Max-Planck-Institut für Meteorologie

REPORT No. 323

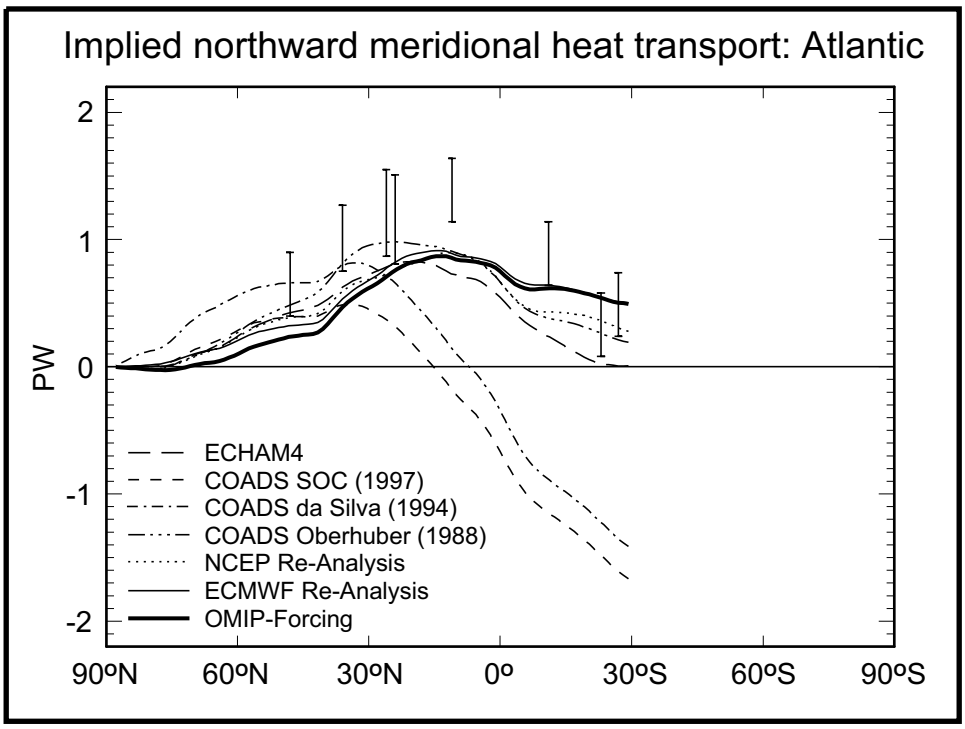

AN ATLAS OF SURFACE FLUXES BASED ON THE ECMWF RE-ANALYSIS- A CLIMATOLOGICAL DATASET TO FORCE GLOBAL OCEAN GENERAL CIRCULATION MODELS

by

Frank Röske

HAMBURG, July 2001

AUTHORS:

Frank Röske

Max-Planck-Institut
für Meteorologie

MAX-PLANCK-INSTITUT
FÜR METEOROLOGIE
BUNDESSTRASSE 55
D - 20146 HAMBURG
GERMANY

Tel.: +49-(0)40-4 11 73-0
Telefax: +49-(0)40-4 11 73-298
E-Mail: <name> @ dkrz.de

An atlas of surface fluxes based on the ECMWF Re-Analysis - a climatological dataset to force global ocean general circulation models

Frank Röske

Max-Planck-Institut für Meteorologie
Bundesstr.55, D-20146 Hamburg
email: roeske@dkrz.de
http://www.mpimet.mpg.de/Depts/Klima/natcli/omip.html

July 2001

ISSN 0937-1060

Abstract

A climatological dataset for forcing global ocean models has been derived from the Re-Analysis (ERA) of the European Centre for Medium-Range Weather Forecasts. This dataset has been constructed for an Ocean Model Intercomparison Project (OMIP), in which the Max-Planck-Institute for Meteorology (MPI), the German Climate Computing Center in Hamburg, and the Alfred Wegener Institute Foundation for Polar and Marine Research in Bremerhaven were involved. The dataset is referred to as "OMIP-Forcing".

In OMIP, the focus was on the intercomparison of the mean global circulation simulated by different ocean models. Therefore, a mean annual cycle has been produced from the 15 years of ERA by using Gaussian filtering with daily fluctuations superimposed.

The precipitation and evaporation over the continents have been transformed into runoff. A scheme has been used which is based on the main drainage basins as well as the catchment areas and annual runoff observations of the 35 largest rivers. The scheme is run independently of the ocean models.

The budgets of the heat and the fresh water fluxes have been closed by modifying the bulk formulae. All three forecast cycles of ERA have been examined with respect to the demands for the closure procedure. The 24 hour cycle has the best properties. Therefore, this cycle has been chosen to be the base of the OMIP-Forcing.

The dataset is compared to six other climatologies: the direct output of ERA, the Re-Analysis of the National Center for Environmental Prediction and the National Center for Atmosperic Research (NCEP/NCAR), the Comprehensive Ocean Atmosphere Data Sets (COADS) in three different versions (Oberhuber, da Silva, and the Southampton Oceanographic Centre), and the output of the atmospheric model ECHAM4 of the MPI.

Contents

1 Introduction

A climatological dataset for forcing global ocean models has been constructed. It has been derived from the data of the re-analysis project of the European Centre for Medium-Range Weather Forecasts (ECMWF). These data are called ECMWF Re-Analysis (ERA; Gibson et al. 1997). A short description of these data is given in section 2.

The motivation to produce such a dataset arose from an ocean model intercomparison project (OMIP). In this project the Max-Planck-Institute for Meteorology (MPI) and the German Climate Computing Center (DKRZ) in Hamburg, and the Alfred Wegener Institute Foundation for Polar and Marine Research (AWI) in Bremerhaven were involved. For this project a dataset was necessary which is global, which provides a temporal resolution resolving weather time scales, and which has a spatial resolution horizontally somewhat better than coarse ocean models have. The ERA seemed to be optimal for this purpose. The dataset is referred to as "OMIP-Forcing".

In OMIP, the focus was on the intercomparison of the mean global oceanic circulation. A forcing was produced consisting of a mean annual cycle with daily fluctuations superimposed. The parameters used will be described in section 3 and the mean annual cycle in section 4.

Since the ocean models considered in OMIP were global, the precipitation und evaporation over the continents had to be considered and transformed into runoff. The runoff model can be and has been run independently of the ocean models so that the resulting output is available. The runoff model will be described in section 5.

In global ocean models the sea ice has to be simulated. Such sea ice modules are e.g. the model of Hibler (1979) with viscous-plastic rheology. The sea ice conditions, such as melting and freezing, are dependent on the heat budget. The budgets of both the heat and the fresh water fluxes have to be closed. The closure procedure has to be independent of the model formulation and will be described in section 6.

An atlas is derived from the OMIP-Forcing. The structure of the atlas is described in section 7. To get an impression of the quality of the OMIP-Forcing dataset it is compared with other climatologies, which will be described in section 8. The intercomparison of the OMIP-Forcing with these climatologies is described in section 9. The major results are summarized in section 10. A list of all figures is given in section 11.

2 Data source

The ERA Project has produced a validated 15 year set of assimilated data for the period 1979 to 1993 (Gibson et al. 1997). The need for a reanalysis arose from developments in

the numerical weather prediction (NWP) procedure over time. Reanalysis with the most up to date NWP then allowed for a consistent dataset. In many areas of the globe the density of available observations is far below that needed to support the analysis with the required accuracy. In such areas the analysis relies mainly on satellite based observations: cloud cleared radiance data or retrieved temperature and humidity data from the NOAA-satellites, and cloud motion wind data from geostationary satellites.

The data assimilation scheme attempts to make use of a numerical forecast model to propagate information concerning the state of the global atmosphere from data dense areas to data sparse areas. Output from the forecast model is used, together with the observations and forcing fields, as input to the analysis. Results from the analysis, after initialization, are then used as initial conditions for the next forecast. These processes are repeated in a cyclic fashion.

Thus, continuous data assimilation over a long period is equivalent to running the forecast model as a global circulation model and restoring towards the observations and forcing fields at six hourly intervals. In addition, two further cycles are included at twelve and twenty-four hourly forecast intervals. These cycles are coupled to the six-hourly cycle, because they are based on the same initializations.

All forecasts are made available through the MARS system. In the corresponding User Guide (MARS, 1995) all parameters are summarized and listed according to their codes. The surface parameters are on a Gaussian grid with T106 truncation, which corresponds to a resolution of $1.125^\circ \times 1.125^\circ$.

3 The parameters

As a first approach, all three forecast cycles have been averaged to daily values: four six-hourly forecasts, two twelve-hourly forecasts and two twenty-four-hourly forecasts per day (one 24 hour forecast begins at 0:00 GMT and one at 12:00 GMT). In the following, the parameters are presented which have been used (Table 1). Some of them had to be combined to generate new ones. The total precipitation has been calculated by summing large-scale precipitation, MARS-code 142, and convective precipitation, MARS-code 143. Runoff has been calculated by the runoff scheme described in section 5 using total precipitation minus evaporation, MARS-code 182.

The scalar wind and its daily standard deviation have been computed from the wind components, MARS-codes 165 and 166. For the first approach, using all three forecast cycles, a total of eight forecasts are available to calculate the daily standard deviation. These parameters together with the mean sea level pressure are needed as input for the bulk formulae described in section 6.

The sea ice modules of the ocean models produce their own albedos as a function of the current ice conditions. Therefore, they have to be forced by the total solar radiation, in which the reflected part of the solar radiation is still included. For this purpose, forecast albedos of ERA have been used. Total solar radiation (R_{tot}) has been computed from net solar radiation (R_{net}), MARS-code 176, and forecast albedo (a), MARS-code 243, according to $R_{tot} = R_{net}/(1-a)$.

The direct outputs of ERA for the long wave radiation, MARS-code 177, and the turbulent heat fluxes, MARS-codes 146 and 147, are used for the heat budget closure considerations and are plotted in the atlas (section 7) over the continents; in addition to those over the oceans which have been computed by using the bulk formulae (see section 6). The long wave radiation is composed of the outgoing grey body radiation and of the incoming atmospheric back radiation. However, these two components are not distinguished explicitly in the following. Only the net outgoing effect is considered and referred to as long wave radiation.

Some of the parameters are accumulated quantities. Therefore, the forecasts of these parameters had to be divided by the corresponding number of seconds, 21600 for six-hourly forecast intervals, 43200 for twelve-hourly forecast intervals and 86400 for twenty-four-hourly forecast intervals prior to the averaging procedure.

New Code	Parameter	MARS-Codes
139	Sea surface temperature	139
142	Total precipitation	142*, 143*
146	Surface sensible heat flux	146*
147	Surface latent heat flux	147*
151	Mean sea level pressure	151
160	Runoff	142*, 143*, 182*
164	Total cloud cover	164
165	Scalar wind	165, 166
166	Standard deviation scalar wind	165, 166
167	2 meter temperature	167
168	2 meter dew point temperature	168
176	Total solar radiation	176*, 243
177	Surface thermal radiation	177*
180	East-west surface stress	180*
181	North-south surface stress	181*
182	Evaporation	182*

Table 1: Parameters. A * denotes: Parameter has been accumulated since start of forecast.

The 2 meter temperatures and 2 meter dew point temperatures in the Arctic Ocean have undergone a correction after Harder et al. (1998). During the period from June 15 to August 15, air temperatures are not allowed to drop below 0°C. Dew point temperatures are adjusted accordingly so that the relative humidity of the air is conserved. This correction has been done for the mean annual cycle (see the following section).

4 Mean annual cycle

For all parameters introduced in the last section a mean annual cycle has been produced. The runoff has been calculated from the mean annual cycles of precipitation and evaporation over the continents (section 5). The daily values are the basis for the mean annual cycle. All daily values of all 15 years were filtered by a Gaussian method. This method divides the data into low-frequency and high-frequency components. The low-pass component has been averaged to one year. From the high-pass component, a particular year (1982, see below) has been selected such that the variability is preserved as well as possible. This selected year has been added to the averaged low-pass component. The sum is called the mean year.

To obtain the low-frequency component of a time series, the filter technique of a "running mean" may be the first choice. The running mean works like a window with rectangular shape, i.e. with constant weights, "running" through the time series. However, the sharp edges of this window produce oscillations of higher frequency which are not desired in this case. In order to obtain only the first element of the corresponding Fourier series, the edges of the window are smoothed exponentially. This technique is called a Gaussian filter (Schönwiese, 1992).

Consider a time series, $a_i, i = 1, \ldots, n$, with n the length of the time series. The filtered time series, $\tilde{a}_j, j = 1, \ldots n - 2m$, m being the filter width, is calculated by multiplication with the weights $w_k, k = -m, \ldots + m$, according to

$$\tilde{a}_j = \sum_{k=-m}^{+m} w_k a_{j+m+k} \quad \text{for } j = 1, \ldots, n - 2m \tag{1}$$

Filter weights are normalized to unity and then averages in the time intervals $(i - m, \ldots, i + m)$ are preserved.

In order to obtain weights implying an exponential characteristic filter function R, the following algorithm is applied. If T_* is the period, for which $R(T < T_*) = 0$ is valid, then $T_* = 6\sigma$, with σ being the standard deviation of the normal distribution, produces the

unnormalized weights

$$w_k = \frac{1}{\sqrt{2\pi}} e^{-\frac{1}{2}\left(k\frac{6}{T_*}\right)^2}, \quad k = 0, \ldots, m \quad \text{and} \quad T_* = 2m + 1 \tag{2}$$

The characteristic filter function for the low-pass yields

$$R_L(f) = e^{-\frac{1}{3}\pi^2 f^2} \tag{3}$$

Normally, it is sufficient to truncate the series w_k, if $w_k < w_0/10$. When the low-pass $\tilde{a}_j(L)$ is determined in this way, the high-pass $\tilde{a}_j(H)$ is calculated by

$$\tilde{a}_j(H) = a_j - \tilde{a}_j(L) \qquad j = 1, 2, \ldots, n - 2m \tag{4}$$

and the characteristic filter function of the high-pass becomes

$$R_H(f) = 1 - R_L(f) \tag{5}$$

This filter has been applied with $m = 15$ so that the averaging interval $(-m, \ldots, +m)$ has a total length of one month. Then, the daily values of the low-pass have been averaged over all 15 years to obtain one mean year.

From the high-pass component a particular year was selected in the following way. Initially, the search for this year was restricted to only one parameter, the zonal wind stress, which is one of the most important parameters to force ocean circulation models. Then, a total of 15 mean years have been calculated by adding each of the 15 years of the high-pass to the mean year.

From these 15 mean years and the 15 original years variances relative to monthly means have been calculated (Table 2), which are approximations to the squared high-pass values. The mean variance of all 15 single years is $1.02 \cdot 10^{-2}(Nm^{-2})^2$. The mean variance of all 15 mean years is $0.77 \cdot 10^{-2}(Nm^{-2})^2$, which is approximately 75% of the value for the single years. In order to preserve the variability of the original data as well as possible, the specific year has to be chosen in such a way that it provides a maximum of variance.

The mean years have a maximum of their variances in the fourth year ($0.80 \cdot 10^{-2}(Nm^{-2})^2$). This corresponds to 1982, a year when a strong El Niño event occured. Therefore, the fourth year has been chosen to be the year of the high-pass component and is added to the averaged low-pass component. This year has also been chosen for the remaining parameters for reasons of dynamical consistency.

The original years of ERA follow the real calendar. Therefore, the months are different in length: there are either 28 or 29 days for February, implying a total of 365 or 366 days. The ocean models compared in OMIP use idealized years, which means 12 months with

No.	Year	Mean Year	Single Year
1	1979	0.78	1.06
2	1980	0.75	0.98
3	1981	0.74	0.99
4	1982	0.80	1.05
5	1983	0.78	1.03
6	1984	0.76	1.02
7	1985	0.77	1.02
8	1986	0.76	1.03
9	1987	0.78	1.04
10	1988	0.77	1.00
11	1989	0.75	1.00
12	1990	0.79	1.05
13	1991	0.76	1.01
14	1992	0.75	0.99
15	1993	0.78	1.03

Table 2: Globally averaged variances of zonal wind stress relative to monthly means for the 15 years of daily averaged ECMWF Re-Analysis data. Unit: $10^{-2}(Nm^{-2})^2$.

30 days, a total of 360 days, which is shorter than the real calendar. Therefore, the mean year was shortened by excluding the last 5 days of December. This procedure is combined with the procedure of producing a periodic cycle, which means adjusting the first and the last days of the shortened mean year.

The resulting mean year is called the mean annual cycle. This cycle has smooth transitions at the beginning and the end of the year. The continuity of time series is preserved, and the variability of the original data is preserved at 78%.

5 Runoff model

The runoff model is based on two datasets provided by Hagemann and Dümenil (1998): the catchment areas of the 35 largest rivers (the Baltic Sea is treated as a river) and the main drainage basins of the world, which correspond to the water sheds. The drainage is a summary of all small rivers which are not resolved by the catchment areas.

These datasets are horizonal distributions of codes $c \in \mathbb{Z}$ $(\mathbb{Z} = \{\ldots, -1, 0, +1, \ldots\})$ defining the regions of the catchment areas $(1 \leq c_{catch} \leq 35)$ and the drainage basins $(-1 \leq c_{drain} \leq 33)$. Code $c_{drain} = -1$ is an exception of the otherwise positive codes and means no runoff. $c_{drain} = 0$ means no land. Some of these basins are defined by the oceans or adjacent seas, to which the fresh water flows, such as the Arctic Ocean ($c_{drain} = 2$),

the Atlantic Ocean ($c_{drain} = 3$), the Mediterranean Sea ($c_{drain} = 4$), the Indian Ocean ($c_{drain} = 5$), and the Pacific Ocean ($c_{drain} = 6$); some of the basins are defined by lakes or seas, such as the Caspian Sea ($c_{drain} = 7$), the Aral Sea, Lake Chad, Lake Balkhash etc.

The codes of the main drainage basins cover the whole area of the continents, whereas the codes of the catchment areas cover only parts of them. Both datasets were combined in such a way that the codes of the drainage basins were used to fill those areas where no catchment areas are defined. The resulting dataset is shown in the figure below.

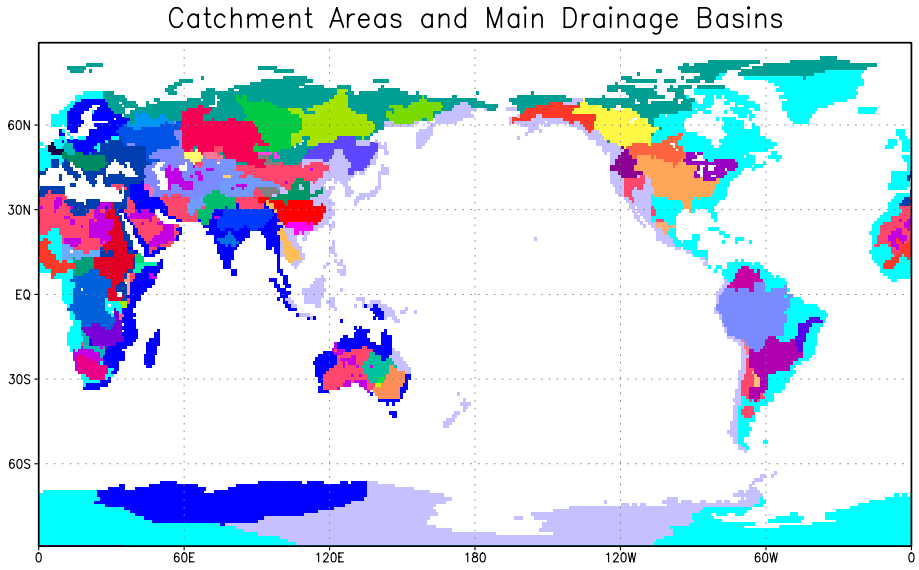

A "quasi coastline" has been derived from this dataset using those grid boxes next to the coasts of the continents where water is defined. This quasi coastline consists of codes of the catchment areas corresponding to the mouth coordinates. The remaining grid boxes of this line are filled with those codes of the drainage basins which correspond to the codes of the nearest land points.

The distance between two points has been measured by the Manhattan distance: given two two-dimensional vectors $\vec{r} = (x, y)^T$ and $\vec{r}' = (x', y')^T$ with $x, x' = 1, \ldots, n$ and $y, y' = 1, \ldots, m$ and n and m being the indices of the T106 grid. The Manhattan distance is defined by:

$$|\vec{r} - \vec{r}'| = |x - x'| + |y - y'| \tag{6}$$

The coordinates of the quasi coastline have been assigned to the land points of the associated catchment areas and the main drainage basins. Assigned were the coordinates

either of the mouths, if the land points were in the catchment areas, or of the nearest quasi coastline points, if the land points were in the drainage-only defined regions. In the latter case, up to seven nearest quasi coastline points with the same Manhattan-distance were possible. This yielded seven horizontal fields of coordinates for each of the two coordinate directions.

These fields were used to gather the differences of the mean annual cycles of precipitation and evaporation at the land points and to put them instantaneously, that means directly for every day, to the quasi coastline, whereby up to seven coordinates per land point were considered. Because the continental runoff is positive or zero by definition, but could become negative during this procedure, negative runoffs were set to zero and positive ones reduced accordingly.

Furthermore, closed basins with no runoff had to be considered, in which the water is circulating only within the basin and does not reach the oceans. Such a basin is, for example, the Caspian basin including the Caspian Sea, with the catchment area of the Volga being the main fresh water provider. To judge the quality of the model, the model estimate for the 35 main rivers is compared with the observations of annual runoff (Dümenil et al. 1993) as shown in Table 3.

It can be seen that there are systematic errors. The runoffs of the Siberian rivers are underestimated and those of the African rivers are overestimated. Assuming that there are no systematic errors in this very simple runoff model this would mean that the precipitation is overestimated over Africa or the evaporation is underestimated. The latter reason dominates as Hagemann points out (pers. comm.). The underestimation of the evaporation can be explained by the observing system. Evaporation during the irrigation of the fields is not recorded.

For a good simulation of the Arctic sea ice by the ocean circulation models, a realistic simulation of the Siberian river runoff and of the glacial runoff is necessary. This is also true for the Antarctic sea ice (Marsland and Wolff, 2001), but has not been considered here. Therefore, the observations of annual runoffs (Dümenil et al. 1993) have been prescribed for every day. The difference between those and the model estimate plus the runoff of the closed basins is put into the Arctic, if the sum is positive, and into the 'Non-Arctic', if it is negative. This procedure has been applied for every day so that the budget is closed on a daily basis.

River	Observations	Model Estimates
Amazon	154943	141505
Congo	40269	85215
Ganges/Brahmaputra	33485	22230
Orinoco	31171	39110
Yangtze	29043	17619
Jenissei	17691	9484
Lena	16640	8449
Parana	16566	35704
Baltic	15323	9915
Mississippi	14779	22032
Ob	12559	10119
Amur	9791	7137
Mekong	9485	17576
Mackenzie	9153	7539
Wolga	8105	6453
St.Lawrence	7657	8684
Xun	6998	7415
Danube	6435	4823
Yukon	6371	5634
Columbia	5446	6906
Sambesi	3342	15589
Dvina	3335	2462
Kolyma	3244	2878
Godavari	3061	1653
Nil	2935	21589
Sao Francisco	2807	15086
Nelson	2405	4157
Rhine	2287	1250
Indus	2262	6724
Huang	1444	2647
Chari	1062	13909
Niger	1055	19766
Elbe	782	978
Murray	258	2319
Oranje	145	1865

Table 3: Annual runoffs of the 35 main rivers. Unit: $m^3 s^{-1}$.

6 Closure procedure

The surface heat budget consists of one incoming component, the short wave solar radiation and three outgoing components, the long wave radiation (the net effect, see section 3), and the two turbulent heat fluxes, namely the latent and the sensible heat fluxes. The fresh water budget consists of two incoming components, the precipitation and the continental runoff, and one outgoing component, the evaporation. Instead of using the evaporation from ERA over the oceans, it is calculated from the latent heat flux as a function of the ice conditions. Because there is no ice concentration (equivalent names: ice compactness or ice coverage) available in ERA, sea surface temperature of ERA has been used instead. Ice conditions are defined when the sea surface temperatures are below the freezing point, which yields ice concentrations of 0% and 100%. In the first case the heat of vaporization and in the latter case the heat of sublimation is used.

In the ocean models the budgets of heat and fresh water must be closed in order to preserve mass and to avoid a long-term drift. The budgets are closed, when the imbalances of the heat and fresh water budgets, i.e. the net heat and fresh water fluxes integrated over all oceans and at least one year, are zero. Because these fluxes are computed from several input parameters, their budgets cannot be closed directly by simply subtracting their mean, but only indirectly by adjusting the formulae for these fluxes. Therefore, a procedure with pre-defined finite precision is necessary. The budgets are considered as closed when the following conditions are fulfilled:

$$\int_{year}\int_{ocean} (Q_{sw} - Q_{lw} - Q_{la} - Q_{se}) d\lambda d\phi dt < \varepsilon_h \tag{7}$$

$$\int_{year}\int_{ocean} (P + R - c \cdot Q_{la}) d\lambda d\phi dt < \varepsilon_f \tag{8}$$

with

Q_{sw}	:	Short wave solar radiation
Q_{lw}	:	Long wave radiation
Q_{la}	:	Latent heat flux
Q_{se}	:	Sensible heat flux
P	:	Precipitation
R	:	Continental runoff
c	:	Heat of vaporization or sublimation, dependent on ice conditions.

and $\varepsilon_h = 0.1$ Wm^{-2} and $\varepsilon_f = 0.1$ mm/month. In subsection 9.2 these conditions will be relaxed by one order of magnitude defining $\varepsilon_h = 1$ Wm^{-2} and $\varepsilon_f = 1$ mm/month. Because the evaporation is calculated from the latent heat flux, its formula is tuned first. It is

distinguished for water (w) and ice (i) conditions. The turbulent heat fluxes are calculated as follows:

$$\begin{aligned} Q_{se} &= \rho_a c_{p,air} c_{se} V (T_a - T_s) \\ Q_{la,w/i} &= \rho_a L_{w/i} c_{la,w/i} V (q_a - q_{w/i}) \end{aligned} \tag{9}$$

where $\rho_a = 1.3$ kg m^{-3} is the air density, $c_{p,air} = 1004$ Ws kg^{-1} K^{-1} is the specific heat of air, V is the scalar wind, T_a is the 2 meter air temperature, T_s is the sea surface temperature, $L_w = 2.5 \cdot 10^6$ Ws kg^{-1} is the latent heat of vaporization and $L_i = 2.834 \cdot 10^6$ Ws kg^{-1} is the latent heat of sublimation. The transfer coefficients $c_{la,w/i}$ and c_{se} correspond to c_L and c_H in Oberhuber (1988), respectively. Oberhuber (1988) used in his study equations following Large and Pond (1982), and these are used also here. In contrast to Oberhuber, the specific humidity of air q_a is not calculated using relative humidity, but using 2 meter dew point temperature T_{dew} instead. Specific humidity is calculated by

$$q = \frac{0.622e}{p - 0.378e}, \tag{10}$$

where e is water vapor pressure and p is air pressure. Instead of using the formula of Magnus for the water vapor pressure (Möller, 1973) as Oberhuber (1988) proposed, the formulae of Buck (1981) are applied, which are dependent on the ice conditions:

$$\left\{ \begin{array}{c} e_w \\ e_i \end{array} \right\} = a \cdot e^{\left[\frac{(b - T/d)T}{T+c}\right]} \tag{11}$$

with the coefficients a,b,c, and d as in Table 4. It is noted that q_a is a function of the water vapor pressure, but q_w and q_i are functions of the saturation water vapor pressure. They are calculated by $q_a = q(e_w(T_{dew}))$, $q_w = 0.9815 \cdot q(e_w(T_s))$, and $q_i = q(e_i(T_s))$.

condition	a	b	c	d
water (e_w)	6.1121	18.729	257.87	227.3
ice (e_i)	6.1078	23.036	279.82	333.7

Table 4: Coefficients for calculating the water vapor pressure (hPa) of pure water as a function of temperature (°C).

Following Oberhuber (1988), the Charnock constant as contained in $c_{la,w/i}$ and c_{se} is modified until (8) is satisfied. Thereafter, to close the heat budget, the formula for the long wave radiation is adapted. The net effect of long wave radiation is taken from Berliand (1952) as proposed by Oberhuber (1988). In the term for the atmospheric downward long wave radiation, the water vapor pressure as defined above is used:

$$Q_{lw} = \varepsilon \sigma T_a^4 (0.39 - 0.05\sqrt{e_w(T_{dew})}(1 - \chi n^2) + 4\varepsilon\sigma T_a^3 (T_s - T_a), \tag{12}$$

where $\varepsilon = 0.97$ is the emissivity of water, $\sigma = 5.5 \cdot 10^{-8}$ $\mathrm{Wm^{-2}K^{-4}}$ is the Stefan-Boltzmann constant and n is the relative cloud cover. In order to account for various properties of different cloud types, Budyko (1974) proposed the cloudiness factor χ in (12) to vary linearly with latitude ϕ. His table has been transformed into a linear equation, which is symmetric about the equator:

$$\chi = 0.5 + 0.4 \frac{|\phi|}{90^\circ} \tag{13}$$

The outgoing components of the heat flux budget are dependent on the sea surface temperature. In principle, these components are calculated from the sea surface temperatures simulated by the ocean models. Here, however, the sea surface temperatures of ERA were used instead.

Initially, both budgets had positive imbalances (35 $\mathrm{Wm^{-2}}$ and 9 mm/month). This means for the heat flux budget that in principle the incoming component, the solar radiation, had to be decreased and the outgoing components had to be increased. Increasing the turbulent heat fluxes would help also to close the fresh water budget. A further increase, however, would imply that also the precipitation has to be increased. However, neither the solar radiation could be decreased nor the precipitation increased, since the data are given.

A chance to change them arose from the heat and fresh water flux budgets of the direct outputs of ERA. Instead of following the first approach of averaging all three forecast cycles, every cycle was considered separately, as proposed by Mikolajewicz (pers. comm.). Oceanic averages of the heat and fresh water fluxes are listed in Table 5.

Parameter	6-hourly fc	12-hourly fc	24-hourly fc
Precipitation	87	91	95
Fresh water flux	-13	-10	-8
Fresh water flux global	-4	-1	1
Solar radiation	165	163	161
Net downward heat flux	8	4	< 1

Table 5: Oceanic averages of heat and fresh water fluxes from mean annual cycles for each forecast cycle (fc) of ERA. First three rows in mm/month. Last two rows in $\mathrm{Wm^{-2}}$.

The precipitation increases and the solar radiation decreases with increasing forecast interval. In addition, the imbalances of the oceanic heat flux and of the fresh water budgets diminish. Therefore, the 24-hourly cycle has been chosen to construct the OMIP-Forcing. However, only two forecasts per day are available for this cycle. Based on these two values, the ratio of the daily standard deviation of the scalar wind (see section 3) to its daily mean

is 18%. The second condition in (8) is satisfied with a Charnock constant 0.0187, which is in the range of values that can be found in the literature: 0.010 - 0.035 (Fairall et al., 1996). The first condition in (7) is fulfilled when the long wave radiation (12) is multiplied by a factor of 1.045.

7 Description of the atlas

The results are presented in the form of an atlas of surface fluxes. The parameters presented in the atlas are listed in Table 6. The parameters have been arranged in the following way. The list begins with the net fluxes and is continued with the individual components. The fresh water flux components are followed by four additional parameters: 1. The mean friction velocity is used as an estimate of the turbulent kinetic energy input into the mixed layer. 2. Buoyancy fluxes are fluxes of potential energy. They reflect changes of density due to heat and fresh water fluxes. For both the turbulent kinetic energy input and the buoyancy flux density must be known. To calculate density, also salinity is required. Data of Levitus (1994) have been used for this purpose. 3. The Newtonian cooling scheme of Oberhuber (1988) is an attempt to simplify the heat flux scheme for use in ocean general circulation models. The coupling coefficients $\partial Q/\partial T$ of that scheme are presented. 4. The transfer coefficients for the latent heat flux conclude the list. They are calculated according to the formulae provided by Oberhuber (1988) which are not given here explicitly.

The order of these parameters is maintained throughout the report. In Table 6 global oceanic averages of the annual mean and of the annually averaged monthly standard deviations are listed.

Table 9 in section 11 summarizes the figures. Figures 1 through 13 show global patterns of key quantities of the OMIP-Forcing: heat, fresh water, and momentum fluxes. The subfigures show monthly means together with monthly standard deviations using the same contour interval, as well as the annual mean together with the annually averaged monthly standard deviations. In Fig. 13, the contour lines correspond to the absolute values of the wind stress and the vectors indicate the directions.

In Fig. 14-21 time-latitude sections of zonally averaged quantities are shown. Daily values are presented to get an impression of the variability. Fig. 22 is a summary of the zonal averages of all components of the heat and fresh water budgets. They are shown for the three basins (Atlantic, Pacific, and Indian Ocean) and the global ocean. The maximum heat gain is at the equator in both the Pacific and the Atlantic Oceans. However, in the Indian Ocean, the heat gain in the northern part is higher than at the equator. The fresh water flux is dominated mainly by the precipitation peak of the Intertropical Convergence Zone (ITCZ) and by the evaporation in the subtropics.

Parameter	Unit	Annual mean	Annually averaged monthly standard deviation
Net downward heat flux	Wm^{-2}	0.01	68.5
Fresh water flux (incl. runoff)	mm/month	0.01	136.0
Short wave solar radiation	Wm^{-2}	160.9	33.5
Long wave radiation	Wm^{-2}	-51.2	16.0
Sensible heat flux	Wm^{-2}	-8.9	12.7
Latent heat flux	Wm^{-2}	-100.9	42.1
Evaporation	mm/month	-104.6	43.6
Precipitation (excl. runoff)	mm/month	-94.9	114.2
Turbulent kinetic energy input	mm s^{-1}	9.8	2.6
Buoyancy	10^{-8} m^2 s^{-3}	0.08	4.3
$\frac{\partial Q}{\partial T}$	$WK^{-1}m^{-2}$	-47.1	11.7
Transfer coeff. for lat. heat flux	10^{-5}	129.4	7.6
Wind stress (τ_x,τ_y)	Nm^{-2}	0.0130, 0.0023	0.060, 0.058

Table 6: Parameters in the atlas of the OMIP-Forcing. Oceanic averages of the annual mean, and of the annually averaged monthly standard deviations.

The runoff is shown in Fig. 23. Zonal and oceanic averages are shown, the latter are represented by bar charts. The representation of river runoff is a matter of resolution. The higher the resolution is, the higher are the peaks of the runoffs. Looking at zonal averages, the strongest peaks are seen in the Atlantic close to the equator (Amazon and Congo) and in the Northern Indian Ocean (Ganges/Brahmaputra). The reason for the high peak at the Northern edge of the Indian Ocean is that only one grid cell is used for the zonal average. This grid cell covers that part of the Persian Gulf which is fed by the Euphrates and Tigris rivers which are modelled by the main drainage basins. The impact of major Siberian rivers can be seen in the zonal averages of net fresh water flux (north of 60°N) in both the Atlantic and global oceans.

The oceanic averages show that the differences between the cases with runoff and without runoff are larger in the Atlantic and the North Indian Ocean than in the Pacific reflecting the orography of the continents. In the North Atlantic and particularly in the Indian Ocean, the runoff changes the sign of the oceanic averages of the fresh water flux. In the Arctic Ocean, the oceanic average of the runoff is larger than that of the precipitation. For the existence of the sea ice cover the presence of a low-salinity surface layer which extends down to about 200 m is of fundamental importance. The presence of this surface layer is determined primarily by continental runoff through mixing from the shelf seas and Bering Strait inflow (Barry et al., 1993).

8 Other climatologies

The OMIP-Forcing is compared with other climatologies (section 9). These datasets must be complete with respect to the heat and fresh water budget components. For practical purposes, it was decided a maximum of one flux could be missing, if the net flux is available. This restriction led to the selection of the following datasets: the Comprehensive Ocean Atmosphere Dataset in three different versions [Oberhuber (1988), da Silva et al. (1994) and SOC (1997)]; the direct outputs of the outgoing heat budget components of ERA (1997) which are considered to study the effect of the bulk formulae in the OMIP-Forcing; the Re-Analysis (NRA) of the National Center for Environmental Prediction (NCEP) and the National Center for Atmosperic Research (NCAR); and the output of the atmospheric general circulation model ECHAM4 of the Max-Planck-Institute für Meteorologie (MPI) (Roeckner et al. 1996, Legutke and Maier-Reimer 1999). Hereafter, these six datasets are referred to as Oberhuber, da Silva, SOC, ERA, NRA, and ECHAM4 respectively.

A monthly long-term mean of the NCEP Re-Analysis supplied by the NOAA-CIRES Climate Diagnostics Center has been used. The ECHAM4 output covers 15 years which have been averaged to obtain a climatology. In Table 7, the time period covered by the datasets and the temporal and spatial resolutions are listed.

Climatology	Time period covered	Temporal resolution	Spatial resolution
ECHAM4 (Roeckner et al. 1996)	15 years	daily	2.8° (T42)
COADS Oberhuber (1988)	1950-1979 (30 years)	monthly	2°
COADS da Silva (1994)	1945-1989 (45 years)	monthly	1°
COADS SOC (1997)	1980-1993 (14 years)	monthly	1°
NCEP Re-Analysis (NRA)	1958-1997 (40 years)	six-hourly	1.9°
ECMWF Re-Analysis (ERA)	1979-1993 (15 years)	six-hourly	1.1° (T106)

Table 7: Intercomparison climatologies.

The datasets differ in their temporal and spatial resolutions and the use of general circulation models. All three COADS have been calculated without the help of any general circulation models, but they have only a monthly resolution. The other datasets (NRA, ERA, and ECHAM4) are based on models, but they have higher temporal resolution than COADS. All the model based datasets and the COADS of da Silva (1994) are global, whereas the COADS of Oberhuber (1988) and SOC (1997) do not cover the whole globe. The ERA and the OMIP-Forcing have comparable spatial resolutions. The same holds for the COADS datasets of da Silva and SOC.

9 Intercomparison

The OMIP-Forcing is compared with the climatologies introduced in section 8. All parameters summarized in Table 6 will be examined except the wind stress. For the intercomparison of the first eight parameters describing the heat and fresh water budgets all six climatologies are used, whereas for the intercomparison of the four additional parameters only Oberhuber's atlas is used (see section 7).

The latitudinal dependence is studied by using implied meridional heat and fresh water transports (Fig. 26) described in section 9.1 and by using zonal averages (Fig. 27-29). The zonal averages are shown for both the annual mean and for each month. All three basins (Atlantic, Pacific, and Indian Ocean) and the global ocean are considered. The global imbalances of the net heat and fresh water budgets are presented in section 9.2. Characteristic values for certain regions are shown as bar charts (Fig. 30-31). The heat budget is described in section 9.3, the fresh water budget in section 9.4, and the additional parameters in section 9.5.

Bar charts are also shown for the flux maxima of the main heat gain and loss regions for the Atlantic and the Pacific Oceans as a function of the calendar month (Fig. 32-33) and described in section 9.3.6. The main heat gain regions are the tropics, and the main heat loss occurs in the western boundary current regions. In these regions, not only the net heat fluxes are considered but also the turbulent heat fluxes. To detect areas with large spreads in the heat fluxes, means and standard deviations of all seven climatologies are calculated (Fig. 34-35) and described in section 9.3.7. The units in these figures are Wm^{-2} for the heat fluxes and mm/month for the fresh water fluxes.

9.1 Meridional transports

To study the latitudinal dependence, the implied northward meridional transports are discussed. They are defined as follows. Let $f(\lambda, \phi)$ be the heat or fresh water flux. Then the meridional heat or fresh water transport $T(\phi)$ is calculated as:

$$T(\phi) = \int_{NorthPole}^{\phi} d\phi' \int_{\lambda_{west}}^{\lambda_{east}} f(\lambda, \phi') d\lambda \tag{14}$$

Here, λ_{west} and λ_{east} are determined by the basin chosen: Atlantic, Pacific, and Indian Ocean, as well as the global ocean.

From the North Pole down to about 40°N, the implied meridional heat transports of the OMIP-Forcing in the global and the Atlantic oceans fall below the lower bound of the

climatologies. From this latitude southward down to 10°N in the Atlantic Ocean and to 15°S in the global ocean, the OMIP-Forcing is within the range of the other climatologies. In the global ocean, the change from positive to negative transports near the equator is made by almost all climatologies including the OMIP-Forcing except the ECHAM4 climatology at the same latitude. South of 30°S, the OMIP-Forcing, as well as the ERA and the ECHAM4 climatologies, show positive implied heat transports, whereas all other climatologies show negative values. In comparison with the ERA climatology, the transports of the OMIP-Forcing are enhanced by using the bulk formulae. This causes a reduction of the absolute values of the transports at about 70°S to < 0.1 PW. Also, the ECHAM4 climatology shows small transports at this latitude (< 0.2 PW).

The meridional transports are compared with heat transport observations at certain latitudes. Such observations have been selected for which also an error estimate is provided (Bryden et al. 1991, Rintoul 1991, Rintoul and Wunsch 1991, Saunders and King 1995, Macdonald and Wunsch 1996, Wijffels et al. 1996, Johns et al. 1997). In the North Atlantic, the transport of almost all climatologies are lower than the observations suggest or reach only the lower error bars (see Fig. 26). Only the climatology of da Silva fits well to the observation at 48°N. In the North Pacific, the agreement of the implied heat transports of the OMIP-Forcing with the observations is improved by using the bulk formulae. In the Indian Ocean, the COADS climatologies fit better to the observations than the model-based datasets.

The transports of the COADS SOC and COADS da Silva climatologies are strongly negative south of 30°N, reflecting high imbalances in the heat budget (see section 9.2 and Table 8). The high heat transports of the climatology of da Silva can be traced to high net heat fluxes in the Arctic Ocean (see section 9.3.1).

The global meridional fresh water transports are shown for two cases: with and without continental runoff. In the case without runoff, the OMIP-Forcing is within the range of the other climatologies. In the case with runoff, the OMIP-Forcing is compared with the output of the ECHAM4 model. In the global ocean, the meridional transports of the OMIP-Forcing south of 70°S are small (< 0.1 Sv). A similar condition holds for the ECHAM4 climatology (< 0.2 Sv). The OMIP-Forcing is in good agreement with the ECHAM4 climatology over the Northern Hemisphere, but there are large differences in the Southern Hemisphere.

9.2 Global imbalances

The global imbalances of the net heat and fresh water flux budgets of all climatologies are summarized in Table 8. Concerning the net downward heat flux, the COADS SOC and COADS da Silva climatologies show the highest imbalances, the imbalances of the COADS

of Oberhuber and NRA are small, and ECHAM4, ERA, and the OMIP-Forcing are closed with respect to the imbalances (see the definition of ε_h and ε_f in (7) and (8) in section 6).

Climatology	Net heat flux	Net fresh water flux without runoff	Net fresh water flux with runoff
ECHAM4	< 1	-7	-1
COADS Oberhuber (1988)	3	4	
COADS da Silva (1994)	28	3	
COADS SOC (1997)	30	-6	
NCEP Re-Analysis (NRA)	3	-8	
ECMWF Re-Analysis (ERA)	< 1	-8	
OMIP-Forcing	< 1	-9	< 1

Table 8: Climatologies and their net budgets. Heat flux is in Wm^{-2}, and fresh water flux is in mm/month ("< 1" means the absolute value is smaller than 1 Wm^{-2} or 1 mm/month, respectively).

9.3 The heat budget

The heat budget is discussed in terms of annual means of zonal averages (Fig. 27-28) and oceanic averages (Fig. 30).

9.3.1 Net heat flux

Concerning the net heat flux in the tropical and subtropical oceans, the OMIP-Forcing is generally in the range of the other climatologies, except for the tropical Atlantic and the southern subtropical Indian Oceans, where it falls below the lower bound. In these regions the OMIP-Forcing is rather similar to the ERA. Northward of 40°N, the OMIP-Forcing tends to be near the upper bound of the other climatologies and exceeds it northward of 60°N.

In the Arctic Ocean, the absolute values of the net heat flux of the OMIP-Forcing are small compared with all three COADS datasets which show rather large values. However, the oceanic averages of the COADS of SOC and Oberhuber are not comparable, because they do not cover the whole Arctic, in contrast to the COADS of da Silva.

In this region a large spread of the climatologies is found, especially in winter, which is a result of large spreads in the turbulent heat fluxes. In the Southern Hemisphere, the behaviour described in the subtropics extends to the midlatitudes. In the high southern latitudes, the OMIP-Forcing tends to be near the upper bound of the other climatologies, exceeding it partially at about 60-70°S.

The characteristics of the OMIP-Forcing in comparison with the other climatologies do not change drastically when the annual cycle is considered. Concerning the net heat flux, the OMIP-Forcing tends to be in the range of the other climatologies in the summer hemisphere, and below its lower bound in the winter hemisphere from the tropics to the midlatitudes.

Differences in the sign of the oceanic averages are found in the global ocean in summer and to a lesser extent in spring. These differences are most obvious in the North Atlantic, the North Pacific, and the South Indian Oceans. Due to the strong annual cycle of the heat budget, one would not expect any differences in the sign in summer or winter looking at the hemispheric averages. However, there are such differences in the northern Indian Ocean, especially in winter.

9.3.2 Short wave solar radiation

Concerning the short wave solar radiation in the tropical and subtropical oceans, the OMIP-Forcing is within the range of the other climatologies. However, the local minimum north of the equator reflecting the ITCZ is more pronounced compared to the other climatologies.

Northward of 40°N in the Pacific Ocean, the OMIP-Forcing tends to be near the upper bound of the other climatologies defined by NRA and exceeds it partly. In the Arctic Ocean, the OMIP-Forcing tends to be near the lower limit and falls below it near the pole. By construction, the zonal averages of the short wave solar radiation and the precipitation of the ERA are identical to those of the OMIP-Forcing. Therefore, they cannot be distinguished in Fig. 27.

9.3.3 Long wave radiation

Concerning the absolute values of the long wave radiation (the net effect, see section 6), the OMIP-Forcing is in the range of the other climatologies, except for the tropical Pacific and the Arctic Oceans, where it falls below the lower limit. In the southern higher latitudes, the bulk formulae reduce the long wave radiation compared to ERA.

9.3.4 Turbulent heat fluxes

Concerning the absolute values of the sensible heat flux, the OMIP-Forcing is within the range of the other climatologies, except in the tropics and in the Arctic Ocean, where it falls below the lower limit. Regarding the absolute values of the latent heat flux, the OMIP-Forcing exceeds clearly the other climatologies in the tropical and subtropical oceans, where this flux is the dominant balancing component against the solar radiation. The local minimum of the latent heat flux slightly southward of the equator agrees rather

well in all seven climatologies. In the subtropics, large spreads of the climatologies can be found in the latent heat flux. The COADS datasets show smaller estimates than the model based datasets. The bulk formulae increase this flux in these regions. The OMIP-Forcing also exceeds the other climatologies in the northern part of the northern Indian Ocean, especially in summer.

At high latitudes, the sensible heat fluxes of the various climatologies differ considerably from one another, even in sign. The OMIP sensible heat flux is relatively close to zero near the north pole. The latent heat fluxes differ considerably only at higher latitudes in the northern hemisphere. The OMIP latent heat flux is relatively close to zero, this time at both poles. Observations in the Arctic Ocean suggest that the mean turbulent heat fluxes are $< \pm$ 5 Wm^{-2} over multiyear ice. Away from coastal regions, about 60% of the ice cover is represented by second year and multiyear ice. On an annual basis the sensible and latent fluxes together account for 20%-50% of the net radiation total, (Barry et al., 1993). Thus, the OMIP-Forcing seems to be in good agreement with the observations.

9.3.5 Northern Indian Ocean

In the northern Indian Ocean, the climatologies show a large spread with regard to the net heat flux. The OMIP heat flux increases with latitude, while the other six climatologies are fairly constant meridionally. Regarding the latent heat flux, all model based climatologies show a meridional gradient. The long wave radiation, however, possesses a gradient which is opposite to that of the latent heat flux in the NRA and ERA climatologies. In addition, the sensible heat flux of the NRA also has such an opposite gradient. In general, those opposite gradients can balance the gradient in the latent heat flux. The OMIP-Forcing, on the other hand, shows an opposite gradient in long wave radiation that is very reduced in comparison with ERA and NRA. It seems as if the bulk formulae reduce this gradient. In addition, no such opposite gradient can be seen in the sensible heat flux of the OMIP-Forcing. Thus, with respect to this climatology, the meridional gradient in the latent heat flux remains unbalanced and is apparent in the net heat flux.

9.3.6 Flux maxima

In the following, the flux maxima in the western boundary current regions of the Atlantic and the Pacific Oceans are discussed (Fig. 32-33, upper 3 panels).

With regard to the net heat flux, the OMIP-Forcing provides the highest absolute values in the Atlantic Ocean for the annual mean and for almost all months, except for May to July, when it is within the range of the other climatologies. In the Pacific Ocean, the OMIP-Forcing provides the highest absolute value together with the ECHAM4 climatology for the

annual mean. The OMIP-Forcing is within the range of the other climatologies for almost all months, except for January to March and August, when it provides the highest values. Changes in the sign of the net heat flux occur during May to August in the Atlantic, and during May, July, and August in the Pacific Ocean. The absolute maximum is at about 540 Wm^{-2} in January in the Kuroshio region.

Regarding the sensible heat flux, the OMIP-Forcing is in the range of the climatologies in the Atlantic and the Pacific Oceans for the annual mean and for all months. However, with respect to the latent heat flux, the OMIP-Forcing provides the highest absolute values for the annual mean, for every month in the Atlantic, and for almost every month in the Pacific Ocean. The absolute maximum is at about 380 Wm^{-2} in January in the Kuroshio region.

In the following, the flux maxima in the tropical oceans are discussed (Fig. 32-33, lowest panels). In the Pacific, the OMIP-Forcing provides the largest annual mean and the largest monthly means of the net heat flux. In the Atlantic, the annual mean, as well as almost all of the monthly means are in the range of the other climatologies. The annual cycle is characterized by peaks in spring and fall. There are large spreads between the climatologies in the tropical Atlantic during the spring months.

9.3.7 Regions with large spreads

To detect regions with large spreads, standard deviations of all seven climatologies have been calculated (Fig. 34-35). In the net downward heat flux, there are regions with standard deviations exceeding 30 Wm^{-2}. The heat flux components are examined to find those which are responsible for these regions. The variation in the central tropical Pacific can be attributed to the short wave solar radiation and the latent heat flux. The regions in the western tropical Indian Ocean and the western tropical Atlantic can be attributed to the latent heat flux (and near the coasts to the short wave solar radiation as well). The variation in the subtropical North Pacific, North Atlantic, and Indian Oceans can be attributed essentially to the latent heat flux. In the Fram Strait region, the main source for the high standard deviations in the net heat flux appears to be the sensible heat flux.

9.4 The fresh water budget

The fresh water budget is discussed with respect to the annual means of zonal averages (Fig. 27-28) and oceanic averages (Fig. 30-31). This budget is less complicated than the heat budget, because it consists only of two components, if the continental runoff is disregarded.

In the tropics, the fresh water flux is strongly determined by the precipitation. In these

regions, the ITCZ produces a strong maximum. The OMIP-Forcing clearly exceeds the upper bound of the other climatologies, except in the Indian Ocean. However, looking at the oceanic averages, the precipitation of the OMIP-Forcing is in the range of the other climatologies, except in the Northern Hemisphere in fall, when the OMIP-Forcing exceeds the upper limit. The position of the ITCZ peak in both the fresh water flux and the precipitation agrees rather well in all seven climatologies. However, a large spread of the climatologies can be seen. In the southern Indian Ocean, the transition from the tropical peak to the subtropical minimum of precipitation agrees remarkably in all climatologies.

In the subtropics, the fresh water flux is dominated by evaporation. Apart from a constant factor, the evaporation is the same as the latent heat flux for the COADS SOC, the NRA, and the OMIP-Forcing. For the COADS Oberhuber, the evaporation has been calculated from the precipitation and the net fresh water flux. The evaporation is different from the latent heat flux for the COADS da Silva and ERA. The absolute values of the fresh water fluxes of the OMIP-Forcing in the subtropics exceed the upper bound of the other climatologies in the Southern Hemisphere and in the Northern Atlantic. At high latitudes, the OMIP-Forcing fresh water flux is consistent with the other climatologies. In these regions, the absolute values of the evaporation fall below the lower bound of the other climatologies, and the precipitation tends to be near the lower bound.

Large spreads of the oceanic averages of the fresh water flux are found in almost all basins for the annual mean, except for the North Atlantic, where the estimates are comparatively similar. In the Arctic Ocean, the spread of the climatologies is especially large in the fresh water flux, as well as in the precipitation and the evaporation. Differences in the sign of the oceanic average of the fresh water flux are found for the annual mean in the South Pacific and the entire Indian Ocean.

The standard deviations in the fresh water flux are mainly determined by the differences in the precipitation (see Fig. 34-35).

9.5 Additional parameters

The four additional parameters (the turbulent kinetic energy input, the buyoancy flux, the coupling coefficients $\partial Q/\partial T$, and the transfer coefficients for the latent heat flux) are discussed with respect to zonal averages (Fig. 29) and oceanic averages (Fig. 31) (see section 7). Comparing the OMIP-Forcing with the COADS of Oberhuber, a similar behaviour in all four parameters can be found. Northward of about 20-30°N, all four OMIP parameters except the coupling coefficients have smaller magnitudes than those of COADS, and southward of these latitudes, the OMIP magnitudes are larger. In the case of the coupling coefficients, the same is true but the inflection point is at about 50°N.

With respect to oceanic averages, all four additional parameters of the OMIP-Forcing are equal to or larger than those of the COADS in almost all basins. This does not hold for the turbulent kinetic energy input in the Northern Hemisphere. Northward of the latitudes given above, this parameter of the COADS is high enough that the averages over the Northern Atlantic and the Northern Pacific exceed the averages of the OMIP-Forcing. With respect to the turbulent kinetic energy input, the differences between both datasets are larger in the winter hemisphere. The minimum of the buoyancy flux at the equator is more pronounced and narrower in the OMIP-Forcing. The largest differences are in the southern winter and in the tropical Indian Ocean. The dependence of the coupling coefficients on the annual cycle is relatively weak.

10 Conclusions

A climatological dataset for forcing global ocean/sea ice models has been derived from the ECMWF Re-Analysis (ERA). This dataset has been derived for an Ocean Model Intercomparison Project (OMIP), in which MPI/DKRZ in Hamburg and AWI in Bremerhaven were involved. The dataset is referred to as "OMIP-Forcing".

In OMIP, the focus was on the intercomparison of the mean global oceanic circulation. Therefore, a mean annual cycle was produced from the 15 years of ERA with daily fluctuations superimposed. Runoff has been calculated from precipitation and evaporation over the continents, and the budgets of the heat and the fresh water fluxes have been closed by modifying the bulk formulae.

The dataset has been compared with six other climatologies: the direct outputs of the ERA, the Re-Analysis of NCEP/NCAR (NRA), the COADS data of Oberhuber (1988), of da Silva (1994), and of the Southampton Oceanographic Centre (SOC; 1997), and the output of the atmospheric general circulation model ECHAM4 of the MPI. In the following, the key results of the intercomparison are summarized.

In general, the OMIP-Forcing provides surface fluxes which are in the range spanned by the comparison climatologies. Most of them display small imbalances in the net heat budget, except for the COADS of da Silva and SOC. In the North Atlantic, the implied meridional heat transports of the OMIP-Forcing and of all other climatologies are essentially smaller than the observed heat transports. In the Gulfstream region, the OMIP-Forcing shows the highest heat loss to the atmosphere compared with the other climatologies. In the North Pacific, the agreement of the implied meridional heat transports of the OMIP-Forcing with the heat transport observations is improved by using the bulk formulae. These also reduce the absolute values of the implied transports in the southern high latitudes. The high heat transports of the climatology of da Silva are based on high net heat fluxes

in the Arctic Ocean. In this region, large differences between the climatologies are found. Such a discrepancy suggests that the Arctic Ocean is identified as a region of particular importance for future observational programs, especially in winter.

In the Indian Ocean, the implied heat transports of the COADS agree better with the observed heat transports than those of the model based datasets. In the North Indian Ocean, there are large spreads in the climatologies, especially with respect to long wave radiation. The model based datasets provide much larger long wave radiation than the COADS. However, it is reduced by using the bulk formulae.

The OMIP-Forcing shows a hydrological cycle which is relatively strong in the tropics and subtropics, where it is even enhanced by using the bulk formulae, and relatively weak in the higher latitudes with respect to the other climatologies. Regarding the latent heat flux, large spreads between the climatologies are found in the subtropics, where the model based datasets provide larger absolute values than the COADS. Large spreads are also found in the precipitation in the ITCZ regions.

The description of the OMIP-Forcing, of the atlas, and of the intercomparison with the other climatologies, as well as the forcing data, and the atlas data and figures are available at the following web-address:

http://www.mpimet.mpg.de/Depts/Klima/natcli/omip.html

11 List of Figures

Figure number	Figure title
1.1-1.13	Net downward heat flux
2.1-2.13	Fresh water flux
3.1-3.13	Short wave solar radiation
4.1-4.13	Long wave radiation
5.1-5.13	Sensible heat flux
6.1-6.13	Latent heat flux
7.1-7.13	Evaporation
8.1-8.13	Precipitation
9.1-9.13	Turbulent kinetic energy input
10.1-10.13	Buoyancy flux
11.1-11.13	The coupling coefficients $\frac{\partial Q}{\partial T}$ with Q: see Fig. 1 and T: sea surface temperature
12.1-12.13	Transfer coefficient for latent heat flux
13.1-13.13	Wind stress
14	Time-latitude section of zonally averaged daily net downward heat flux
15	Time-latitude section of zonally averaged daily fresh water flux
16	Time-latitude section of zonally averaged daily short wave solar radiation
17	Time-latitude section of zonally averaged daily long wave radiation
18	Time-latitude section of zonally averaged daily sensible heat flux
19	Time-latitude section of zonally averaged daily latent heat flux
20	Time-latitude section of zonally averaged daily evaporation
21	Time-latitude section of zonally averaged daily precipitation
22	Zonal averages: the flux components
23	Zonal and oceanic averages: the runoff
24	Net downward heat flux: other climatologies
25	Net downward fresh water flux: other climatologies
26	Implied northward meridional transports
27.1-27.13	Zonal averages - part I
28.1-28.13	Zonal averages - part II
29.1-29.13	Zonal averages - part III
30.1-30.5	Oceanic averages - part I
31.1-31.5	Oceanic averages - part II
32	Flux maxima in the Atlantic
33	Flux maxima in the Pacific
34	Mean and standard deviation of all 7 climatologies - part I
35	Mean and standard deviation of all 7 climatologies - part II

Table 9: Subfigure numerals indicate:
Fig. 1-13 and 27-29: 1-13: January, February, ..., December, and Annual Mean.
Fig. 30-31: 1-5: DJF, MAM, JJA, SON, and Annual Mean.

Acknowledgement

I would like to thank the staff of the Max-Planck-Institute for Meteorology and the German Climate Computing Center for their help and assistance, and the staff of the Alfred Wegener Institute Foundation for Polar and Marine Research for the fruitful cooperation. NCEP Re-Analysis data were provided by the NOAA-CIRES Climate Diagnostics Center, Boulder, Colorado, USA, from their Web site at http://www.cdc.noaa.gov/. This work was supported by the German Government under grant no. 01 LA 9859/6. I would also like to thank Scot Johnson, Mojib Latif, Ernst Maier-Reimer, and Simon Marsland for specific comments that improved the readability of this report. Soli Deo Gloria.

References

Barry, R.G., M.C. Serreze, J.A. Maslanik, R.H. Preller, 1993: The Arctic Sea Ice-Climate System: Observations And Modelling. Reviews of Geophysics, 31, 4, p.397-422.
Bryden,H.L., D.H.Roemmich, and J.A.Church, 1991: Ocean heat transport across 24°N in the Pacific. DSR, 38, No.3, 297-324.

Buck, A.L., 1981: New Equations for Computing Vapor Pressure and Enhancement Factor. J.Appl.Met., Vol.20, p.1527-1532.

Budyko, M.I., 1974: Climate and life. English edition ed. by D.H.Miller. Academic Press, Internat. Geophysics Series, New York.

Dümenil, L., K. Isele, H.-J. Liebscher, U. Schröder, M. Schumacher, K. Wilke, 1993: Discharge data from 50 selected rivers for GCM Validation. Global Runoff Data Centre, Koblenz und Max-Planck-Institut für Meteorologie, Rep. No. 100, Hamburg.

Gibson, J.K., P.Kallberg, S.Uppala, A.Hernandez, A.Nomura, E.Serrano, 1997: ECMWF Re-Analysis, Project Report Series, 1.ERA Description. European Centre for Medium-Range Weather Forecasts, Reading, England.

Fairall, C.W., E.F.Bradley, D.P.Rogers, J.B.Edson und G.S.Young, 1996: Bulk parameterization of air-sea fluxes for Tropical Ocean-Global Atmosphere Coupled-Ocean Atmosphere Response Experiment. J.Geophys.Res., Vol.101, No. C2, p.3747-3764.

Hagemann, S. and L. Dümenil, 1998: A parametrization of the lateral waterflow for the global scale. Clim. Dyn. 14 (1), p. 17-31.

Harder, M., P.Lemke, M.Hilmer, 1998: Simulation of sea ice transport through Fram Strait: Natural variability and sensitivity to forcing. J.Geophys.Res., Vol.103, No. C3, p.5595-5606.

Hibler, W.D.III, 1979: A Dynamic Thermodynamic Sea Ice Model, J.Phys.Oceanogr.,9,815-846.

Johns,W.E., T.N.Lee, R.J.Zantopp, and E.Fillenbaum, 1997: Updated Transatlantic Heat Flux at 26.5°N. WOCE Newsletter No.27, p.15-22.

Josey, S.A., E.C.Kent and P.K.Taylor, 1999: New insights into the ocean heat budget closure problem from analysis of the SOC air-sae flux climatology. Journal of Climate, 12(9), p.2856-2880.

Large, W.G., and Pond, S., 1982: Sensible and Latent Heat Flux Measurements over the Ocean. J.Phys.Oceanogr.,12,464-482.

Legutke, S. and E. Maier-Reimer, 1999: Climatology ot the HOPE-G Global Ocean General Circulation Model. Techn. Rep. No.21, Deutsches Klimarechenzentrum, Hamburg.

Levitus, S., R. Burgett and T. Boyer, 1994: World Ocean Atlas: Volume 3, Salinity. NOAA Atlas NESDIS 3.

Macdonald, A.M. and C.Wunsch, 1996: Oceanic Estimates of Global Ocean Heat Transport. WOCE Newsletter No.24, p.5-6.

MARS, 1995: Meteorological Archival and Retrieval System User Guide, Computer Bulletin B6.7/2 for Data Retrieval, ECMWF Meteorological Bulletin M1.9/2.

Marsland, S.J. and J.O.Wolff, 2001: On the sensitivity of Southern Ocean sea ice to the surface freshwater flux: A model study. Journal of Geophysical Research-Oceans 106 (C2), 2723-2741.

Möller, F., 1973: Einführung in die Meteorologie, Band 1. Bibliographisches Institut Mannheim, B.I.-Wissenschaftsverlag.

Oberhuber, J.M., 1988: An Atlas Based on the 'COADS' Data Set: The Budgets of Heat, Buoyancy and Turbulent Kinetic Energy at the Surface of the Global Ocean. Report No.15, Max-Planck-Institut für Meteorologie, Hamburg.

Rintoul,S.R., 1991: South Atlantic Interbasin Exchange. J. Geophys. Res., 96(C2), 2675-2692.

Rintoul,S.R. and C.Wunsch, 1991: Mass, heat, oxygen and nutrient fluxes and budgets in the North Atlantic Ocean. DSR, 38, Suppl.1, S355-S377.

Roeckner, E., K.Arpe, L.Bengtsson, M.Christoph, M.Claussen, L.Dümenil, M.Esch, M.Giorgetta, U.Schlese, U.Schulzweida, 1996: The Atmospheric General Circulation Model ECHAM-4: Model Description and Simulation of Present-Day Climate. Max-Planck-Institut für Meteorologie, Rep. No. 218, Hamburg.

Saunders, P.M. and B.A.King, 1995: Oceanic fluxes on the WOCE A11 section. JPO, 25(9), 1942-1958.

Schönwiese, C.-D., 1992: Praktische Statistik für Meteorologen und Geowissenschaftler. Gebrüder Bornträger, Berlin.

da Silva, A.M., C.C.Young und S.Levitus, 1994: Atlas of surface marine data, Vol.1-5, NOAA Atlas NESDIS 6-10.

da Silva, A.M., C.Young-Molling und S.Levitus, 1995: Revised Surface Marine Fluxes over the Global Oceans: The UWM/COADS Data Set. WCRP Workshop on Air-sea Fluxes, ECMWF, Reading, England.

SOC, 1997: Surface Flux Climatology (Version 1.1) of the Southampton Oceanography Centre. Int. WOCE Newsletter, No.29, p.10.

Wijffels,S.E., J.M.Toole, H.L.Bryden, R.A.Fine, W.J.Jenkins, and J.L.Bullister, 1996: The water masses and circulation at 10°N in the Pacific. DSR, 43, No.4, 501-544.

Fig.1.1 Net downward heat flux January

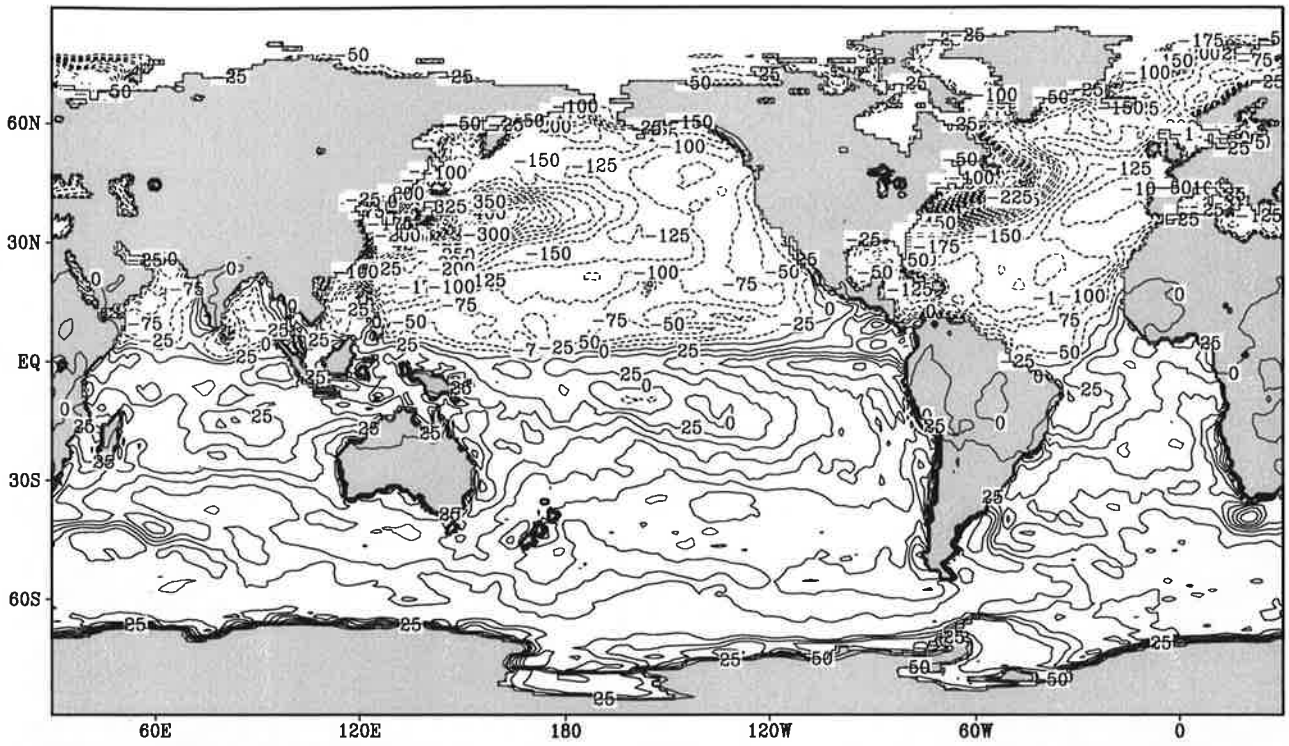

Contour interval: 25 Wm^{-2}

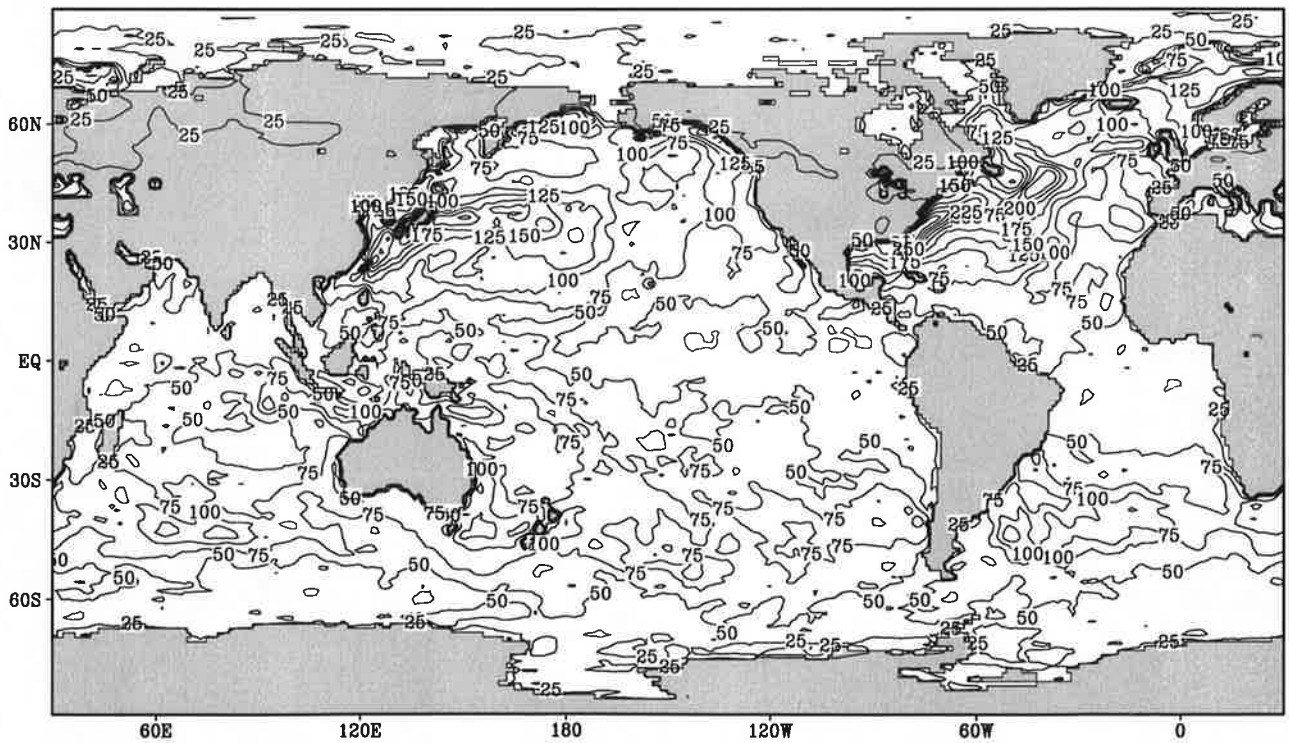

Contour interval: 25 Wm^{-2}

Fig.1.2 Net downward heat flux February

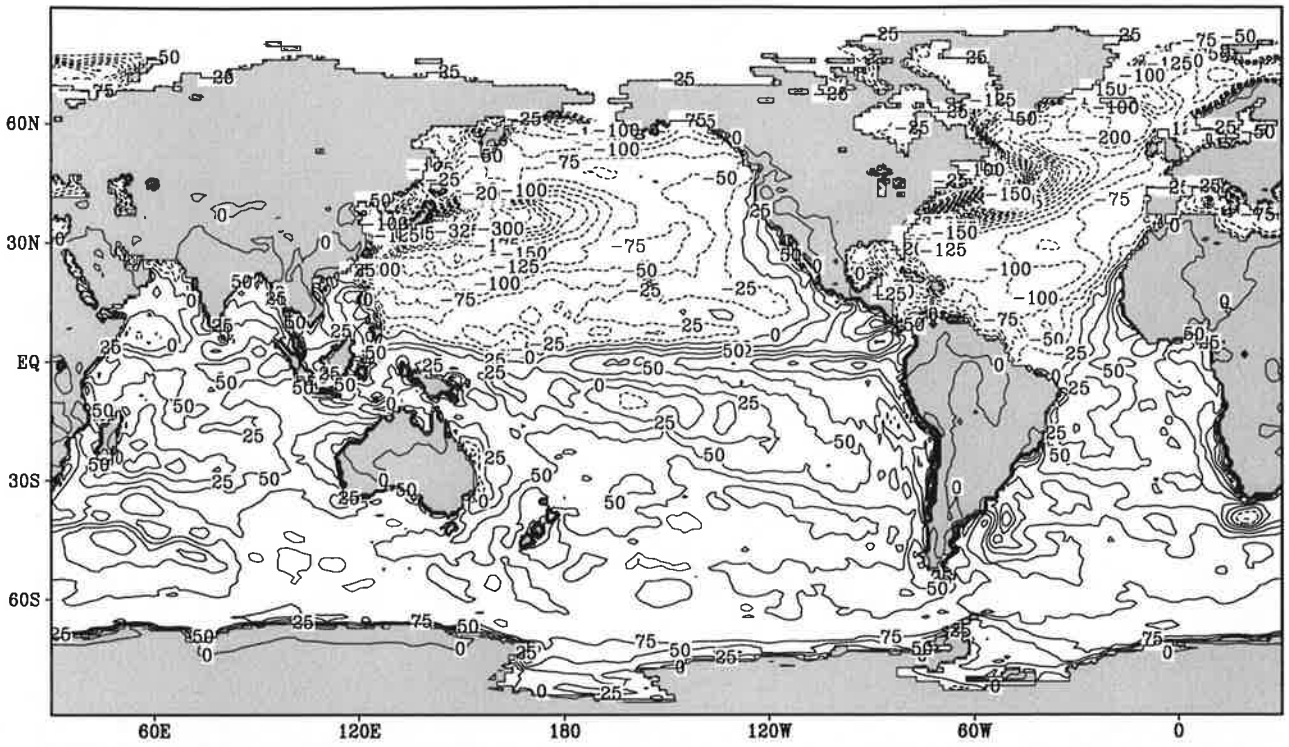

Contour interval: 25 Wm^{-2}

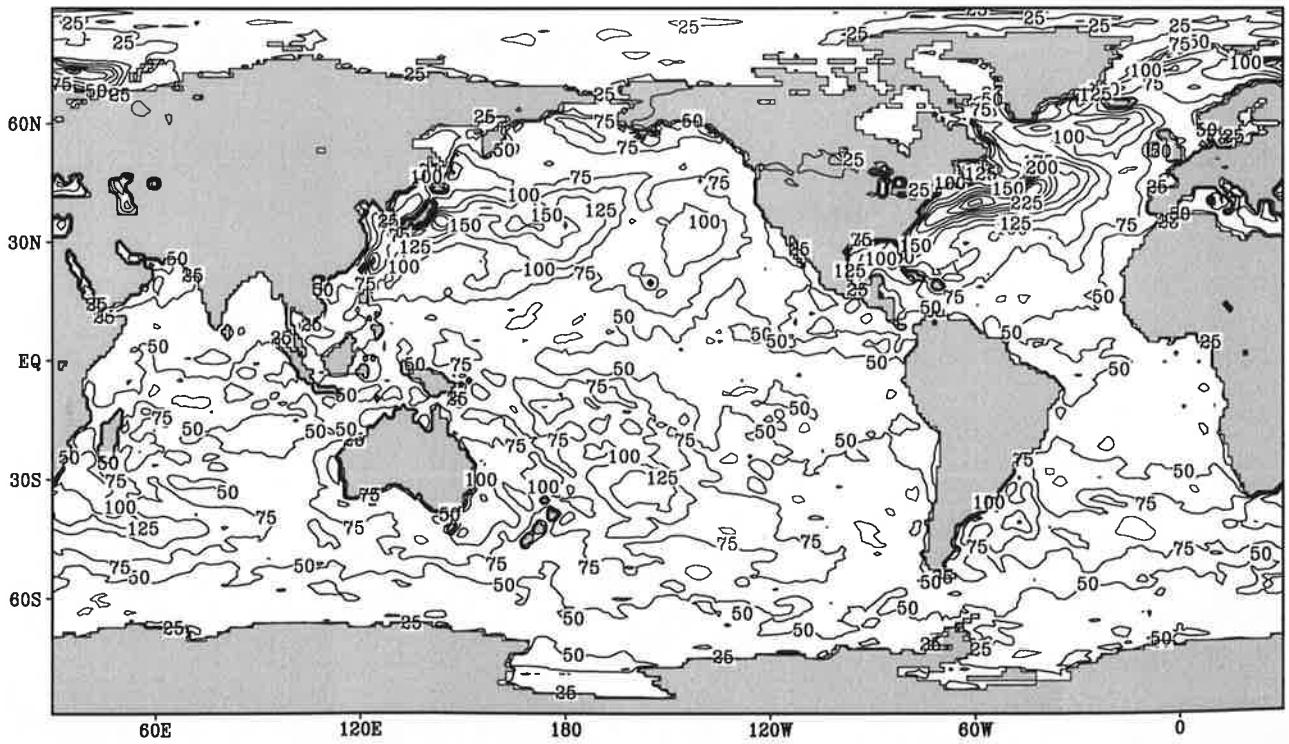

Contour interval: 25 Wm^{-2}

Fig.1.3 Net downward heat flux March

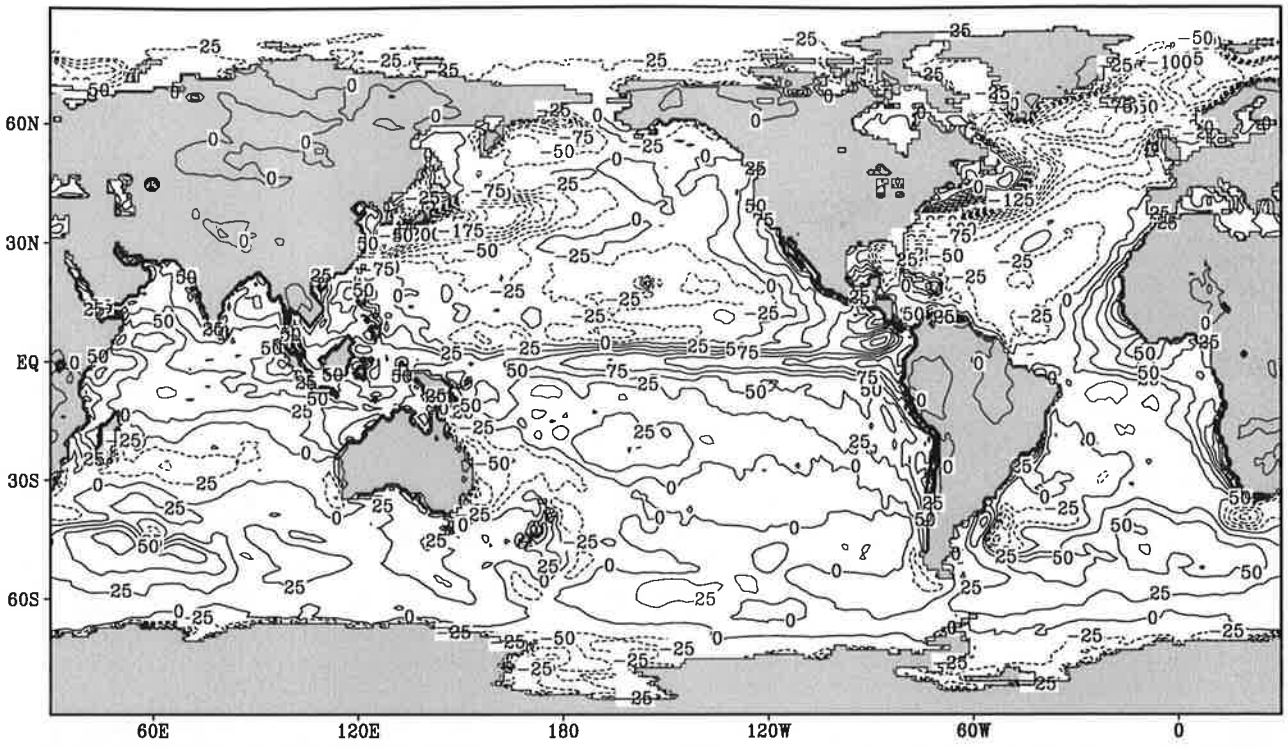

Contour interval: 25 Wm^{-2}

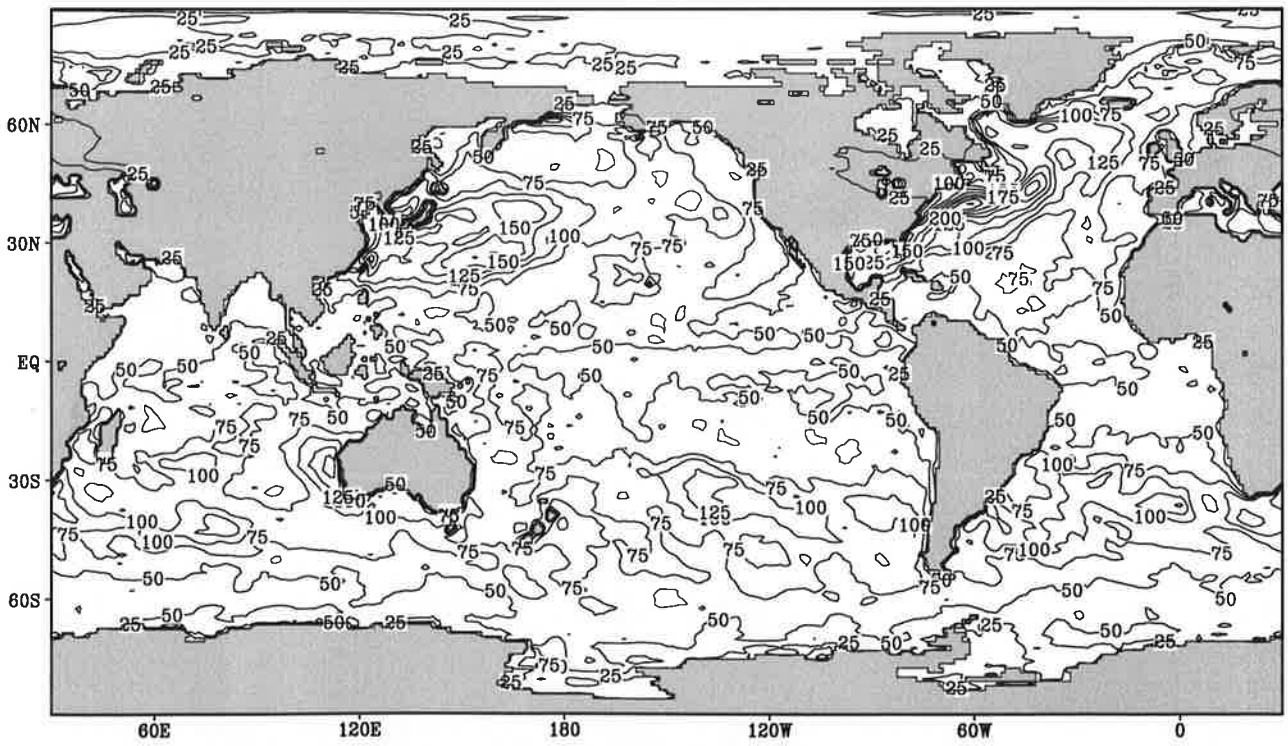

Contour interval: 25 Wm^{-2}

Fig.1.4 Net downward heat flux April

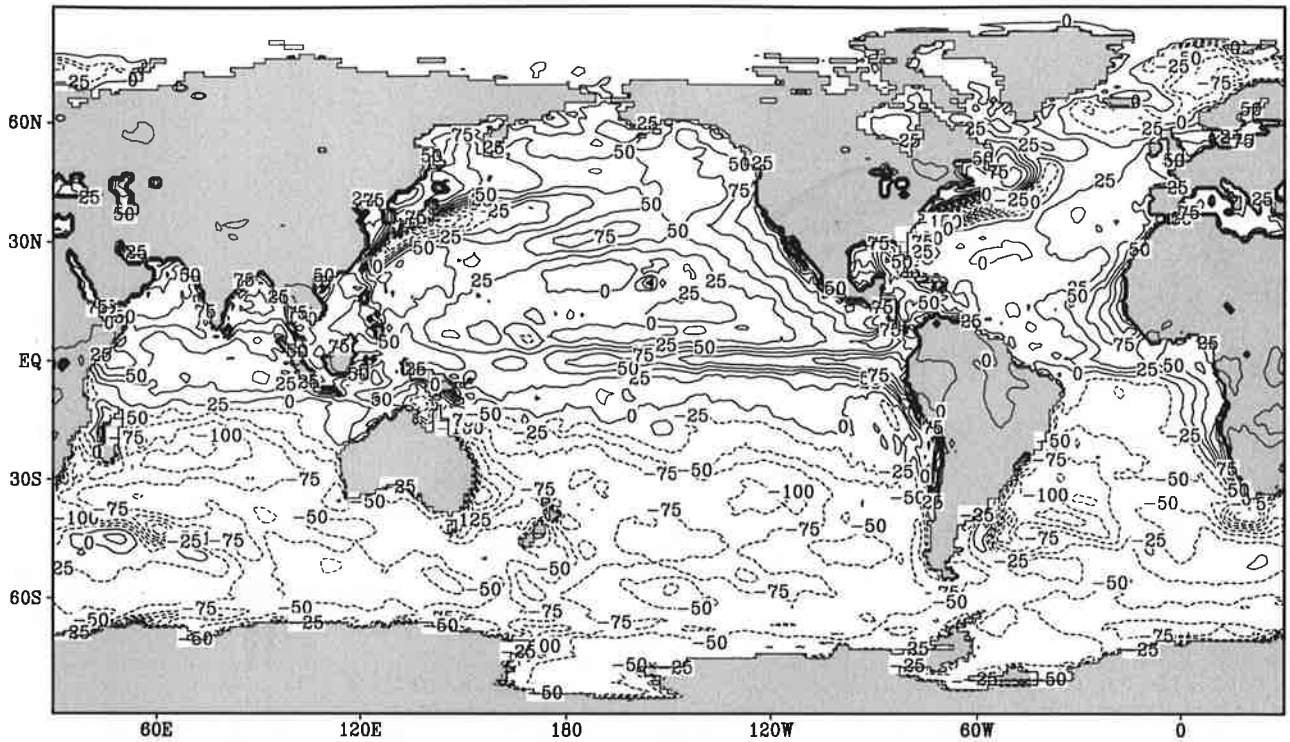

Contour interval: 25 Wm^{-2}

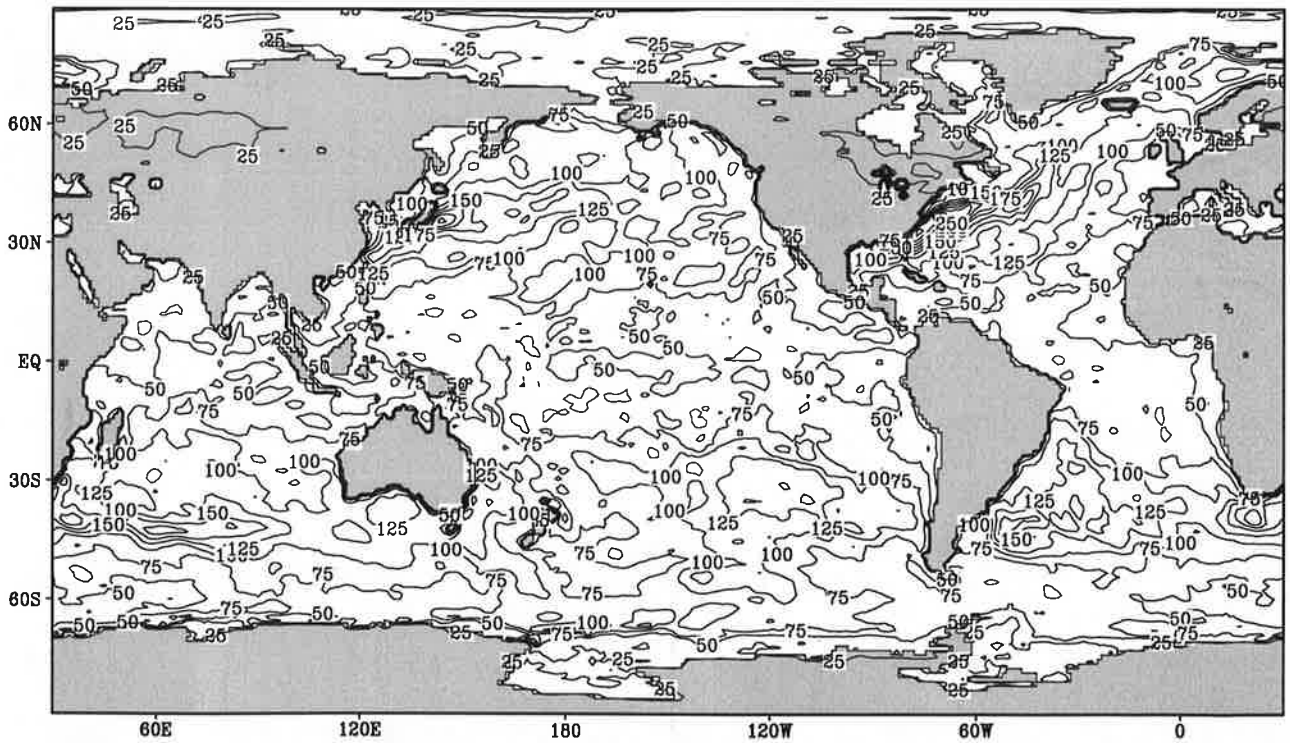

Contour interval: 25 Wm^{-2}

Fig.1.5 Net downward heat flux May

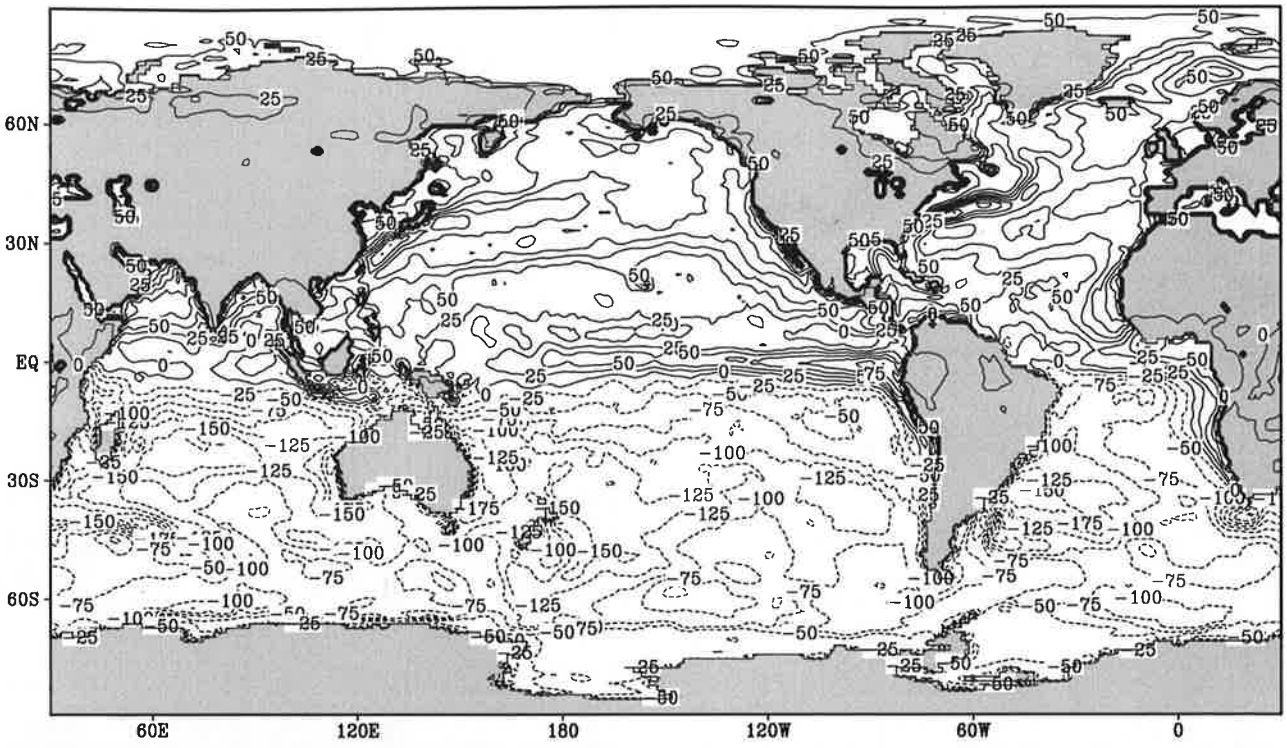

Contour interval: 25 Wm^{-2}

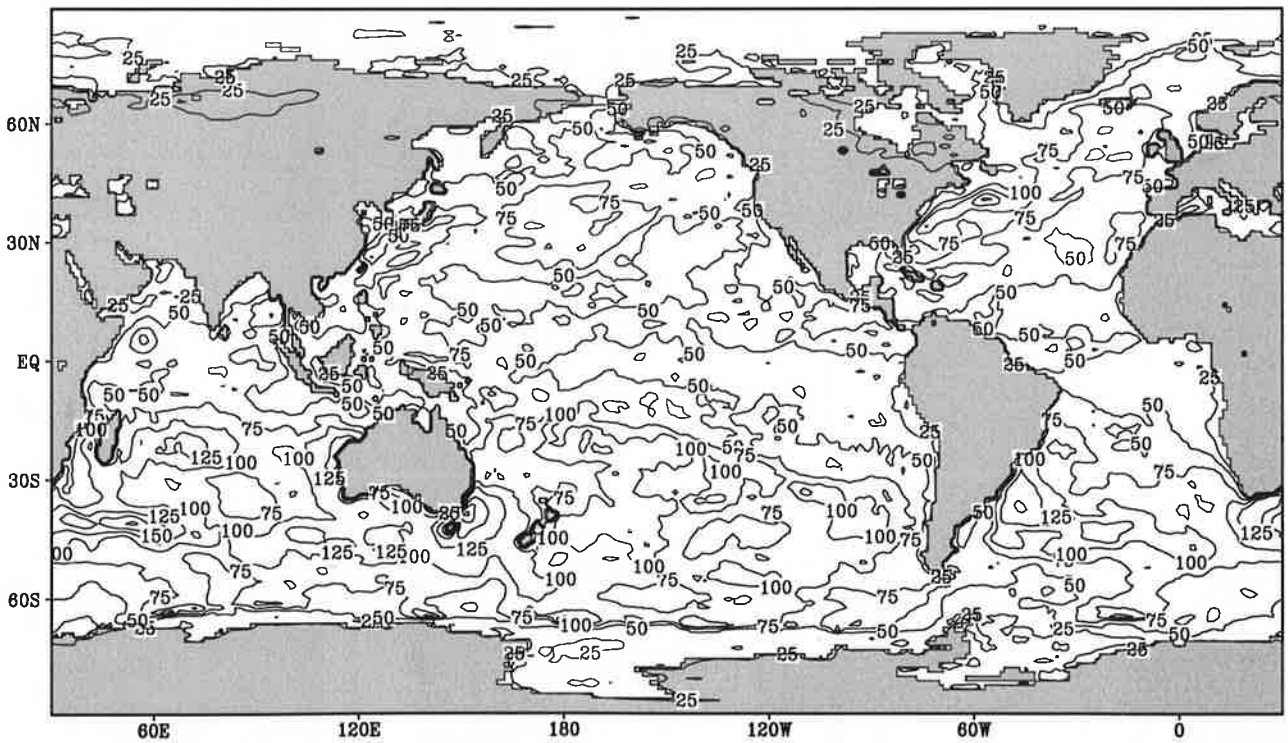

Contour interval: 25 Wm^{-2}

Fig.1.6 Net downward heat flux June

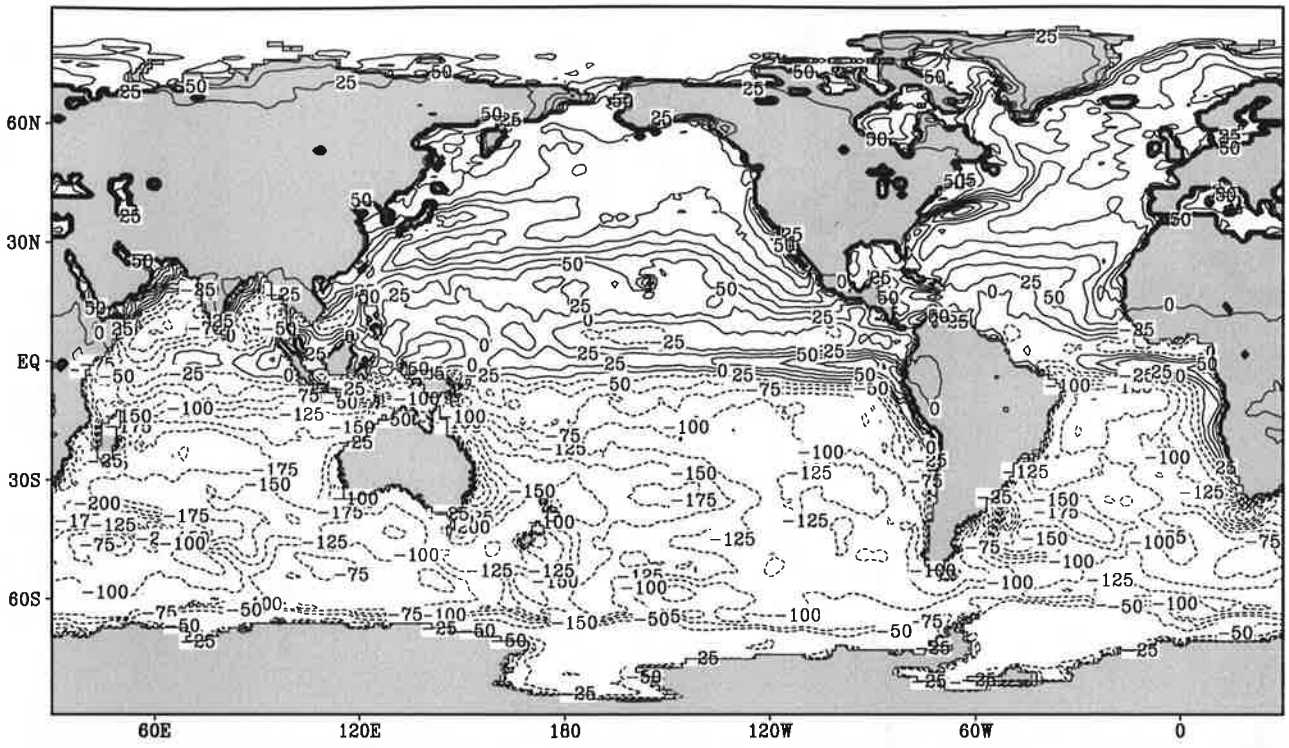

Contour interval: 25 Wm^{-2}

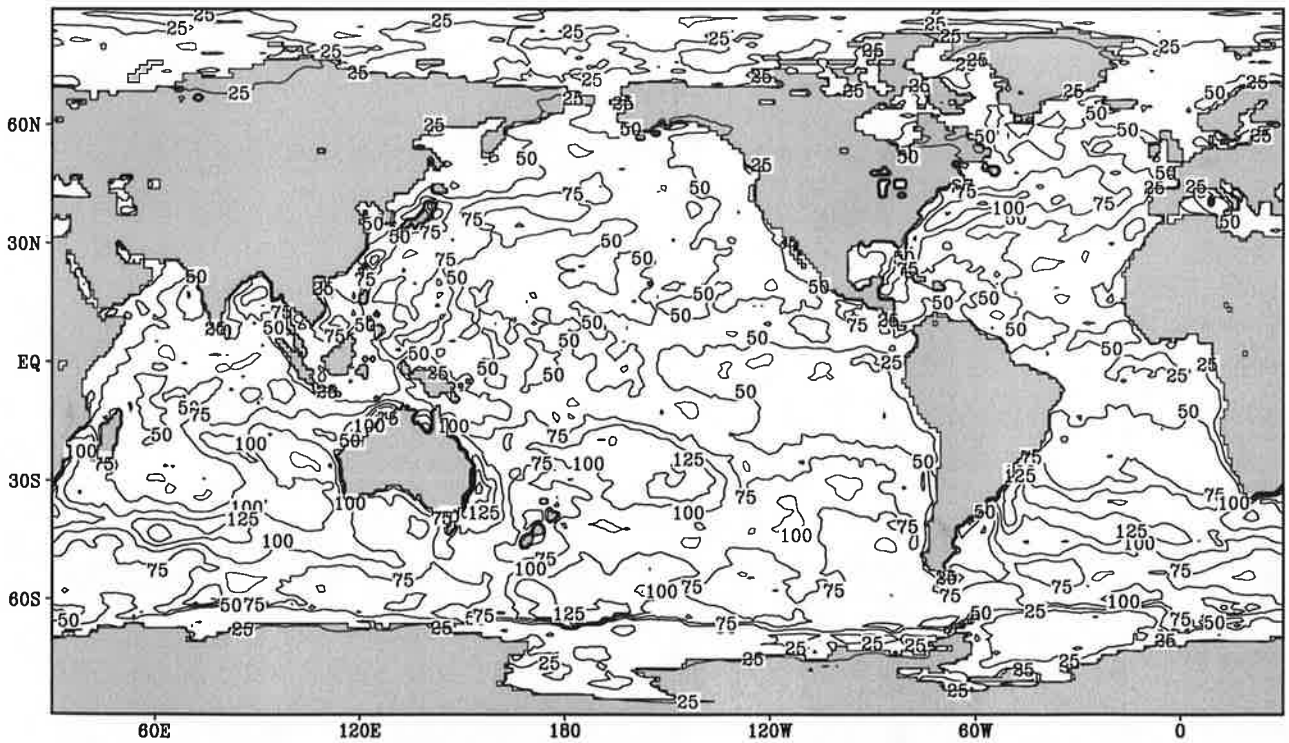

Contour interval: 25 Wm^{-2}

Fig.1.7 Net downward heat flux July

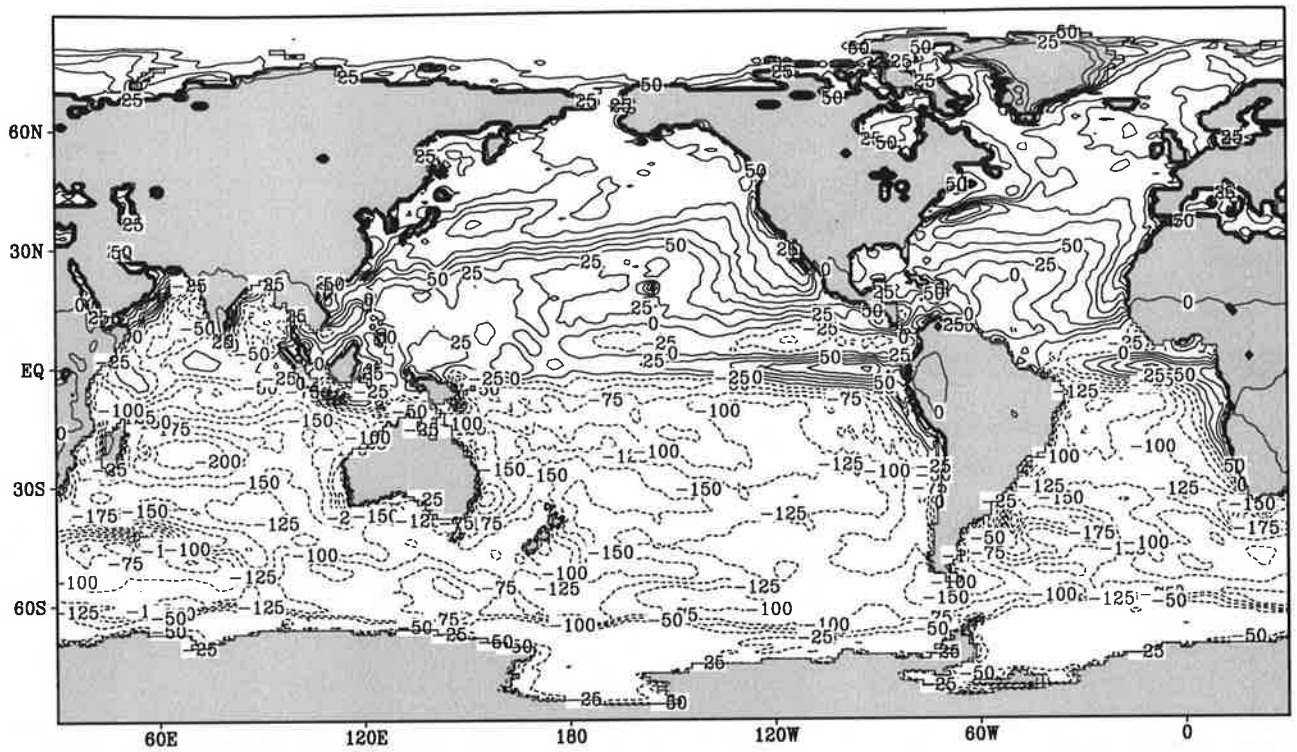

Contour interval: 25 Wm^{-2}

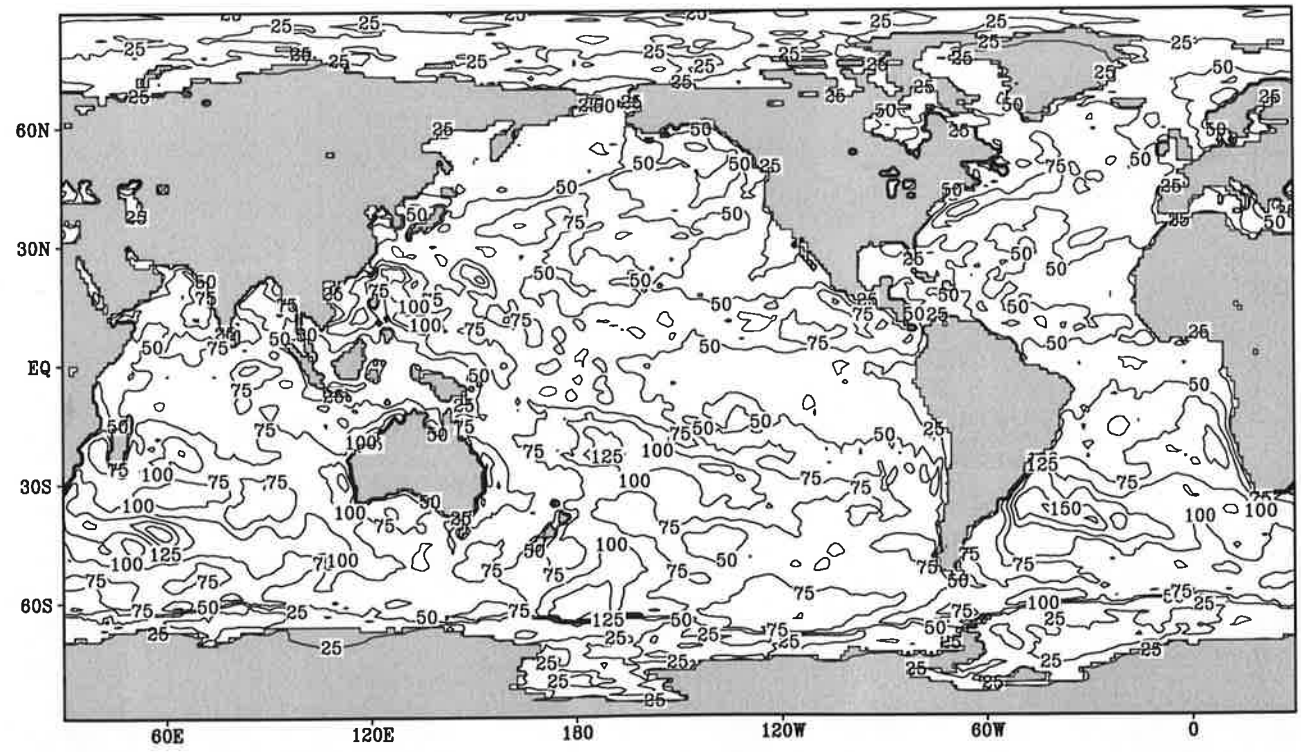

Contour interval: 25 Wm^{-2}

Fig.1.8 Net downward heat flux August

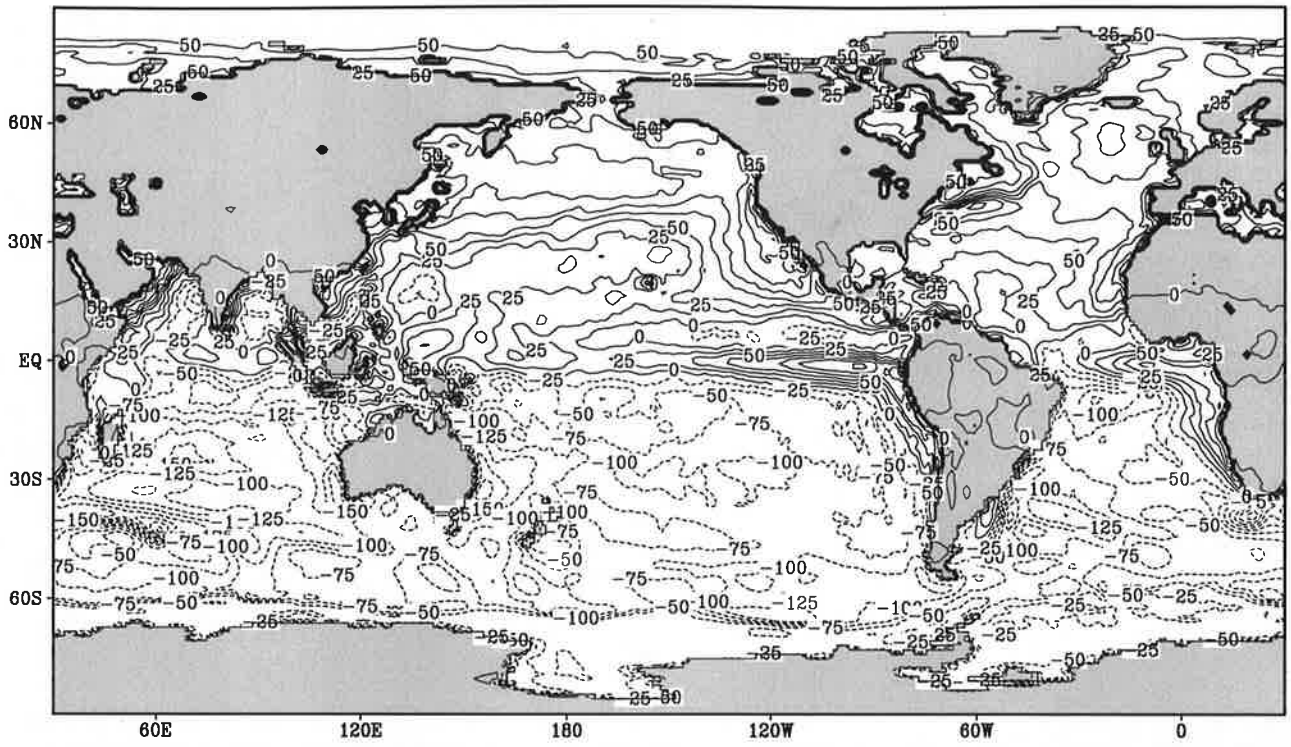

Contour interval: 25 Wm^{-2}

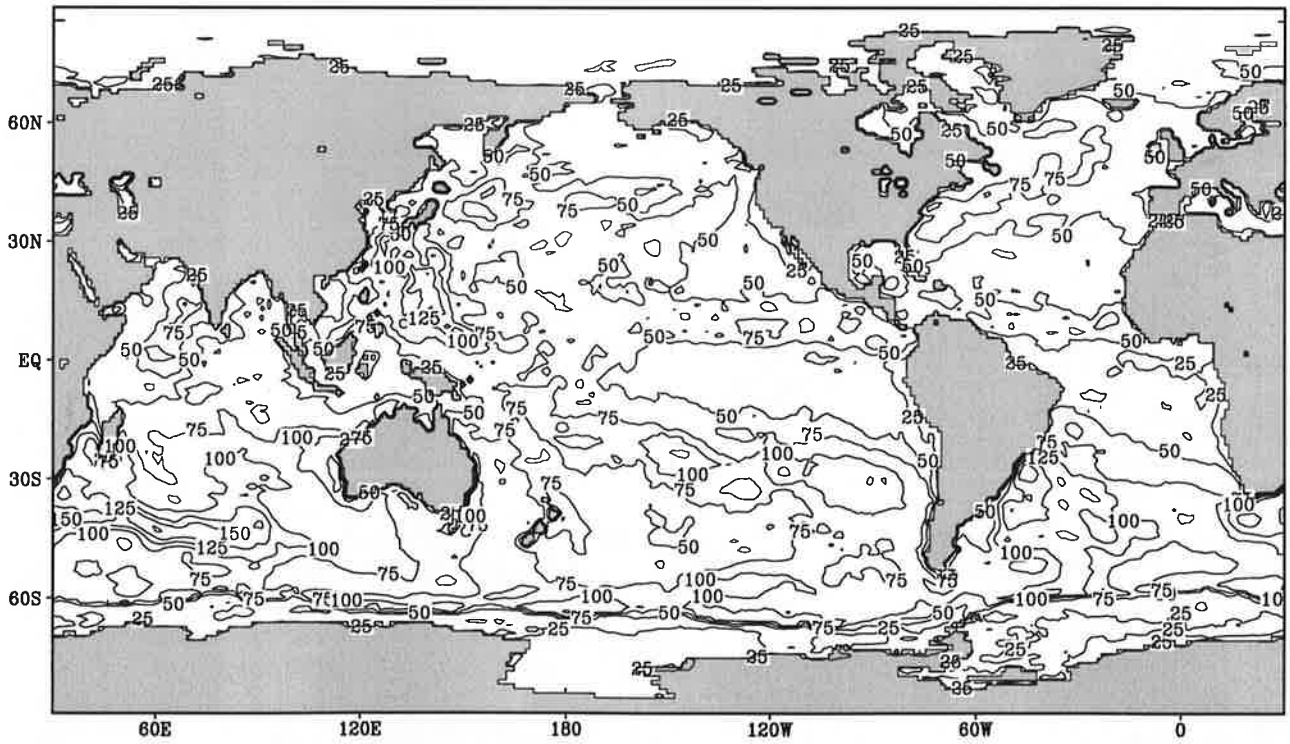

Contour interval: 25 Wm^{-2}

Fig.1.9 Net downward heat flux September

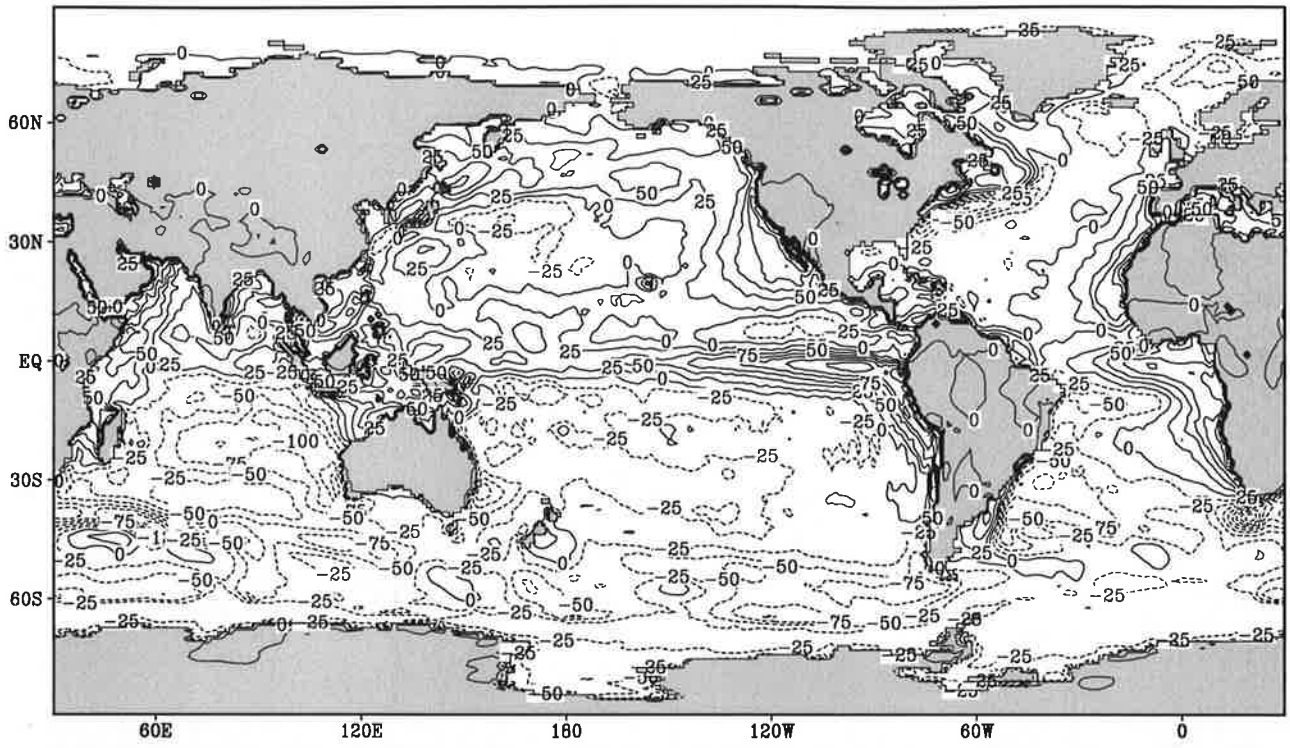

Contour interval: 25 Wm^{-2}

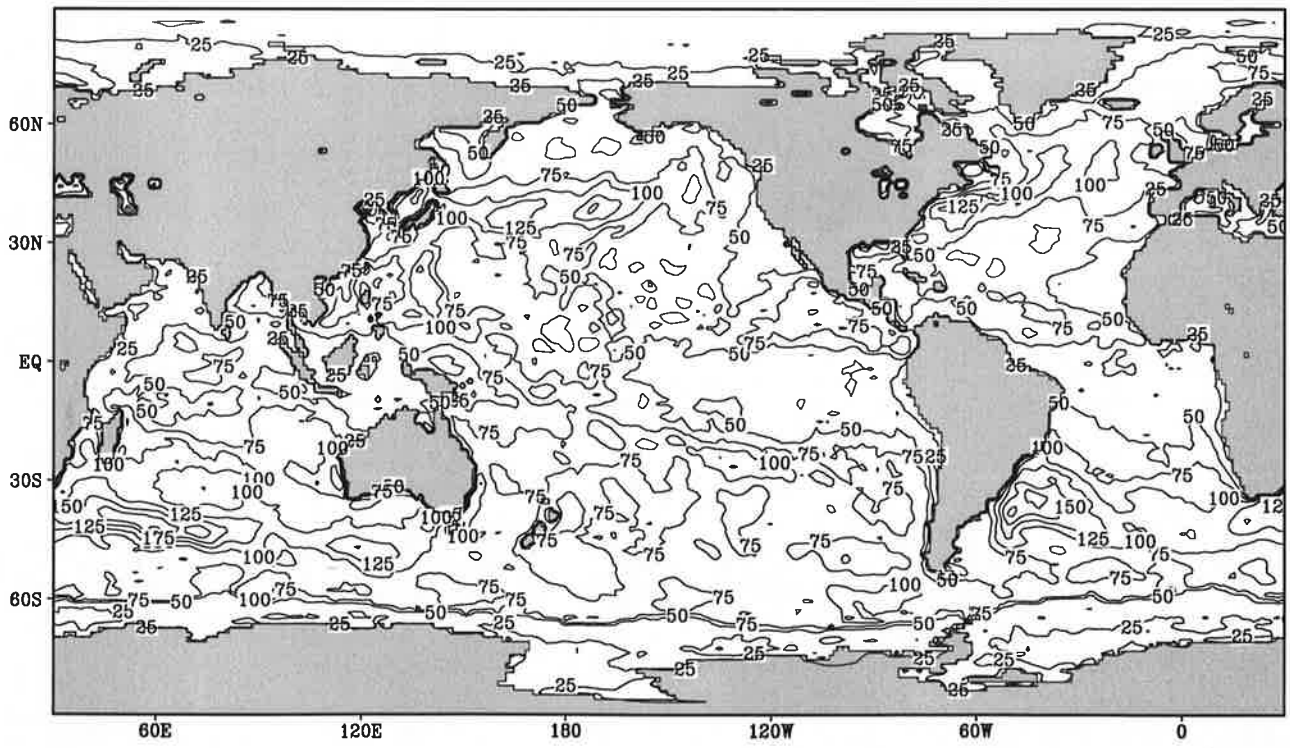

Contour interval: 25 Wm^{-2}

Fig.1.10 Net downward heat flux October

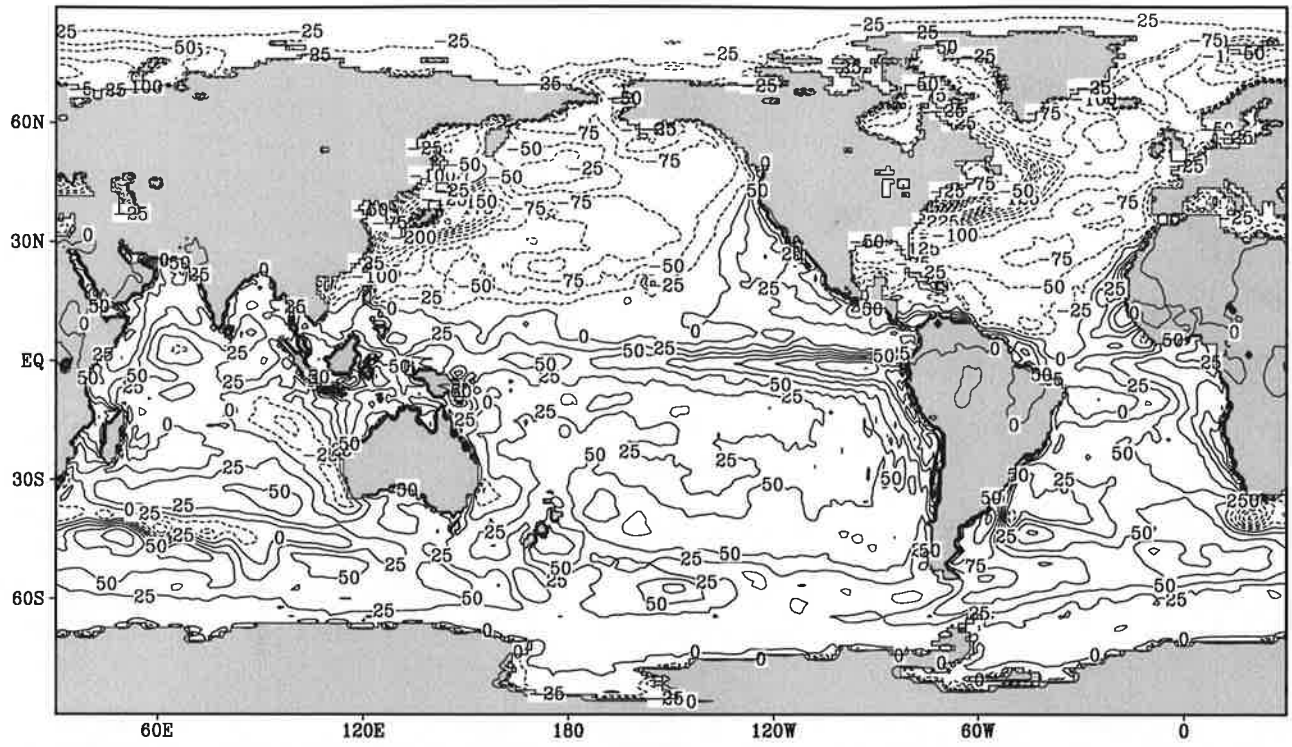

Contour interval: 25 Wm^{-2}

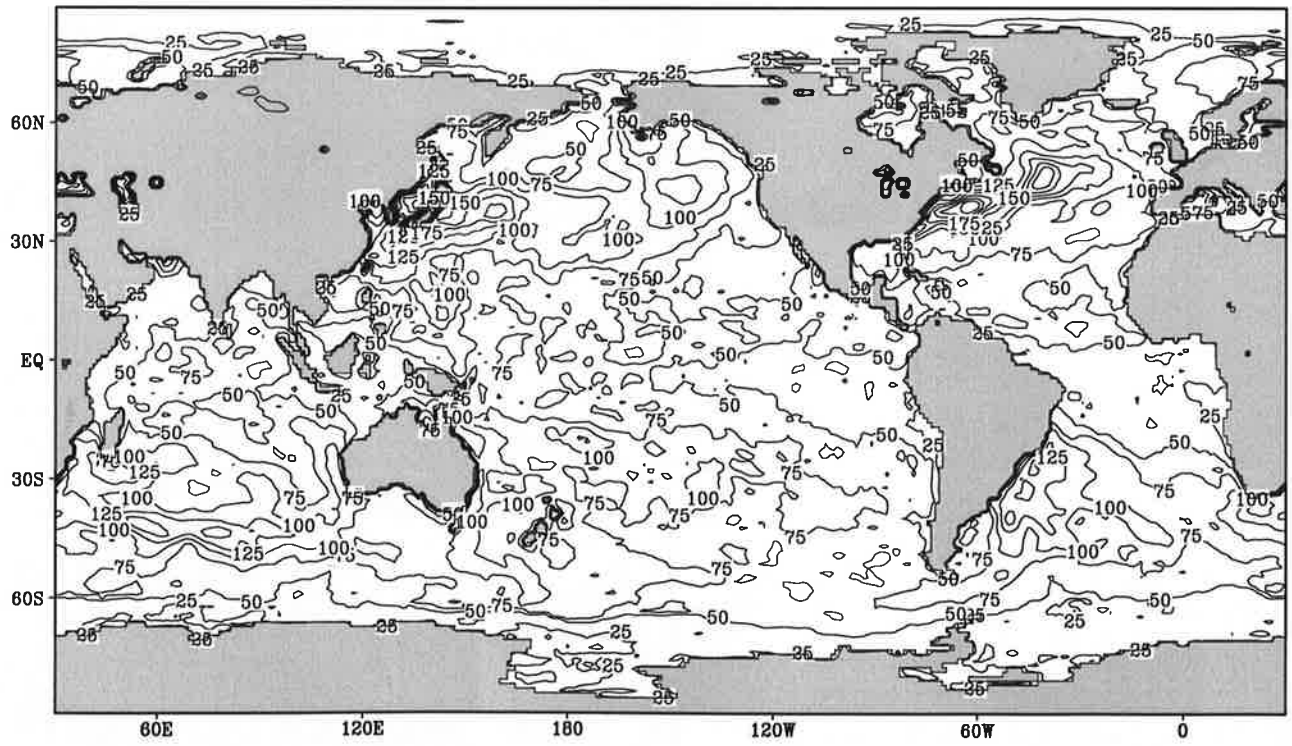

Contour interval: 25 Wm^{-2}

Fig.1.11 Net downward heat flux November

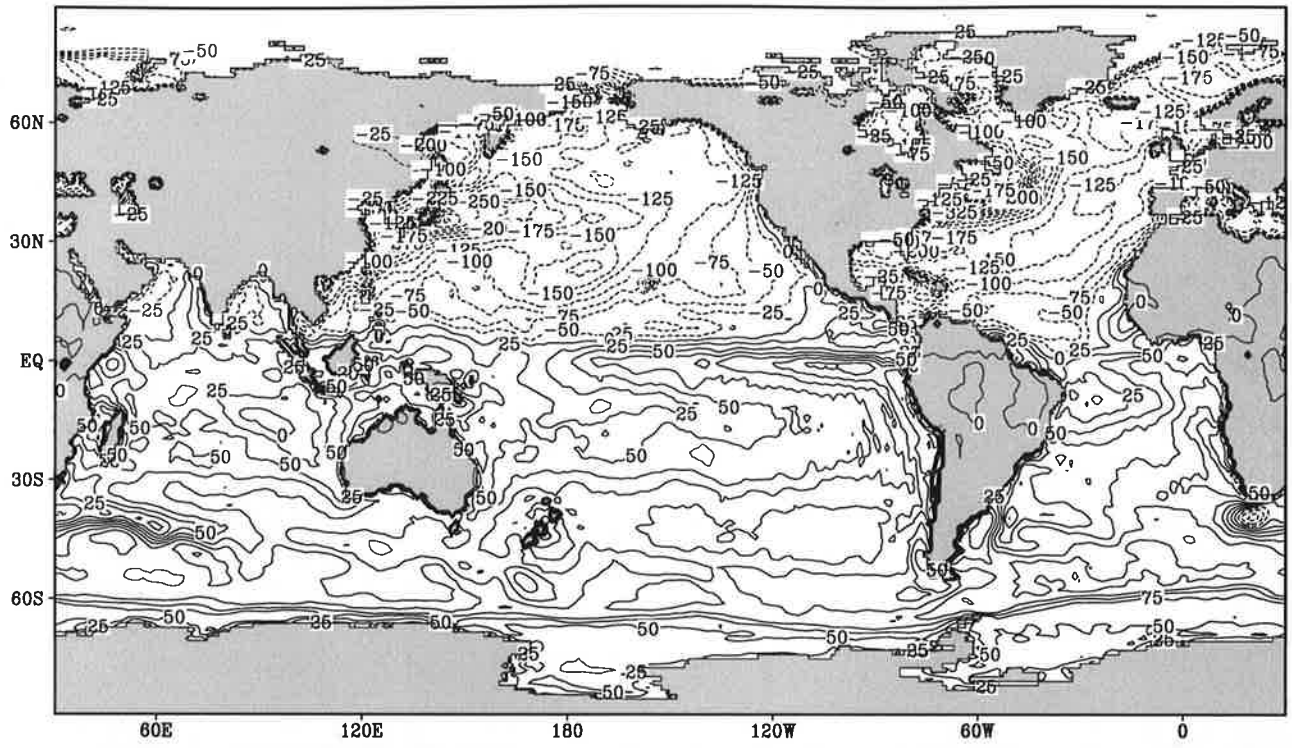

Contour interval: 25 Wm^{-2}

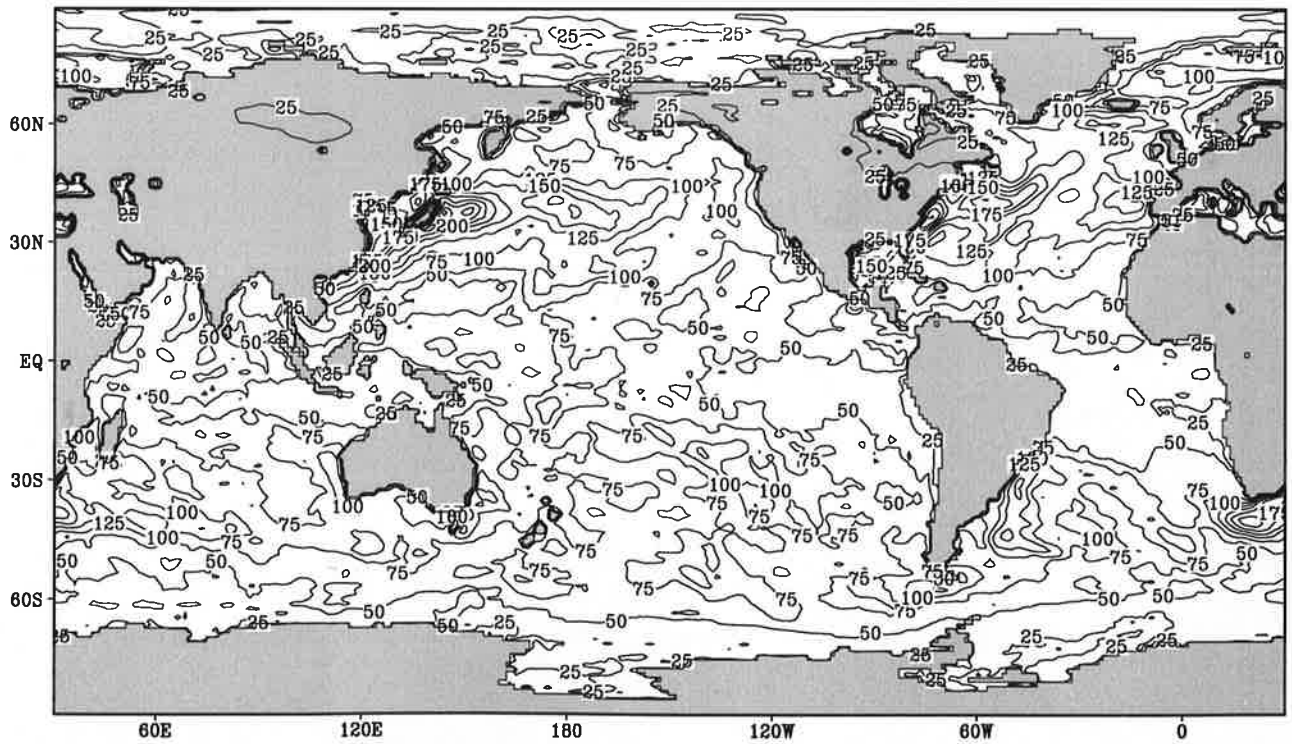

Contour interval: 25 Wm^{-2}

Fig.1.12 Net downward heat flux December

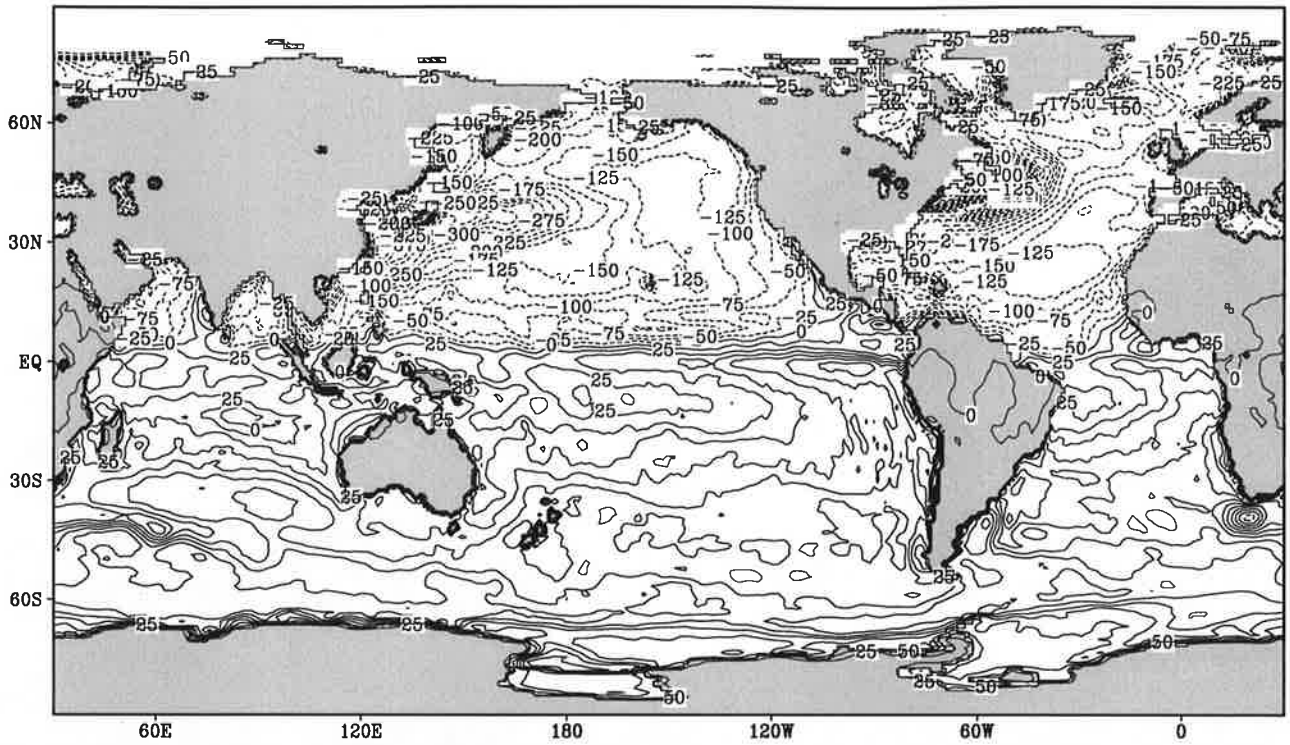

Contour interval: 25 Wm^{-2}

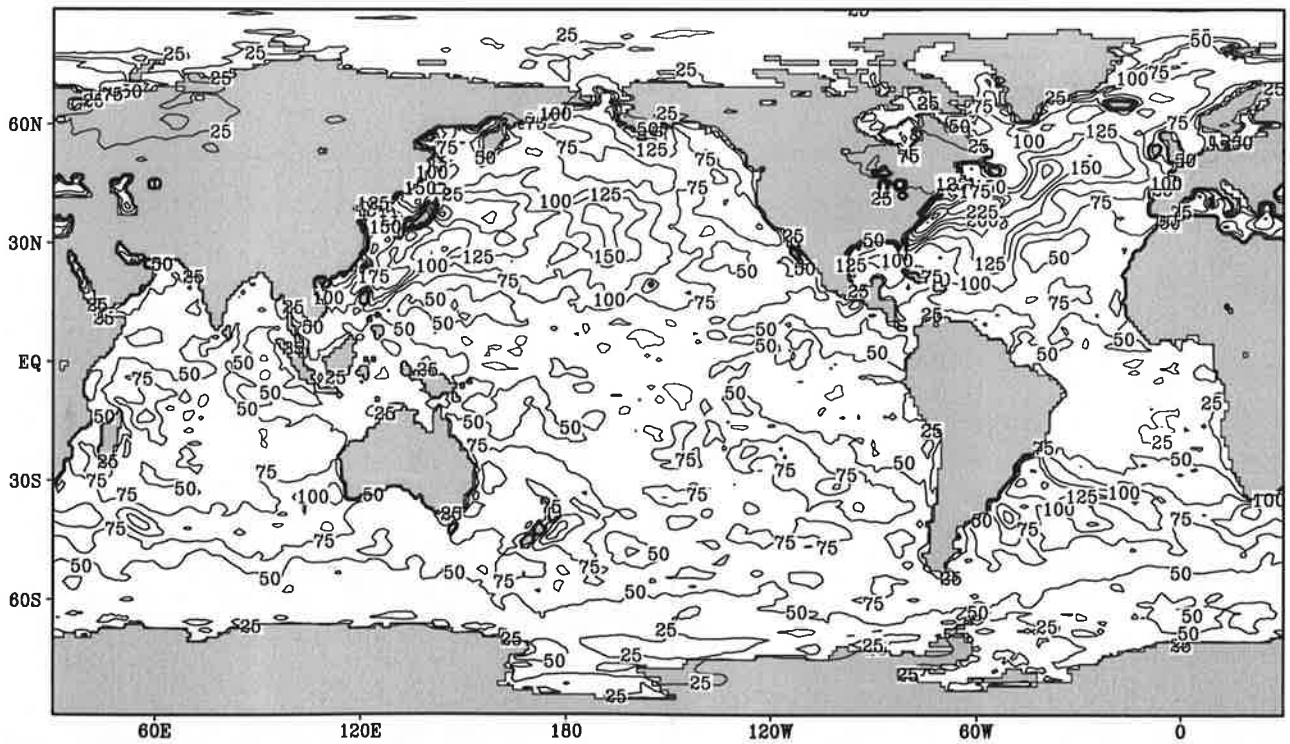

Contour interval: 25 Wm^{-2}

Fig.1.13 Net downward heat flux Annual Mean

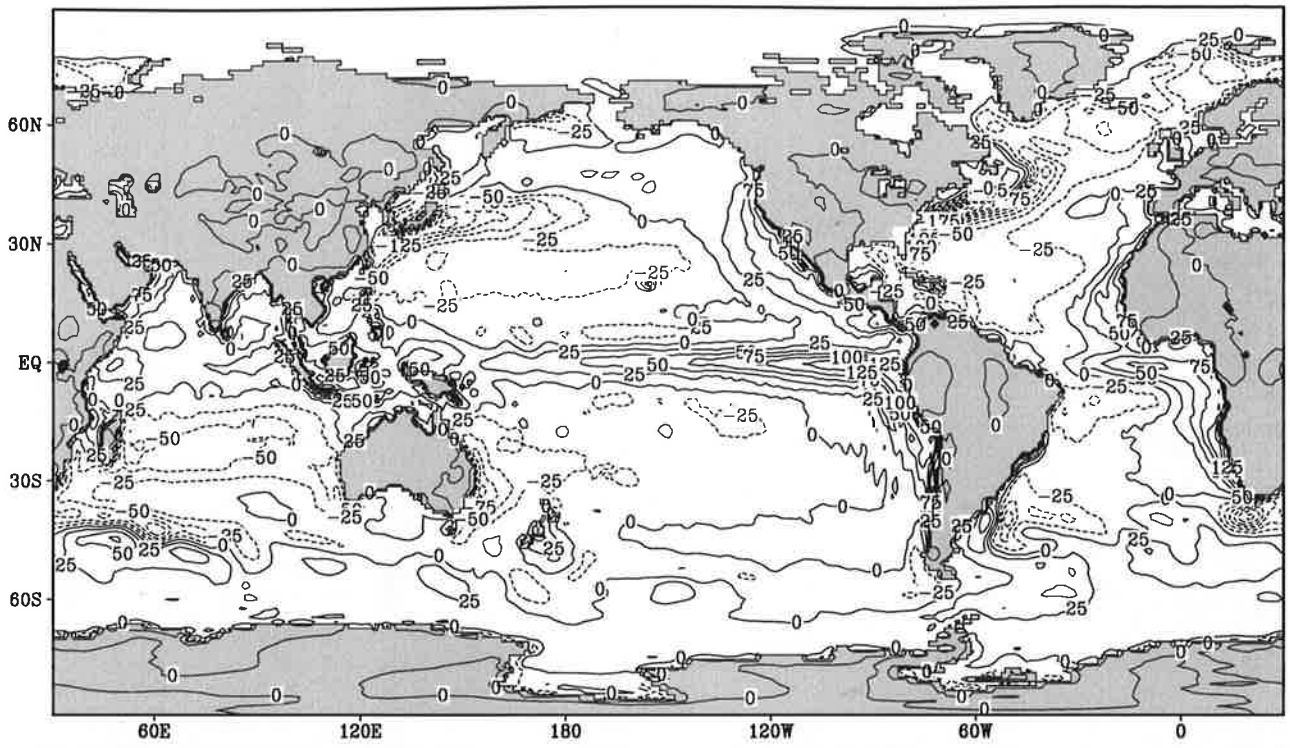

Contour interval: 25 Wm^{-2}

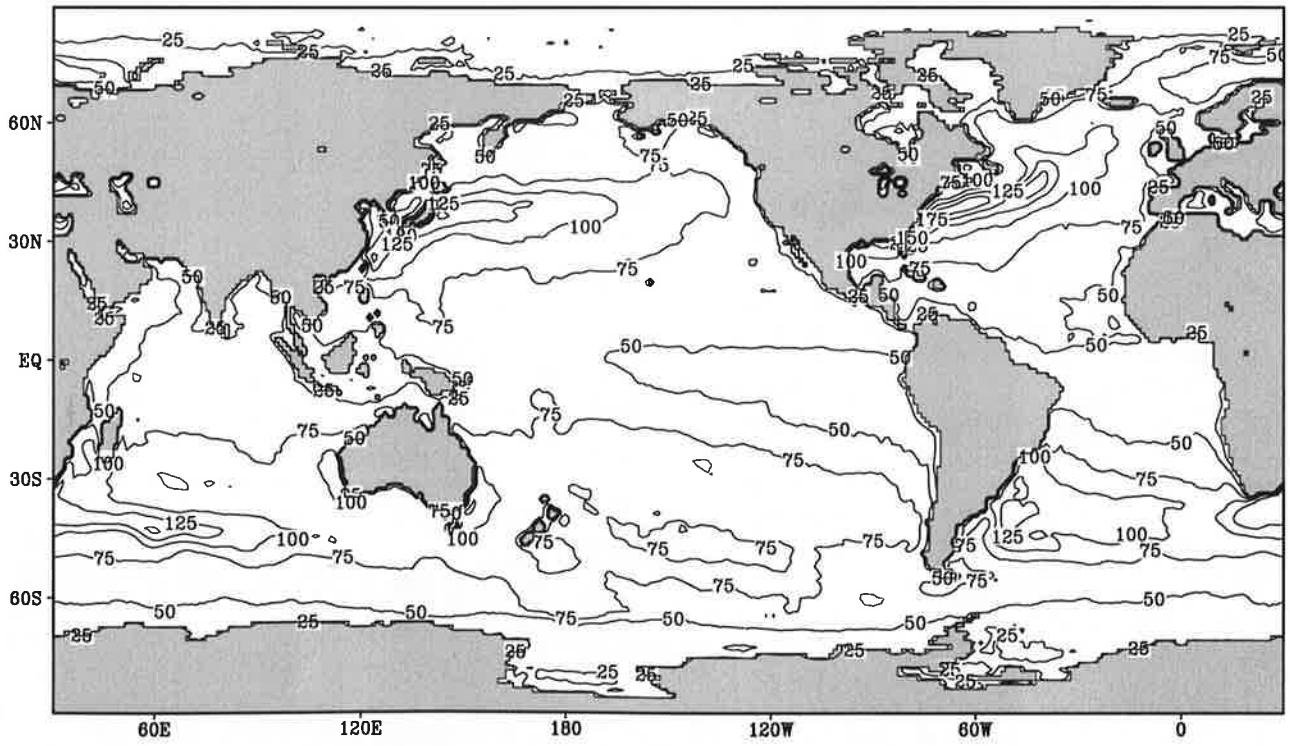

Contour interval: 25 Wm^{-2}

Fig.2.1 Fresh water flux January

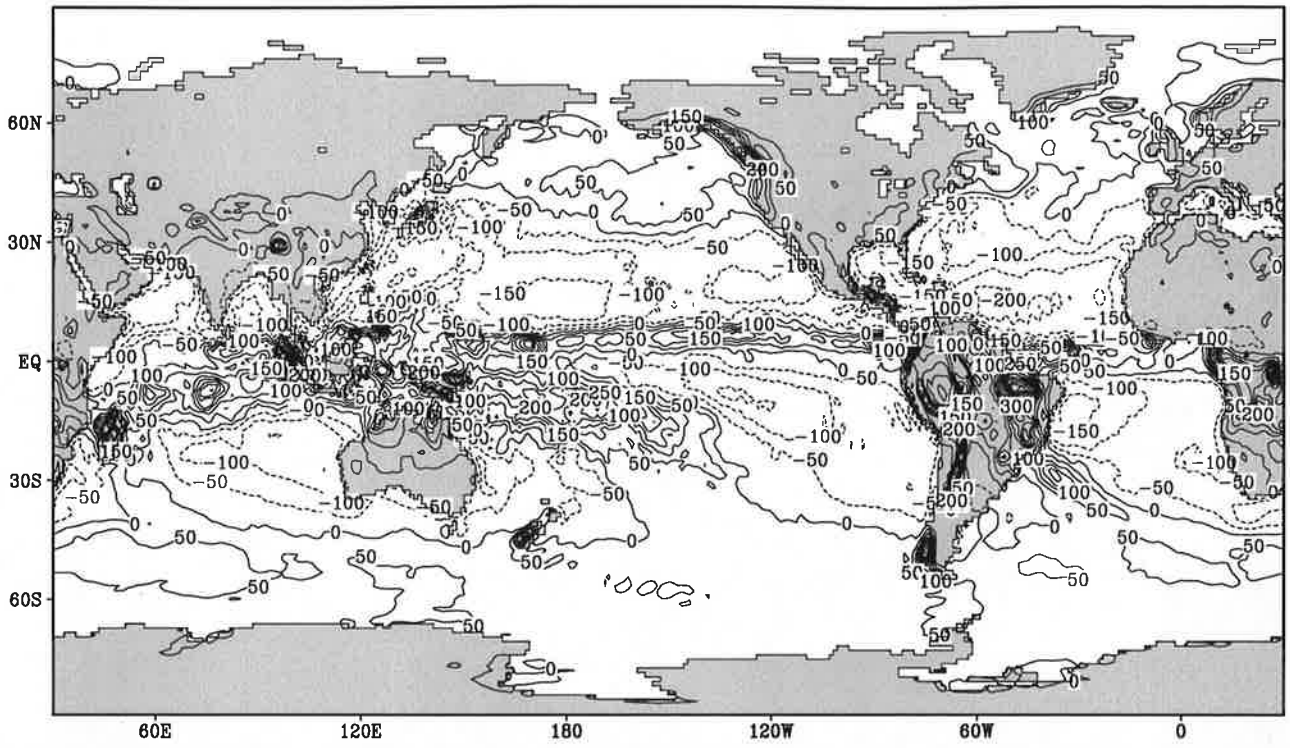

Contour interval: 50 mm month^{-1}

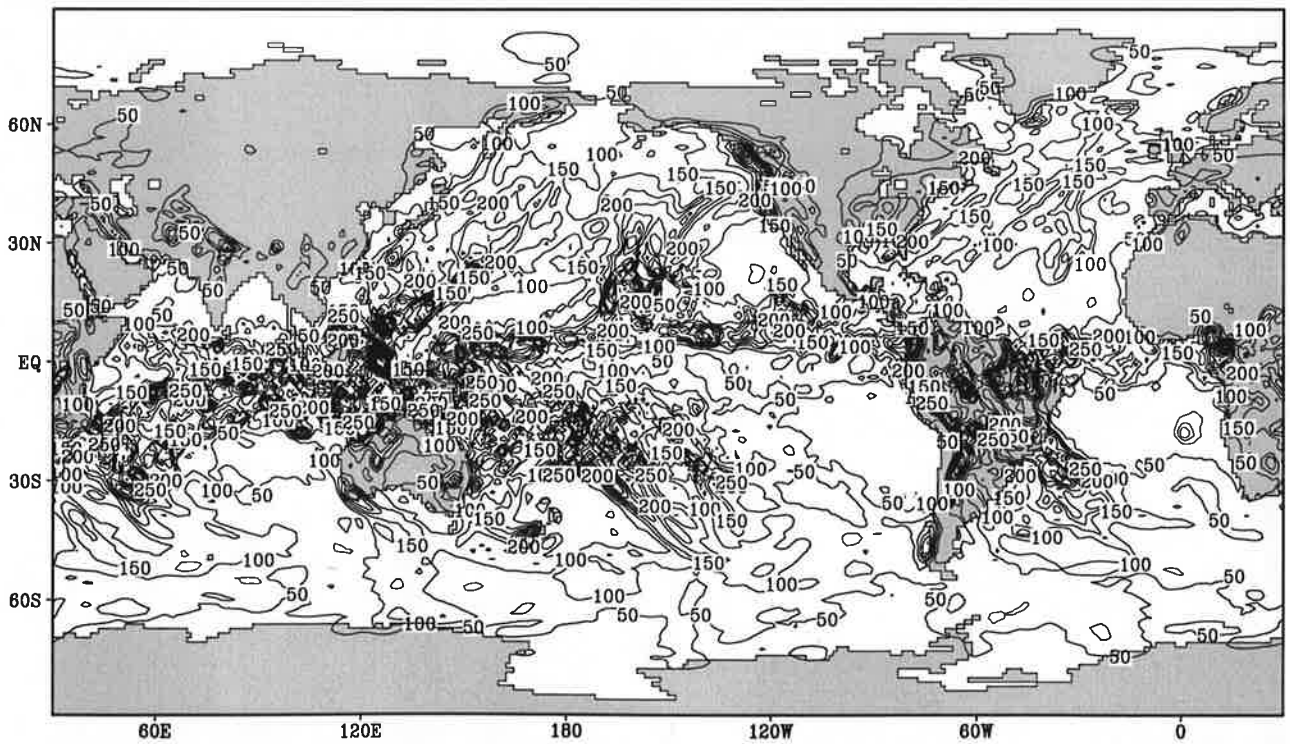

Contour interval: 50 mm month^{-1}

Fig.2.2 Fresh water flux February

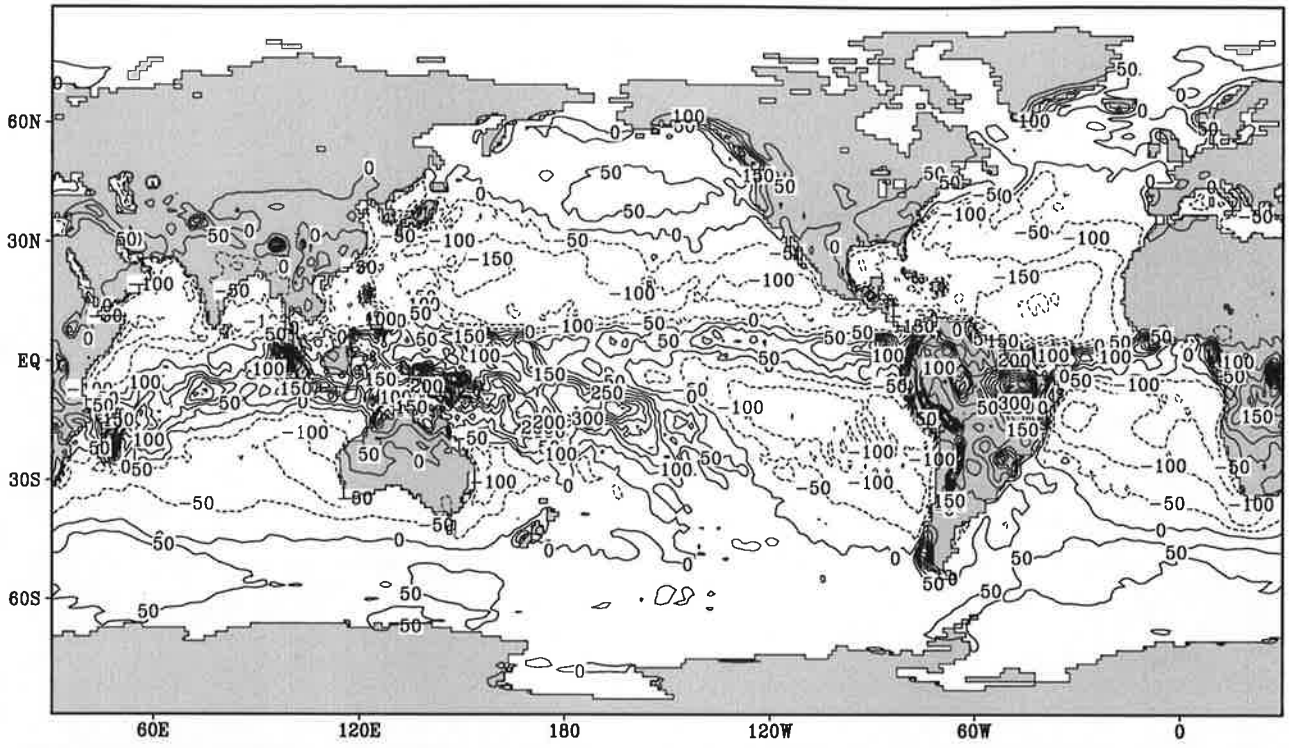

Contour interval: 50 mm month^{-1}

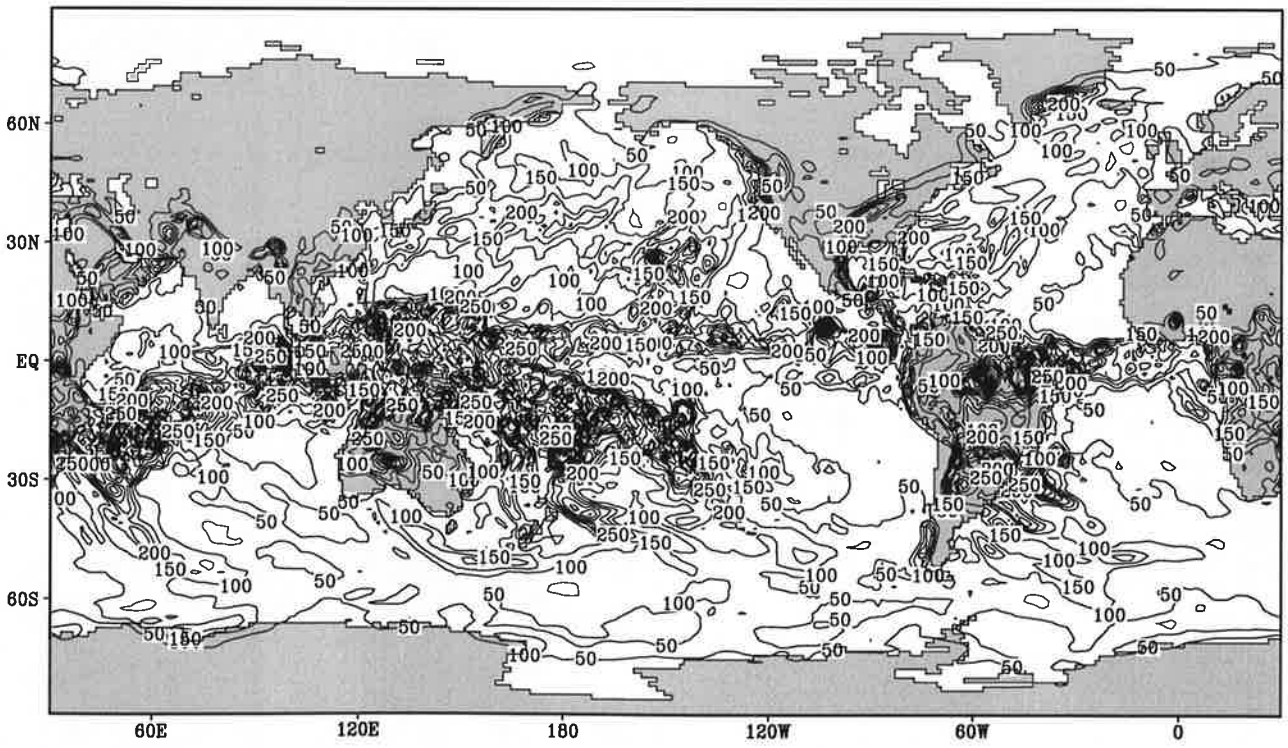

Contour interval: 50 mm month^{-1}

Fig.2.3 Fresh water flux March

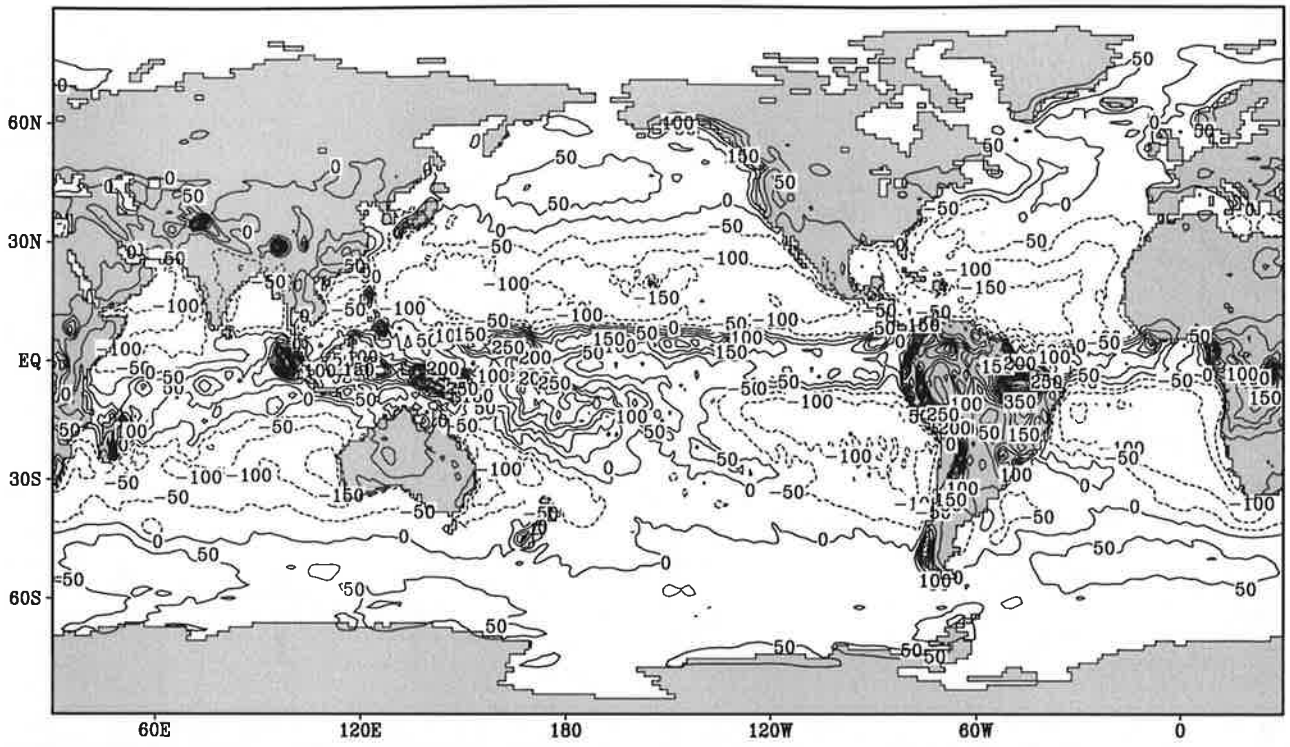

Contour interval: 50 mm month^{-1}

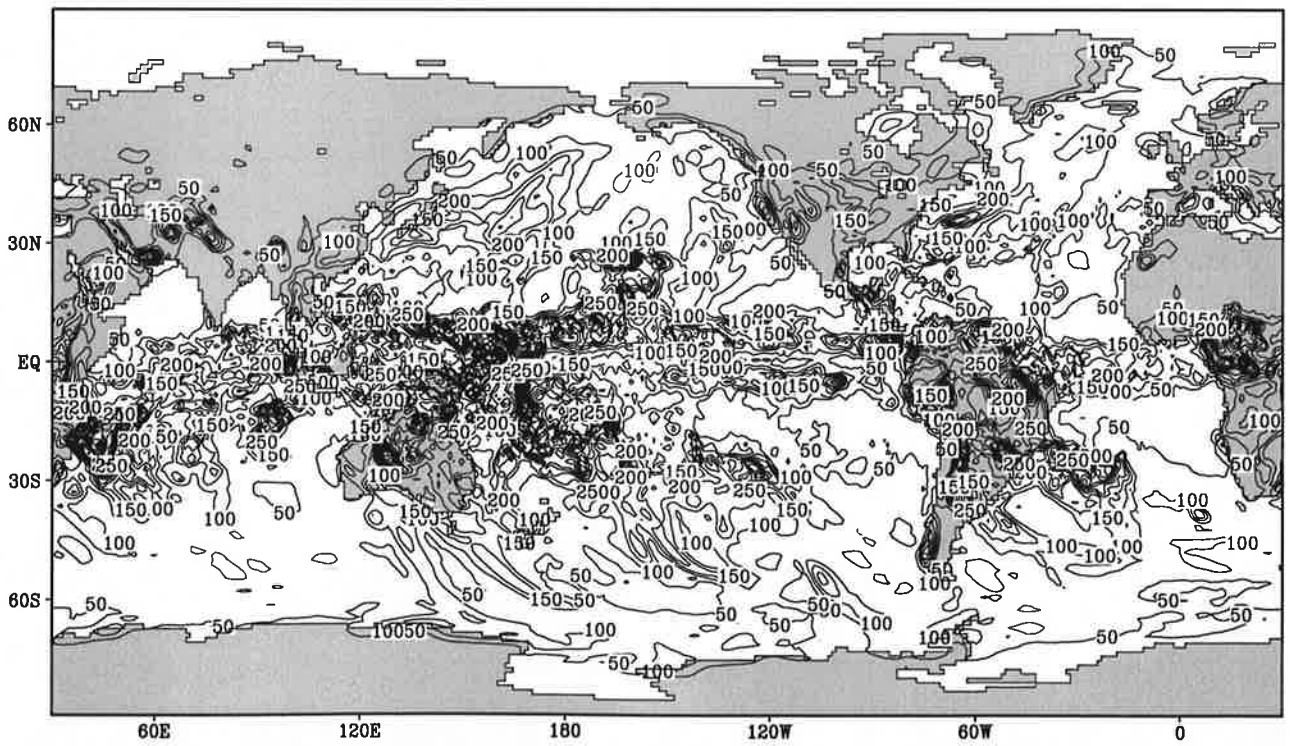

Contour interval: 50 mm month^{-1}

Fig.2.4 Fresh water flux April

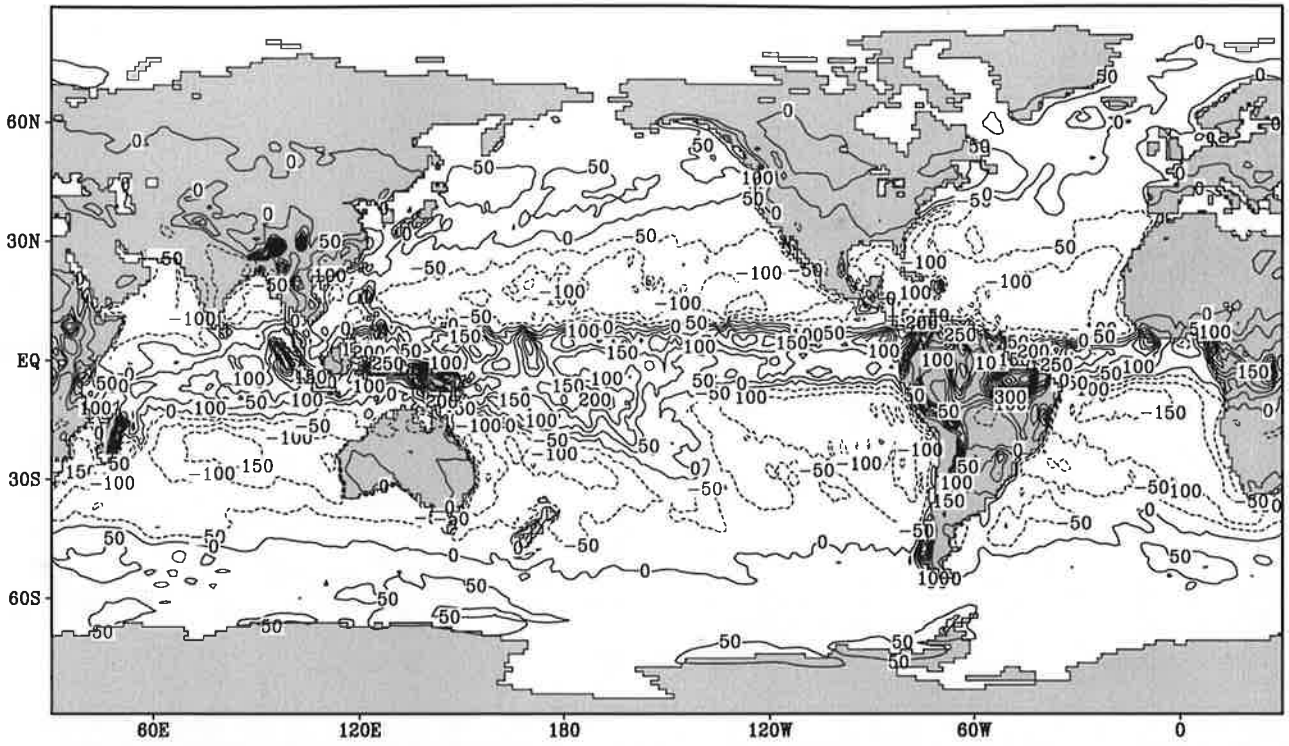

Contour interval: 50 mm month^{-1}

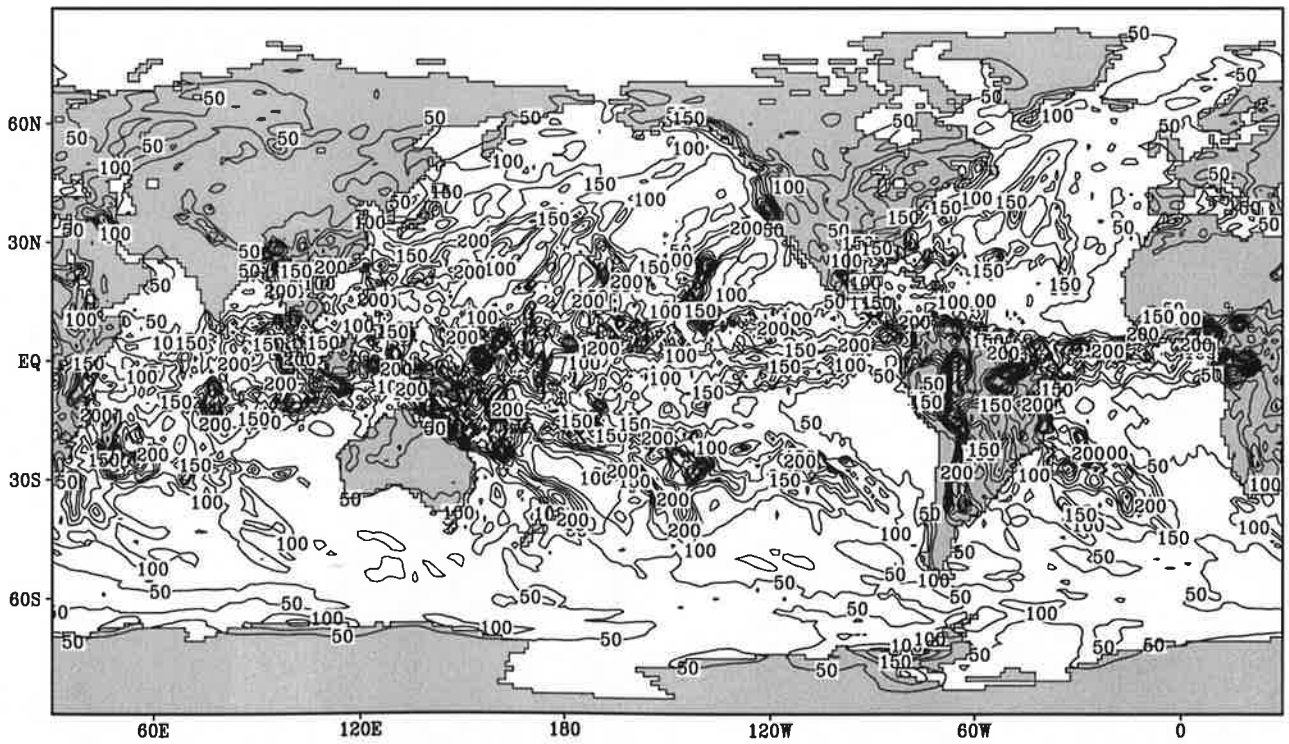

Contour interval: 50 mm month^{-1}

Fig.2.5 Fresh water flux May

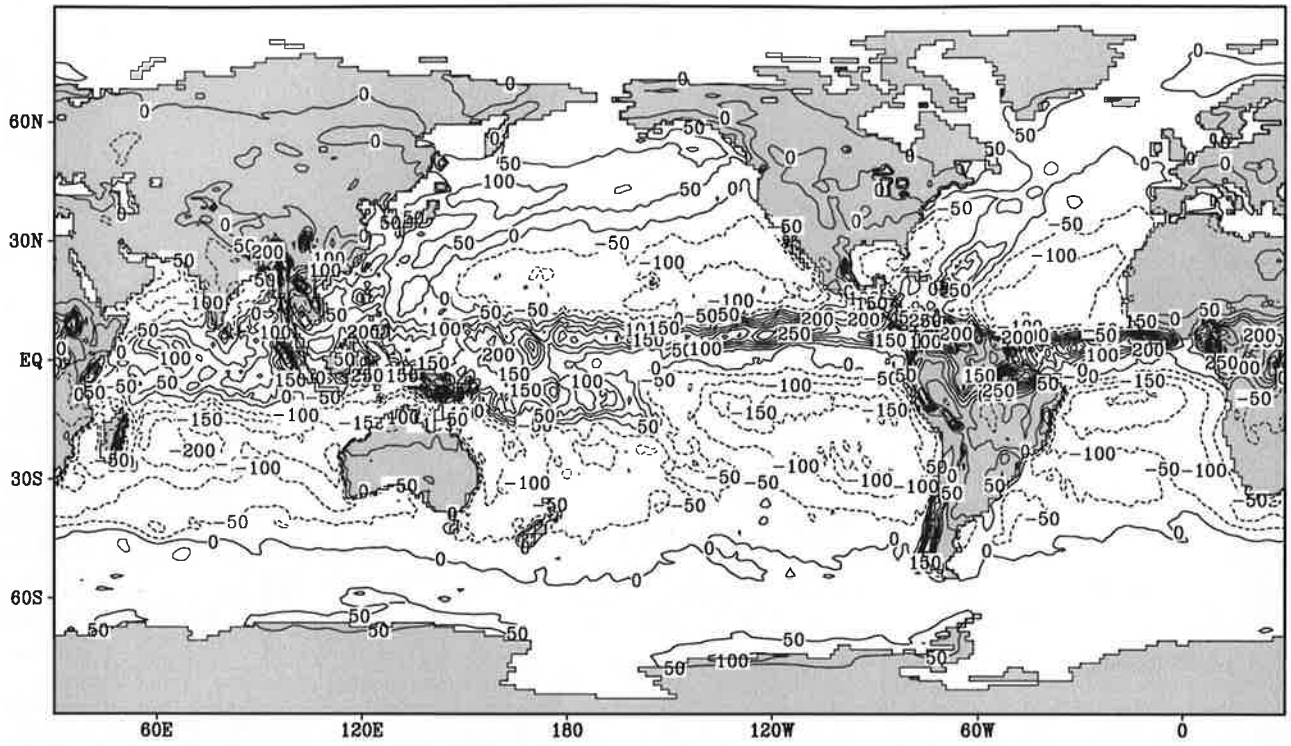

Contour interval: 50 mm month^{-1}

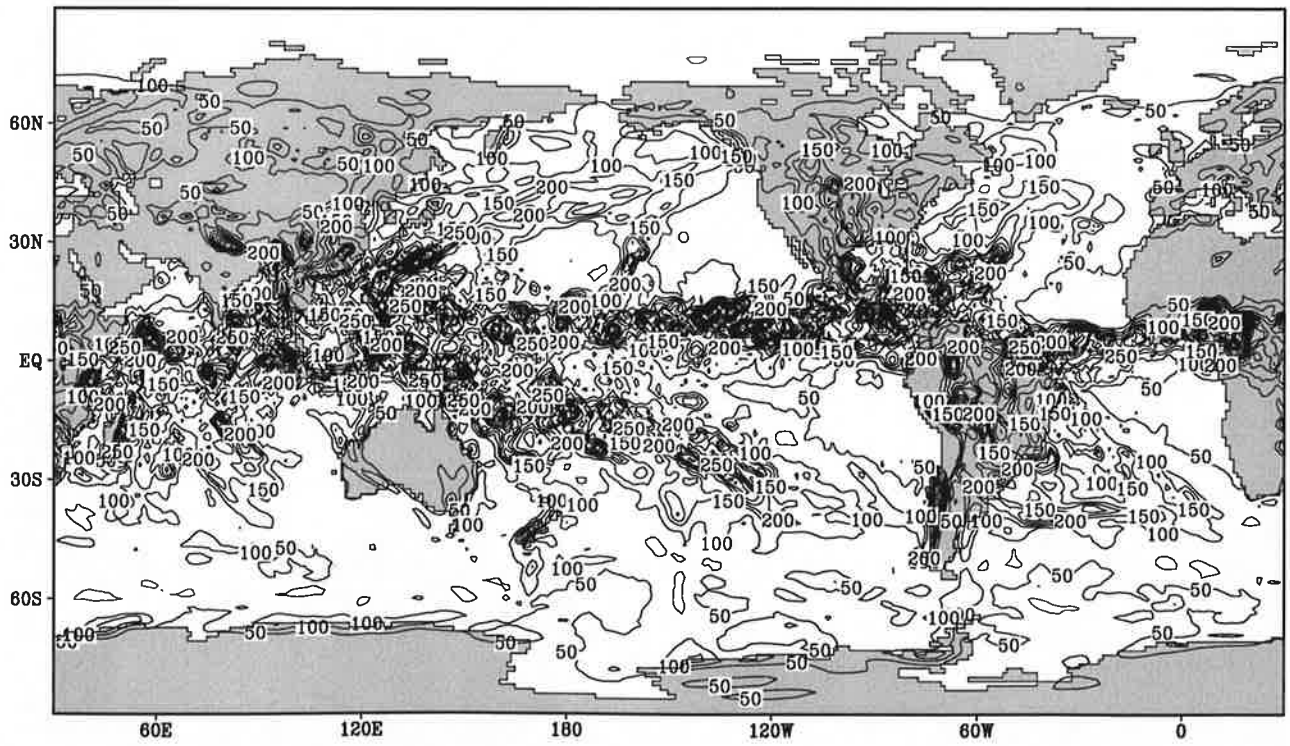

Contour interval: 50 mm month^{-1}

Fig.2.6 Fresh water flux June

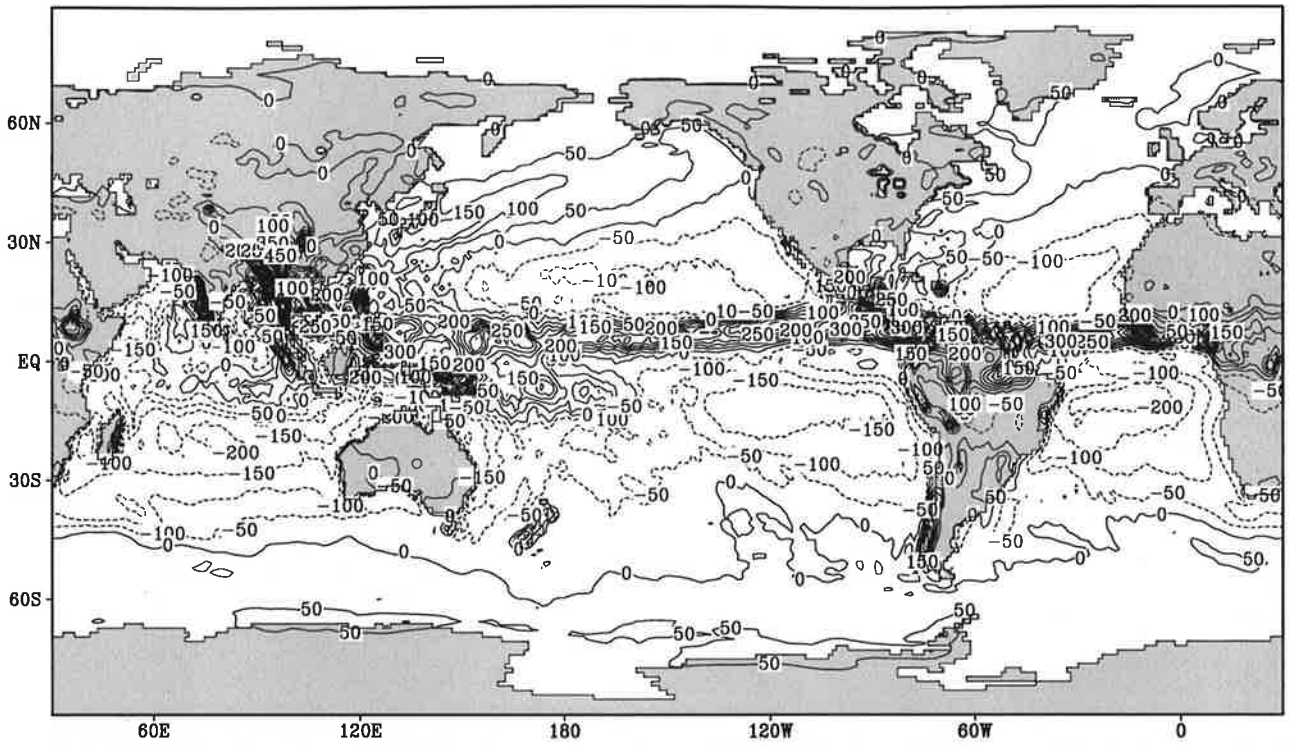

Contour interval: 50 mm month^{-1}

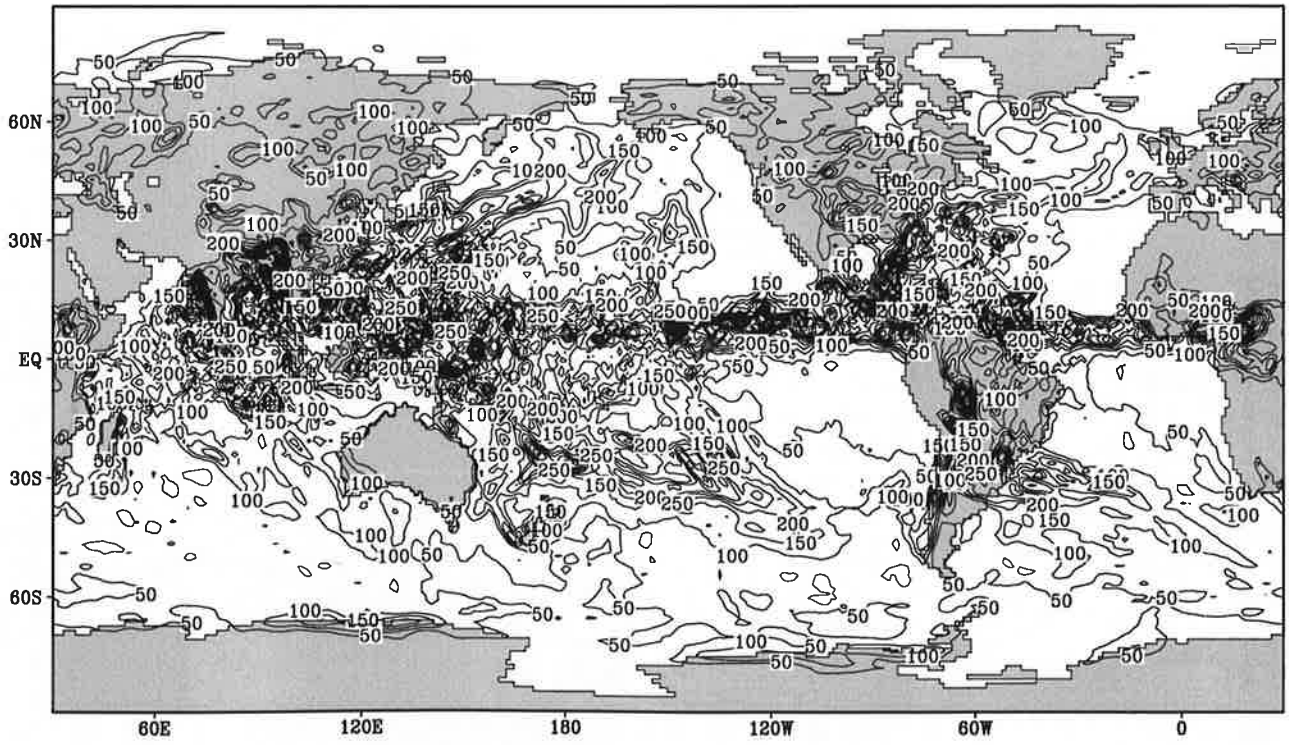

Contour interval: 50 mm month^{-1}

Fig.2.7 Fresh water flux July

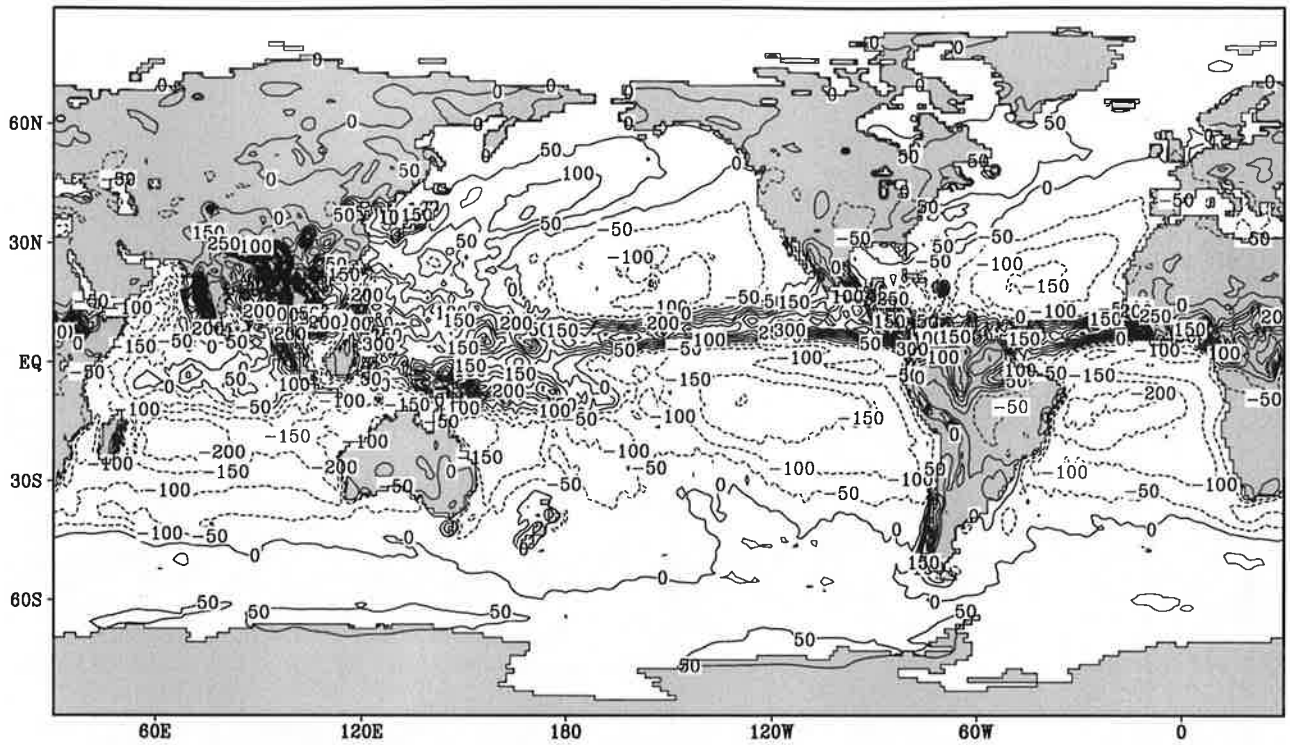

Contour interval: 50 mm month^{-1}

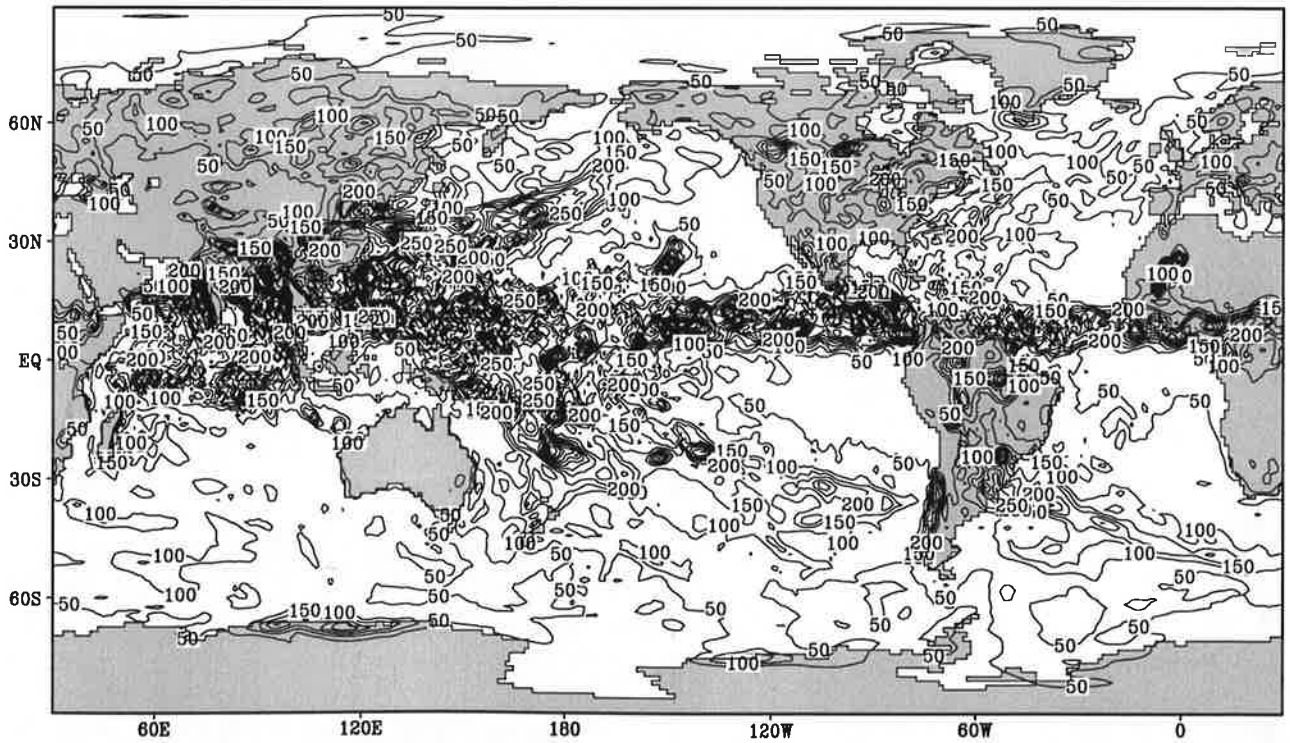

Contour interval: 50 mm month^{-1}

Fig.2.8 Fresh water flux August

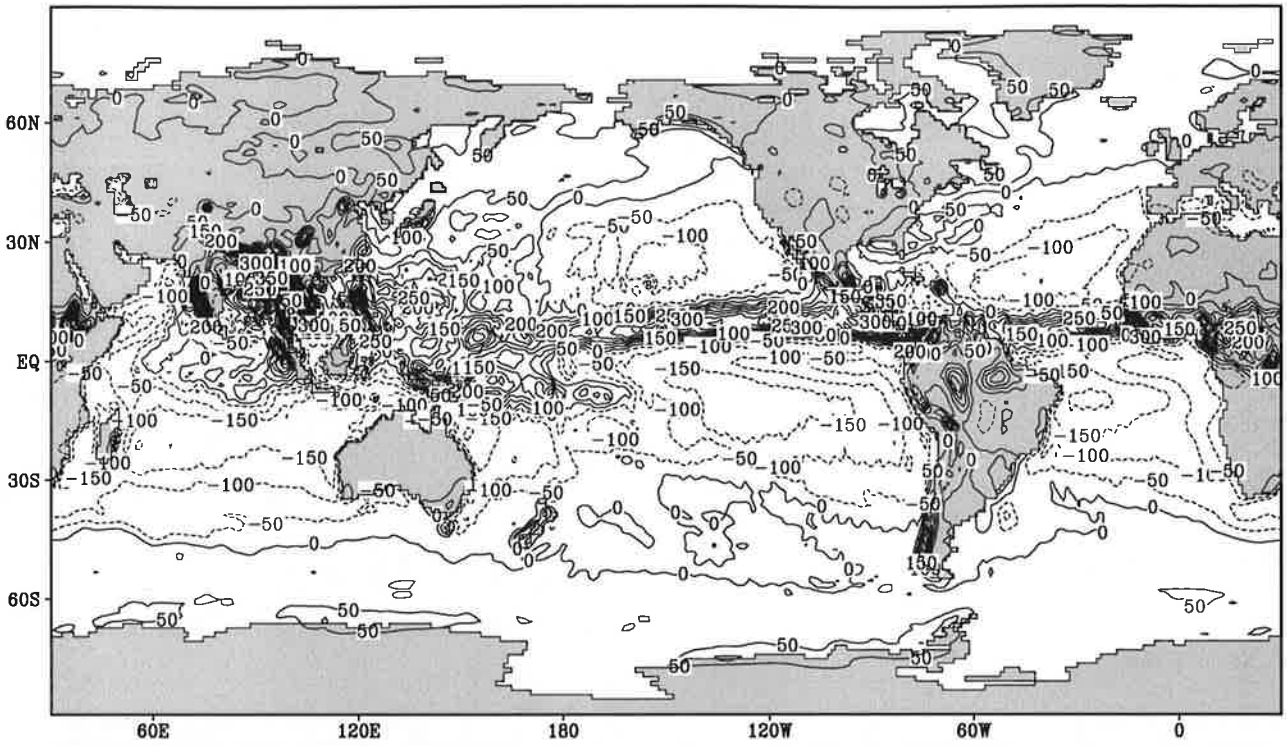

Contour interval: 50 mm month^{-1}

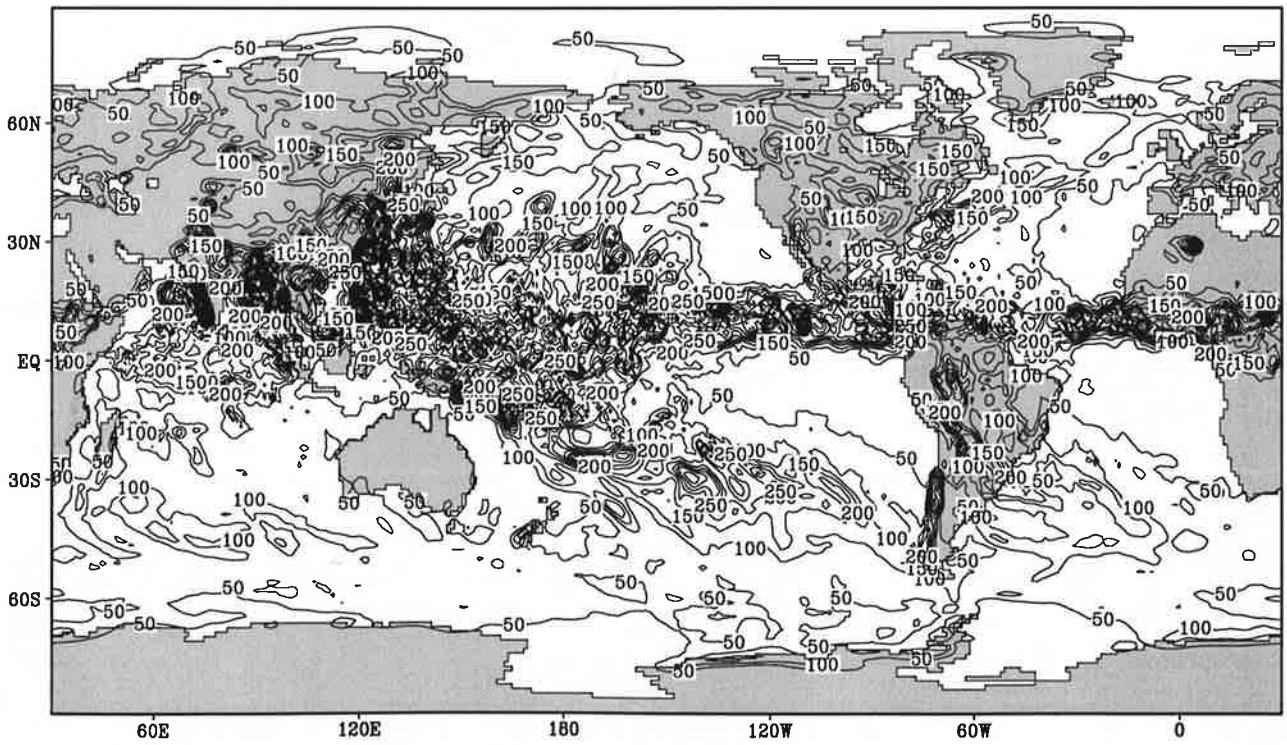

Contour interval: 50 mm month^{-1}

Fig.2.9 Fresh water flux September

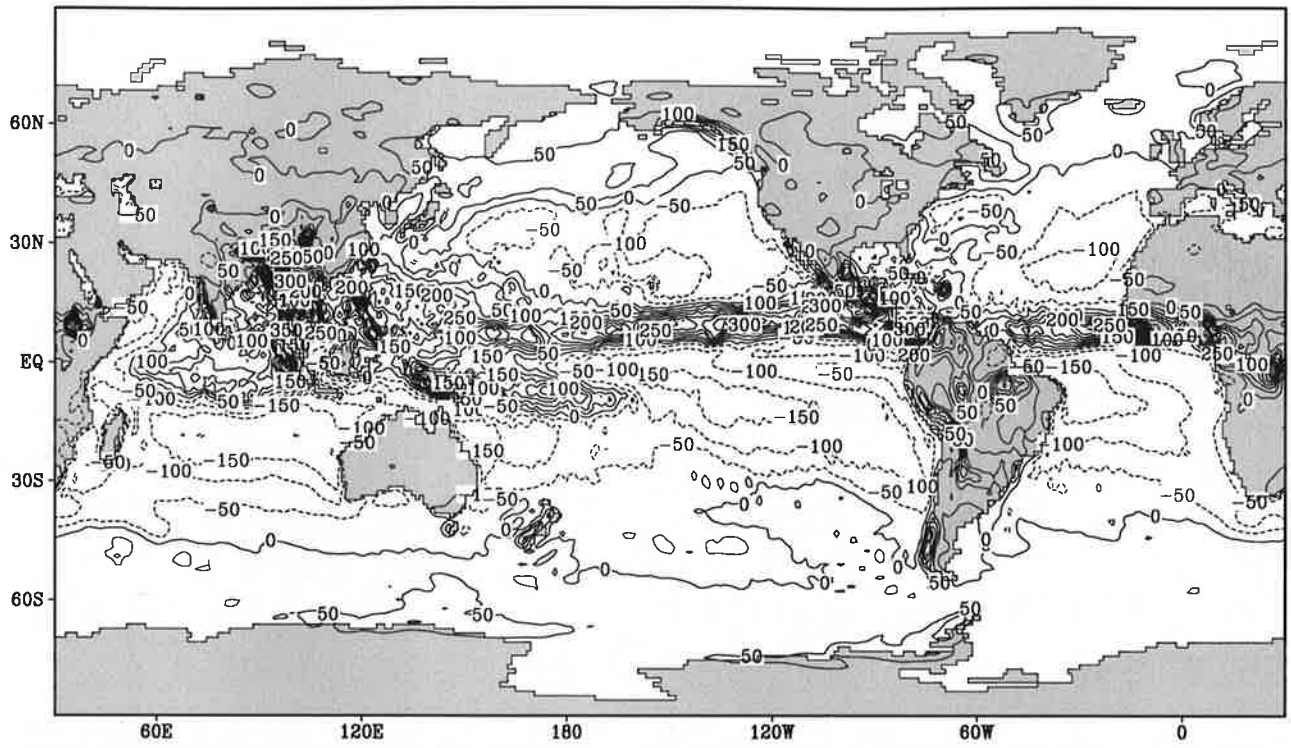

Contour interval: 50 mm month^{-1}

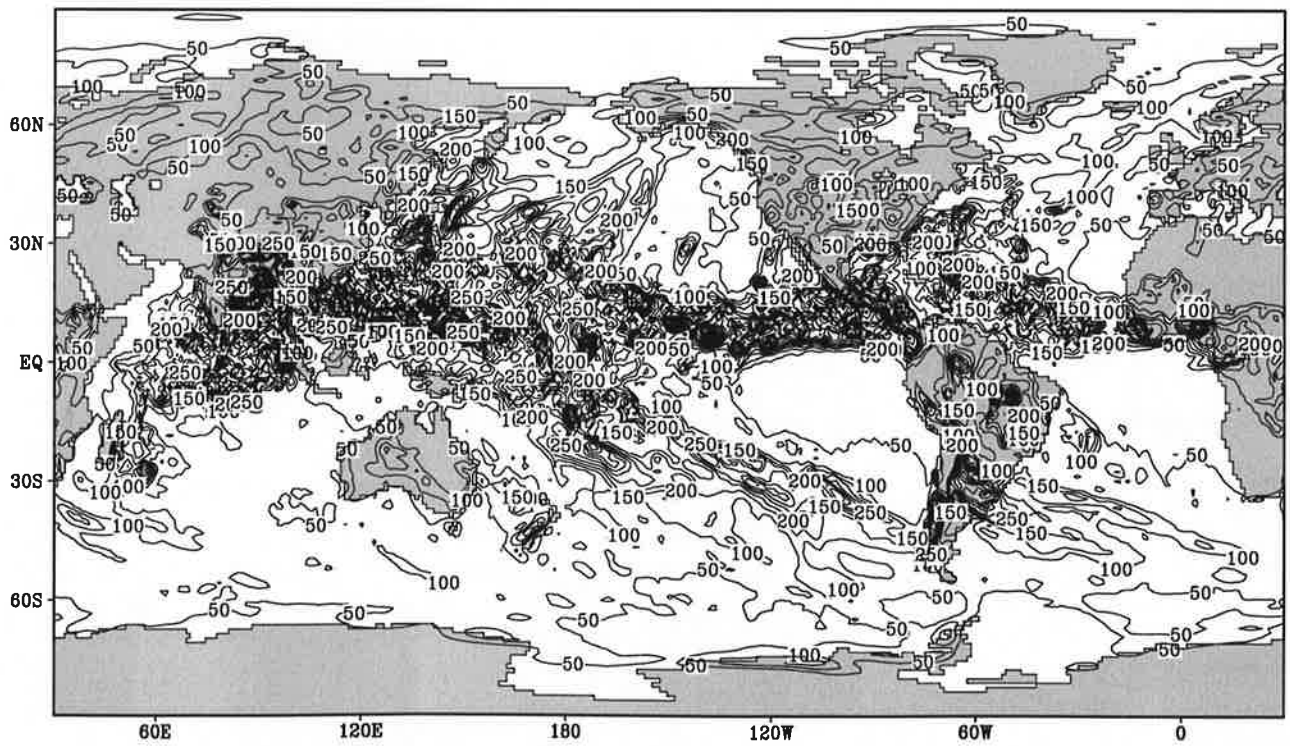

Contour interval: 50 mm month^{-1}

Fig.2.10 Fresh water flux October

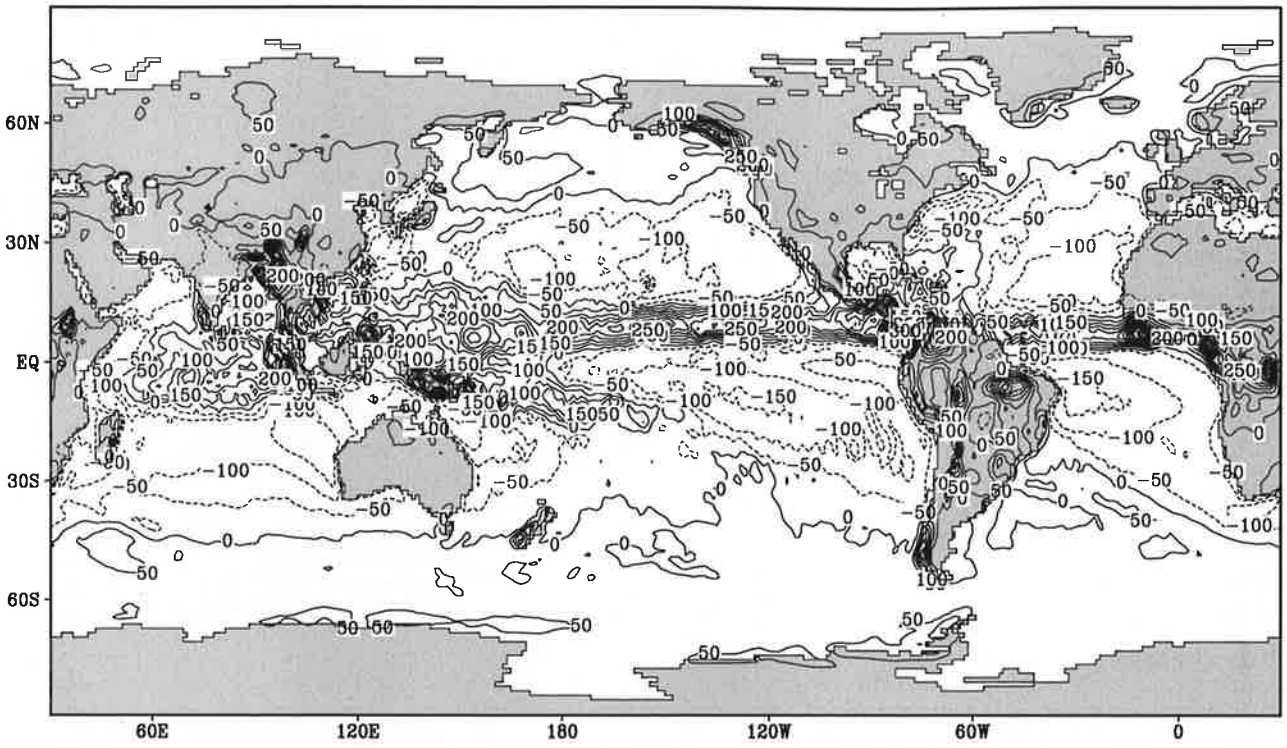

Contour interval: 50 mm month^{-1}

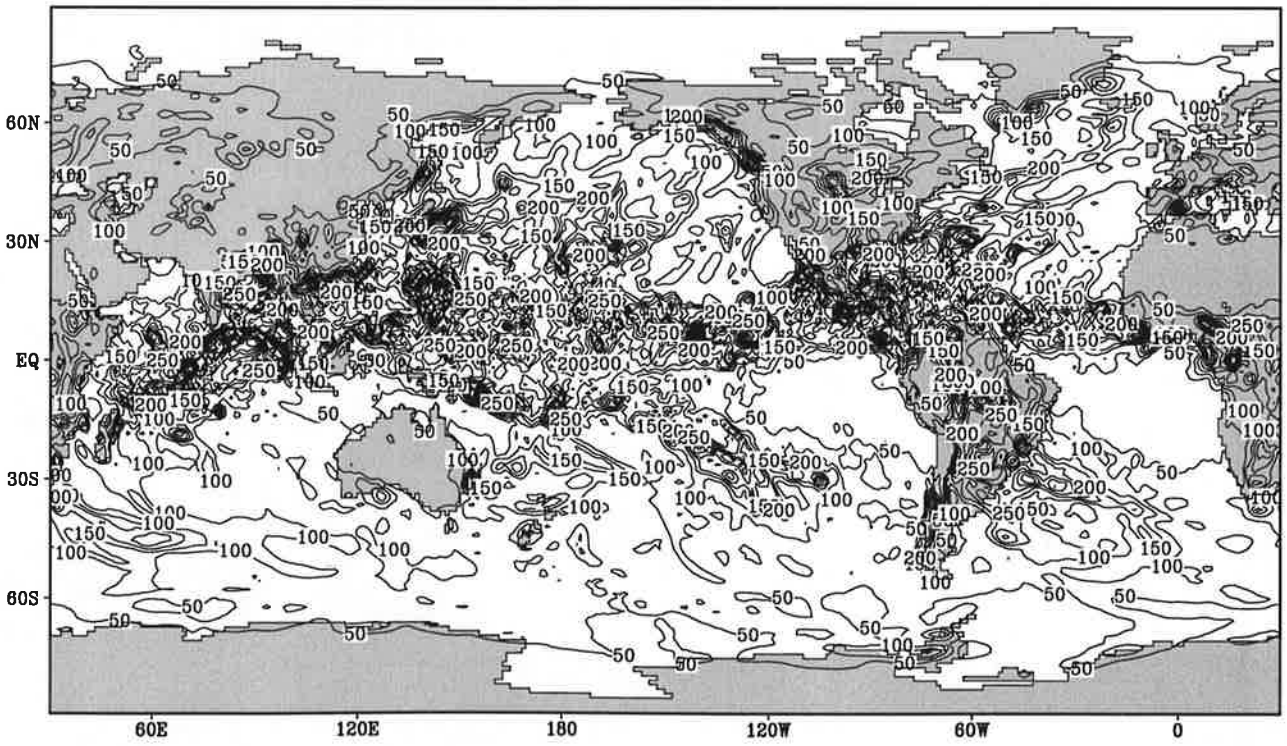

Contour interval: 50 mm month^{-1}

Fig.2.11 Fresh water flux November

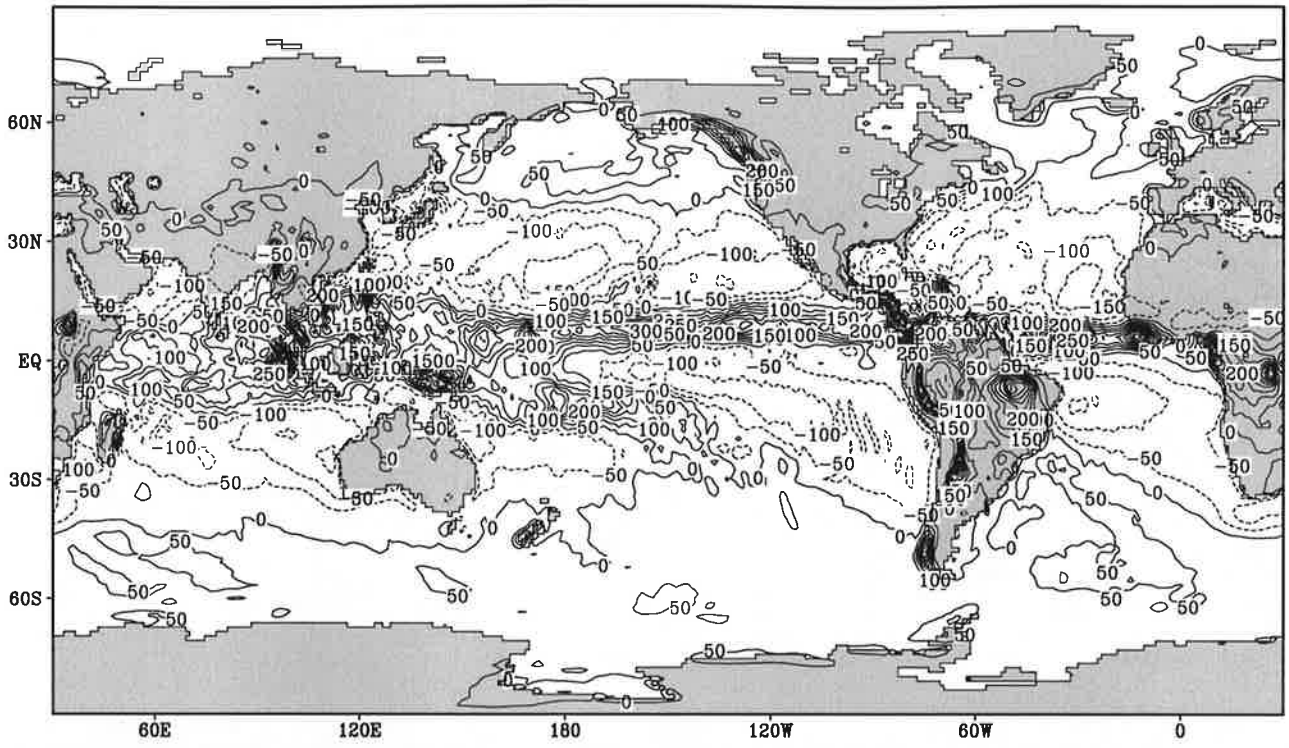

Contour interval: 50 mm month^{-1}

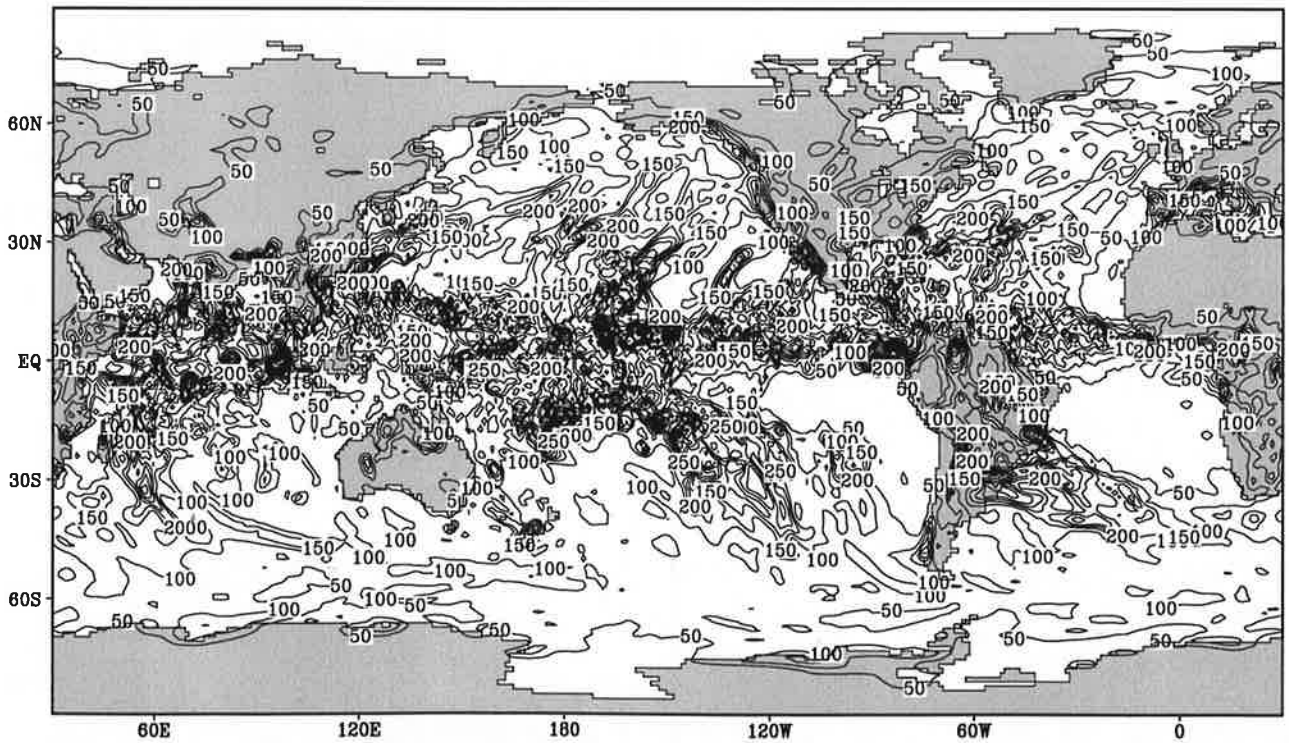

Contour interval: 50 mm month^{-1}

Fig.2.12 Fresh water flux December

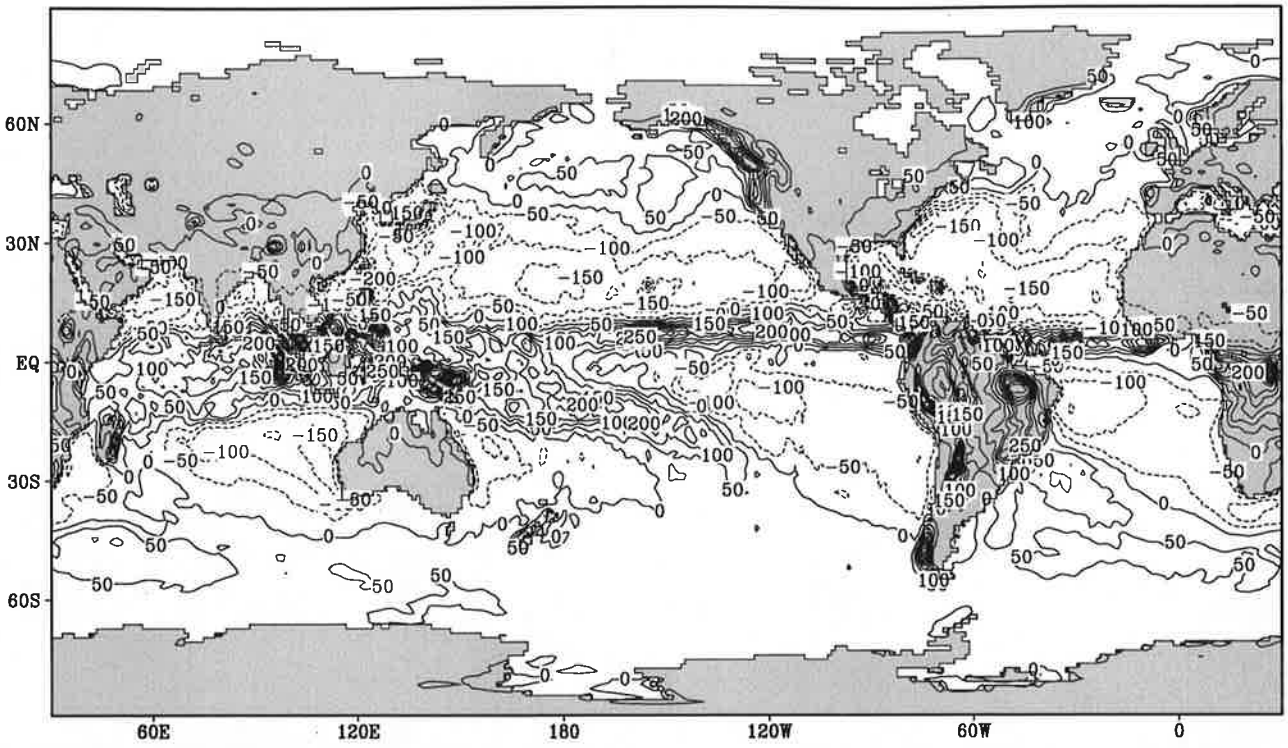

Contour interval: 50 mm month^{-1}

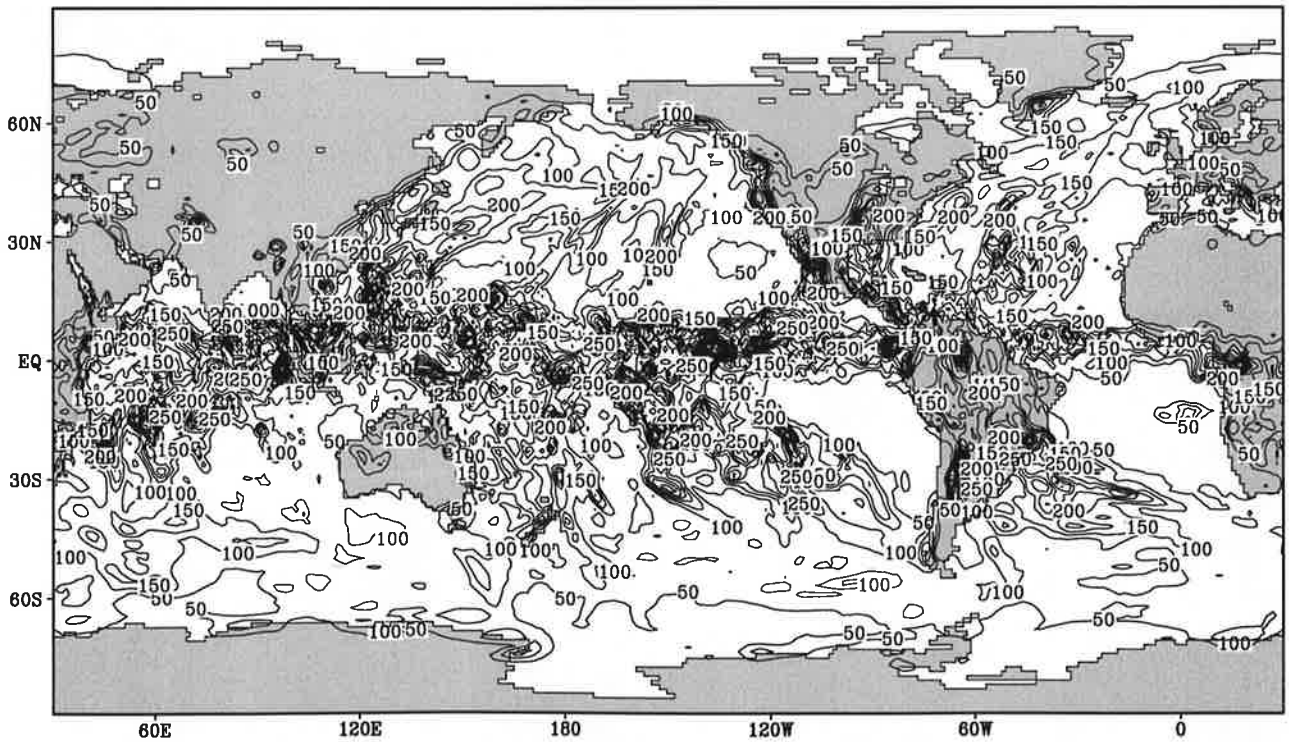

Contour interval: 50 mm month^{-1}

Fig.2.13 Fresh water flux Annual Mean

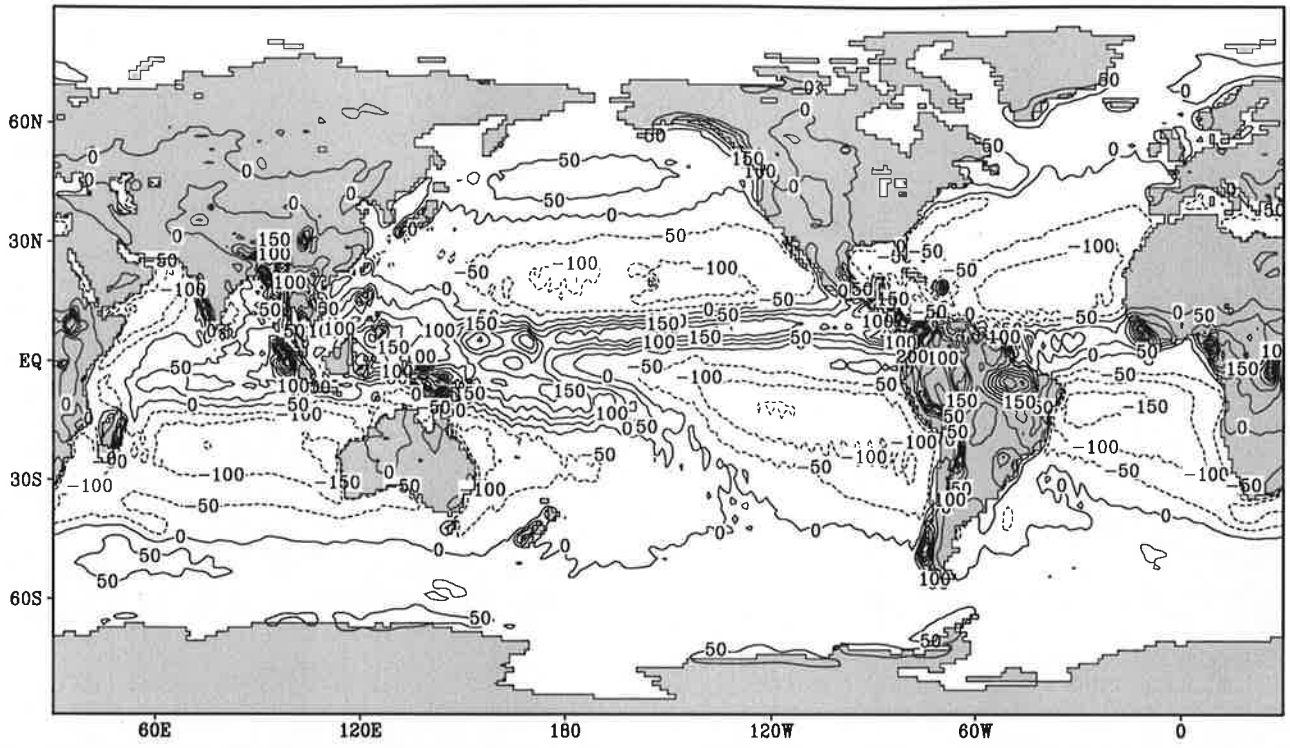

Contour interval: 50 mm month^{-1}

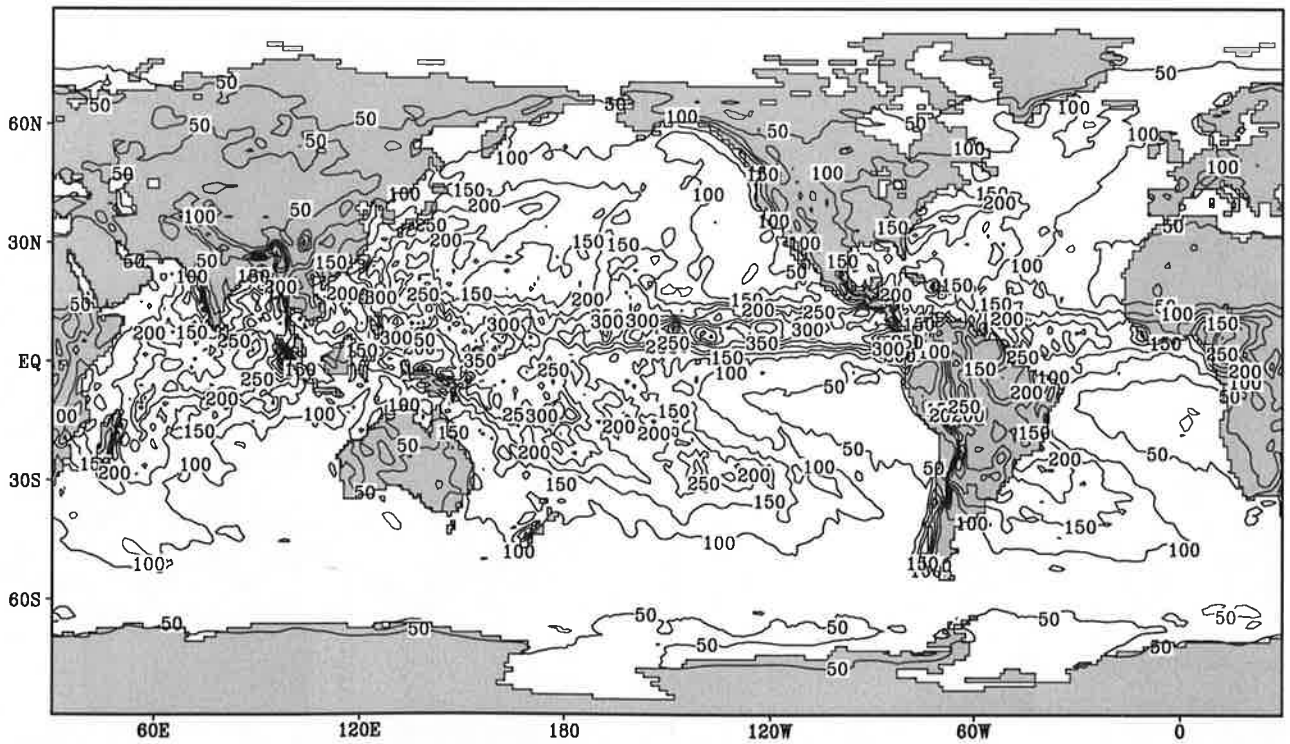

Contour interval: 50 mm month^{-1}

Fig.3.1 Short wave solar radiation January

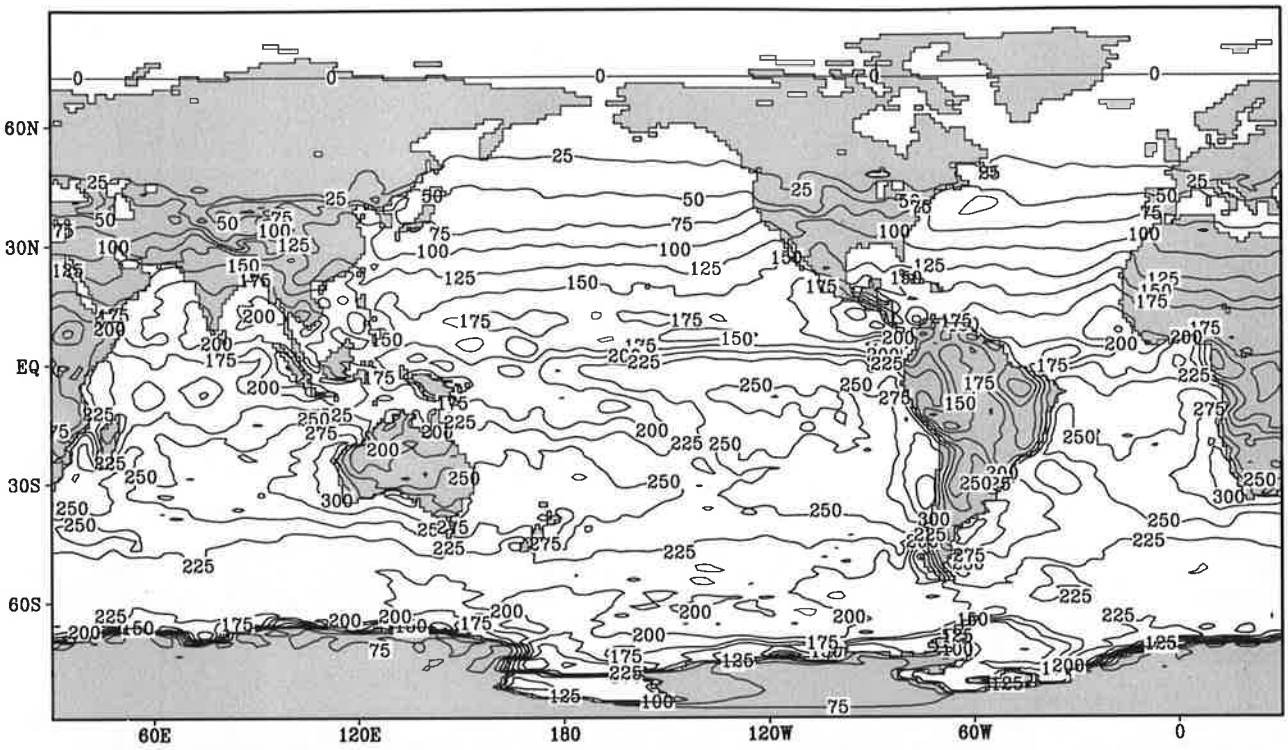

Contour interval: 25 Wm^{-2}

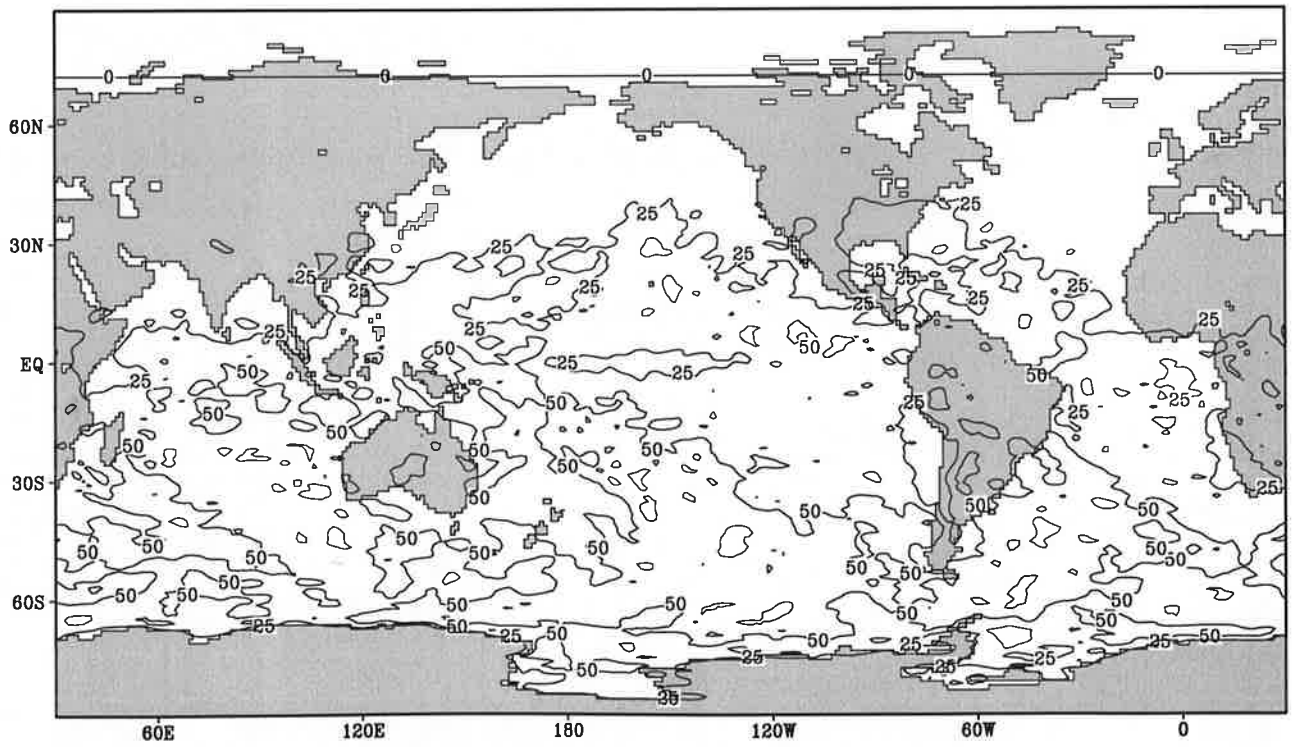

Contour interval: 25 Wm^{-2}

Fig.3.2 Short wave solar radiation February

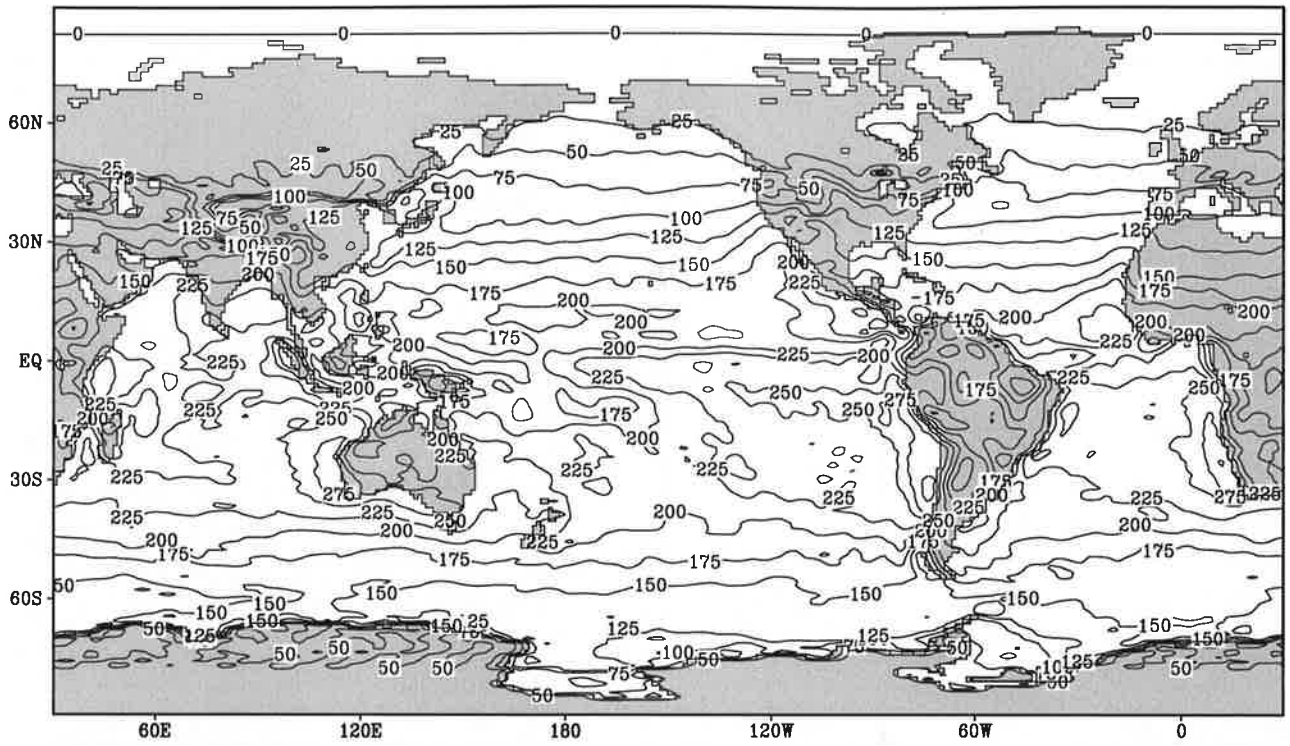

Contour interval: 25 Wm^{-2}

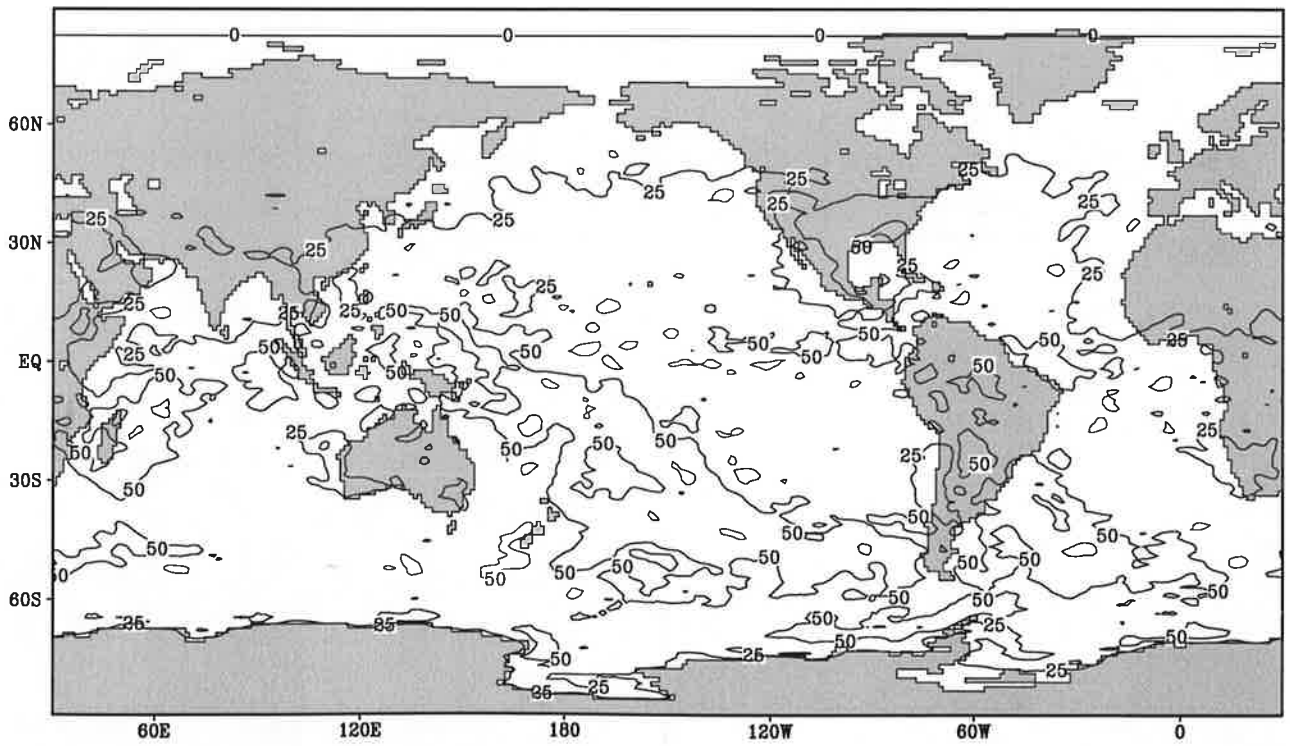

Contour interval: 25 Wm^{-2}

Fig.3.3 Short wave solar radiation March

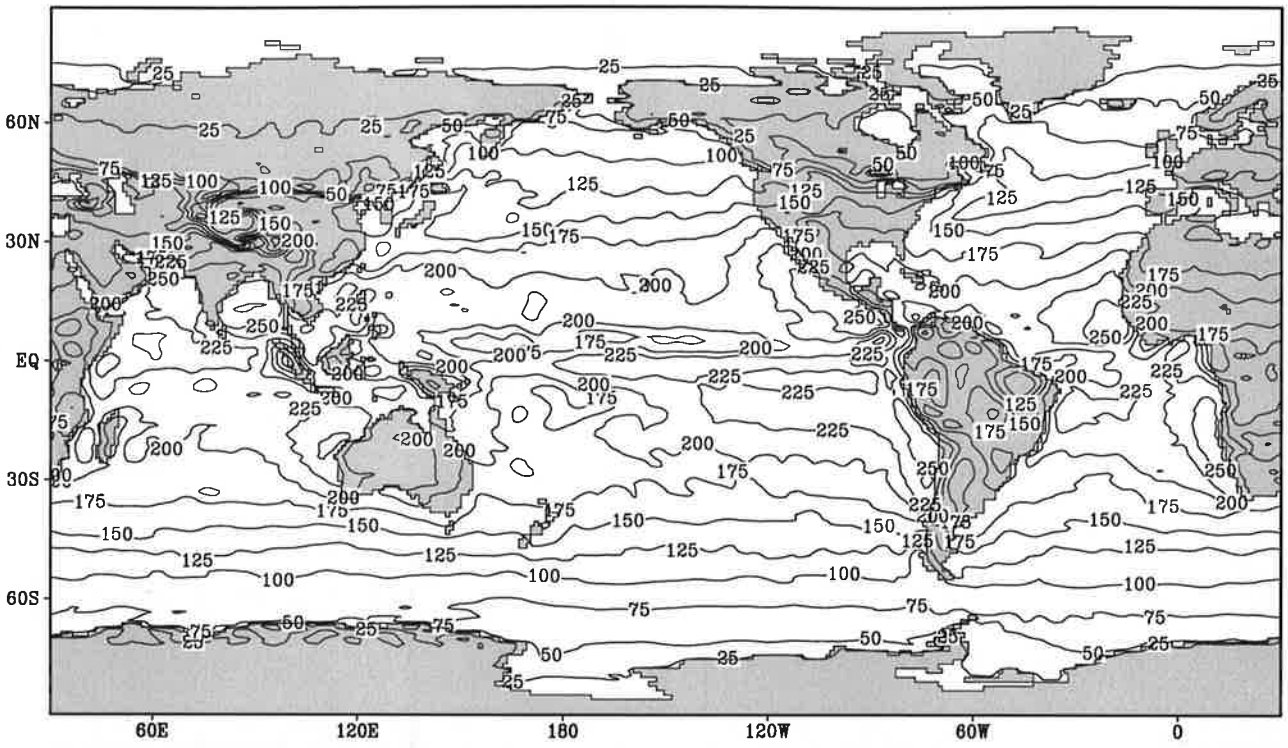

Contour interval: 25 Wm^{-2}

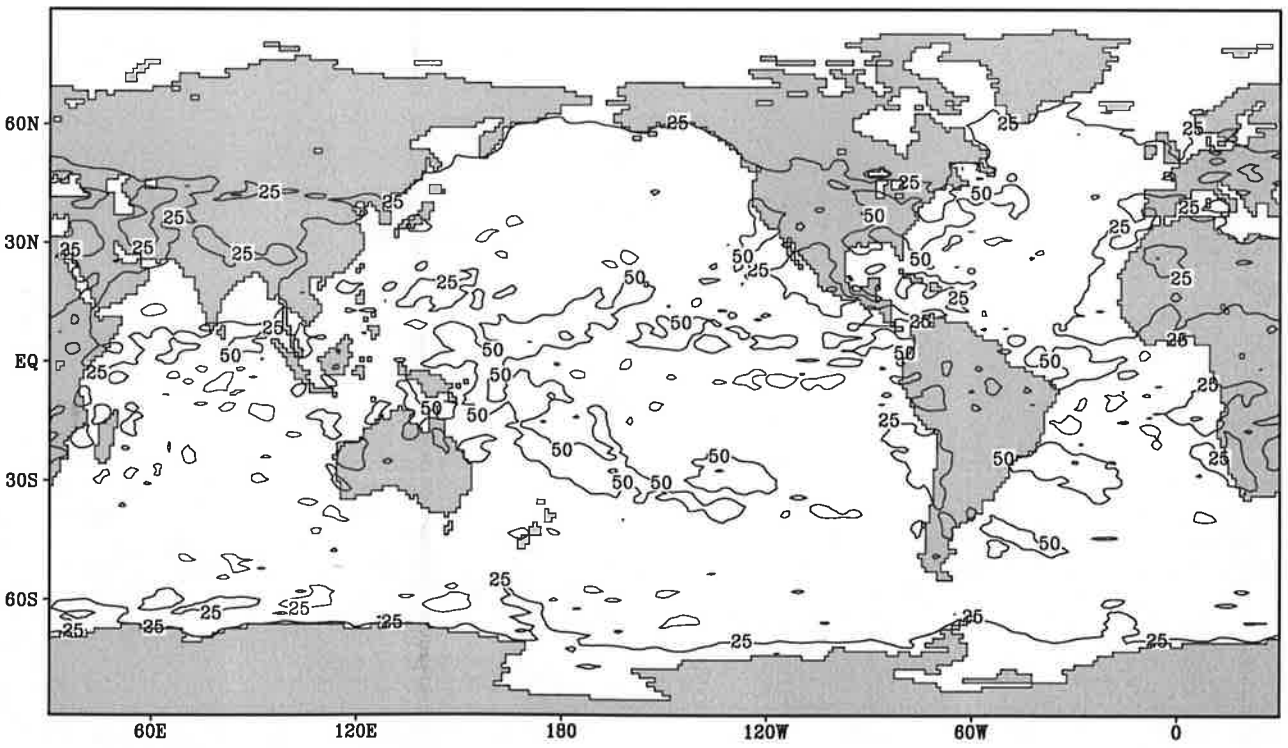

Contour interval: 25 Wm^{-2}

Fig.3.4 Short wave solar radiation April

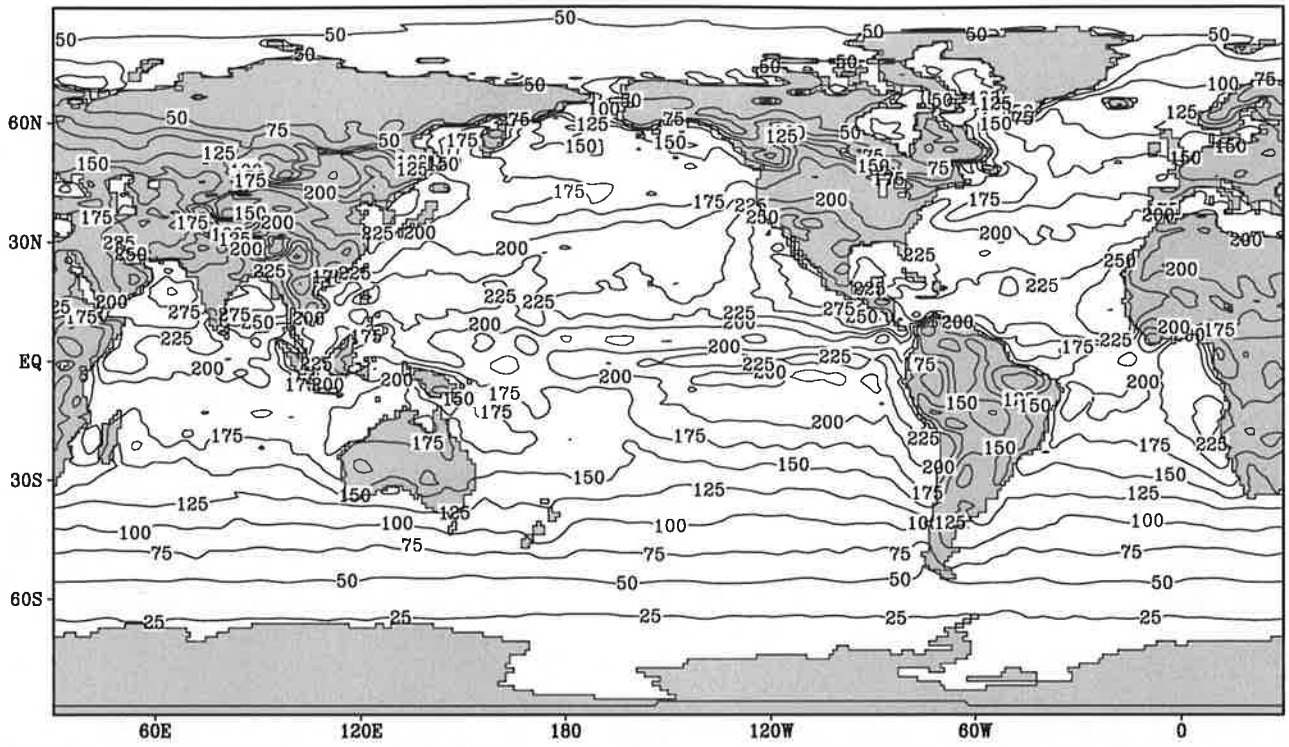

Contour interval: 25 Wm^{-2}

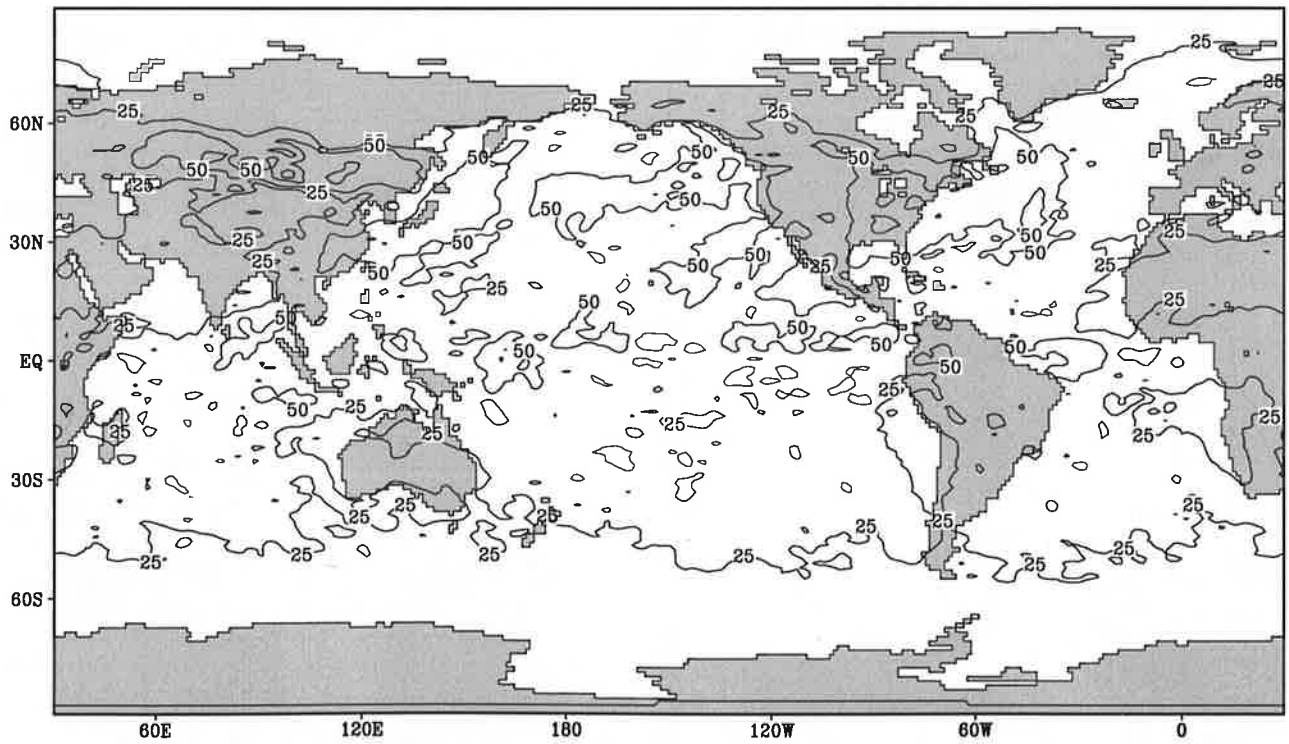

Contour interval: 25 Wm^{-2}

Fig.3.5 Short wave solar radiation May

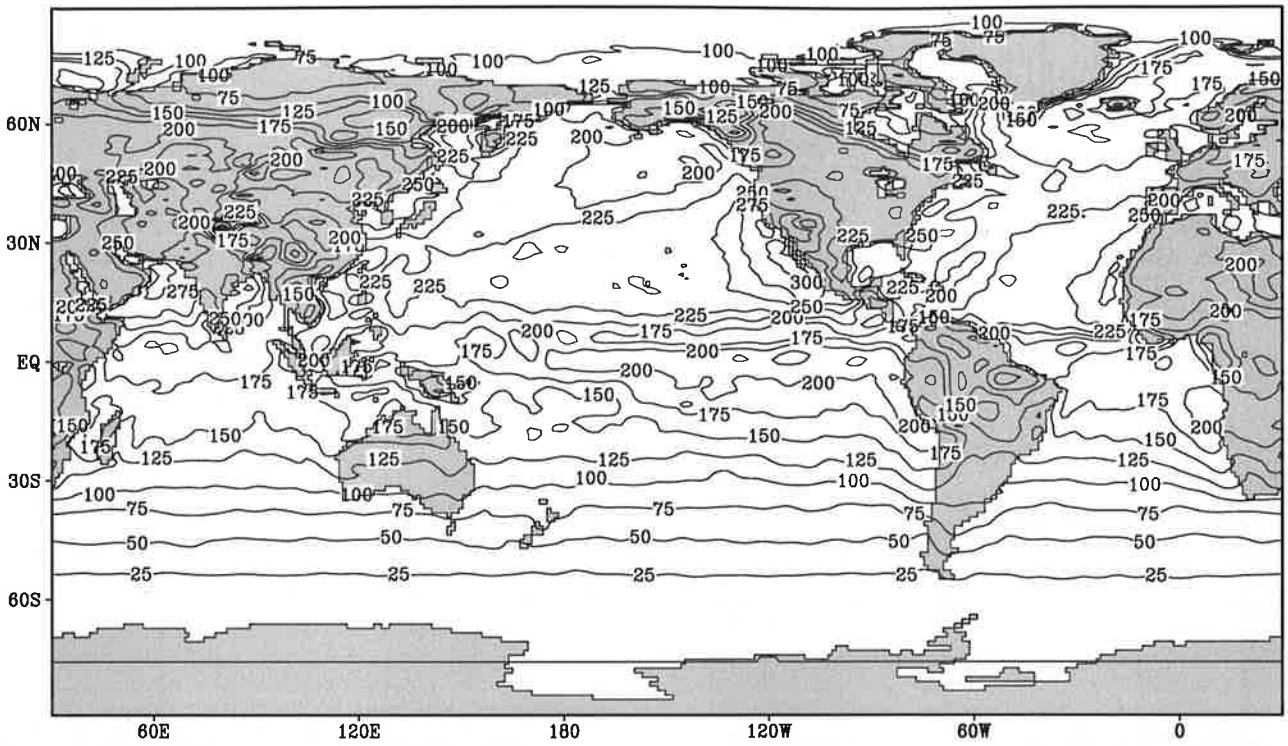

Contour interval: 25 Wm^{-2}

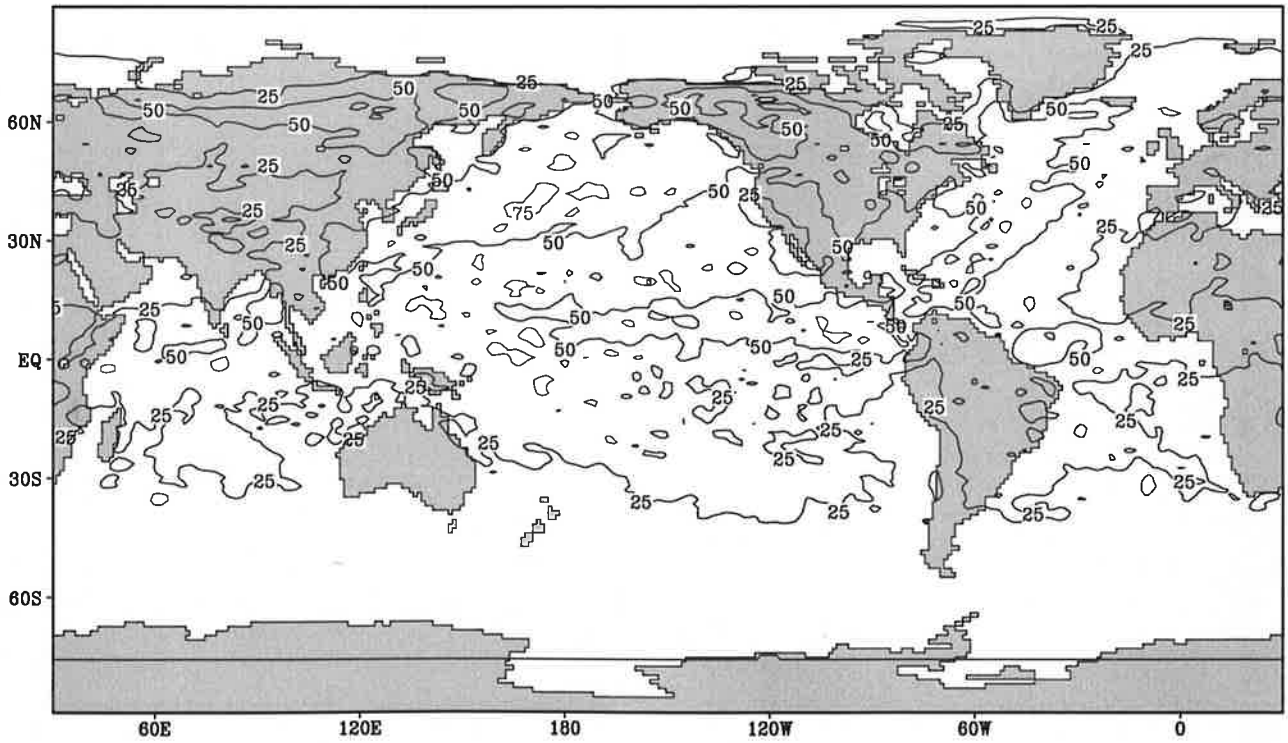

Contour interval: 25 Wm^{-2}

Fig.3.6 Short wave solar radiation June

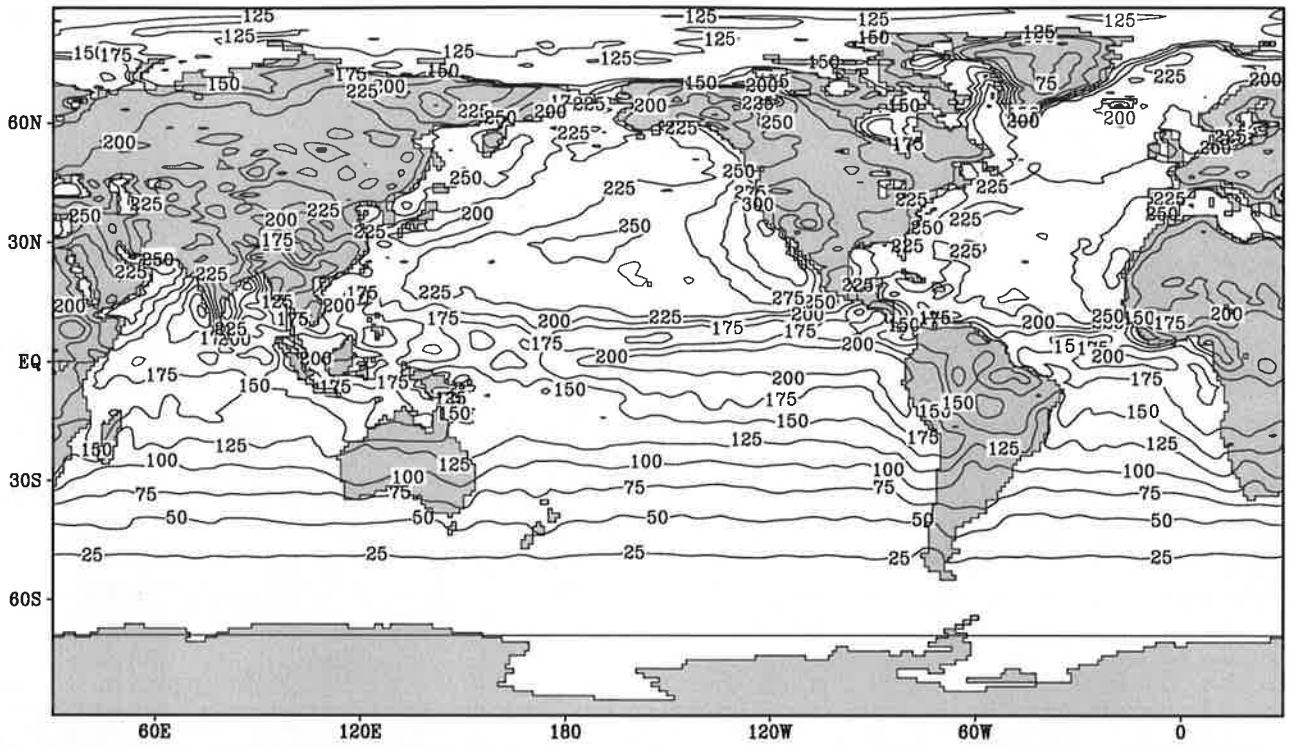

Contour interval: 25 Wm^{-2}

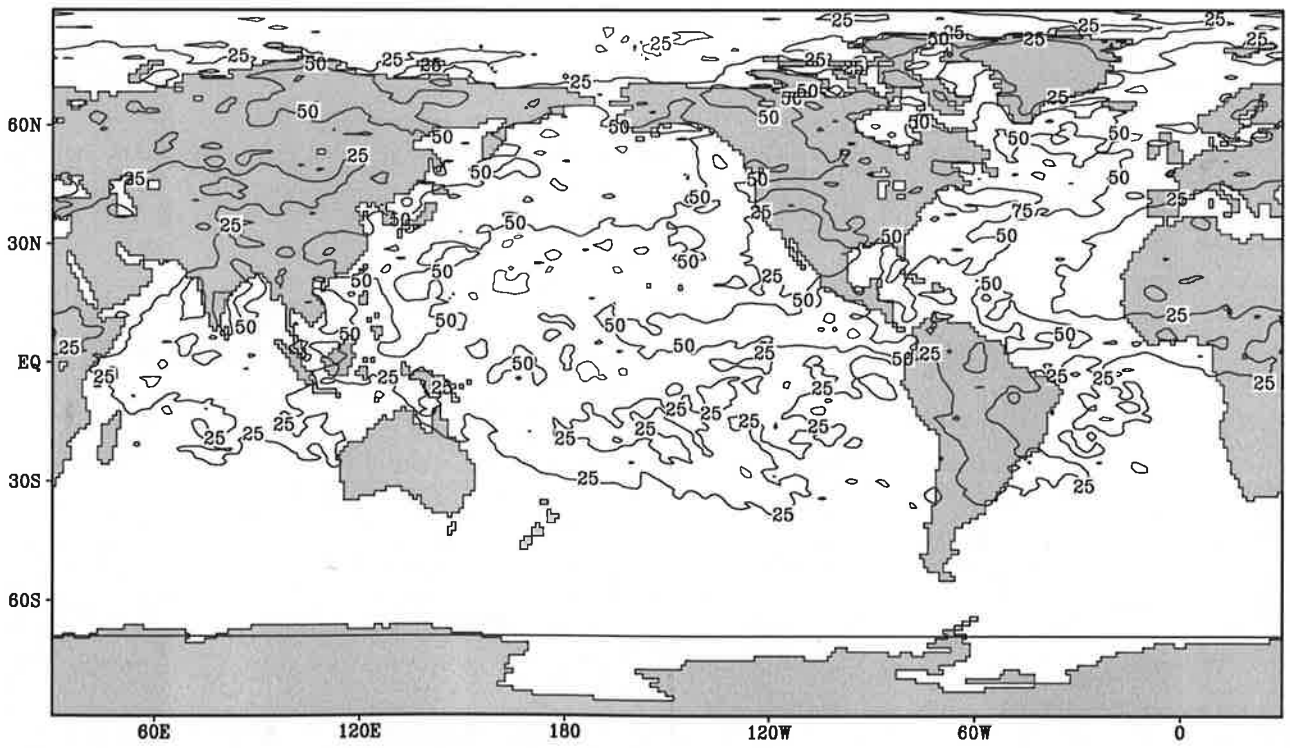

Contour interval: 25 Wm^{-2}

Fig.3.7 Short wave solar radiation July

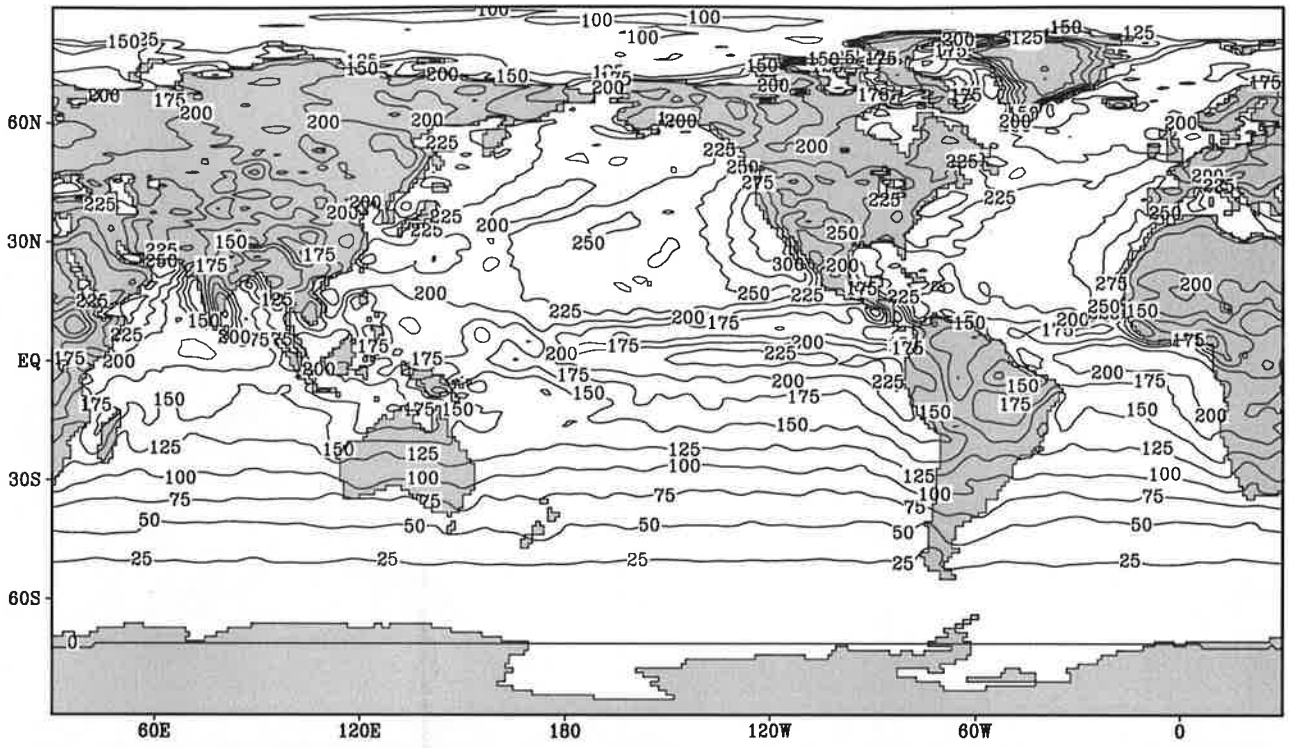

Contour interval: 25 Wm^{-2}

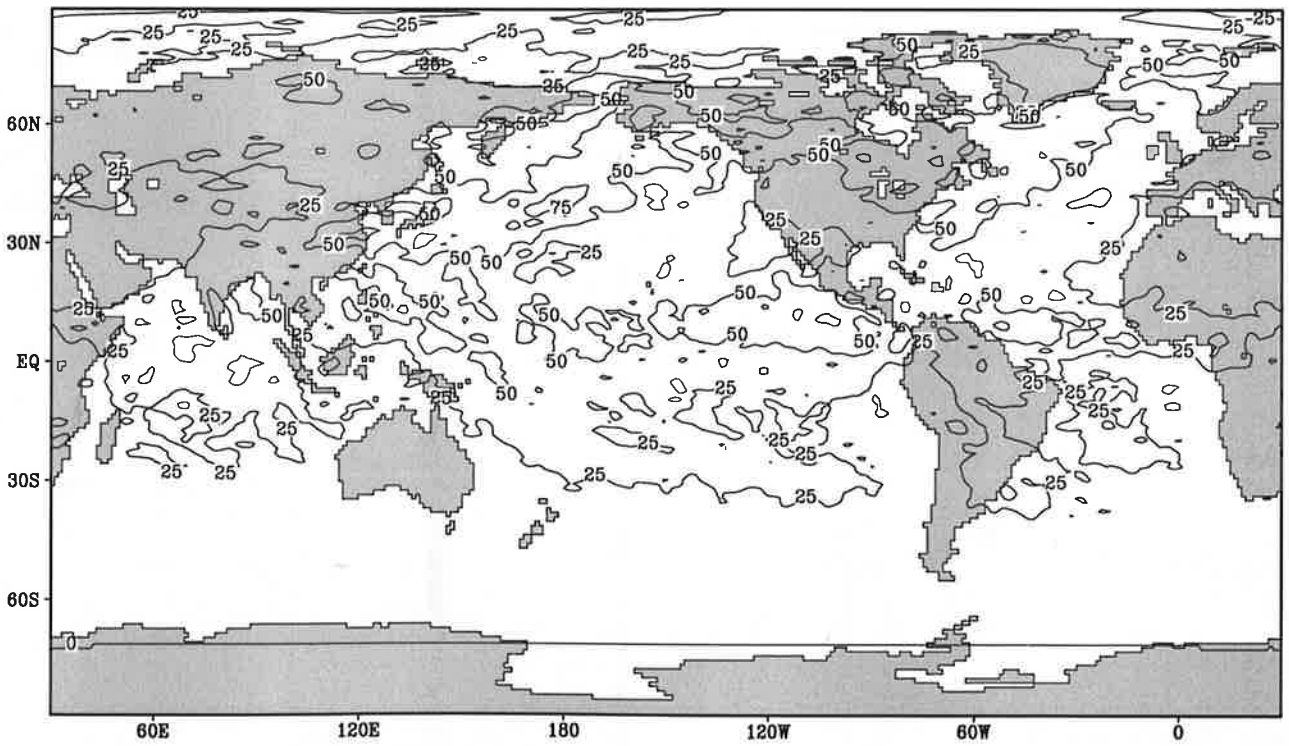

Contour interval: 25 Wm^{-2}

Fig.3.8 Short wave solar radiation August

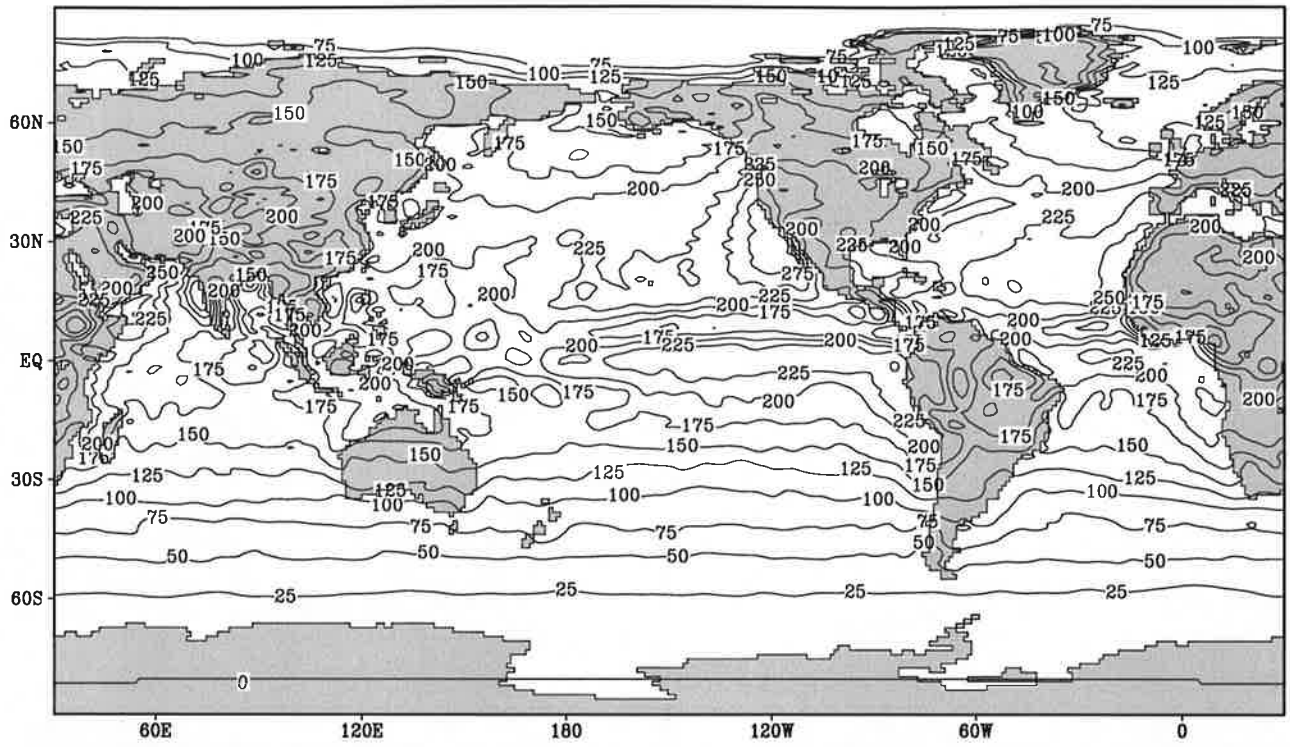

Contour interval: 25 Wm^{-2}

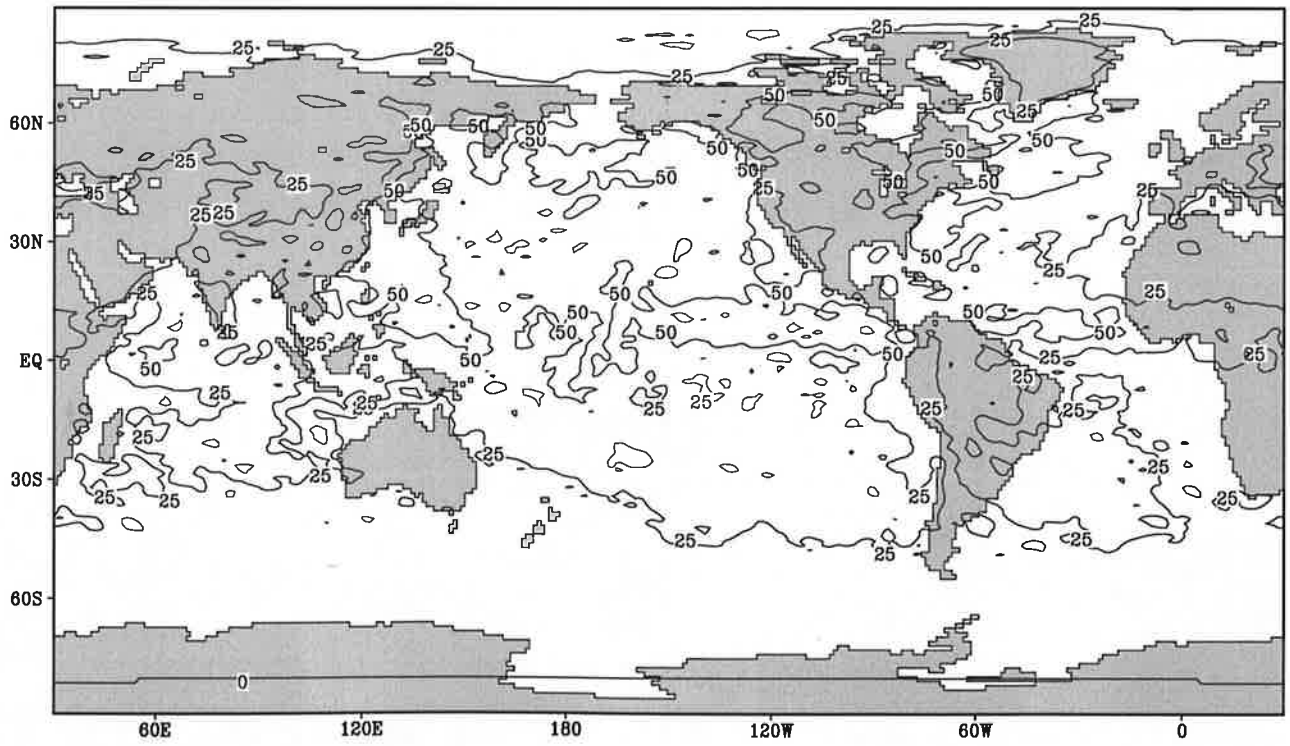

Contour interval: 25 Wm^{-2}

Fig.3.9 Short wave solar radiation September

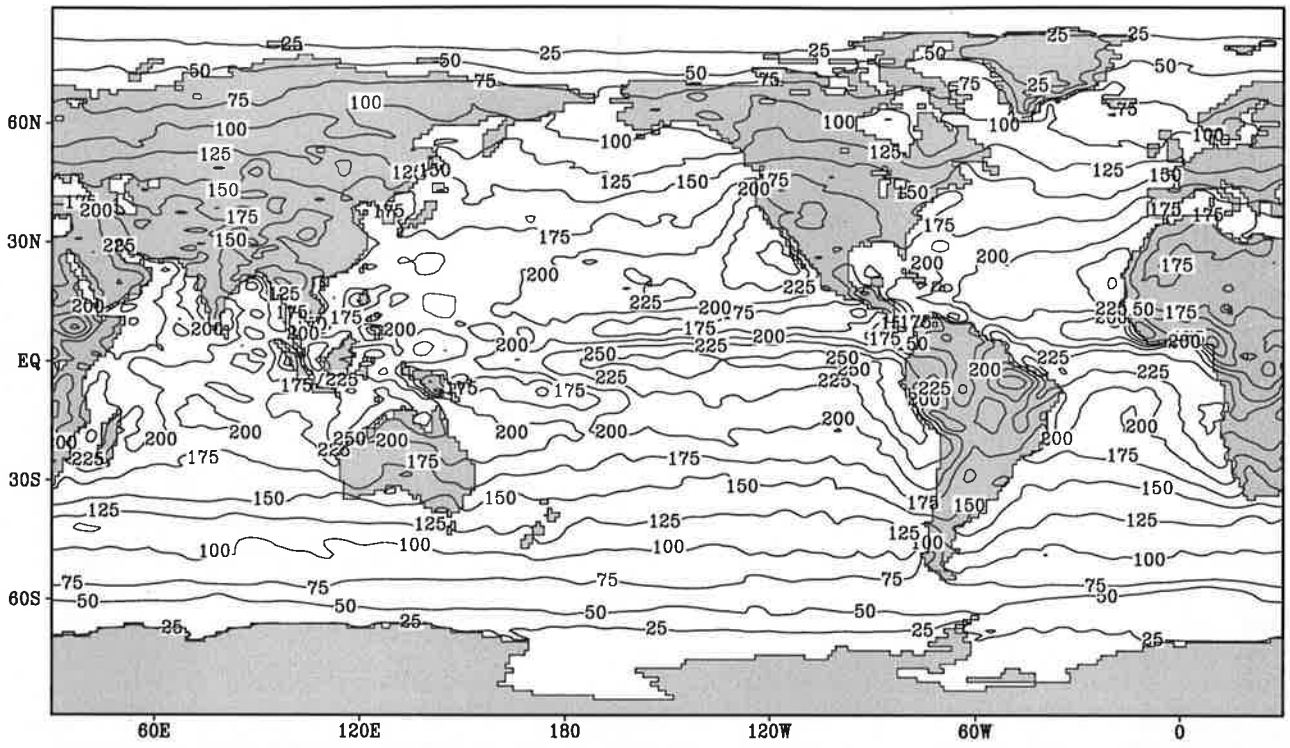

Contour interval: 25 Wm^{-2}

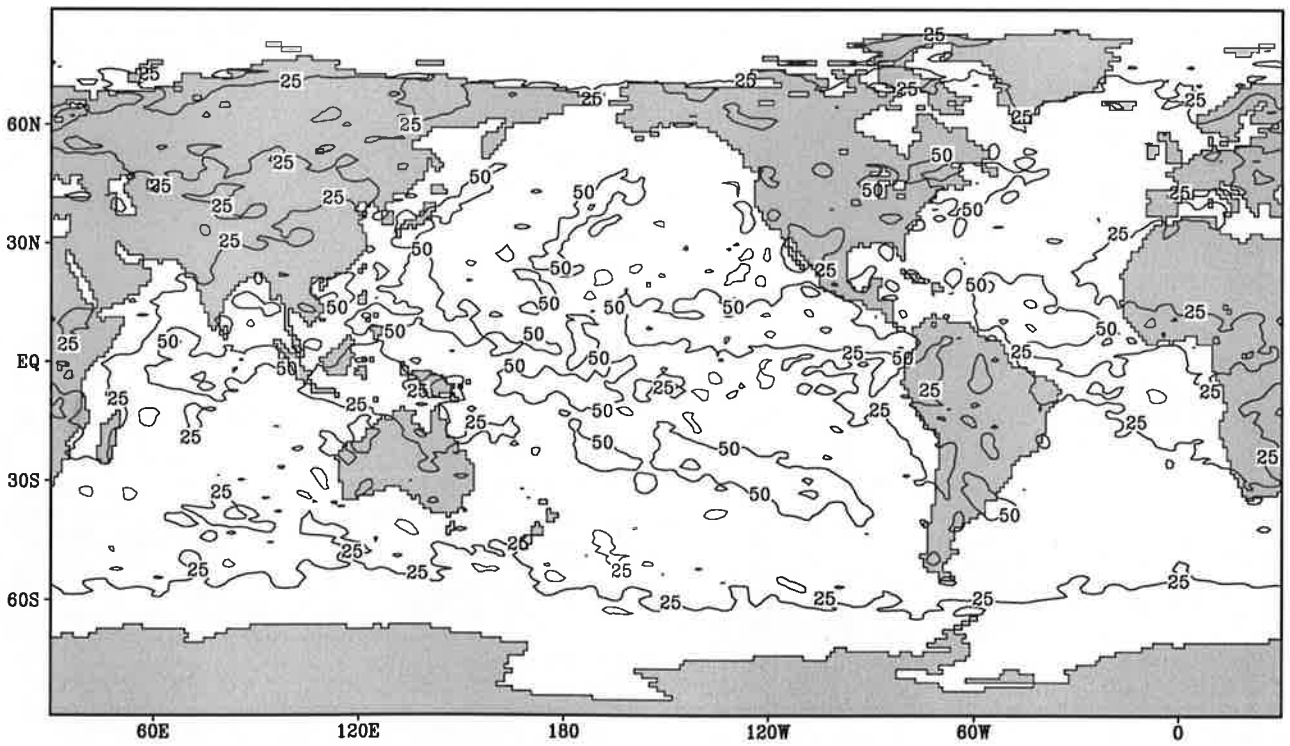

Contour interval: 25 Wm^{-2}

Fig.3.10 Short wave solar radiation October

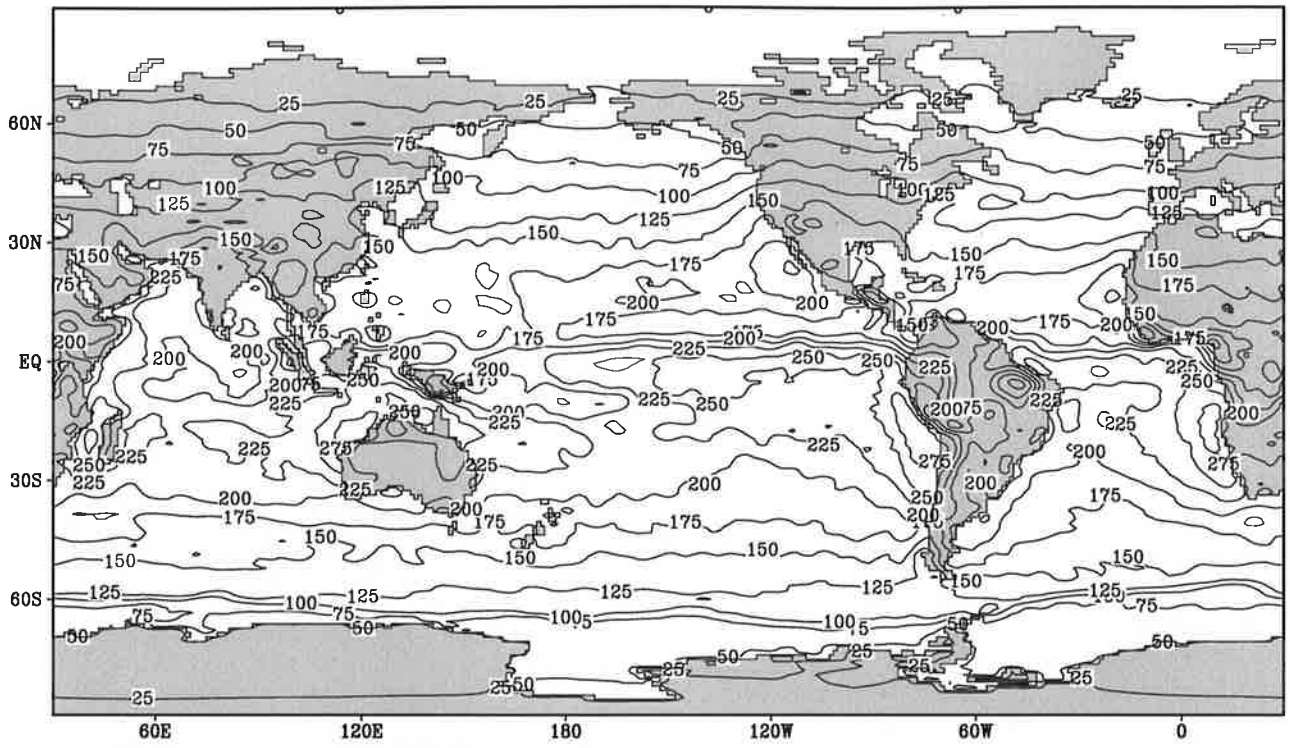

Contour interval: 25 Wm^{-2}

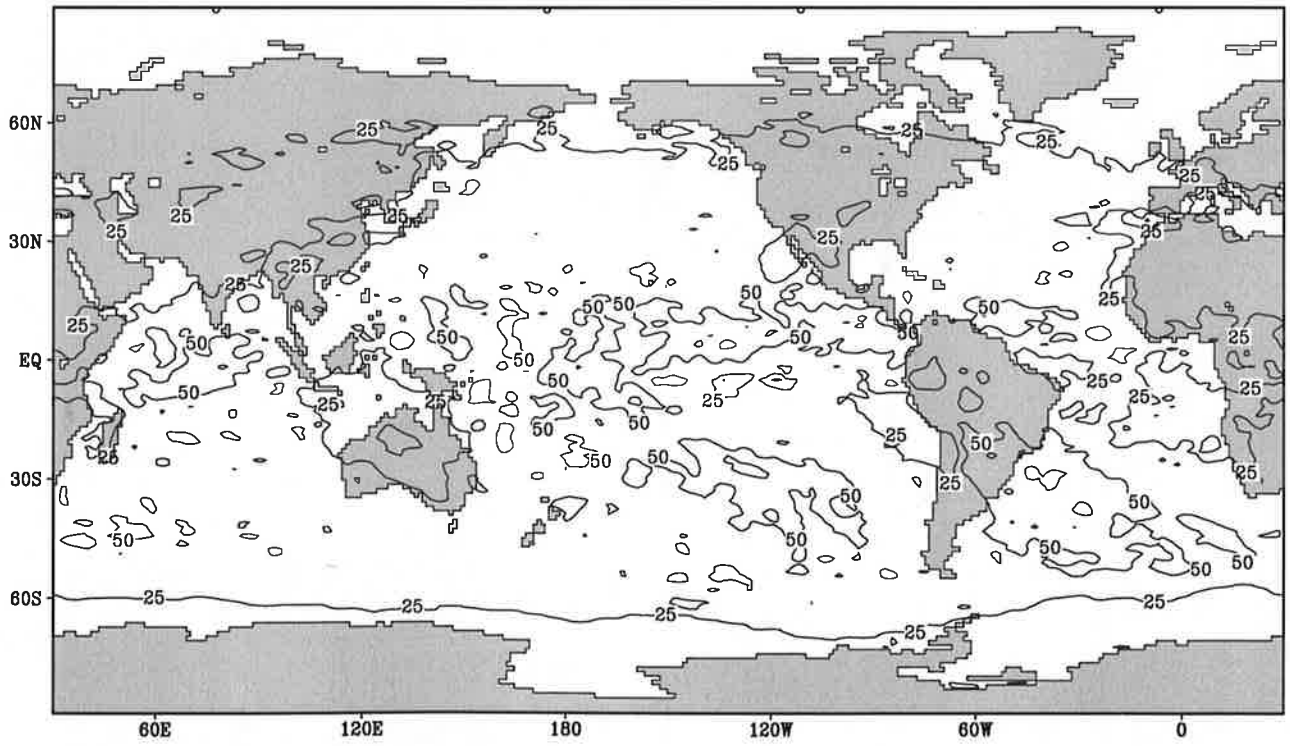

Contour interval: 25 Wm^{-2}

Fig.3.11 Short wave solar radiation November

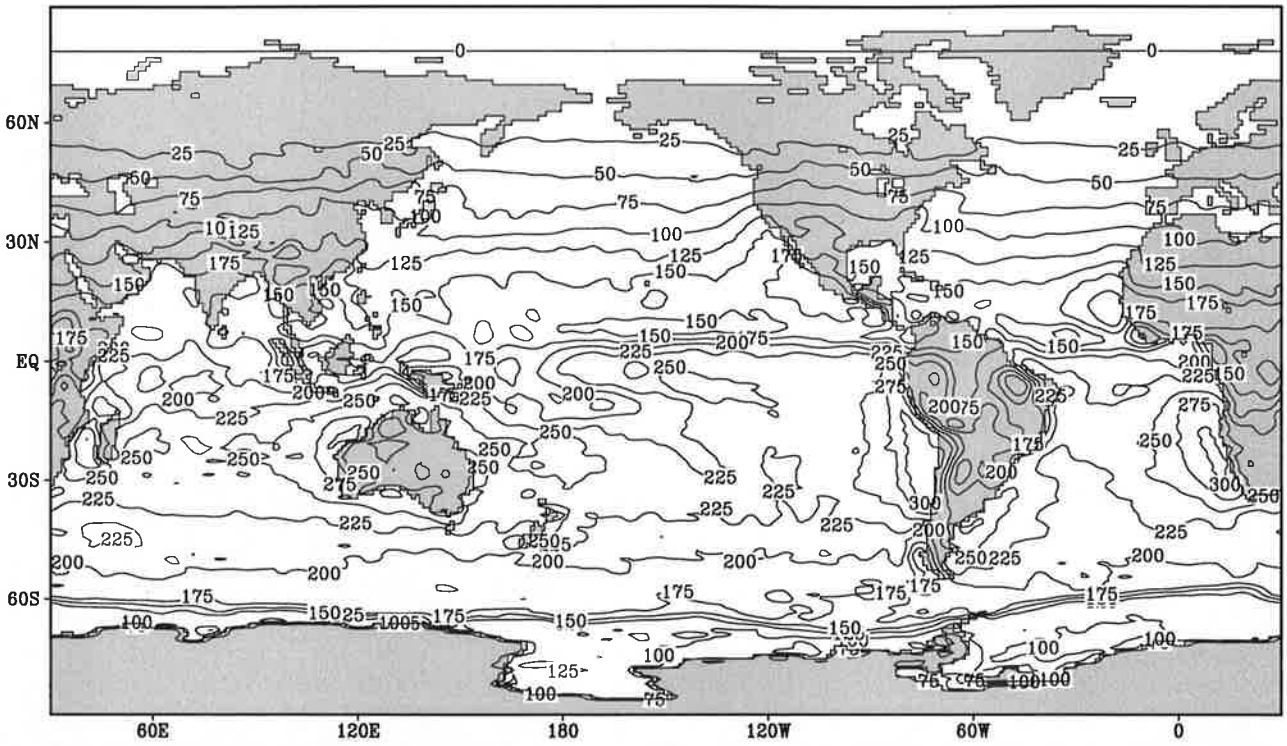

Contour interval: 25 Wm^{-2}

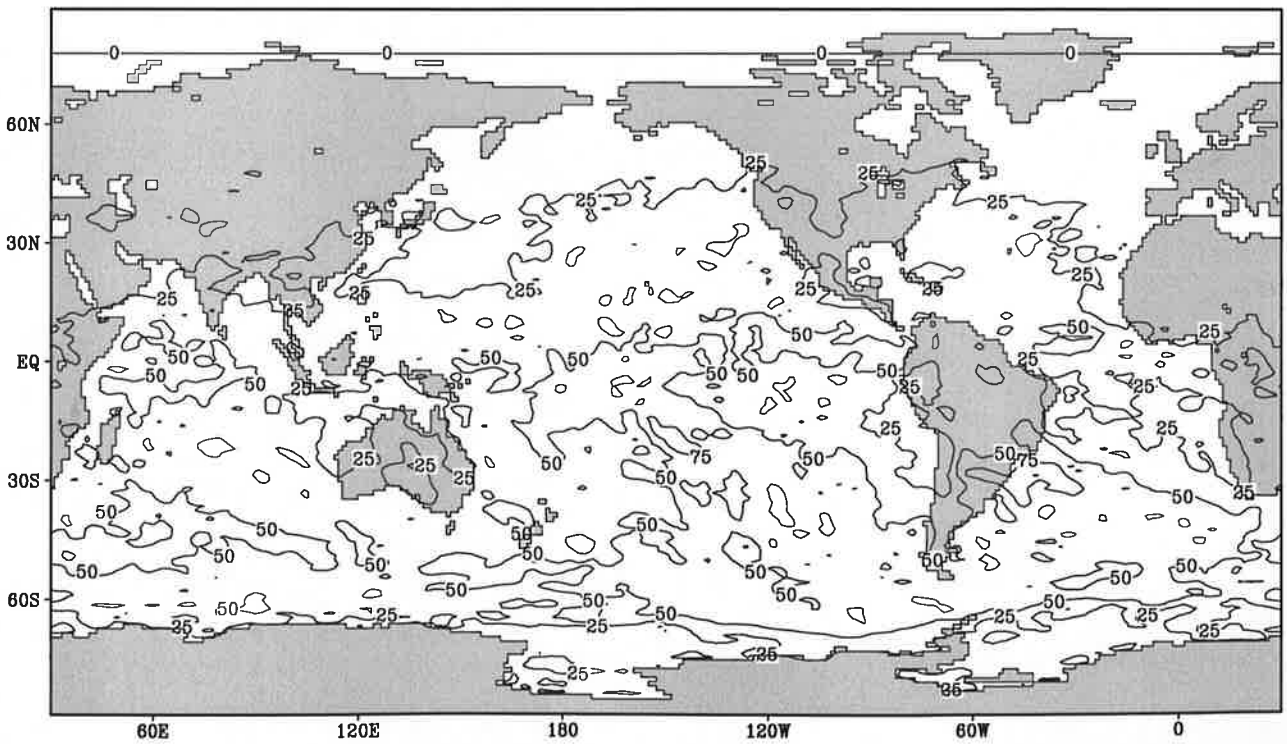

Contour interval: 25 Wm^{-2}

Fig.3.12 Short wave solar radiation December

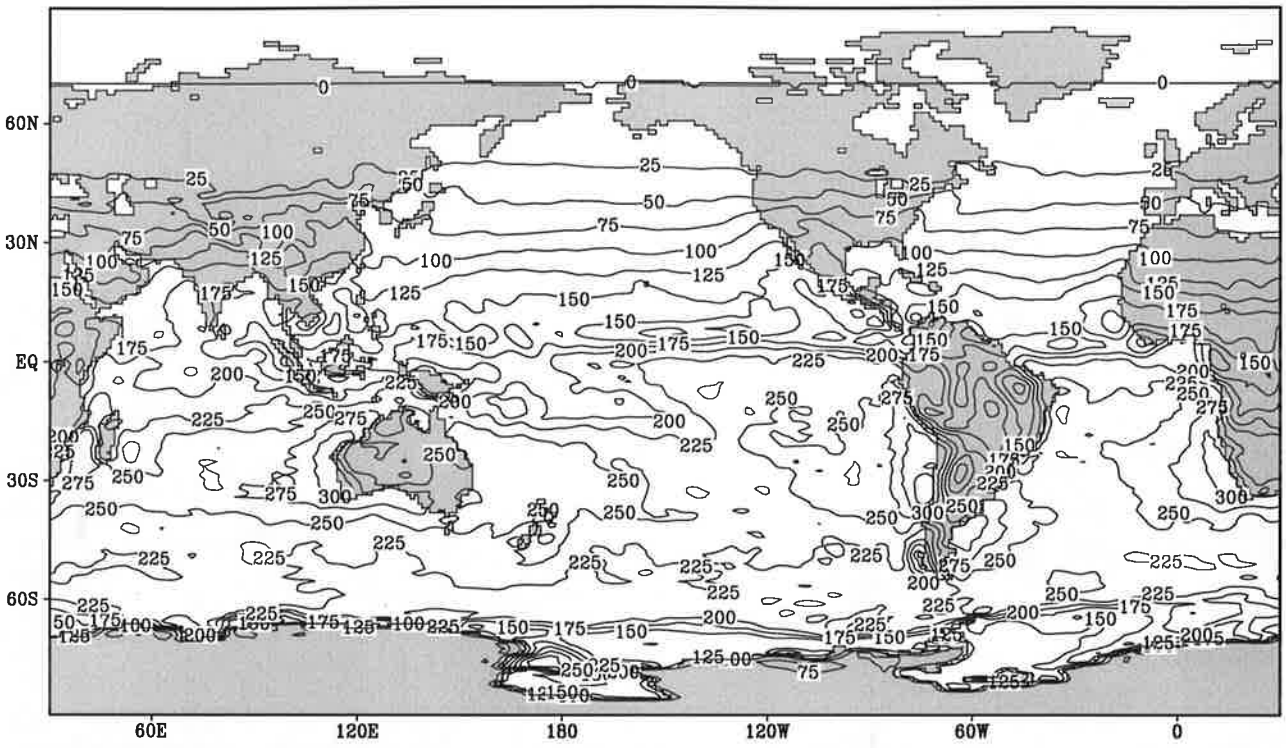

Contour interval: 25 Wm^{-2}

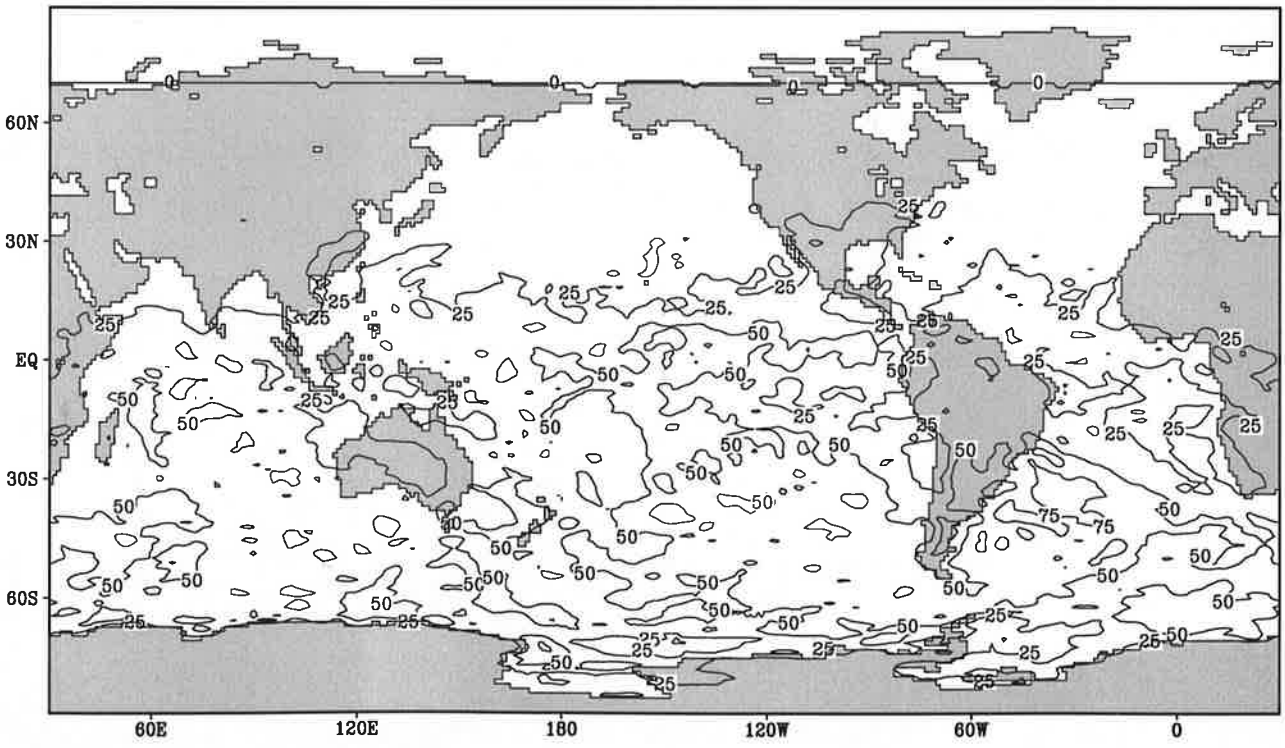

Contour interval: 25 Wm^{-2}

Fig.3.13 Short wave solar radiation Annual Mean

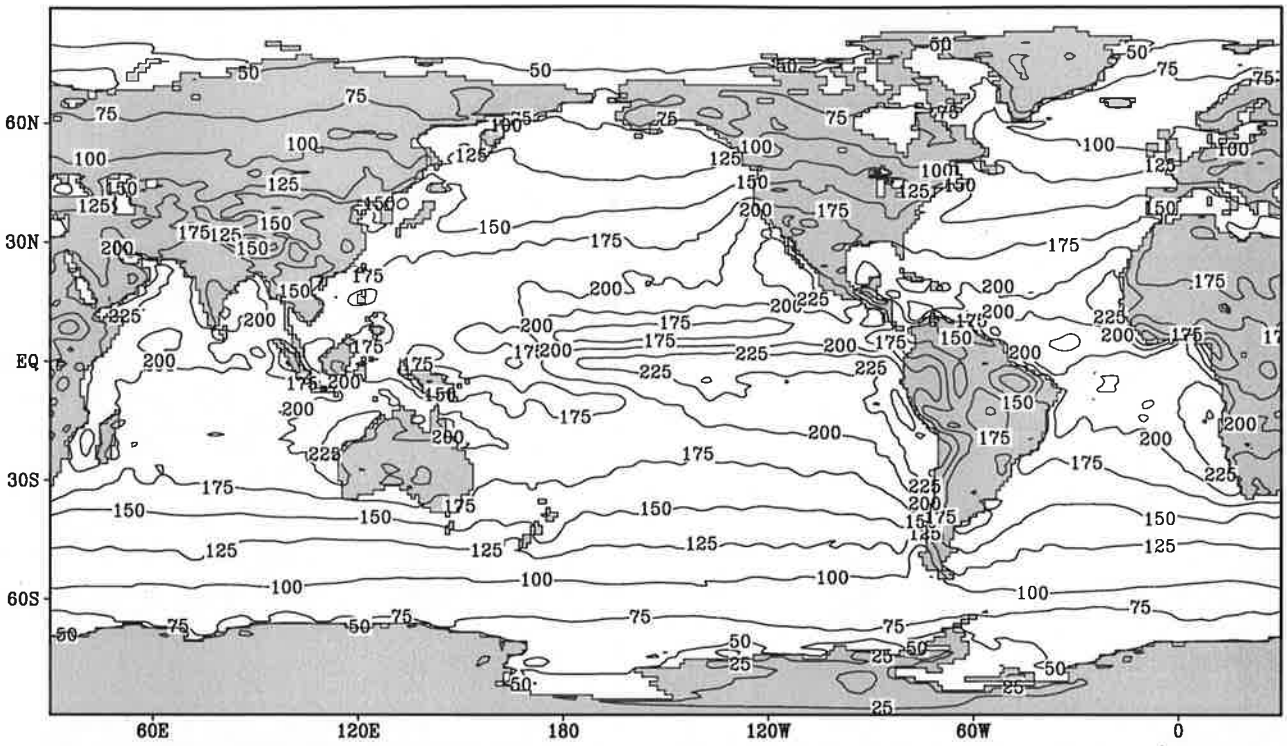

Contour interval: 25 Wm^{-2}

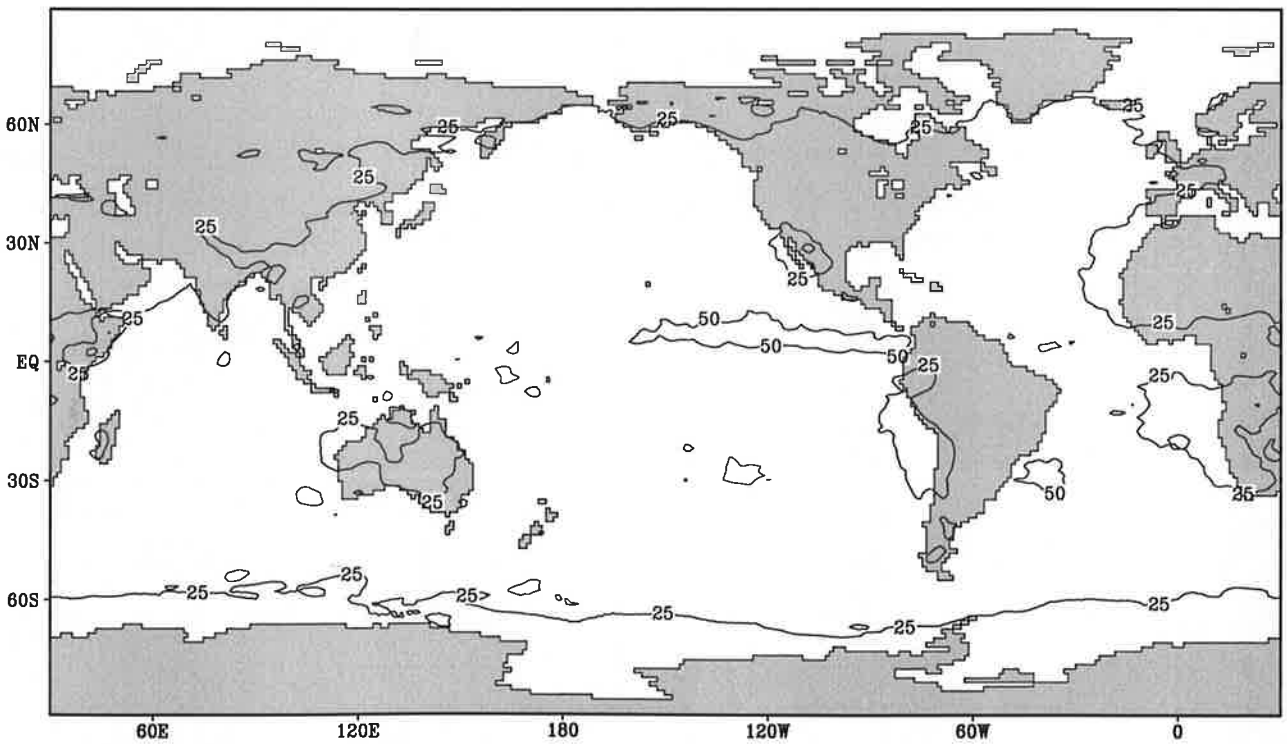

Contour interval: 25 Wm^{-2}

Fig.4.1 Long wave radiation January

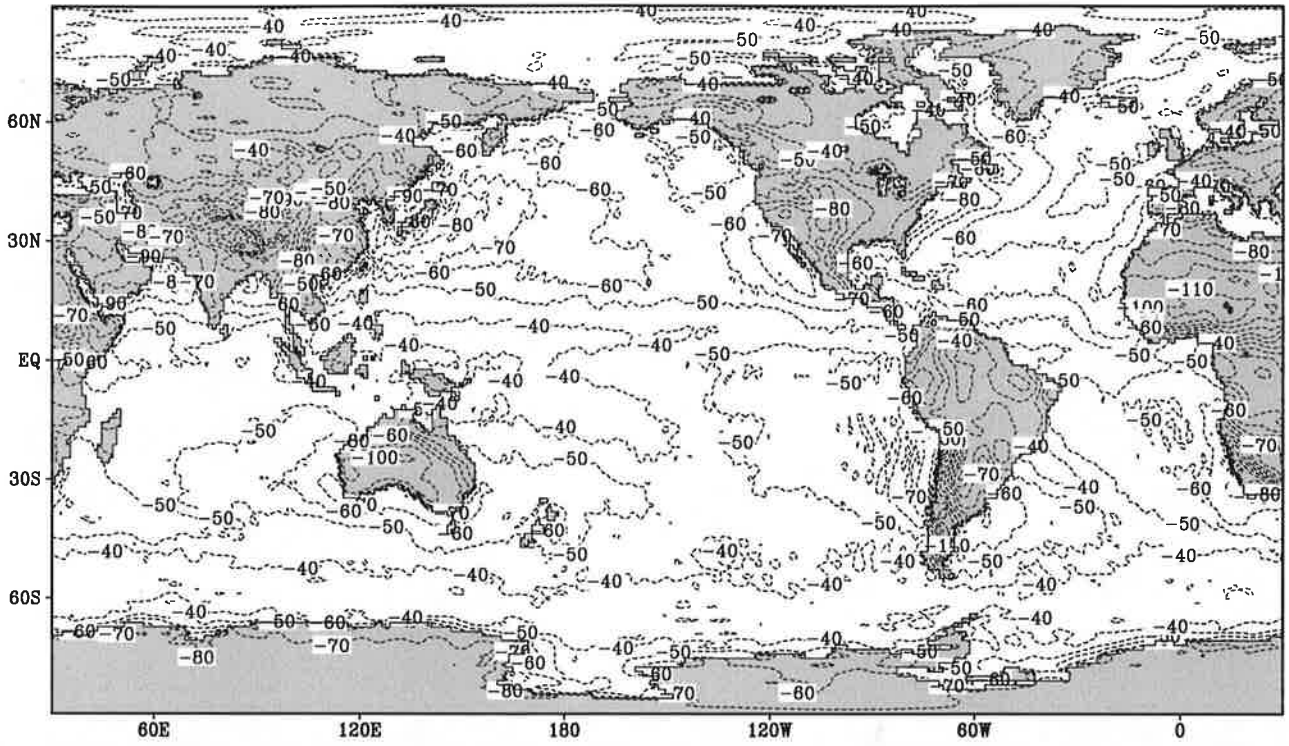

Contour interval: 10 Wm^{-2}

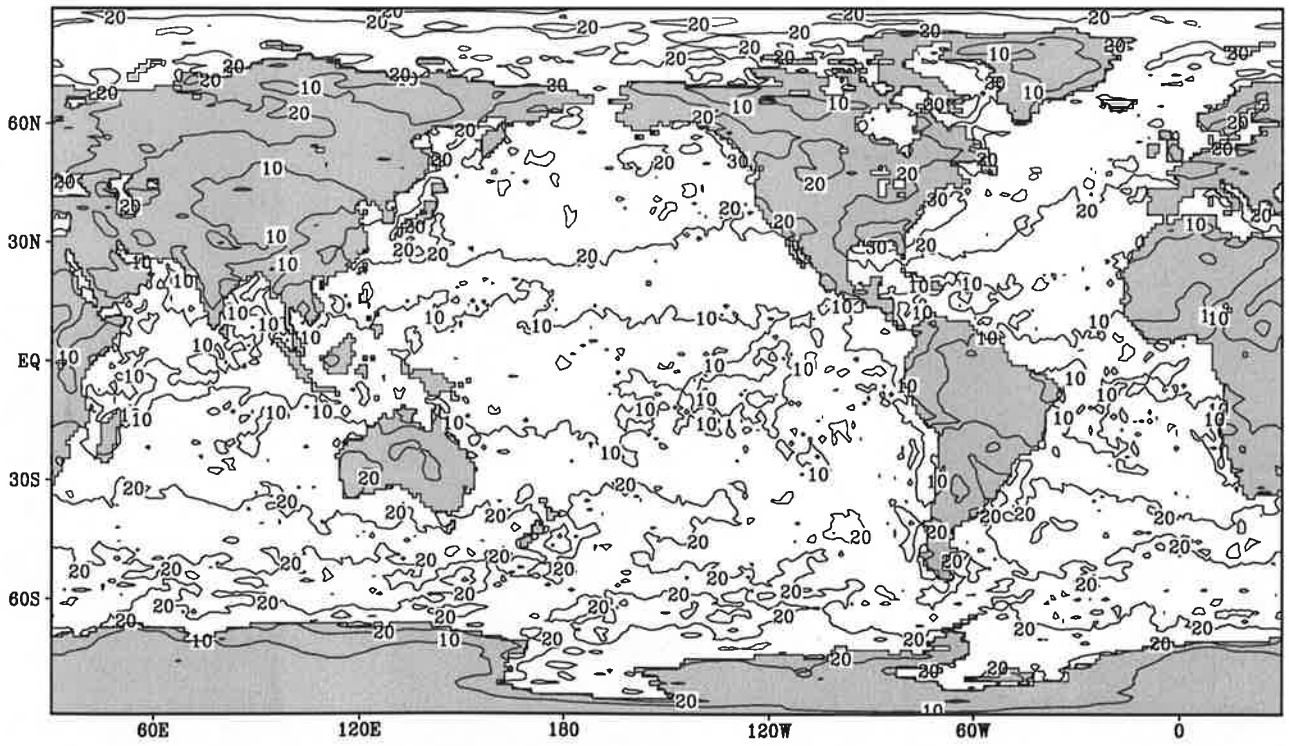

Contour interval: 10 Wm^{-2}

Fig.4.2 Long wave radiation February

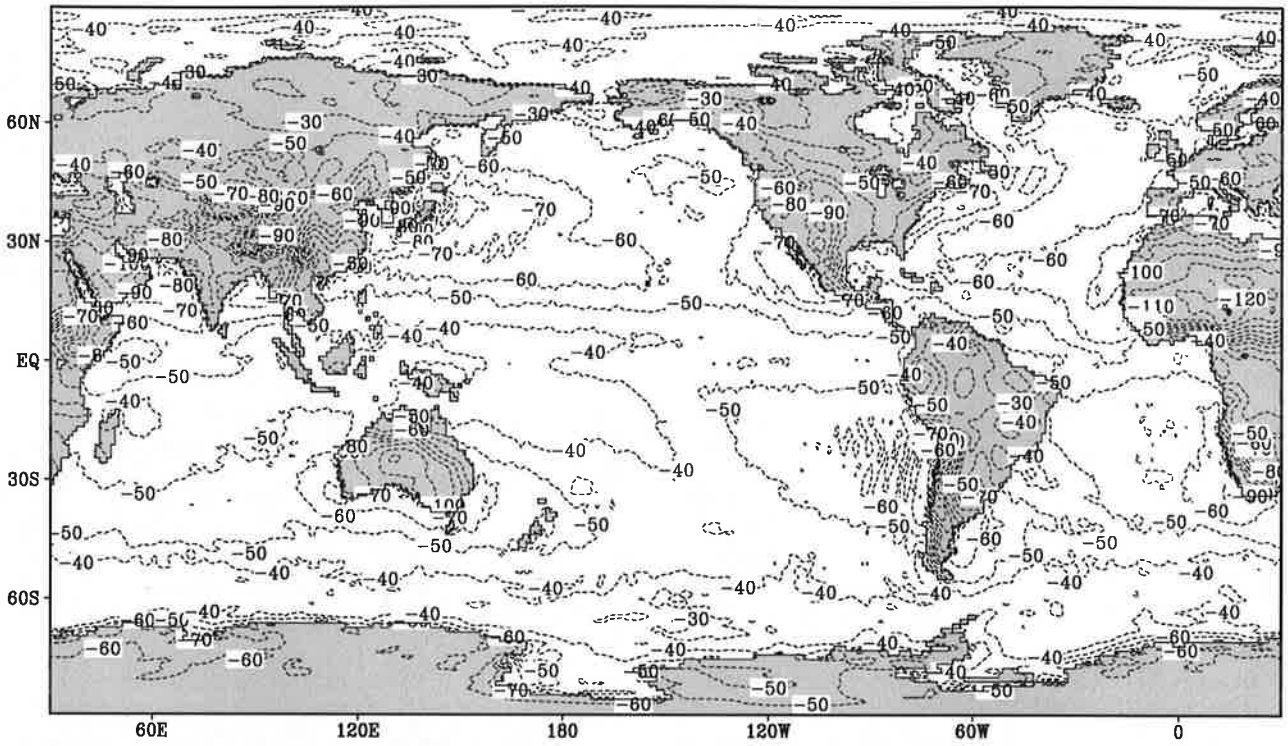

Contour interval: 10 Wm^{-2}

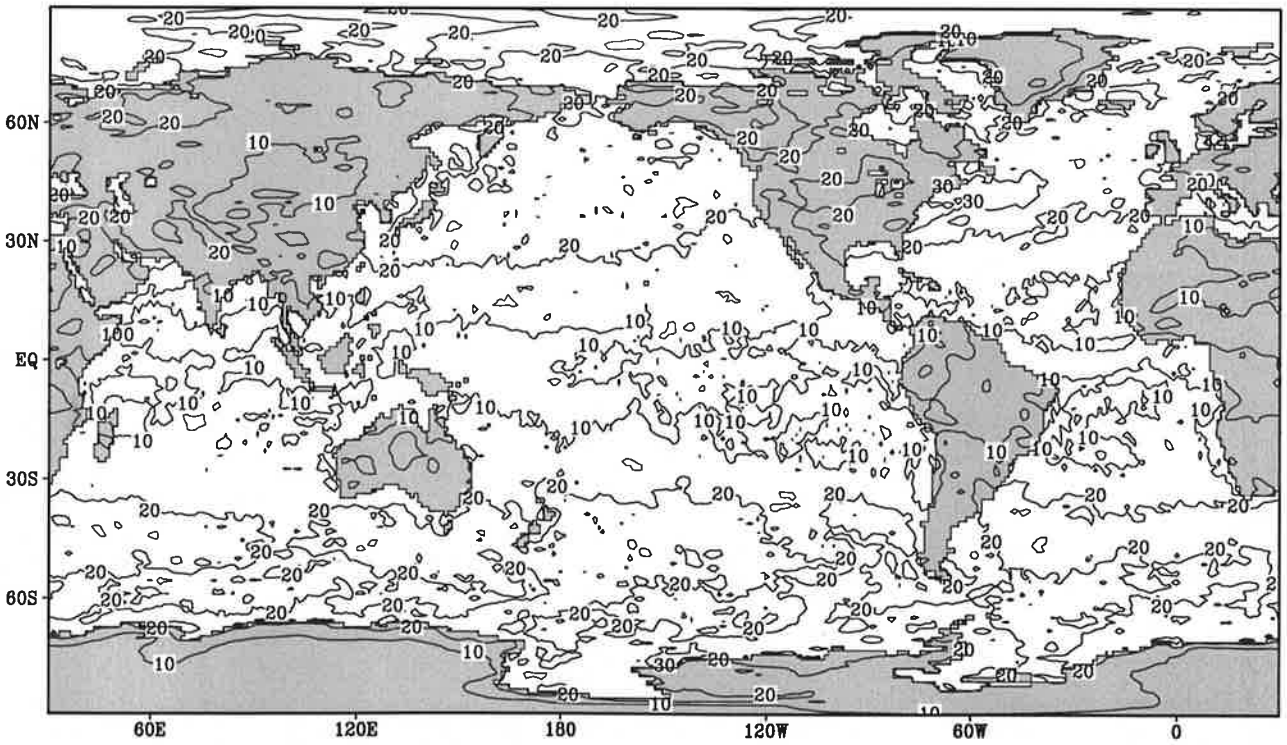

Contour interval: 10 Wm^{-2}

Fig.4.3 Long wave radiation March

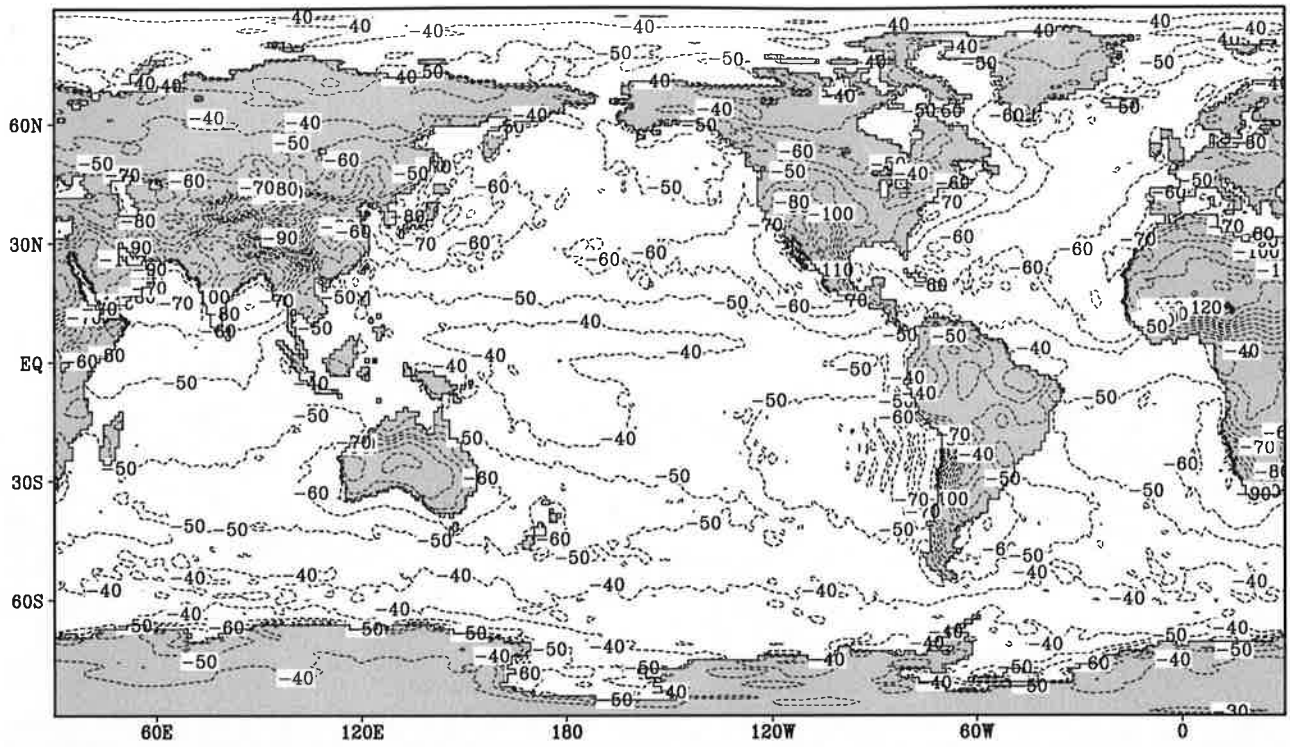

Contour interval: 10 Wm^{-2}

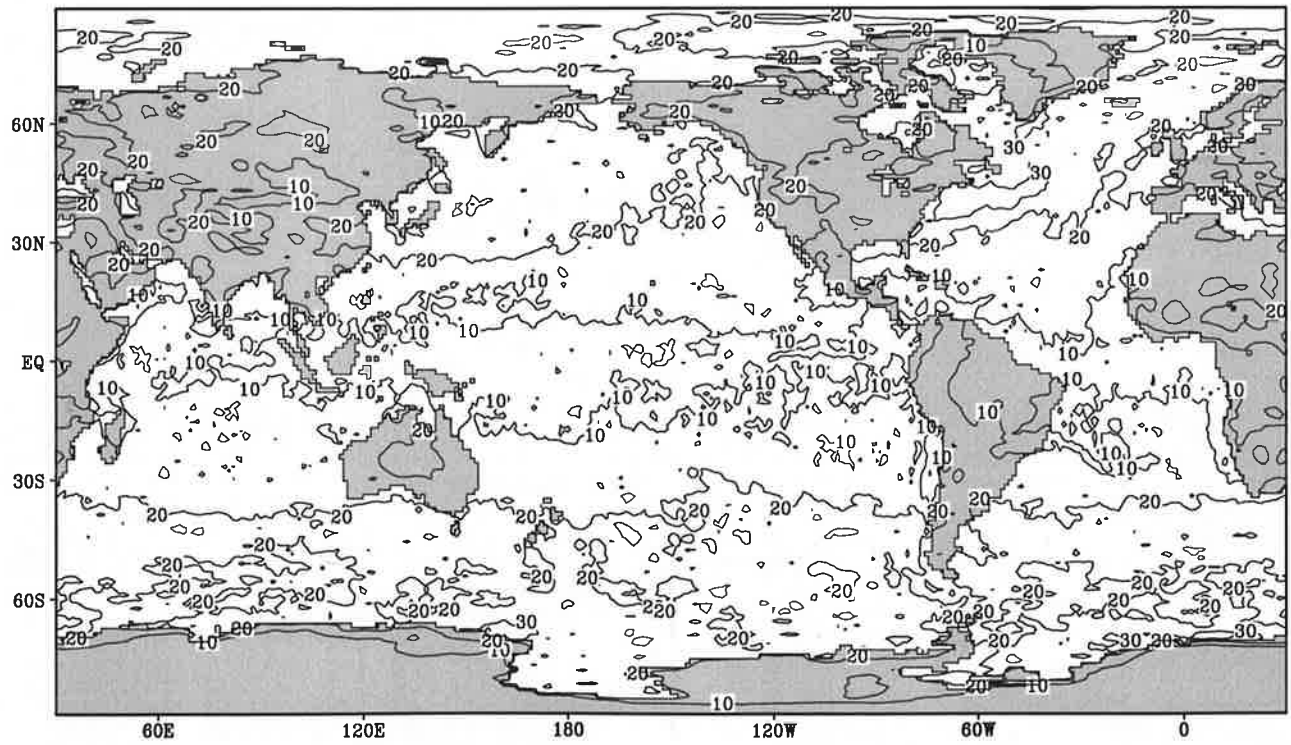

Contour interval: 10 Wm^{-2}

Fig.4.4 Long wave radiation April

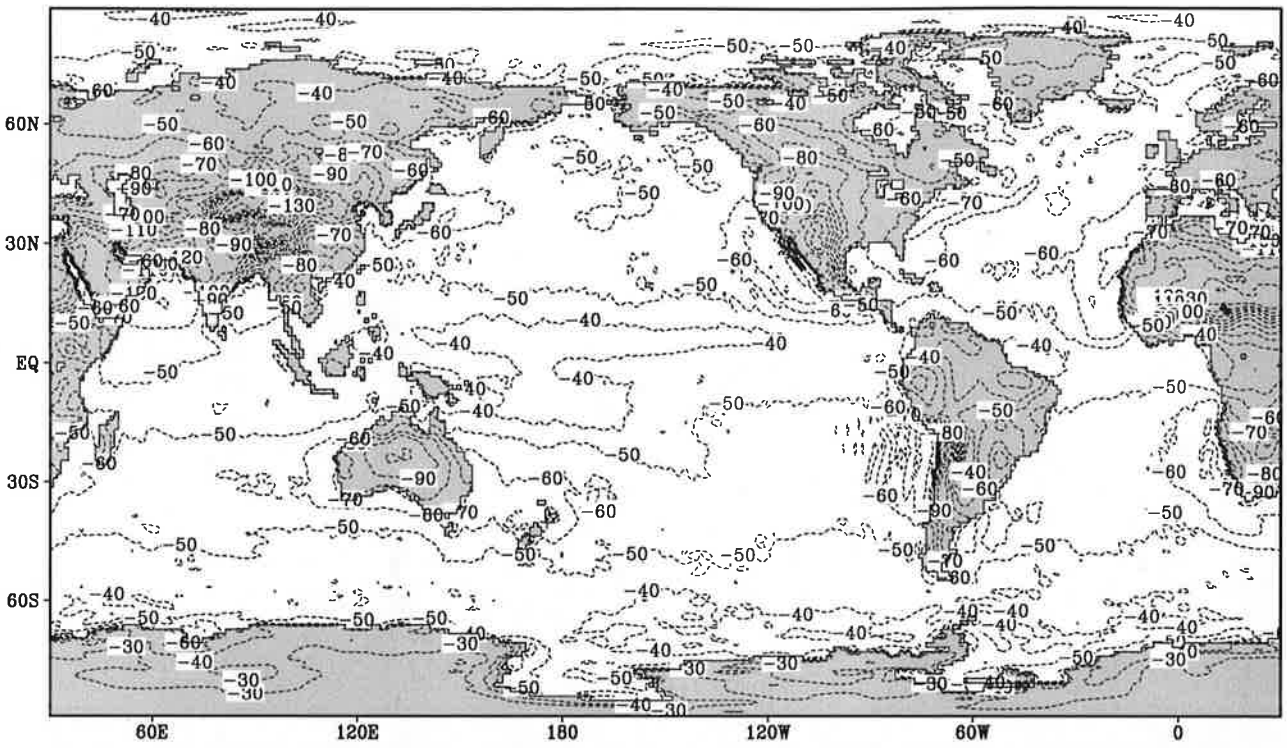

Contour interval: 10 Wm^{-2}

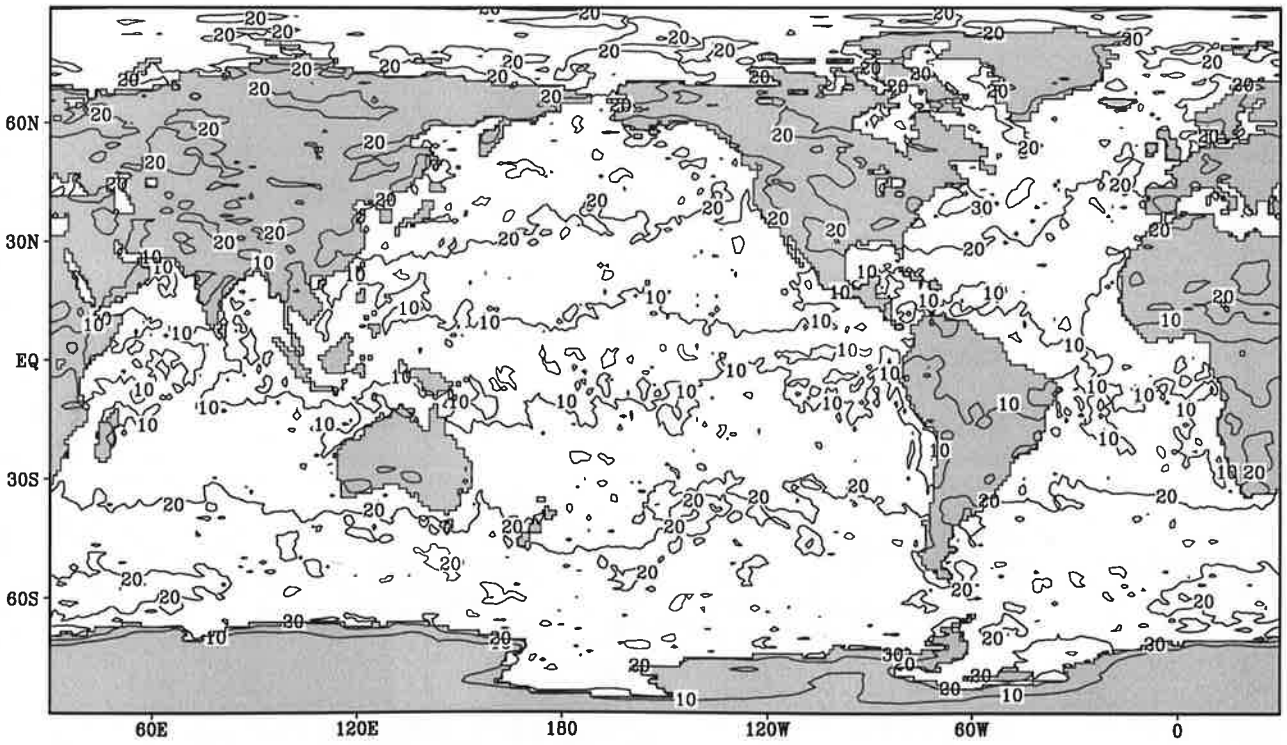

Contour interval: 10 Wm^{-2}

Fig.4.5 Long wave radiation May

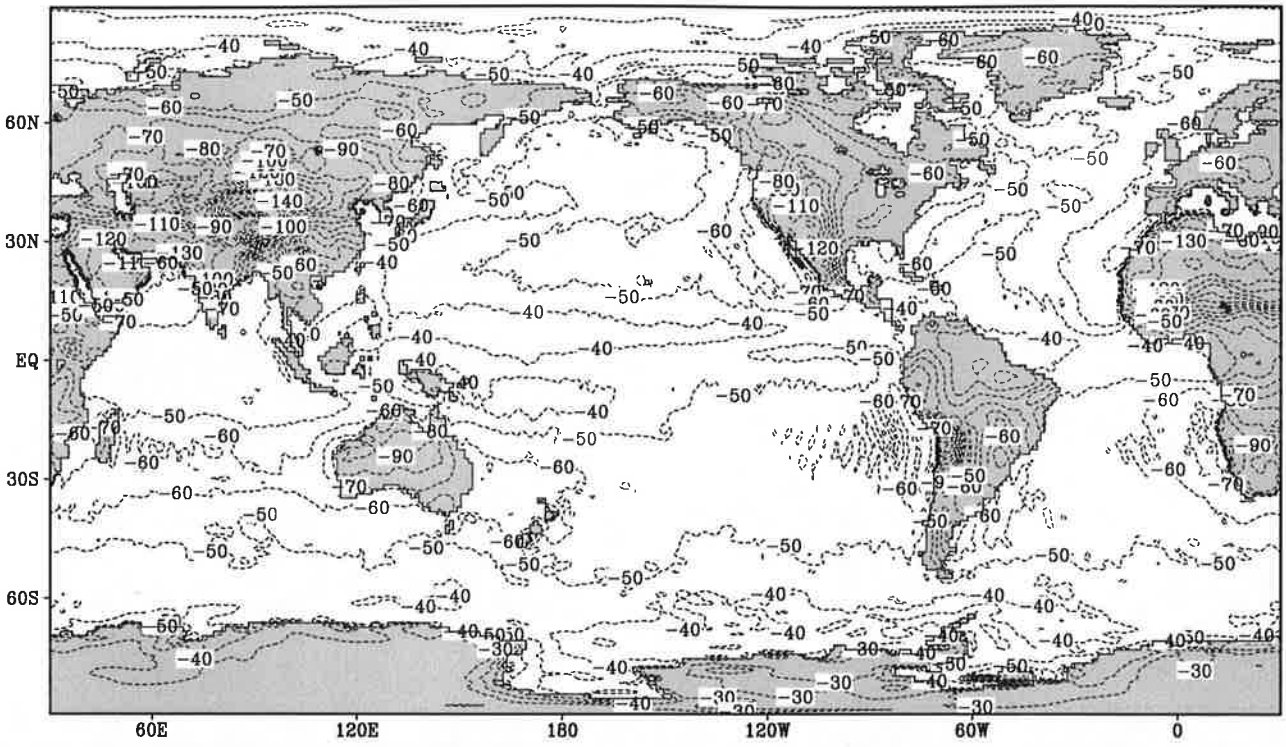

Contour interval: 10 Wm^{-2}

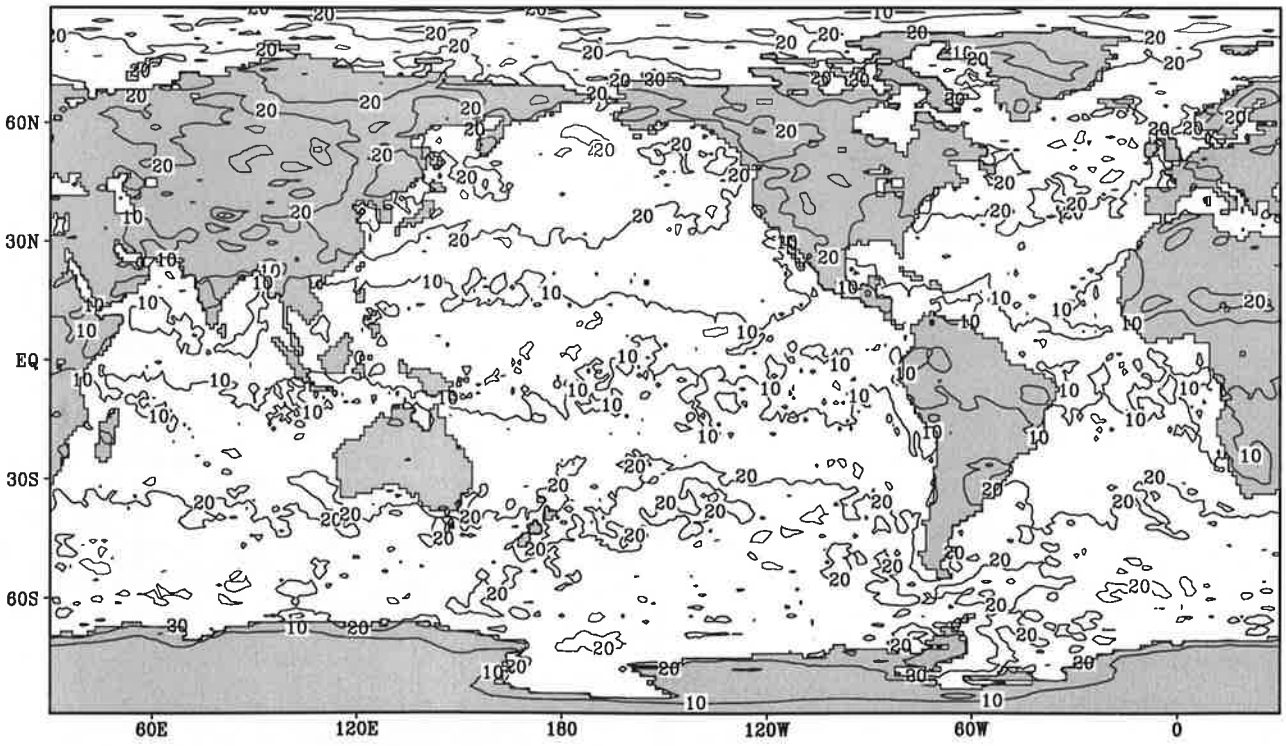

Contour interval: 10 Wm^{-2}

Fig.4.6 Long wave radiation June

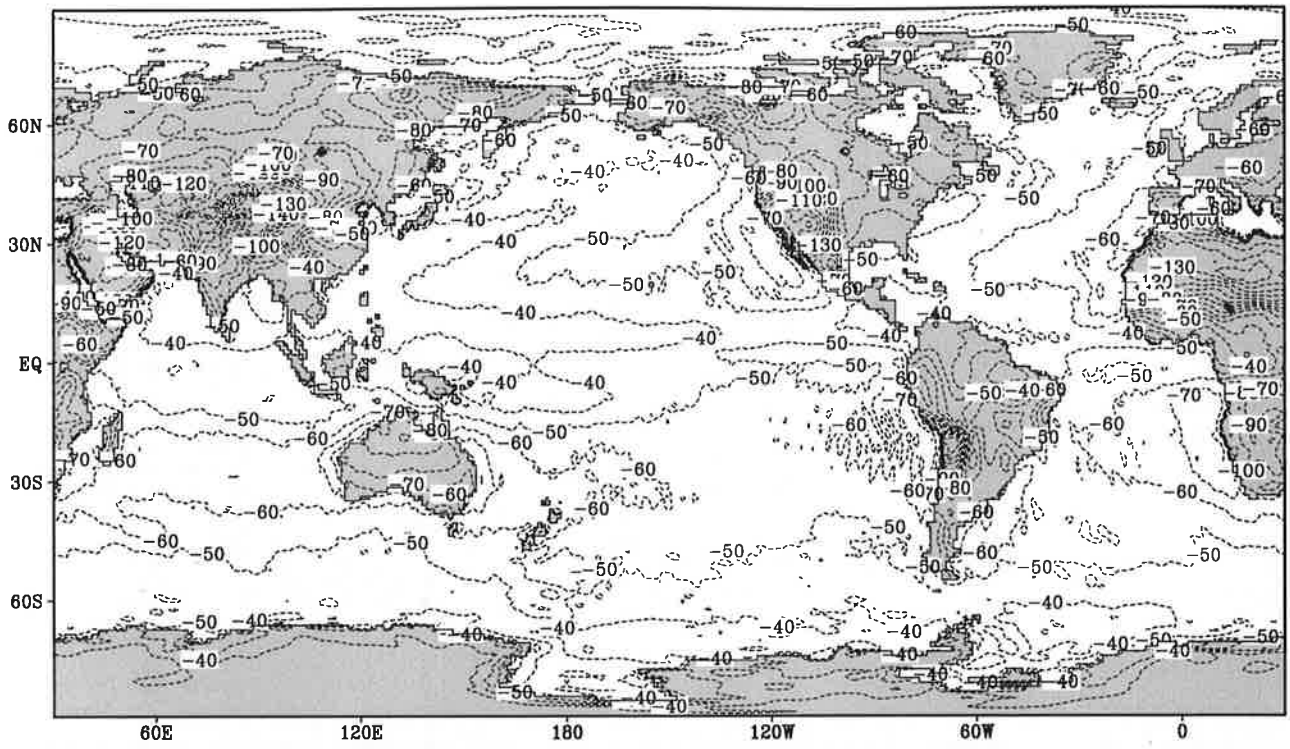

Contour interval: 10 Wm^{-2}

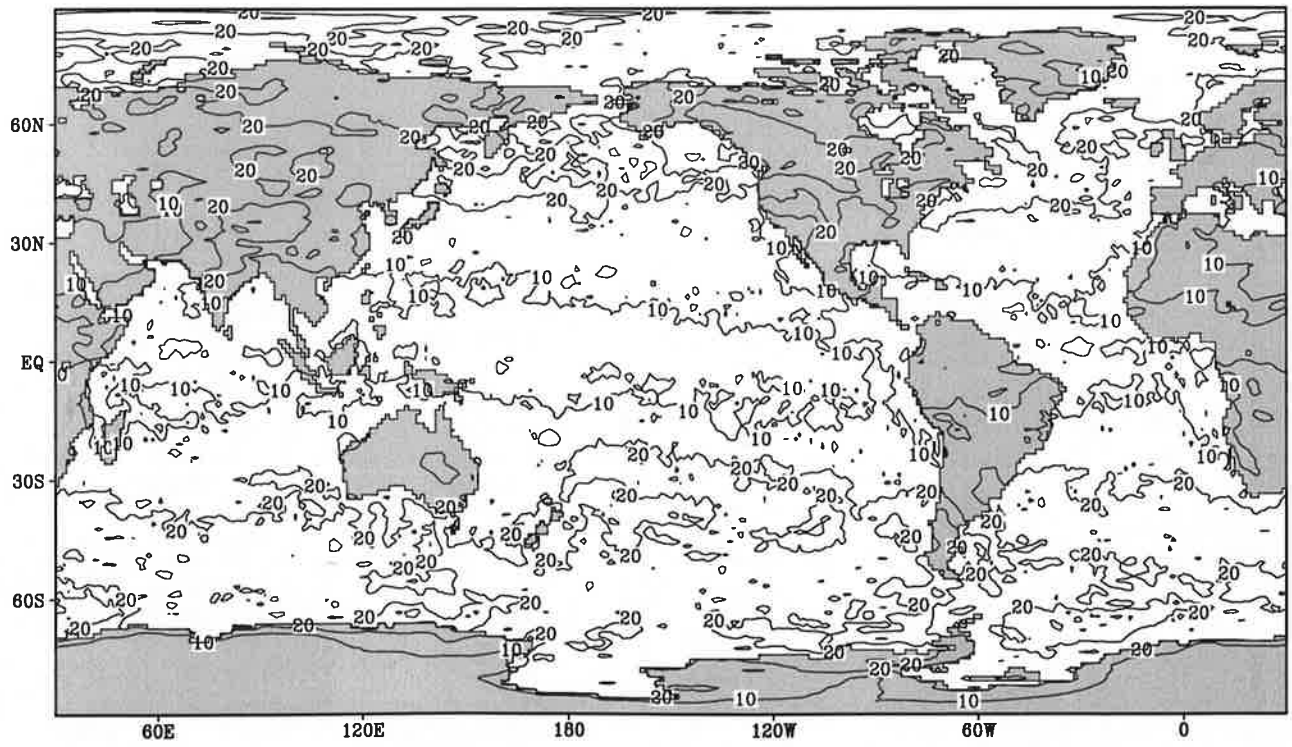

Contour interval: 10 Wm^{-2}

Fig.4.7 Long wave radiation July

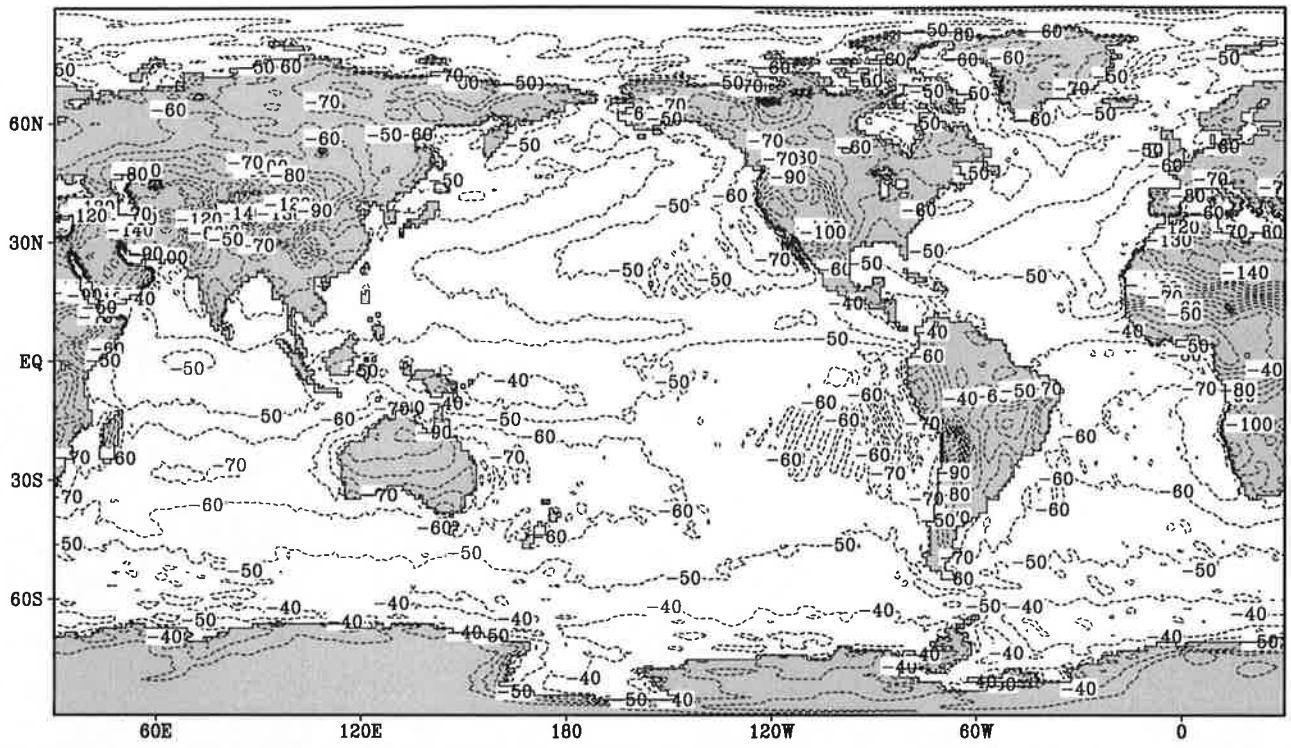

Contour interval: 10 Wm^{-2}

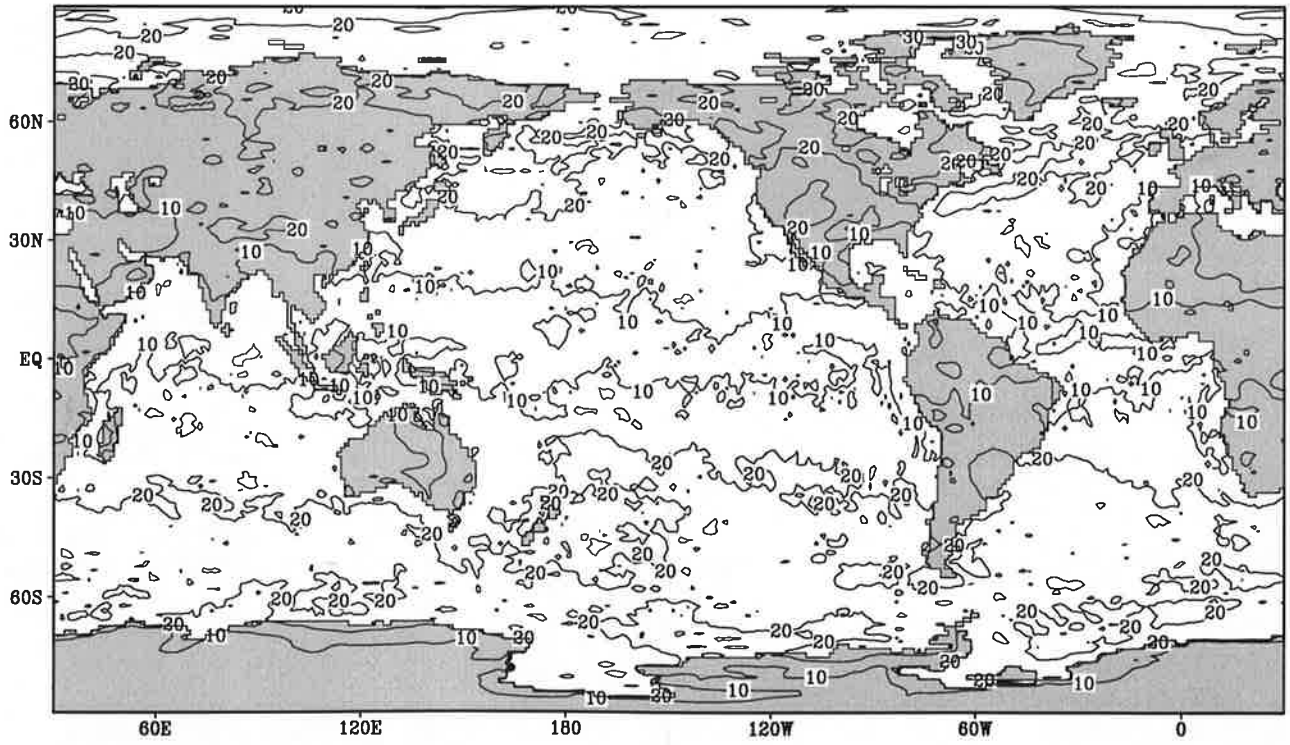

Contour interval: 10 Wm^{-2}

Fig.4.8 Long wave radiation August

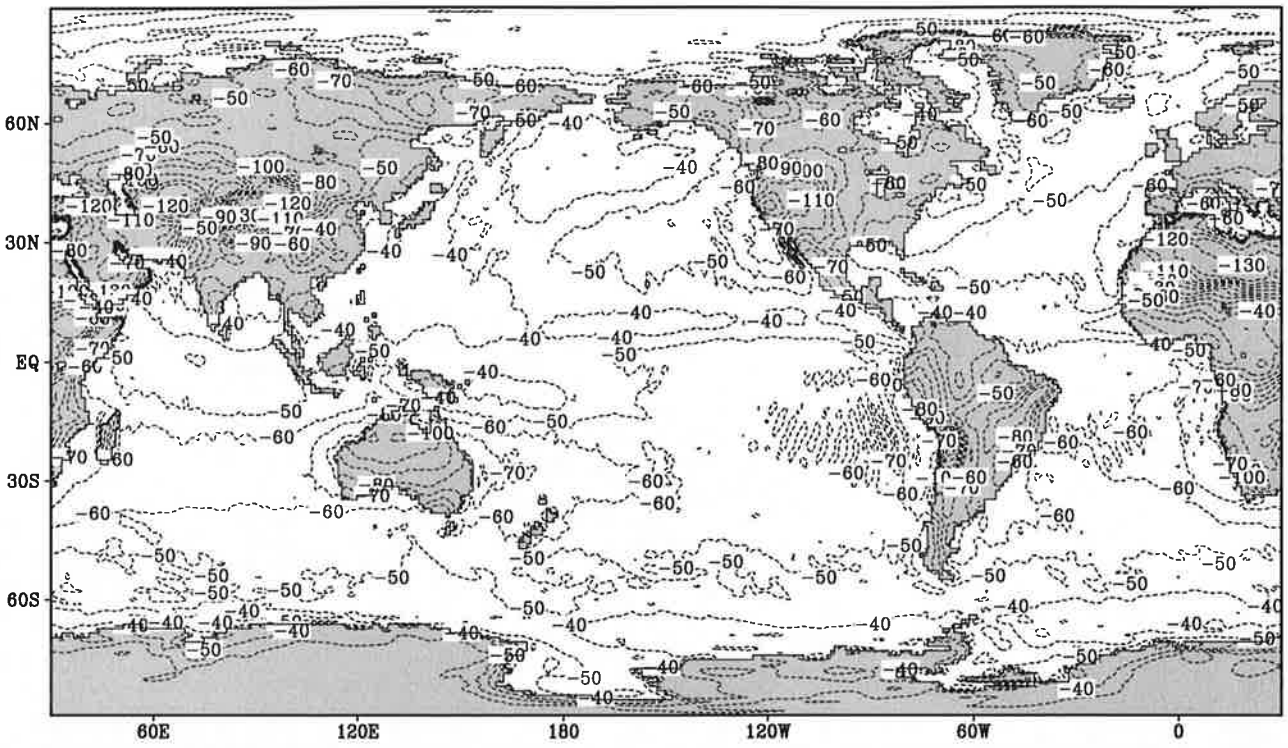

Contour interval: 10 Wm^{-2}

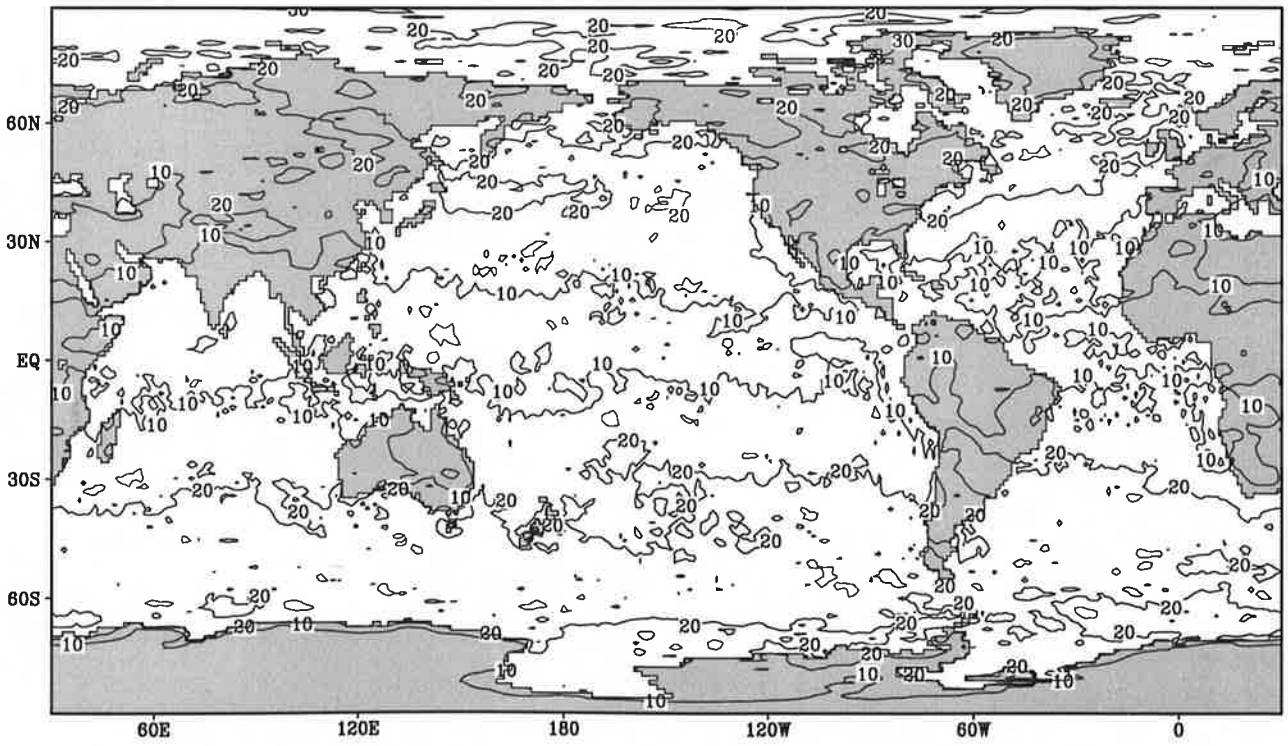

Contour interval: 10 Wm^{-2}

Fig.4.9 Long wave radiation September

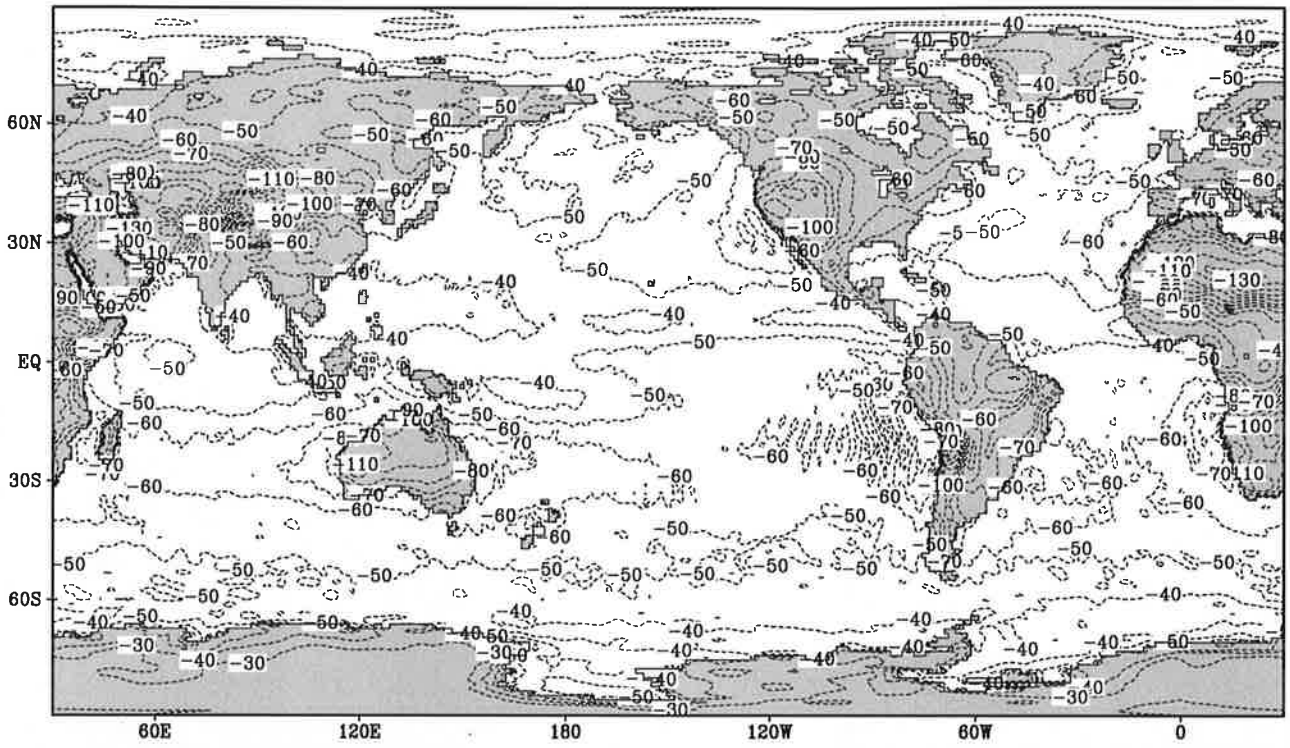

Contour interval: 10 Wm^{-2}

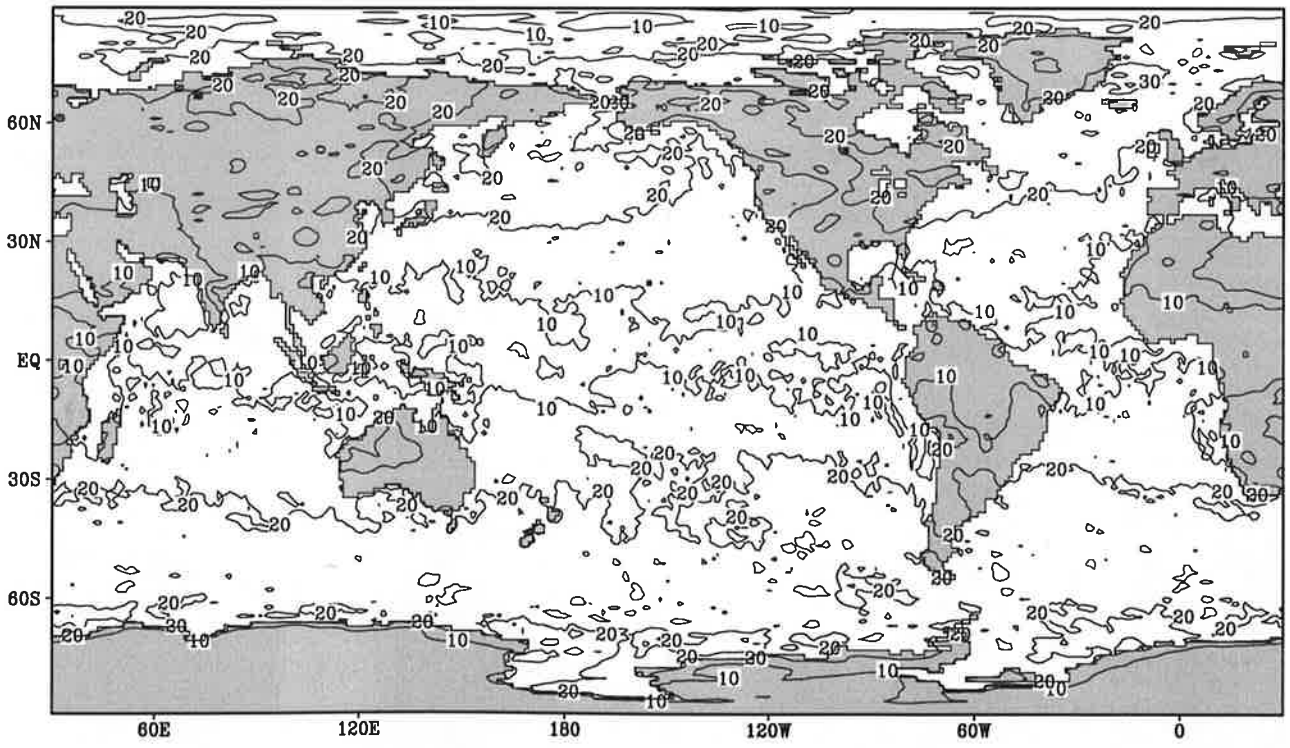

Contour interval: 10 Wm^{-2}

Fig.4.10 Long wave radiation October

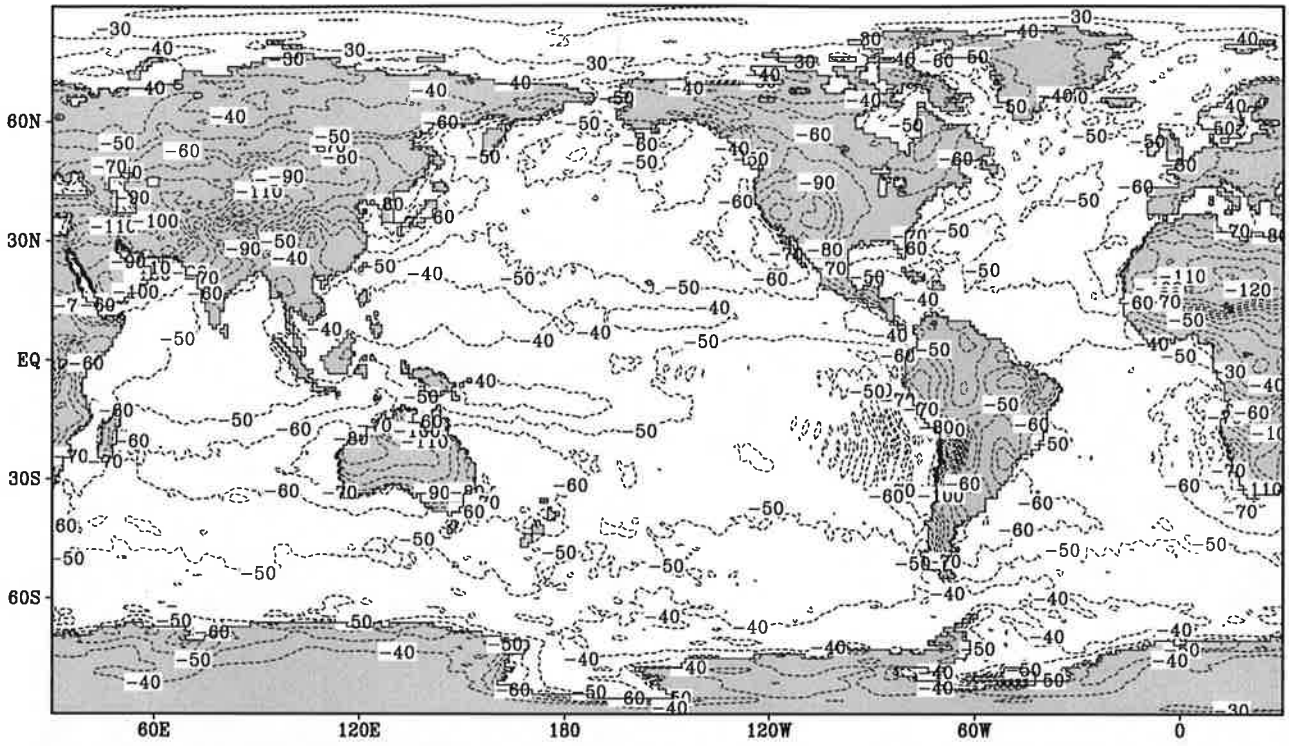

Contour interval: 10 Wm^{-2}

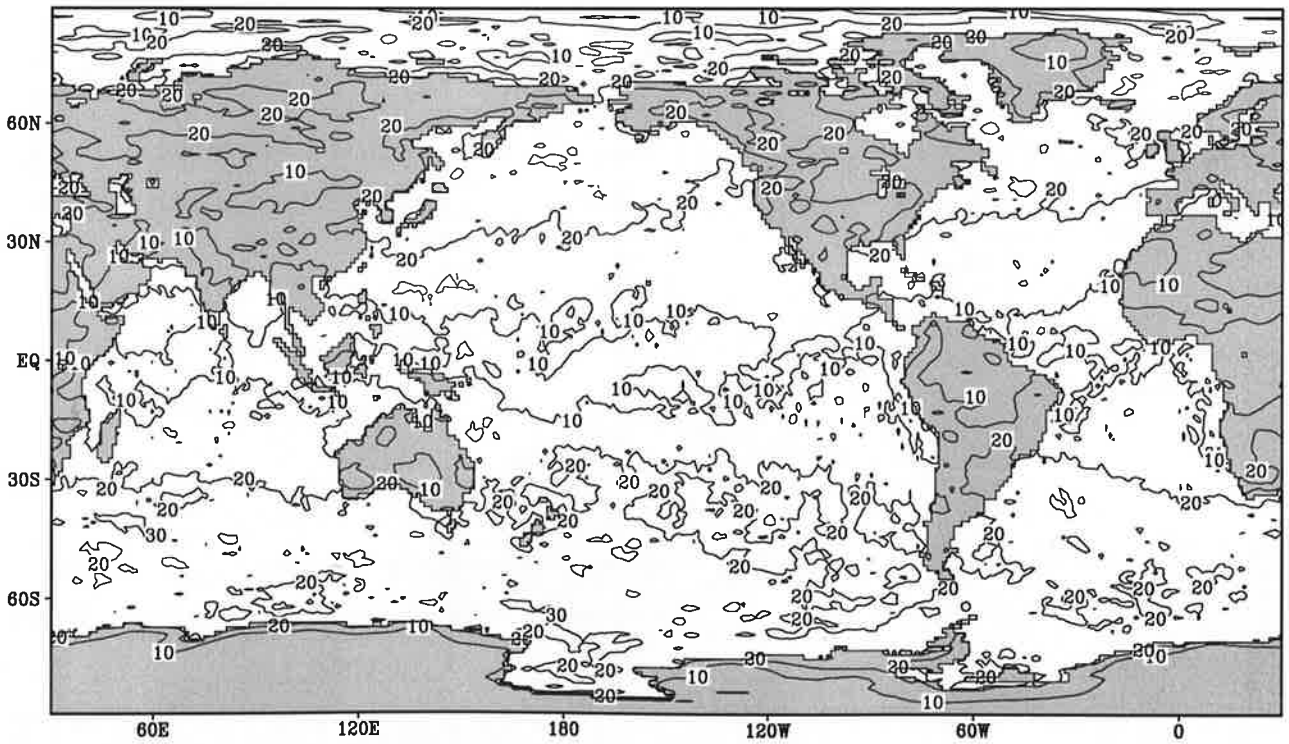

Contour interval: 10 Wm^{-2}

Fig.4.11 Long wave radiation November

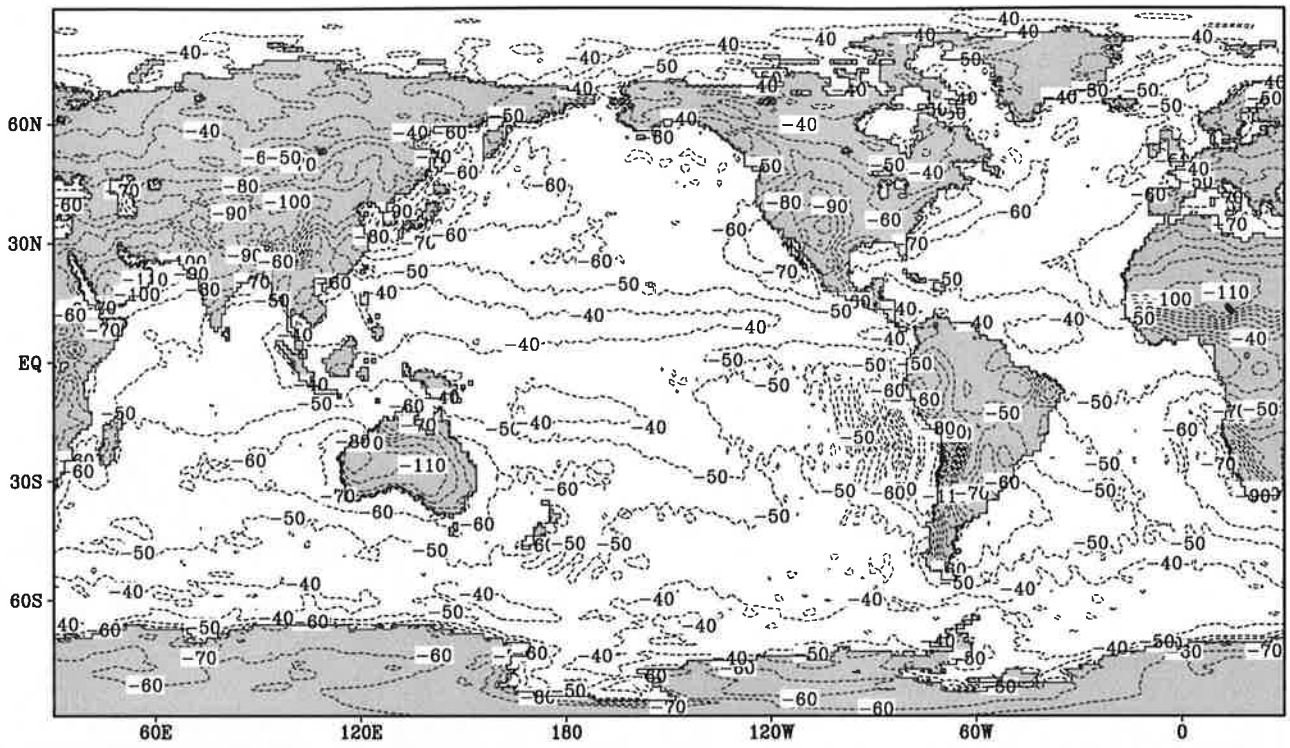

Contour interval: 10 Wm^{-2}

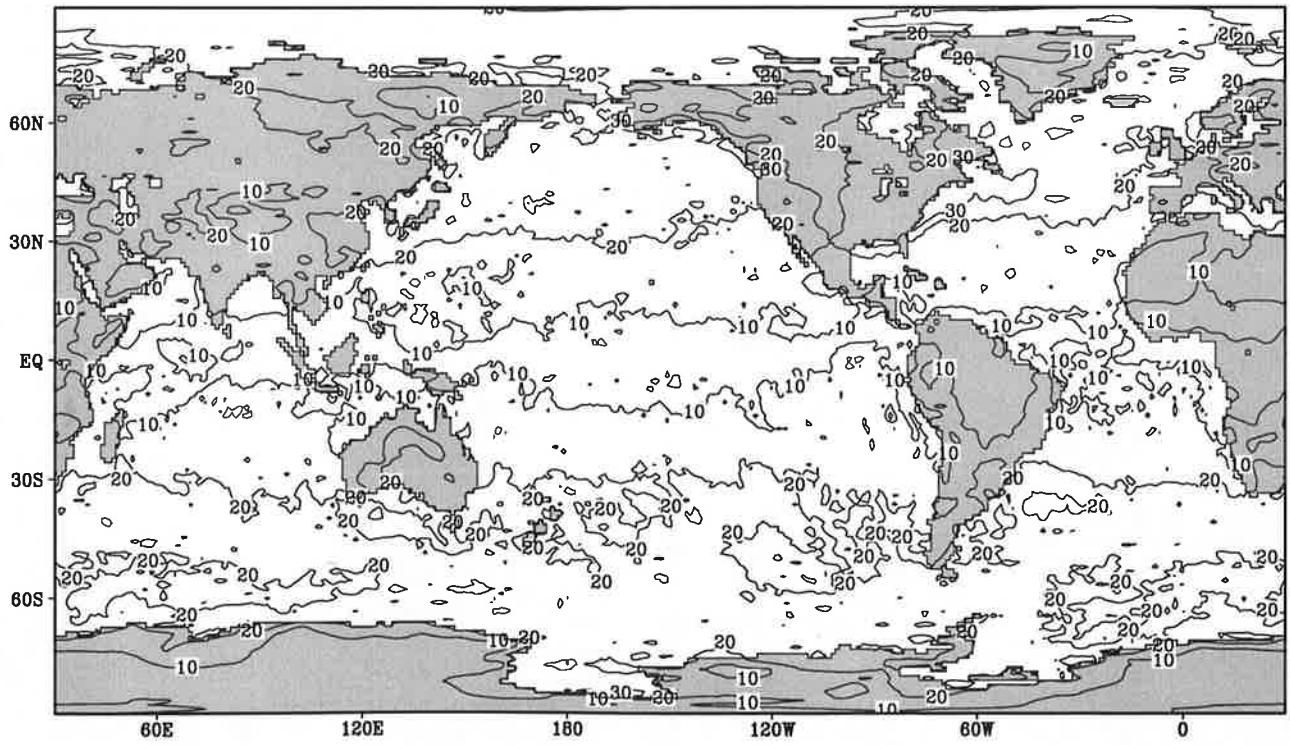

Contour interval: 10 Wm^{-2}

Fig.4.12 Long wave radiation December

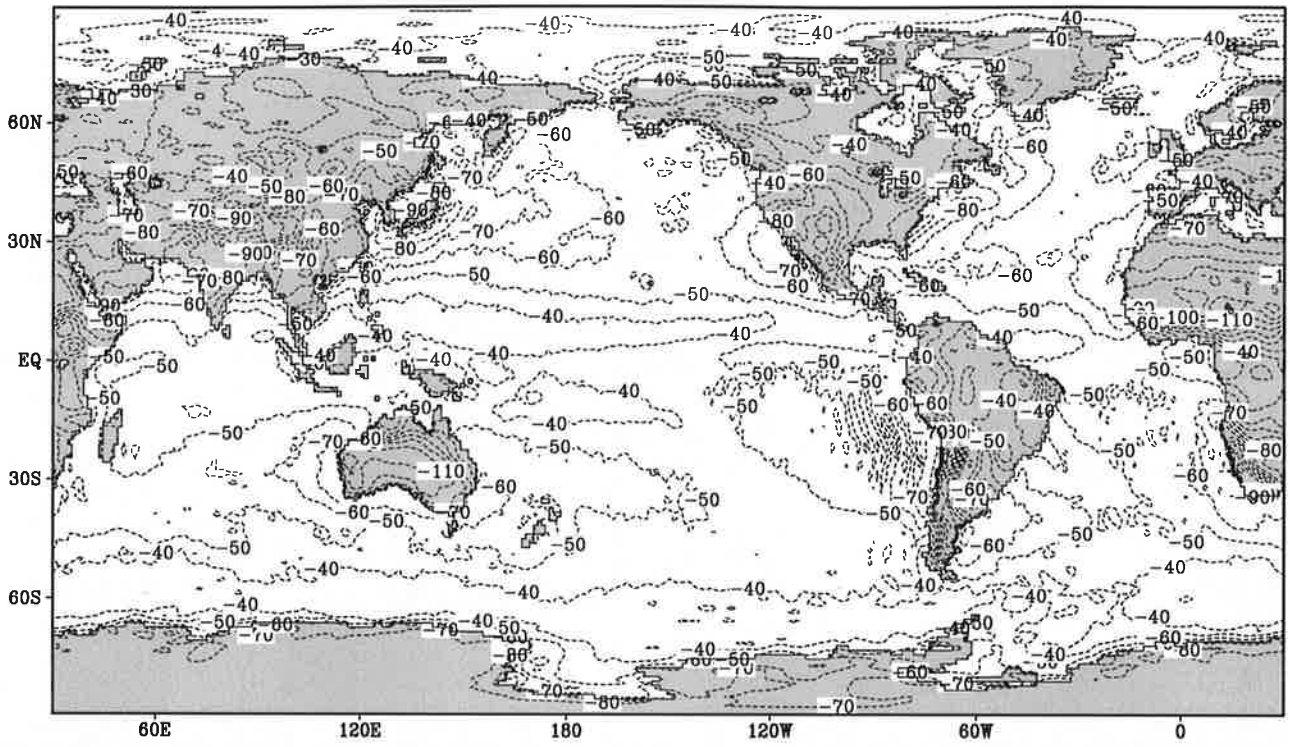

Contour interval: 10 Wm^{-2}

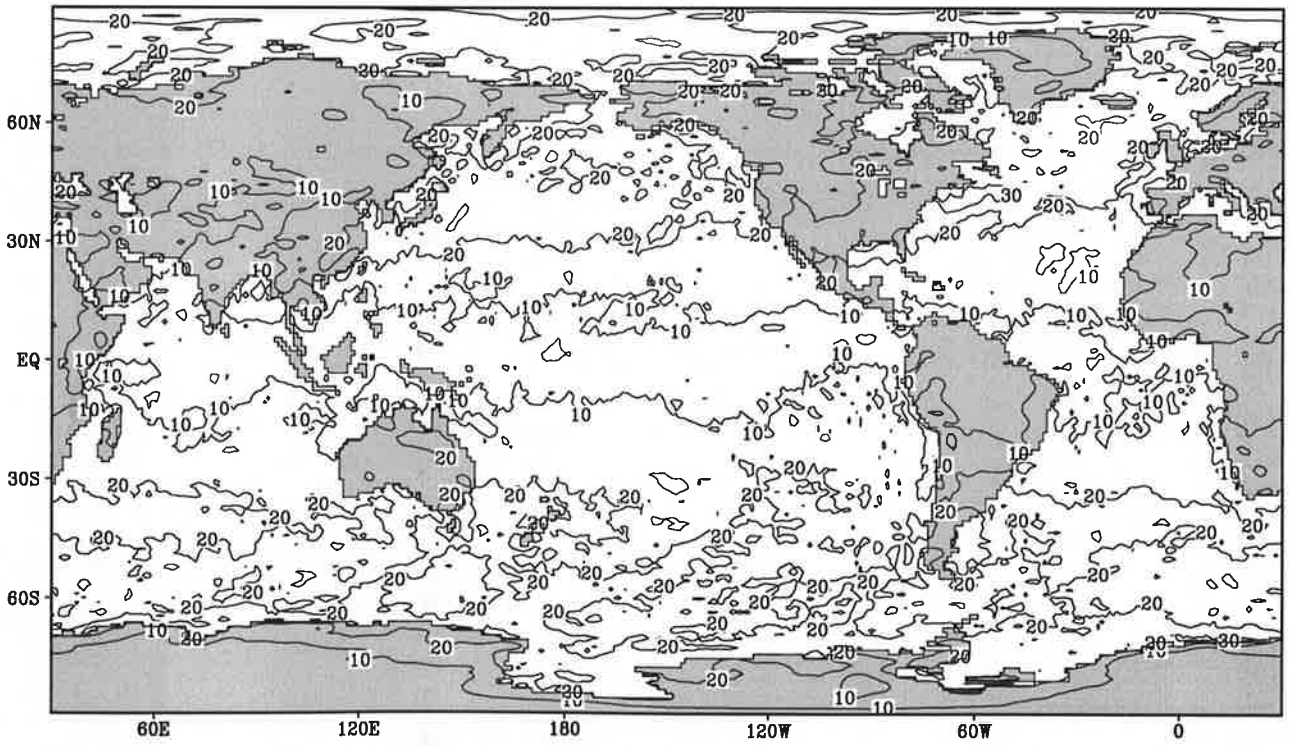

Contour interval: 10 Wm^{-2}

Fig.4.13 Long wave radiation Annual Mean

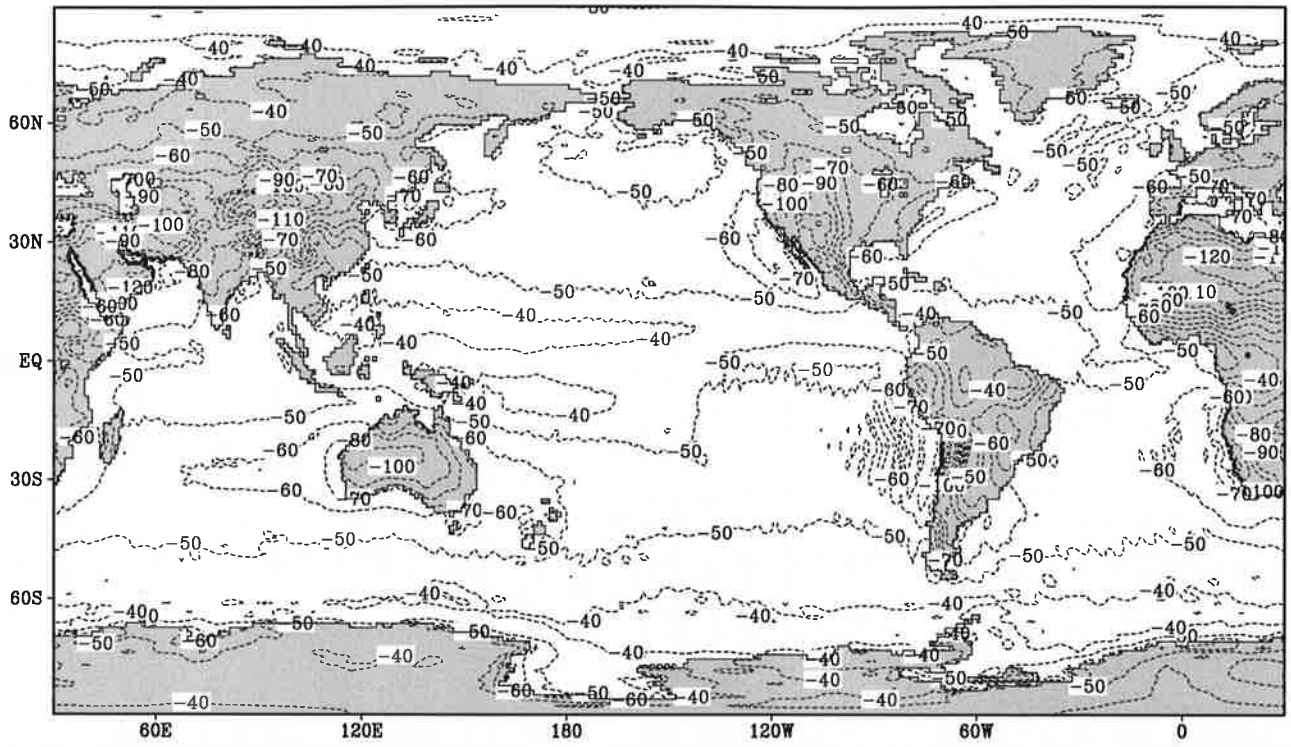

Contour interval: 10 Wm^{-2}

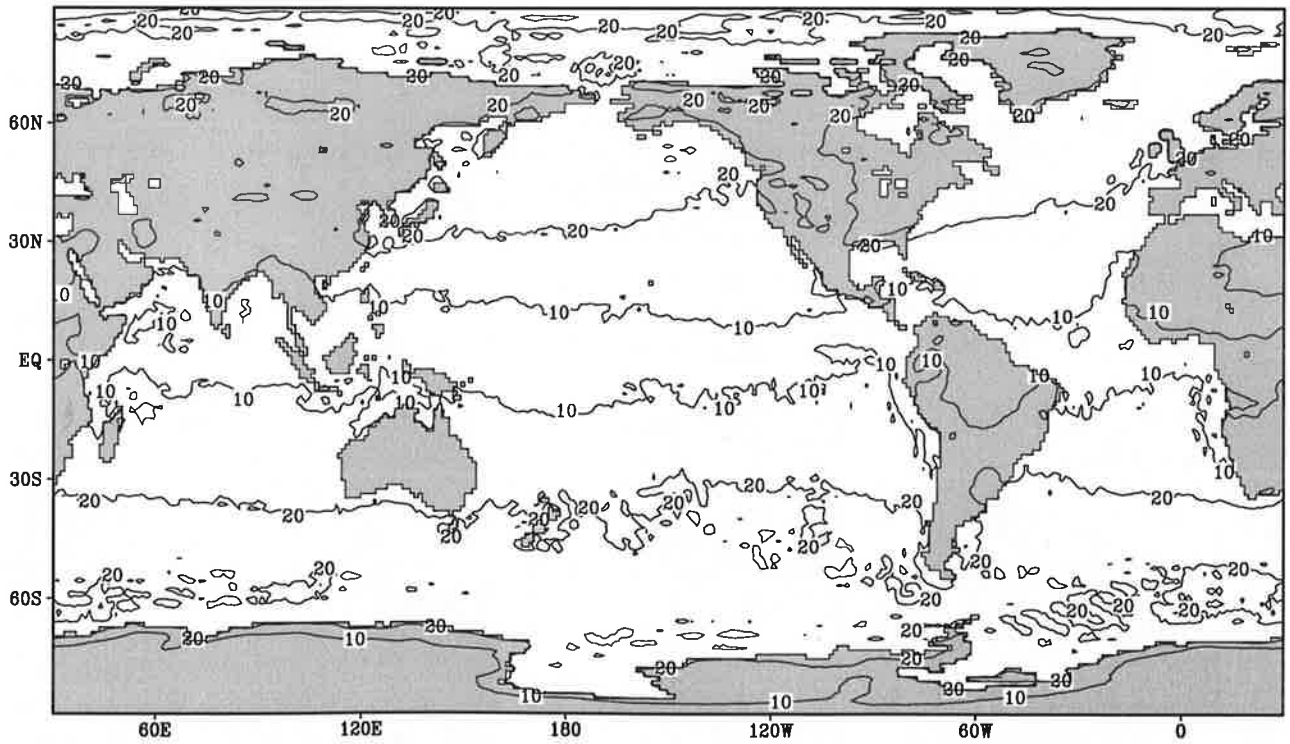

Contour interval: 10 Wm^{-2}

Fig.5.1 Sensible heat flux January

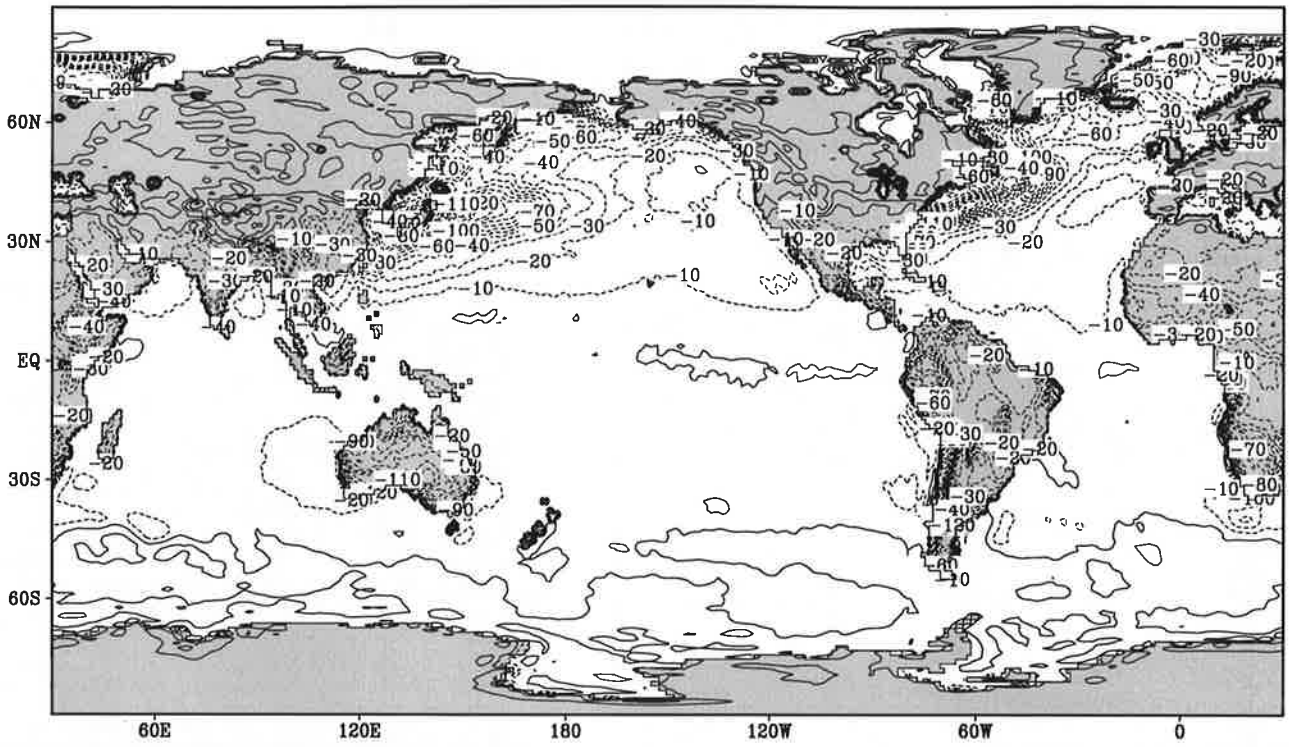

Contour interval: 10 Wm^{-2}

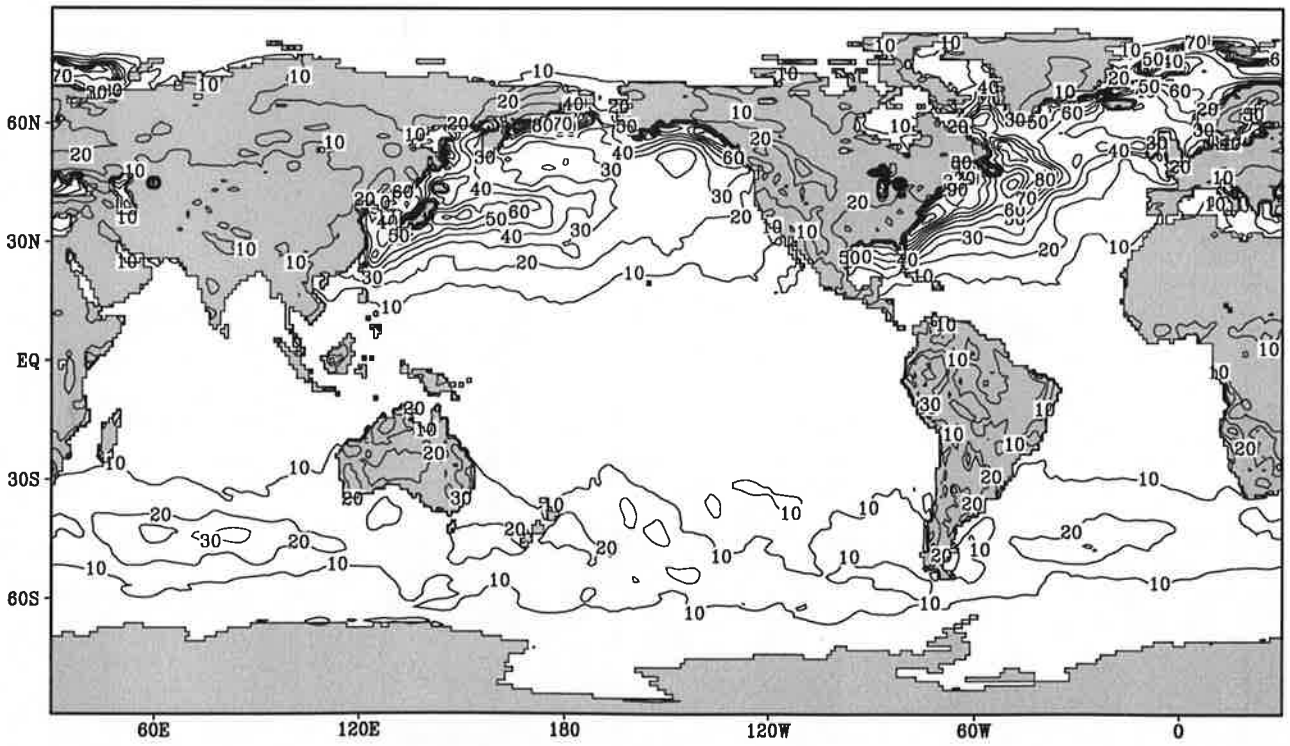

Contour interval: 10 Wm^{-2}

Fig.5.2 Sensible heat flux February

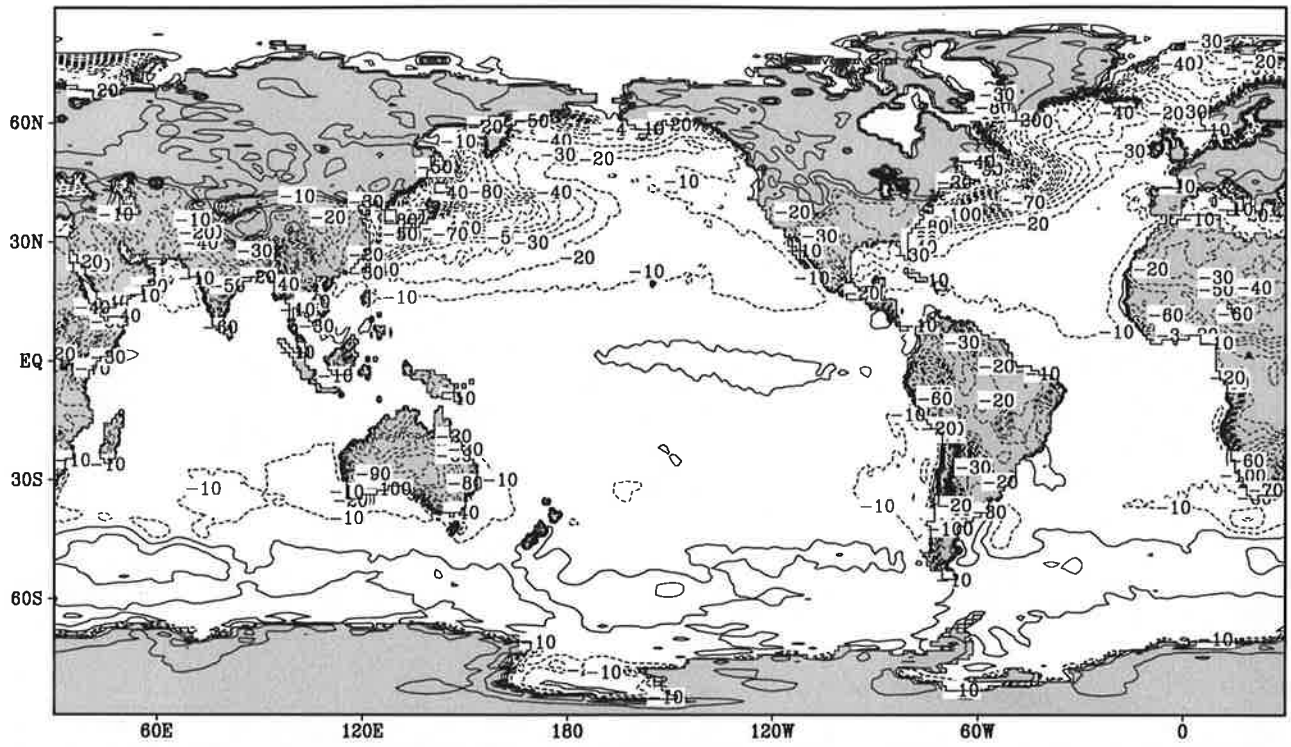

Contour interval: 10 Wm^{-2}

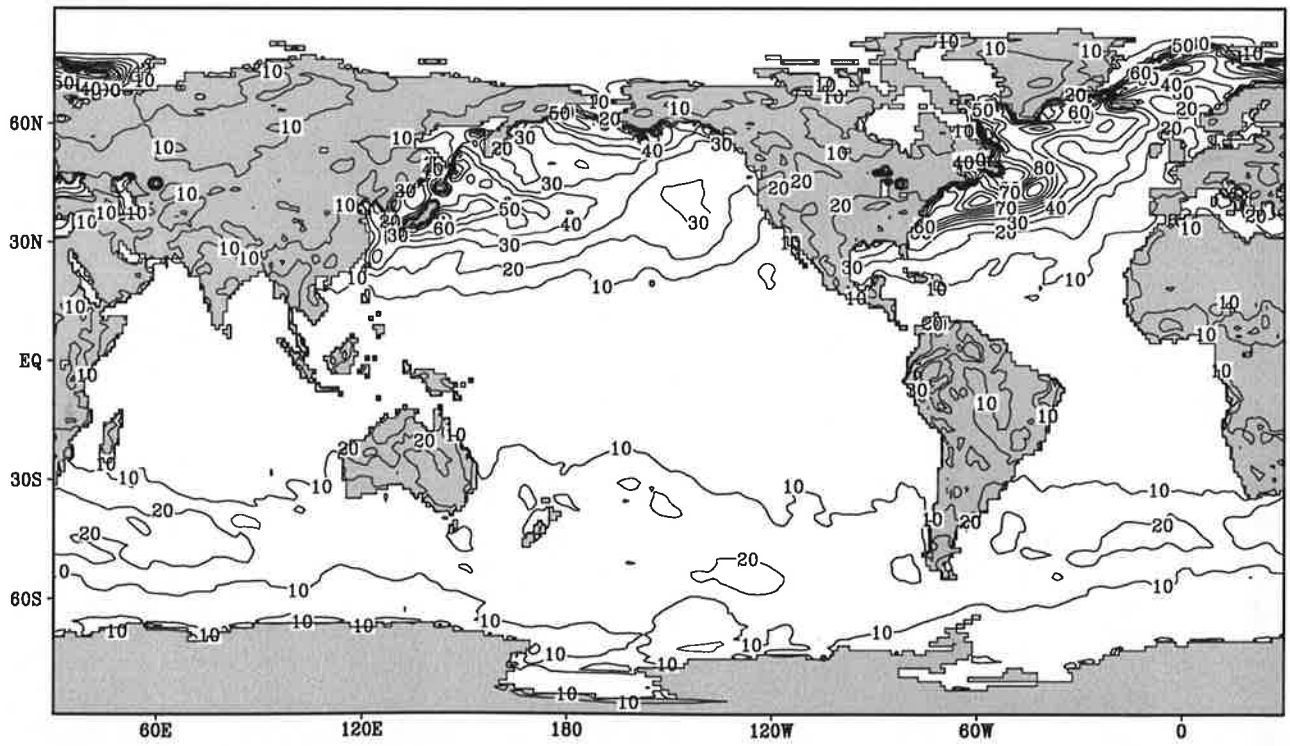

Contour interval: 10 Wm^{-2}

Fig.5.3 Sensible heat flux March

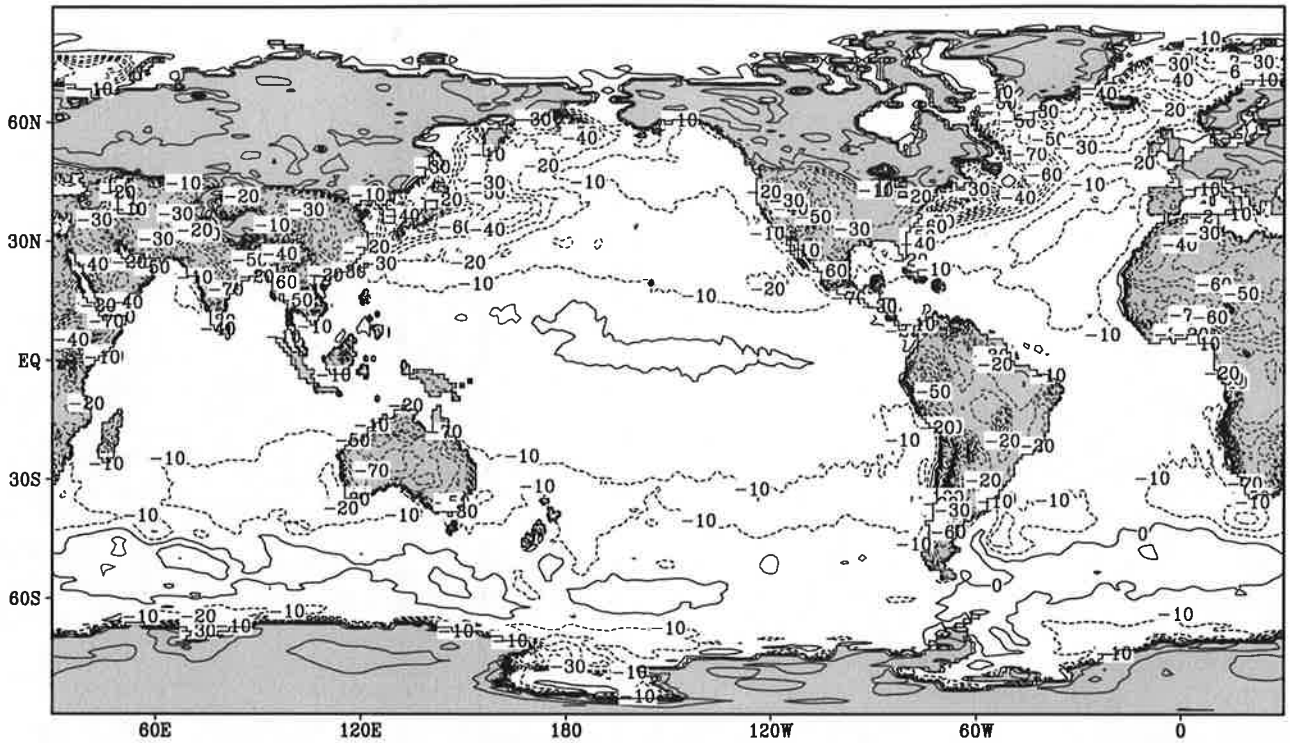

Contour interval: 10 Wm^{-2}

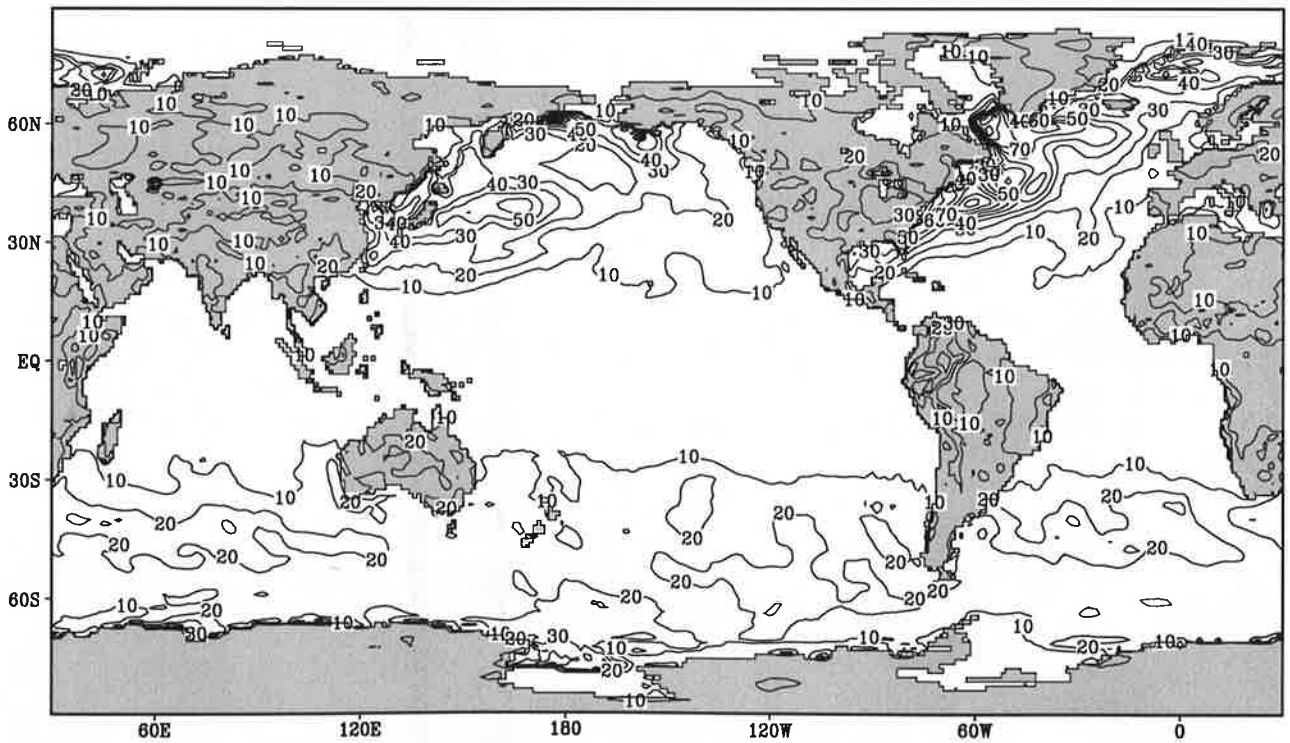

Contour interval: 10 Wm^{-2}

Fig.5.4 Sensible heat flux April

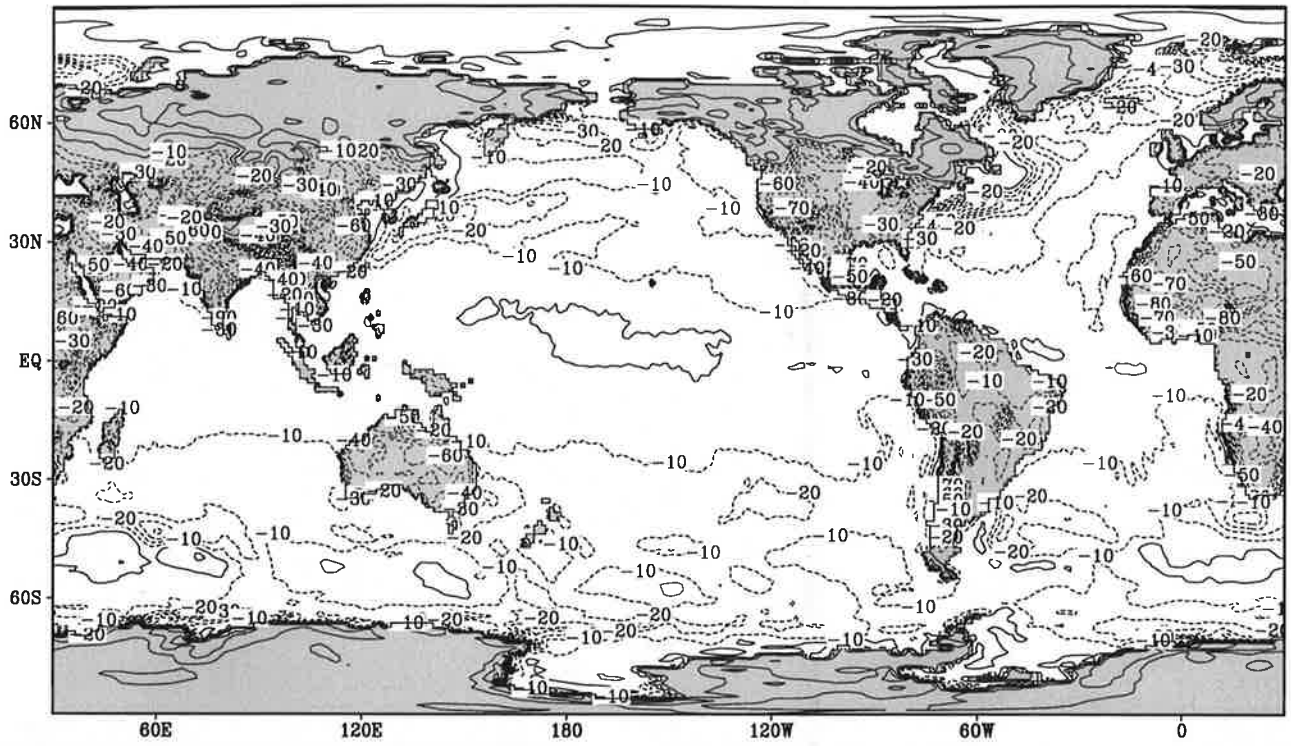

Contour interval: 10 Wm^{-2}

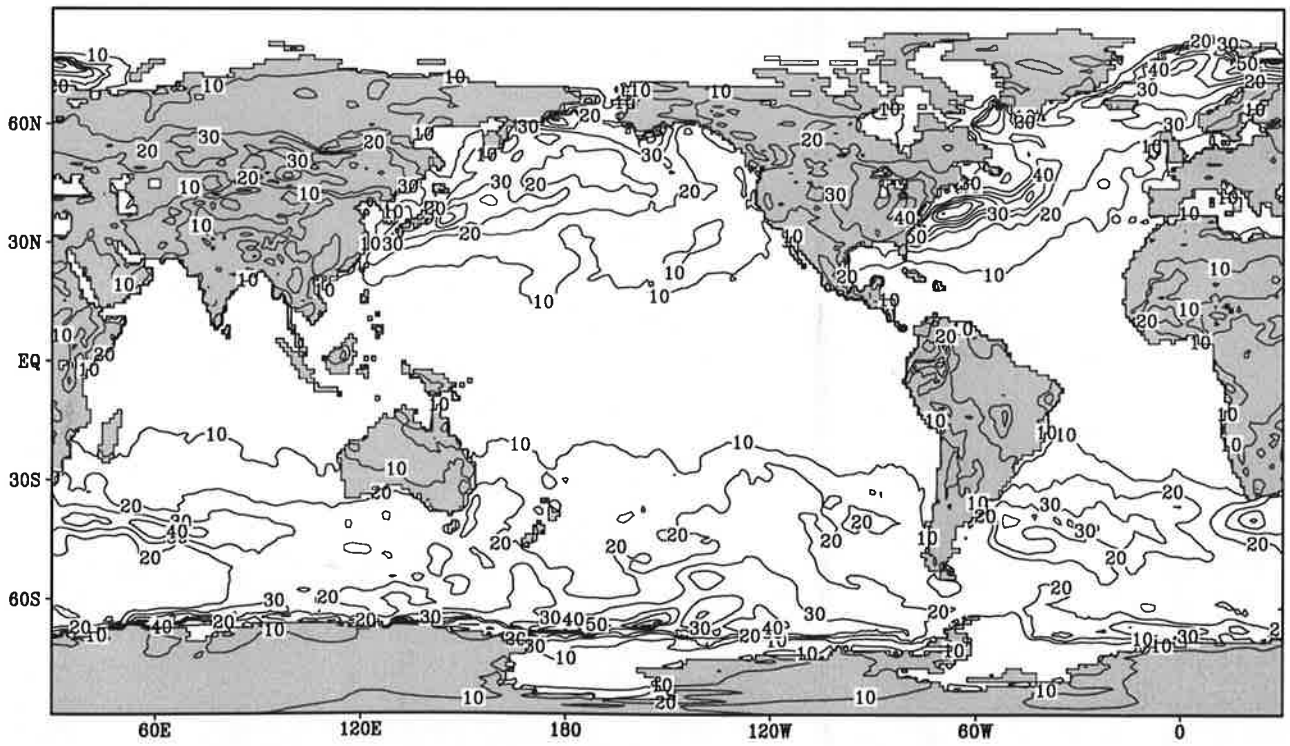

Contour interval: 10 Wm^{-2}

Fig.5.5 Sensible heat flux May

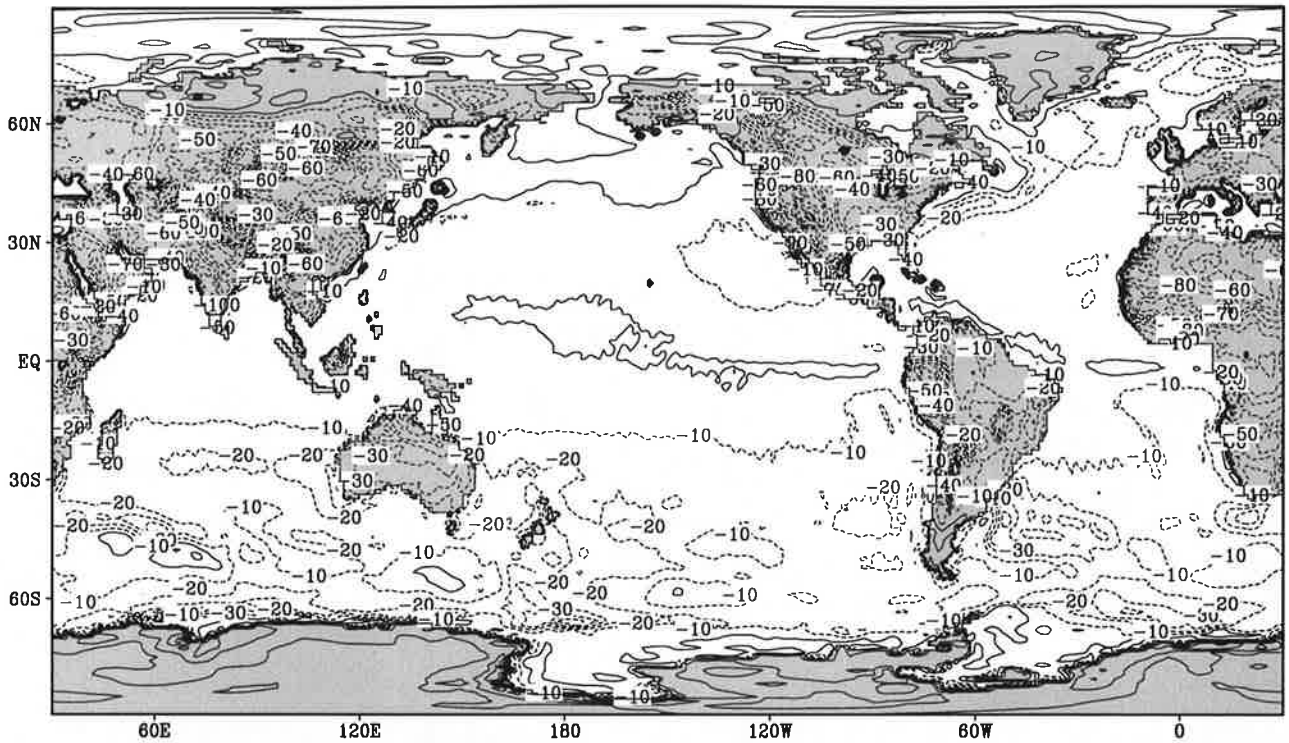

Contour interval: 10 Wm^{-2}

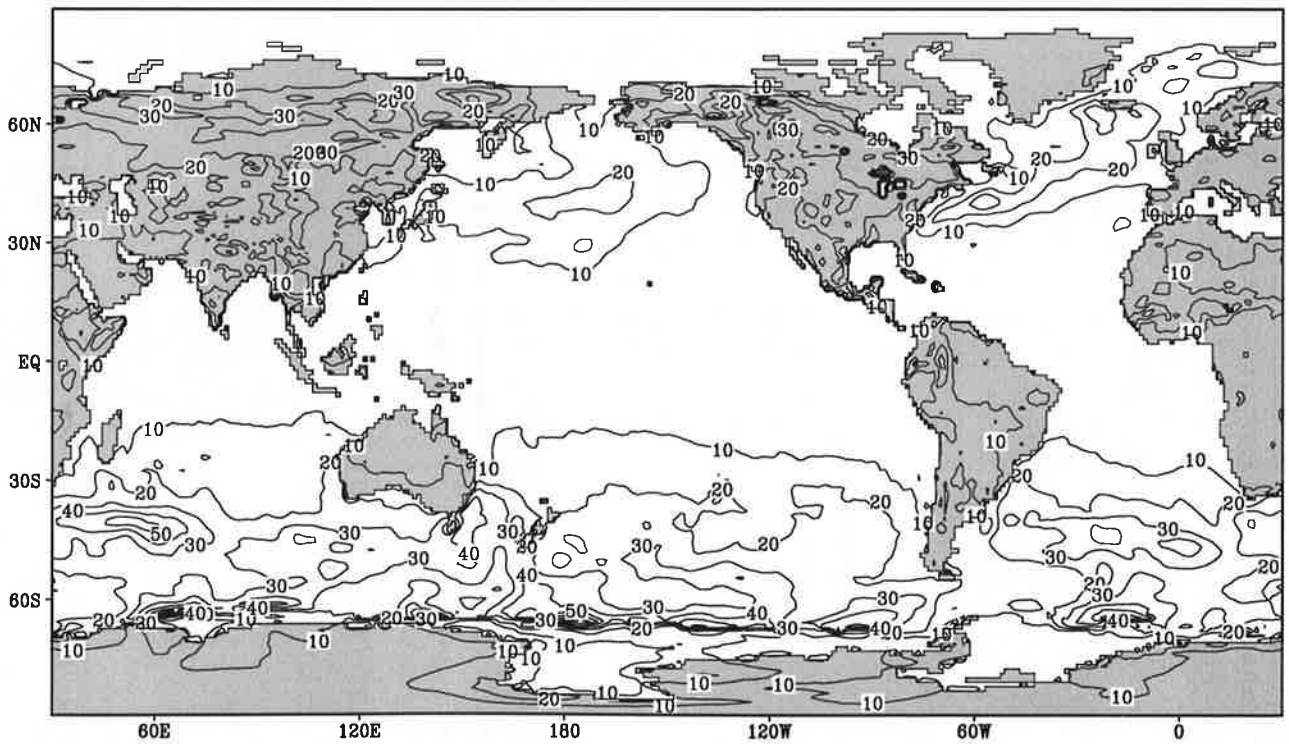

Contour interval: 10 Wm^{-2}

Fig.5.6 Sensible heat flux June

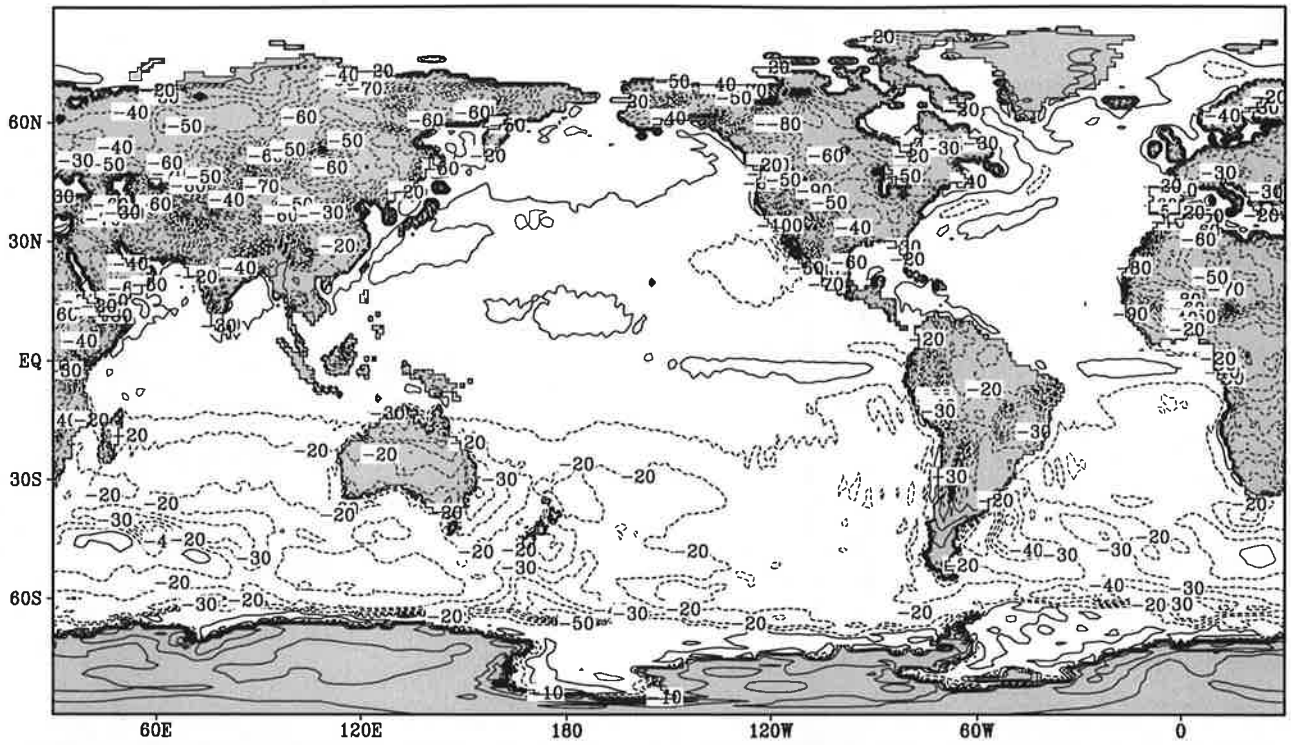

Contour interval: 10 Wm^{-2}

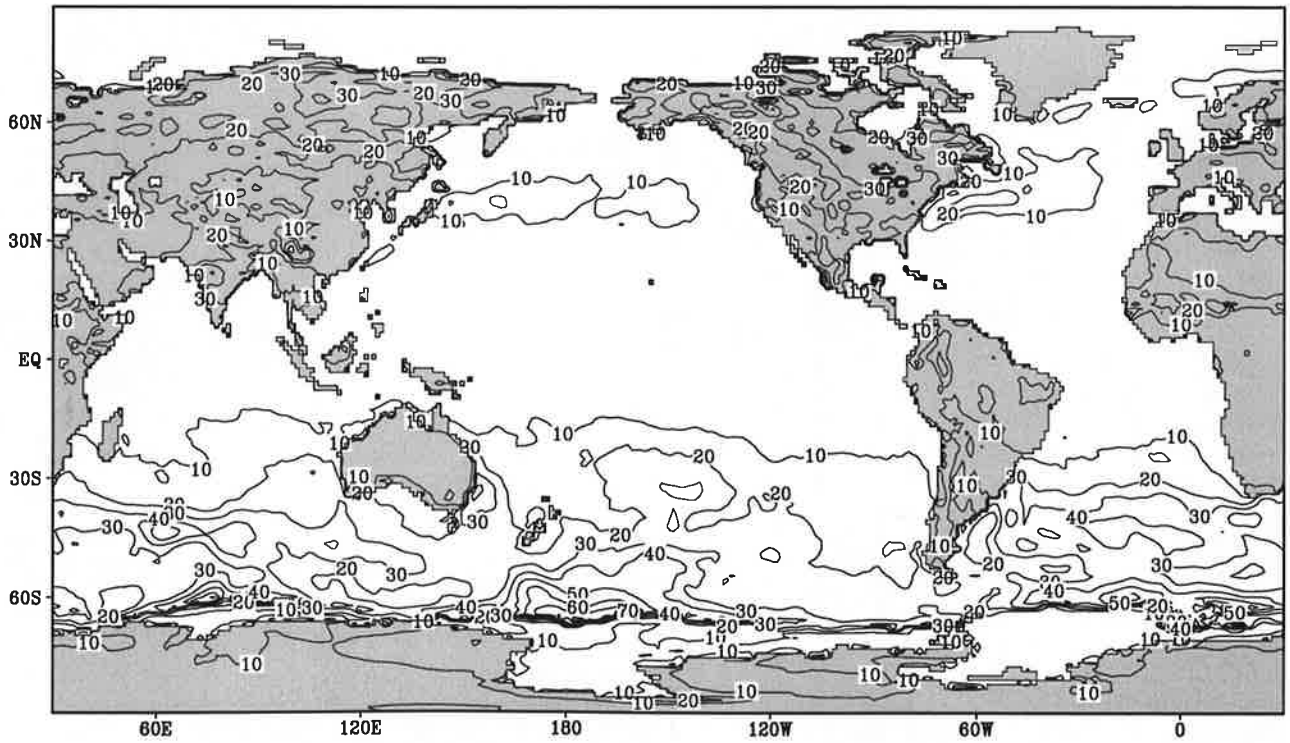

Contour interval: 10 Wm^{-2}

Fig.5.7 Sensible heat flux July

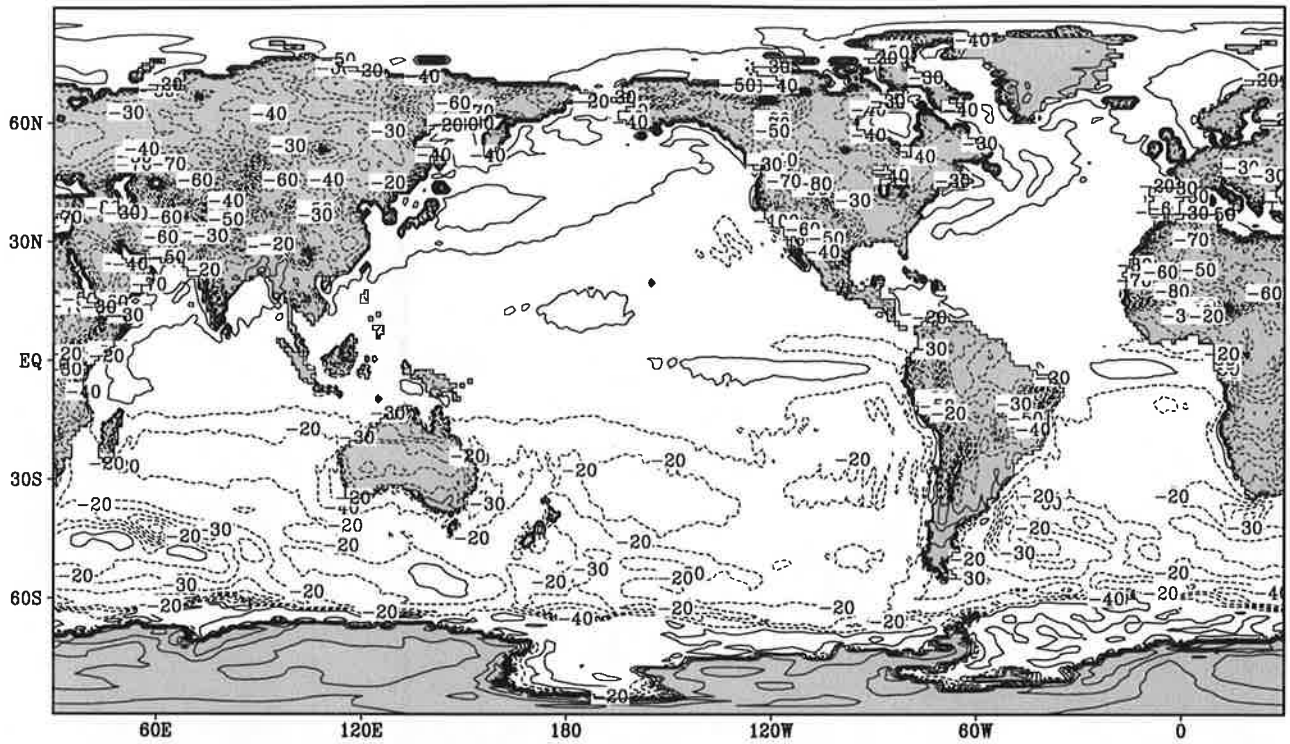

Contour interval: 10 Wm^{-2}

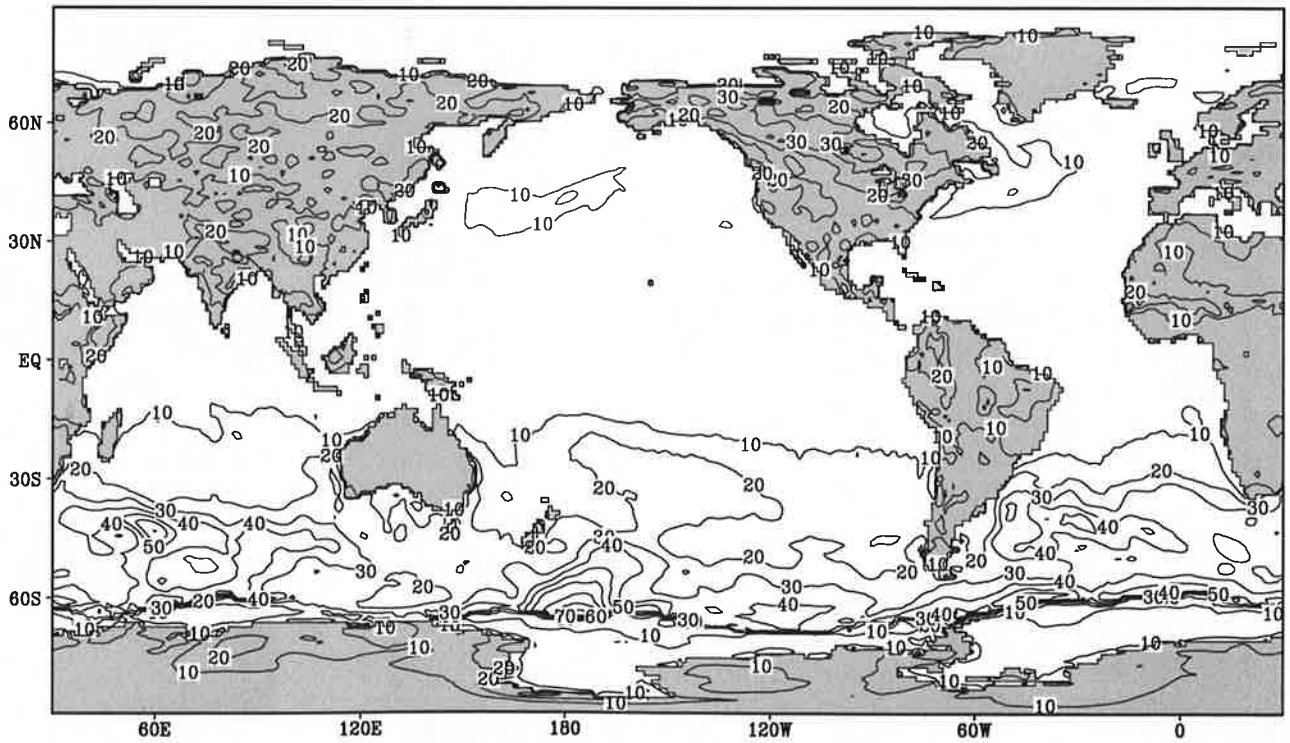

Contour interval: 10 Wm^{-2}

Fig.5.8 Sensible heat flux August

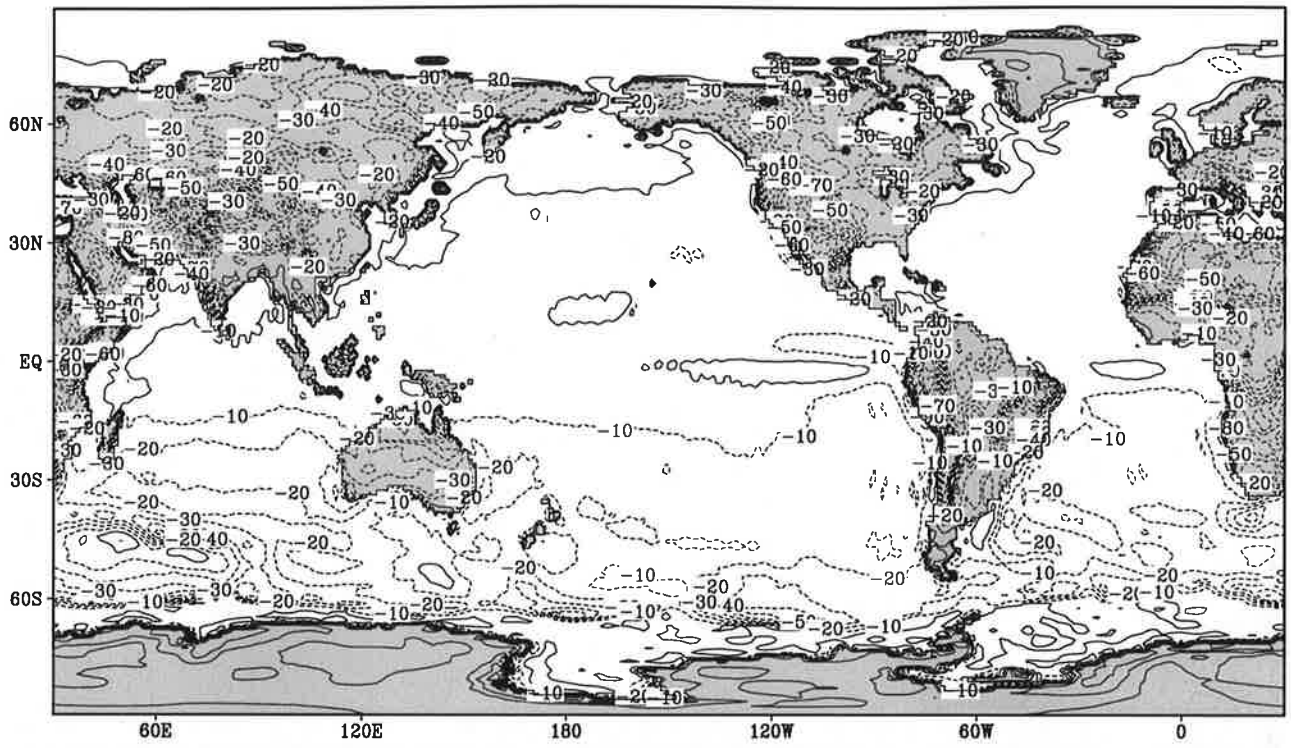

Contour interval: 10 Wm^{-2}

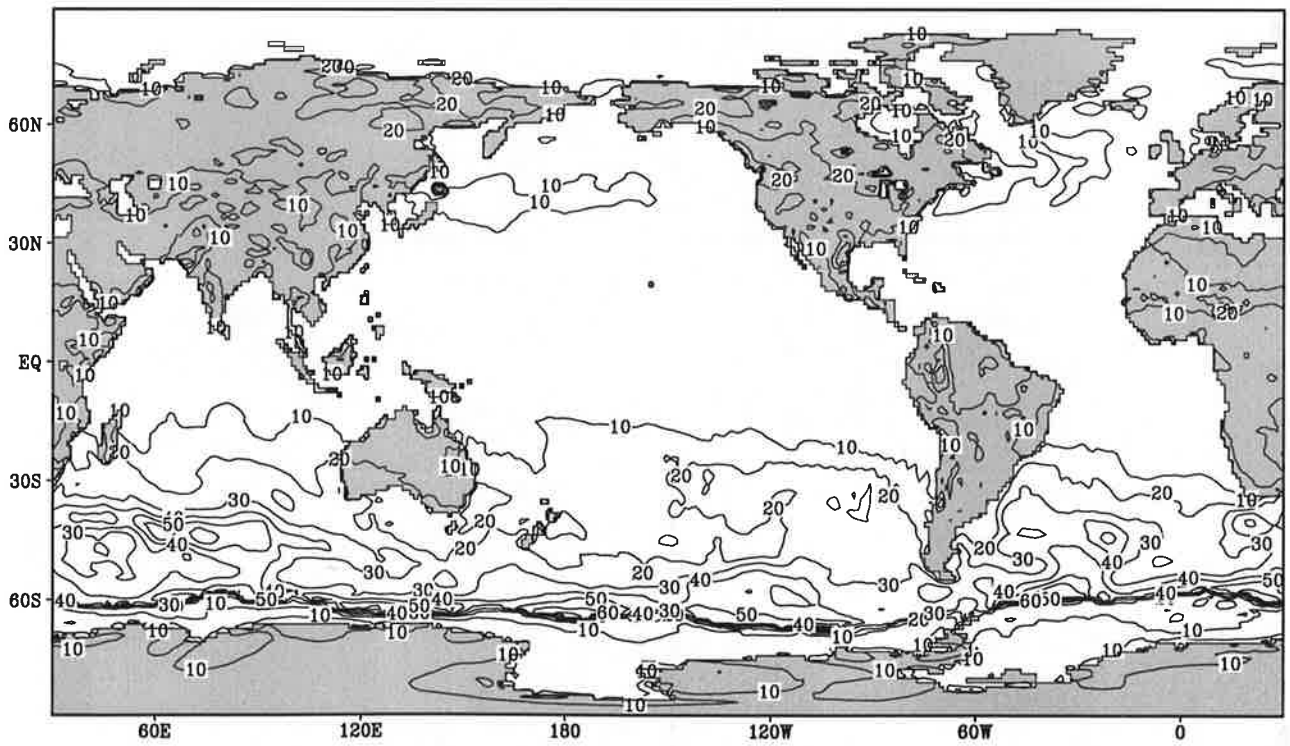

Contour interval: 10 Wm^{-2}

Fig.5.10 Sensible heat flux October

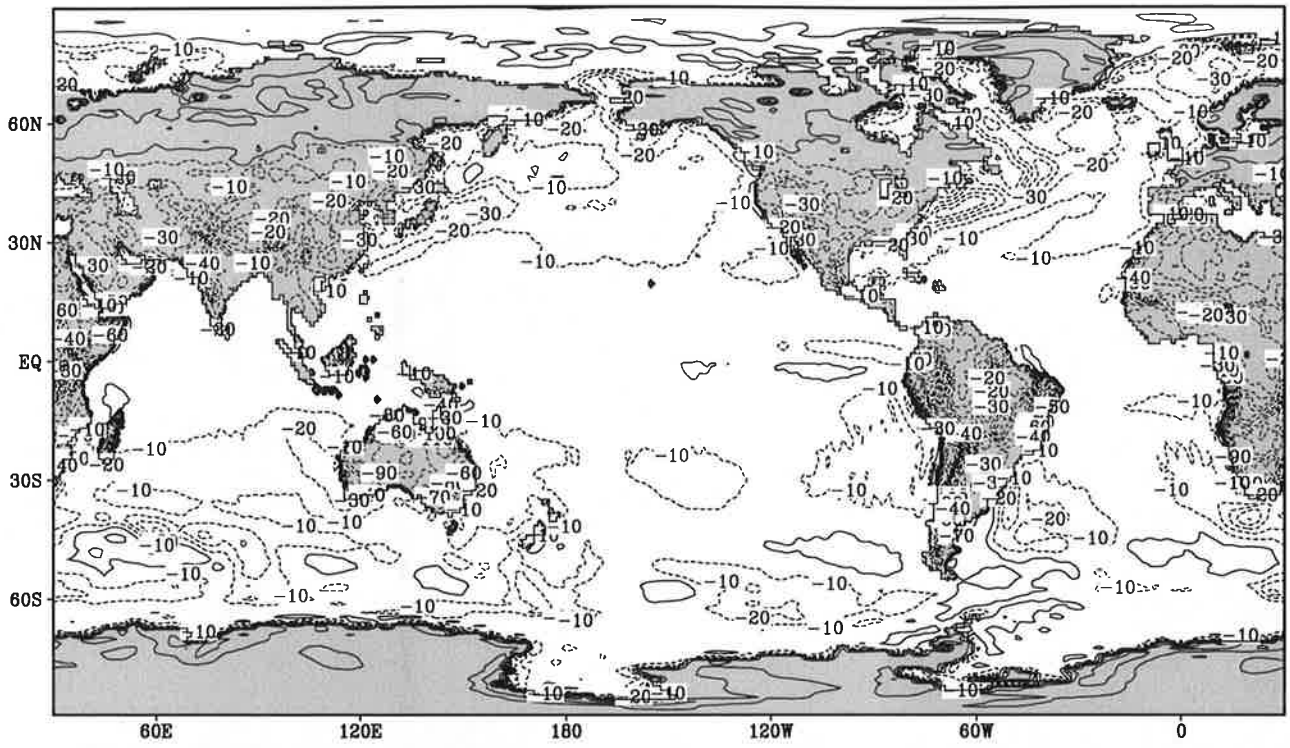

Contour interval: 10 Wm^{-2}

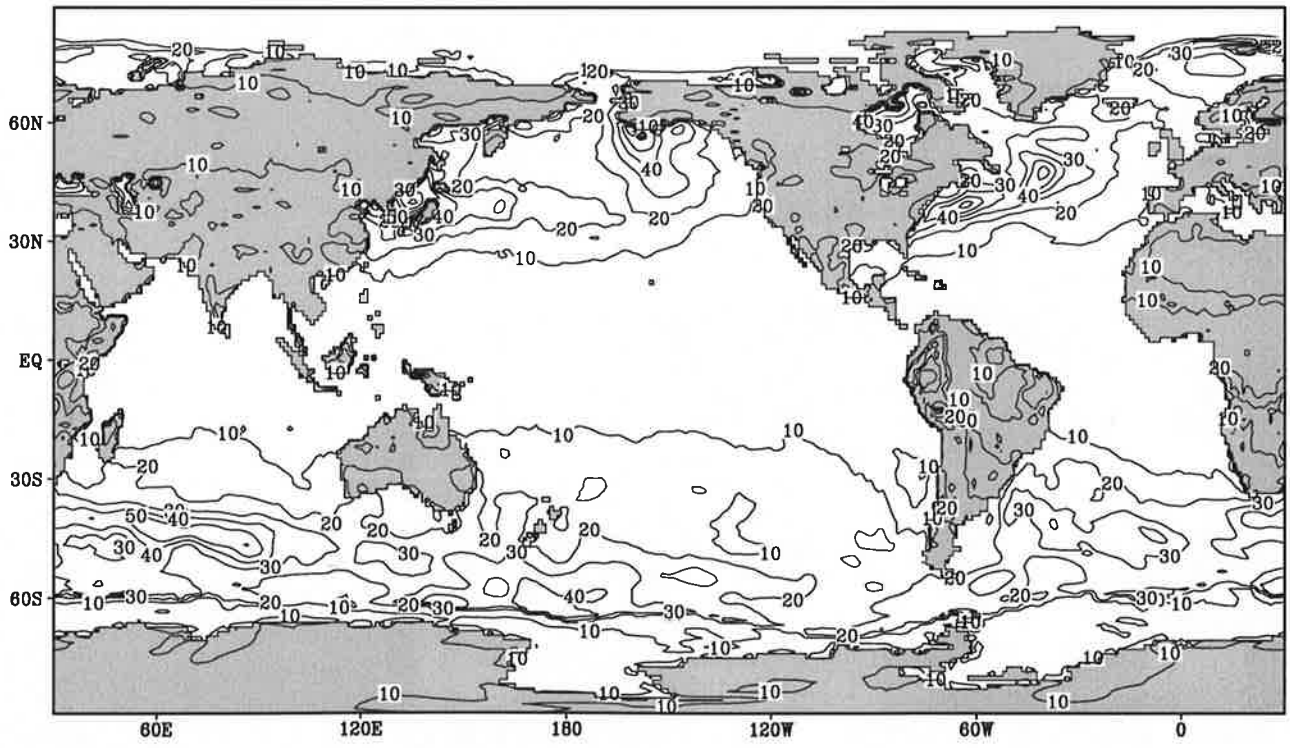

Contour interval: 10 Wm^{-2}

Fig.5.11 Sensible heat flux November

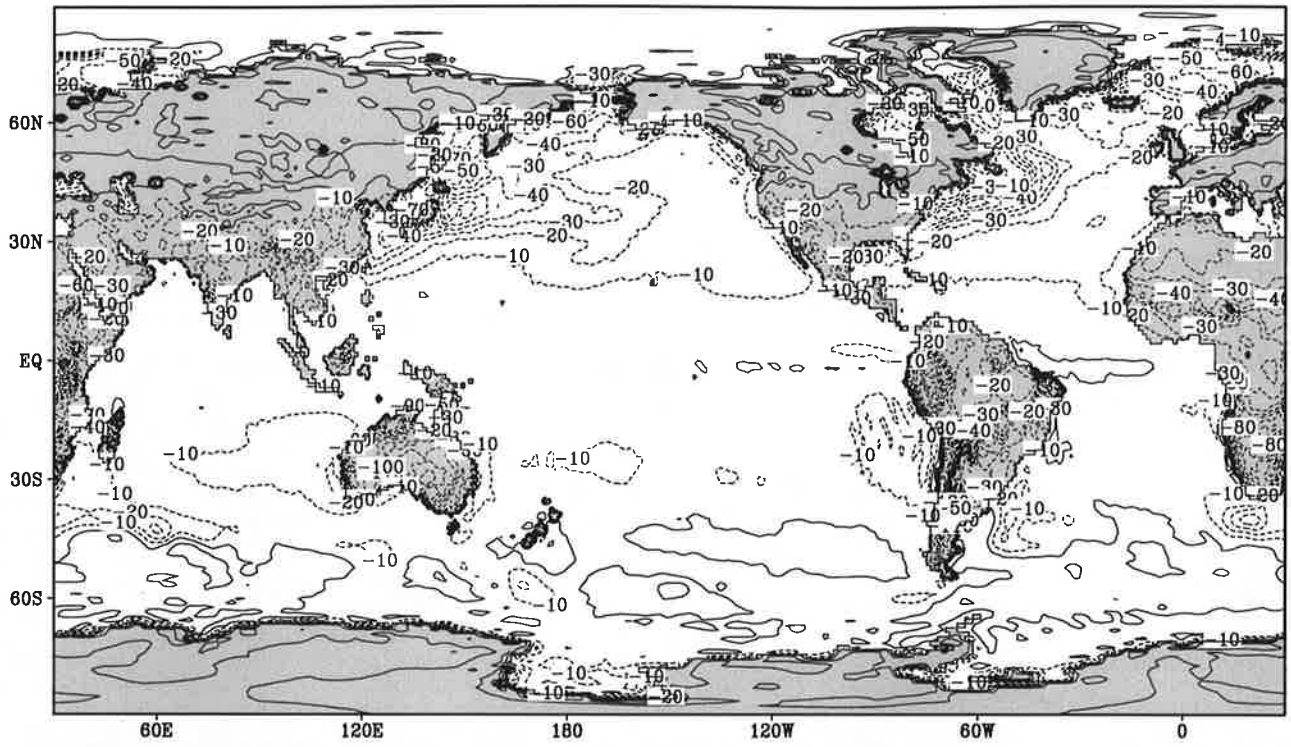

Contour interval: 10 Wm^{-2}

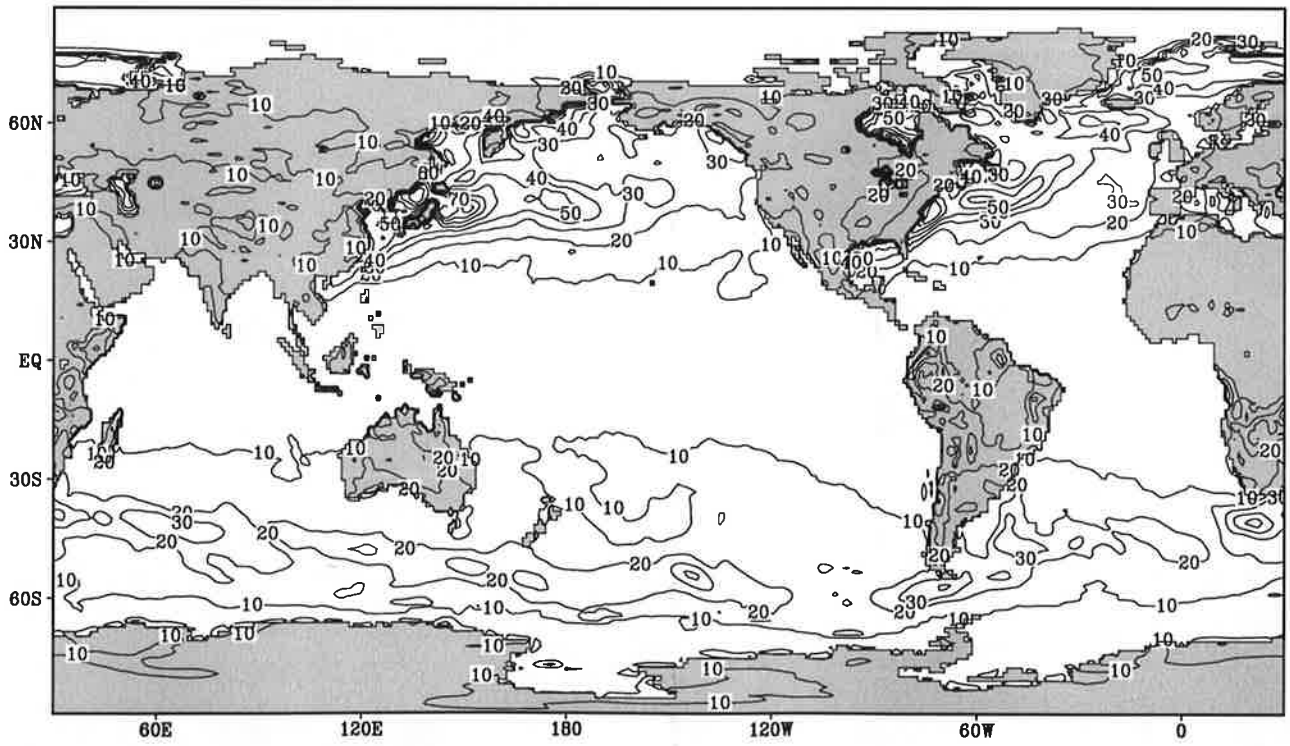

Contour interval: 10 Wm^{-2}

Fig.5.12 Sensible heat flux December

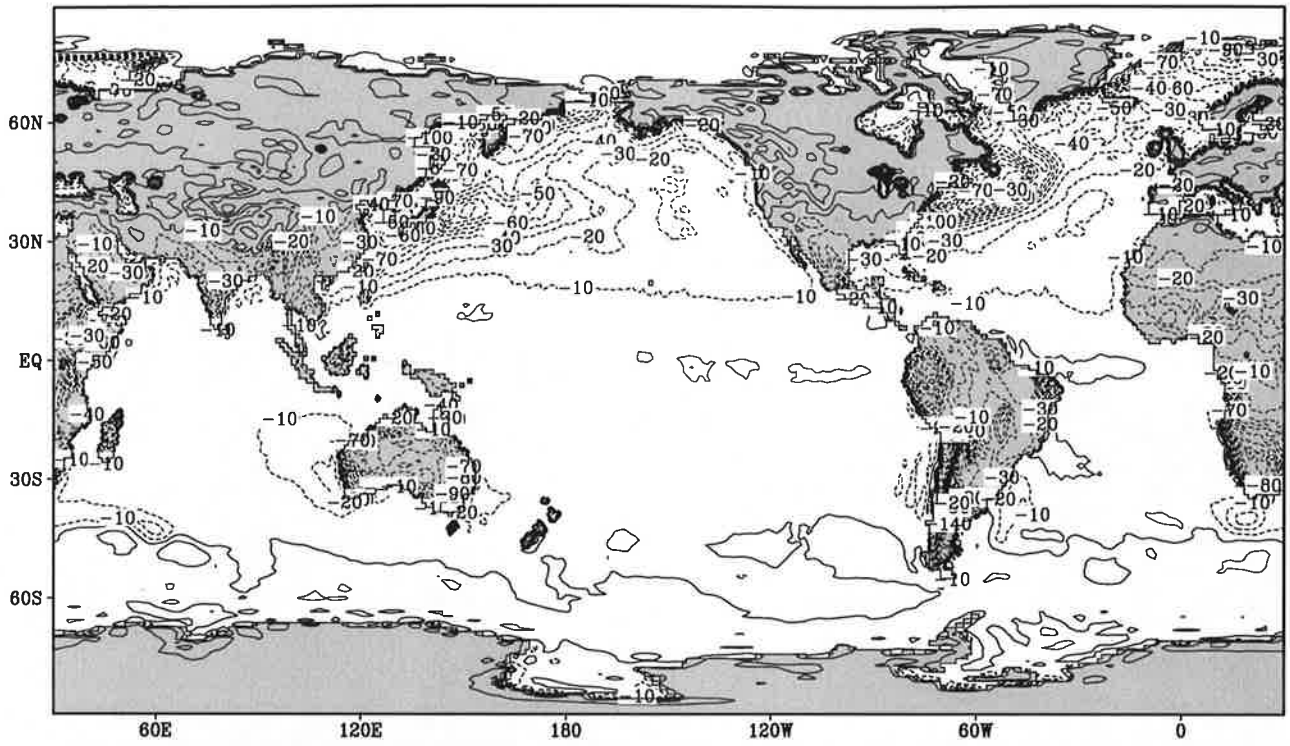

Contour interval: 10 Wm^{-2}

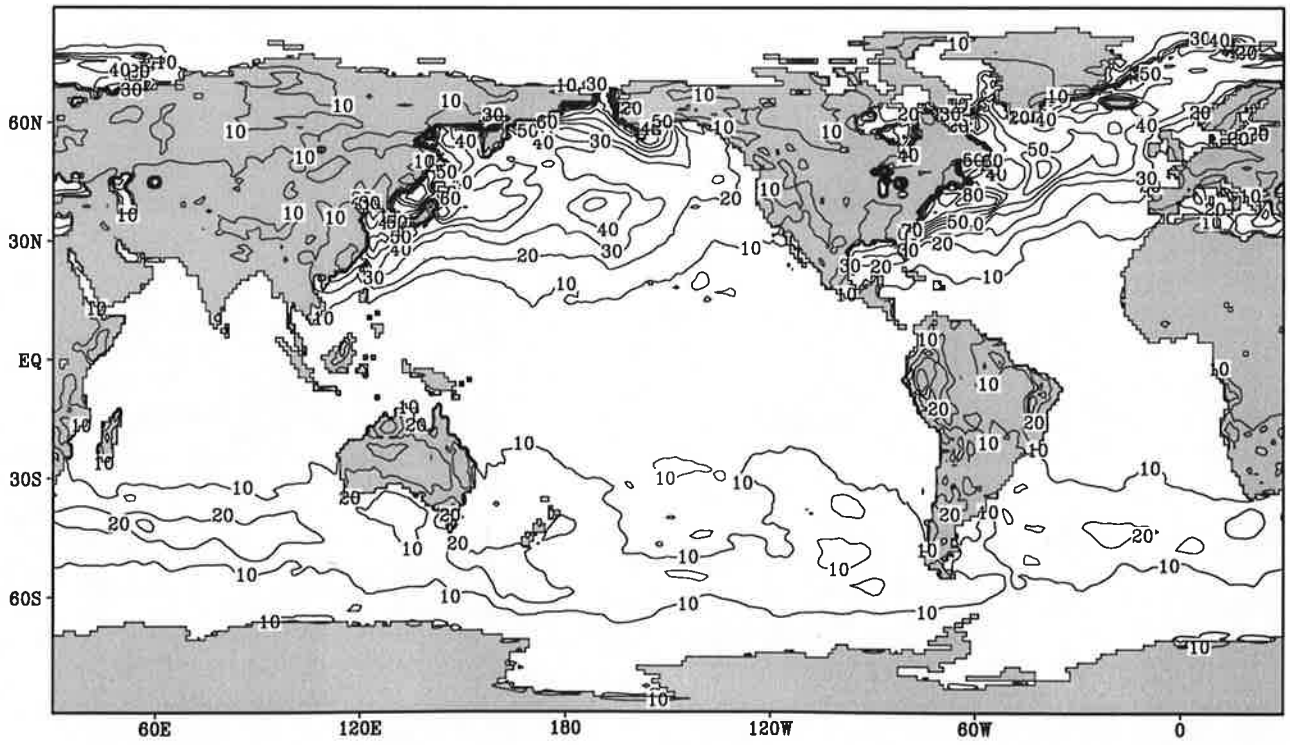

Contour interval: 10 Wm^{-2}

Fig.5.13 Sensible heat flux Annual Mean

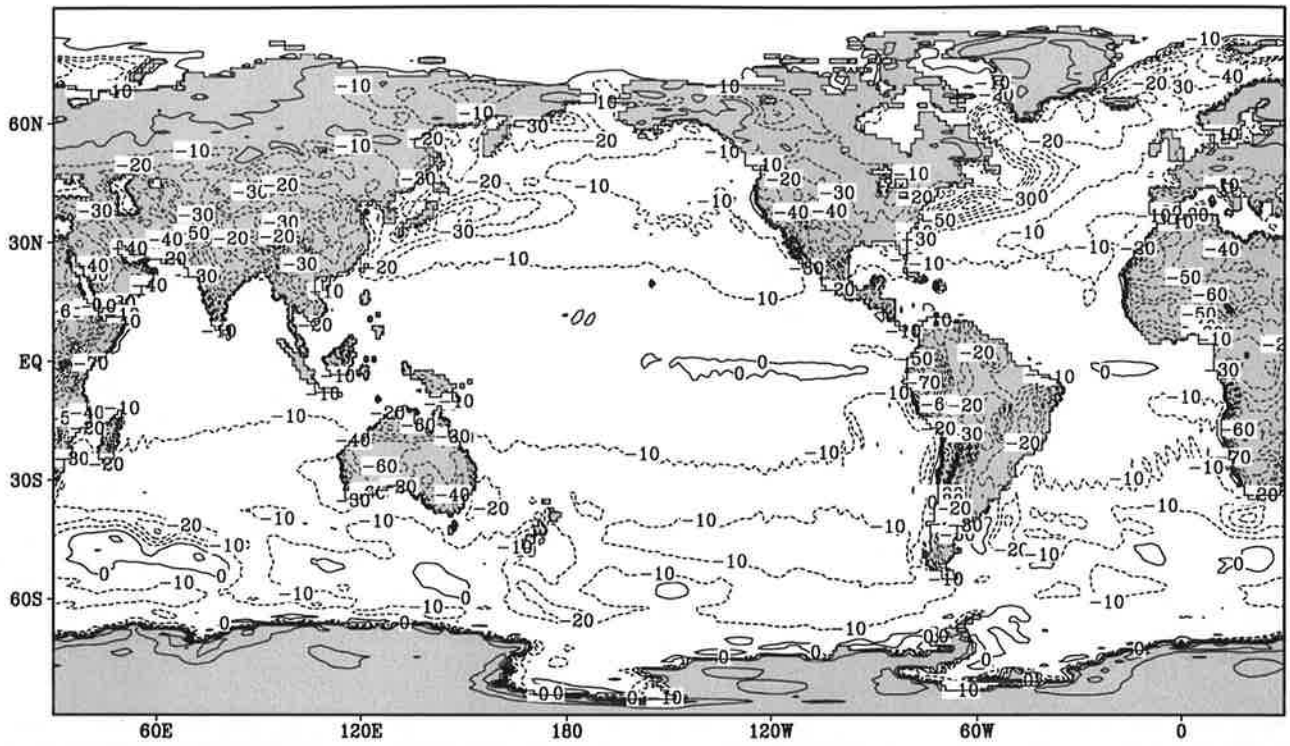

Contour interval: 10 Wm^{-2}

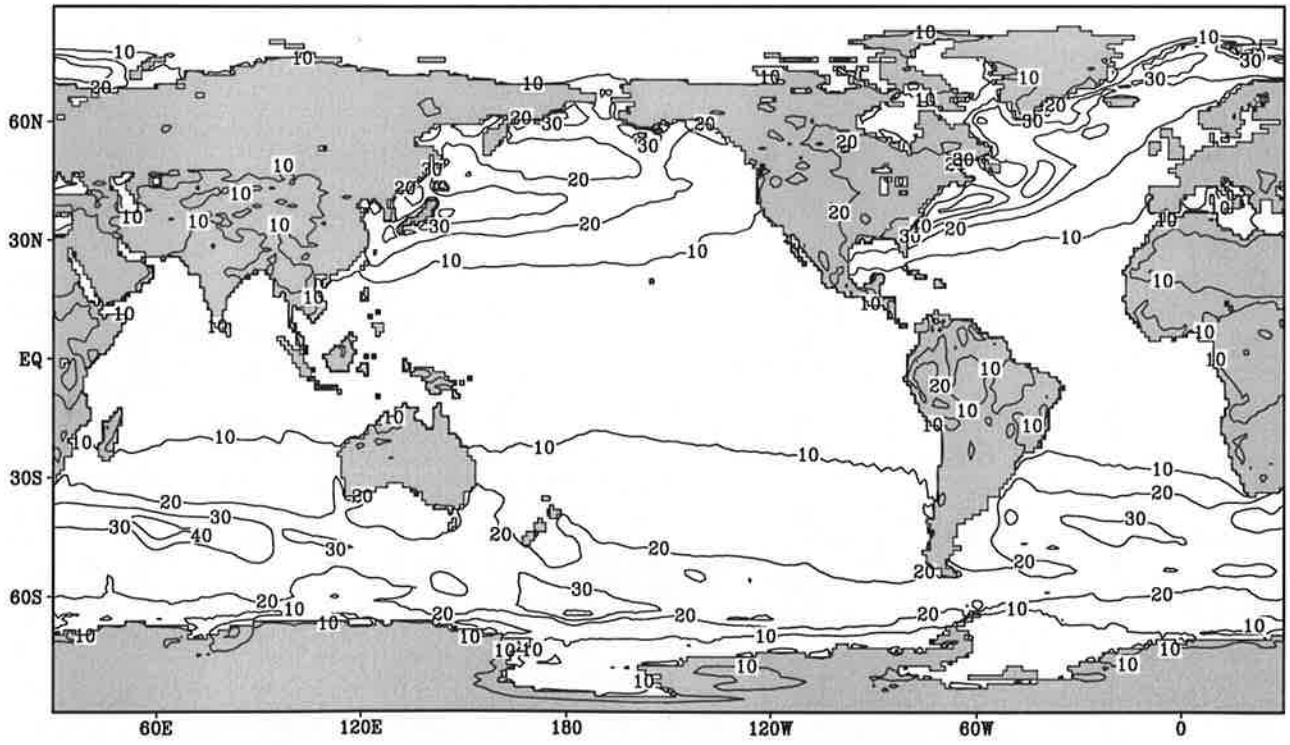

Contour interval: 10 Wm^{-2}

Fig.6.1 Latent heat flux January

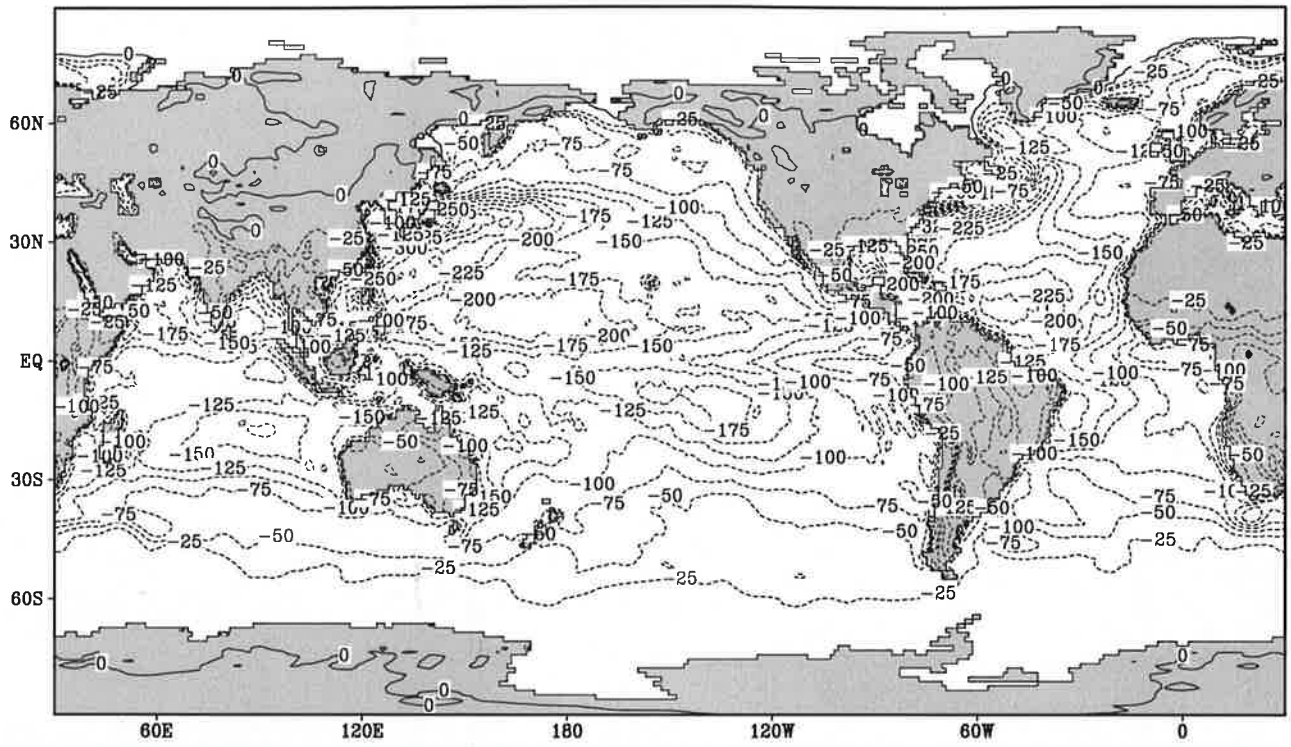

Contour interval: 25 Wm^{-2}

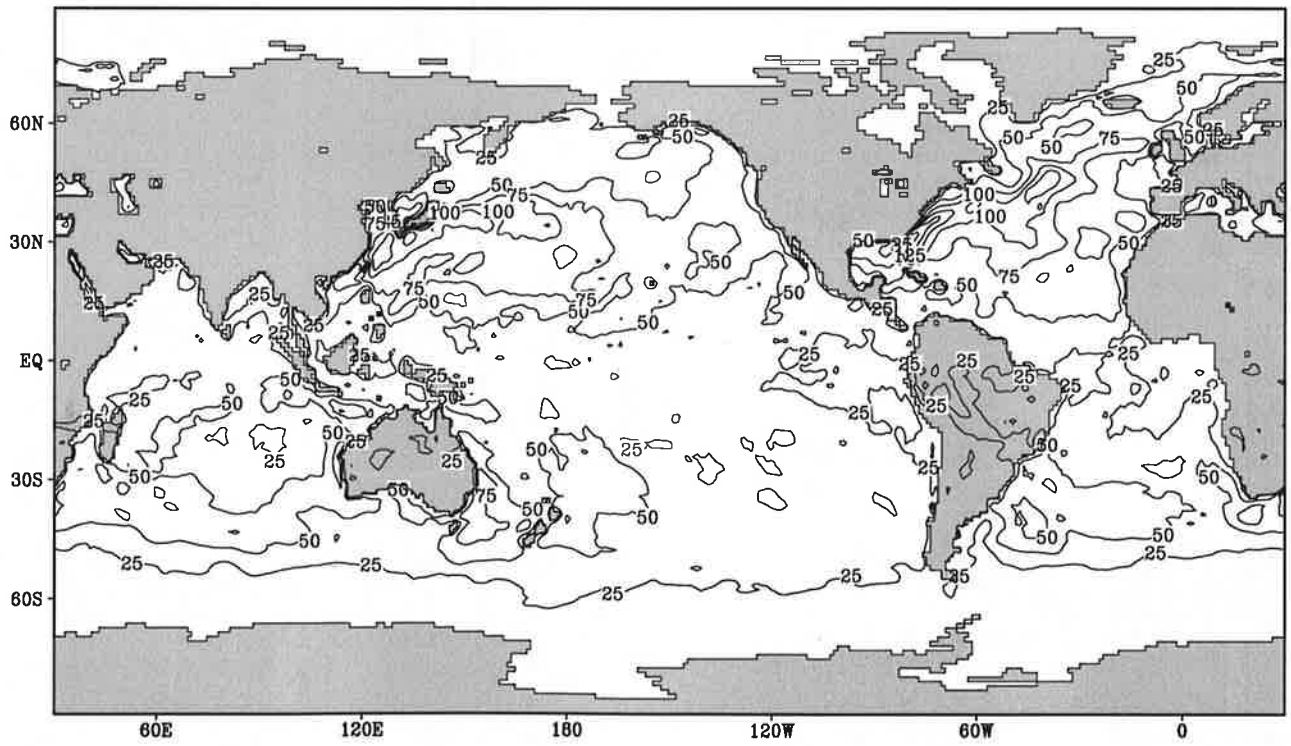

Contour interval: 25 Wm^{-2}

Fig.6.2 Latent heat flux February

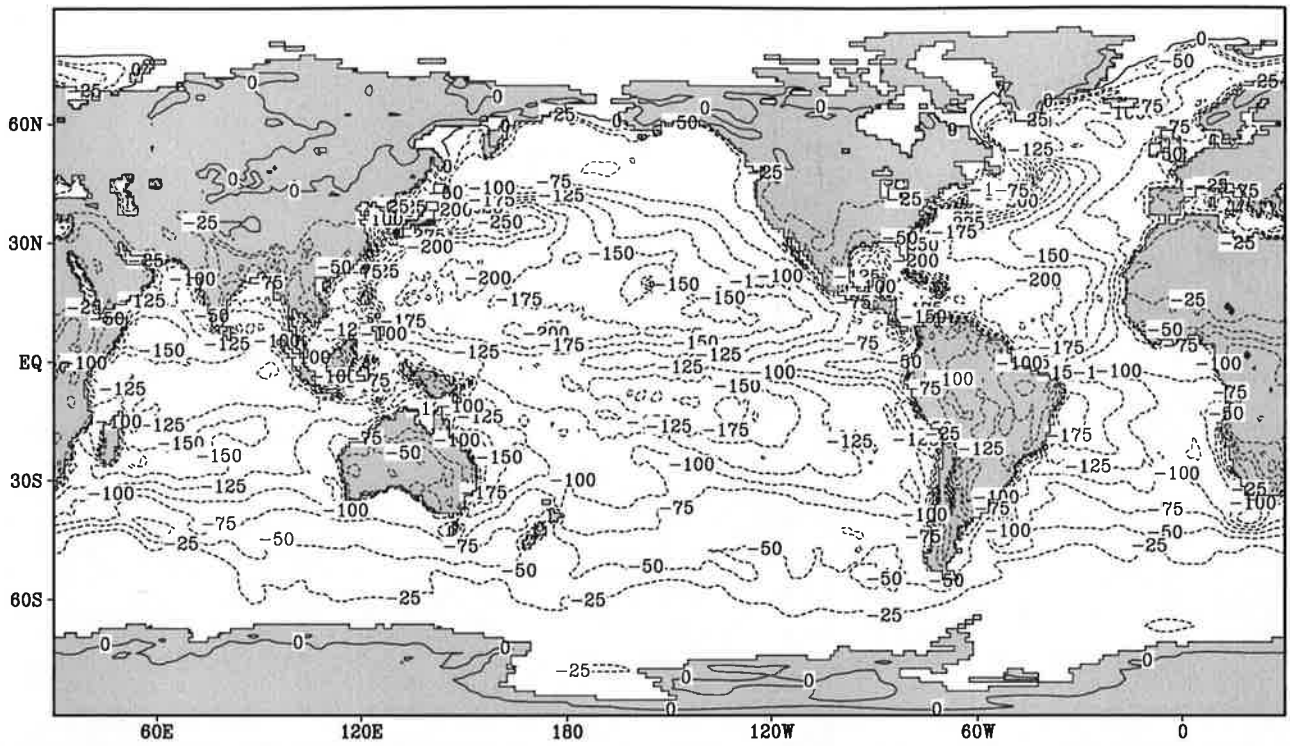

Contour interval: 25 Wm^{-2}

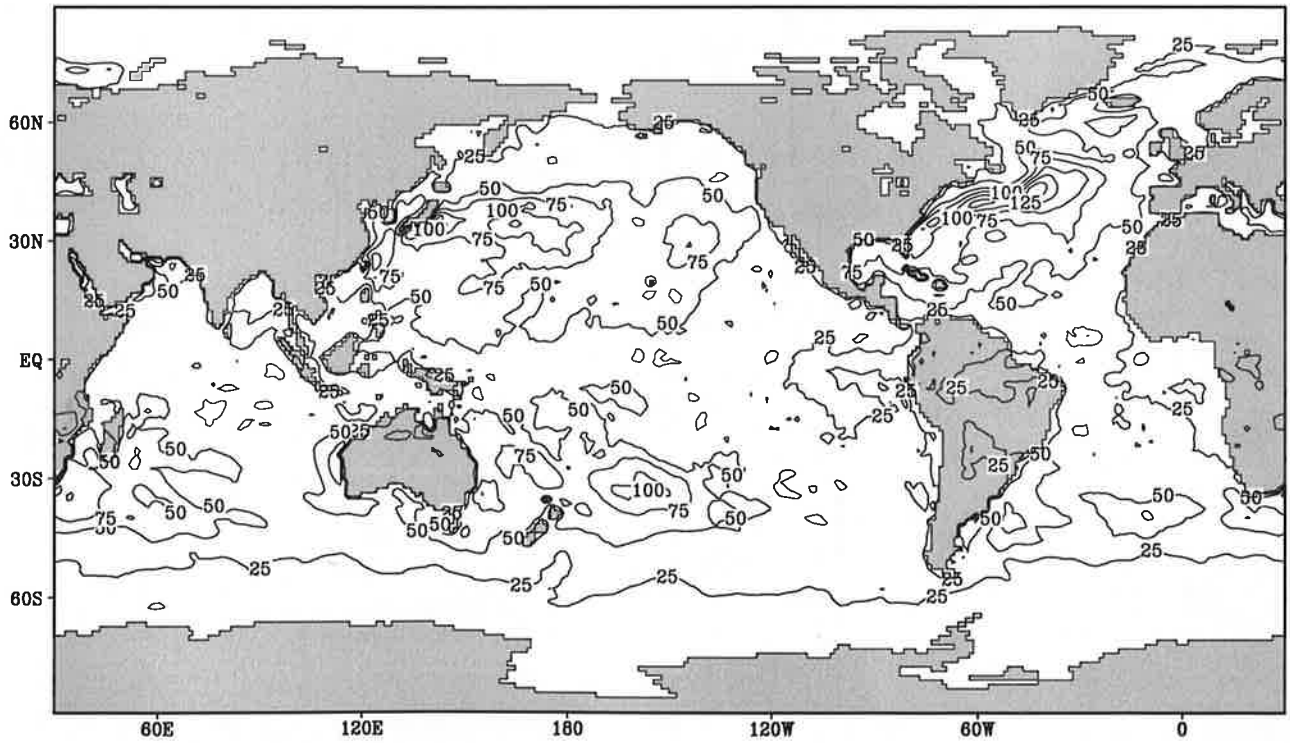

Contour interval: 25 Wm^{-2}

Fig.6.3 Latent heat flux March

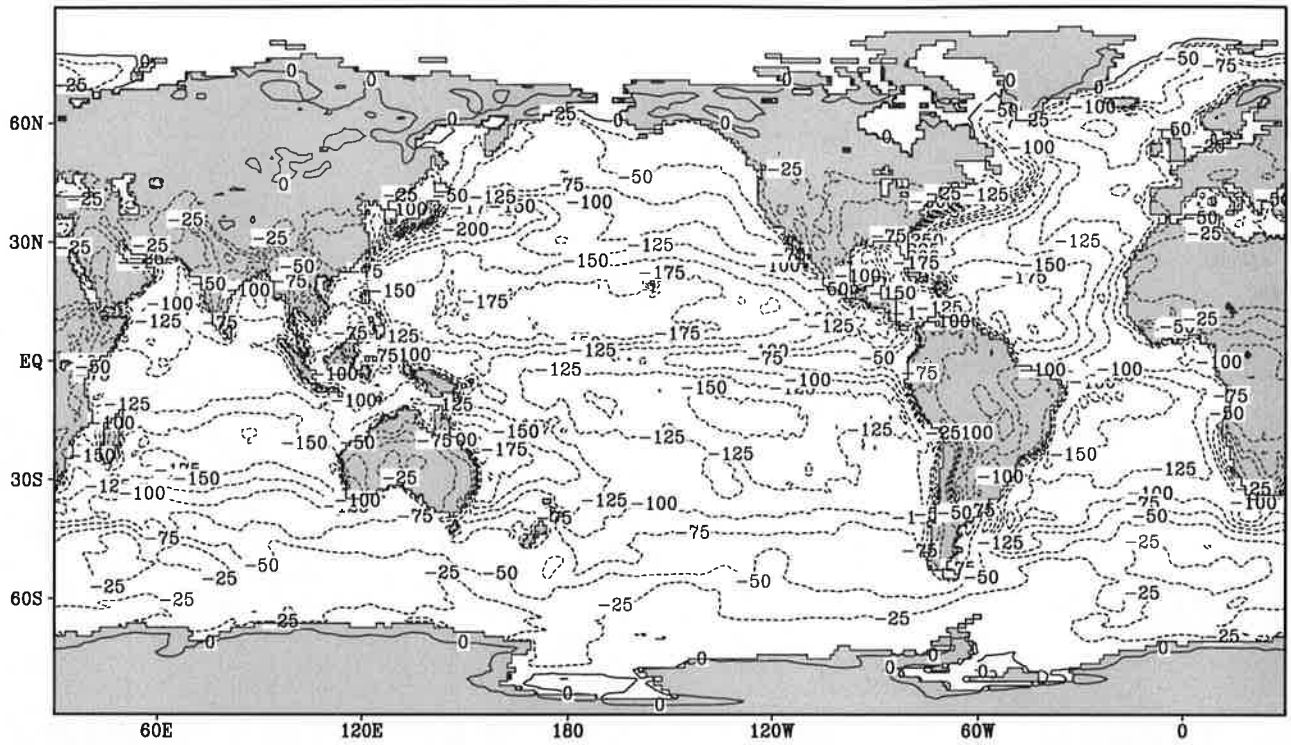

Contour interval: 25 Wm^{-2}

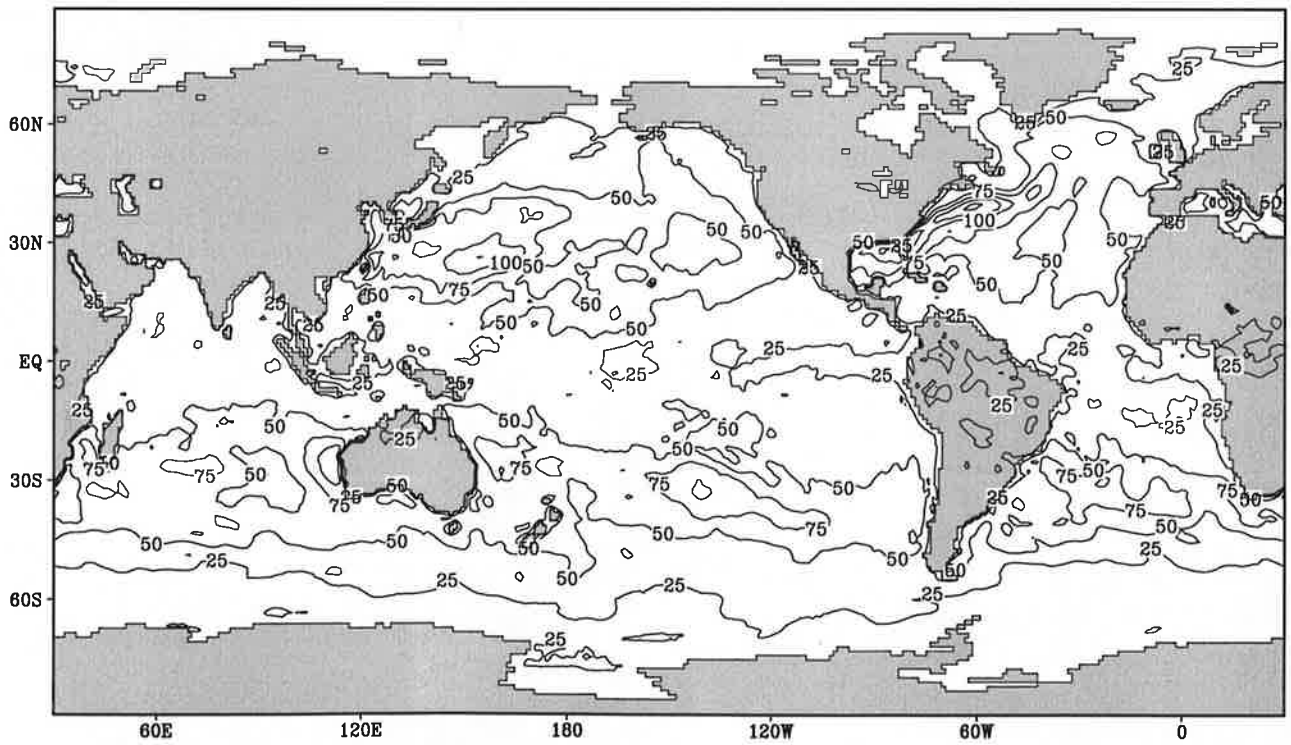

Contour interval: 25 Wm^{-2}

Fig.6.4 Latent heat flux April

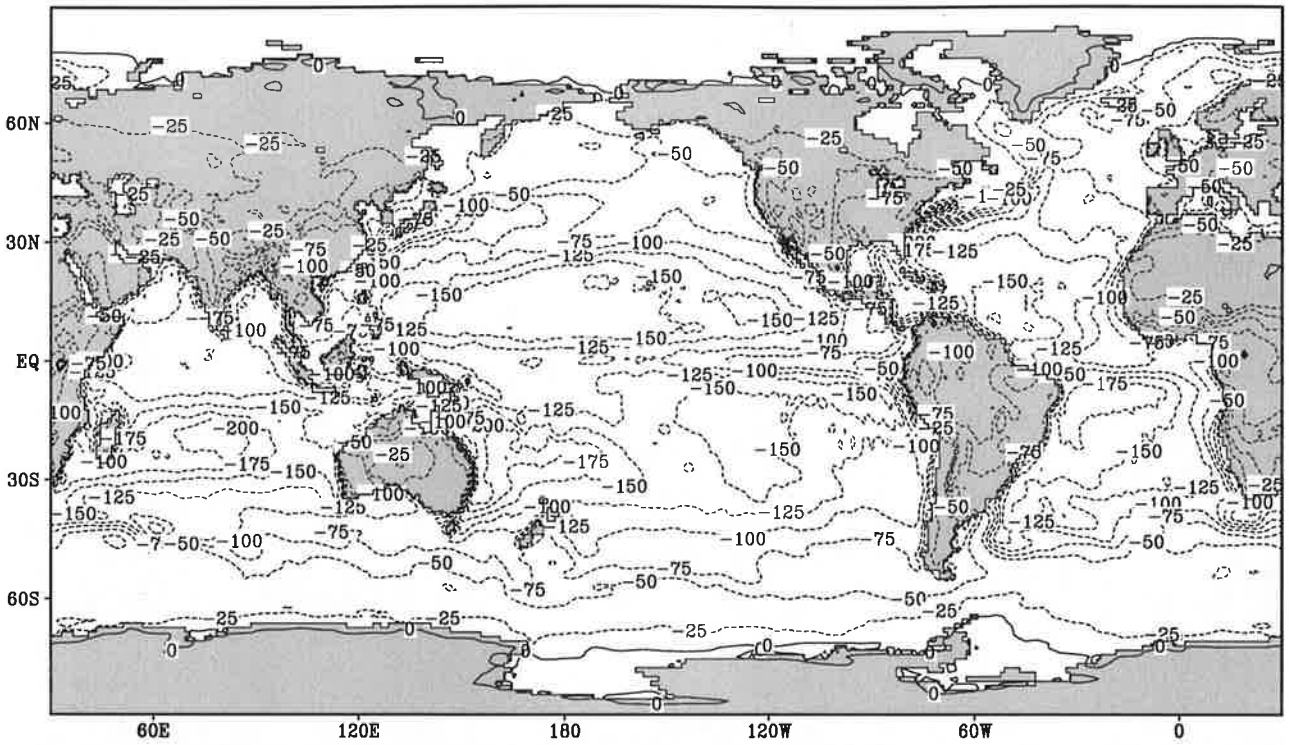

Contour interval: 25 Wm^{-2}

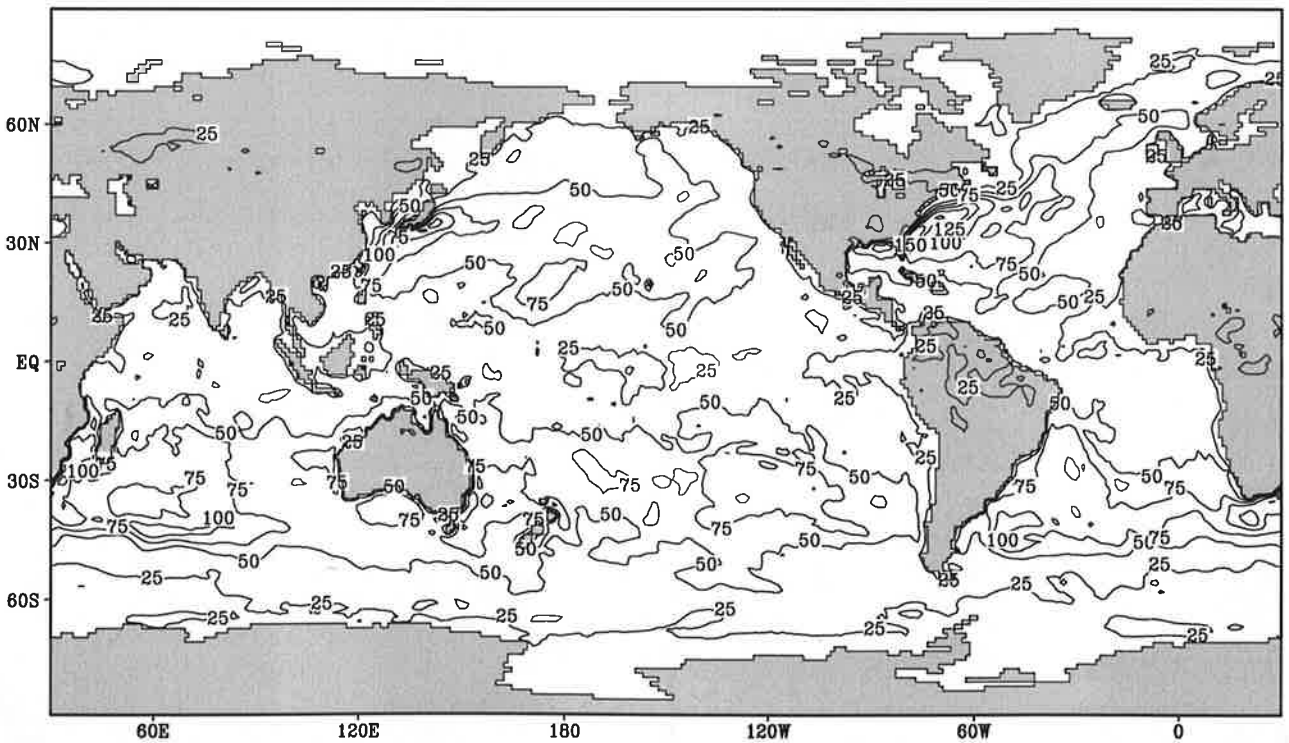

Contour interval: 25 Wm^{-2}

Fig.6.5 Latent heat flux May

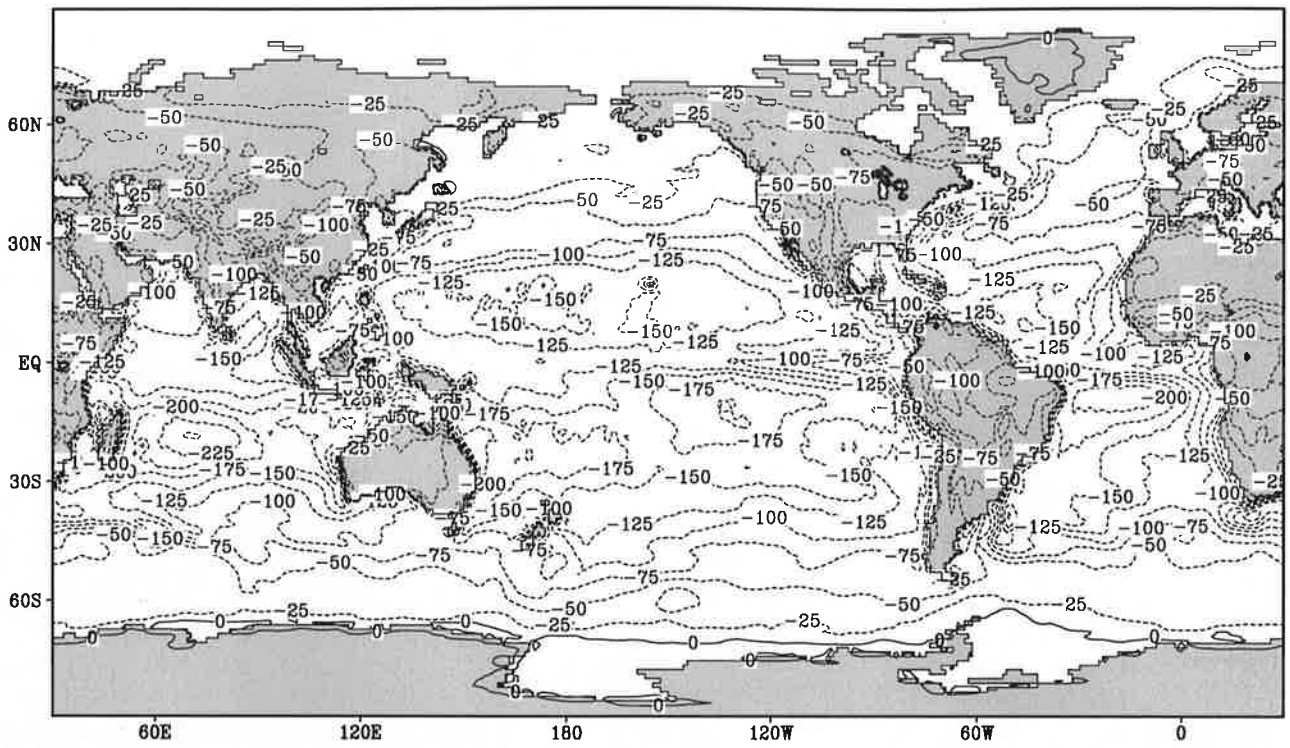

Contour interval: 25 Wm^{-2}

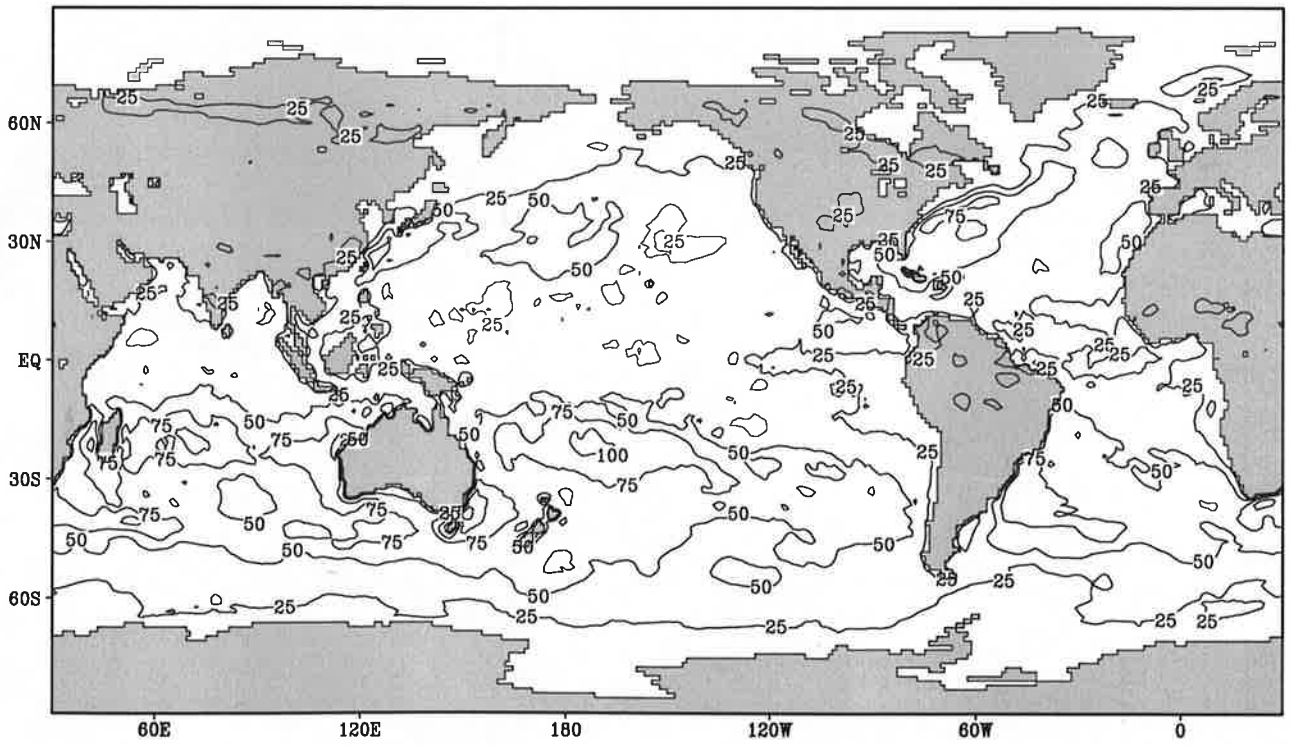

Contour interval: 25 Wm^{-2}

Fig.6.6 Latent heat flux June

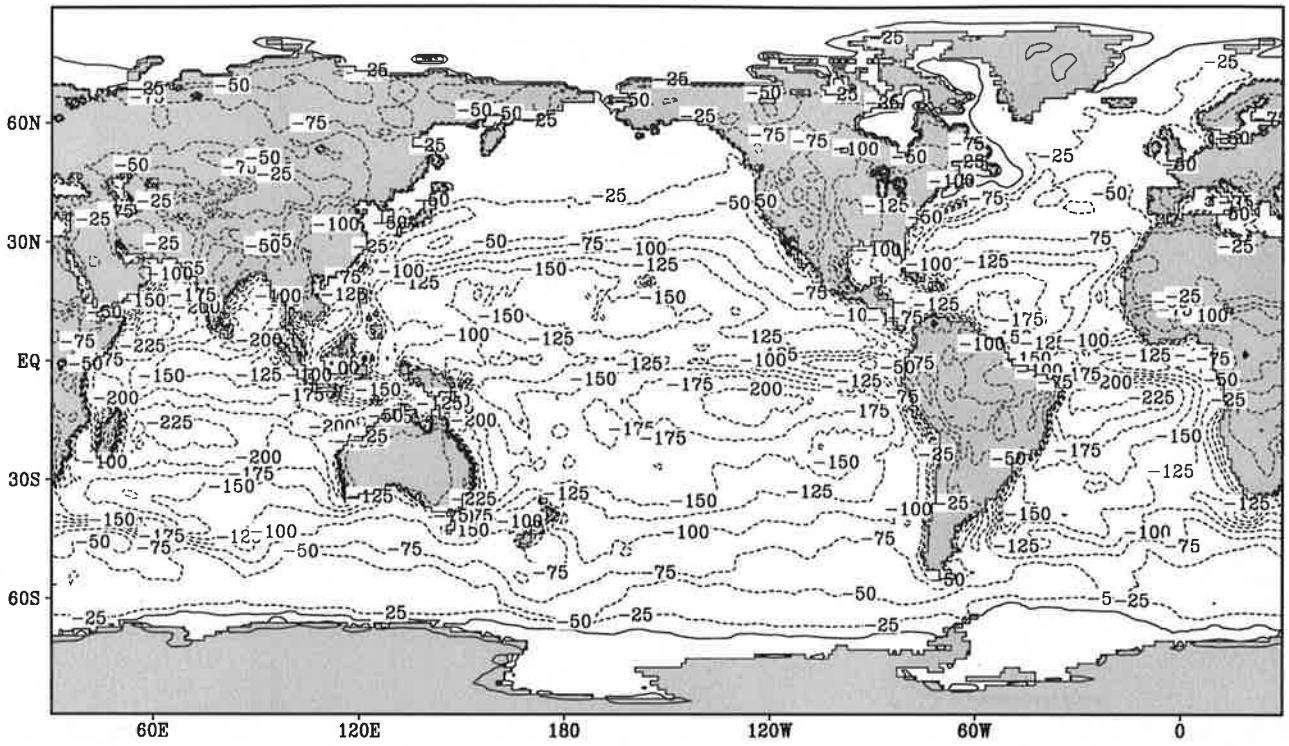

Contour interval: 25 Wm^{-2}

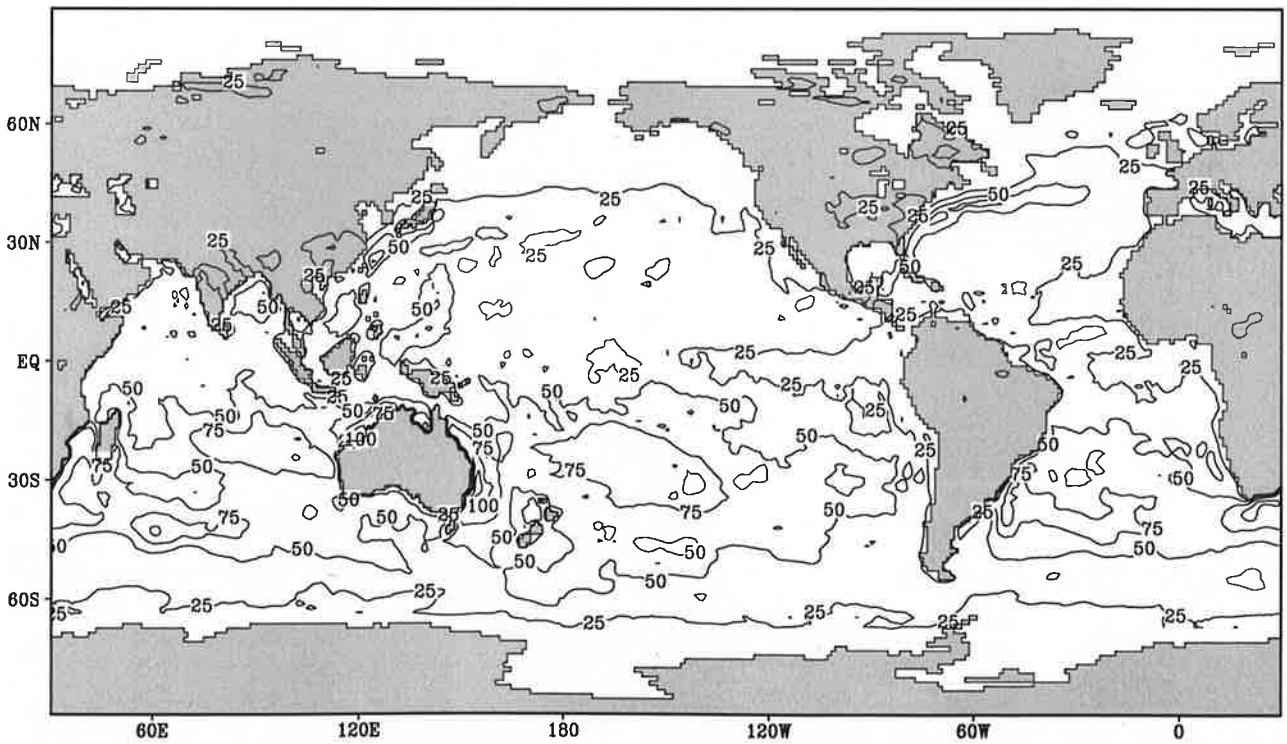

Contour interval: 25 Wm^{-2}

Fig.6.7 Latent heat flux July

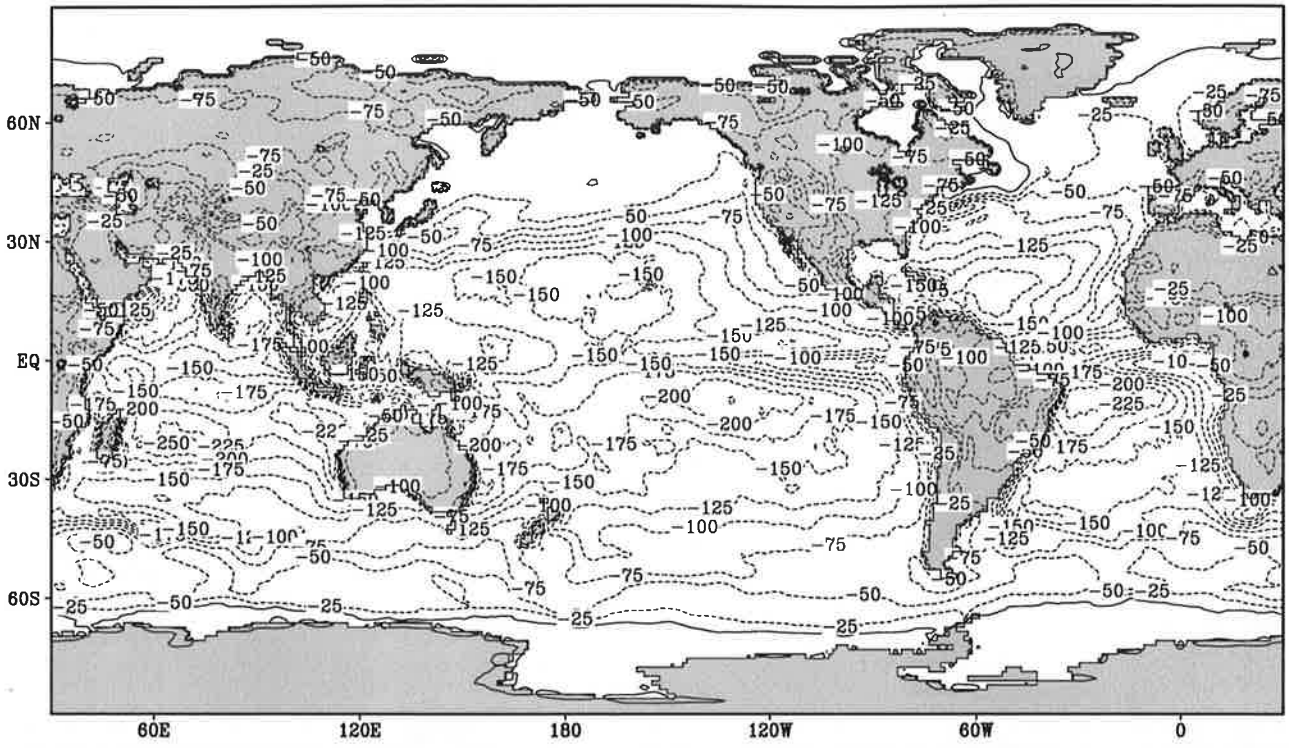

Contour interval: 25 Wm^{-2}

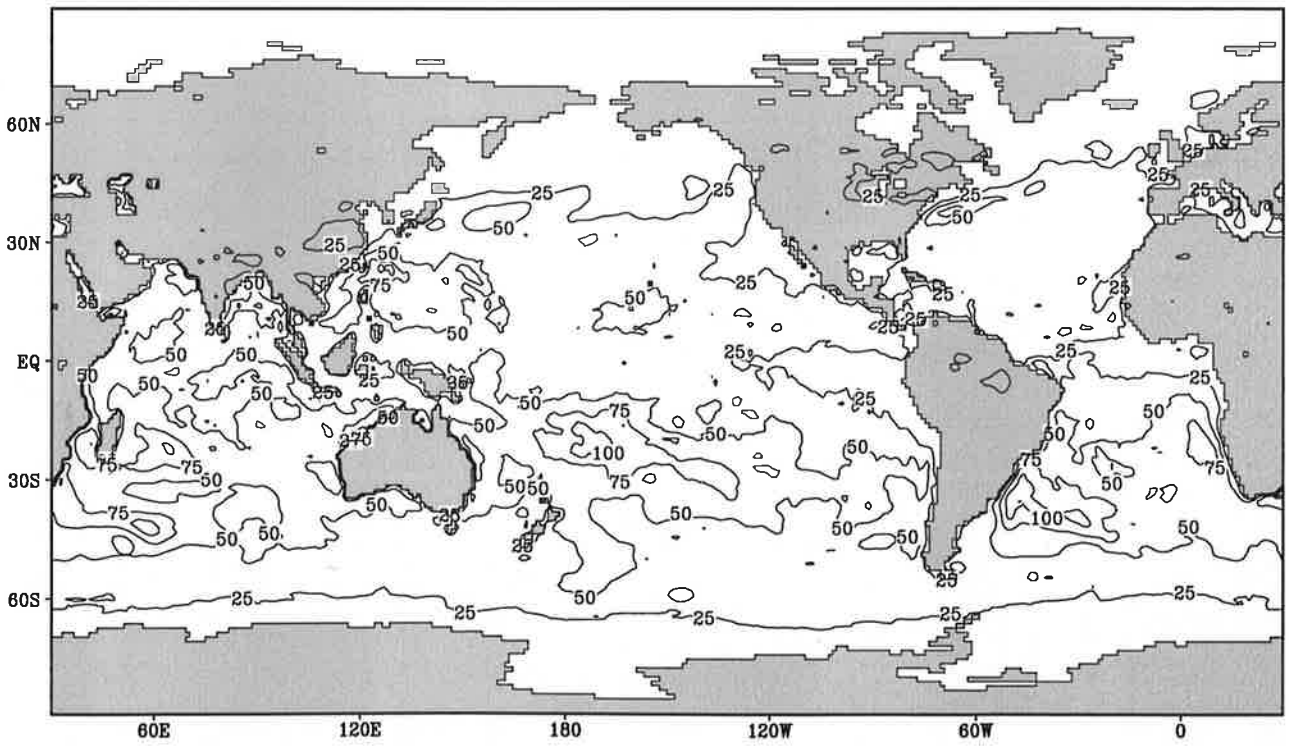

Contour interval: 25 Wm^{-2}

Fig.6.8 Latent heat flux August

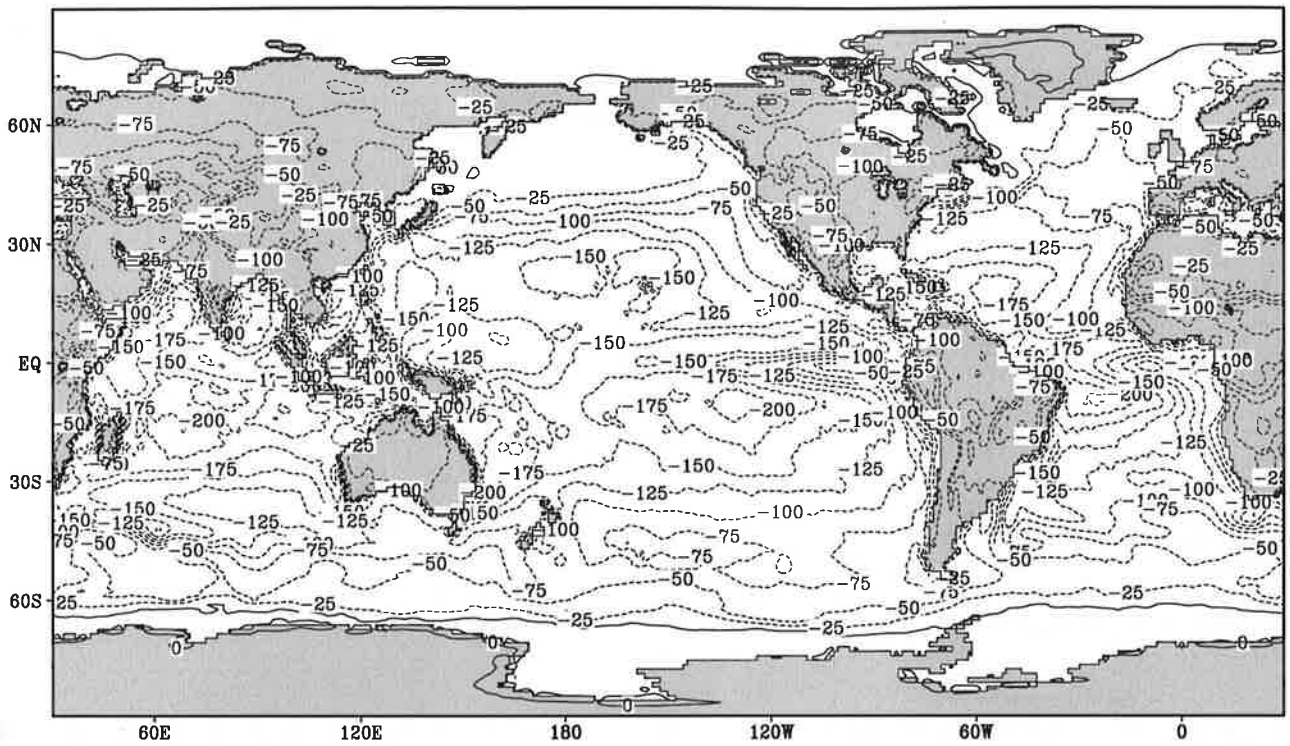

Contour interval: 25 Wm^{-2}

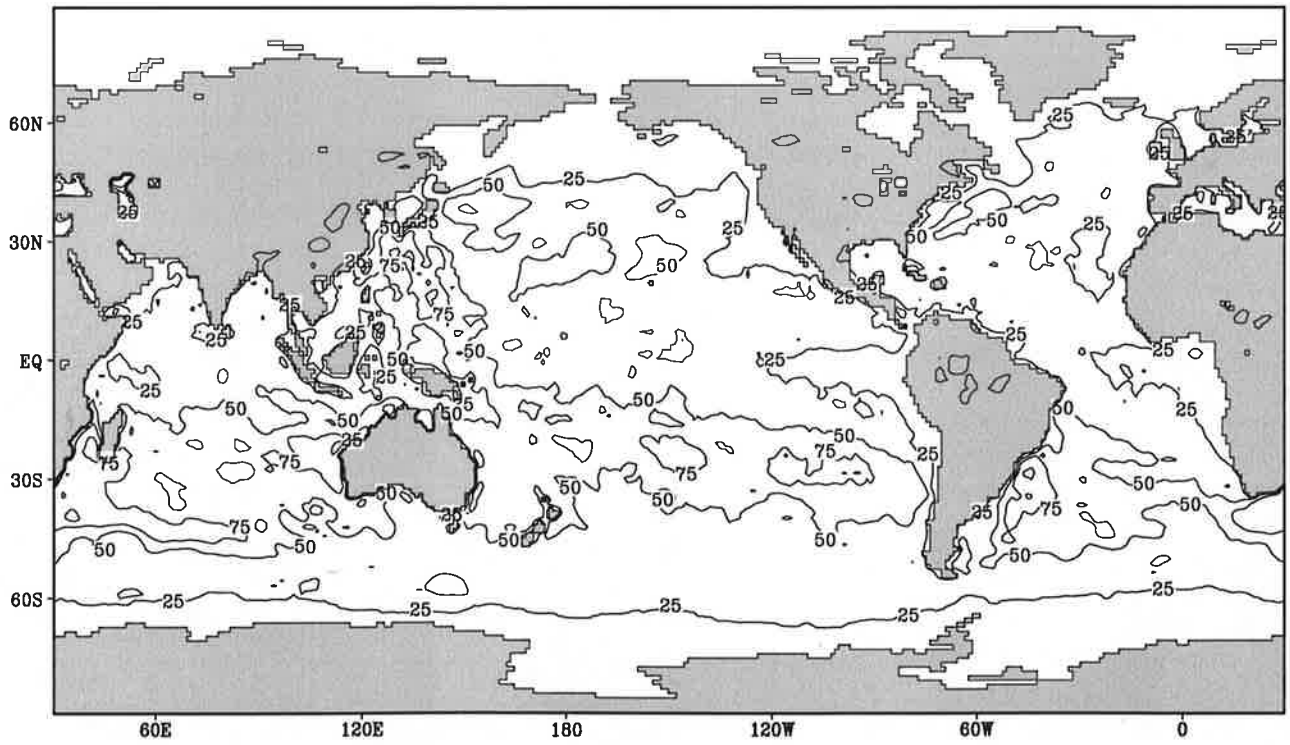

Contour interval: 25 Wm^{-2}

Fig.6.9 Latent heat flux September

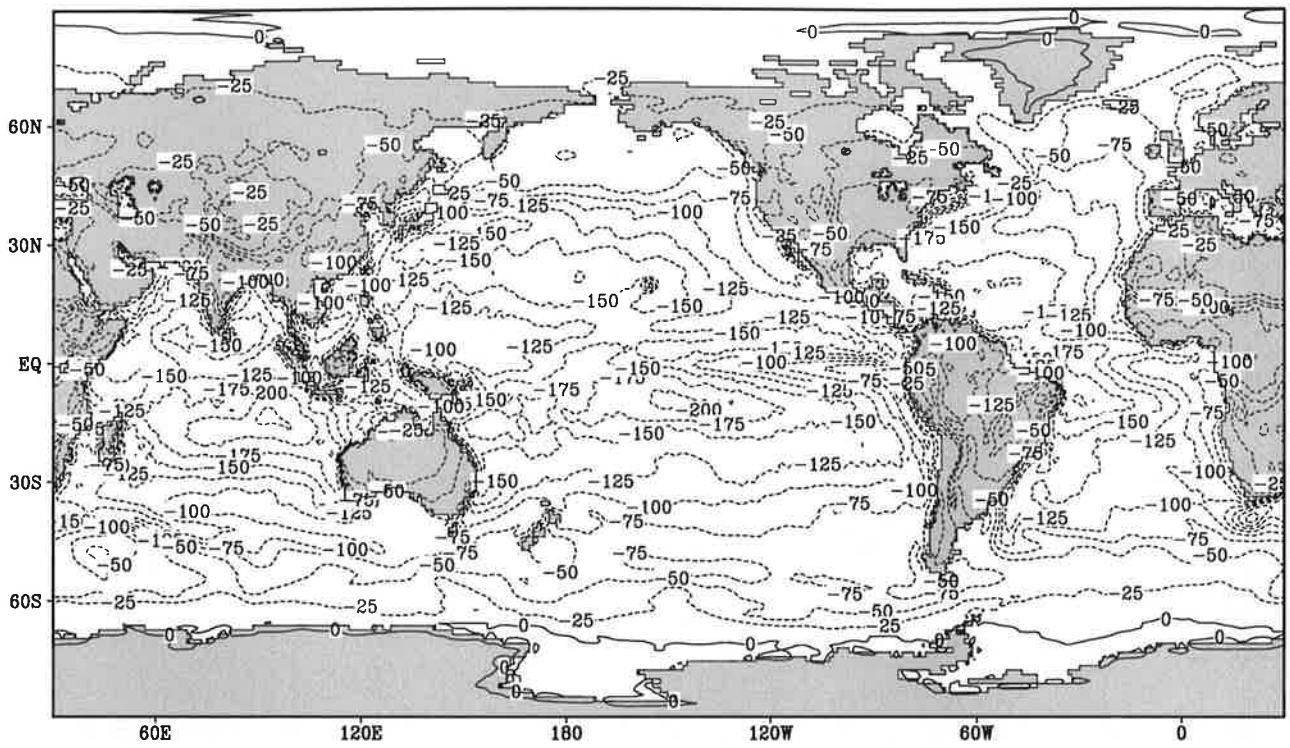

Contour interval: 25 Wm^{-2}

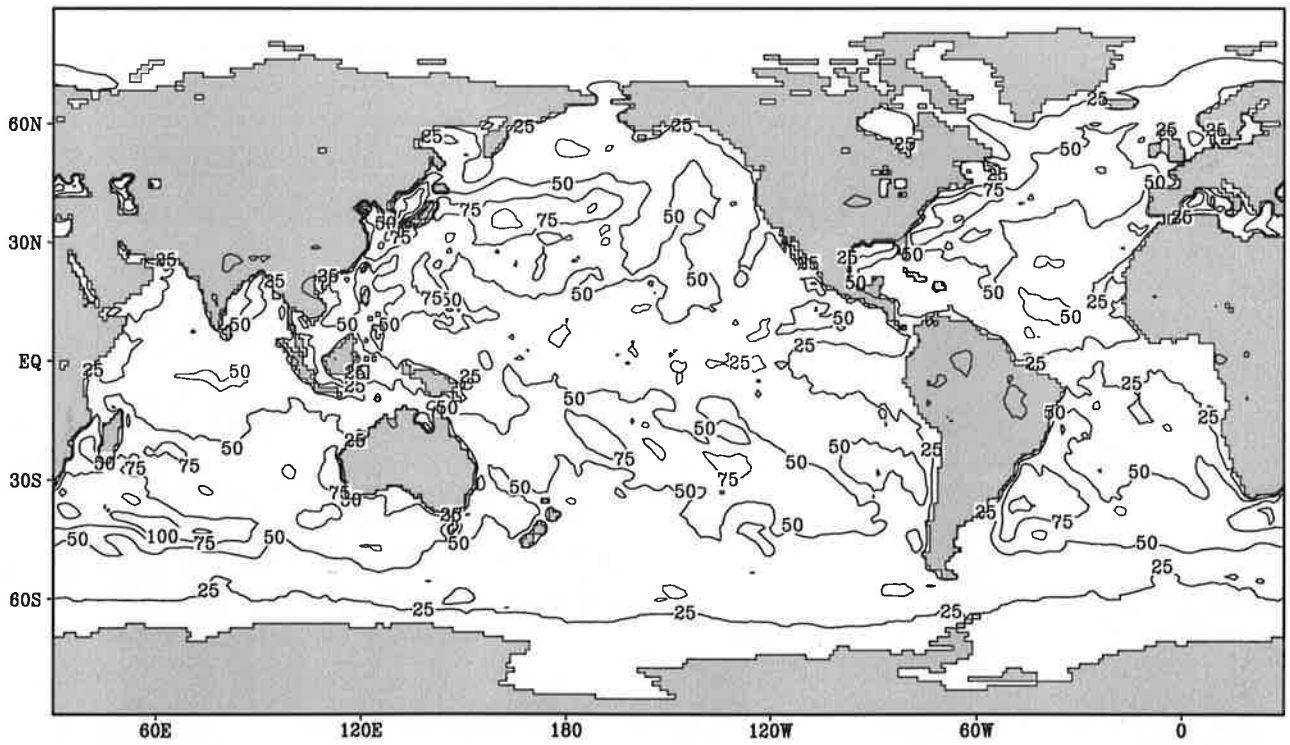

Contour interval: 25 Wm^{-2}

Fig.6.10 Latent heat flux October

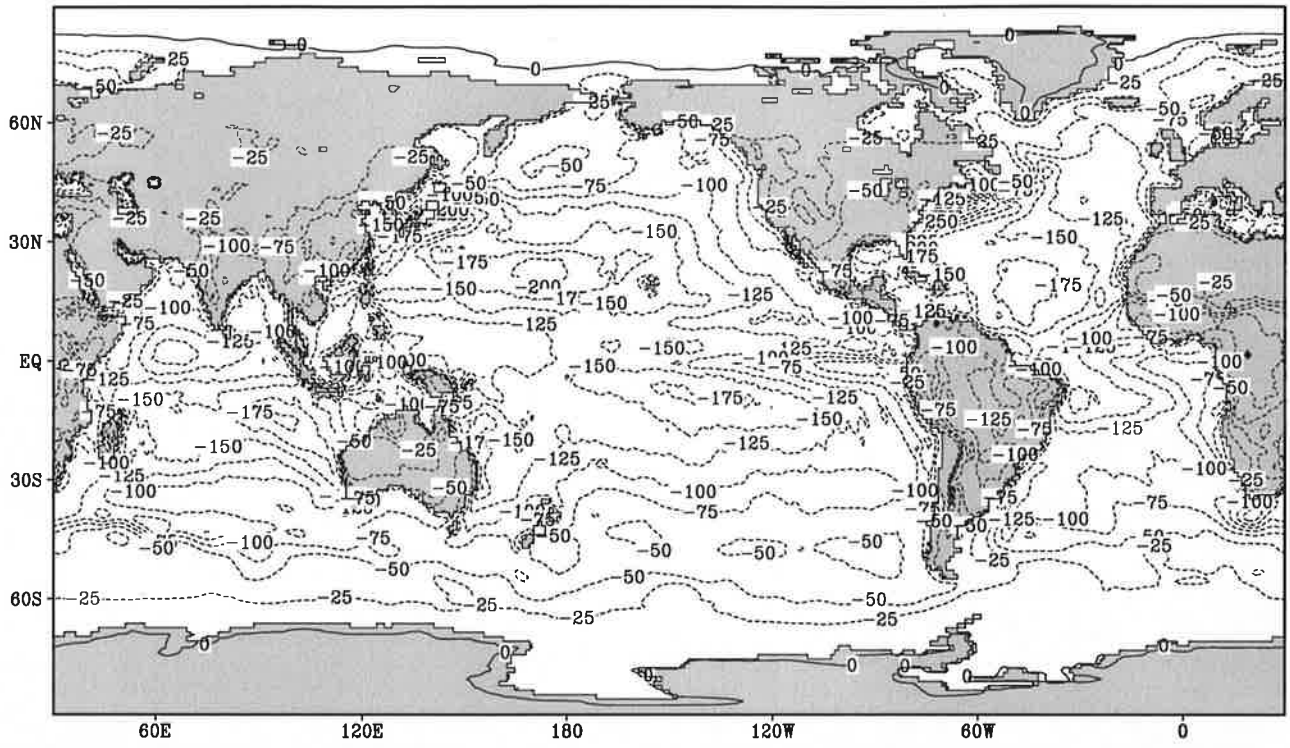

Contour interval: 25 Wm^{-2}

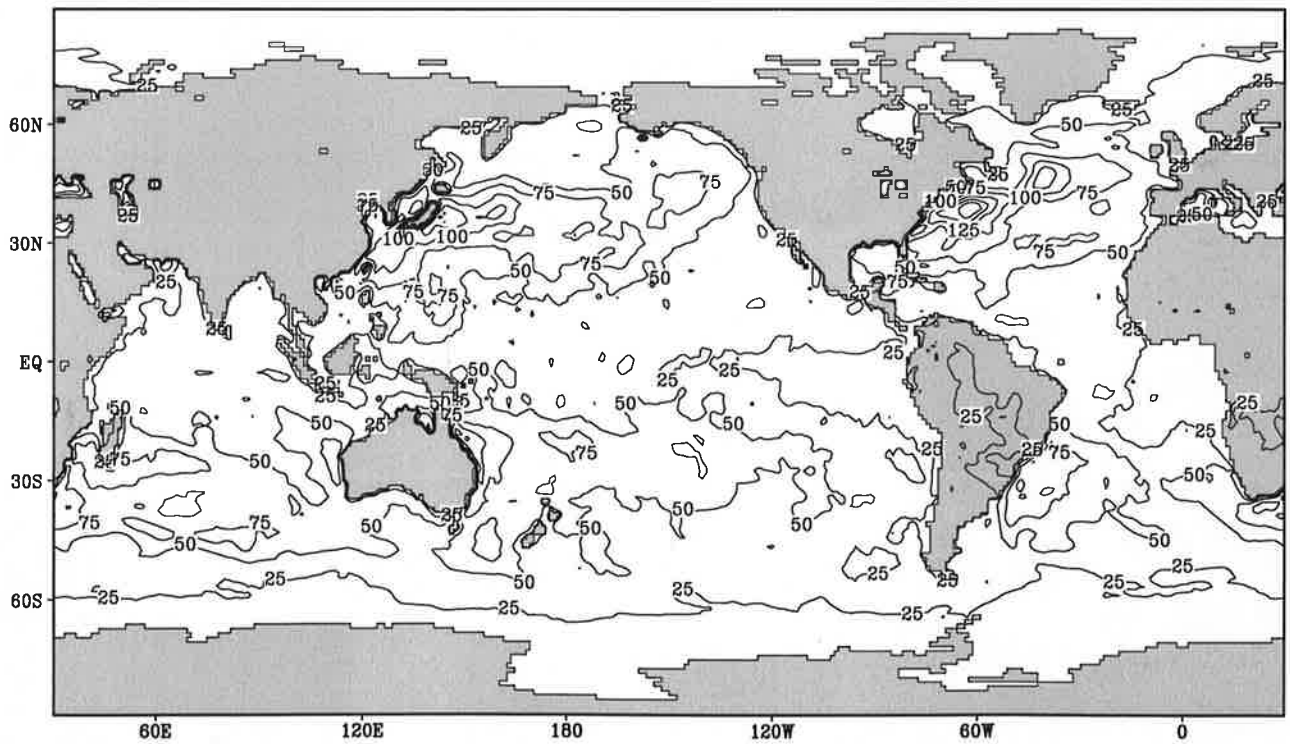

Contour interval: 25 Wm^{-2}

Fig.6.11 Latent heat flux November

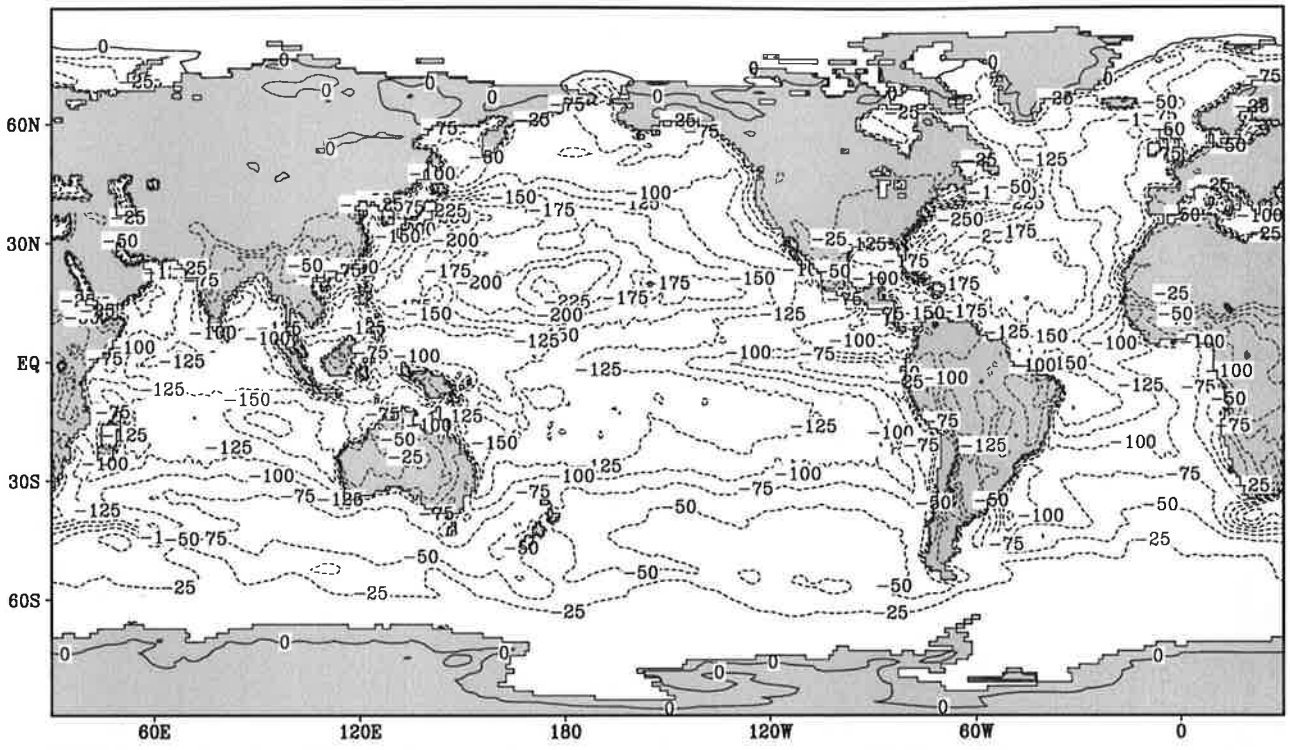

Contour interval: 25 Wm^{-2}

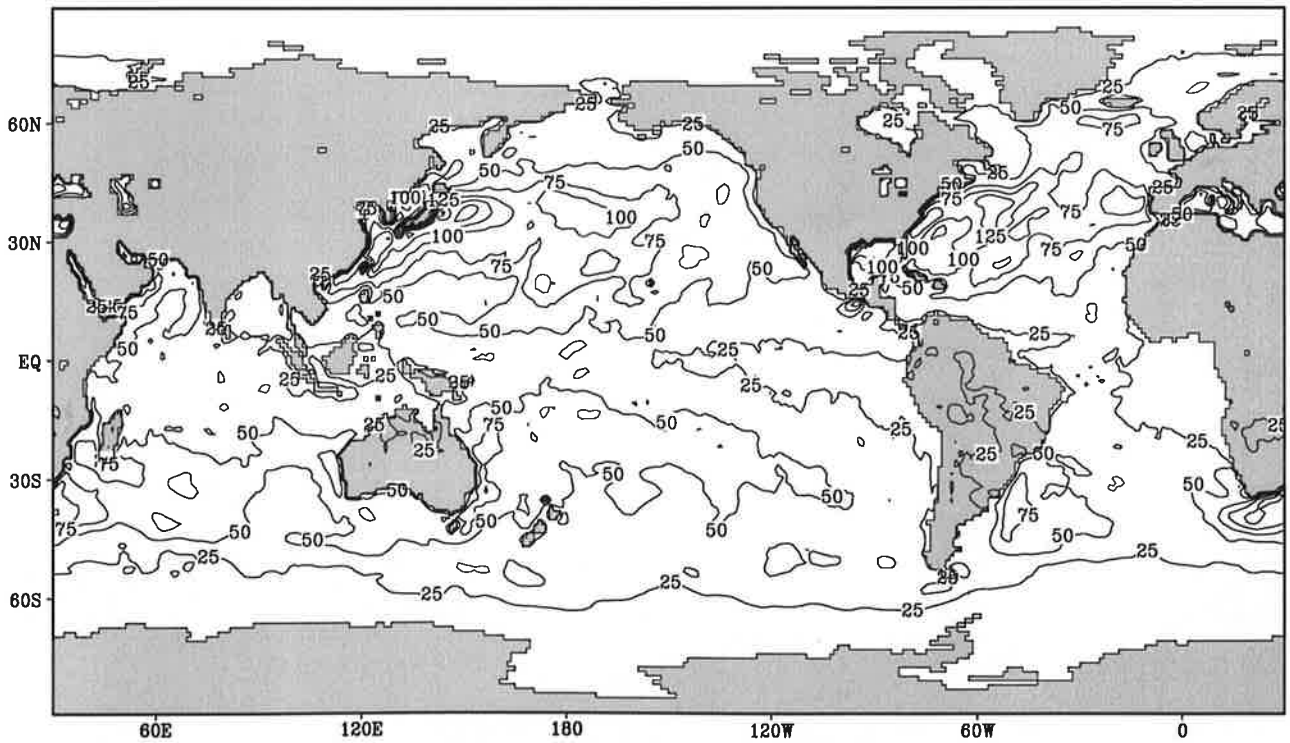

Contour interval: 25 Wm^{-2}

Fig.6.12 Latent heat flux December

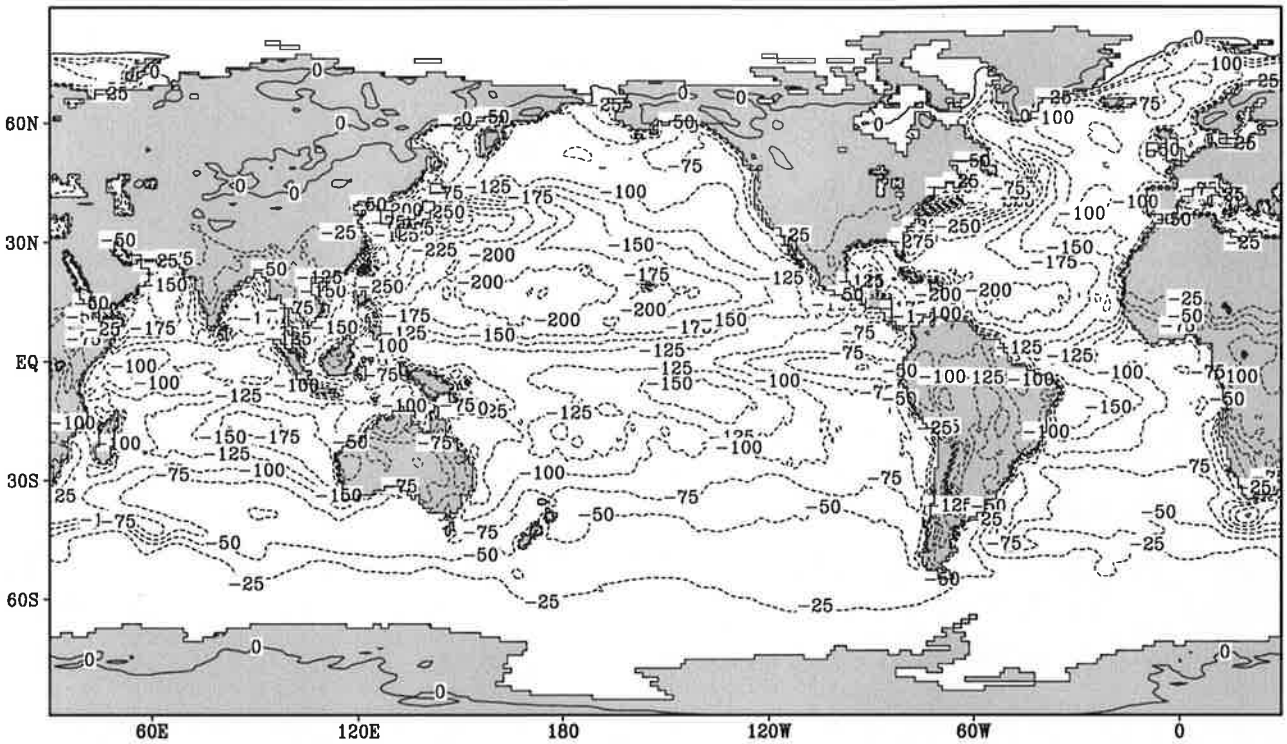

Contour interval: 25 Wm^{-2}

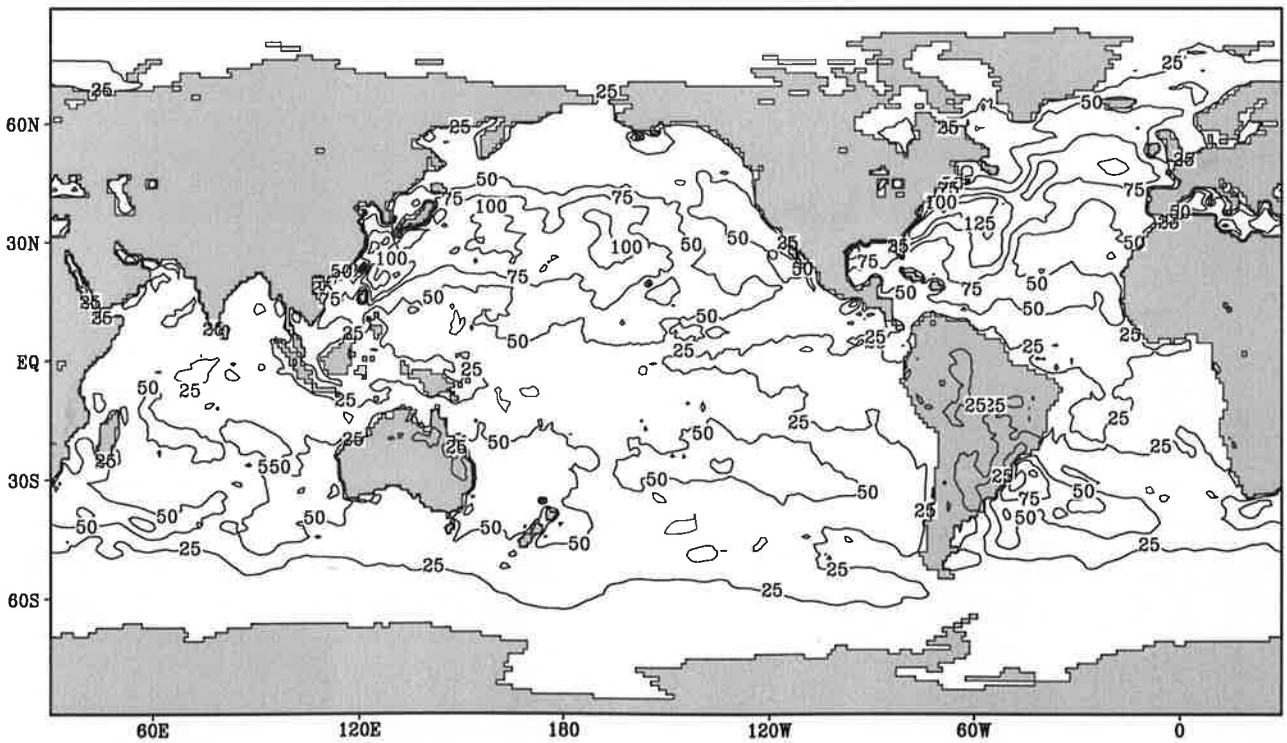

Contour interval: 25 Wm^{-2}

Fig.6.13 Latent heat flux Annual Mean

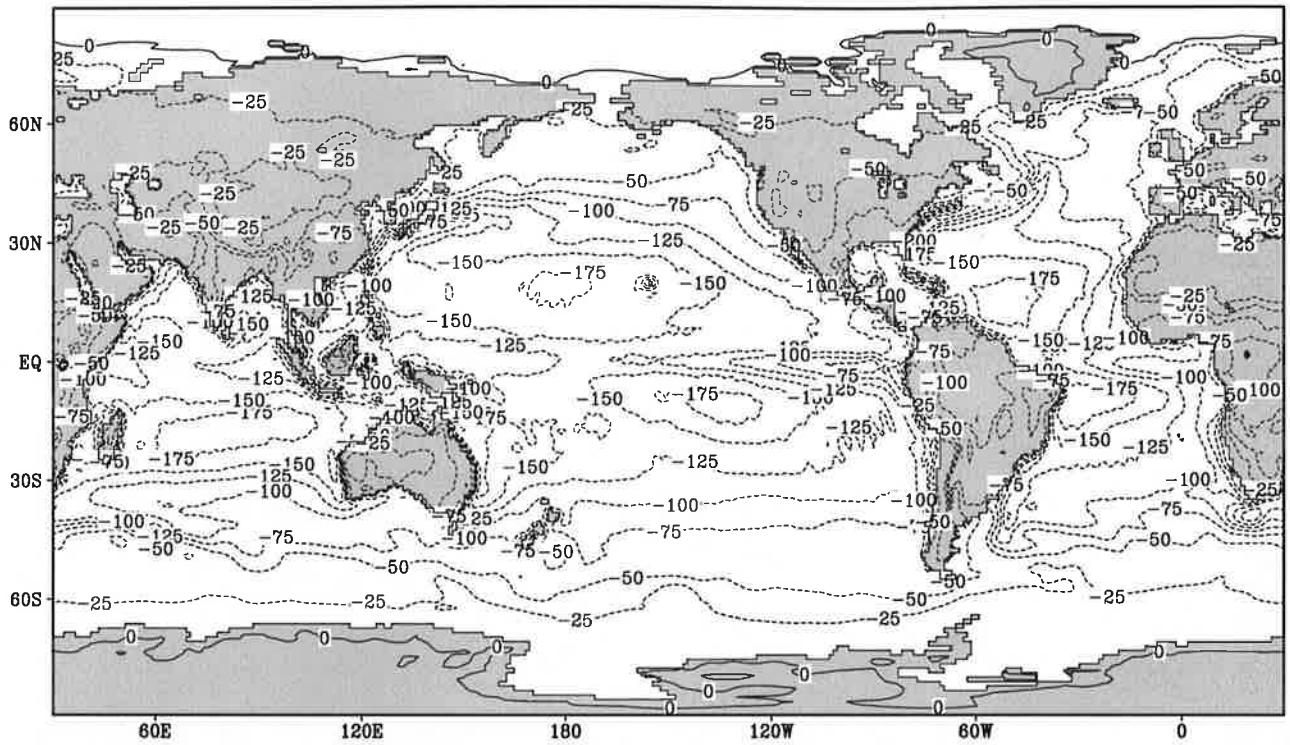

Contour interval: 25 Wm^{-2}

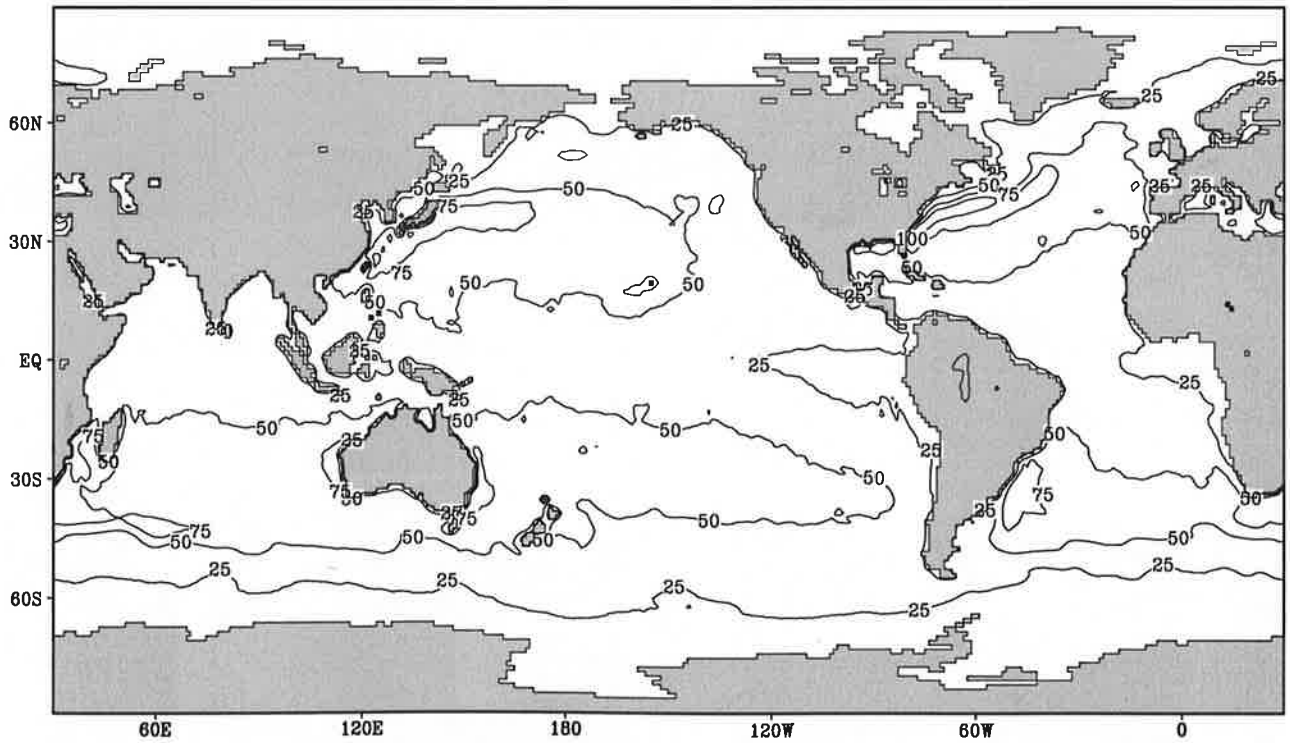

Contour interval: 25 Wm^{-2}

Fig.7.1 Evaporation January

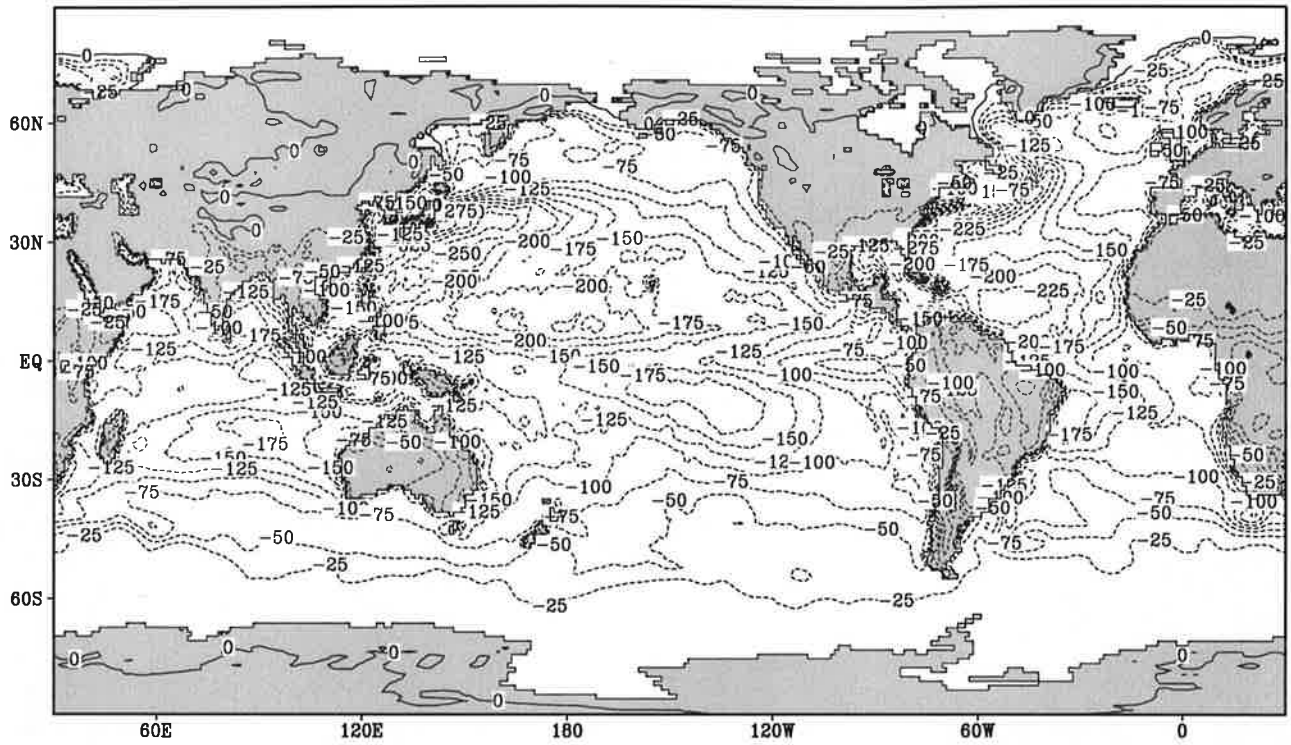

Contour interval: 25 mm month^{-1}

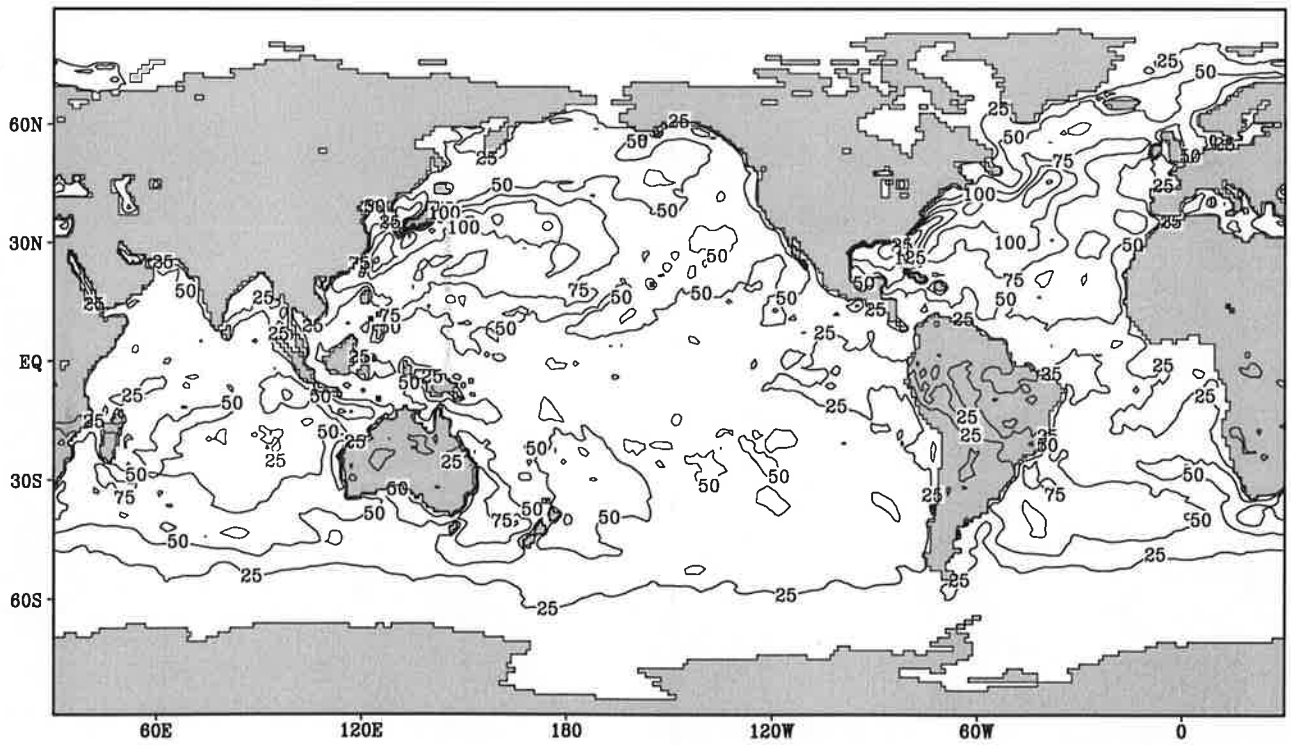

Contour interval: 25 mm month^{-1}

Fig.7.2 Evaporation February

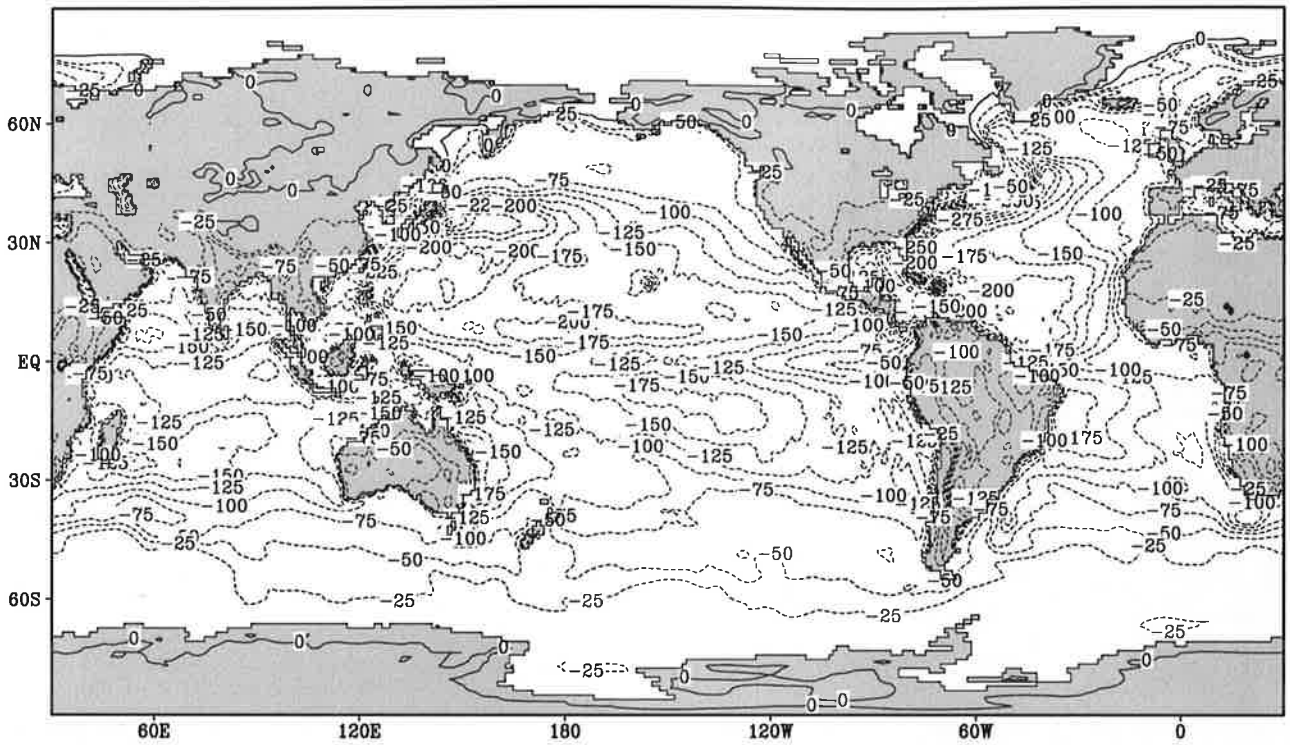

Contour interval: 25 mm month^{-1}

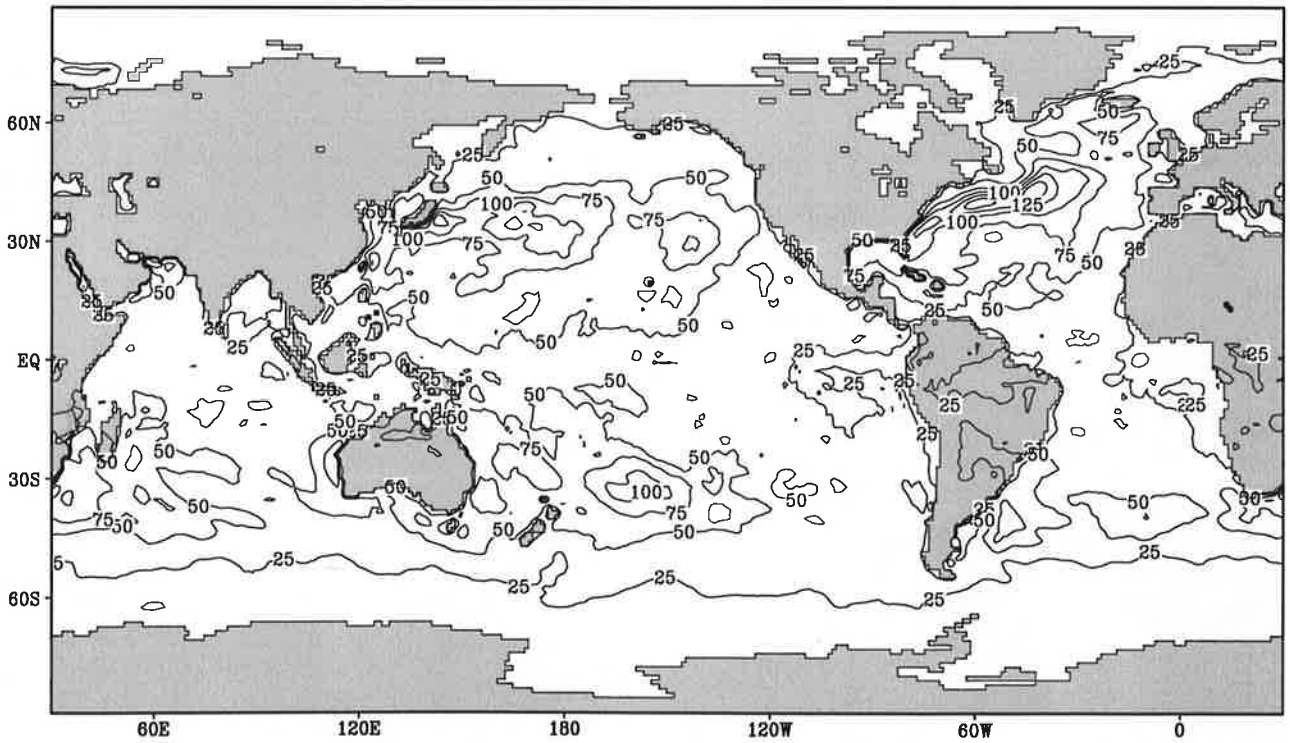

Contour interval: 25 mm month^{-1}

Fig.7.3 Evaporation March

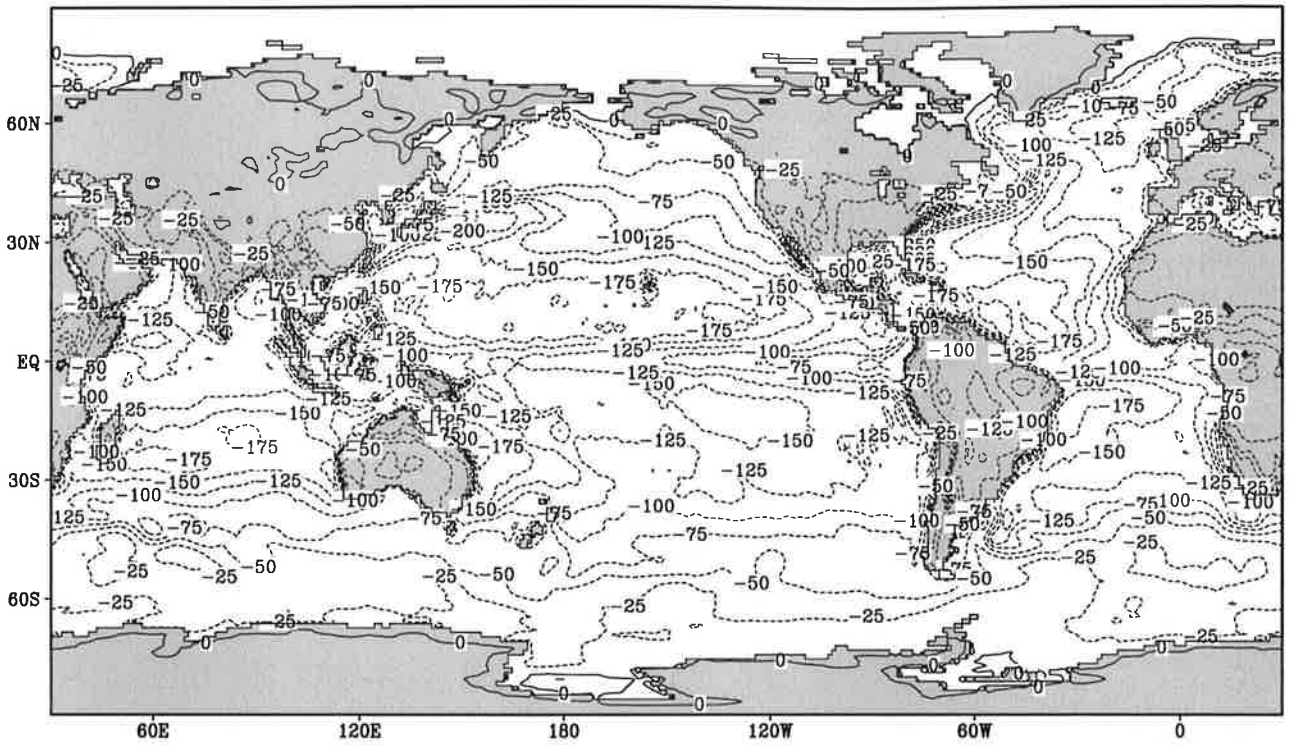

Contour interval: 25 mm month^{-1}

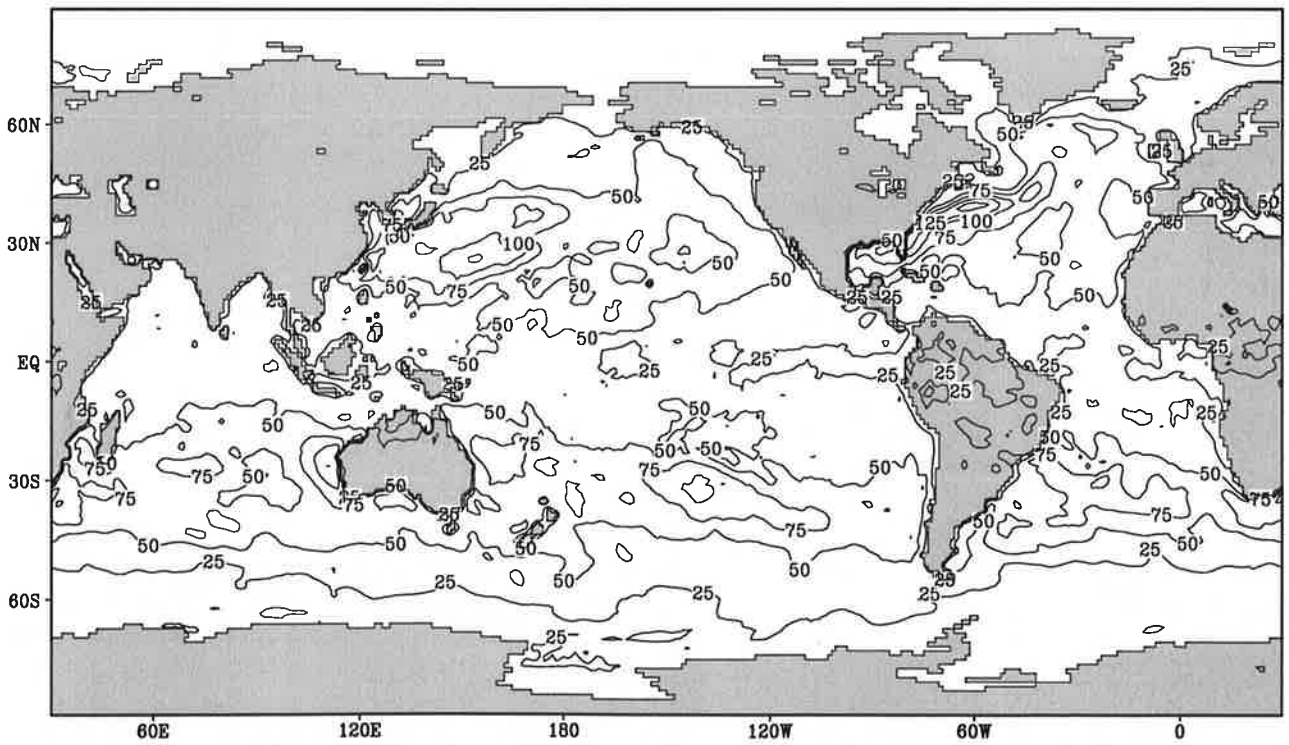

Contour interval: 25 mm month^{-1}

Fig.7.4 Evaporation April

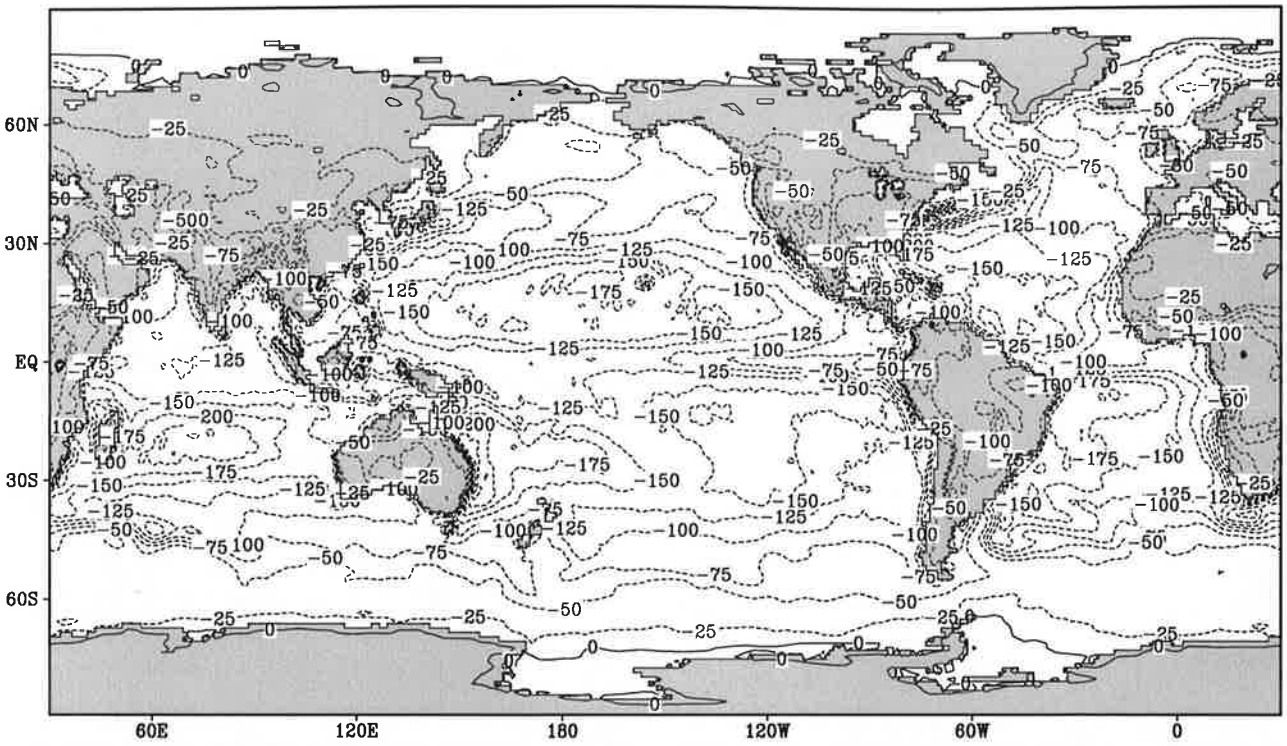

Contour interval: 25 mm month^{-1}

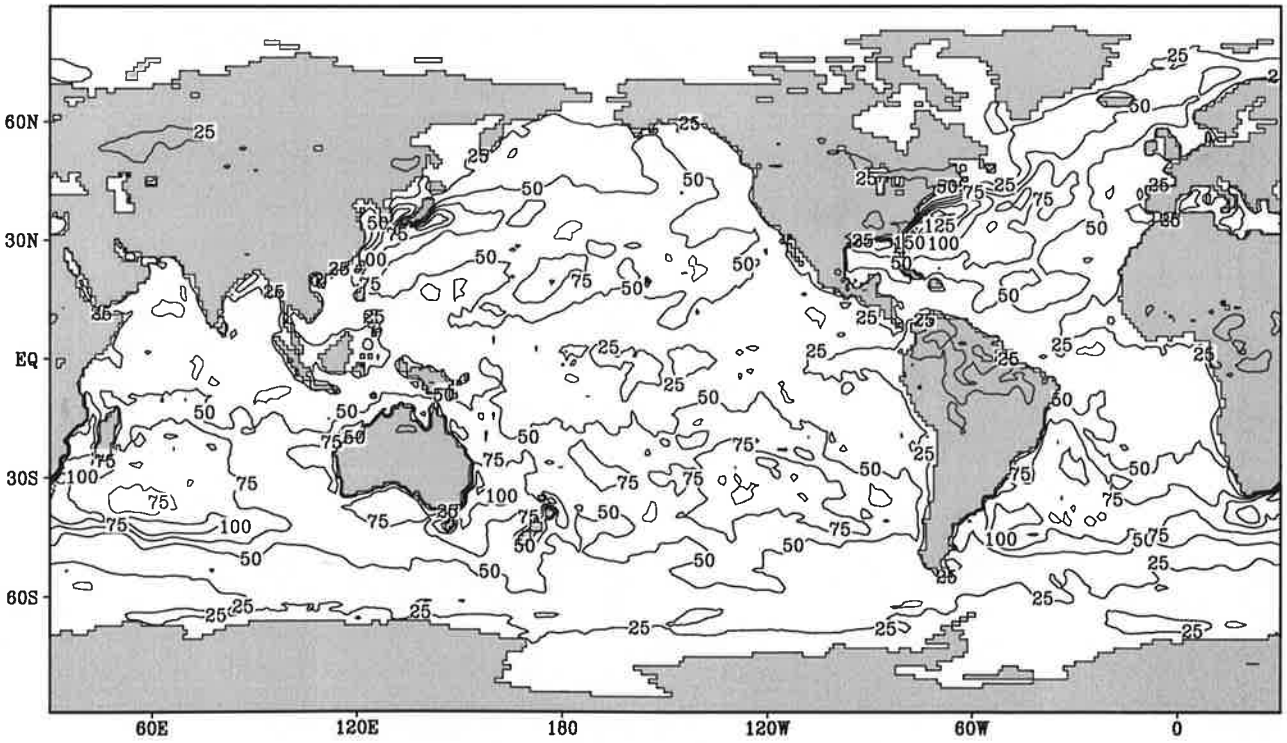

Contour interval: 25 mm month^{-1}

Fig.7.5 Evaporation May

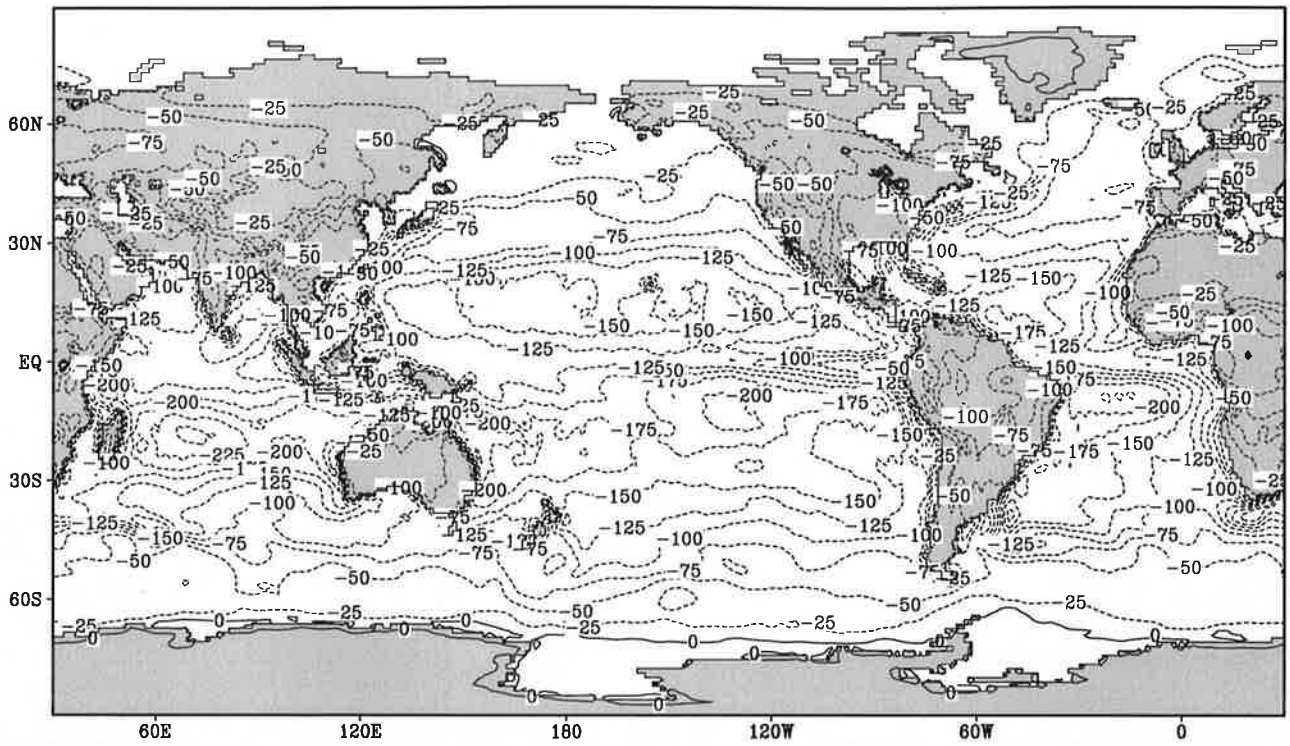

Contour interval: 25 mm month^{-1}

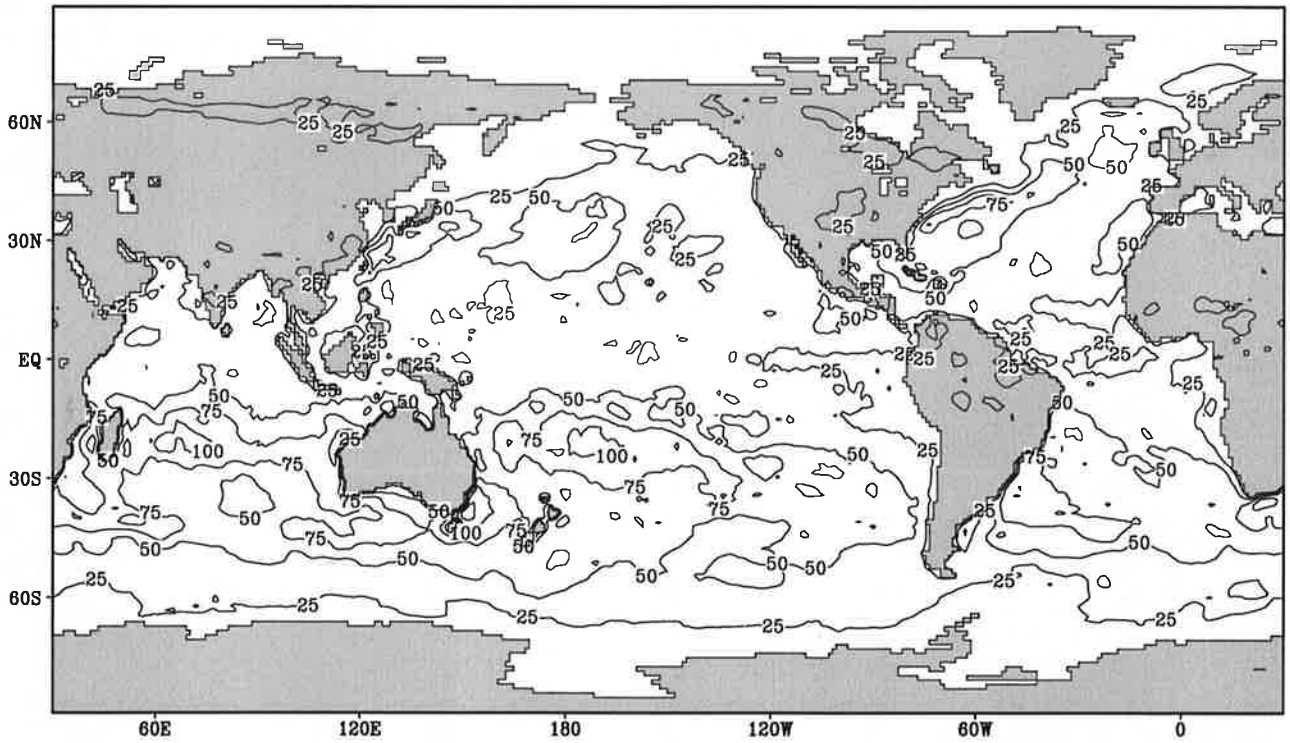

Contour interval: 25 mm month^{-1}

Fig.7.6 Evaporation June

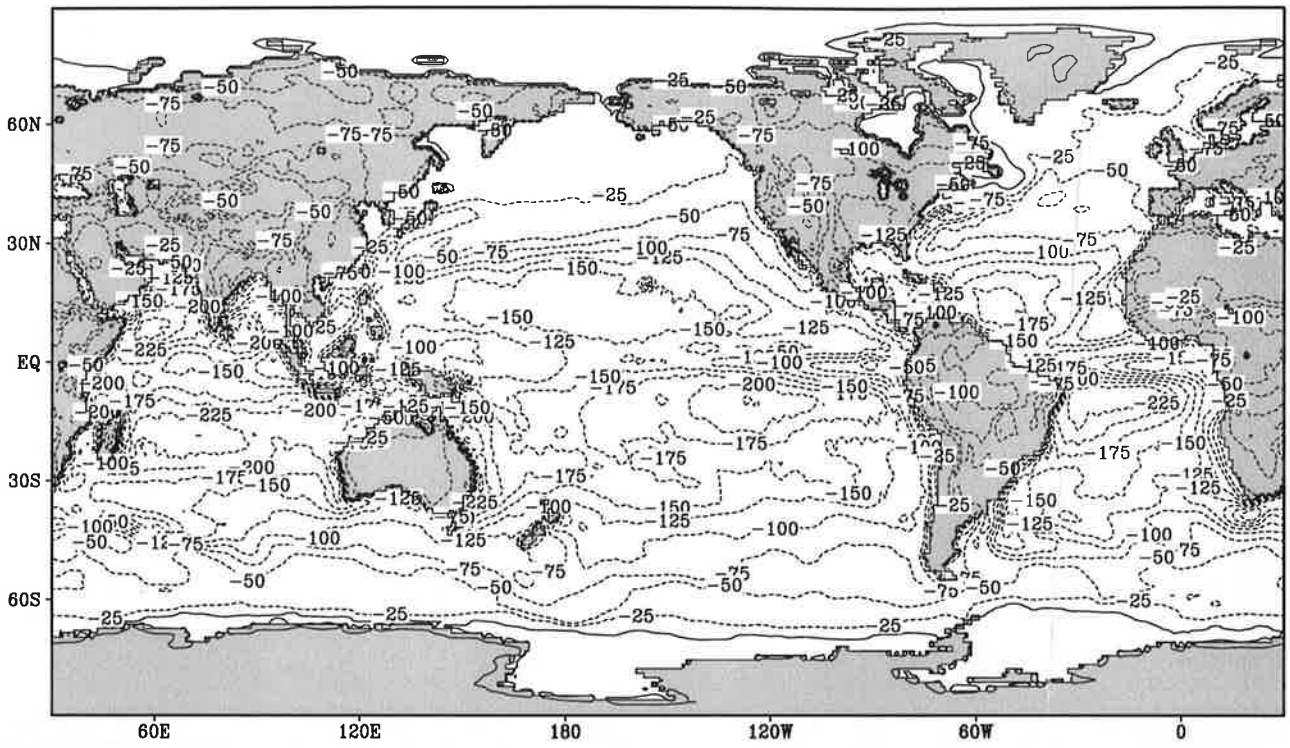

Contour interval: 25 mm month^{-1}

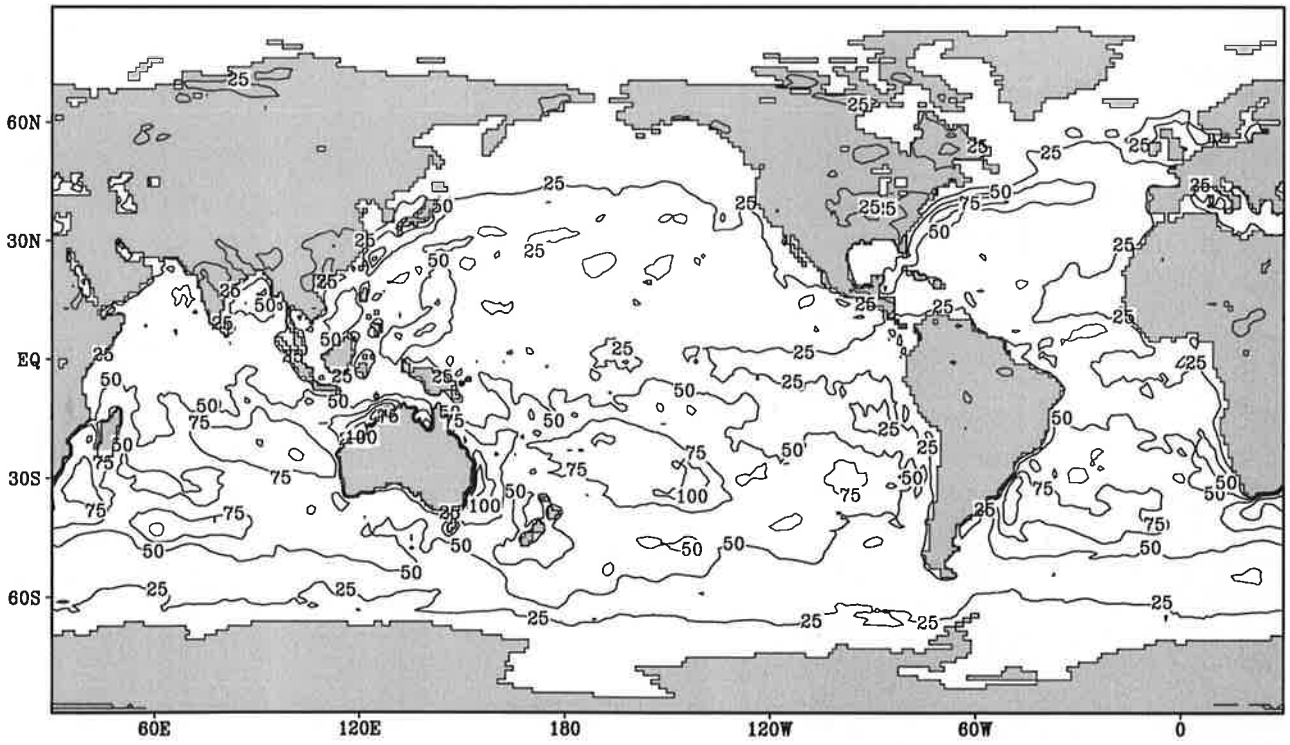

Contour interval: 25 mm month^{-1}

Fig.7.7 Evaporation July

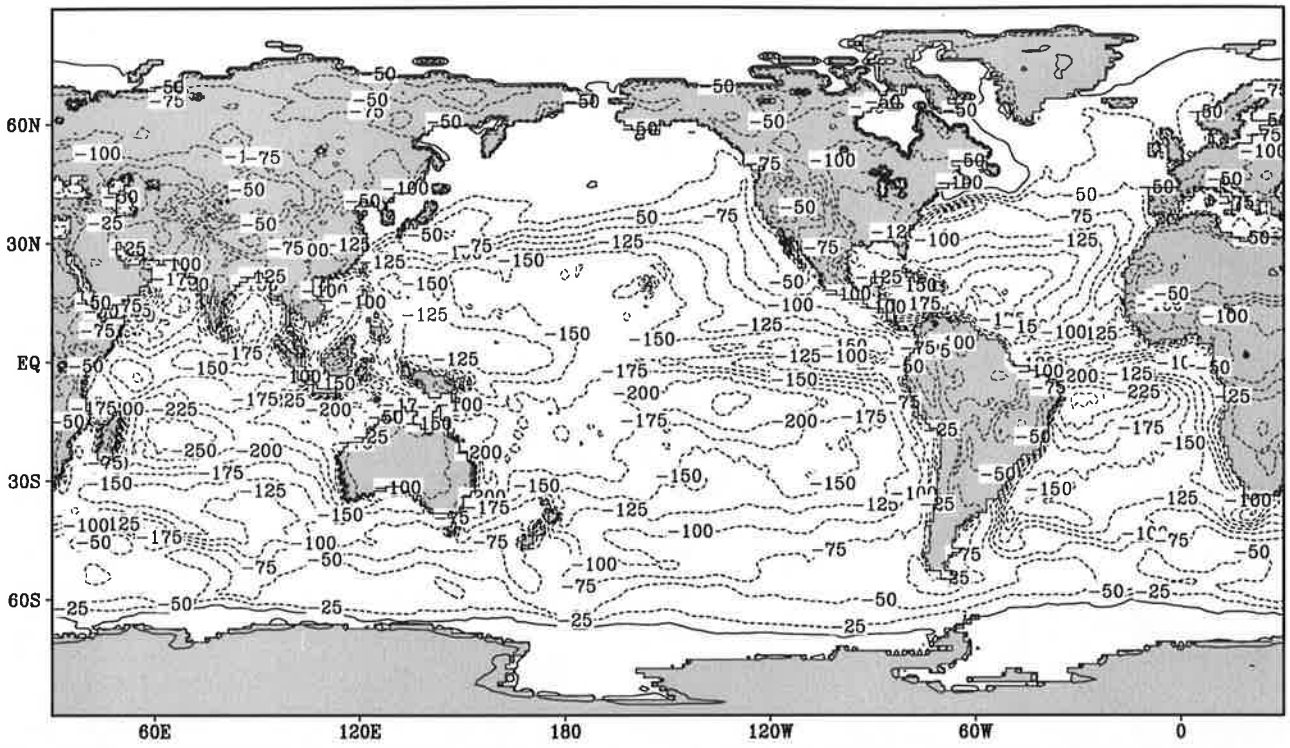

Contour interval: 25 mm month^{-1}

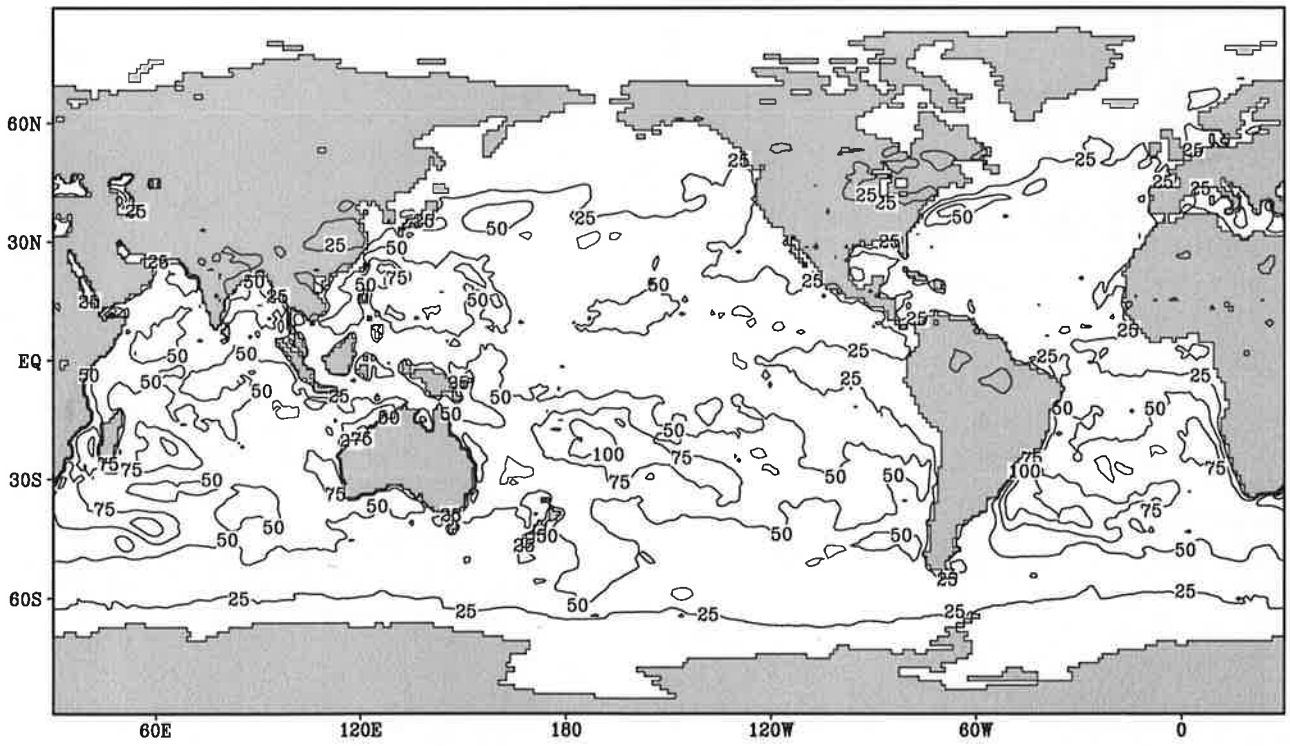

Contour interval: 25 mm month^{-1}

Fig.7.8 Evaporation August

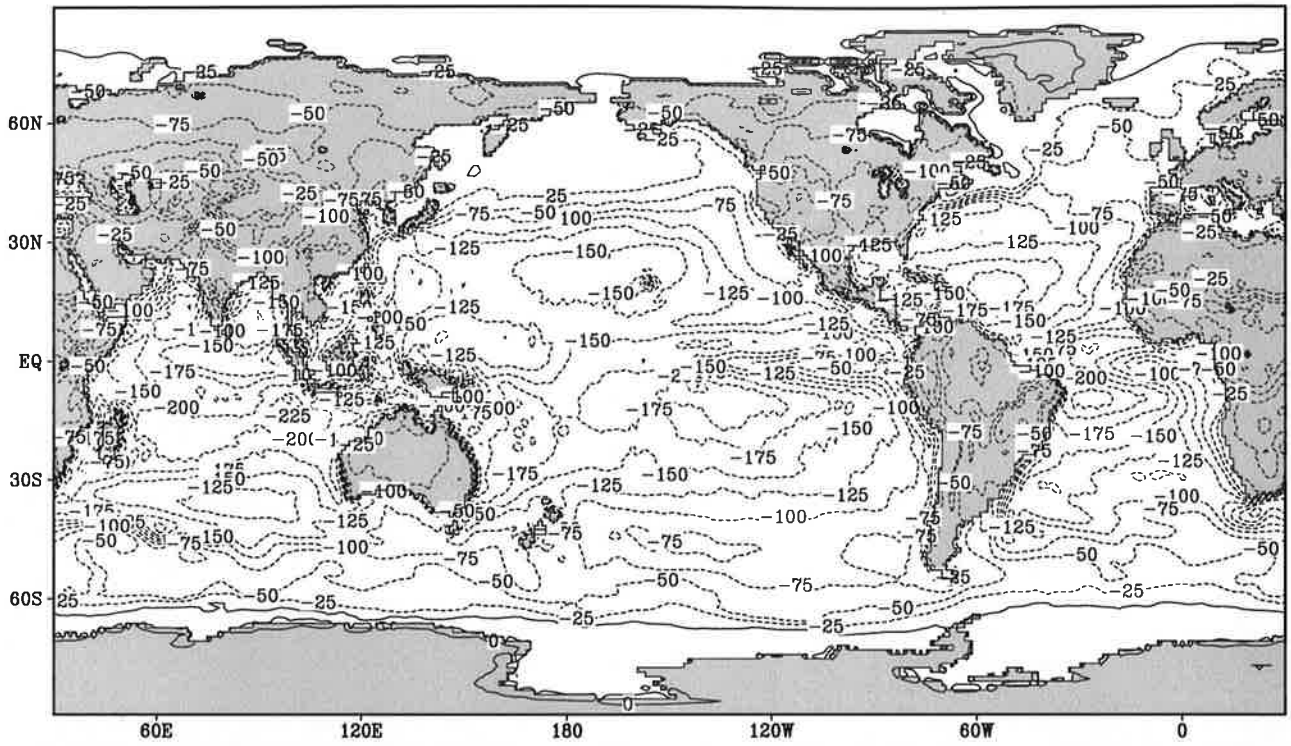

Contour interval: 25 mm month^{-1}

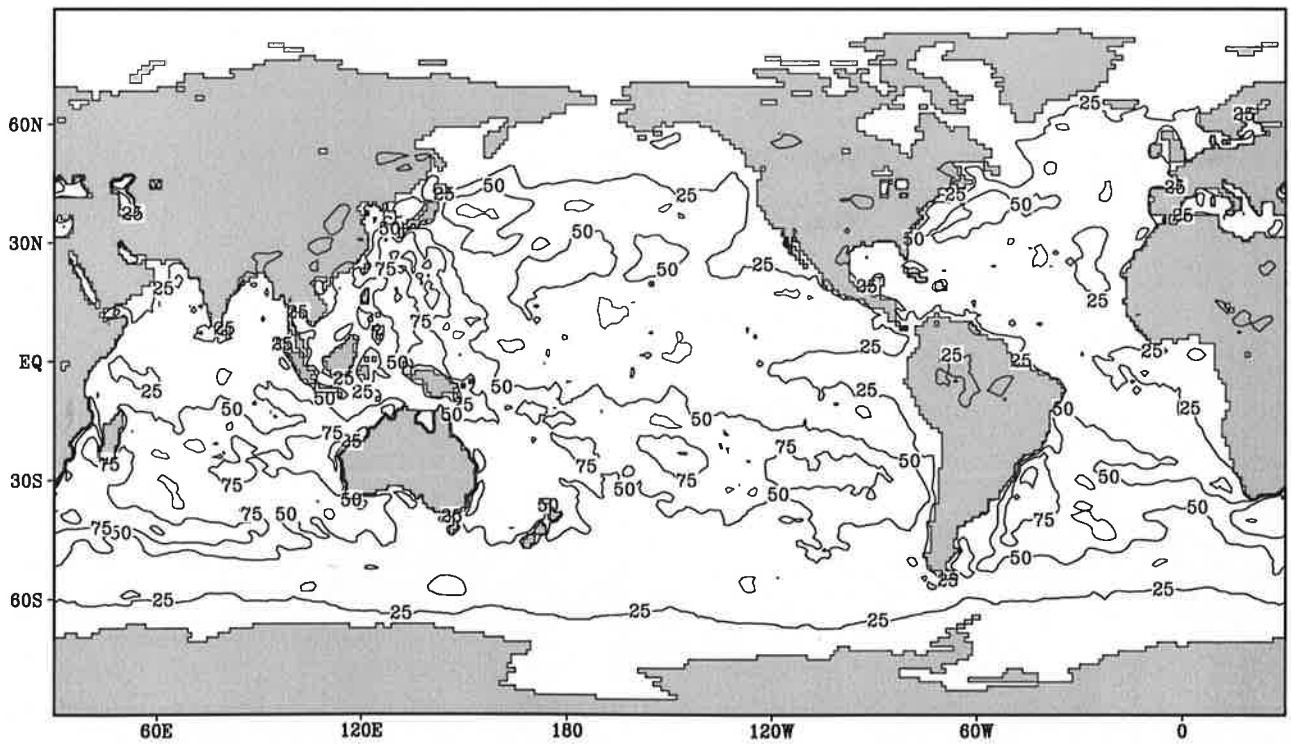

Contour interval: 25 mm month^{-1}

Fig.7.9 Evaporation September

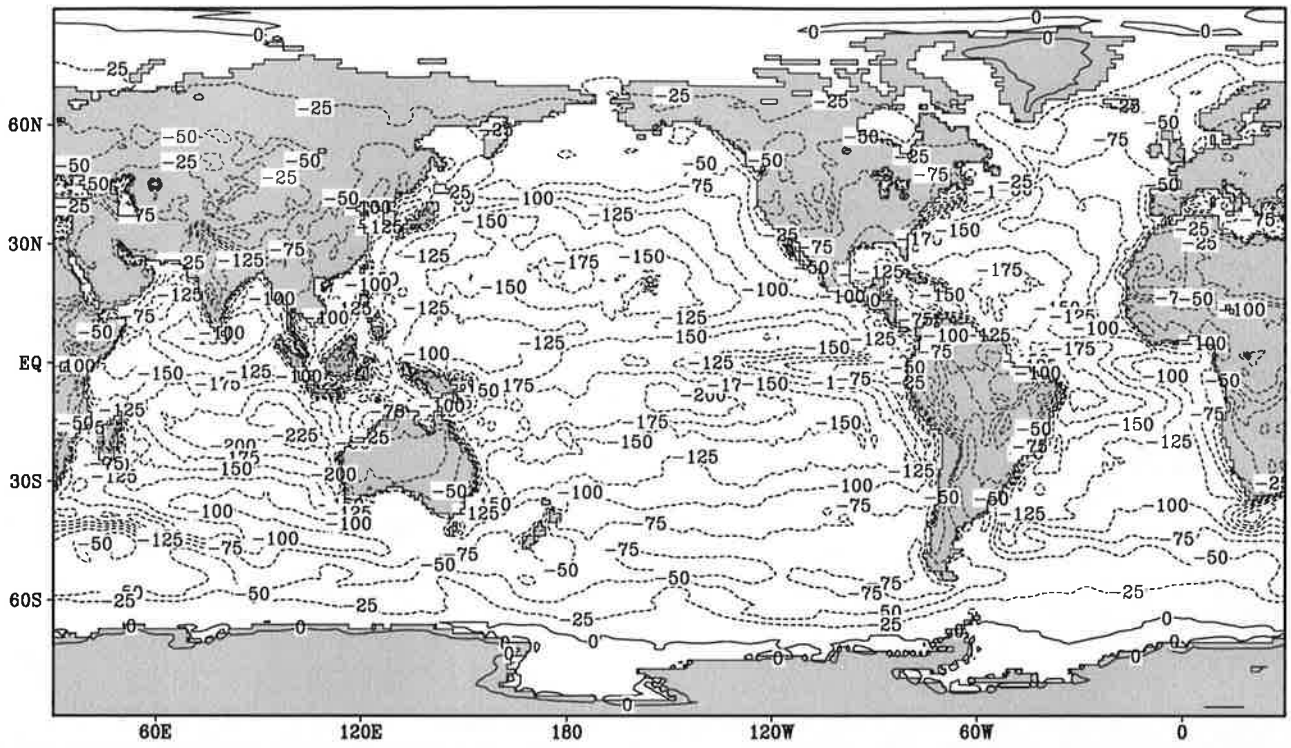

Contour interval: 25 mm month^{-1}

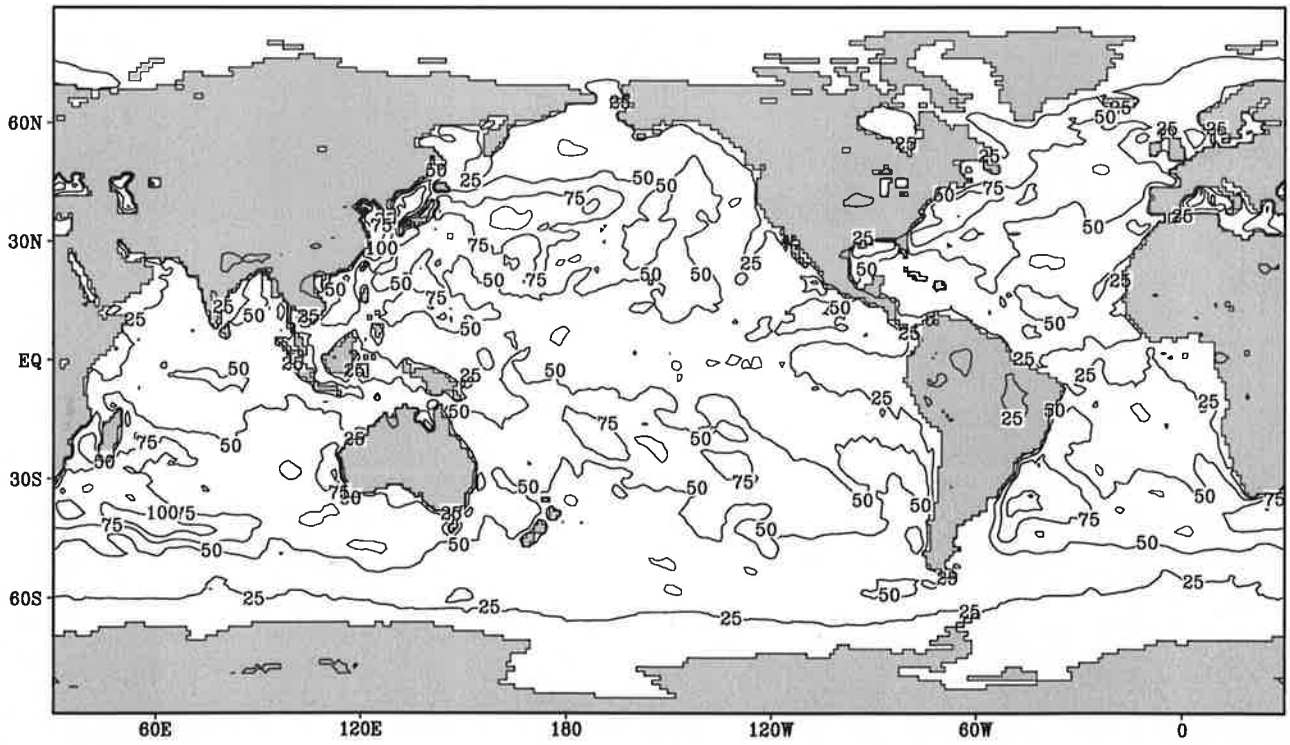

Contour interval: 25 mm month^{-1}

Fig.7.10 Evaporation October

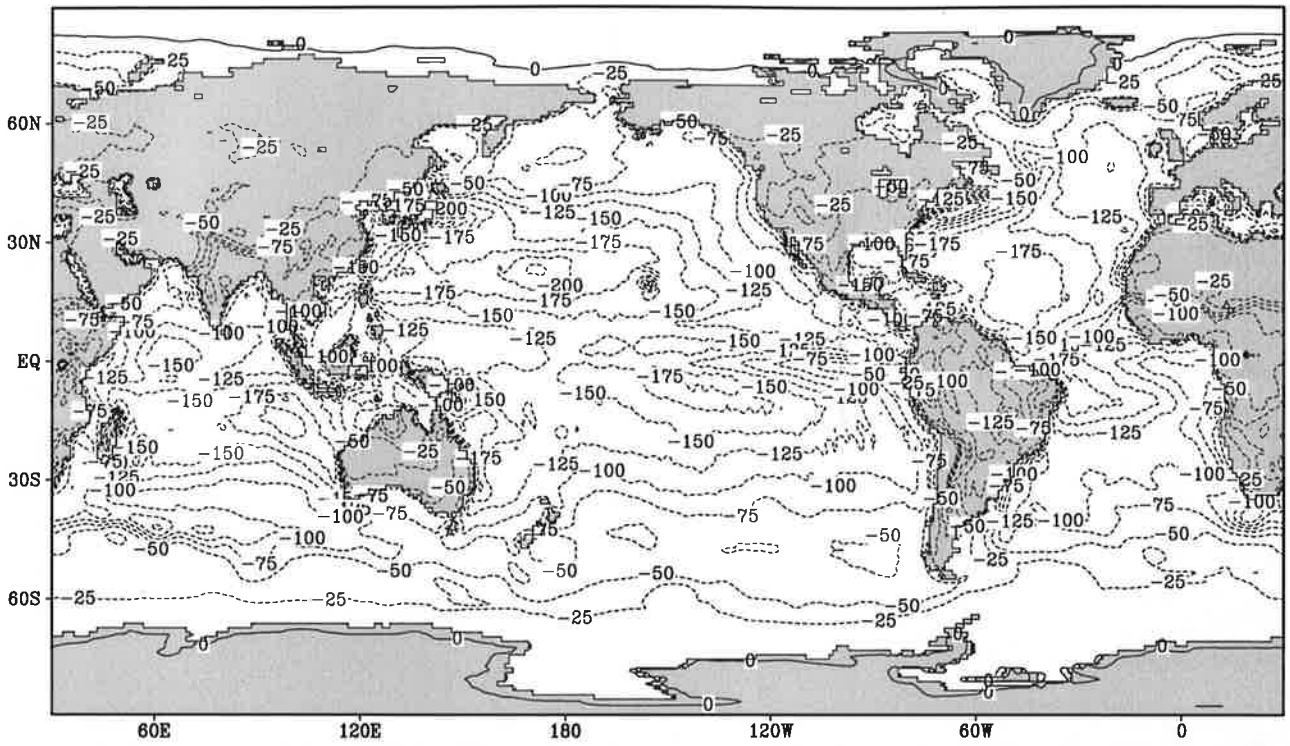

Contour interval: 25 mm month^{-1}

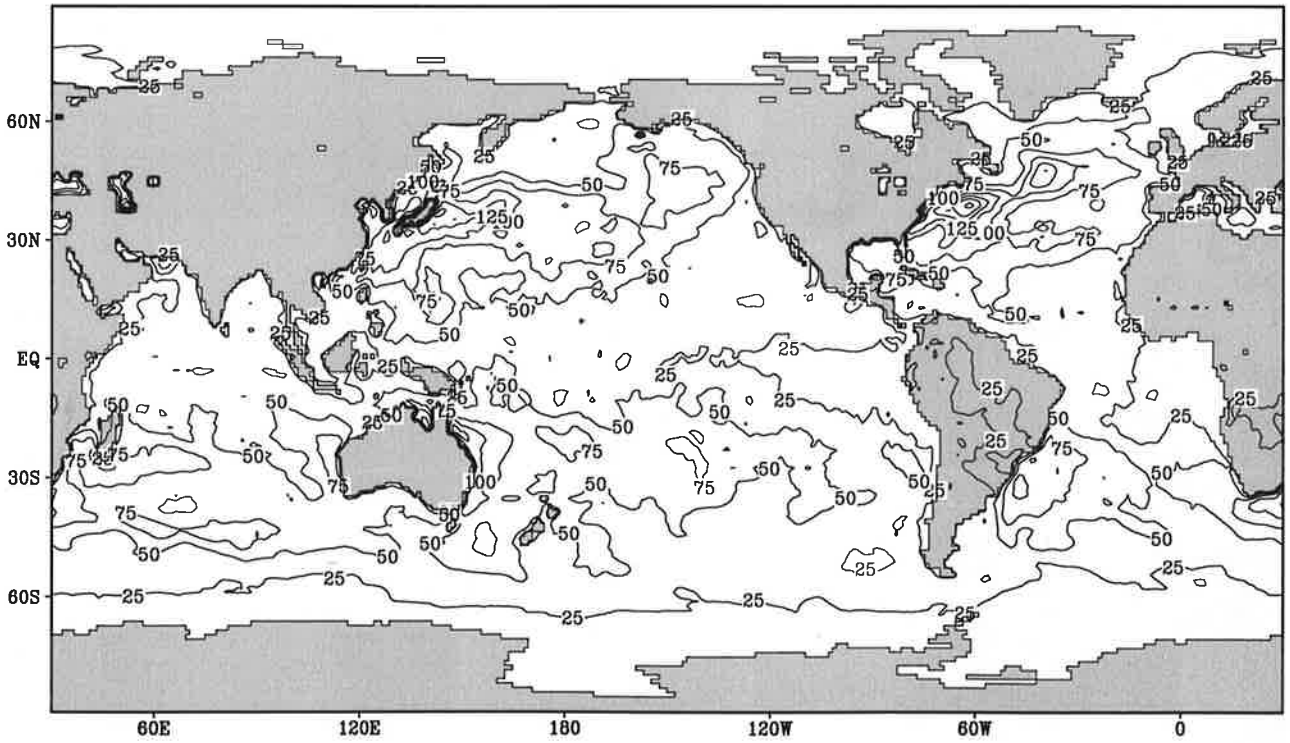

Contour interval: 25 mm month^{-1}

Fig.7.11 Evaporation November

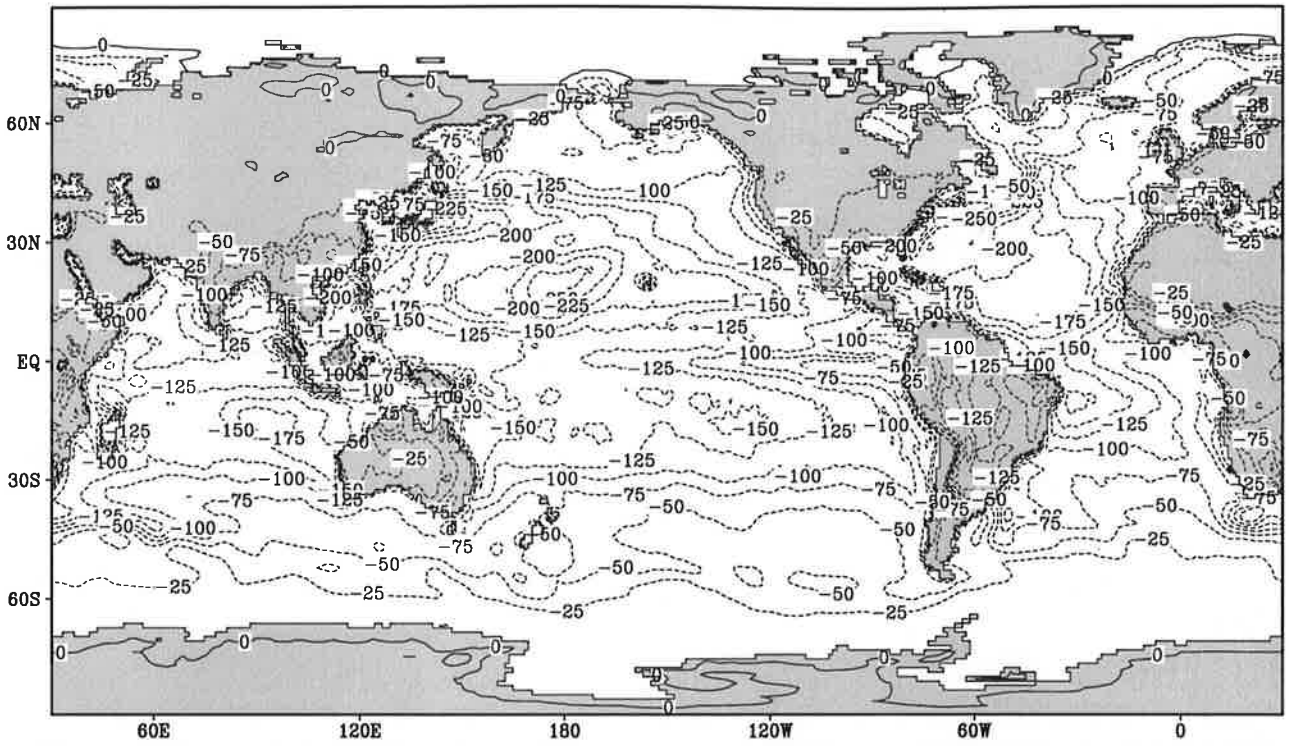

Contour interval: 25 mm month^{-1}

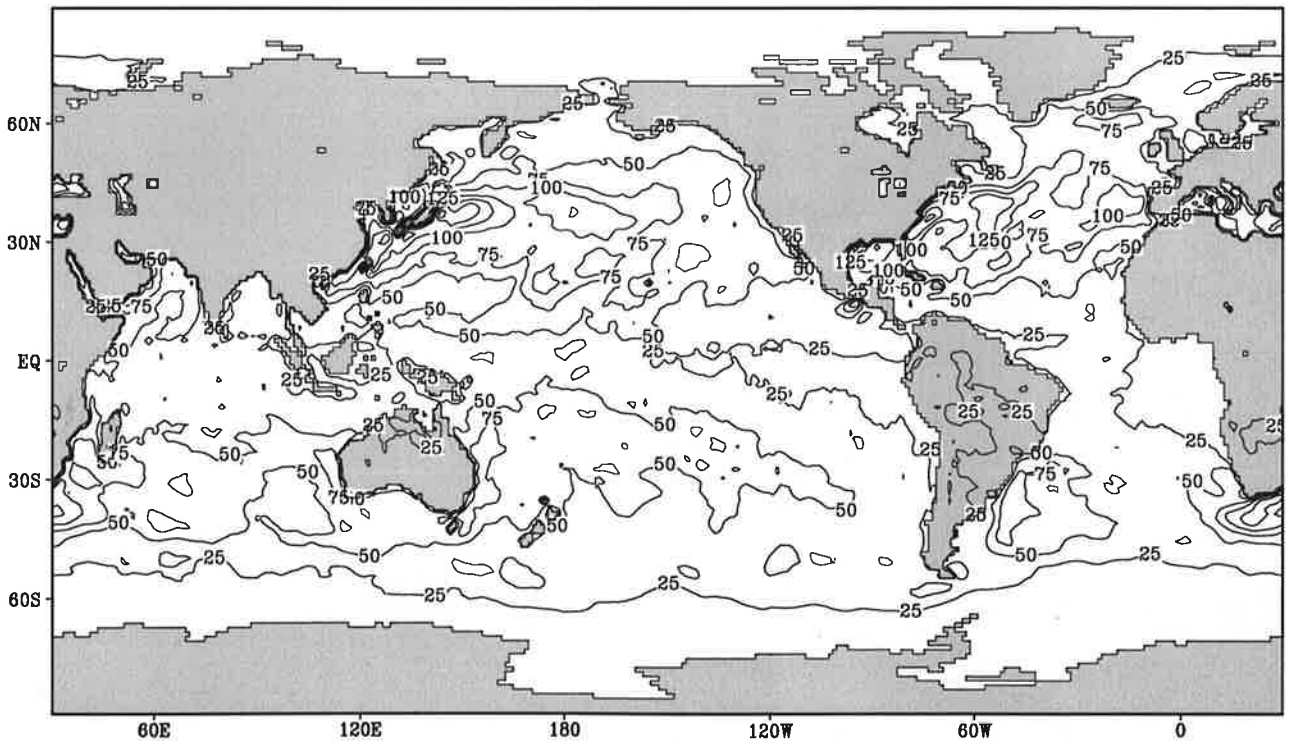

Contour interval: 25 mm month^{-1}

Fig.7.12 Evaporation December

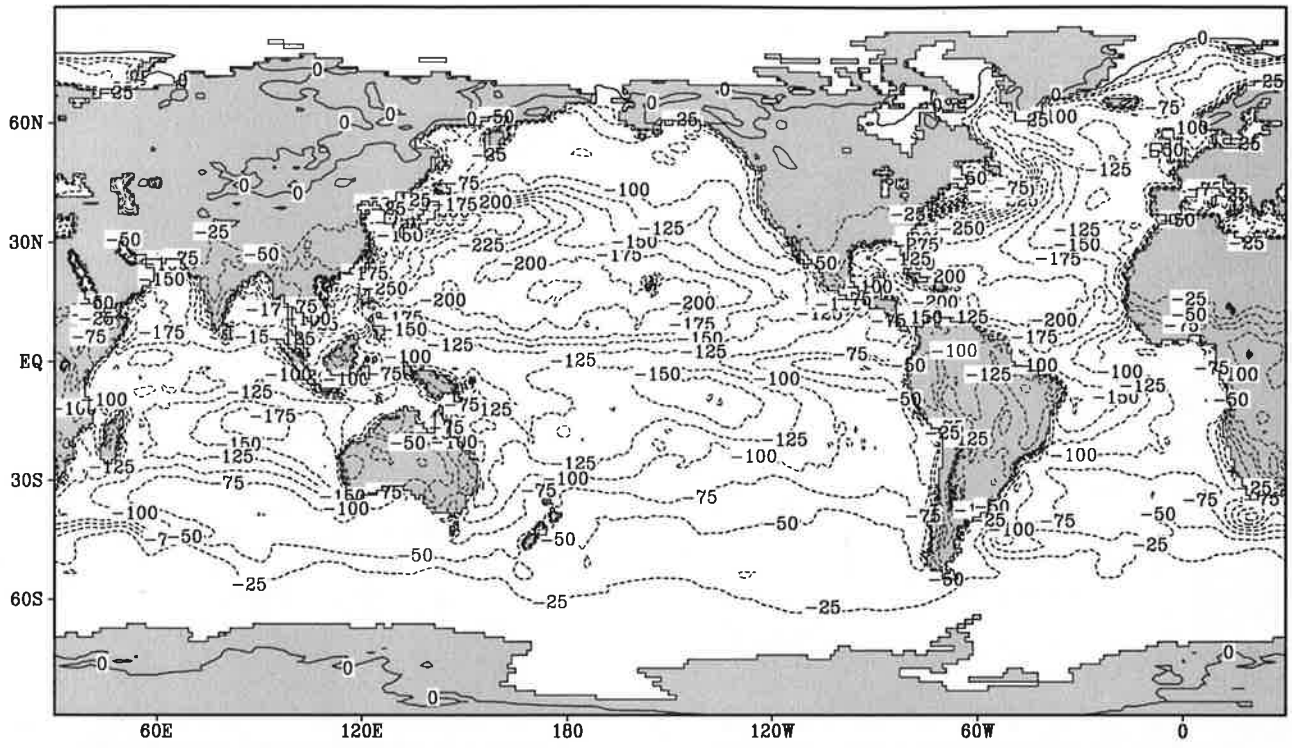

Contour interval: 25 mm month^{-1}

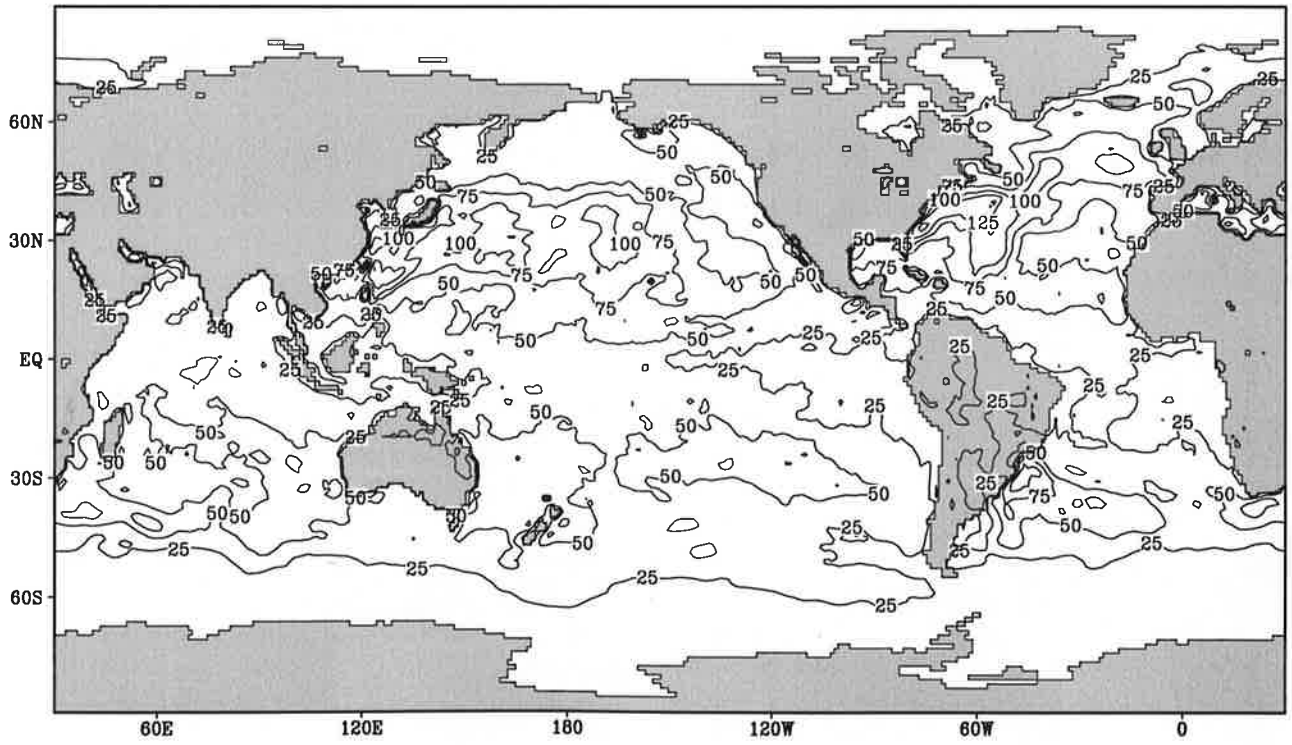

Contour interval: 25 mm month^{-1}

Fig.7.13 Evaporation Annual Mean

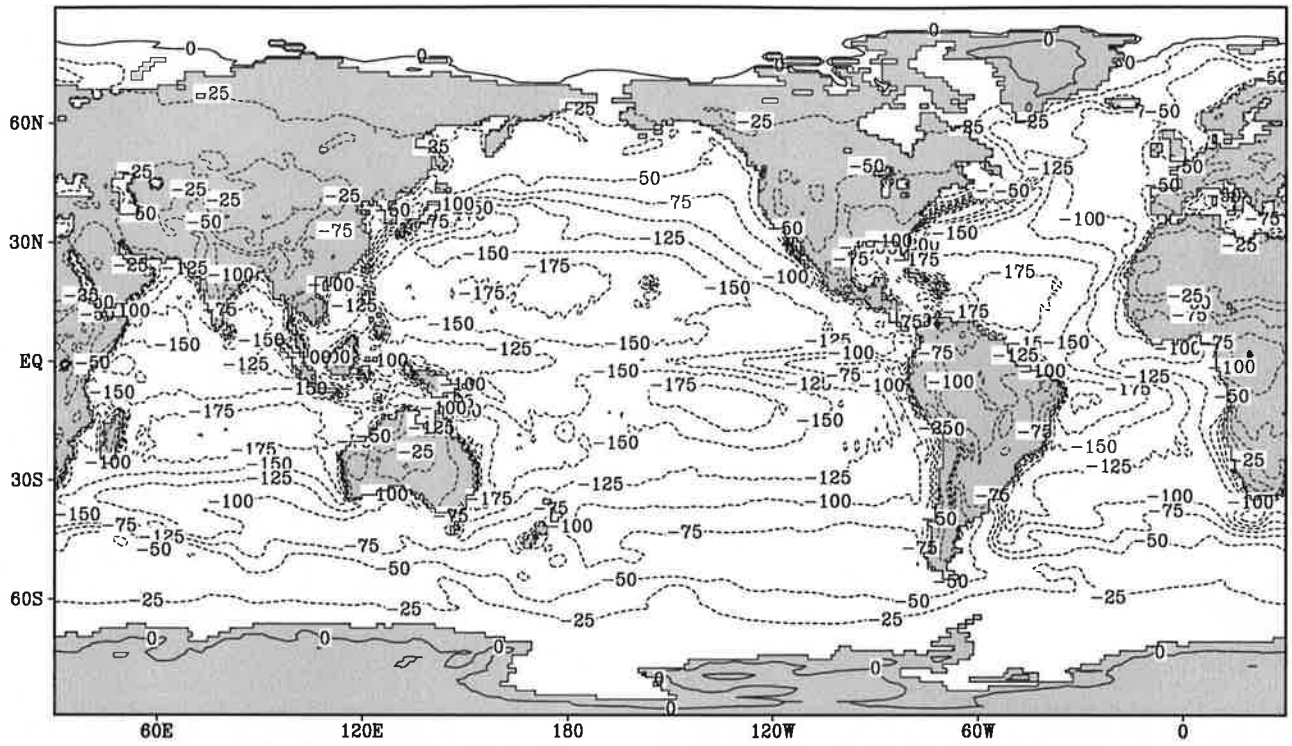

Contour interval: 25 mm month^{-1}

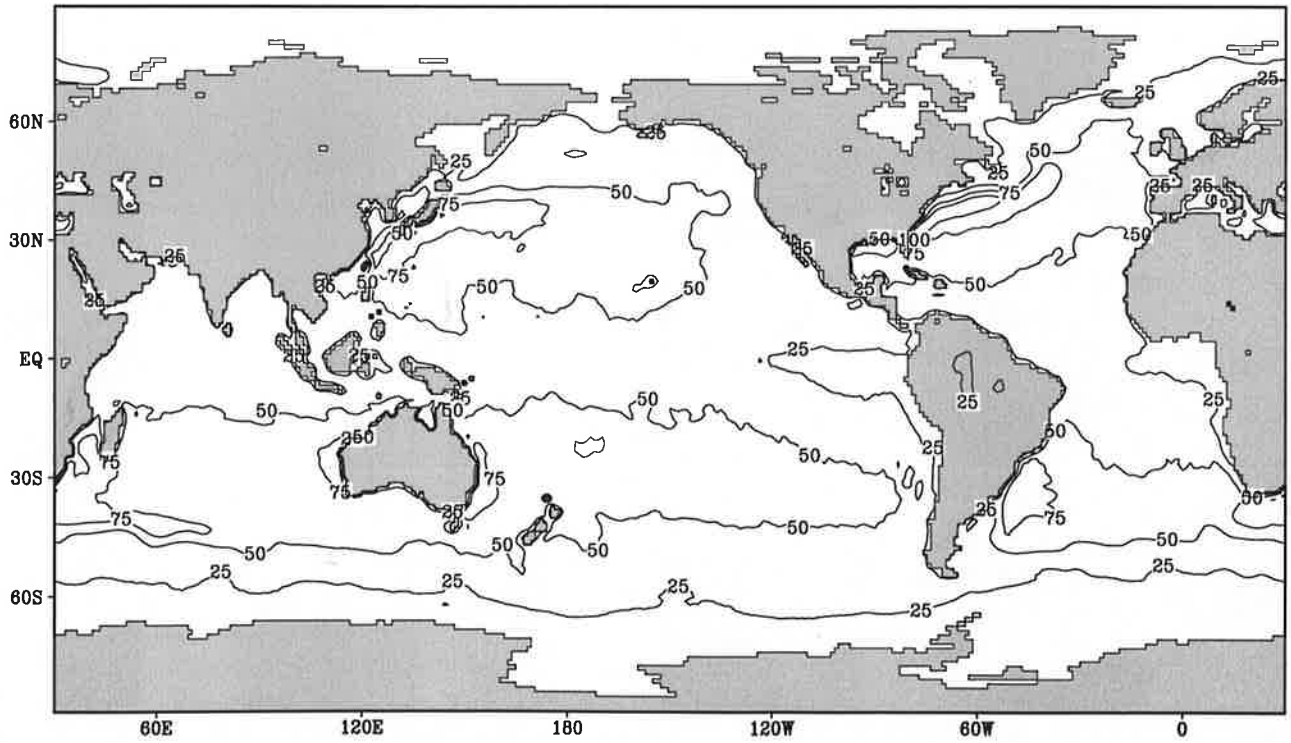

Contour interval: 25 mm month^{-1}

Fig.8.1 Precipitation January

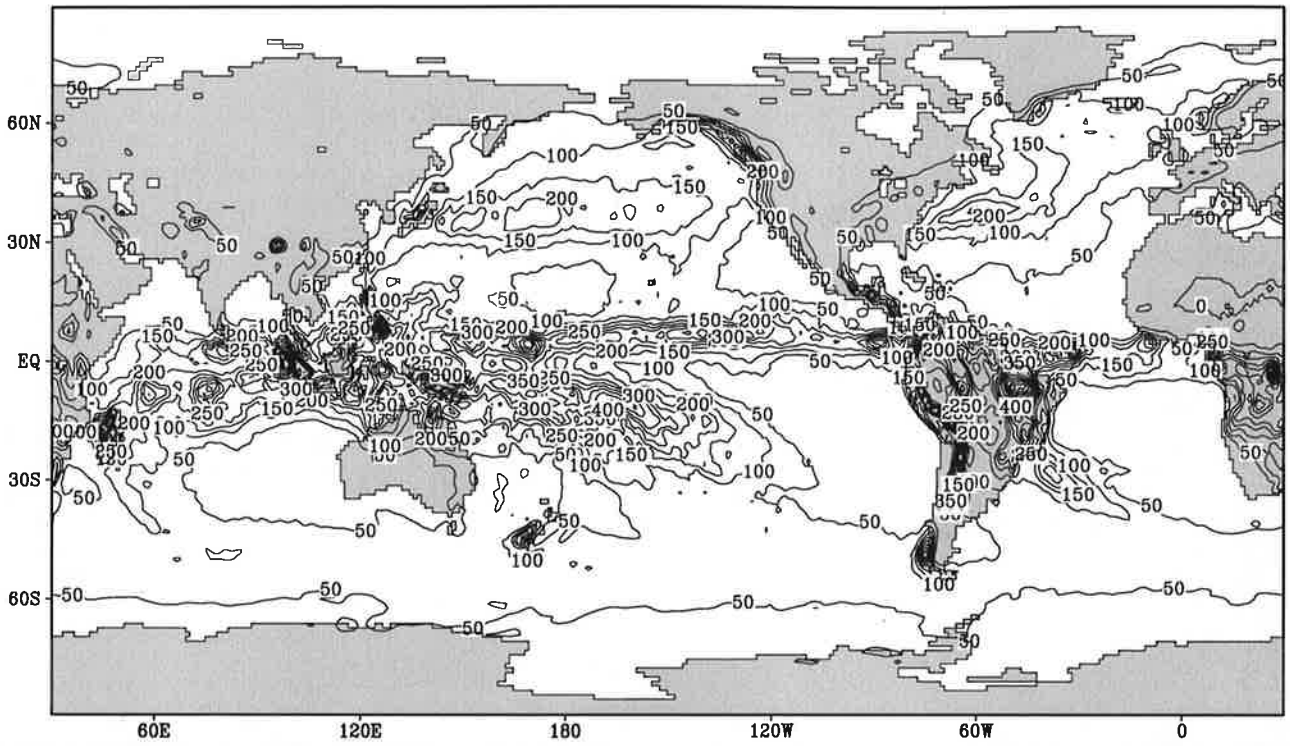

Contour interval: 50 mm month^{-1}

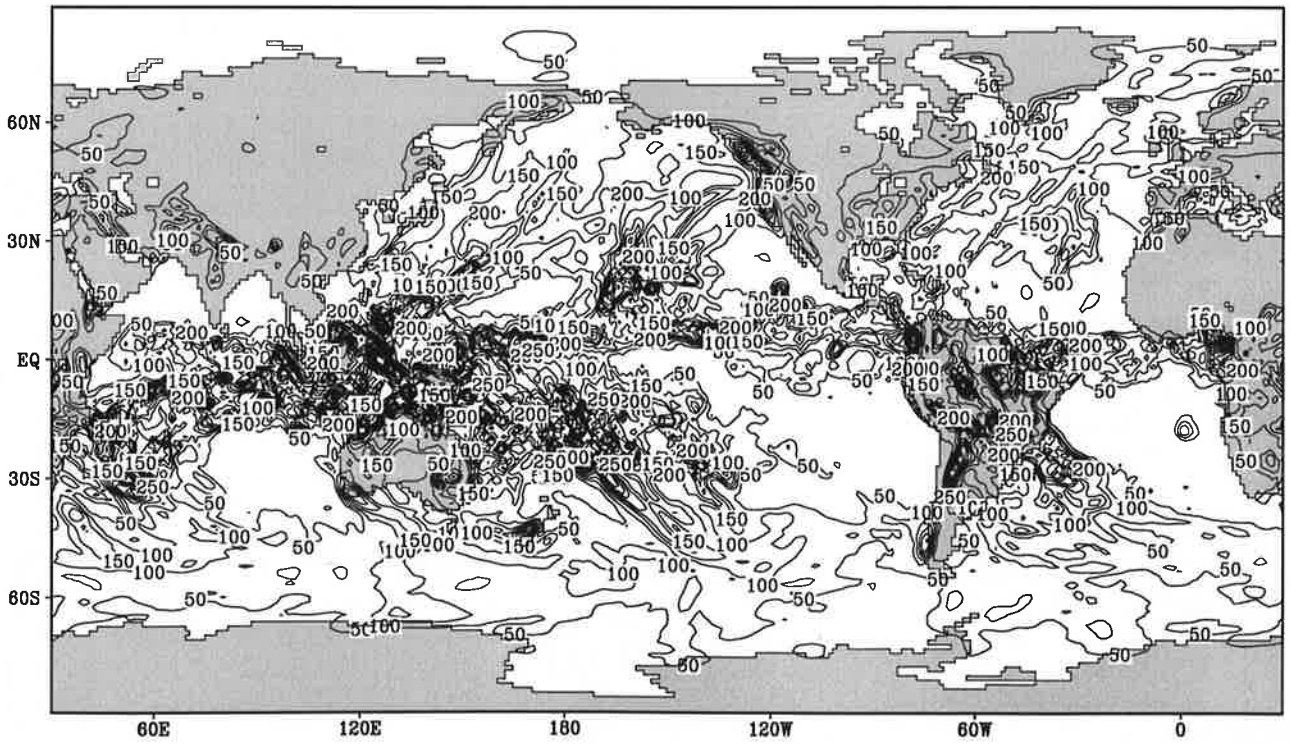

Contour interval: 50 mm month^{-1}

Fig.8.2 Precipitation February

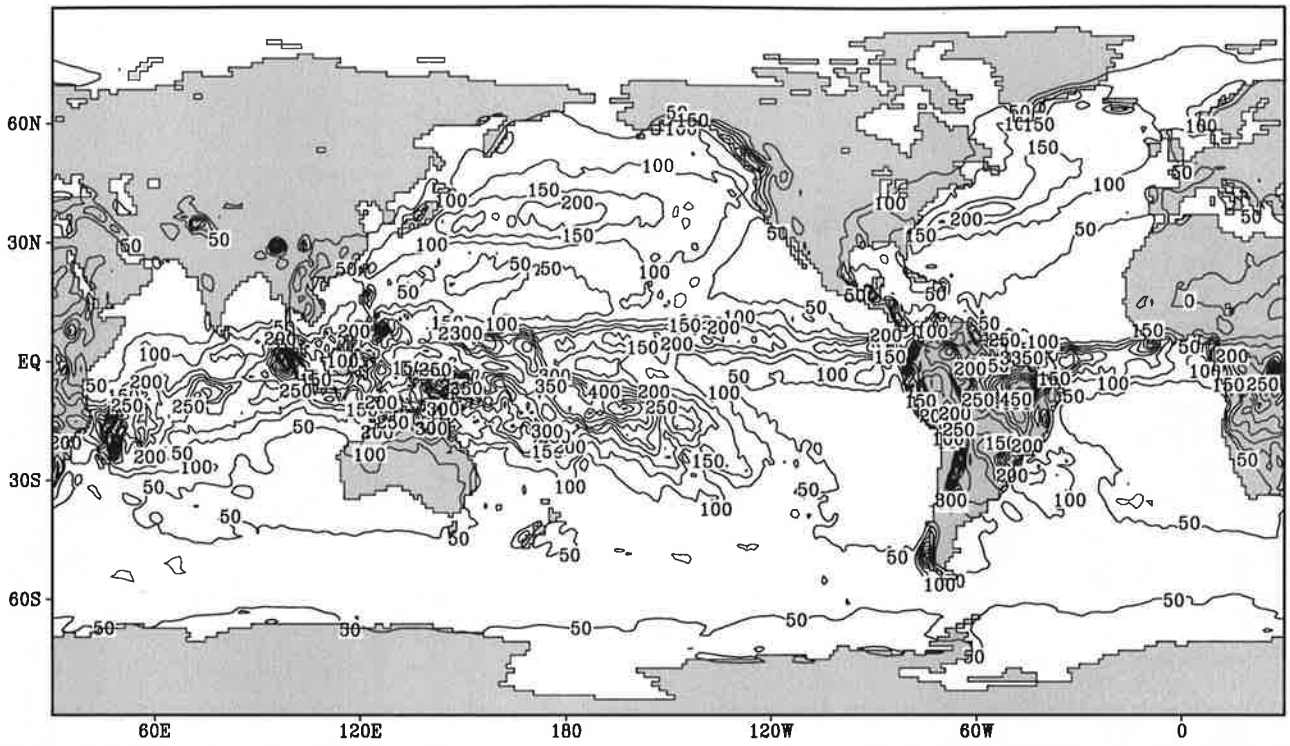

Contour interval: 50 mm month^{-1}

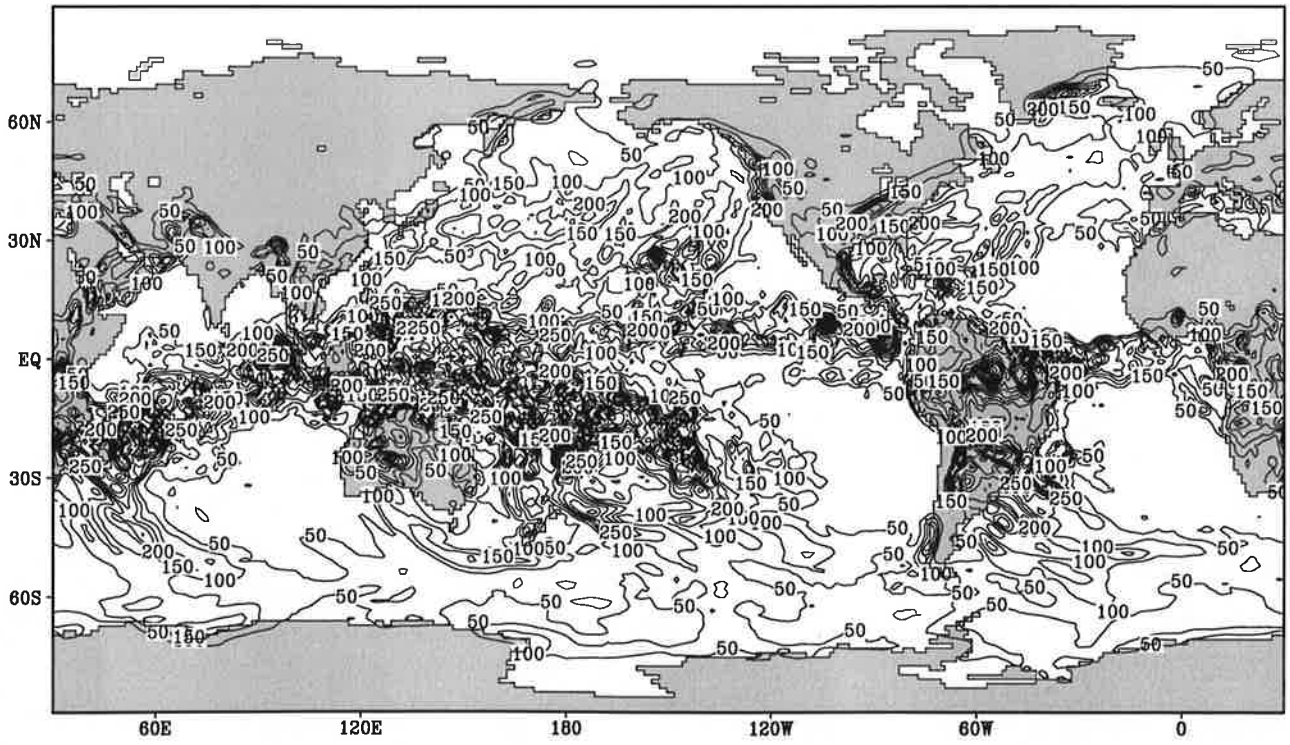

Contour interval: 50 mm month^{-1}

Fig.8.3 Precipitation March

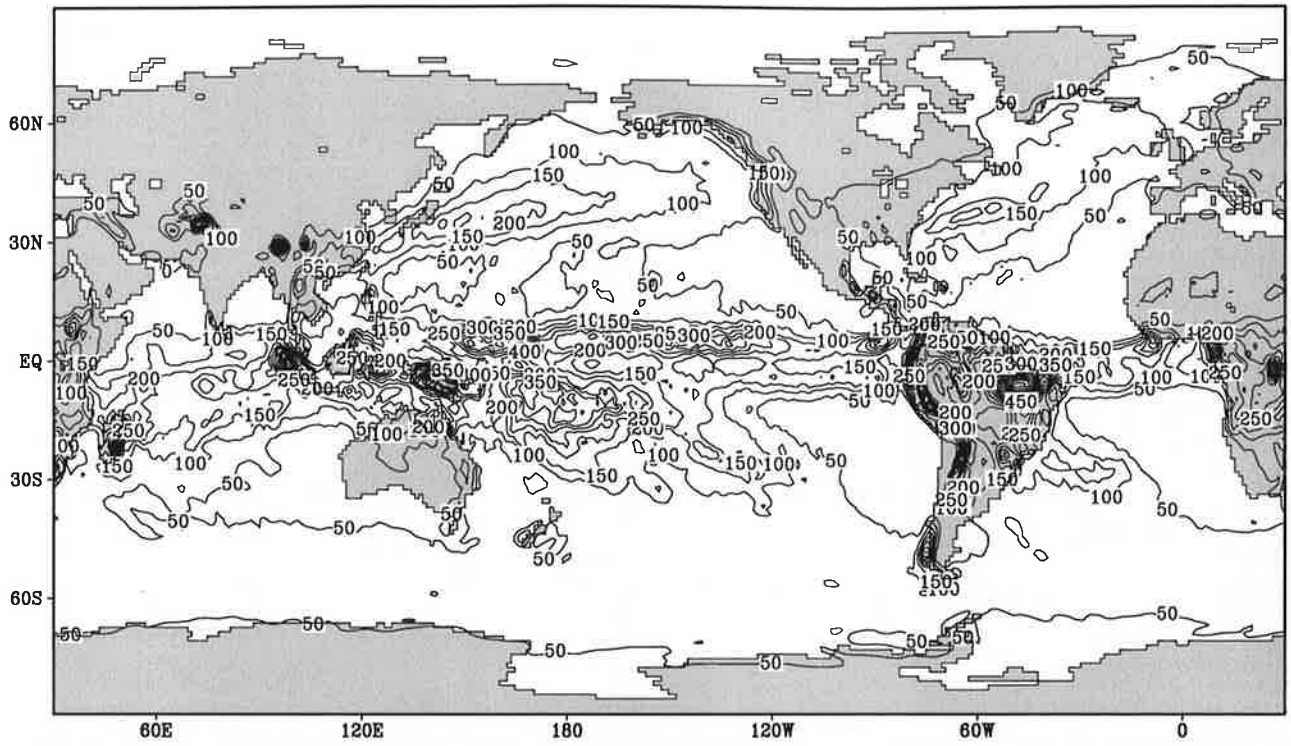

Contour interval: 50 mm month^{-1}

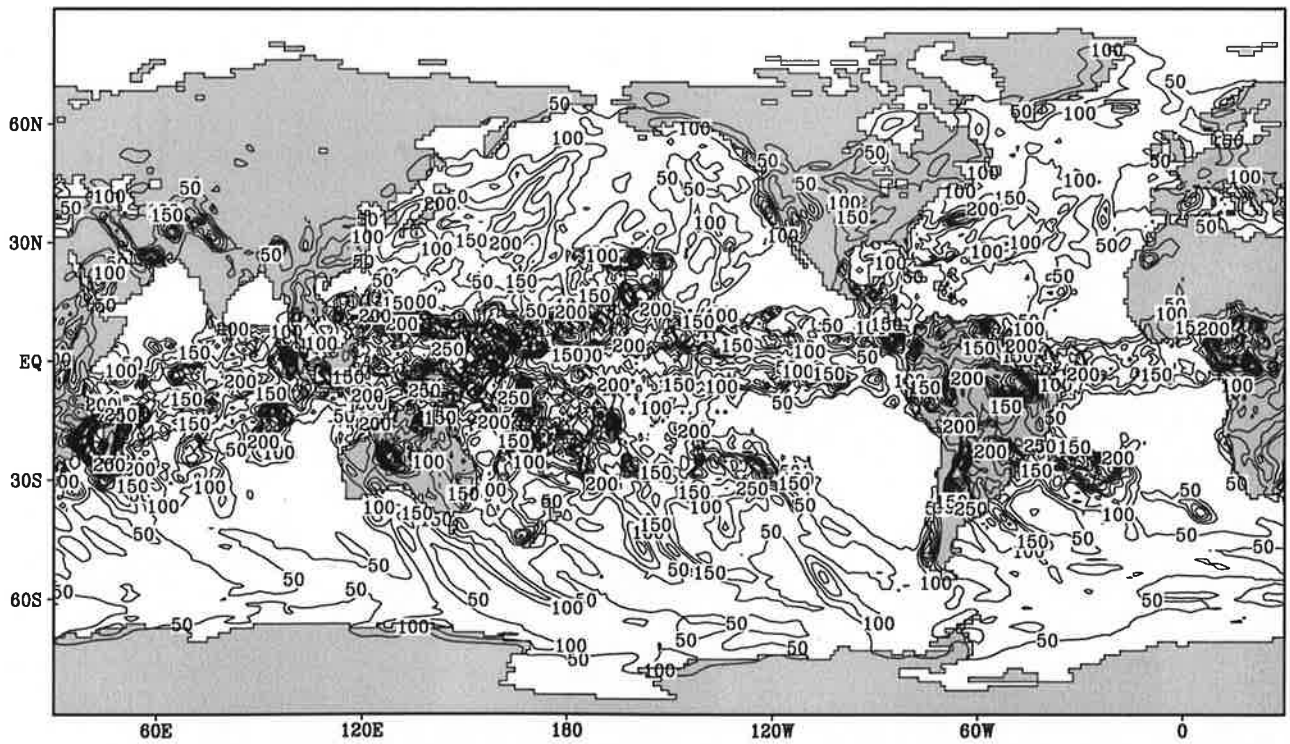

Contour interval: 50 mm month^{-1}

Fig.8.4 Precipitation April

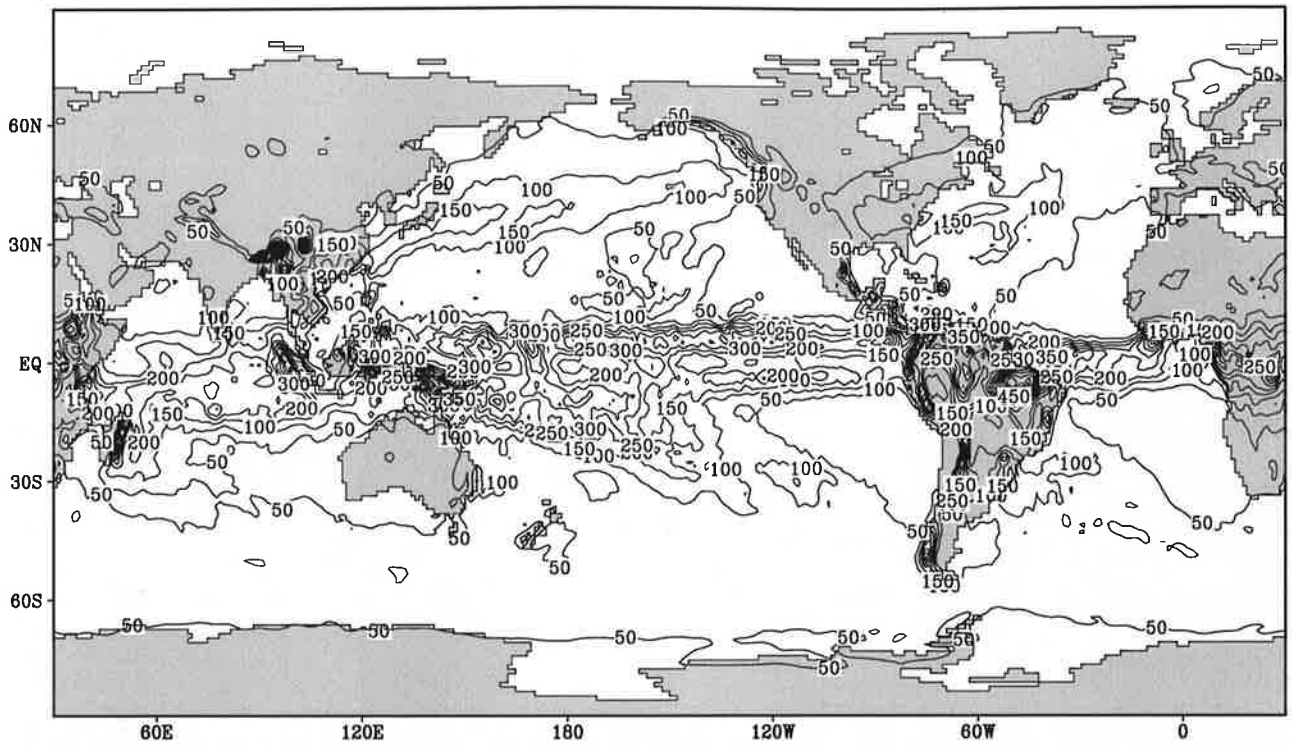

Contour interval: 50 mm month^{-1}

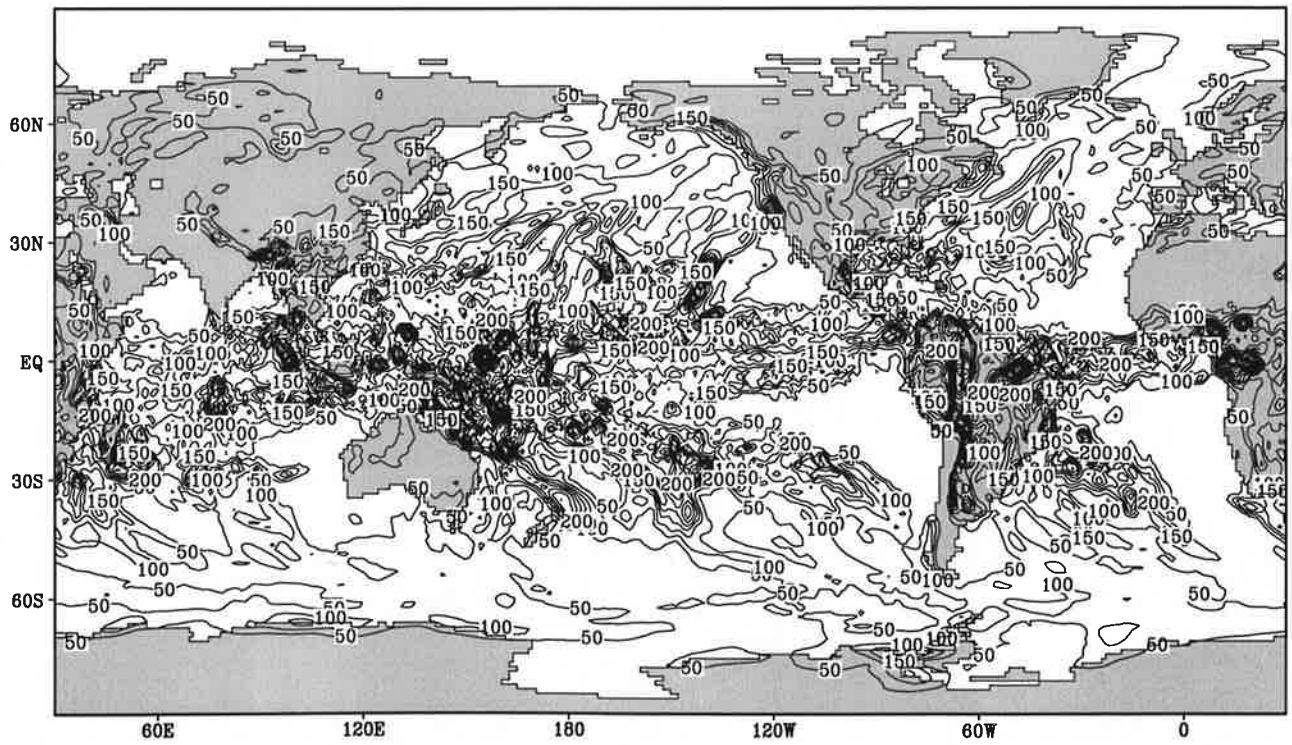

Contour interval: 50 mm month^{-1}

Fig.8.5 Precipitation May

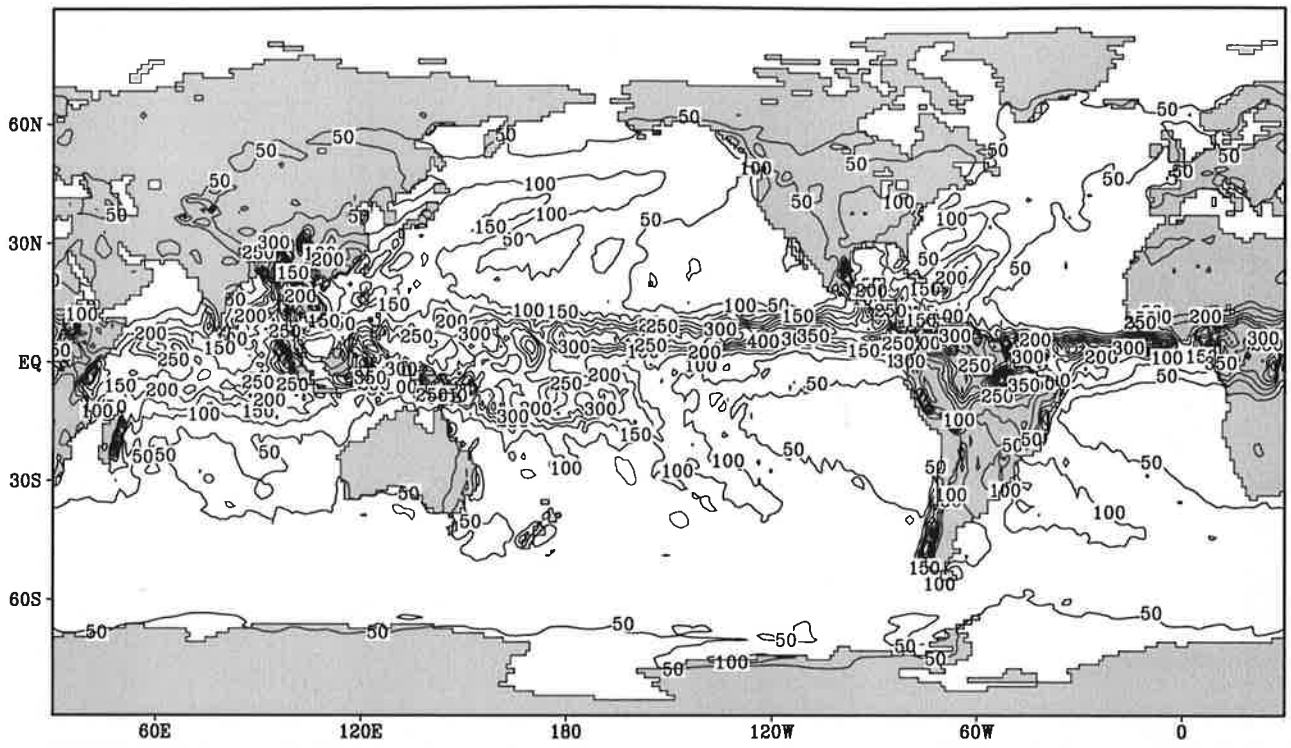

Contour interval: 50 mm month^{-1}

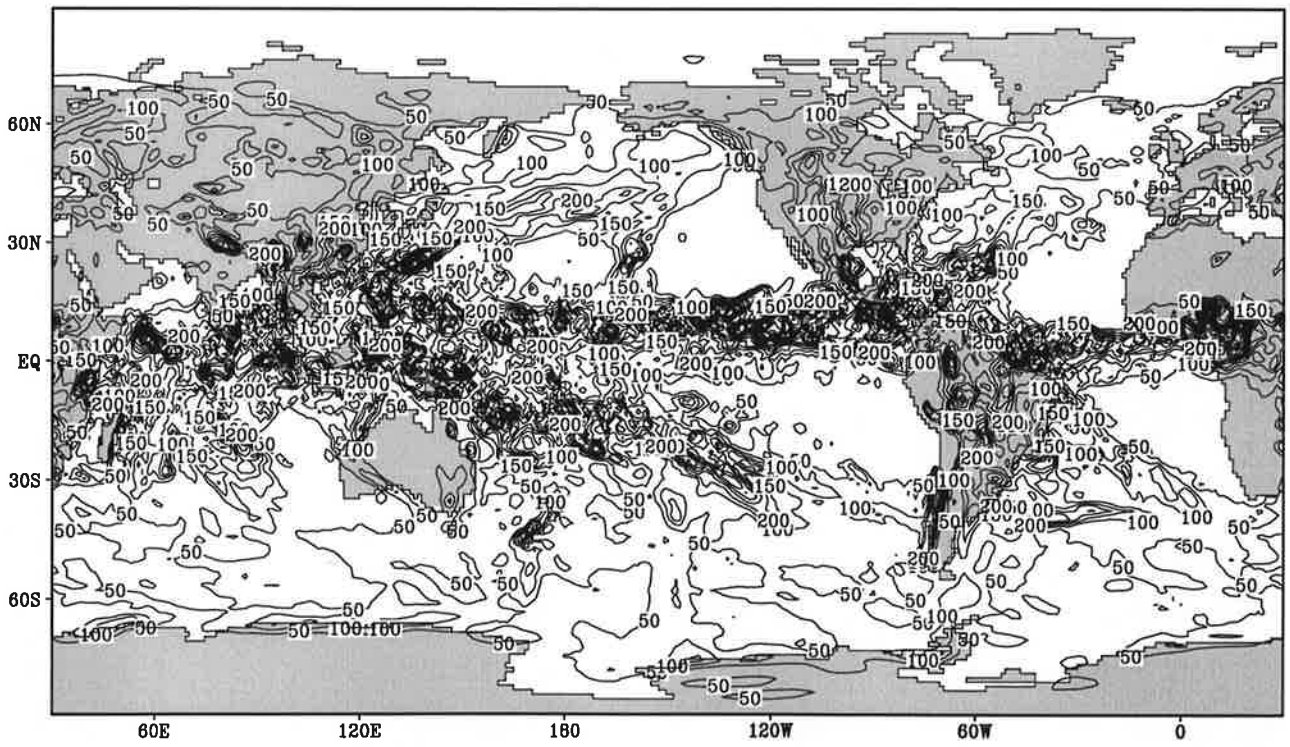

Contour interval: 50 mm month^{-1}

Fig.8.6 Precipitation June

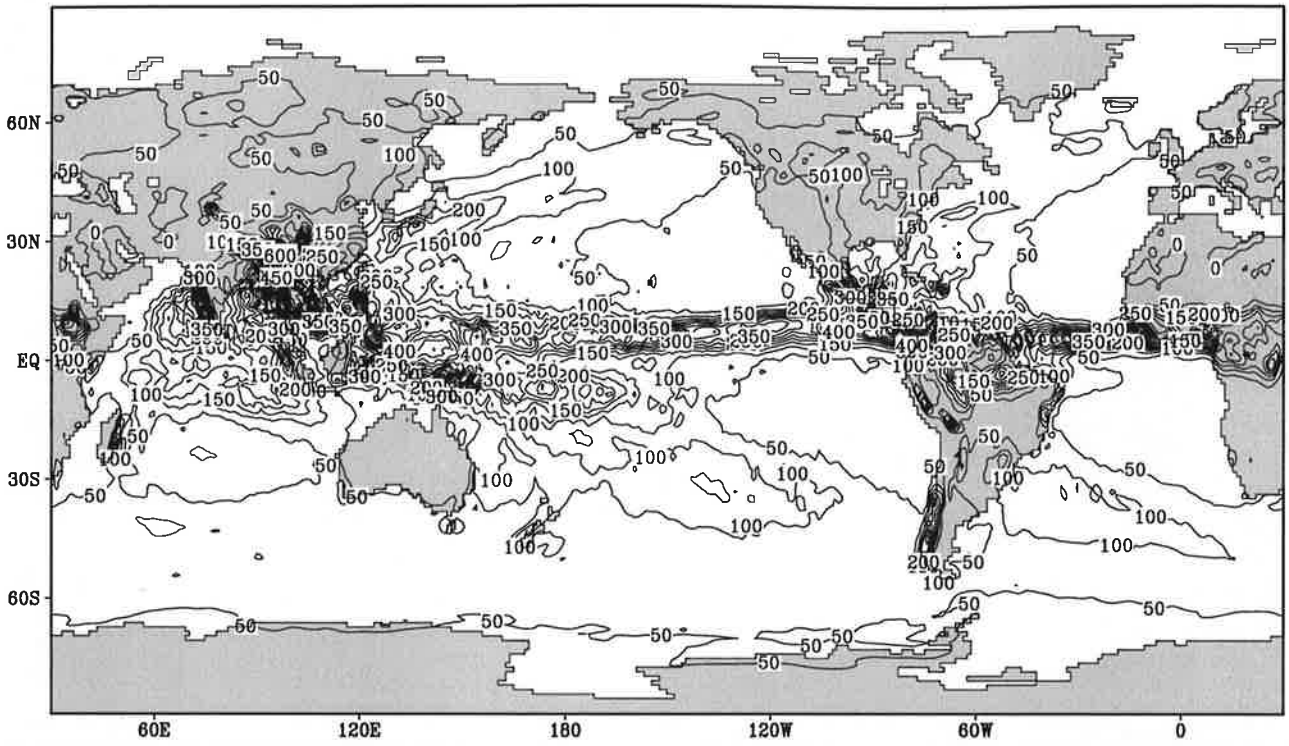

Contour interval: 50 mm month^{-1}

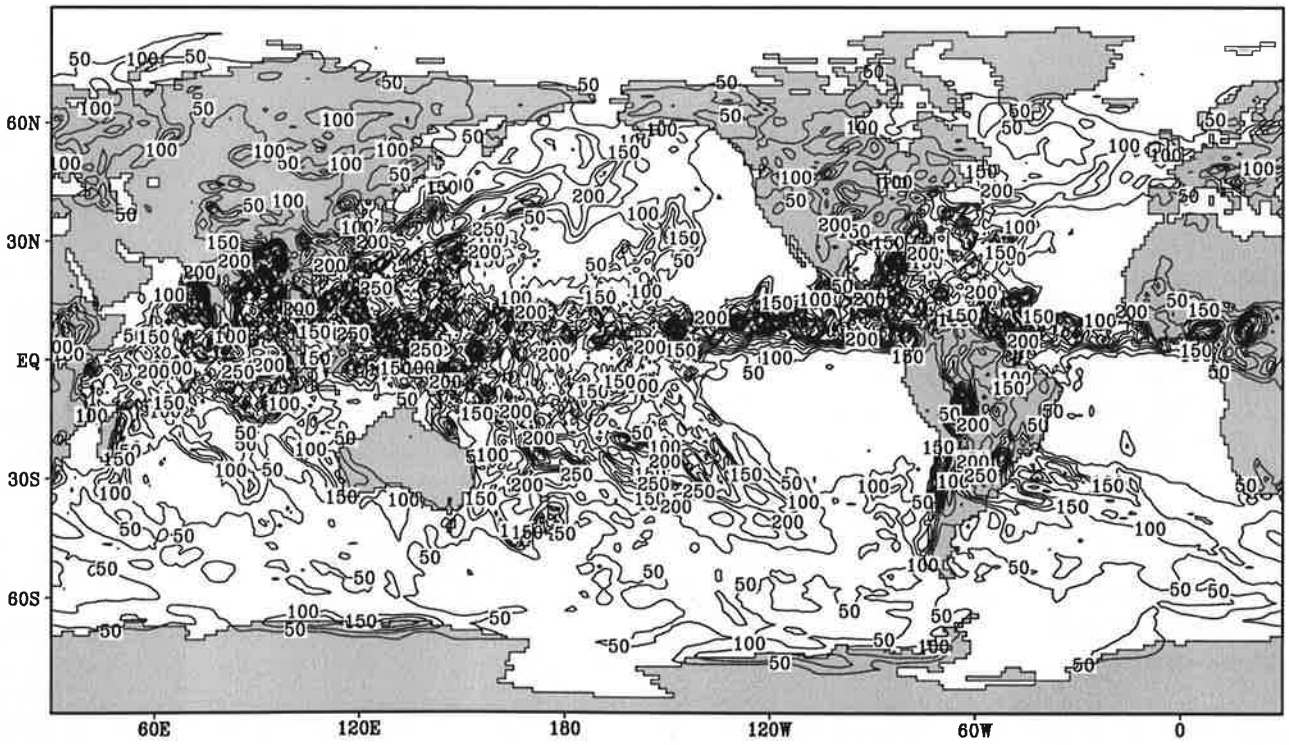

Contour interval: 50 mm month^{-1}

Fig.8.7 Precipitation July

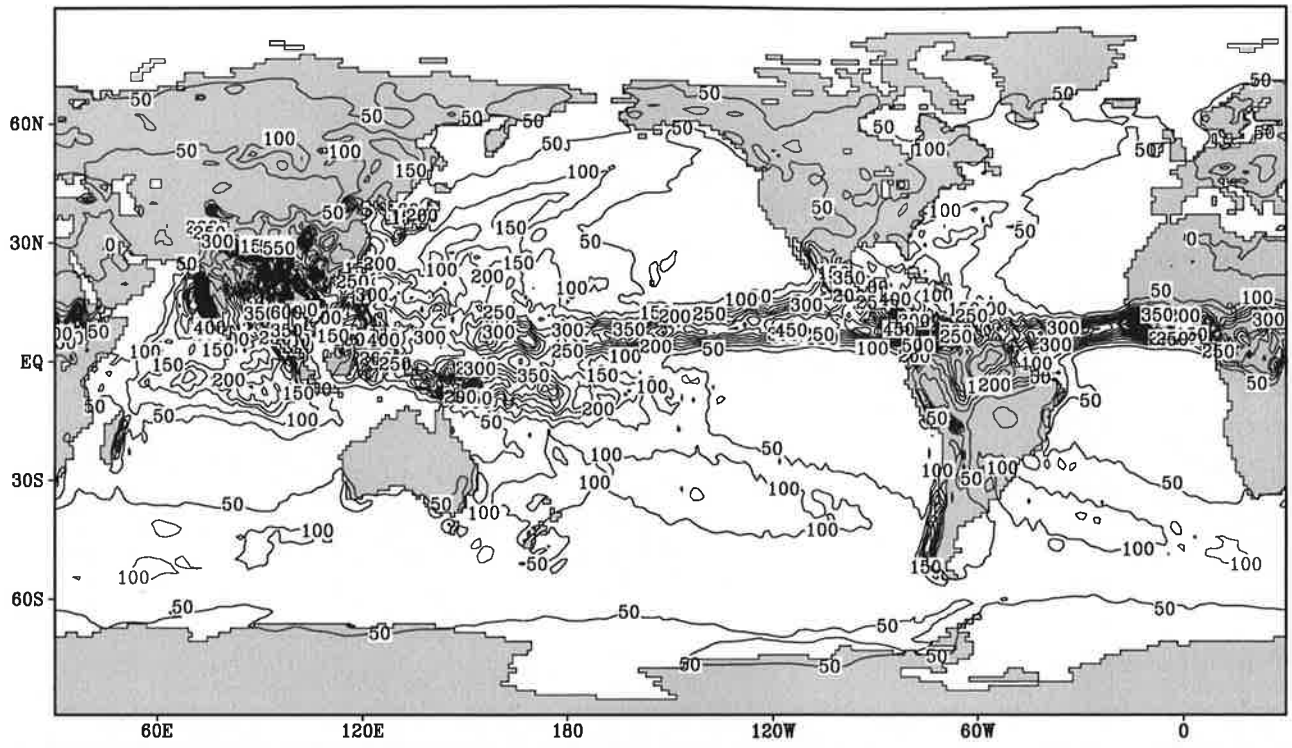

Contour interval: 50 mm month^{-1}

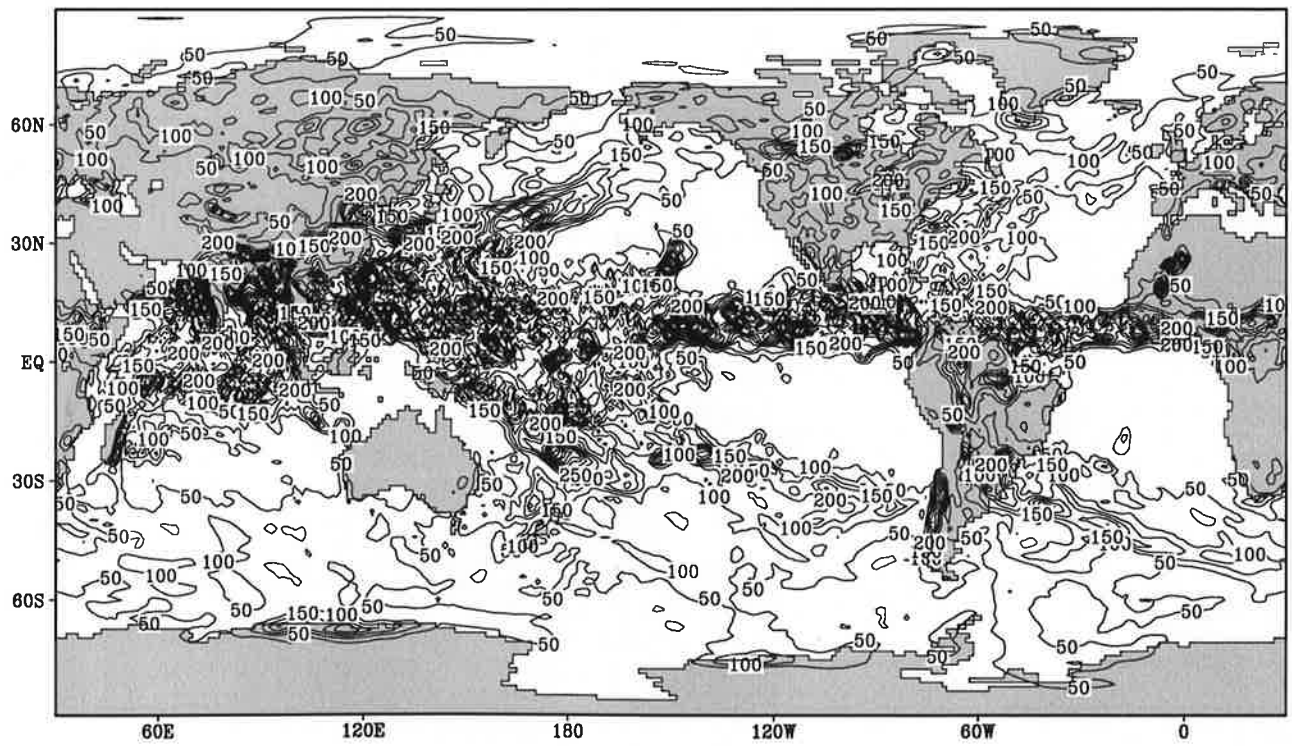

Contour interval: 50 mm month^{-1}

Fig.8.8 Precipitation August

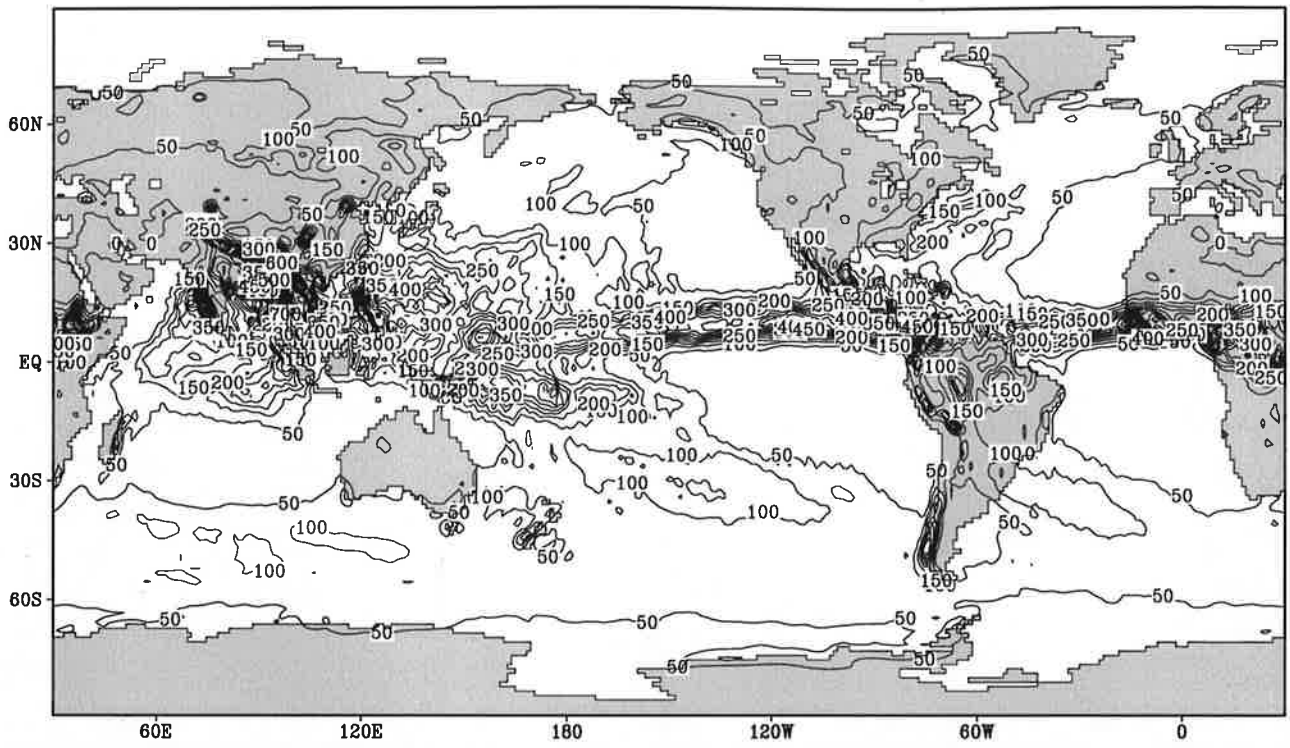

Contour interval: 50 mm month^{-1}

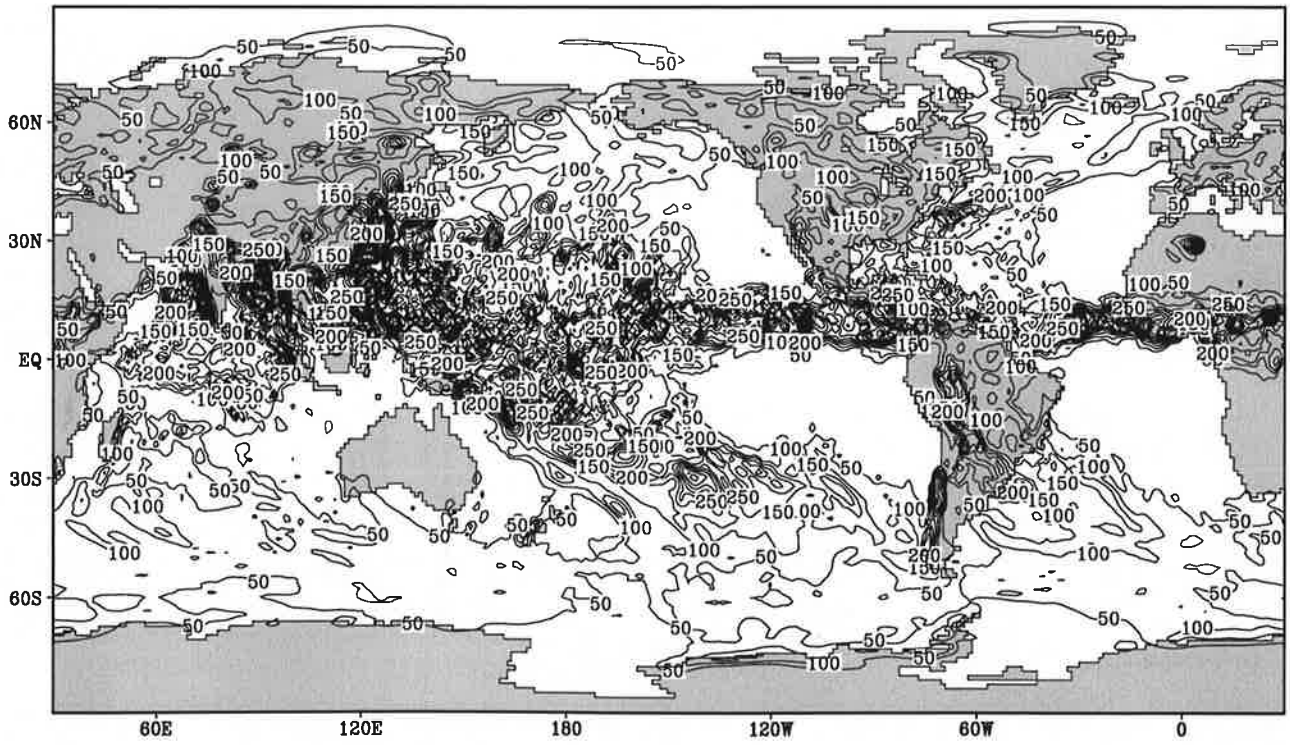

Contour interval: 50 mm month^{-1}

Fig.8.9 Precipitation September

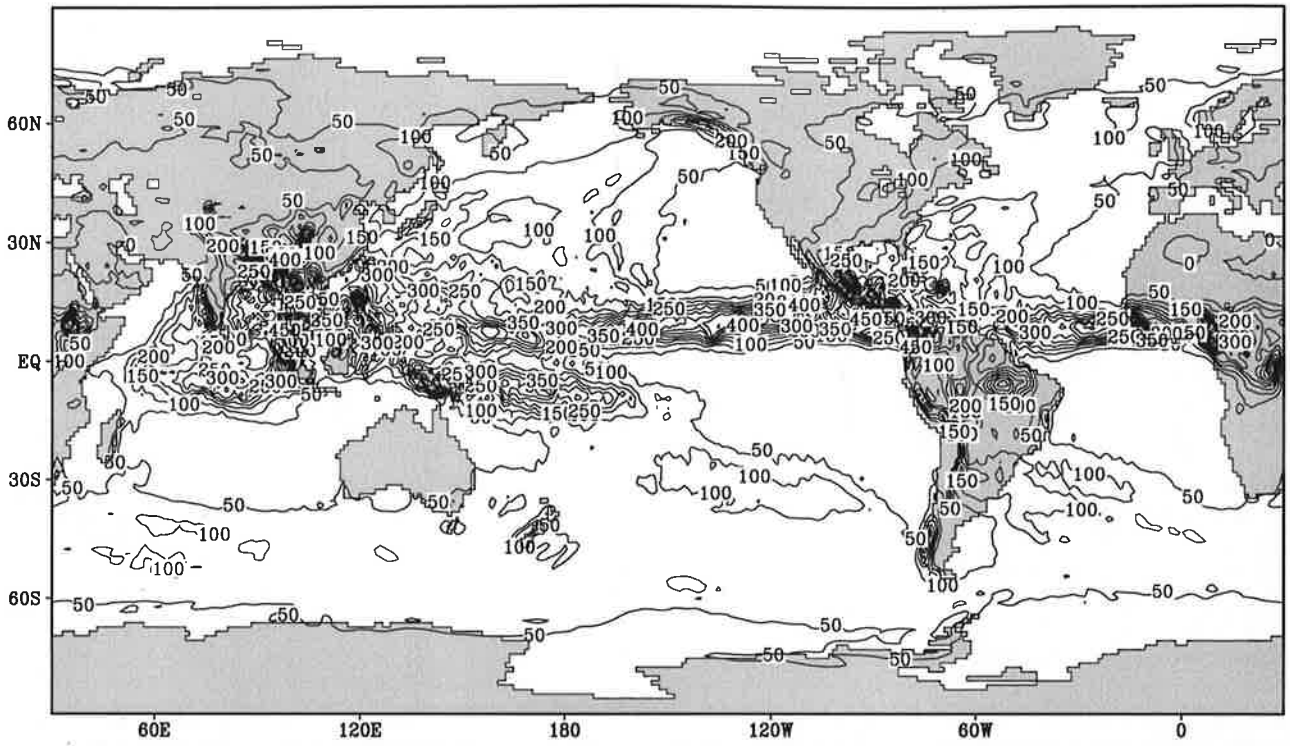

Contour interval: 50 mm month^{-1}

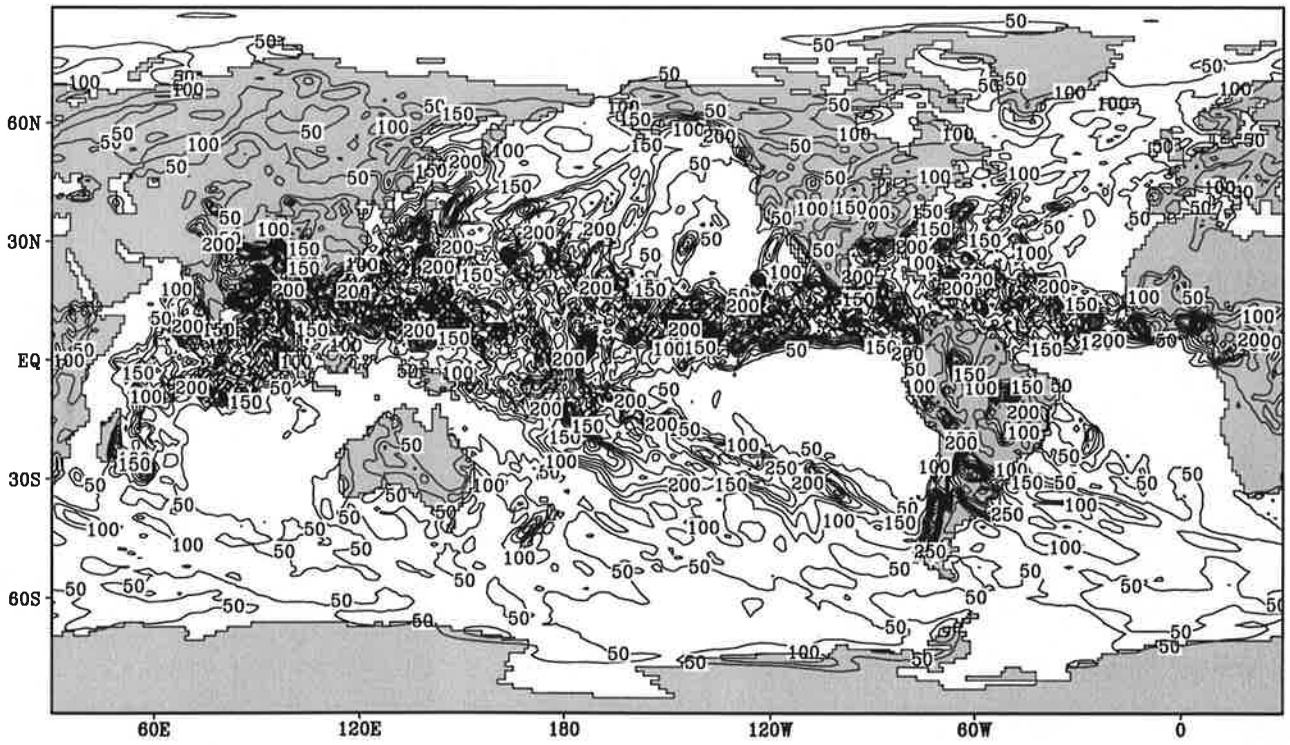

Contour interval: 50 mm month^{-1}

Fig.8.10 Precipitation October

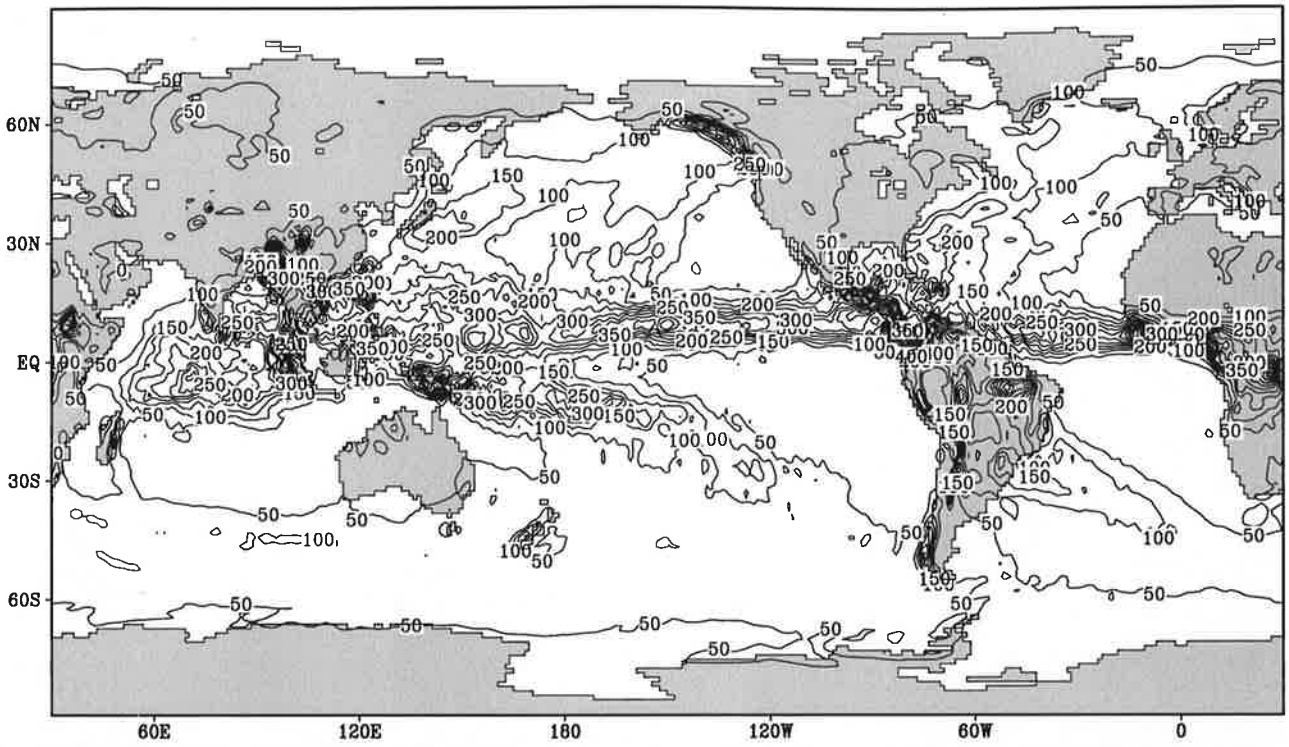

Contour interval: 50 mm month^{-1}

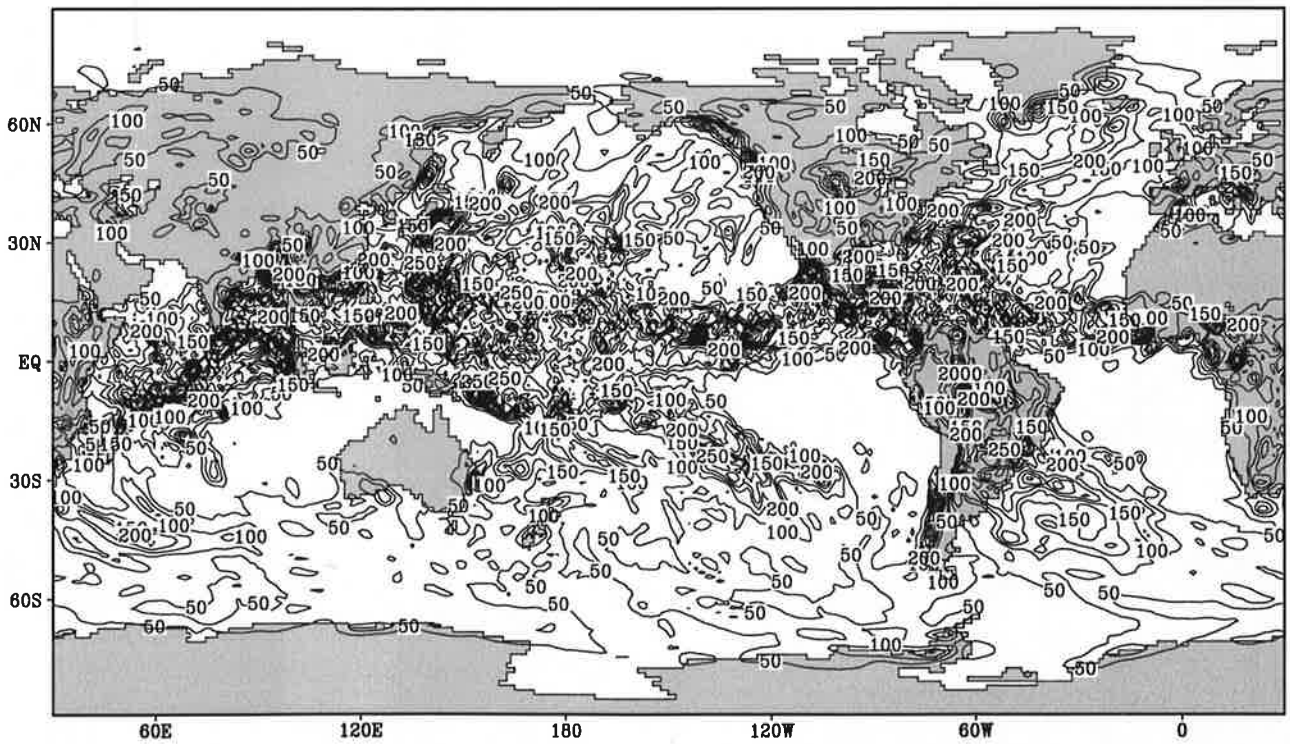

Contour interval: 50 mm month^{-1}

Fig.8.11 Precipitation November

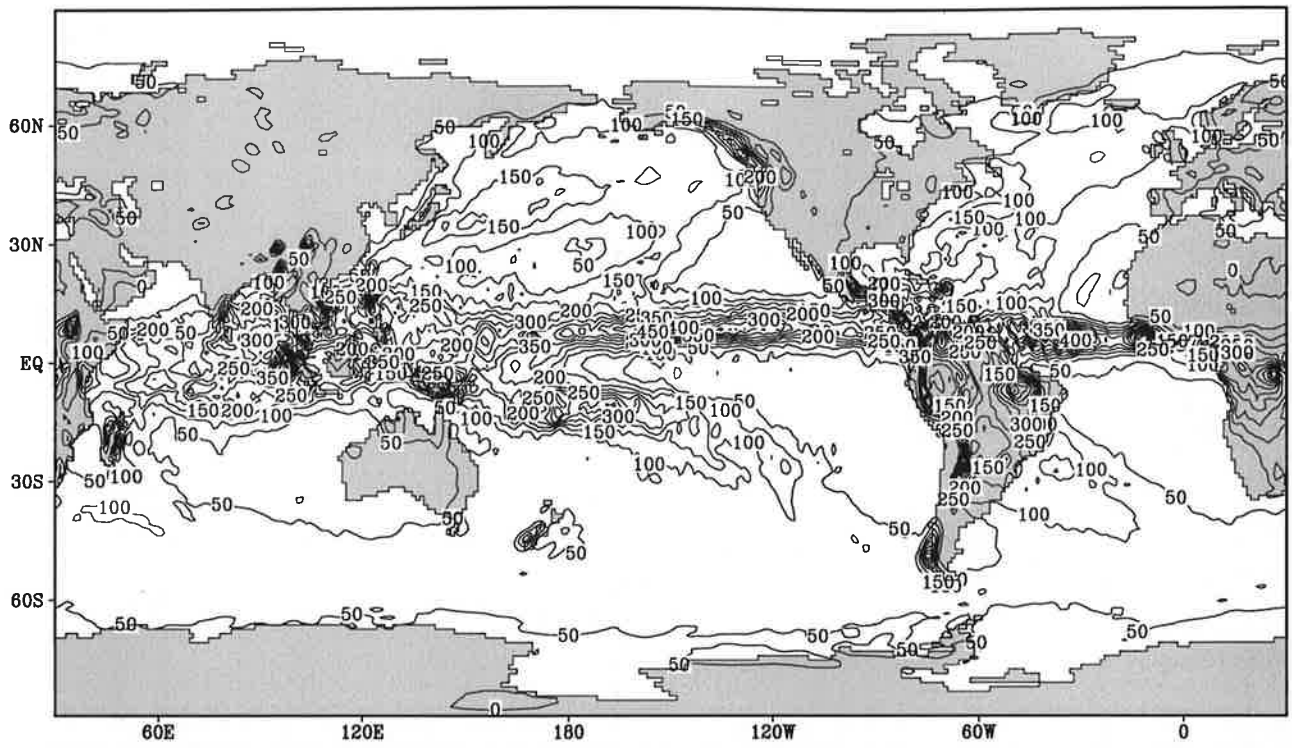

Contour interval: 50 mm month^{-1}

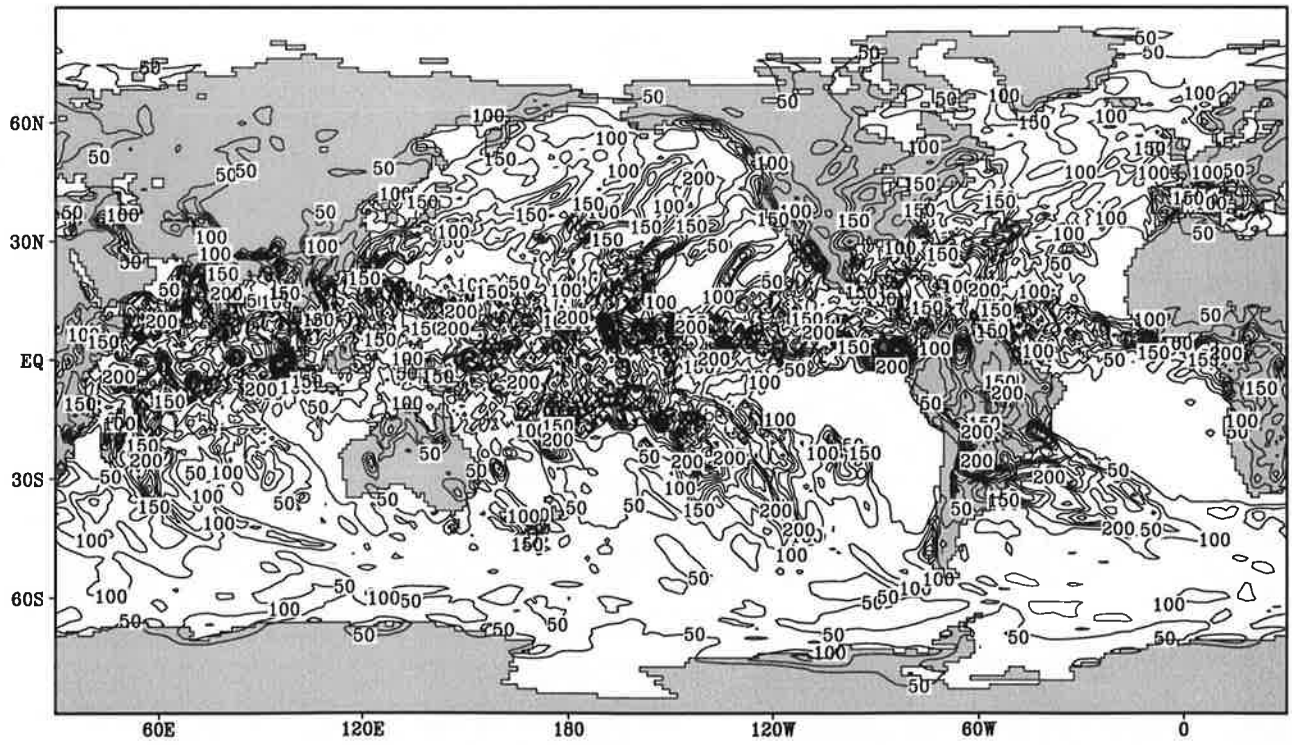

Contour interval: 50 mm month^{-1}

Fig.8.12 Precipitation December

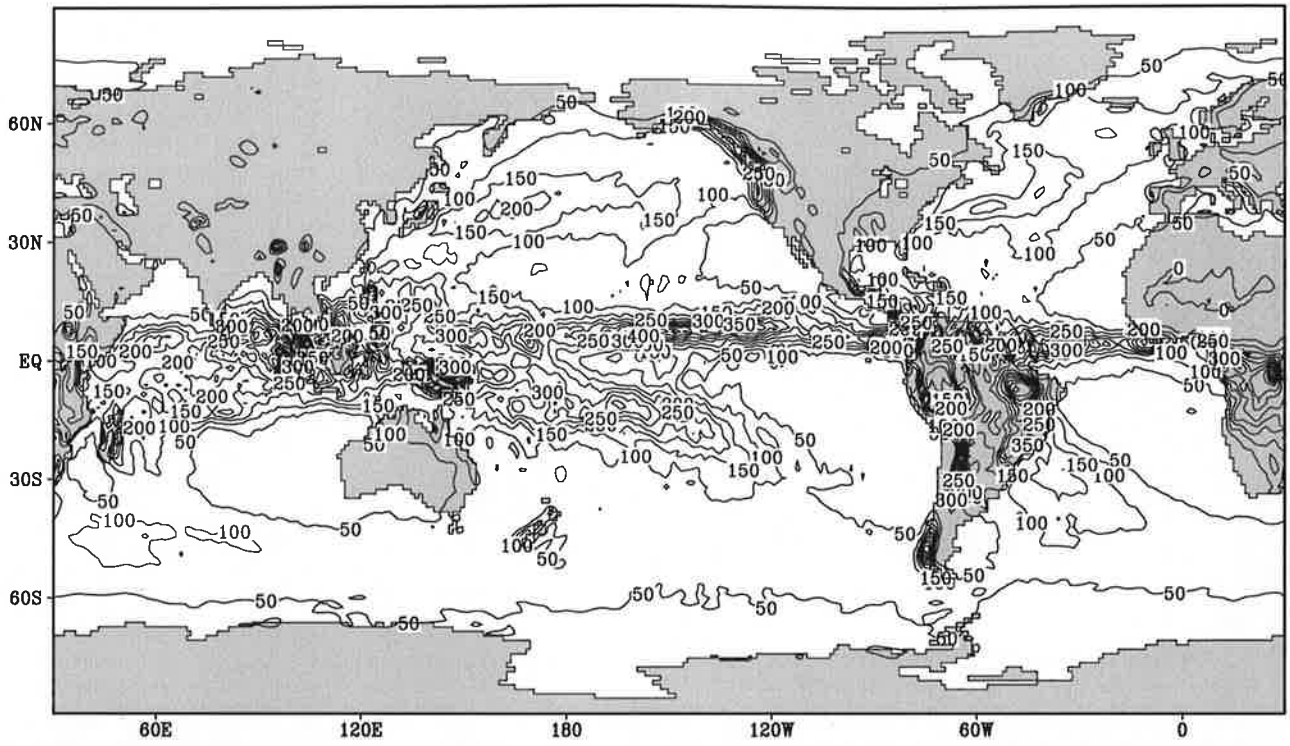

Contour interval: 50 mm month^{-1}

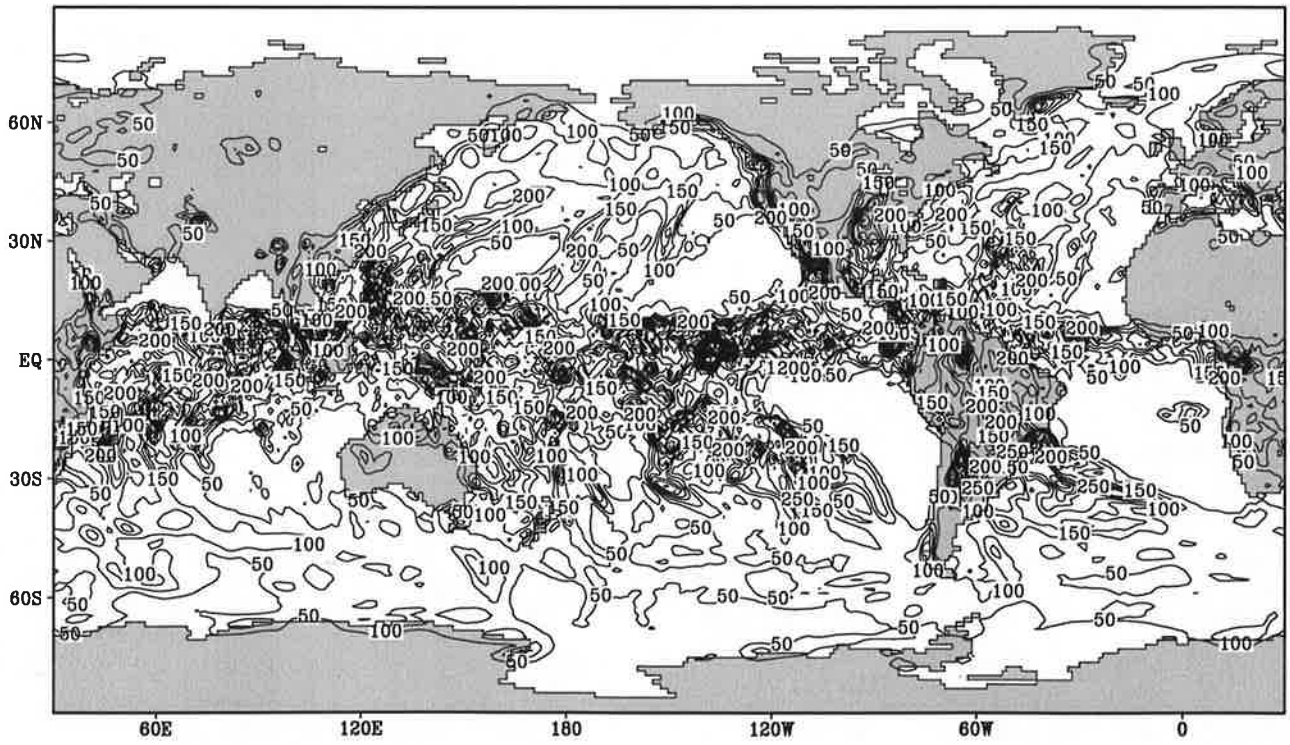

Contour interval: 50 mm month^{-1}

Fig.8.13 Precipitation Annual Mean

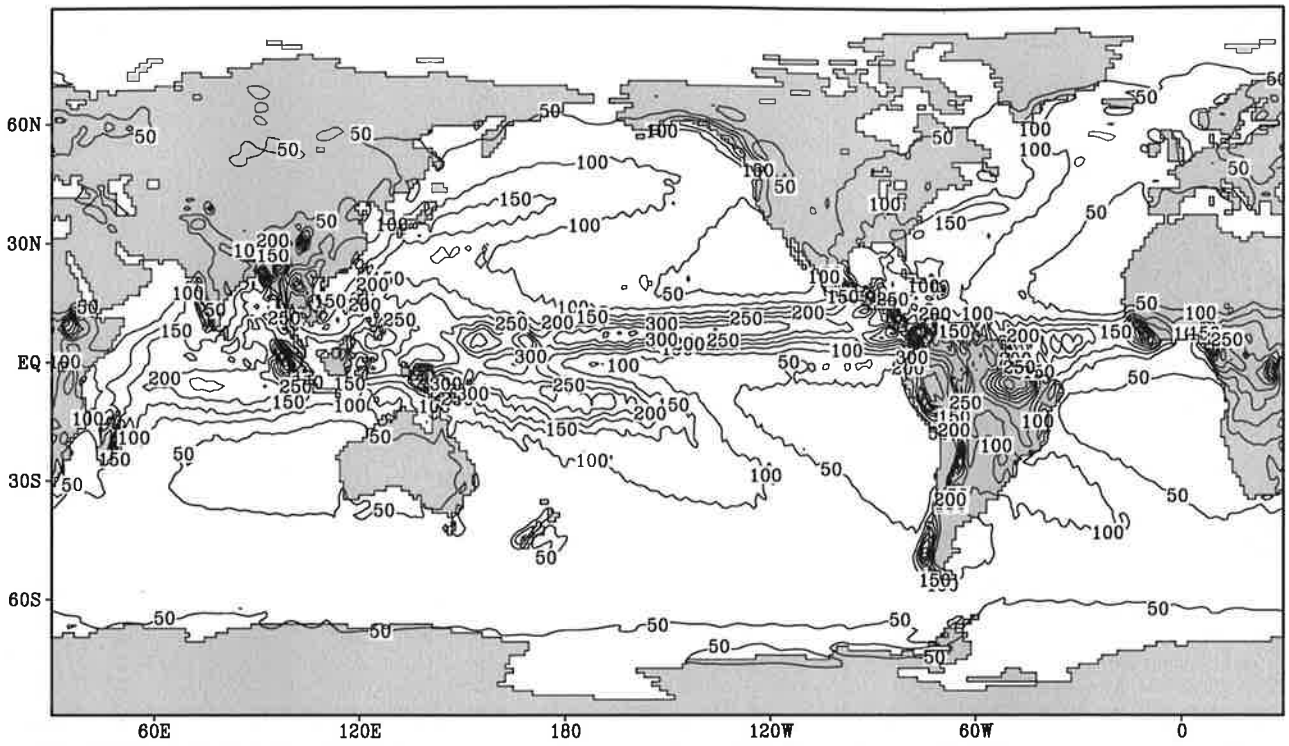

Contour interval: 50 mm month^{-1}

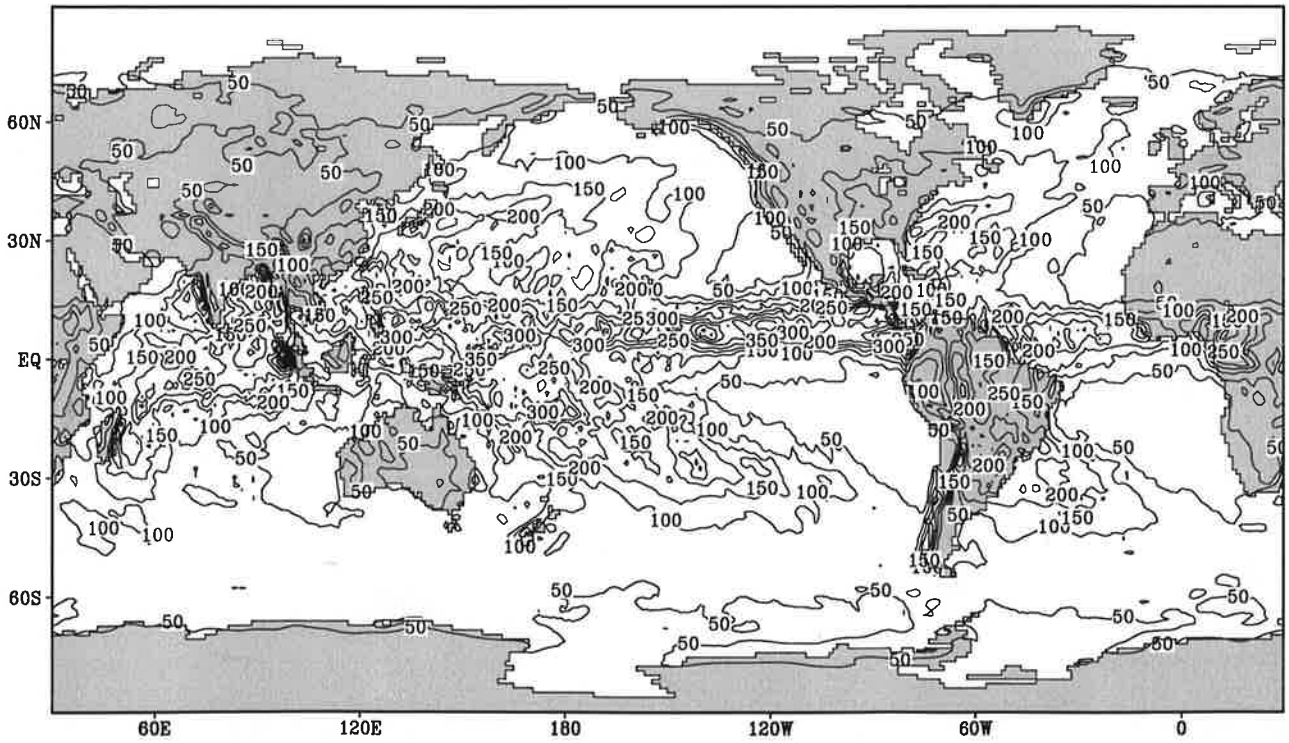

Contour interval: 50 mm month^{-1}

Fig.9.1 Turbulent kinetic energy input January

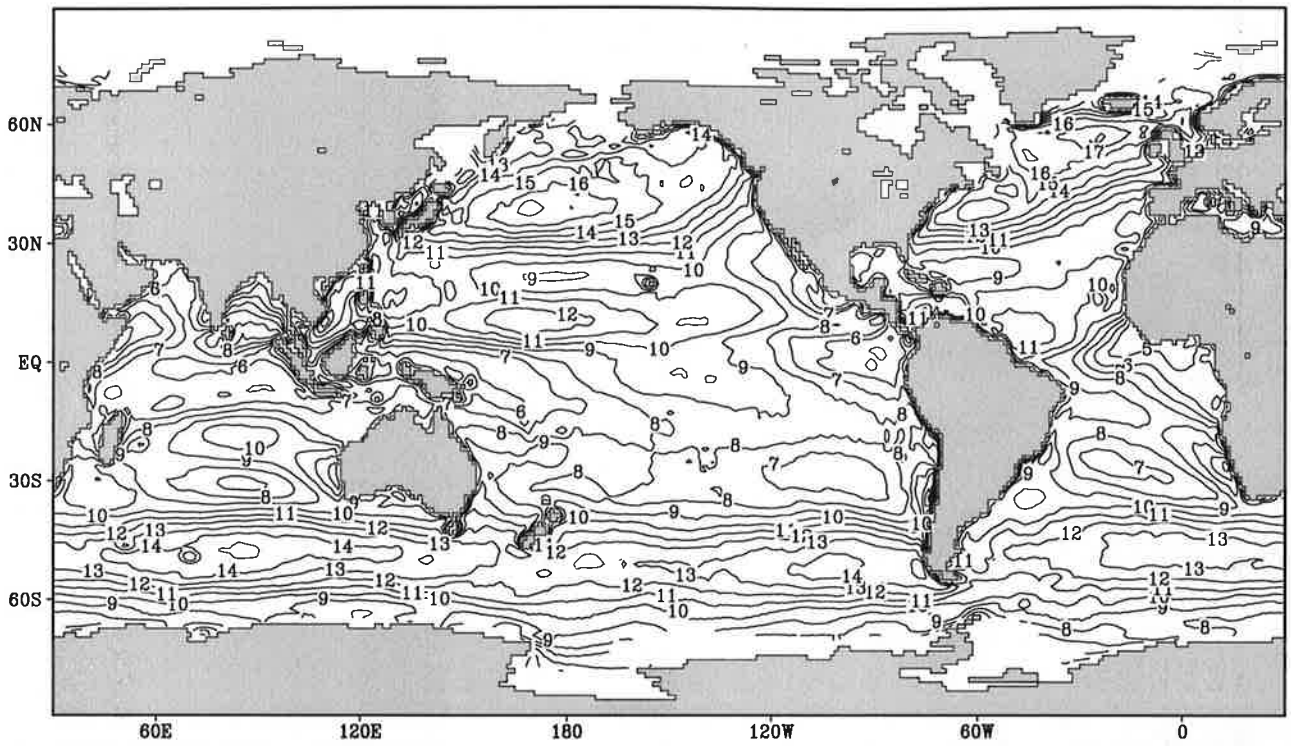

Contour interval: 1 mms^{-1}

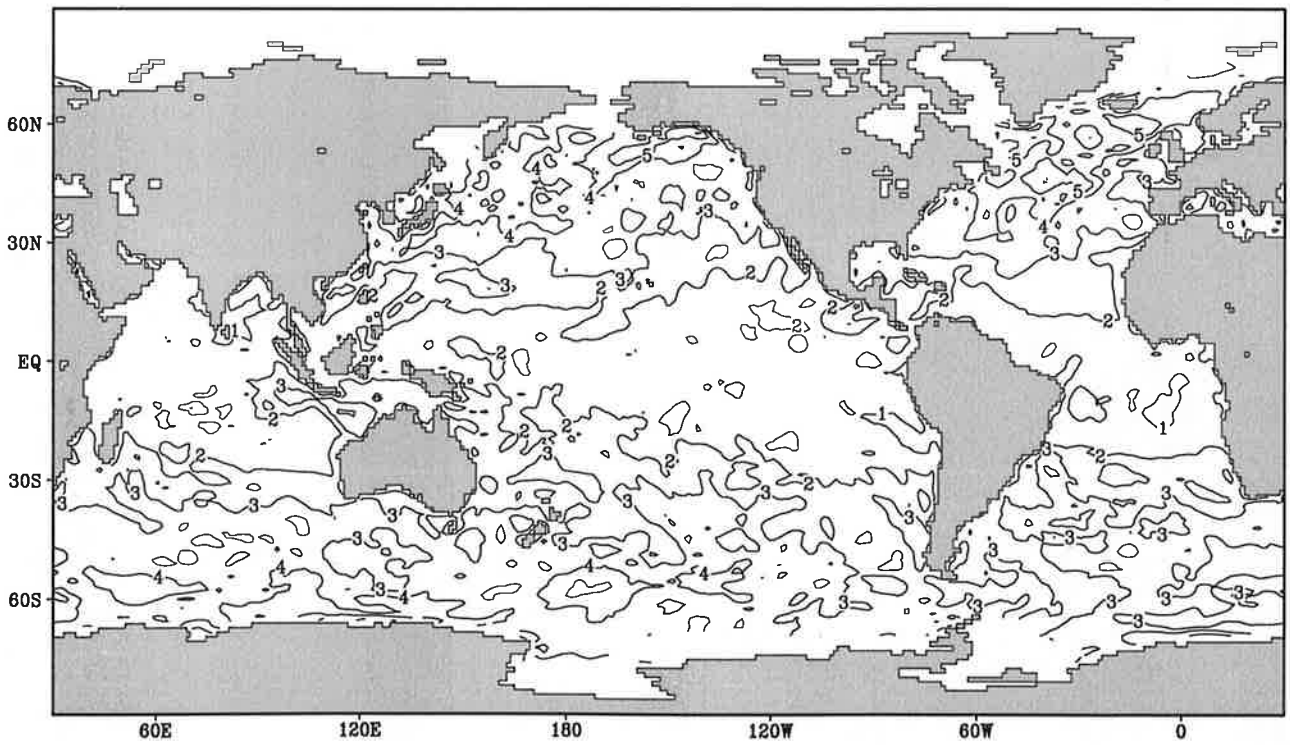

Contour interval: 1 mms^{-1}

Fig.9.2 Turbulent kinetic energy input February

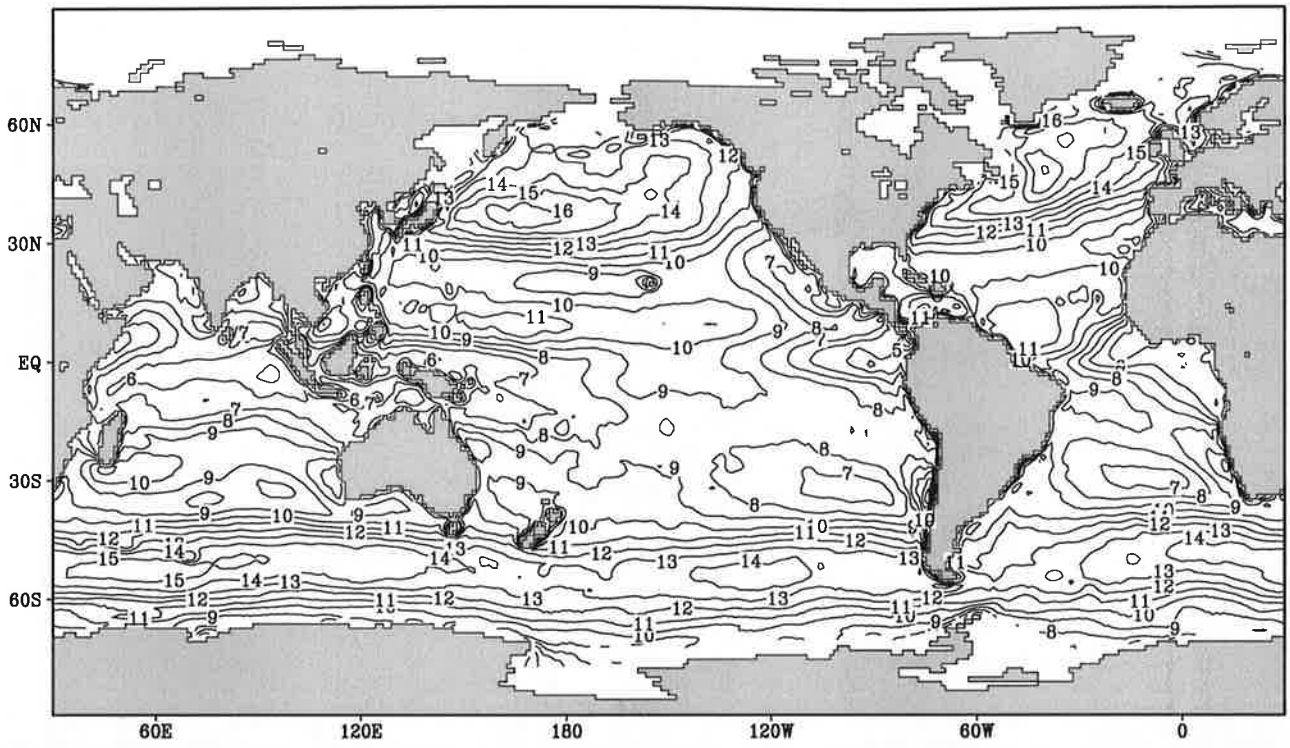

Contour interval: 1 mms^{-1}

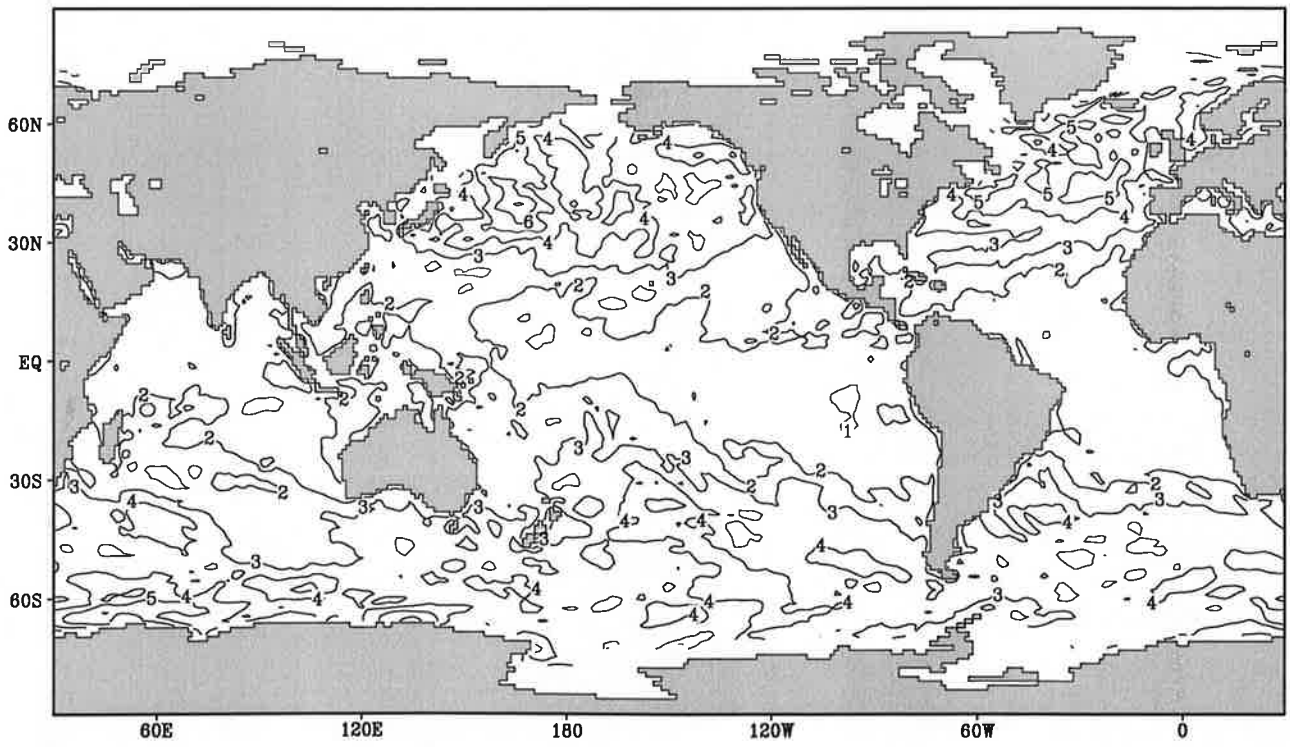

Contour interval: 1 mms^{-1}

Fig.9.3 Turbulent kinetic energy input March

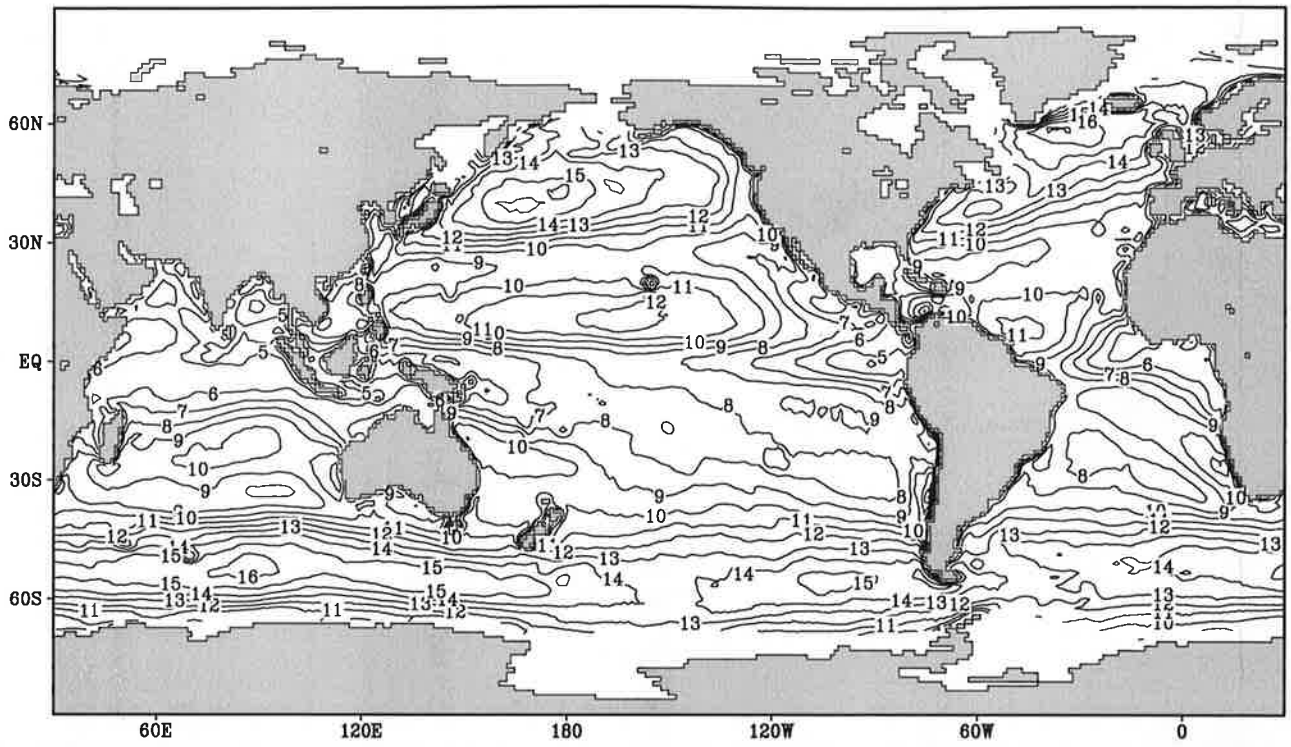

Contour interval: 1 mms^{-1}

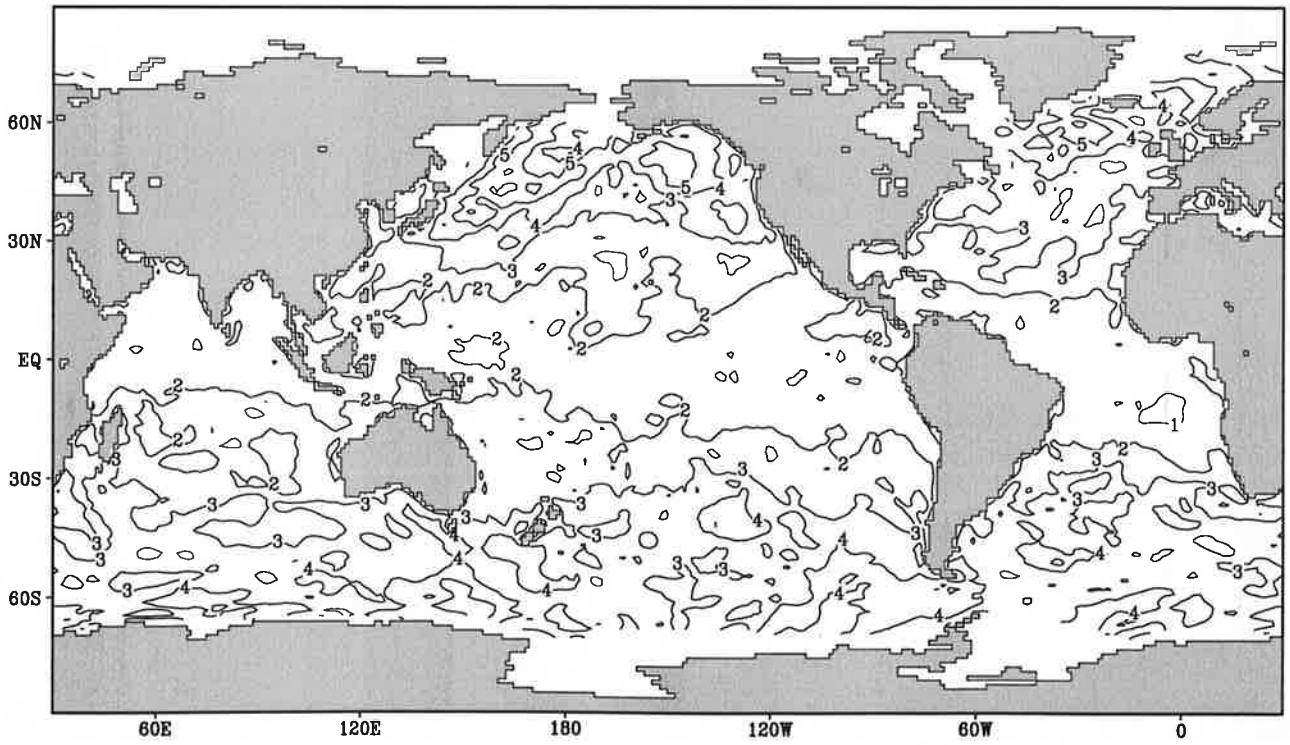

Contour interval: 1 mms^{-1}

Fig.9.4 Turbulent kinetic energy input April

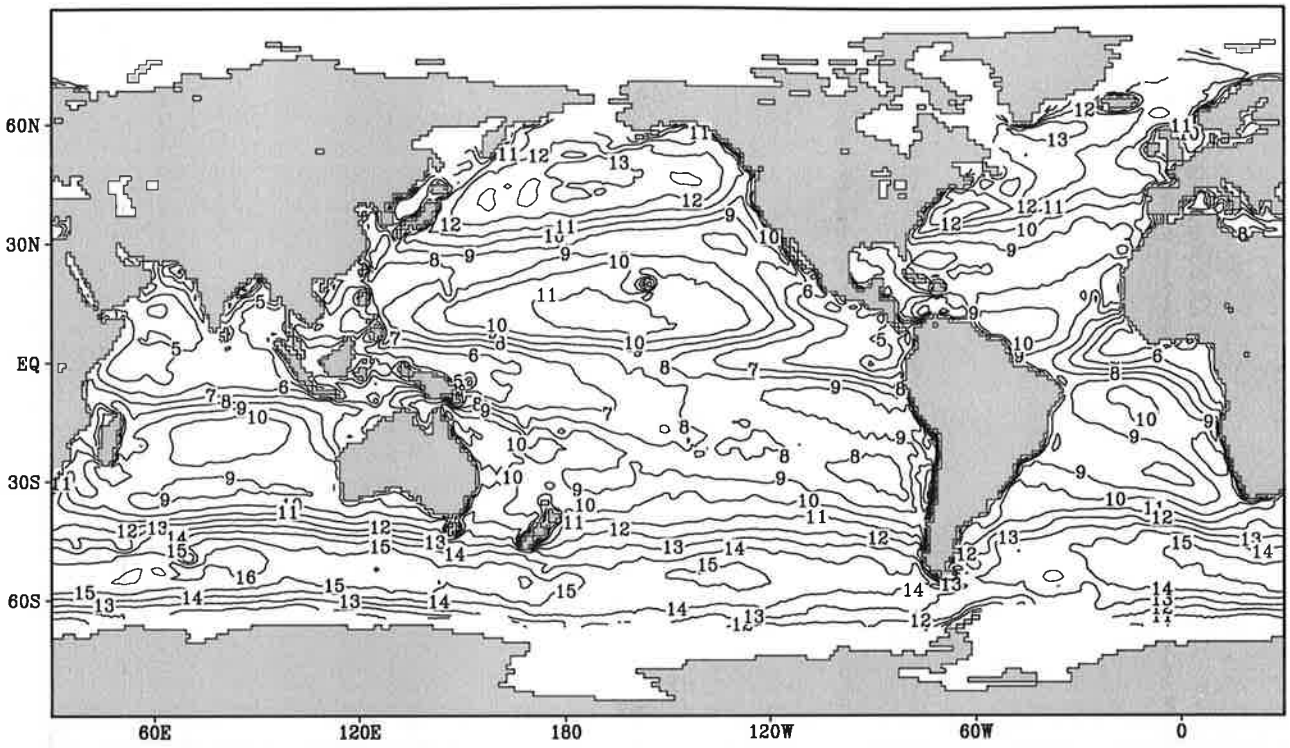

Contour interval: 1 mms^{-1}

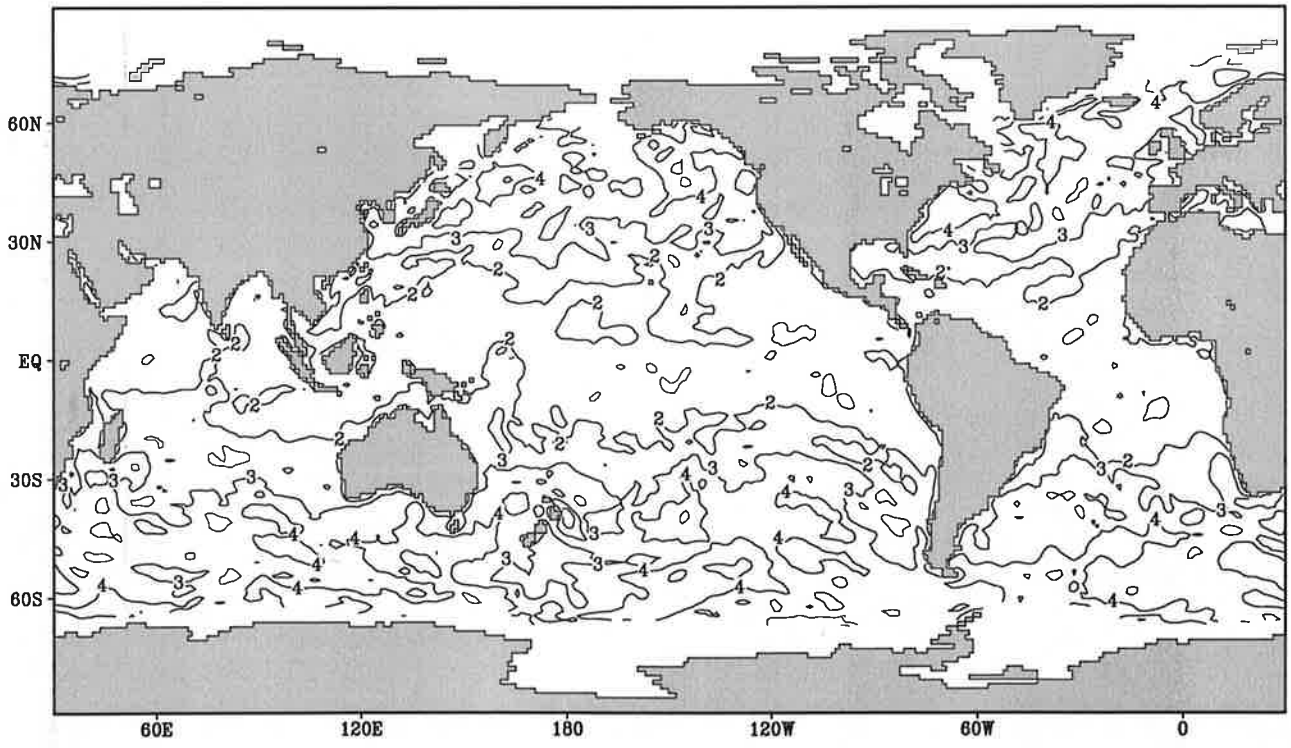

Contour interval: 1 mms^{-1}

Fig.9.5 Turbulent kinetic energy input May

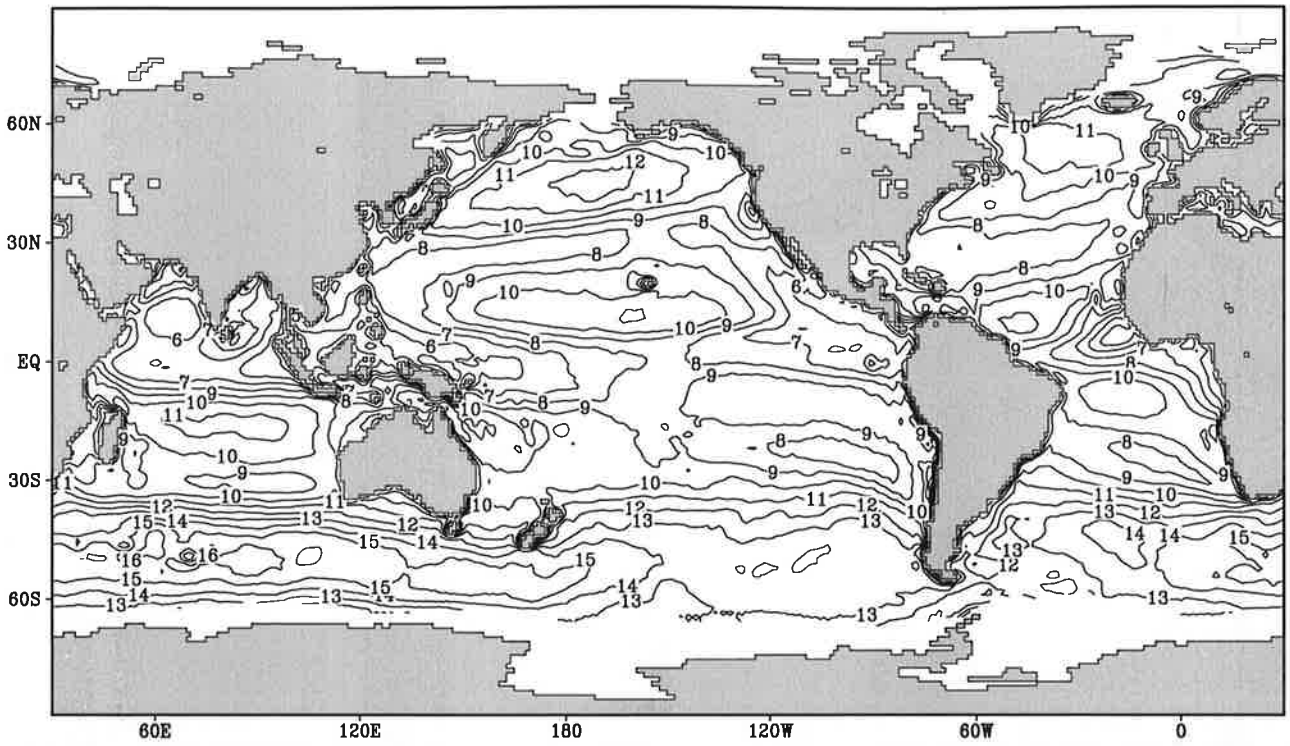

Contour interval: 1 mms^{-1}

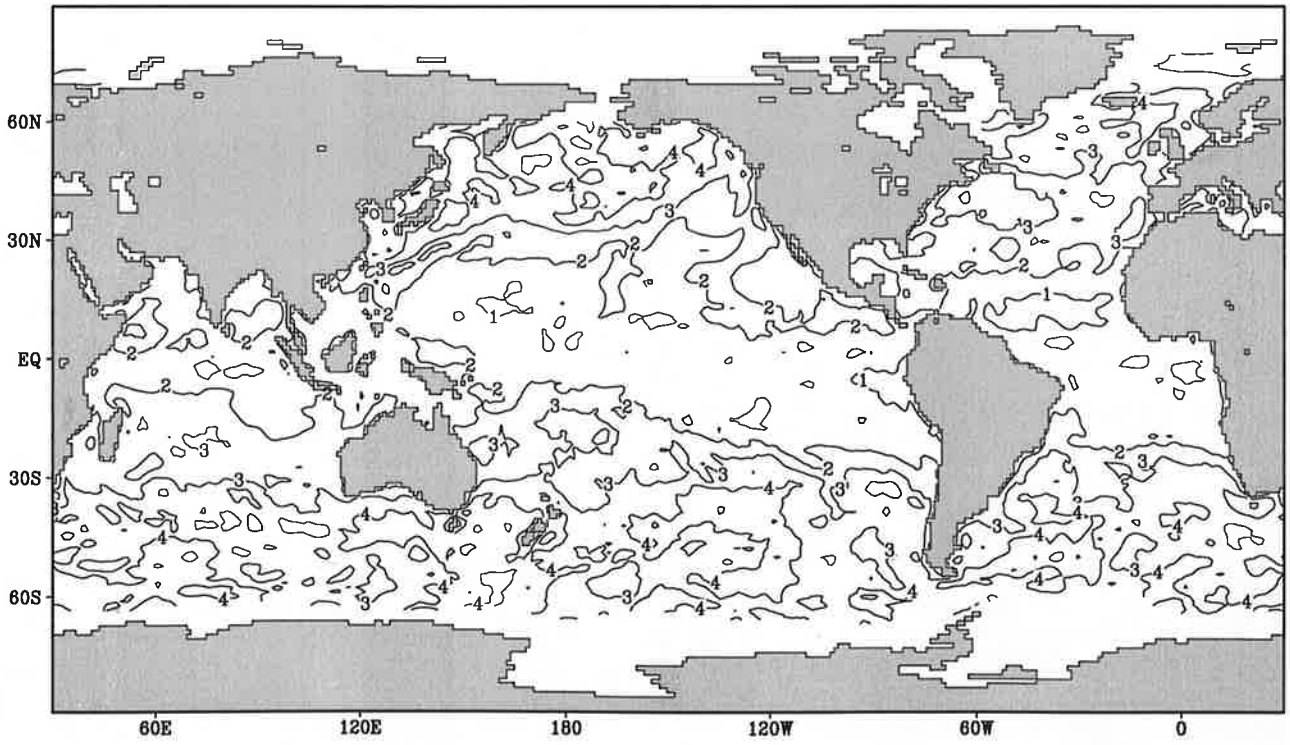

Contour interval: 1 mms^{-1}

Fig.9.6 Turbulent kinetic energy input June

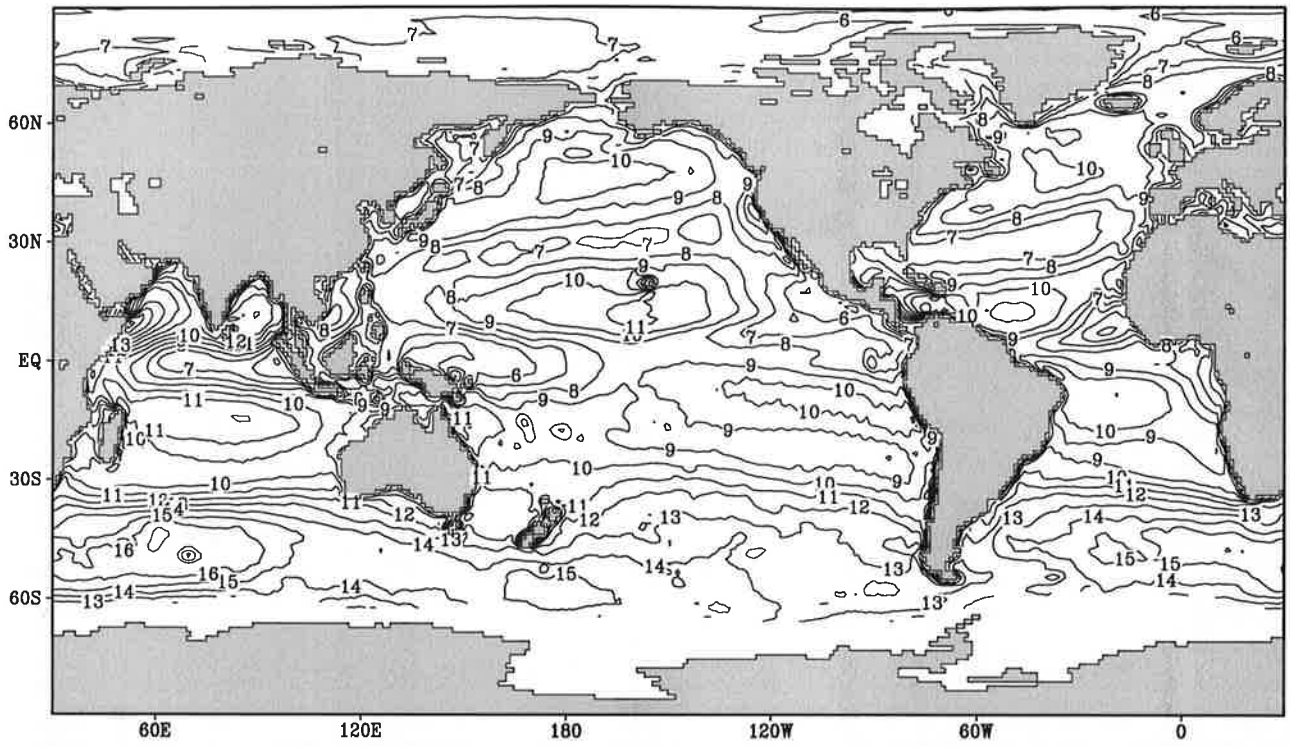

Contour interval: 1 mms^{-1}

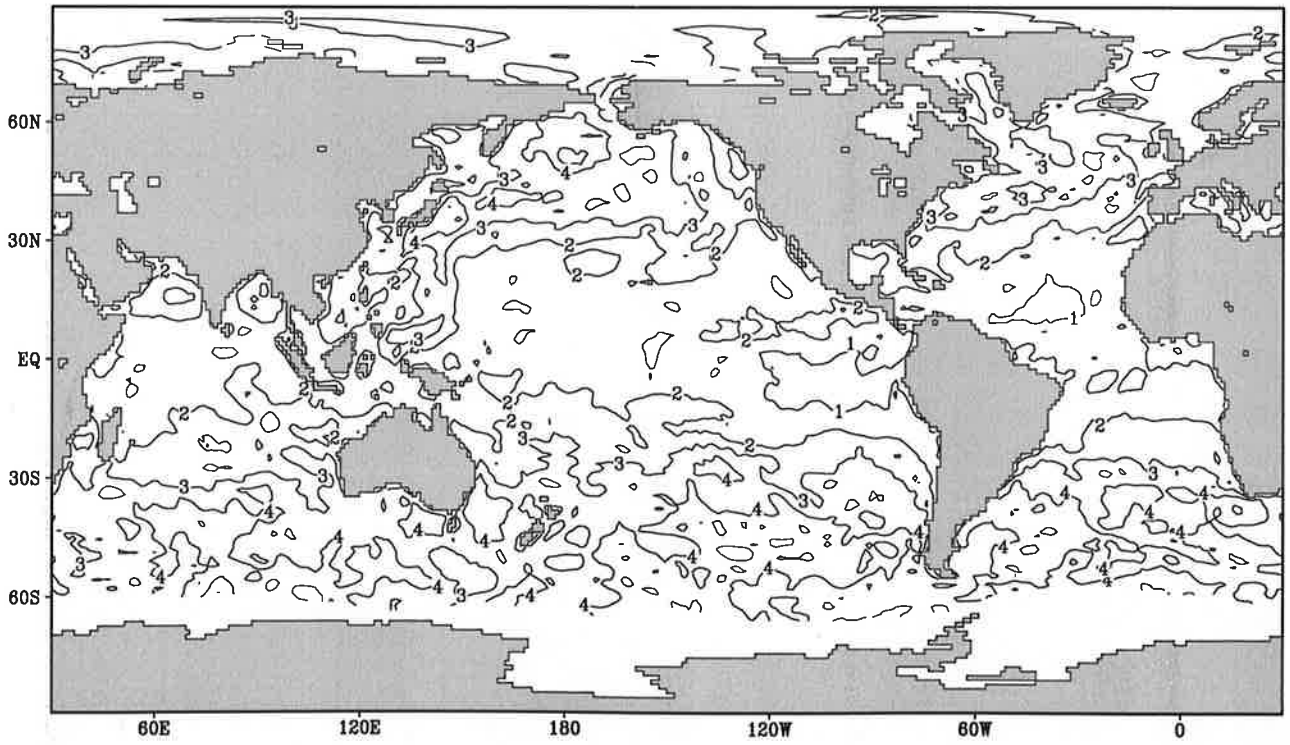

Contour interval: 1 mms^{-1}

Fig.9.7 Turbulent kinetic energy input July

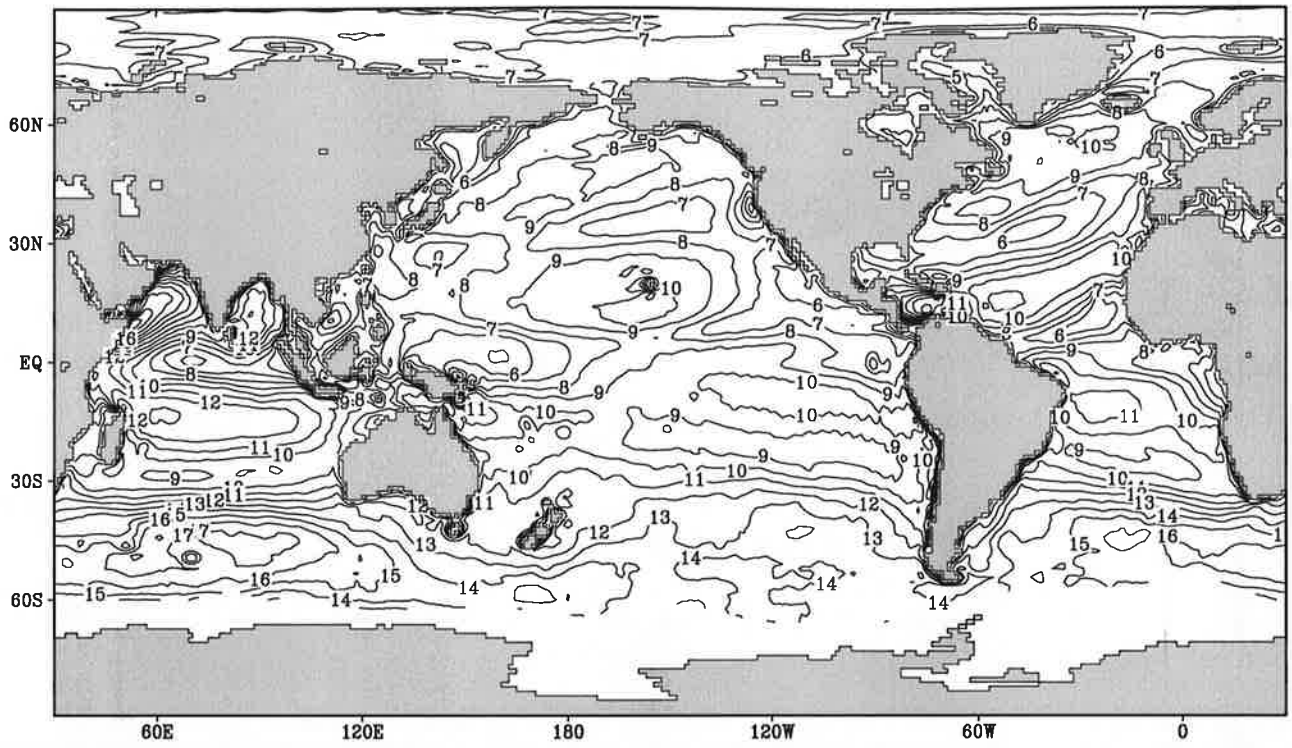

Contour interval: 1 mms^{-1}

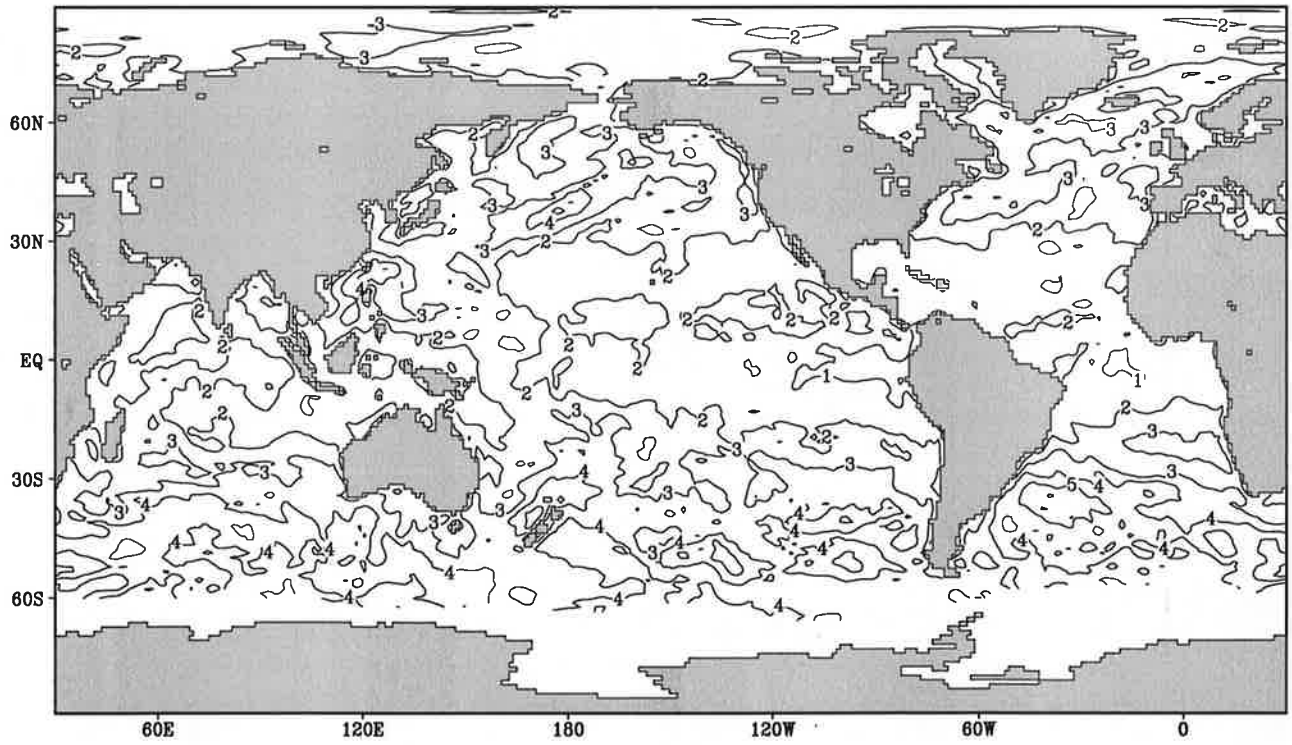

Contour interval: 1 mms^{-1}

Fig.9.8 Turbulent kinetic energy input August

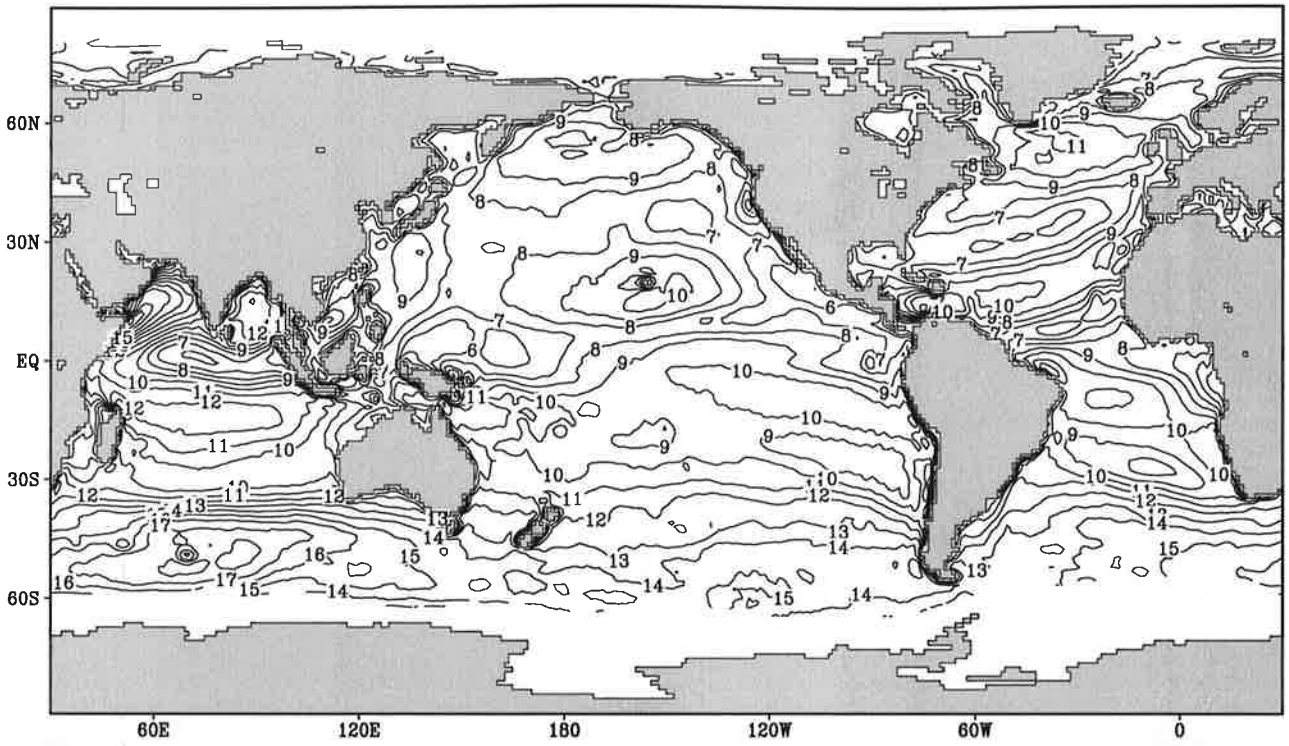

Contour interval: 1 mms^{-1}

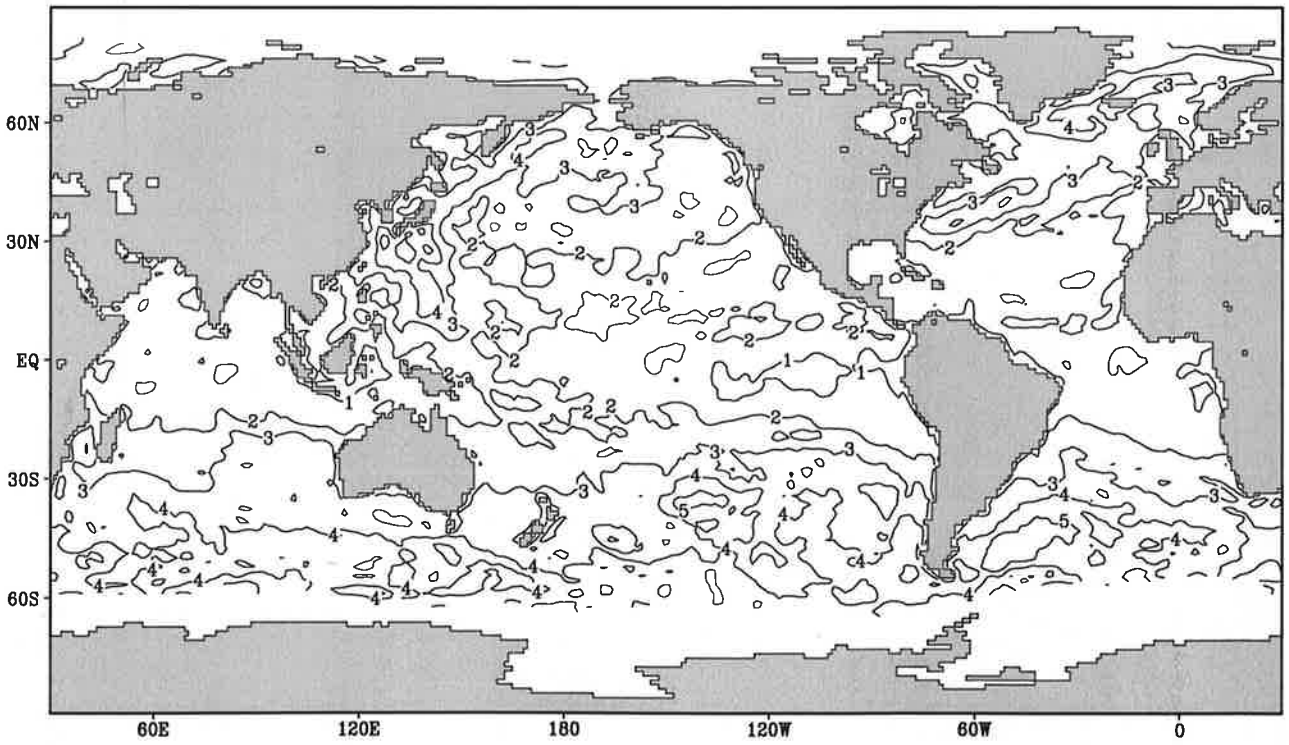

Contour interval: 1 mms^{-1}

Fig.9.9 Turbulent kinetic energy input September

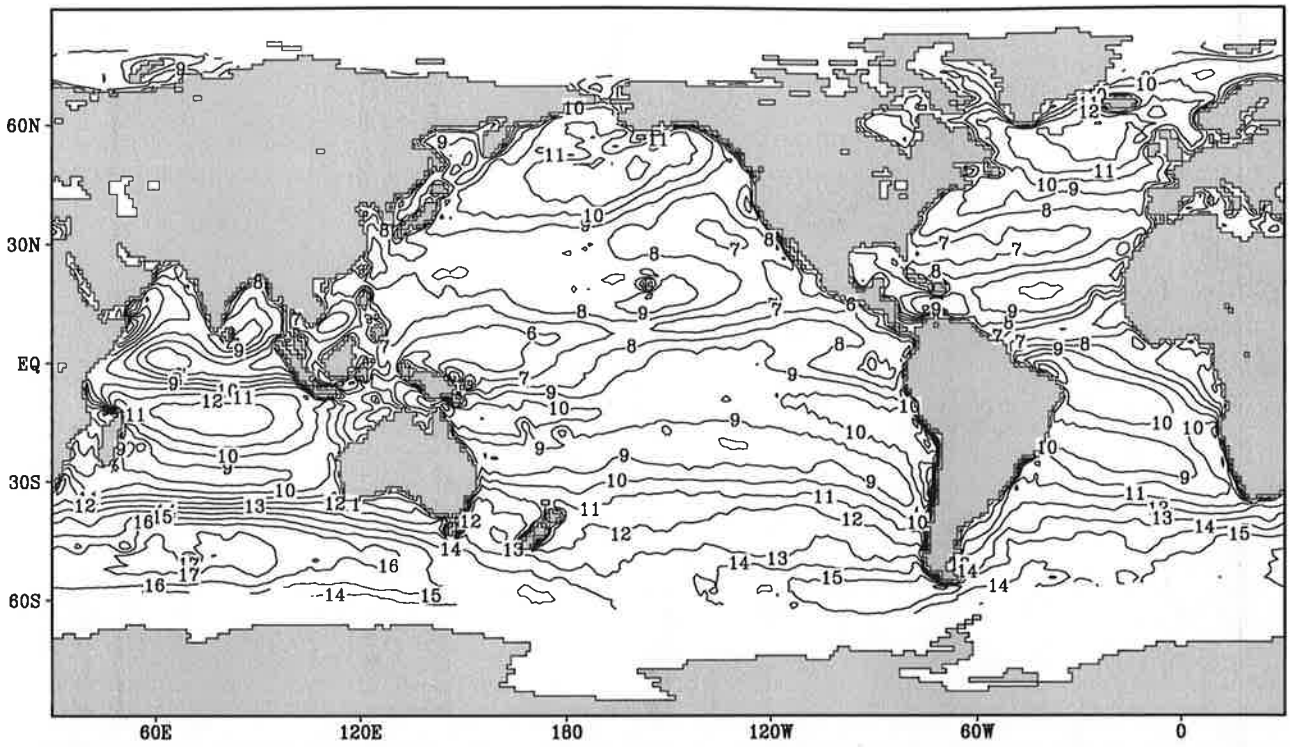

Contour interval: 1 mms^{-1}

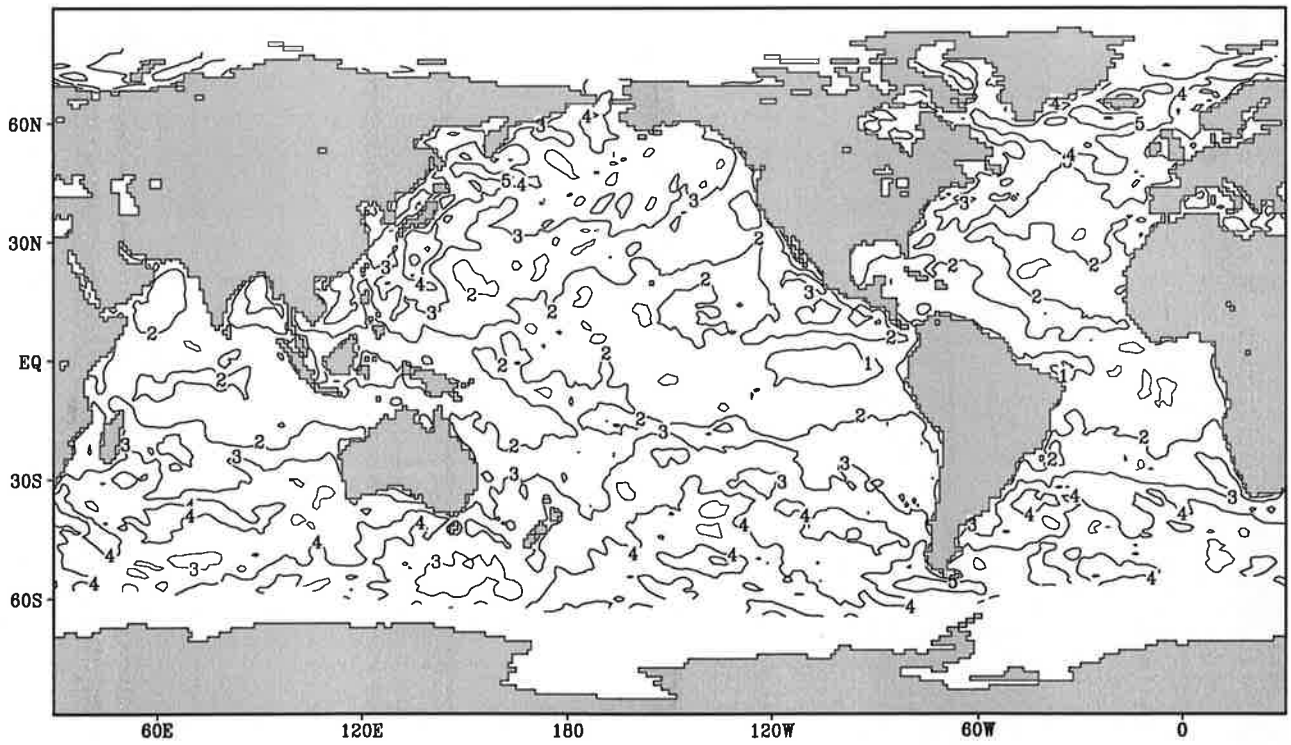

Contour interval: 1 mms^{-1}

Fig.9.10 Turbulent kinetic energy input October

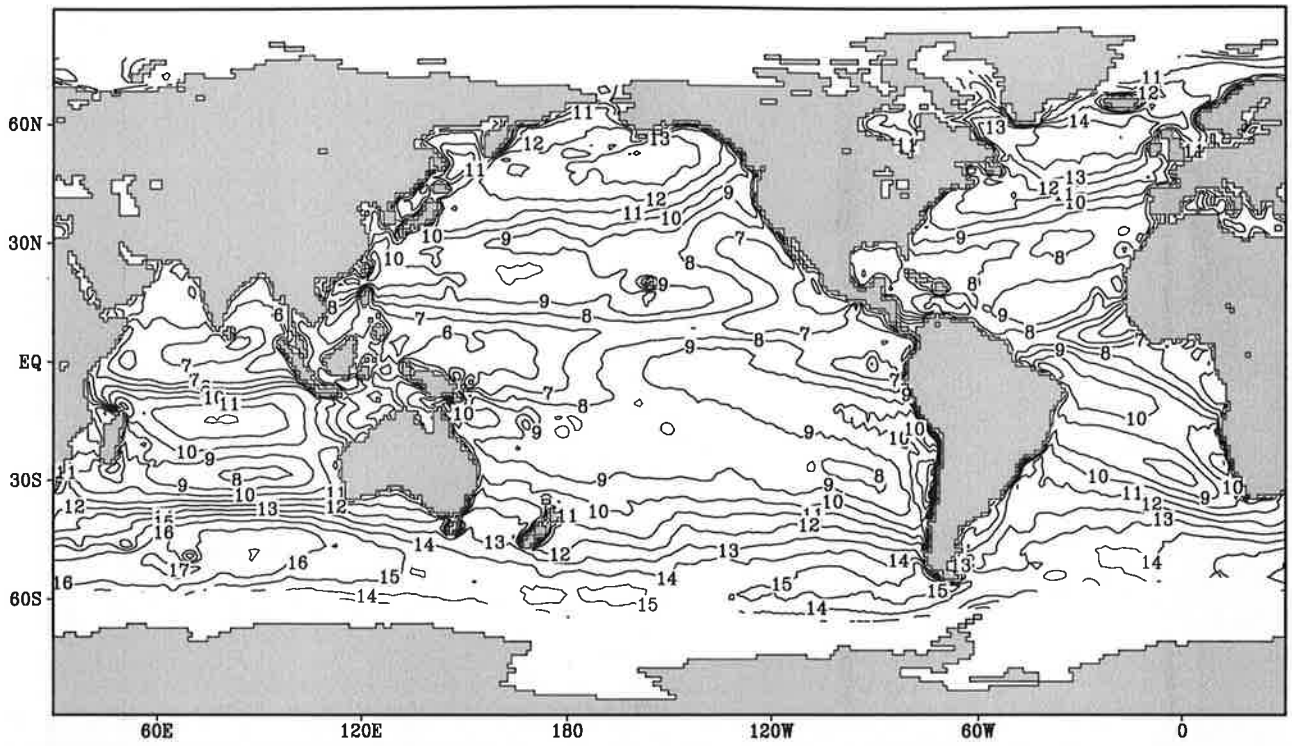

Contour interval: 1 mms^{-1}

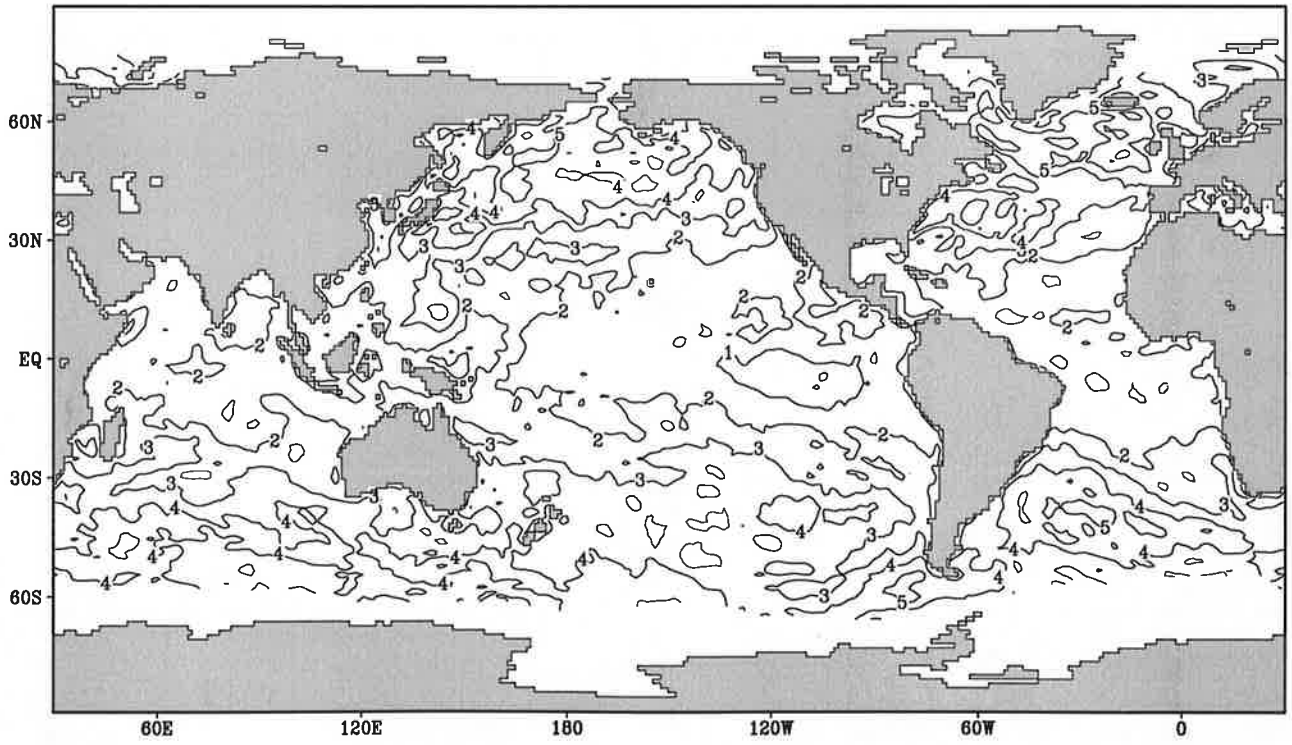

Contour interval: 1 mms^{-1}

Fig.9.11 Turbulent kinetic energy input November

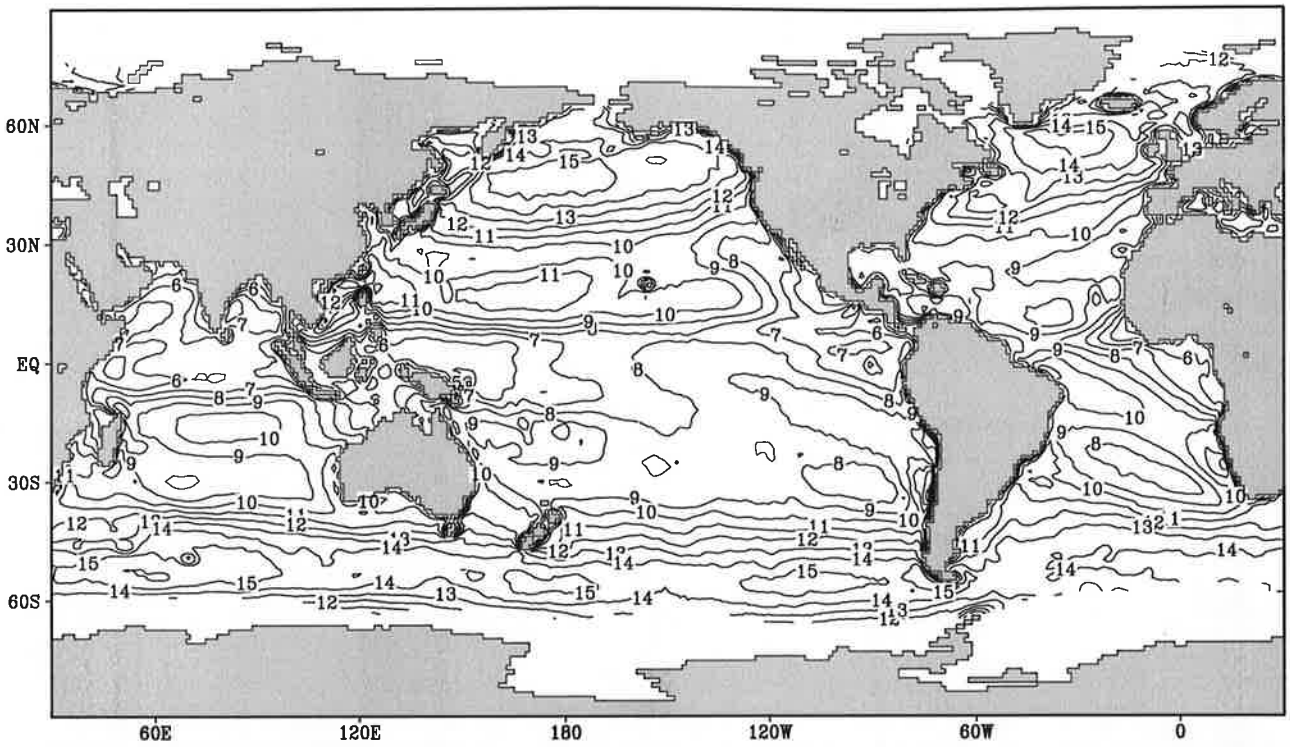

Contour interval: 1 mms^{-1}

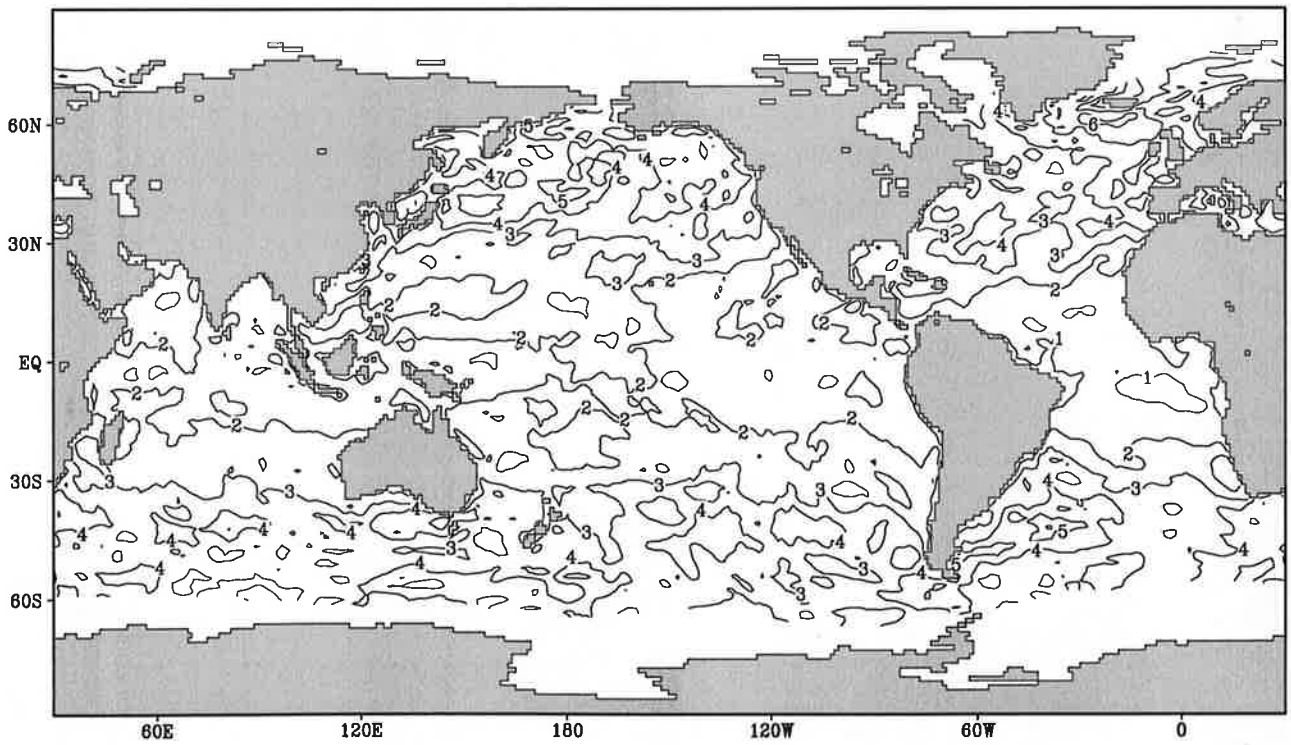

Contour interval: 1 mms^{-1}

Fig.9.12 Turbulent kinetic energy input December

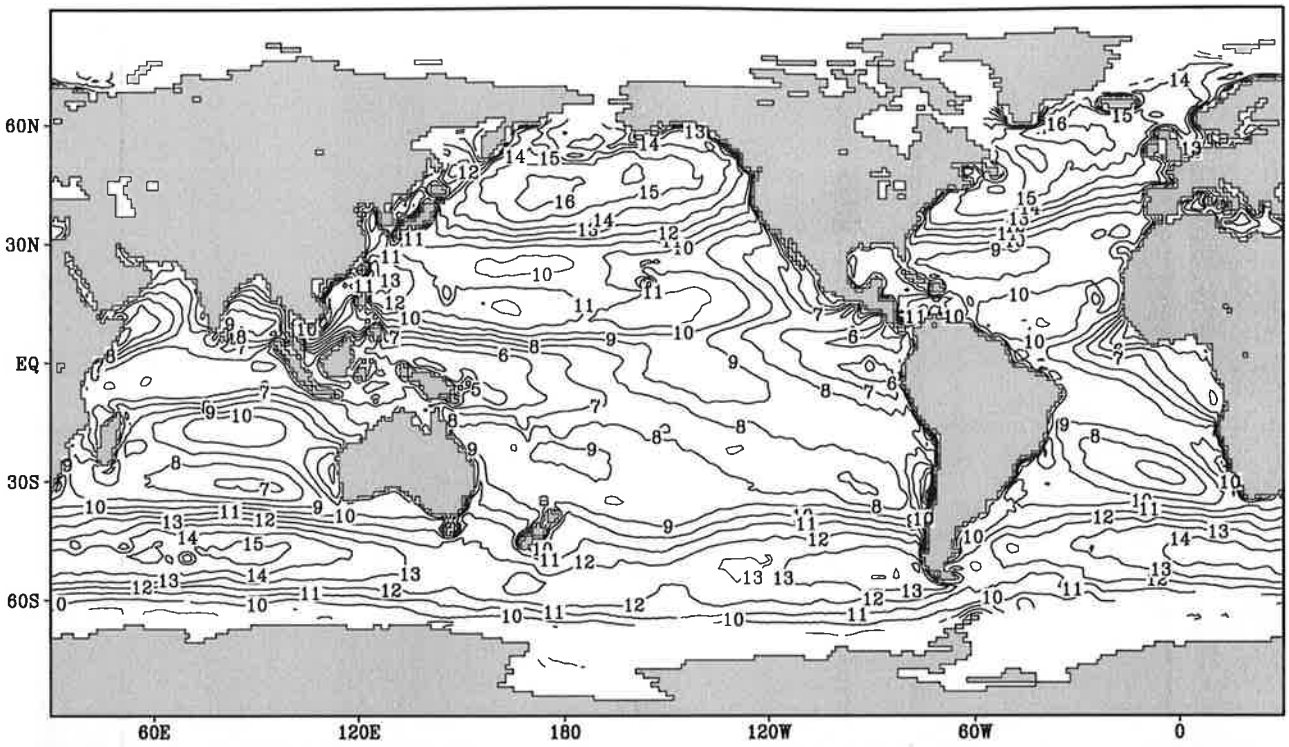

Contour interval: 1 mms^{-1}

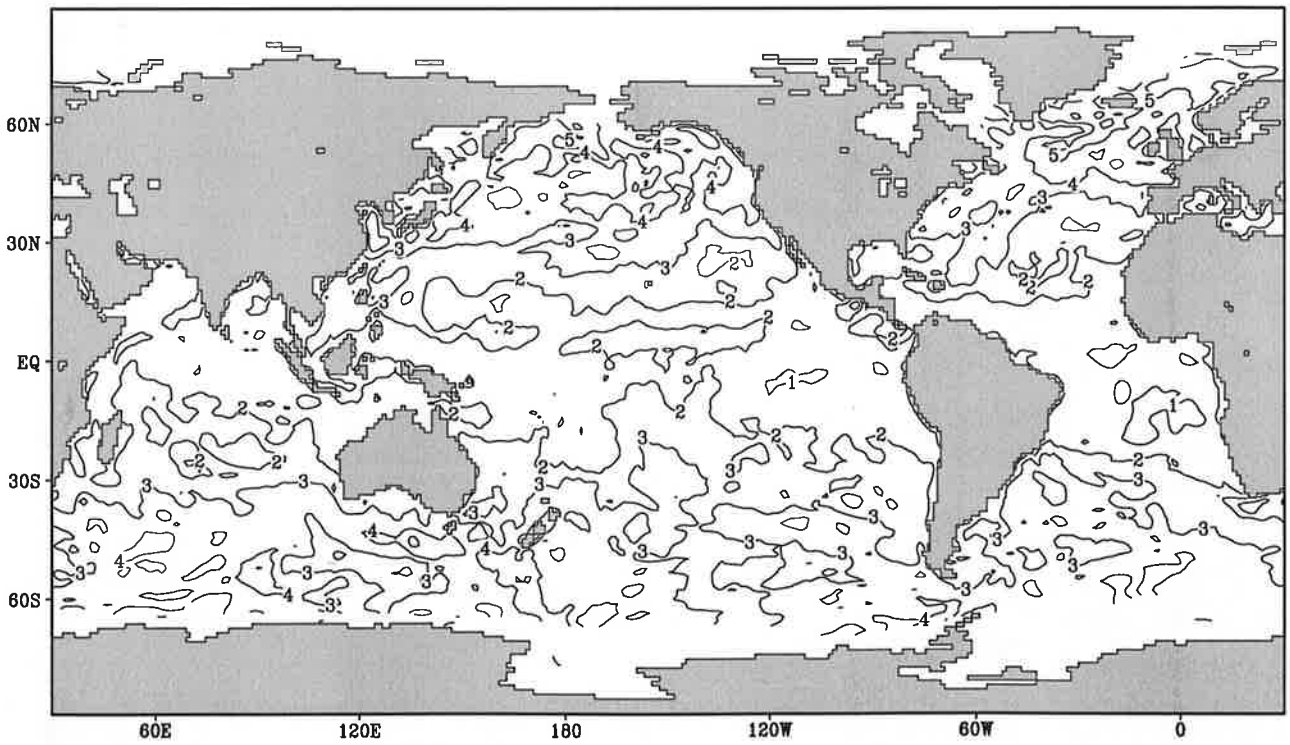

Contour interval: 1 mms^{-1}

Fig.9.13 Turbulent kinetic energy input Annual Mean

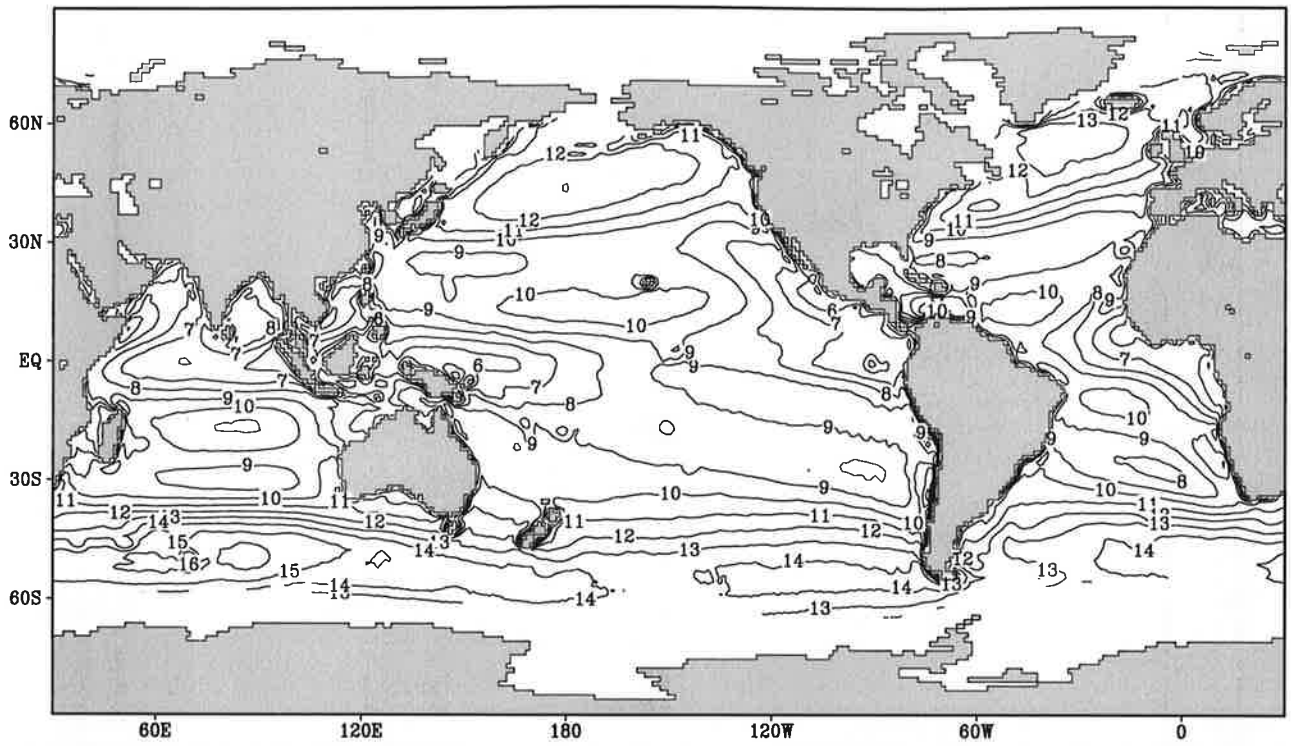

Contour interval: 1 mms^{-1}

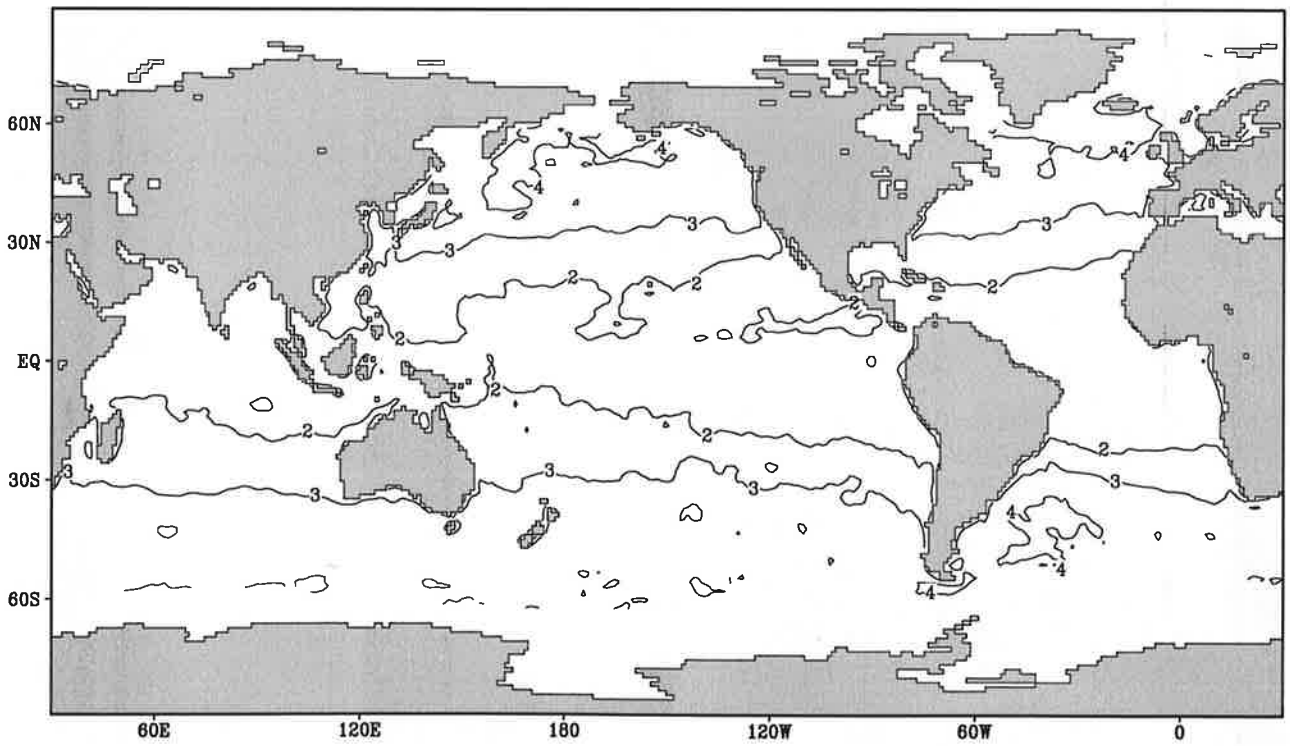

Contour interval: 1 mms^{-1}

Fig.10.1 Buoyancy flux January

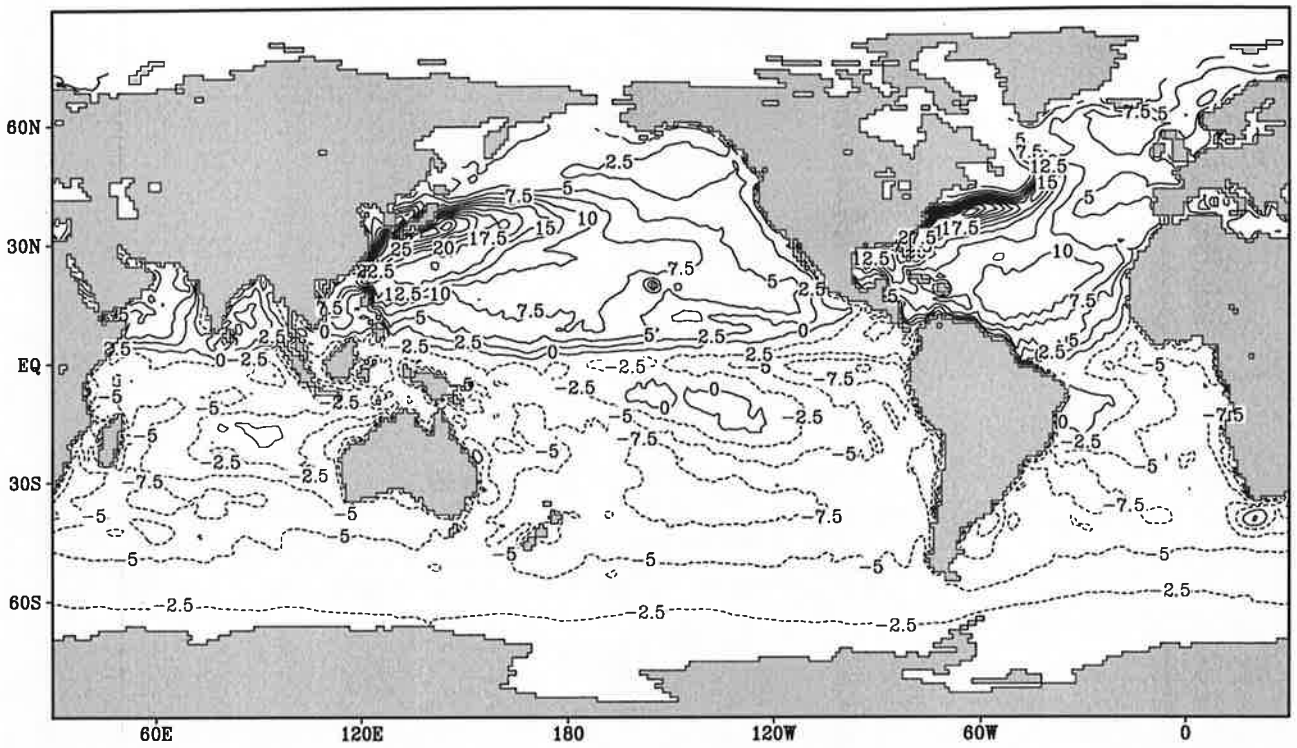

Contour interval: 2.5 10^{-8} m^2s^{-3}

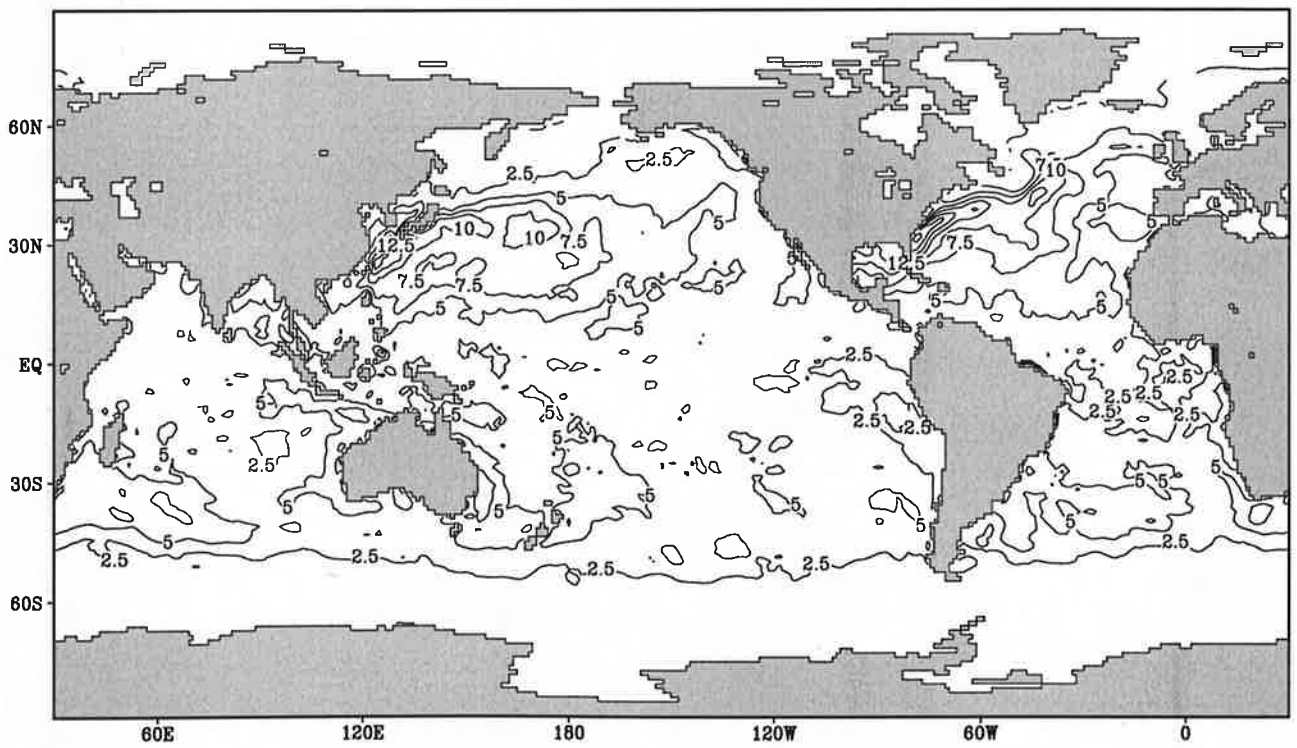

Contour interval: 2.5 10^{-8} m^2s^{-3}

Fig.10.2 Buoyancy flux February

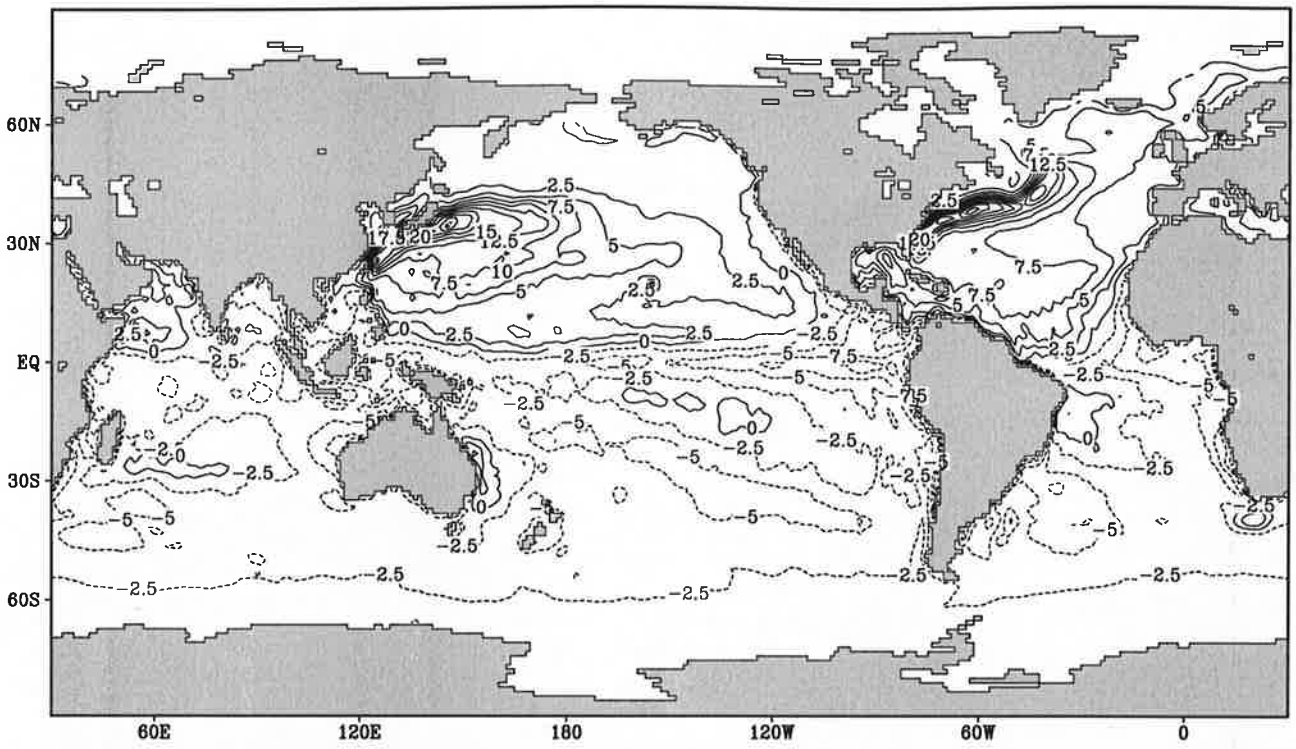

Contour interval: 2.5 10^{-8} m^2s^{-3}

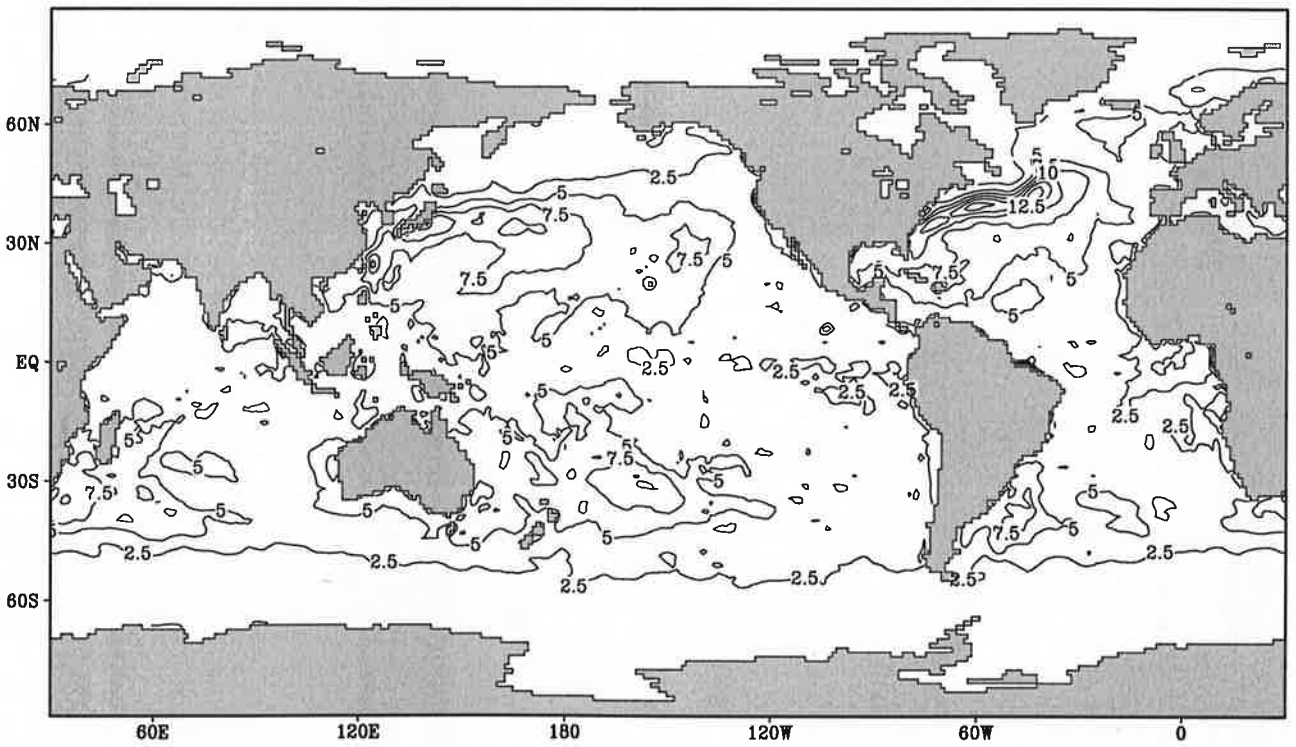

Contour interval: 2.5 10^{-8} m^2s^{-3}

Fig.10.3 Buoyancy flux March

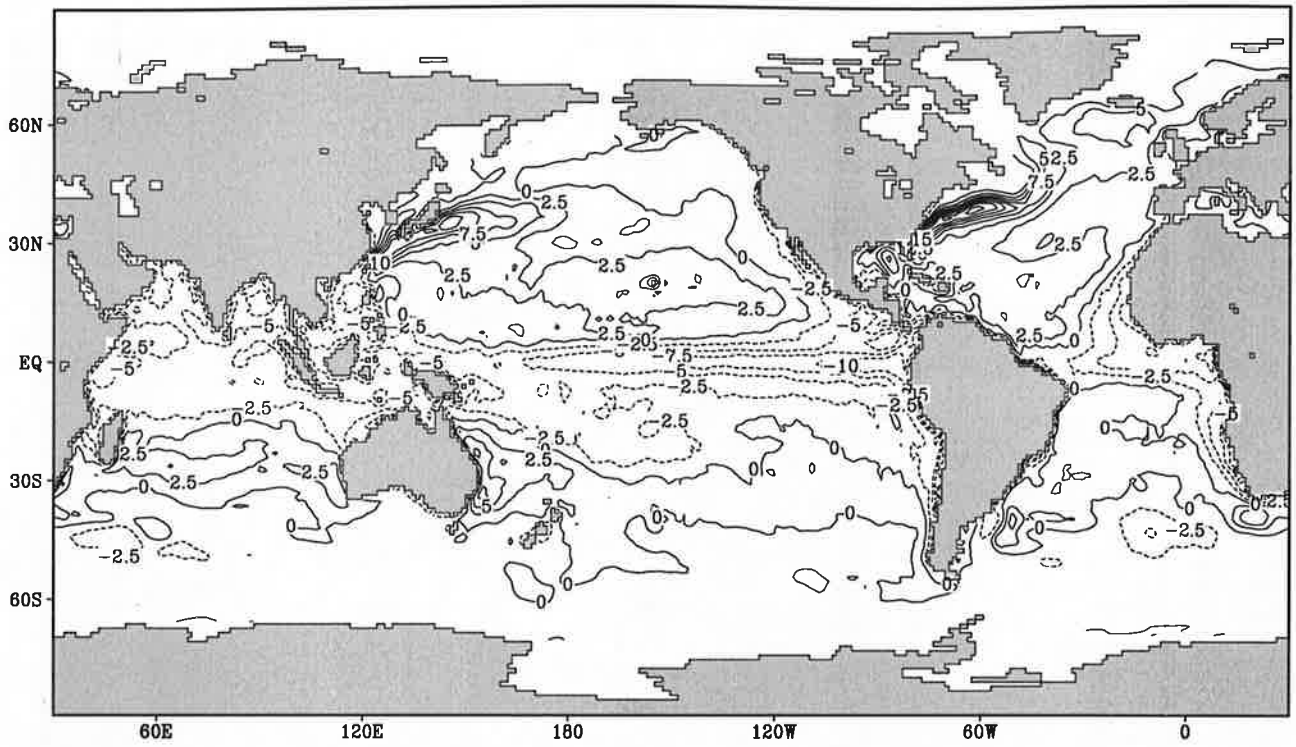

Contour interval: 2.5 10^{-8} m^2s^{-3}

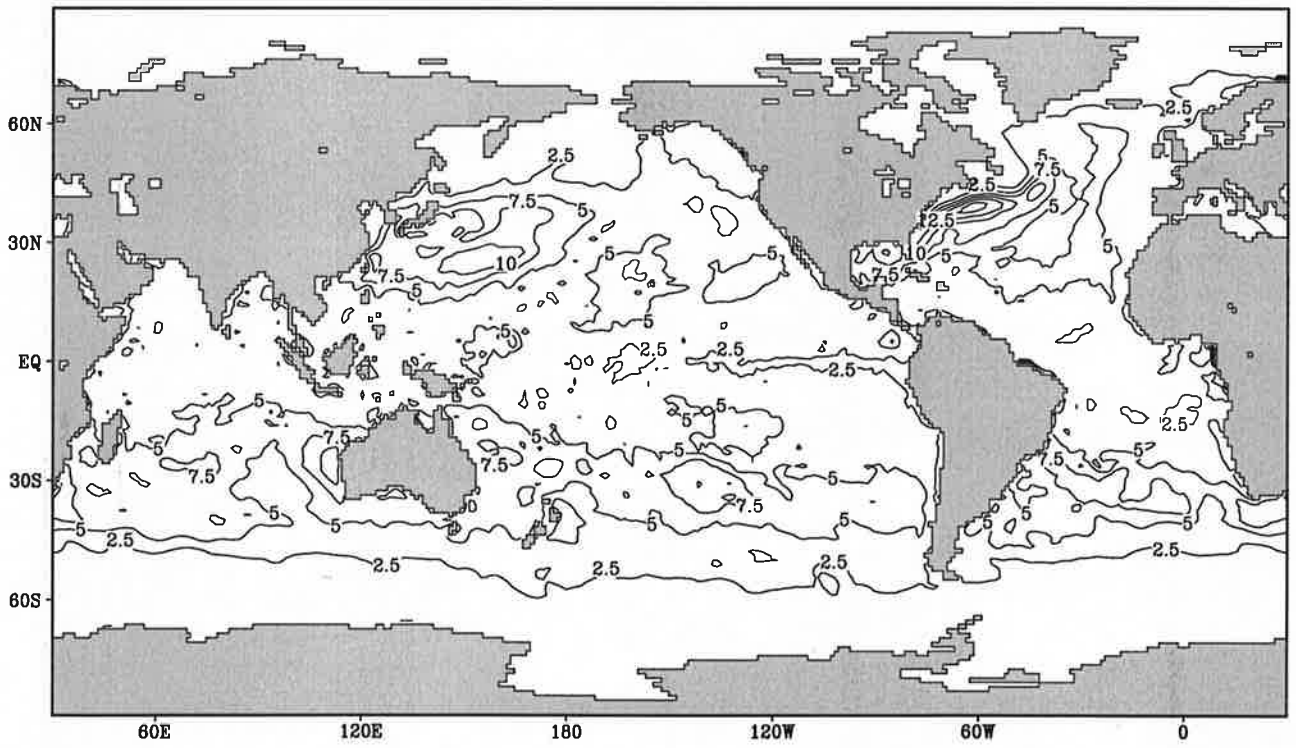

Contour interval: 2.5 10^{-8} m^2s^{-3}

Fig.10.4 Buoyancy flux April

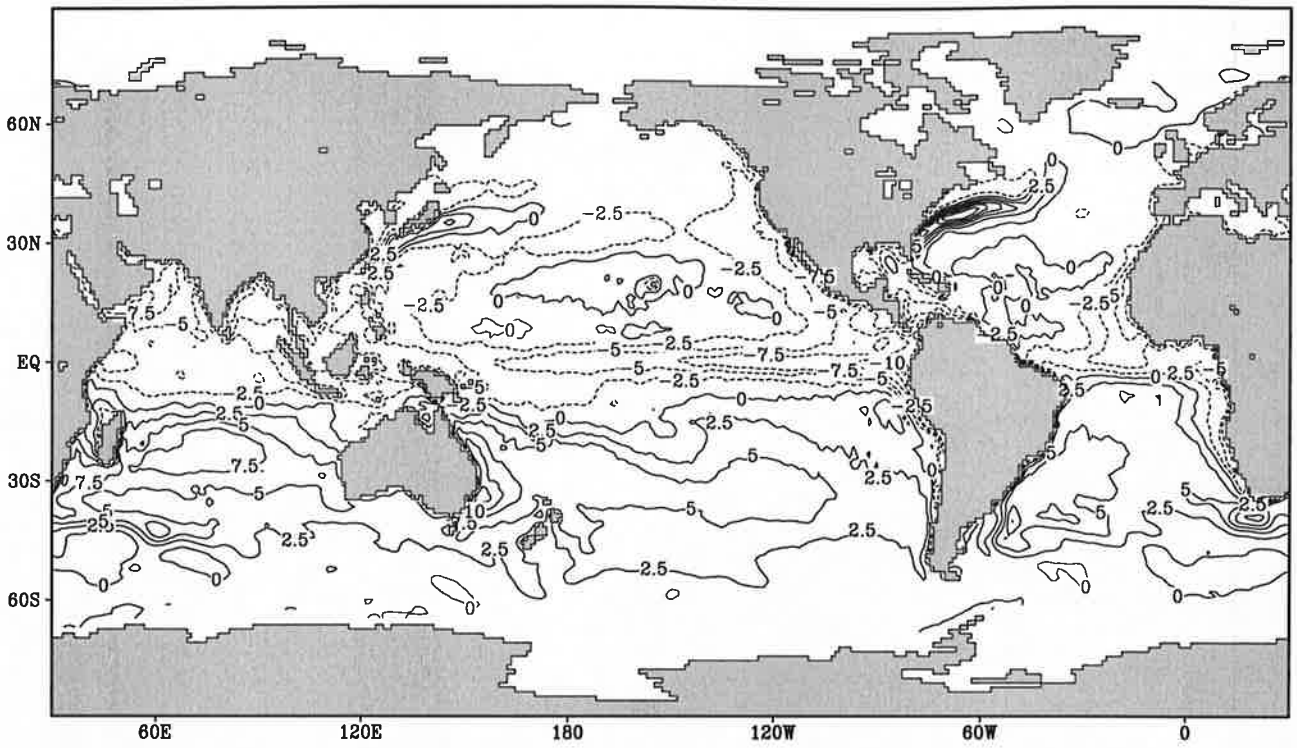

Contour interval: 2.5 10^{-8} m^2s^{-3}

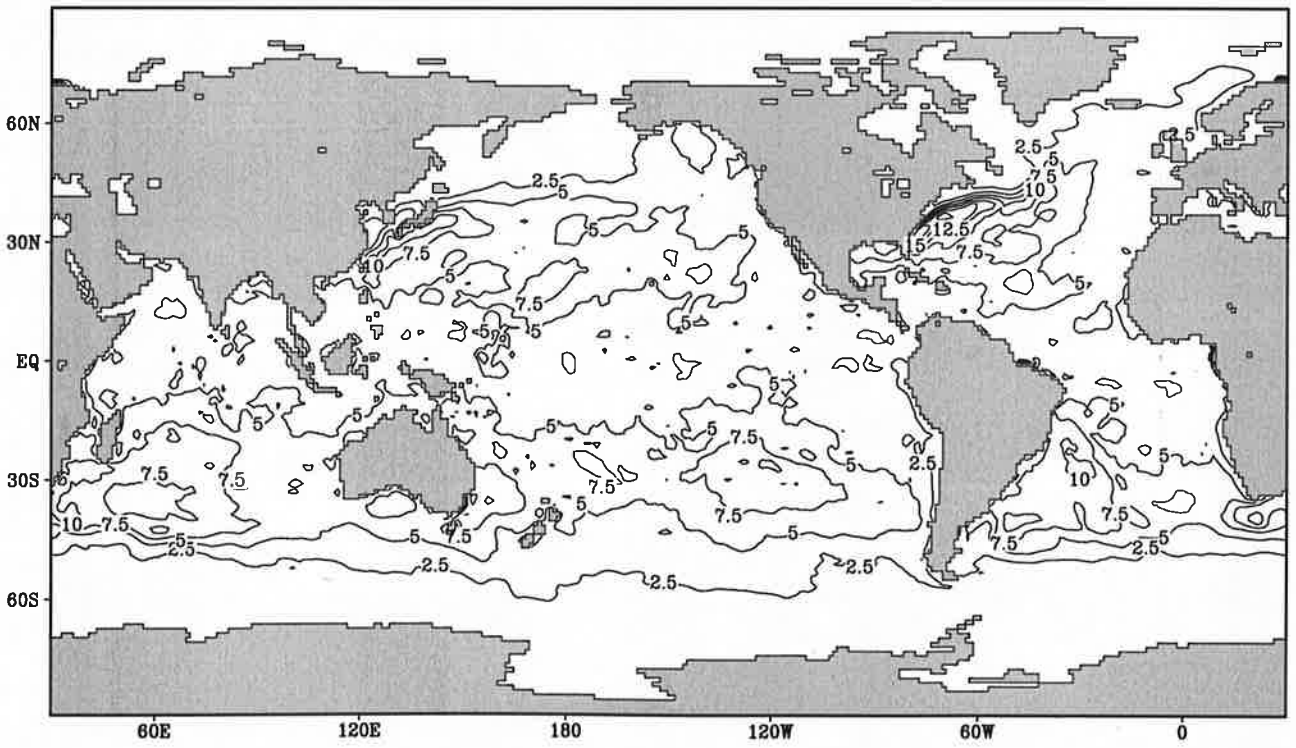

Contour interval: 2.5 10^{-8} m^2s^{-3}

Fig.10.5 Buoyancy flux May

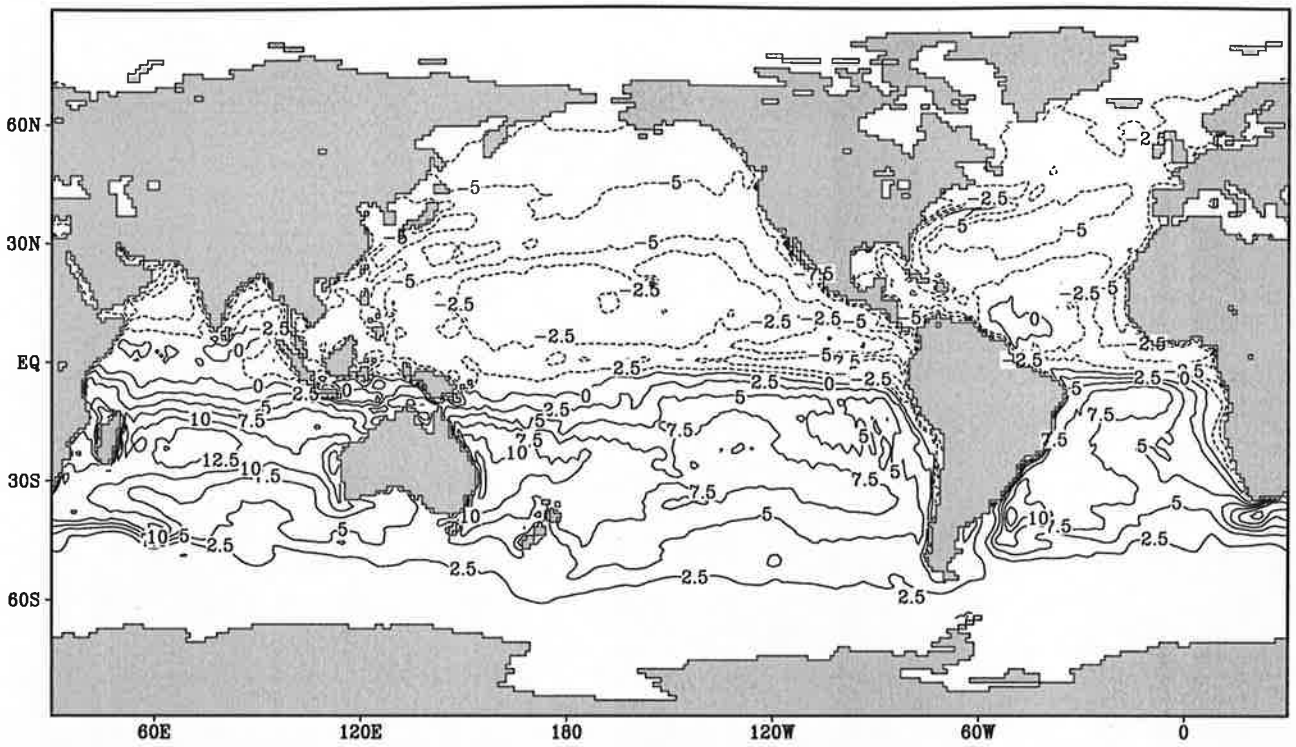

Contour interval: 2.5 10^{-8} m^2s^{-3}

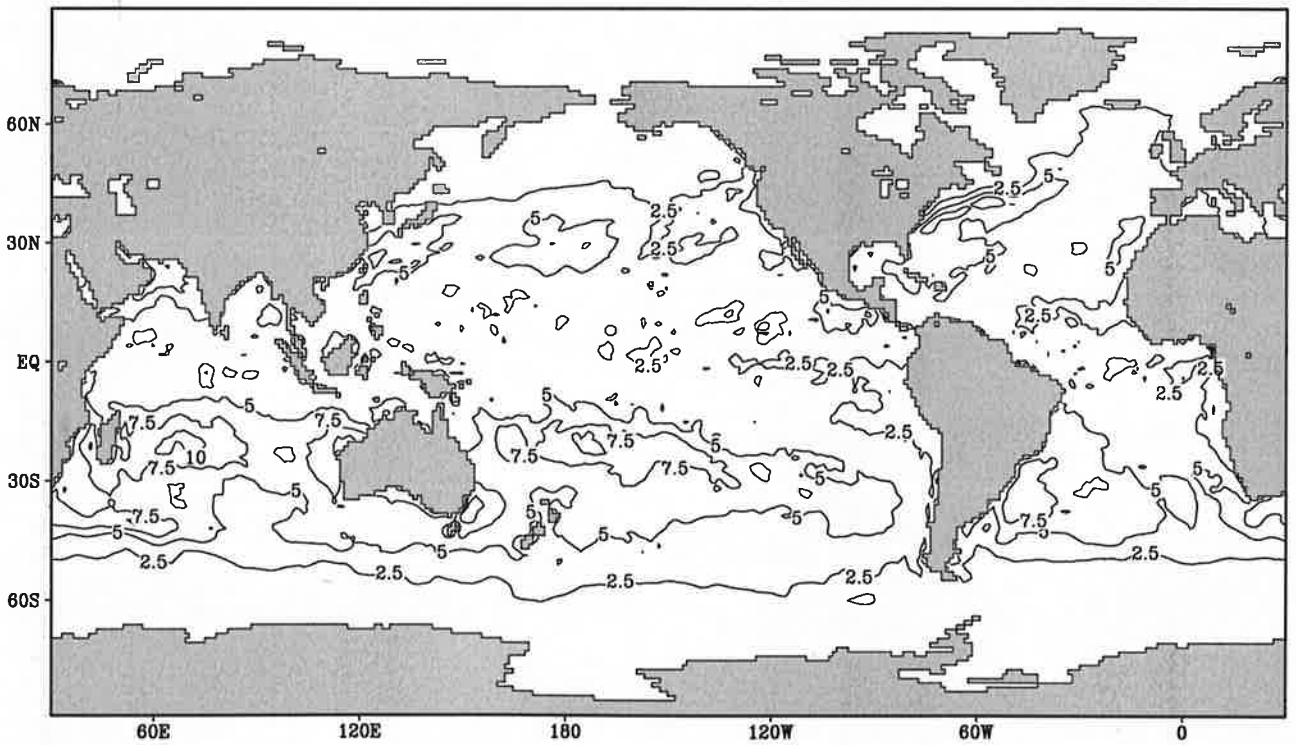

Contour interval: 2.5 10^{-8} m^2s^{-3}

Fig.10.6 Buoyancy flux June

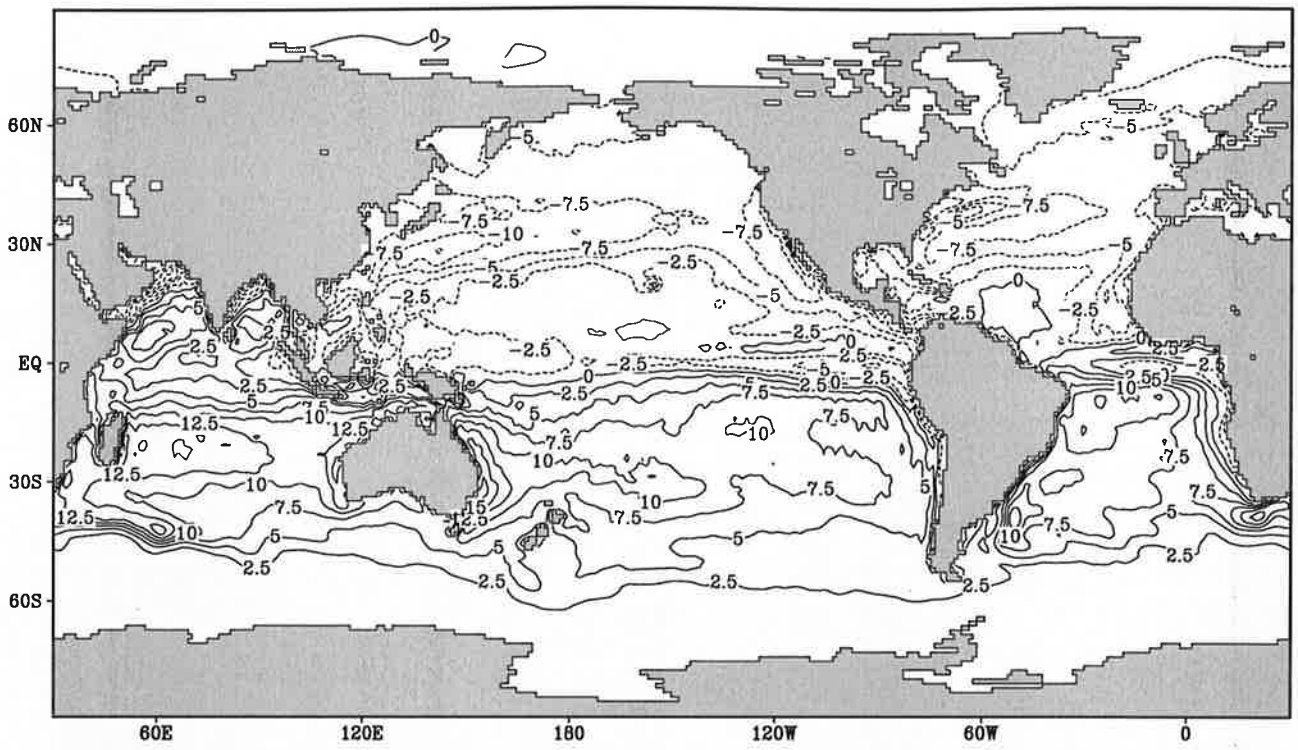

Contour interval: 2.5 10^{-8} m^2s^{-3}

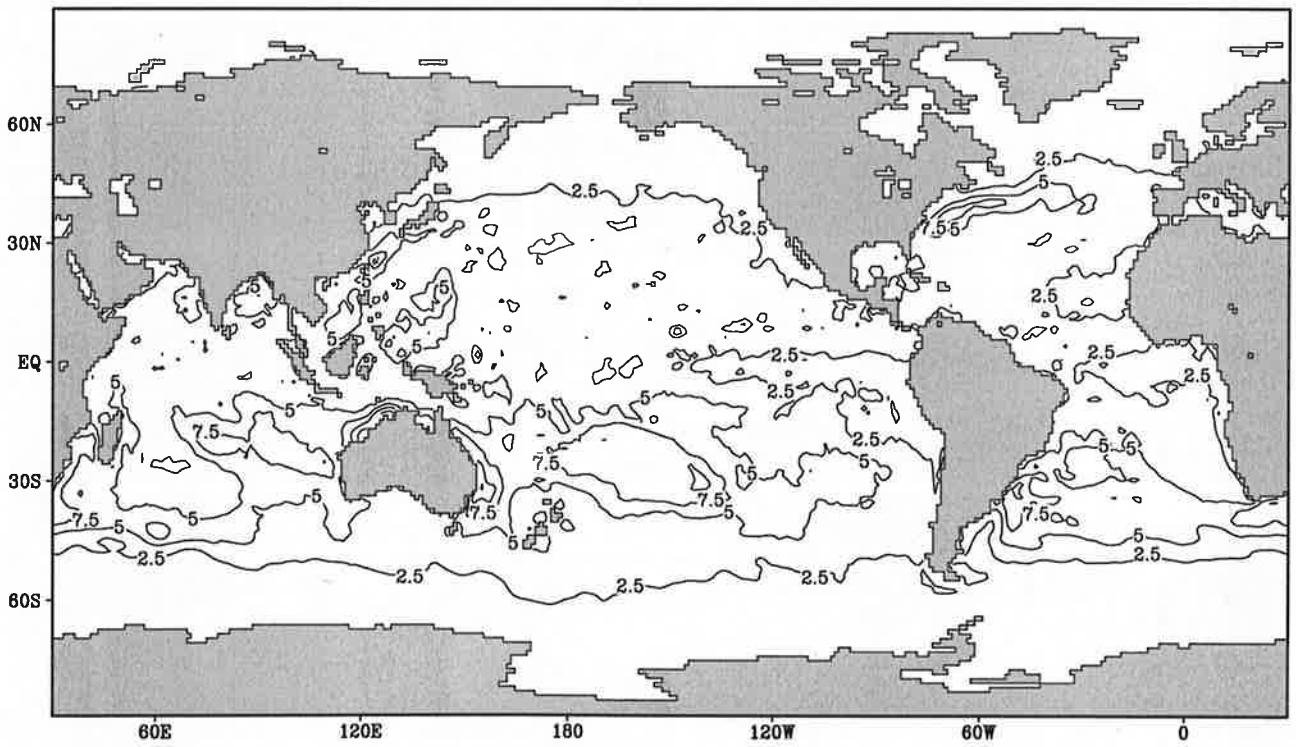

Contour interval: 2.5 10^{-8} m^2s^{-3}

Fig.10.7 Buoyancy flux July

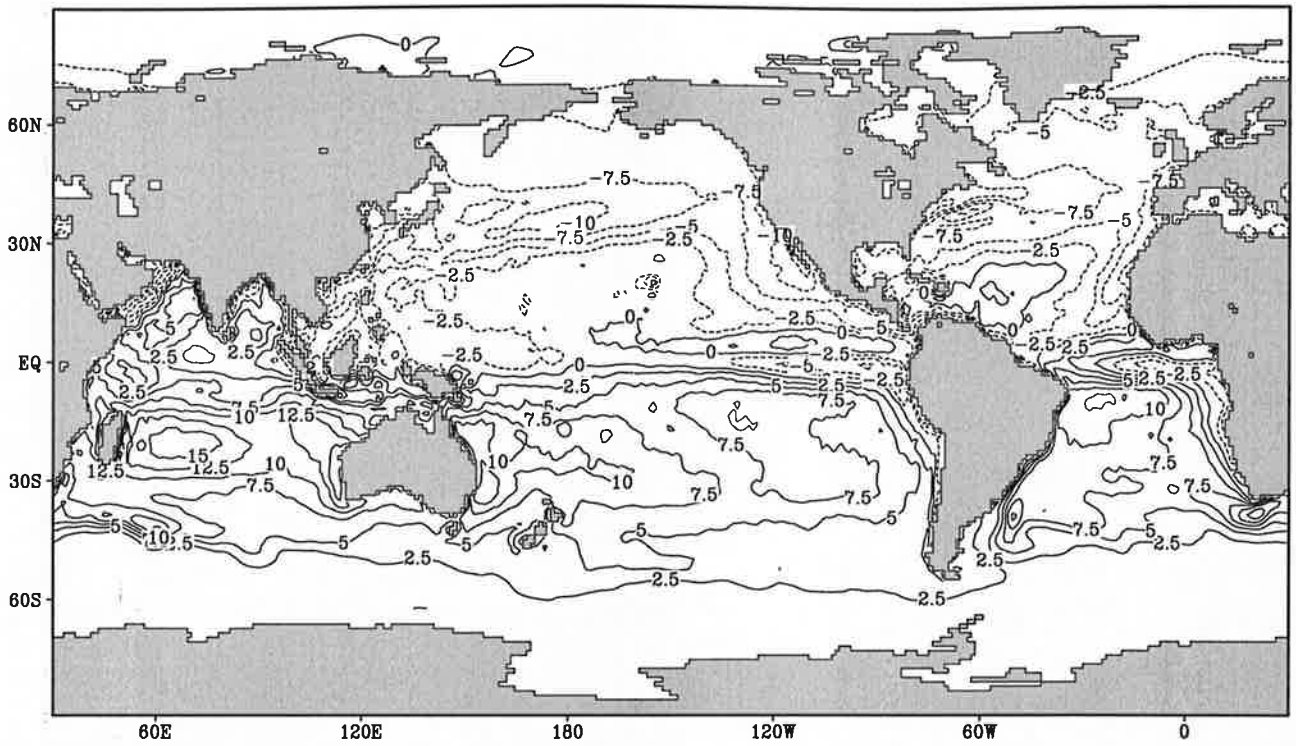

Contour interval: 2.5 10^{-8} m^2s^{-3}

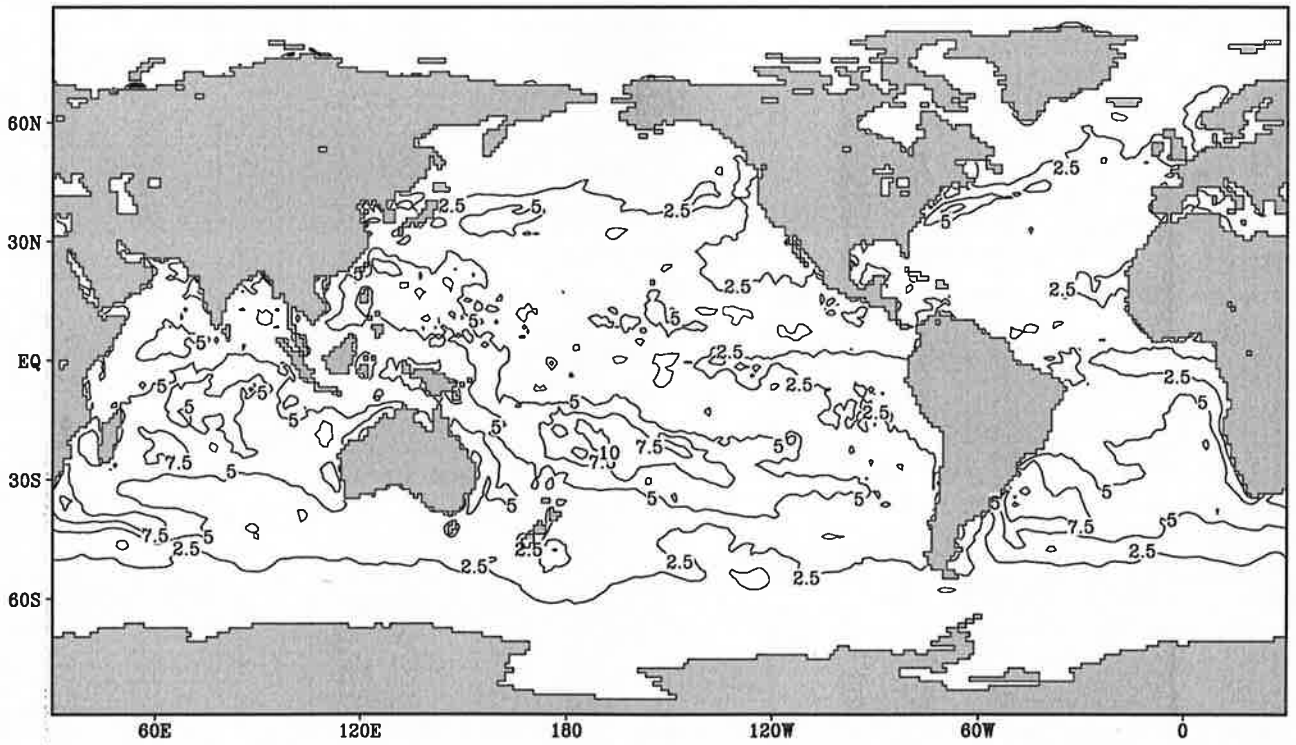

Contour interval: 2.5 10^{-8} m^2s^{-3}

Fig.10.8 Buoyancy flux August

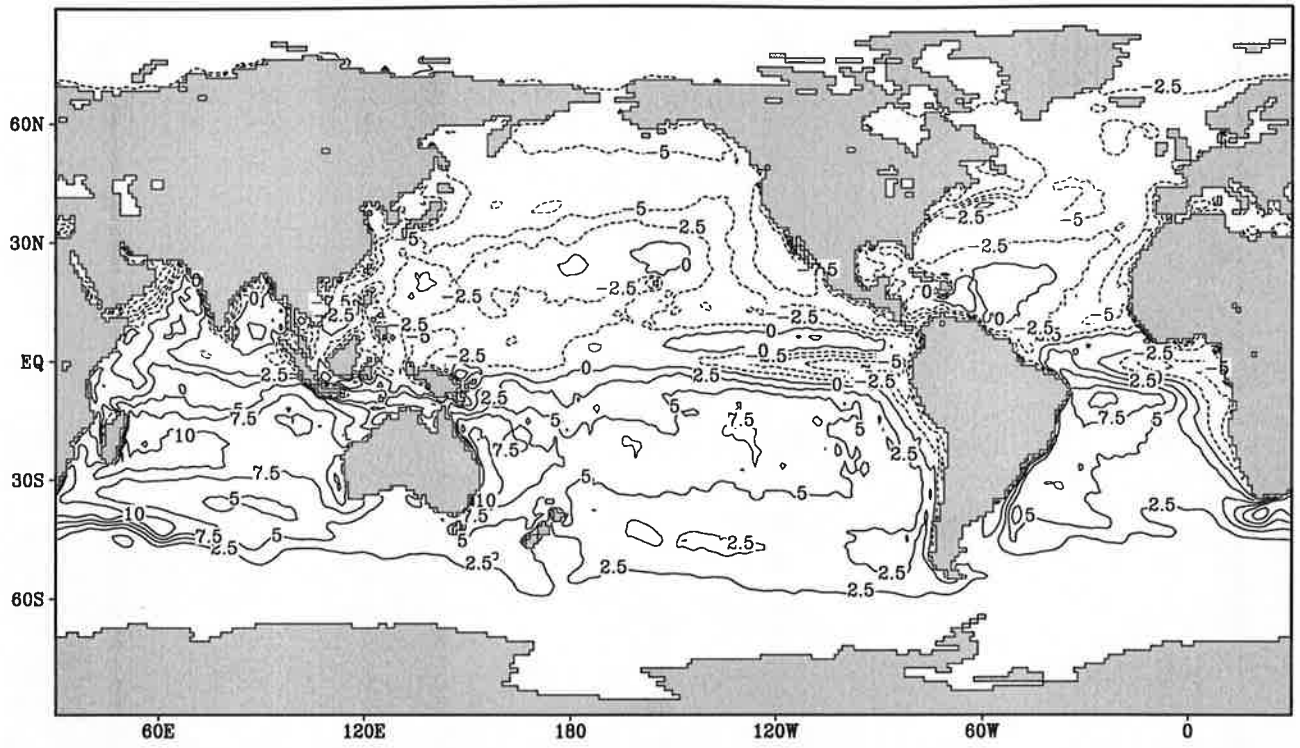

Contour interval: 2.5 10^{-8} m^2s^{-3}

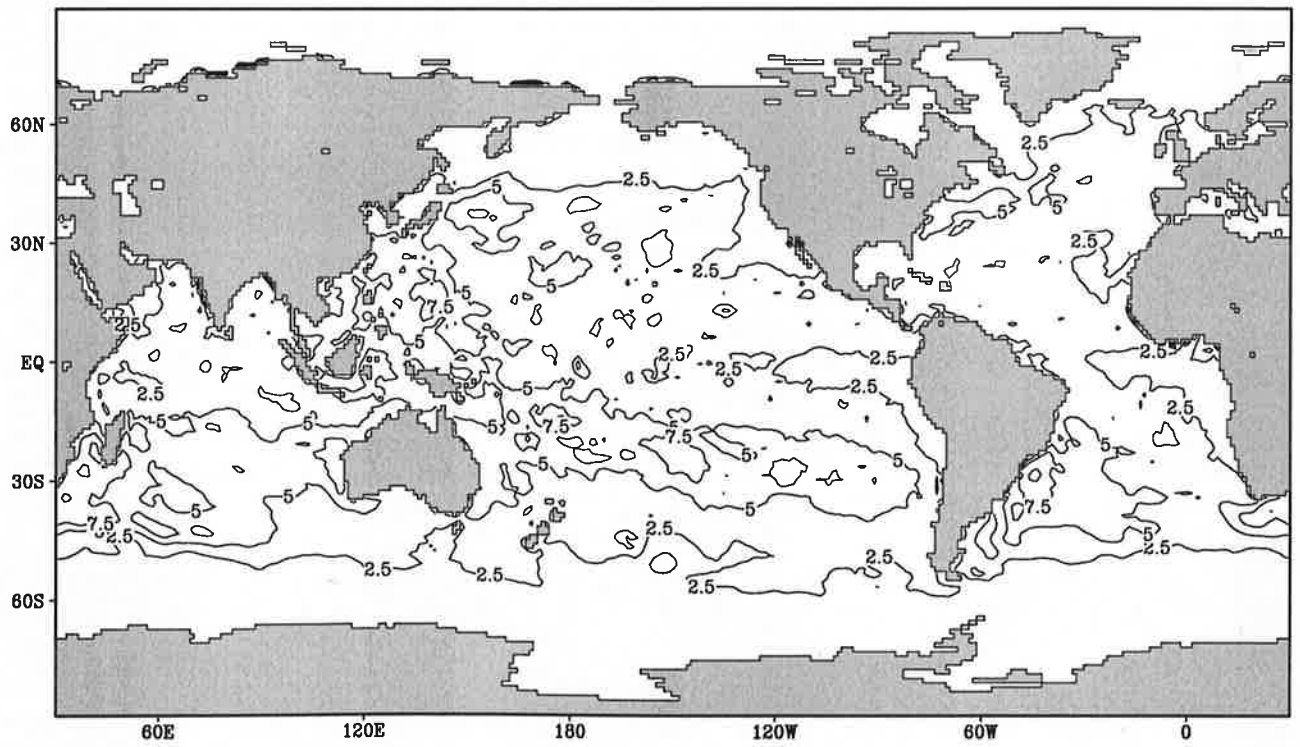

Contour interval: 2.5 10^{-8} m^2s^{-3}

Fig.10.9 Buoyancy flux September

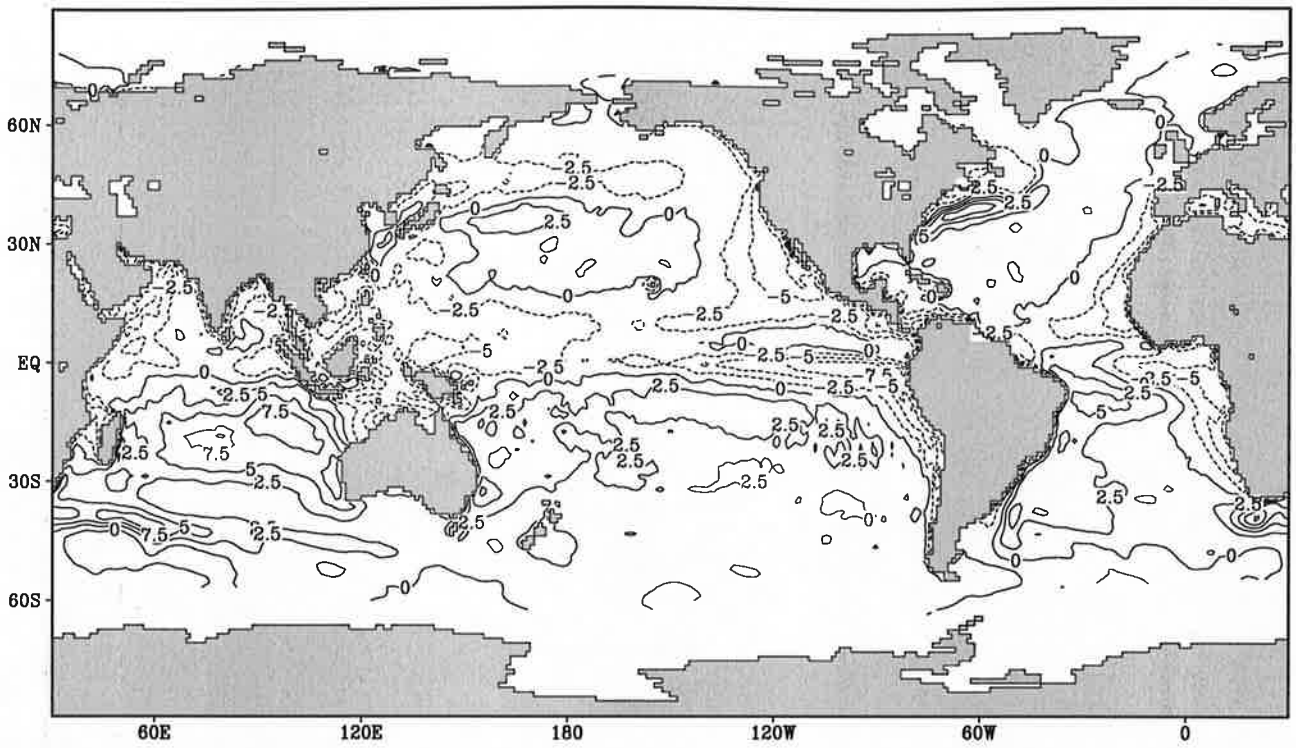

Contour interval: 2.5 10^{-8} m^2s^{-3}

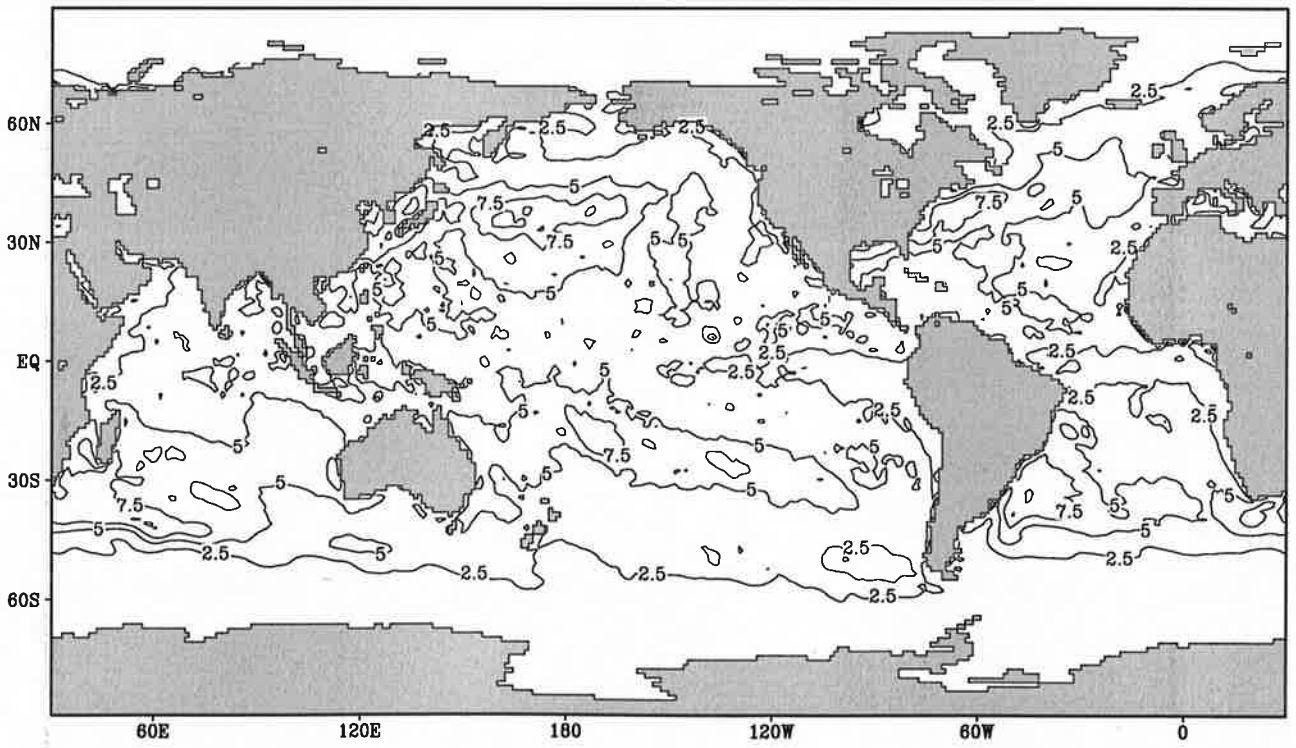

Contour interval: 2.5 10^{-8} m^2s^{-3}

Fig.10.10 Buoyancy flux October

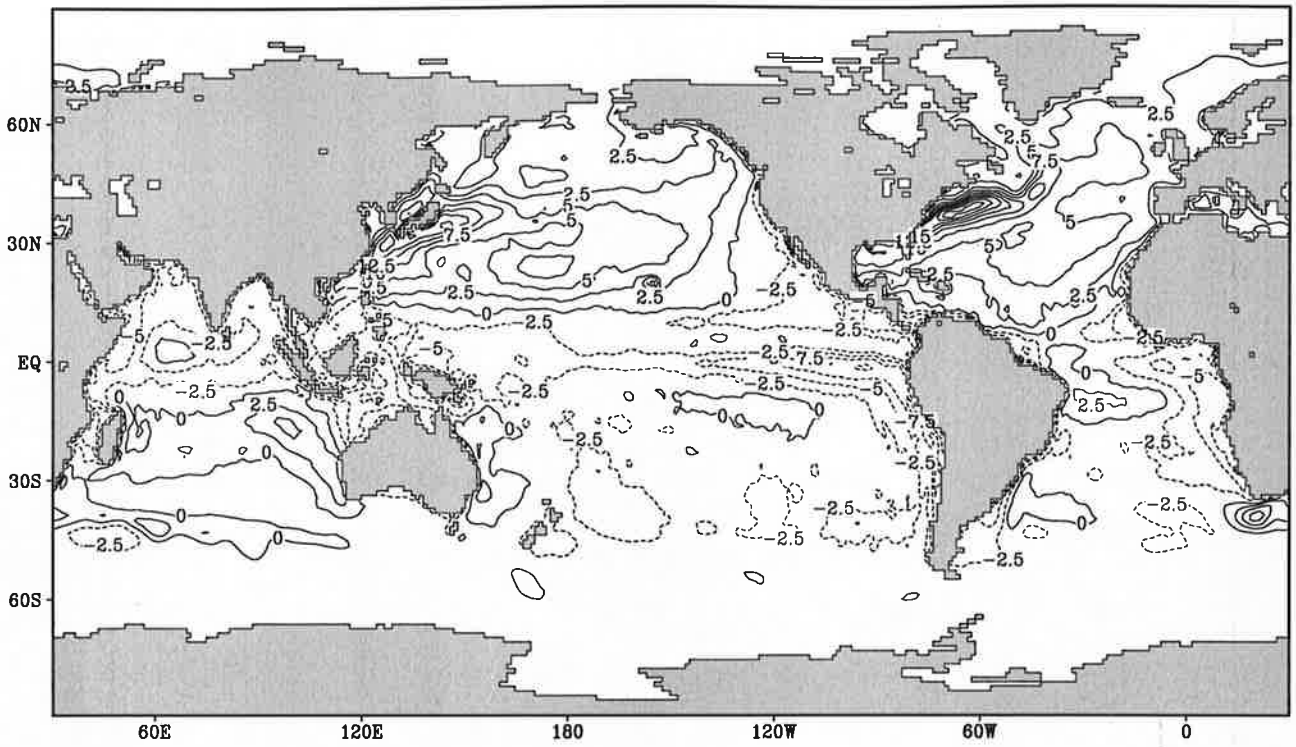

Contour interval: 2.5 10^{-8} m^2s^{-3}

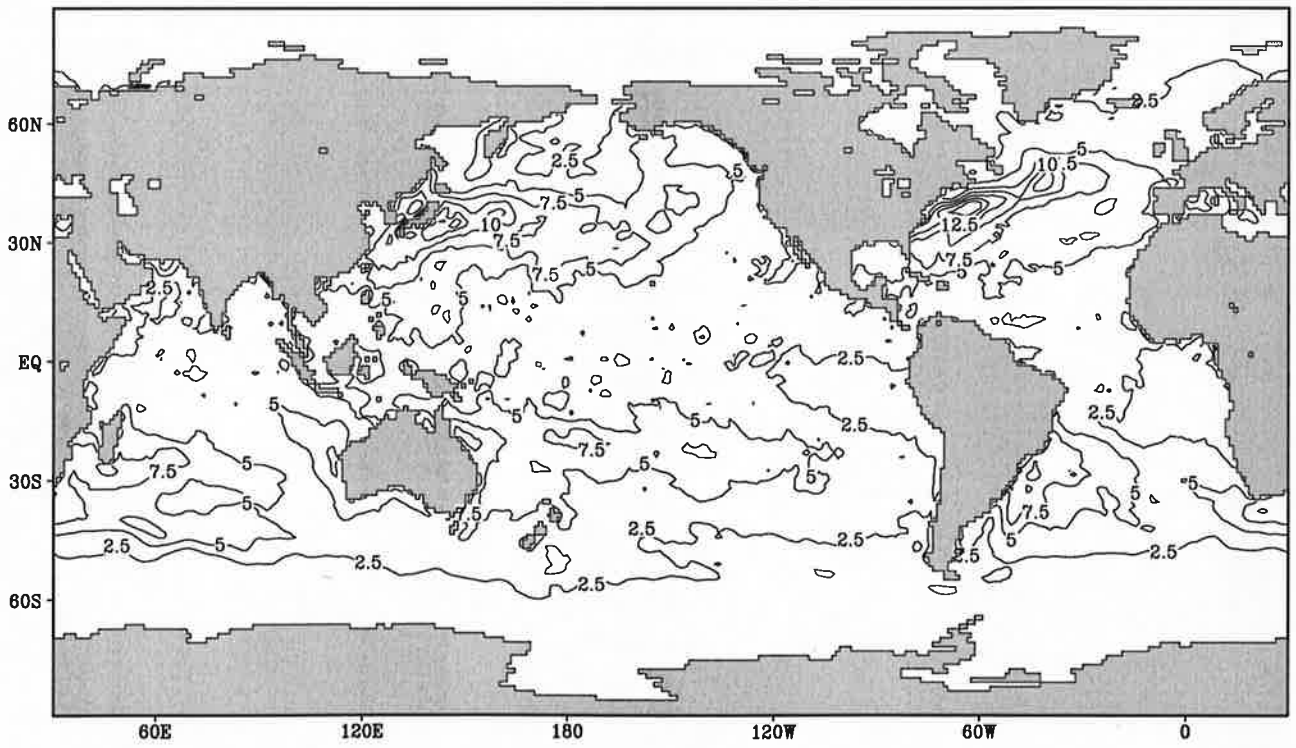

Contour interval: 2.5 10^{-8} m^2s^{-3}

Fig.10.11 Buoyancy flux November

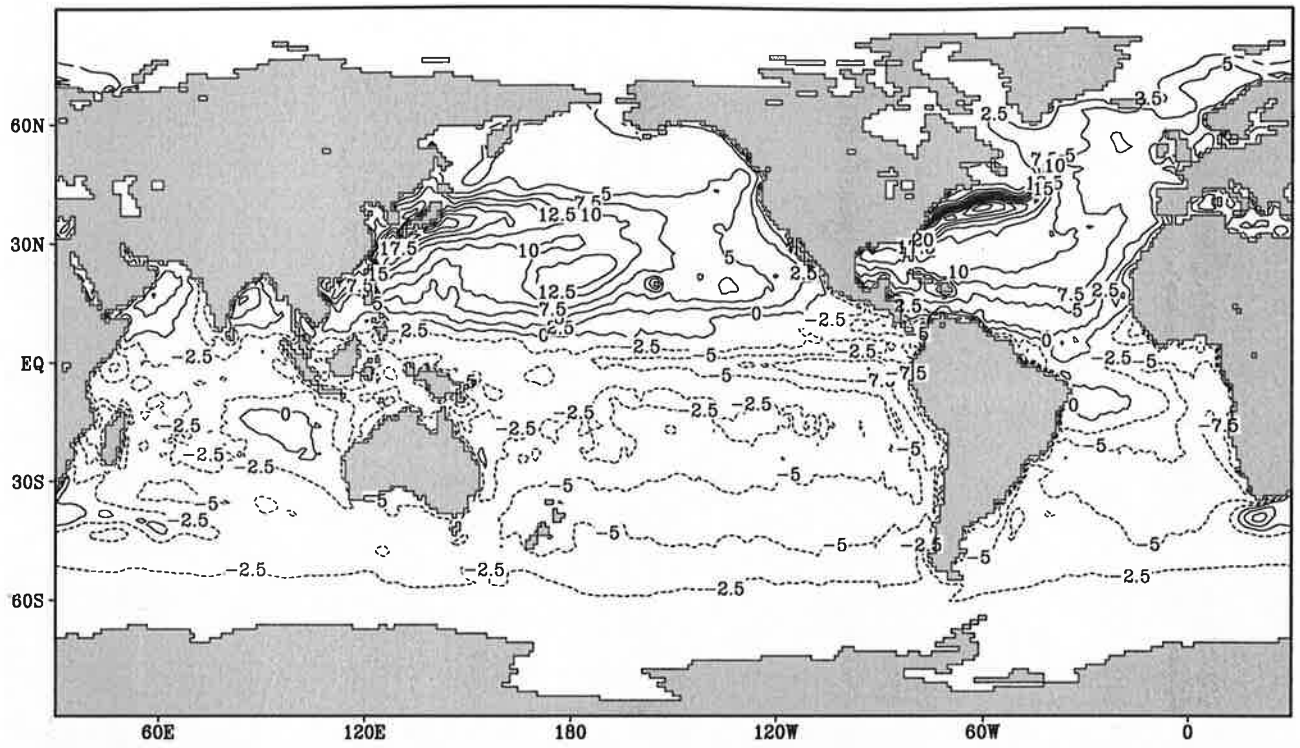

Contour interval: 2.5 10^{-8} m^2s^{-3}

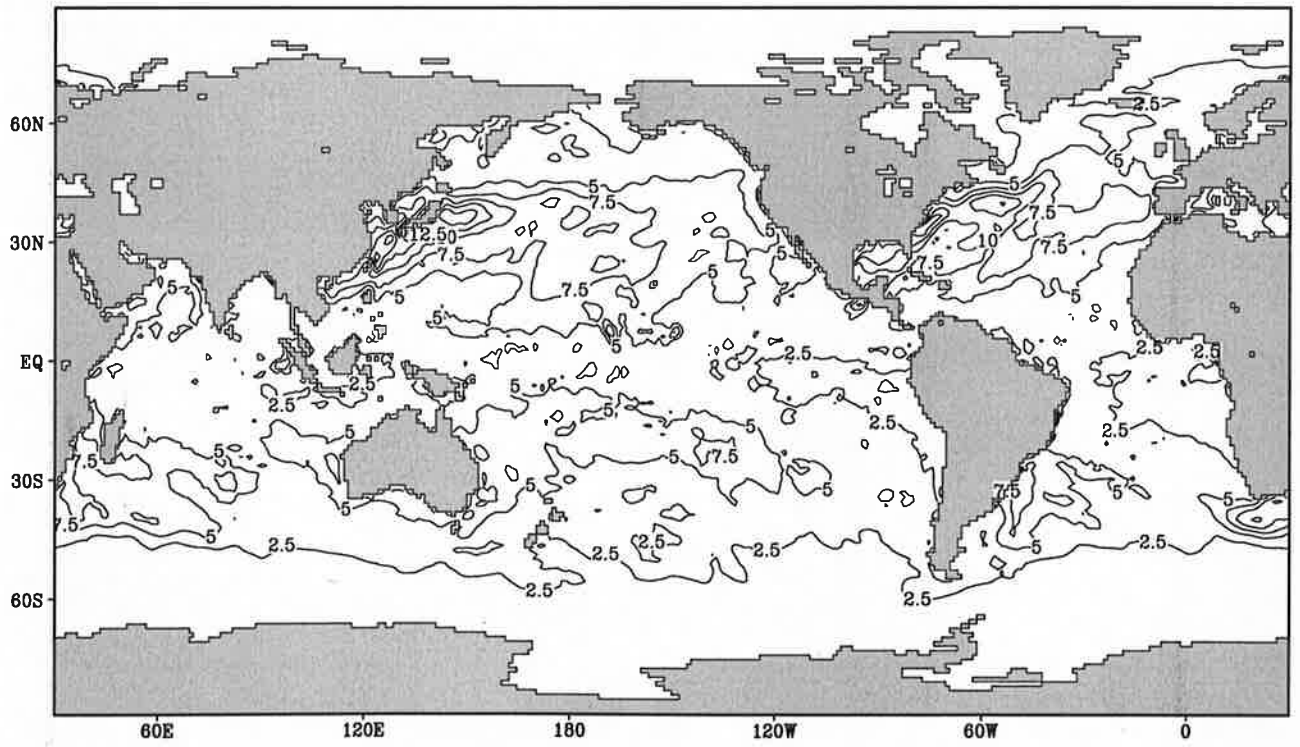

Contour interval: 2.5 10^{-8} m^2s^{-3}

Fig.10.12 Buoyancy flux December

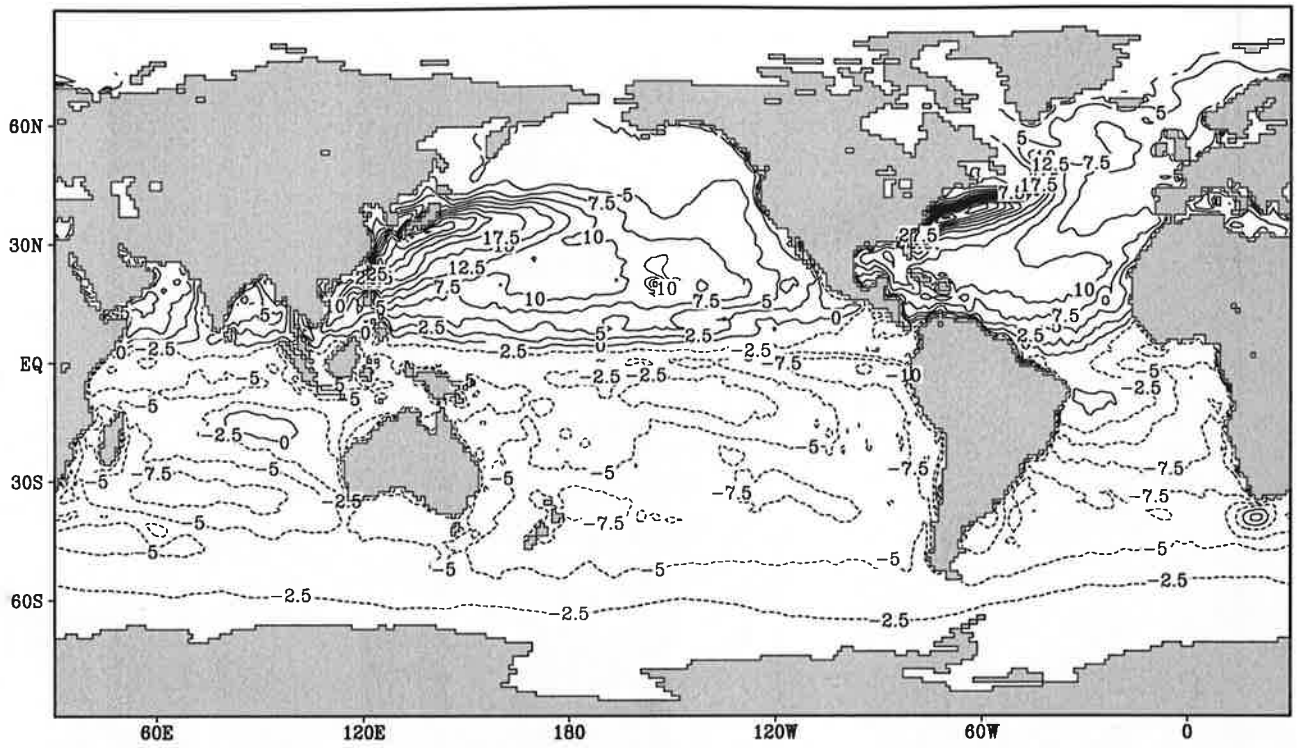

Contour interval: 2.5 10^{-8} m^2s^{-3}

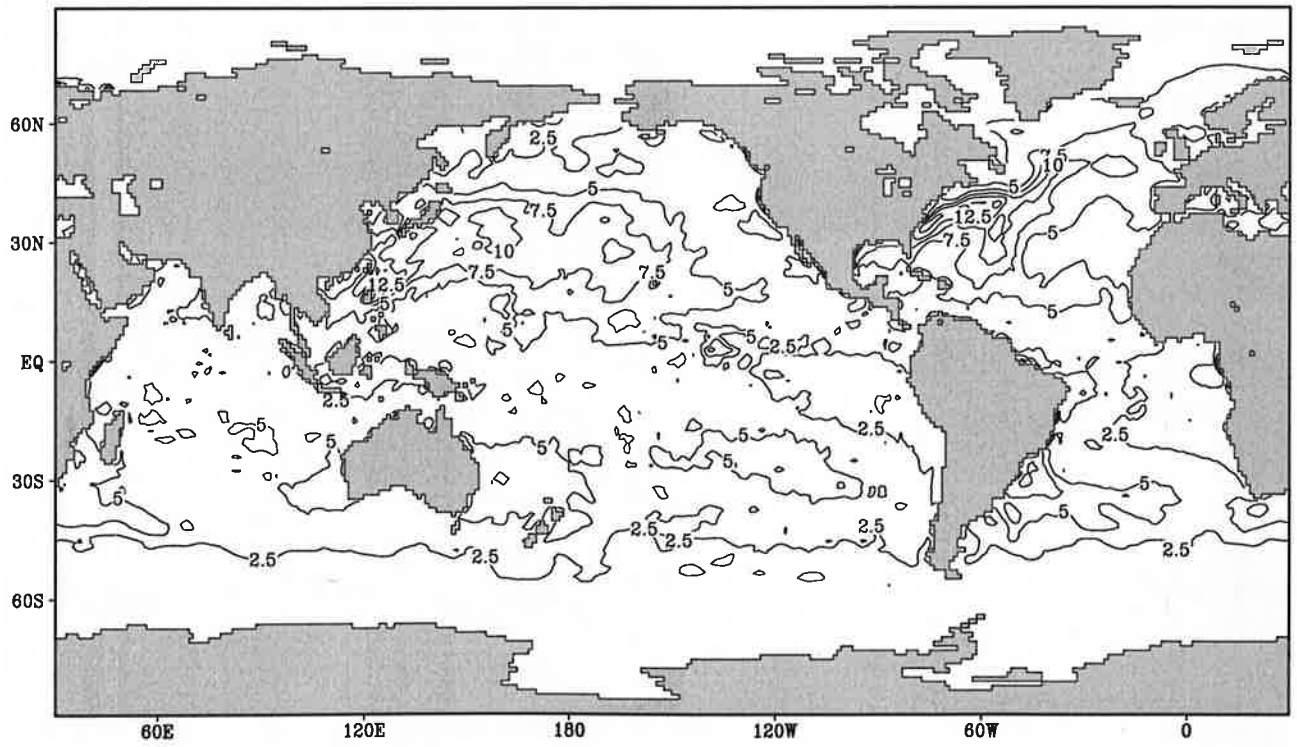

Contour interval: 2.5 10^{-8} m^2s^{-3}

Fig.10.13 Buoyancy flux Annual Mean

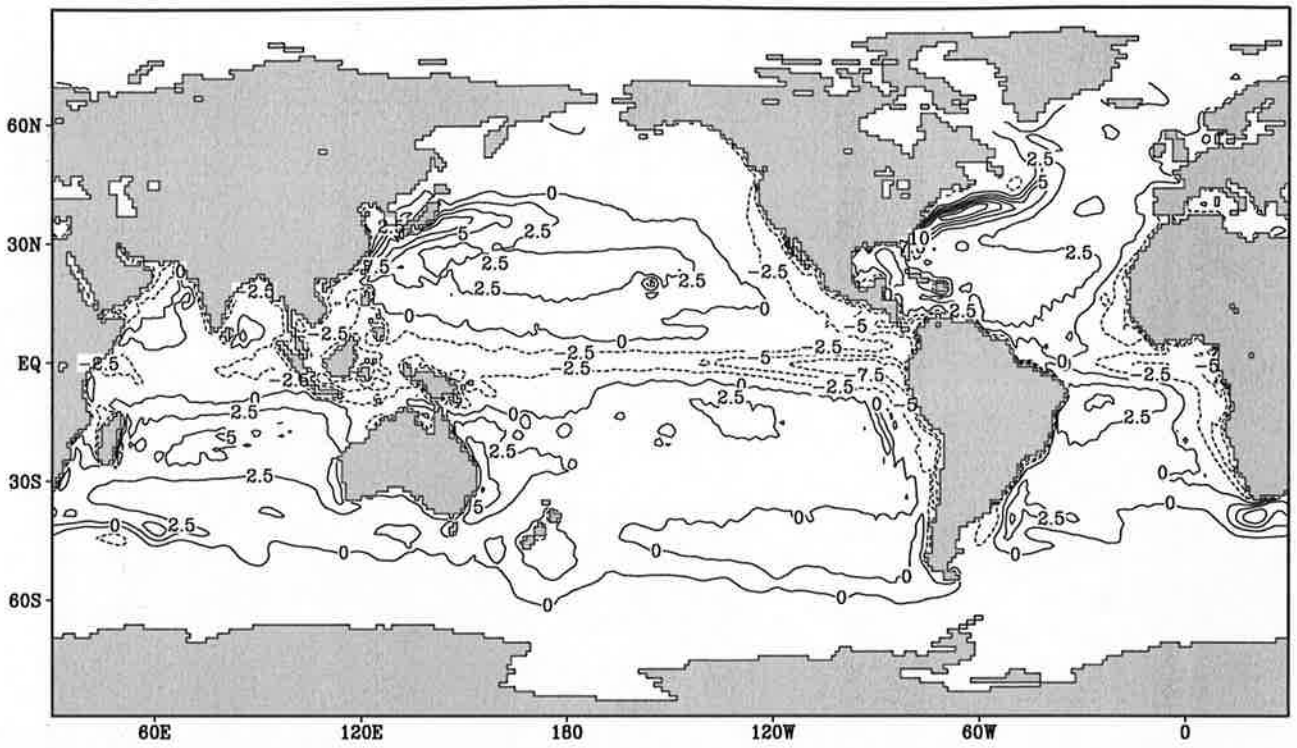

Contour interval: 2.5 10^{-8} m^2s^{-3}

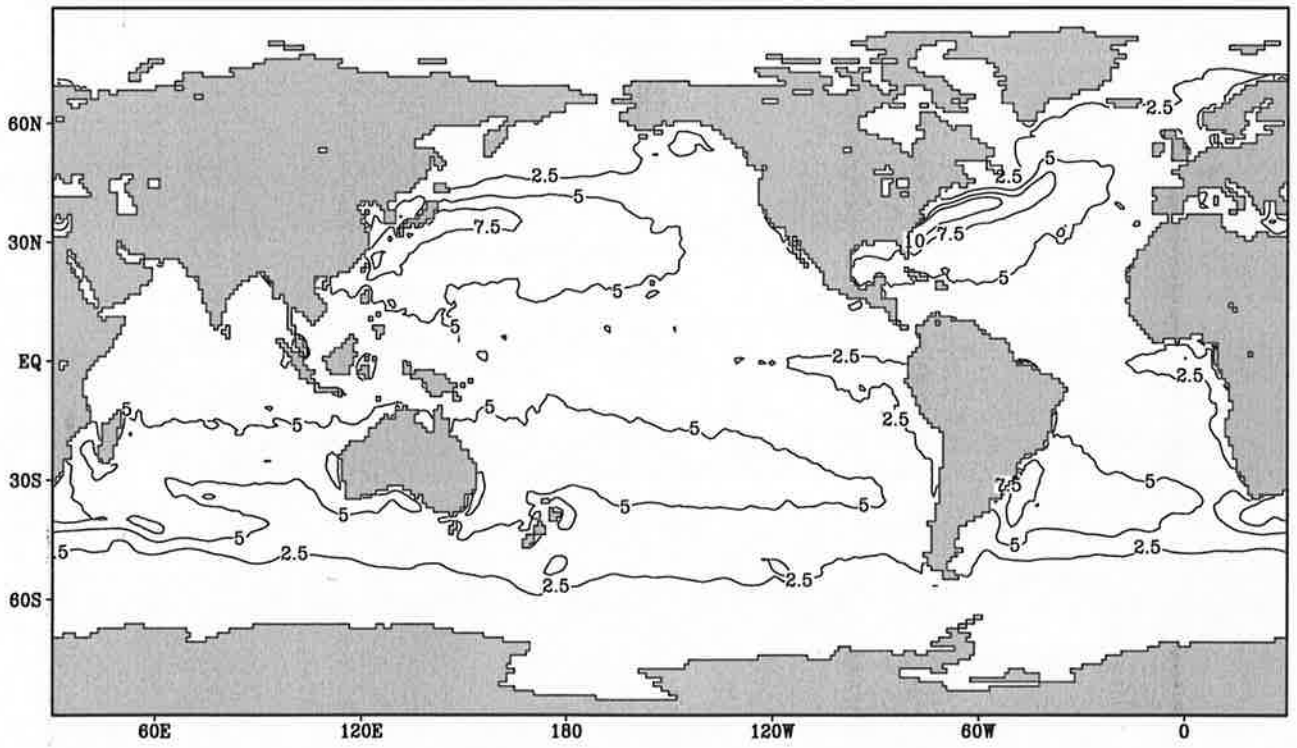

Contour interval: 2.5 10^{-8} m^2s^{-3}

Fig.11.1 $\frac{\partial Q}{\partial T}$ January

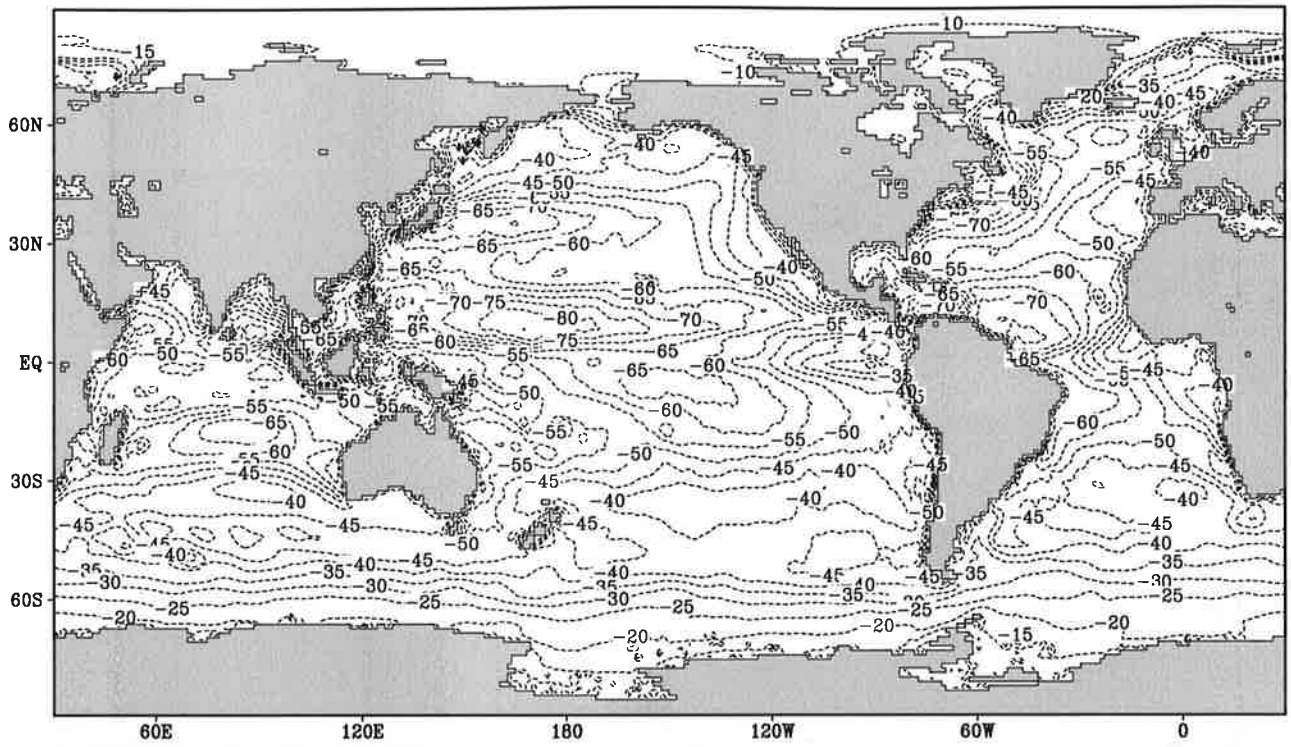

Contour interval: 5 $WK^{-1}m^{-2}$

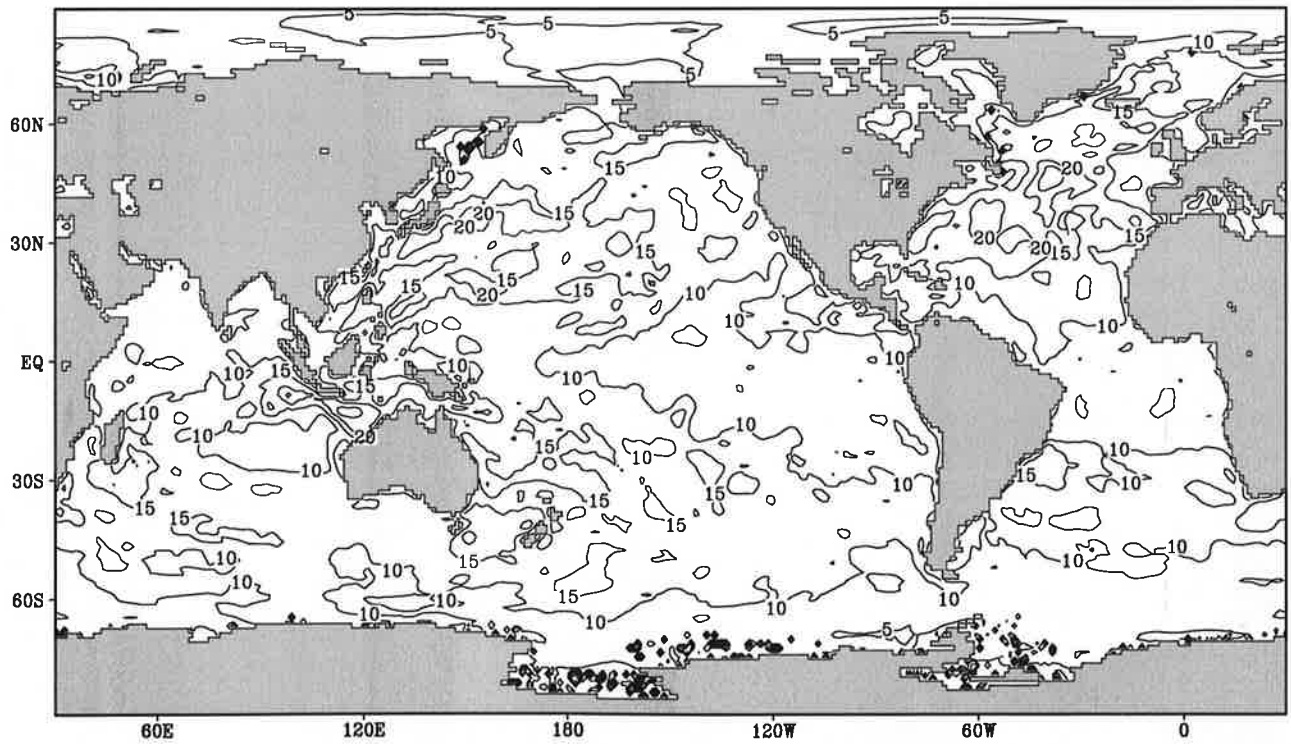

Contour interval: 5 $WK^{-1}m^{-2}$

Fig.11.2 $\frac{\partial Q}{\partial T}$ February

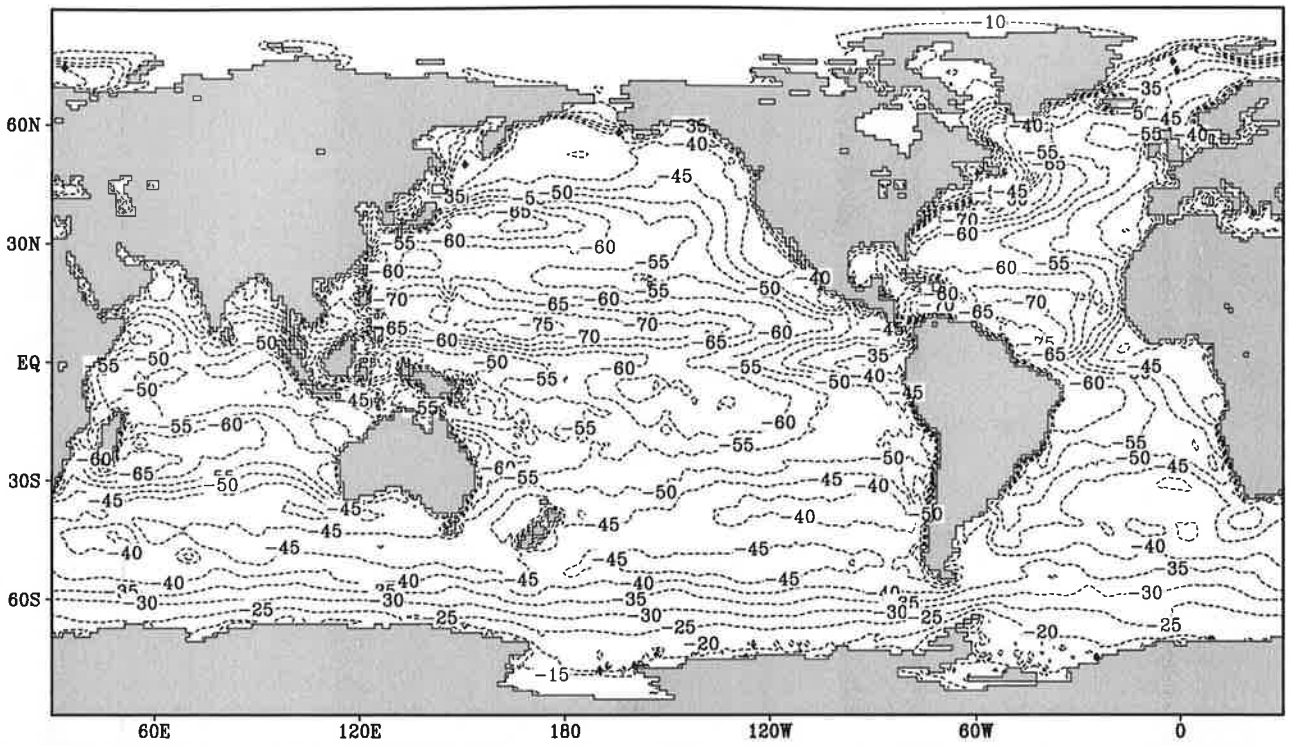

Contour interval: 5 $WK^{-1}m^{-2}$

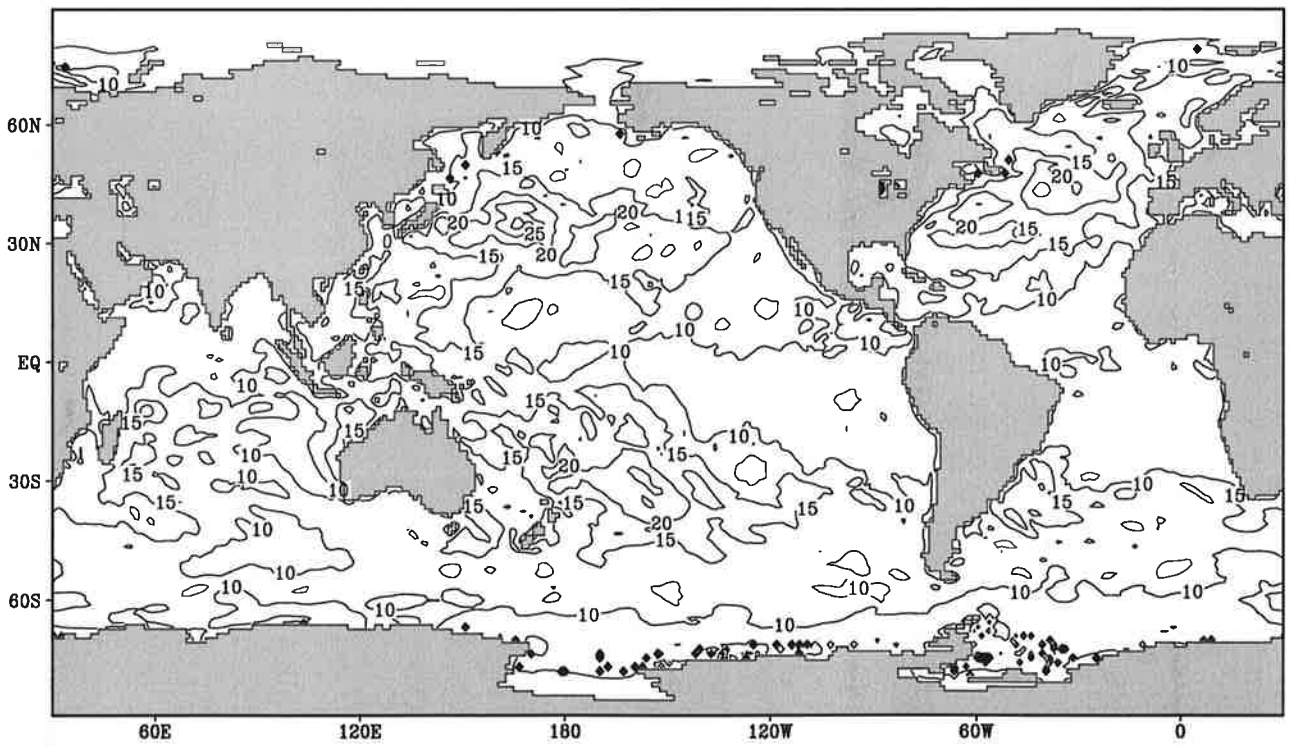

Contour interval: 5 $WK^{-1}m^{-2}$

Fig.11.3 $\frac{\partial Q}{\partial T}$ March

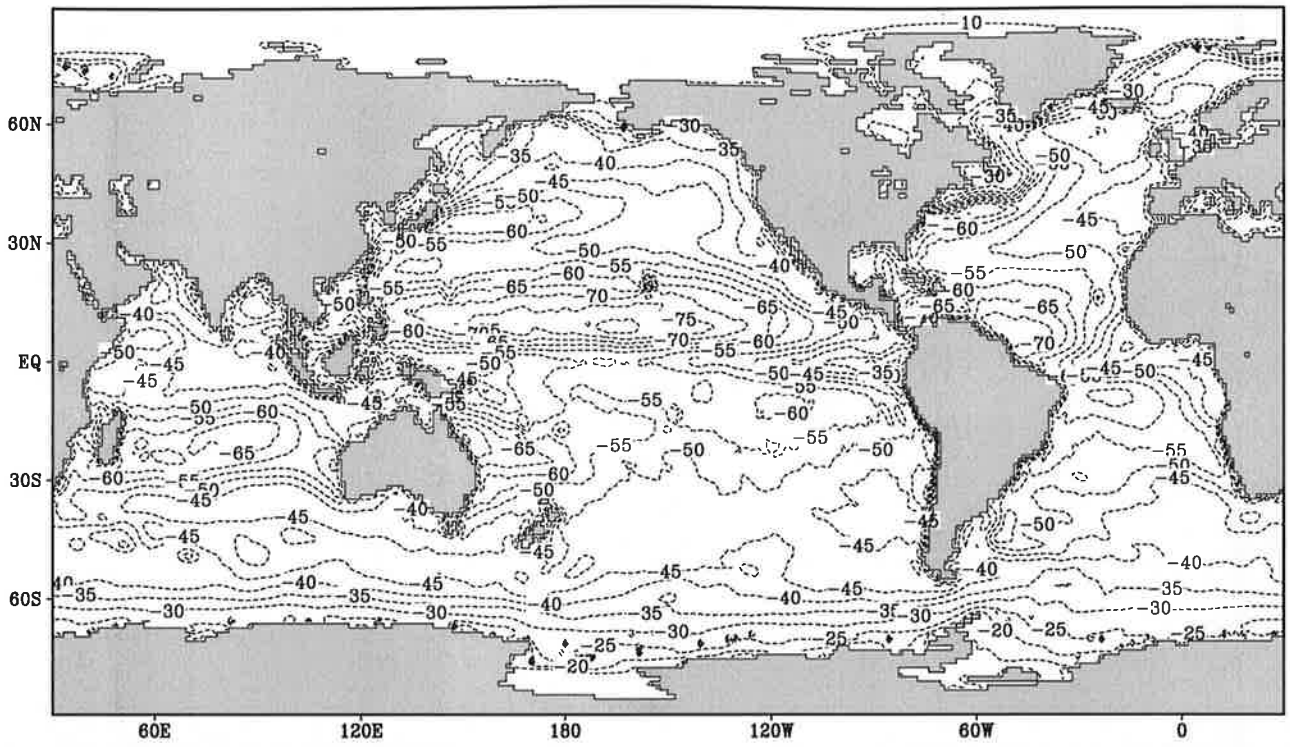

Contour interval: 5 $WK^{-1}m^{-2}$

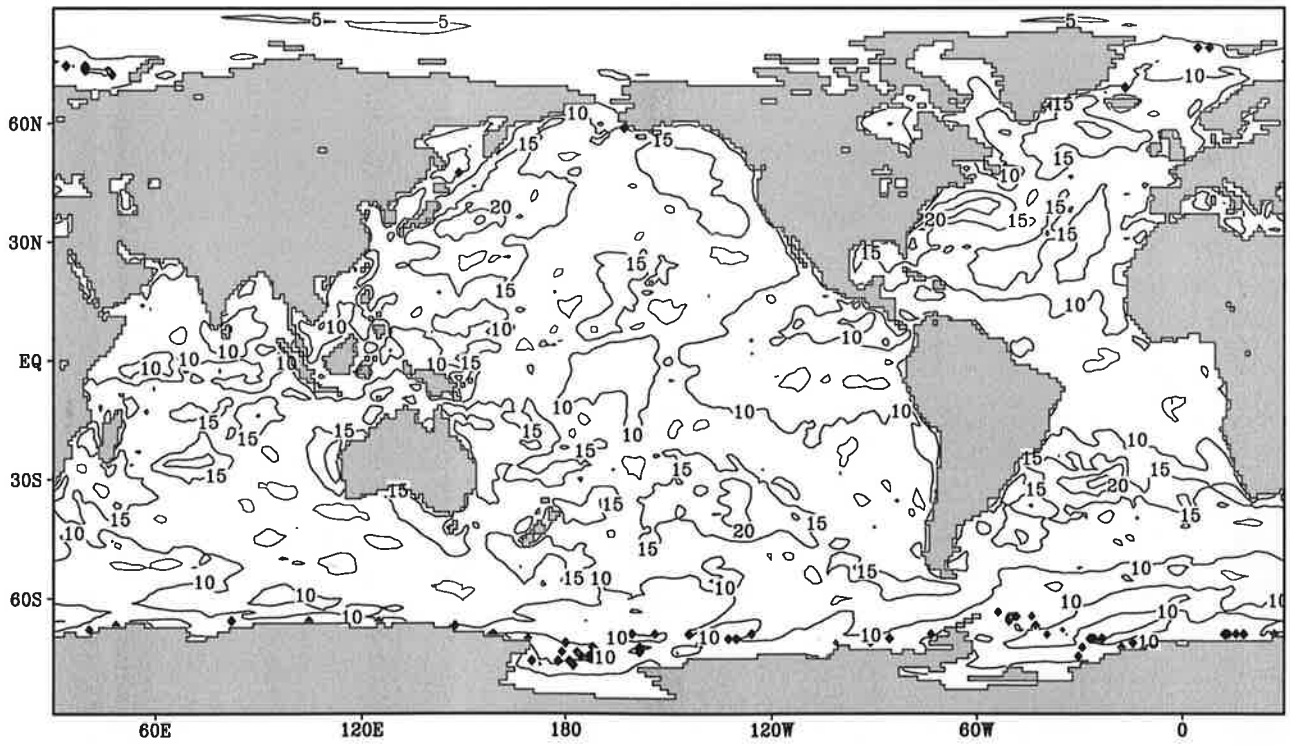

Contour interval: 5 $WK^{-1}m^{-2}$

Fig.11.4 $\frac{\partial Q}{\partial T}$ April

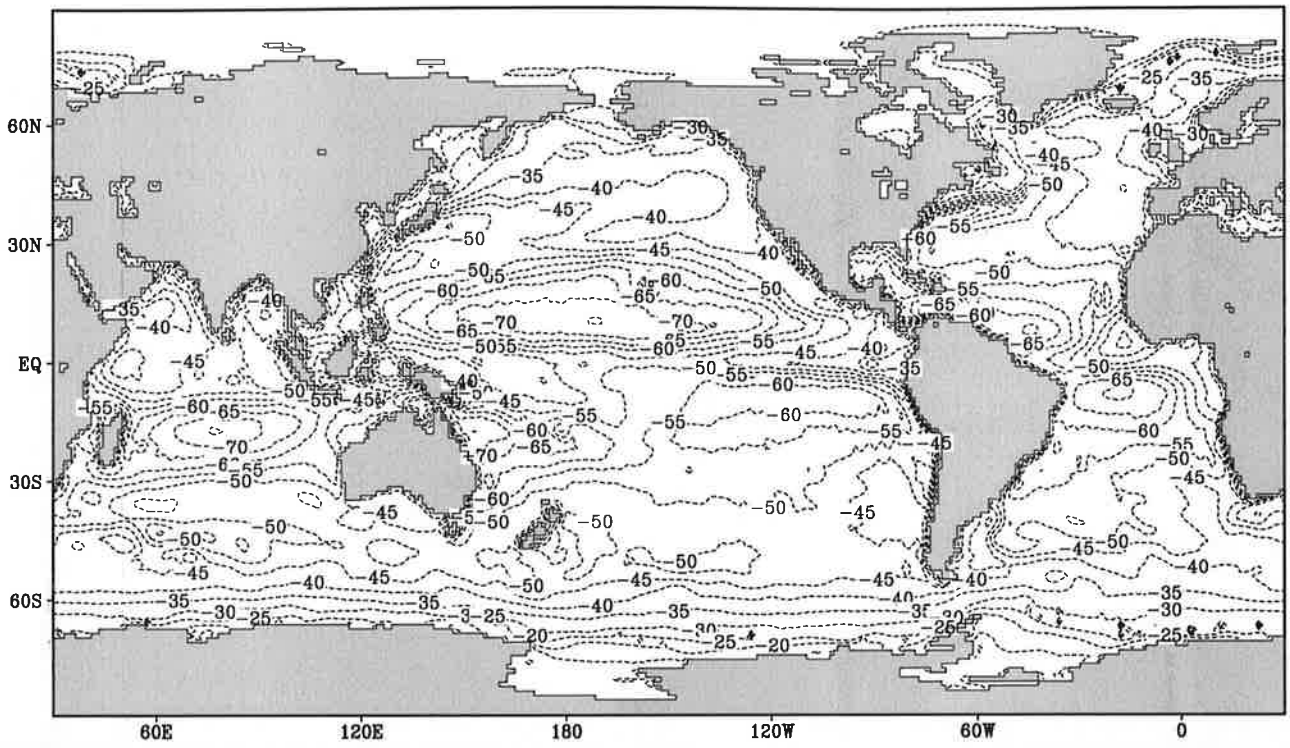

Contour interval: 5 $WK^{-1}m^{-2}$

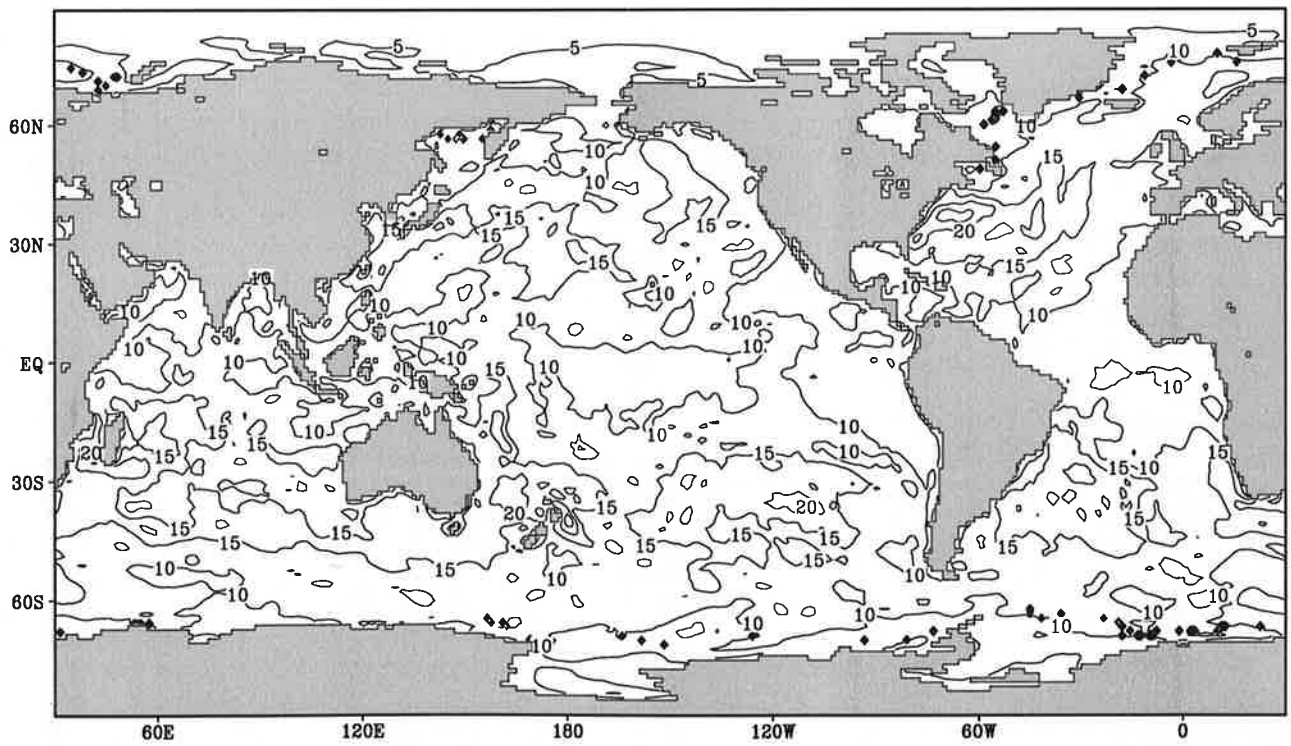

Contour interval: 5 $WK^{-1}m^{-2}$

Fig.11.5 $\frac{\partial Q}{\partial T}$ May

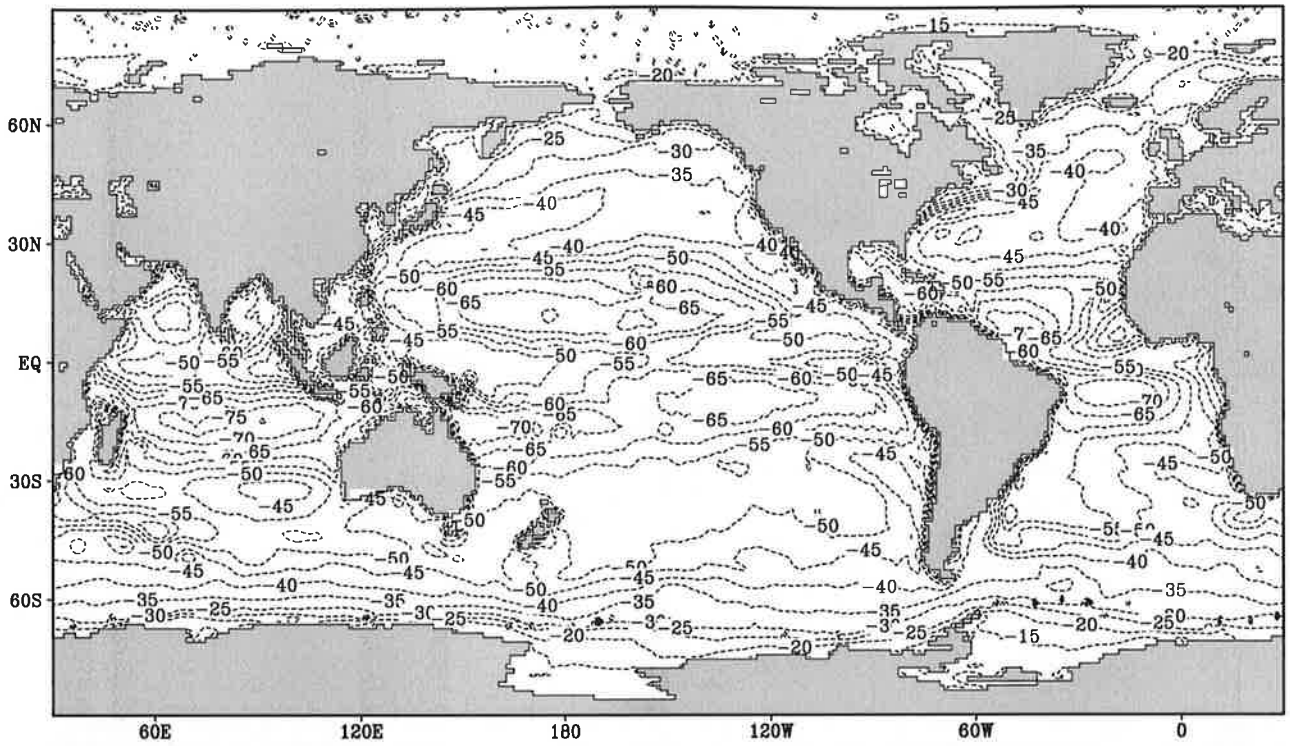

Contour interval: 5 $WK^{-1}m^{-2}$

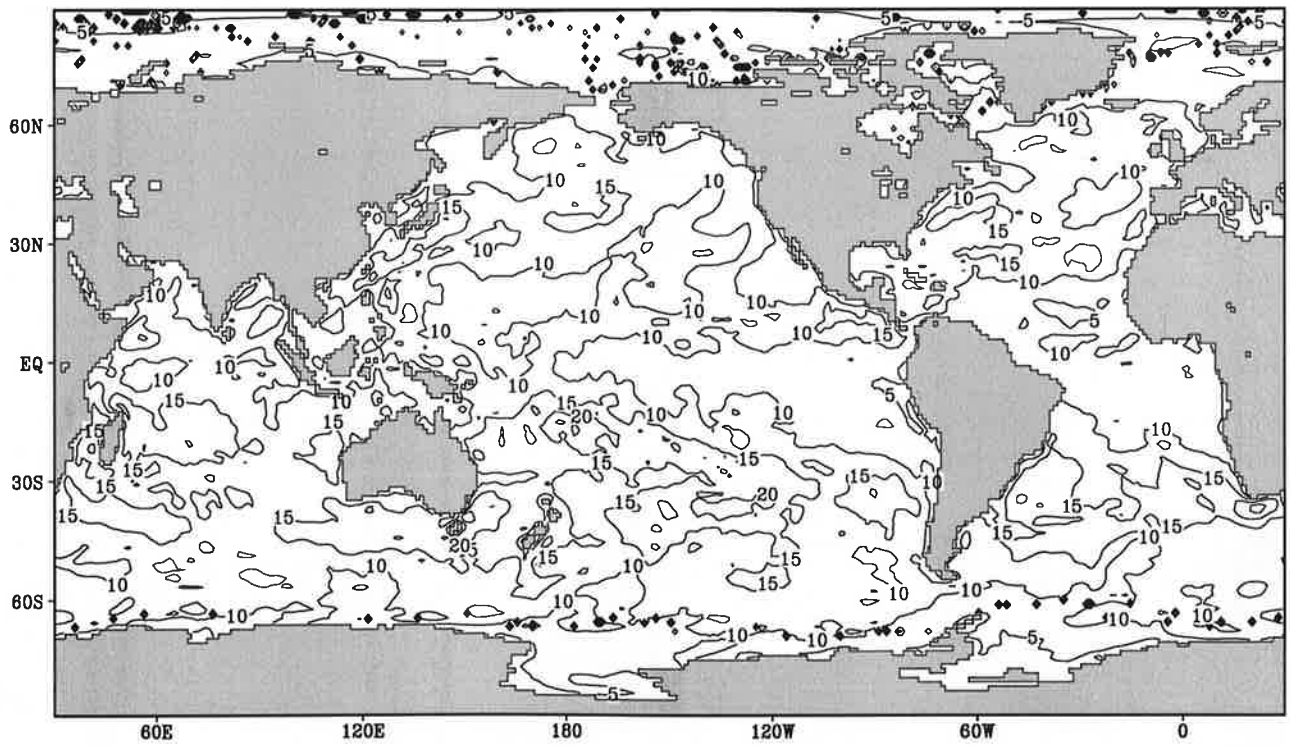

Contour interval: 5 $WK^{-1}m^{-2}$

Fig.11.6 $\frac{\partial Q}{\partial T}$ June

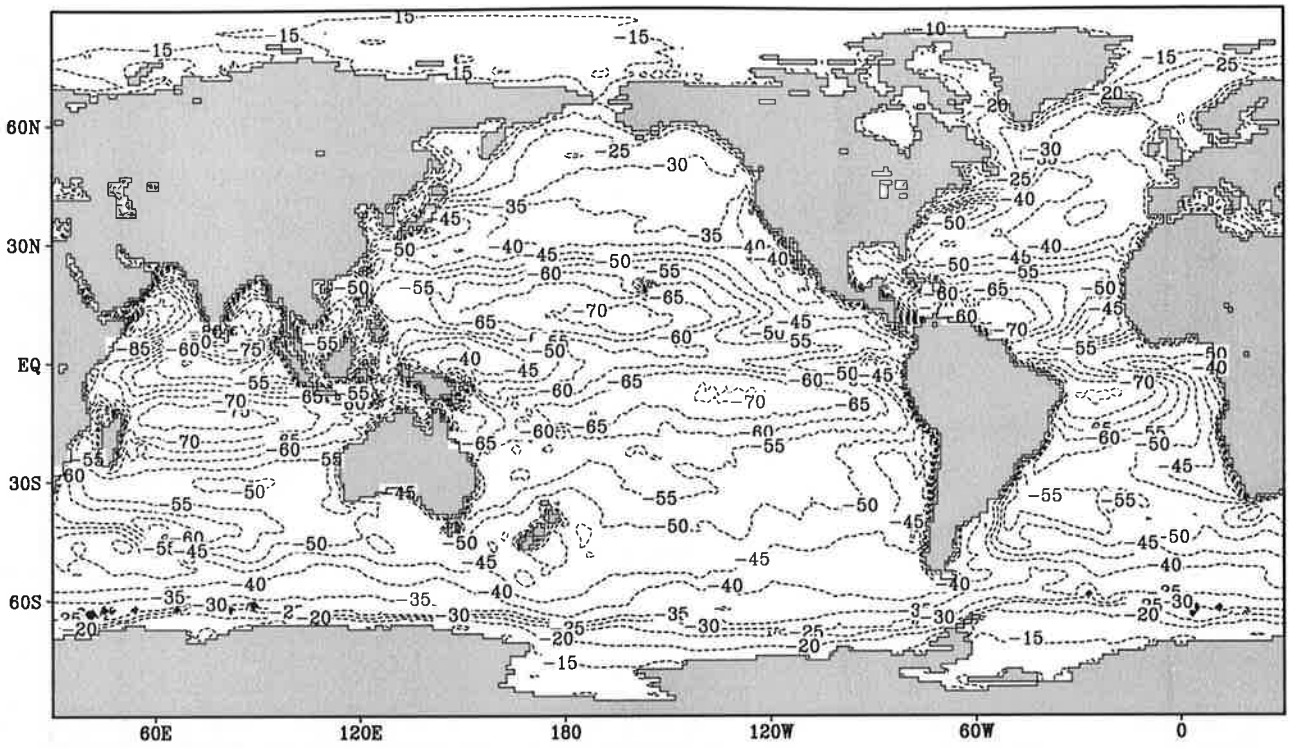

Contour interval: 5 $WK^{-1}m^{-2}$

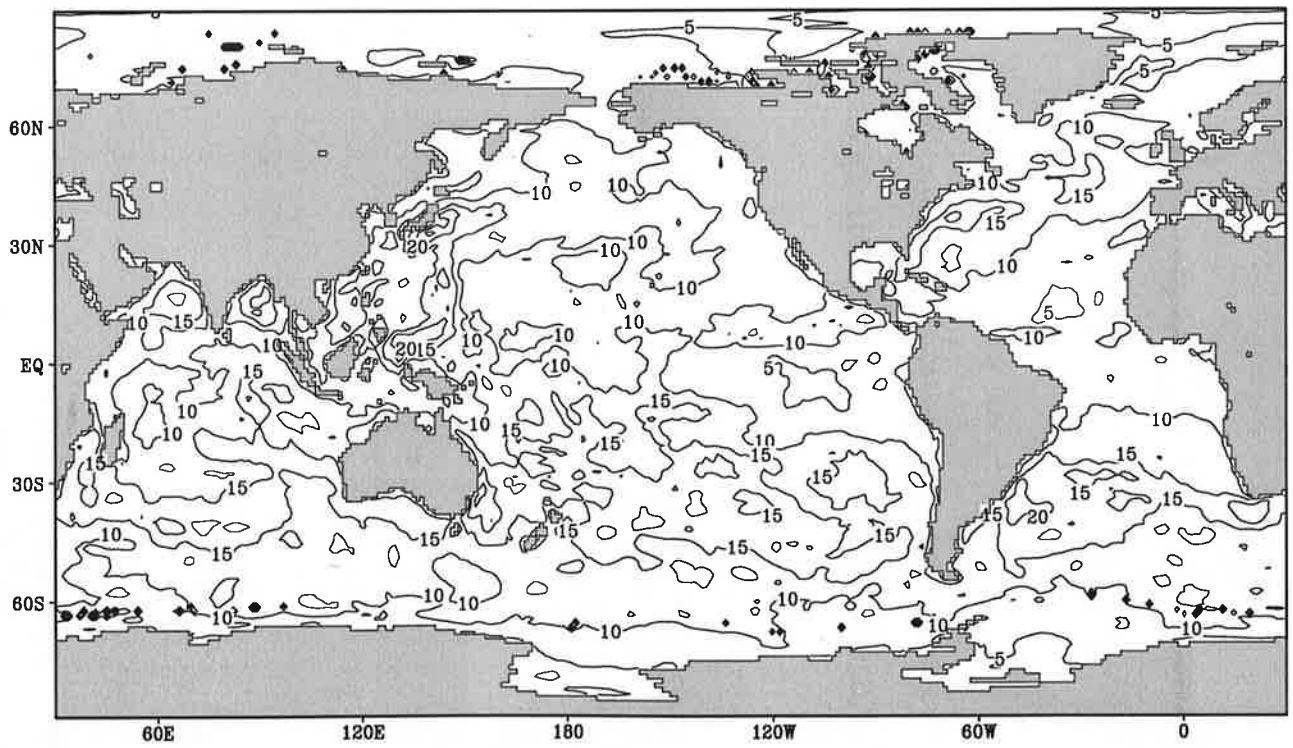

Contour interval: 5 $WK^{-1}m^{-2}$

Fig.11.7 $\frac{\partial Q}{\partial T}$ July

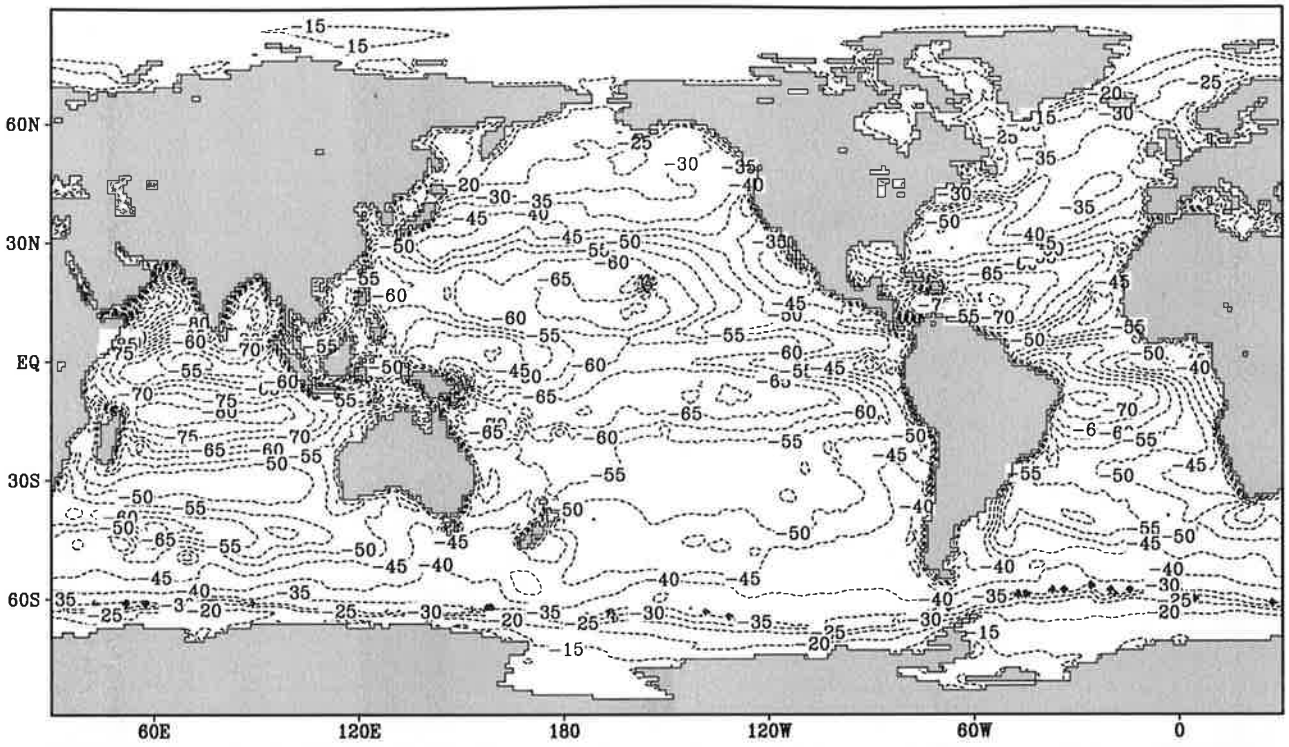

Contour interval: 5 $WK^{-1}m^{-2}$

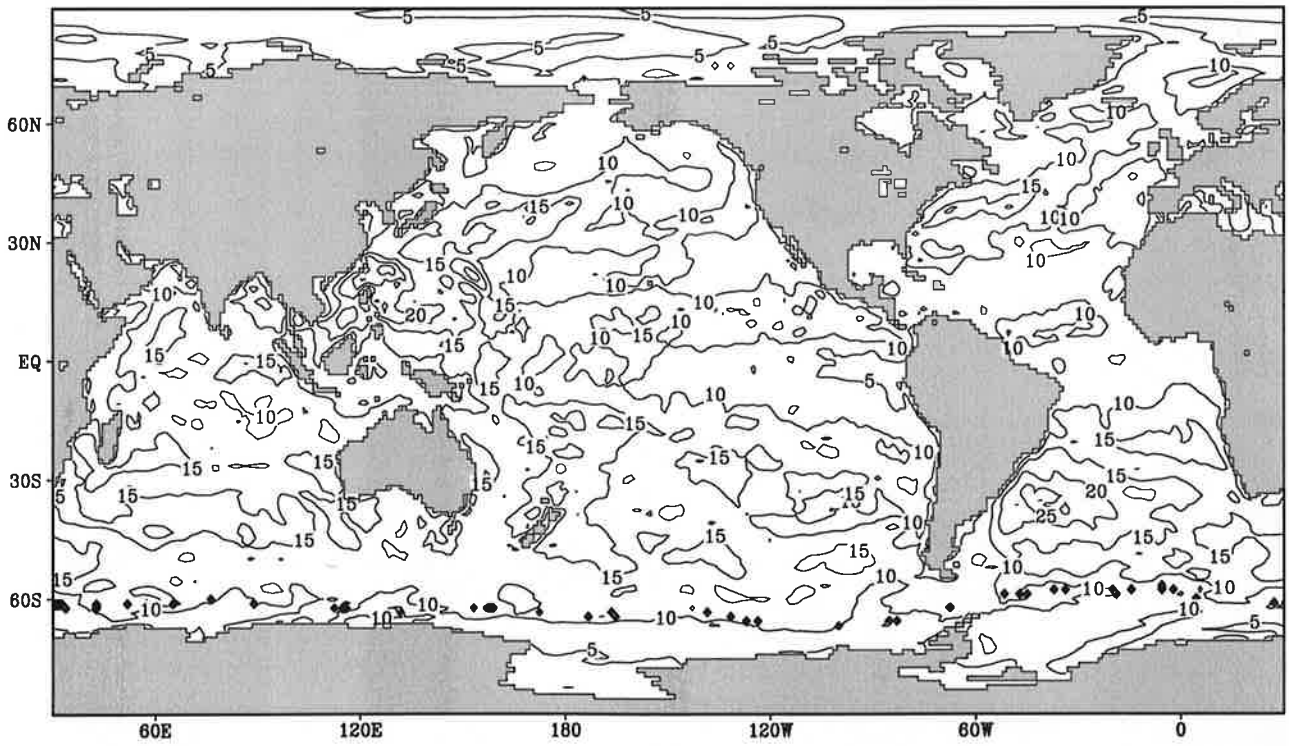

Contour interval: 5 $WK^{-1}m^{-2}$

Fig.11.8 $\frac{\partial Q}{\partial T}$ August

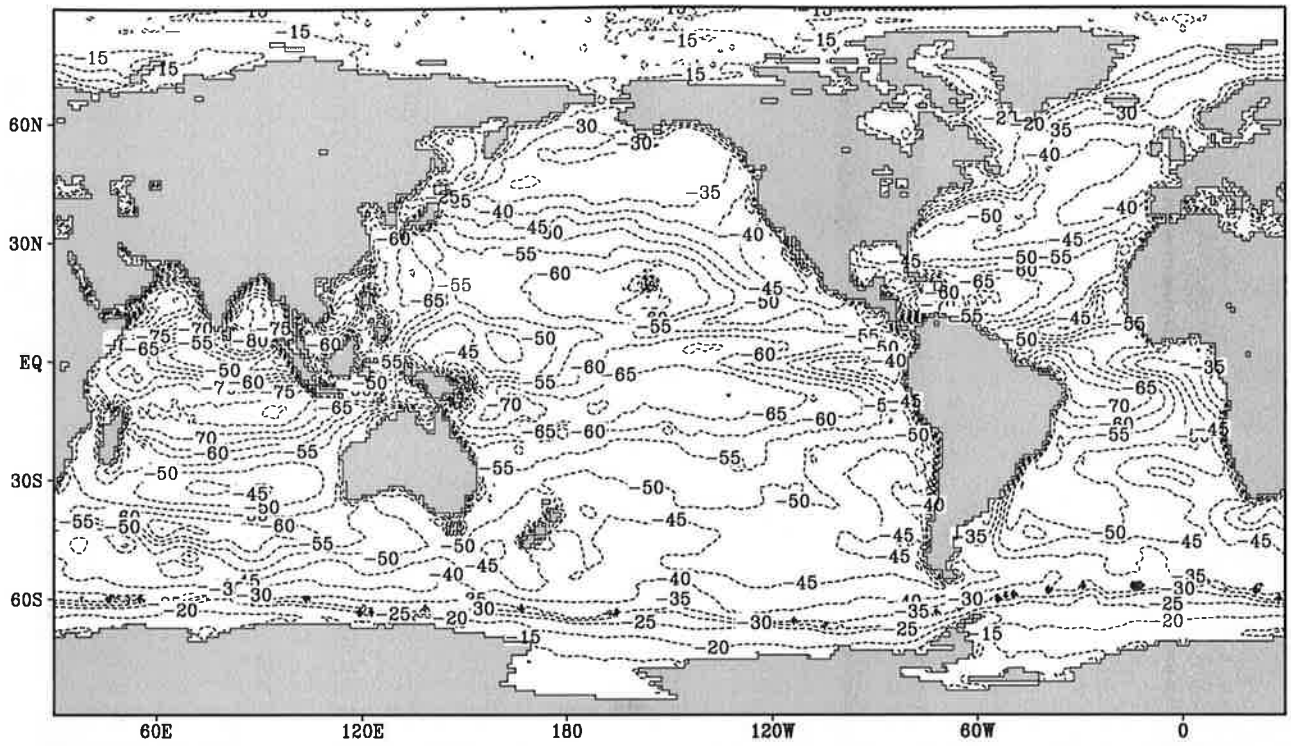

Contour interval: 5 $WK^{-1}m^{-2}$

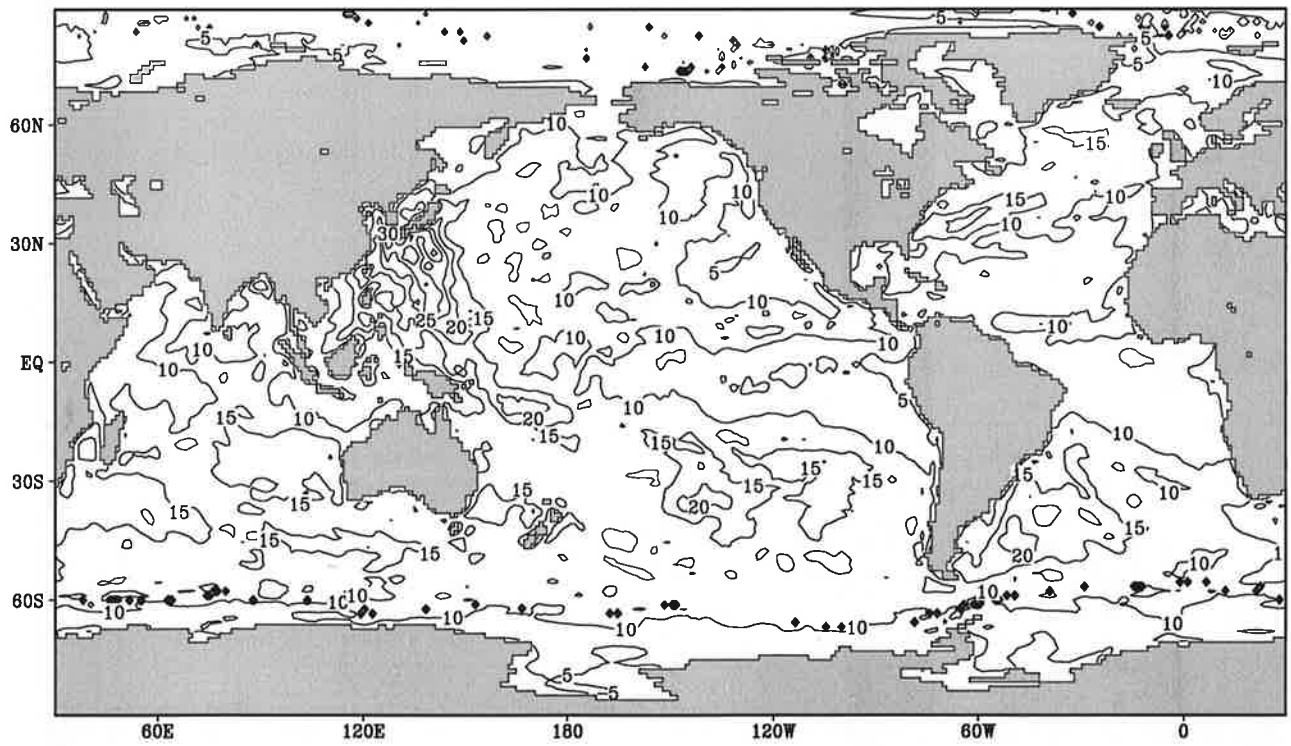

Contour interval: 5 $WK^{-1}m^{-2}$

Fig.11.9 $\frac{\partial Q}{\partial T}$ September

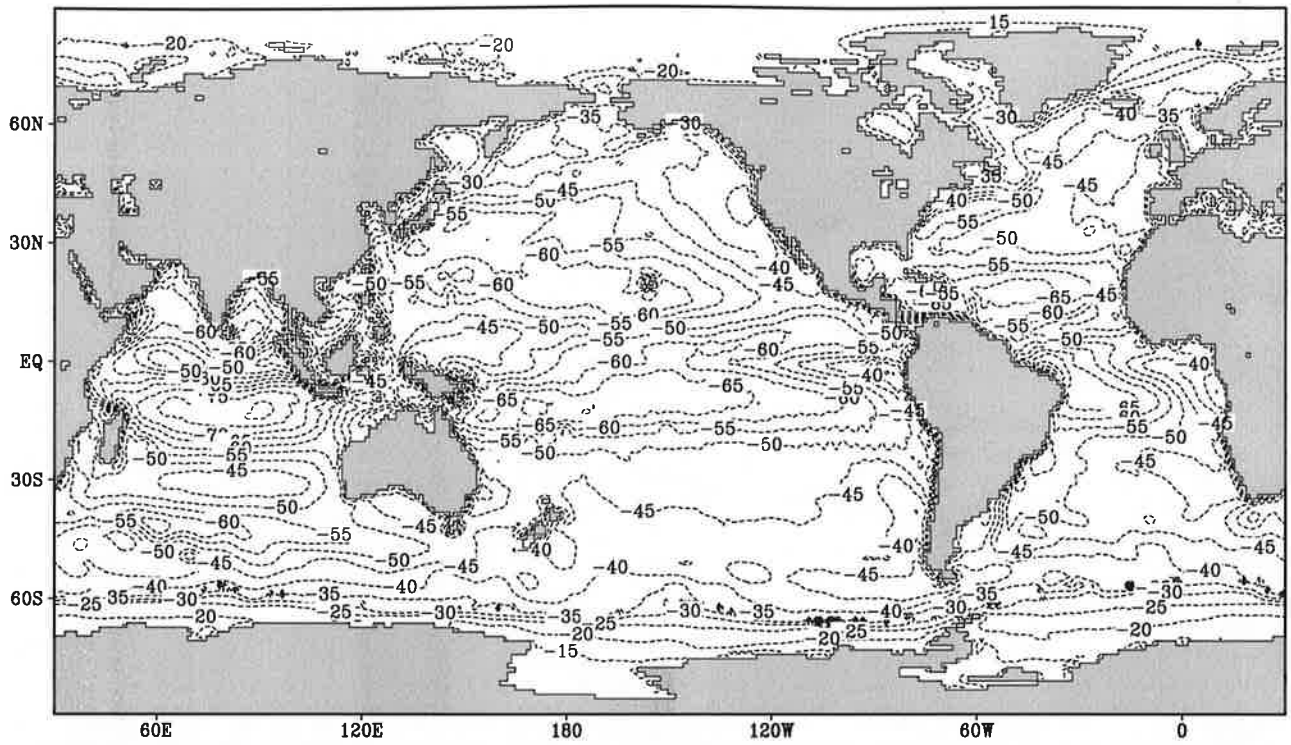

Contour interval: 5 $WK^{-1}m^{-2}$

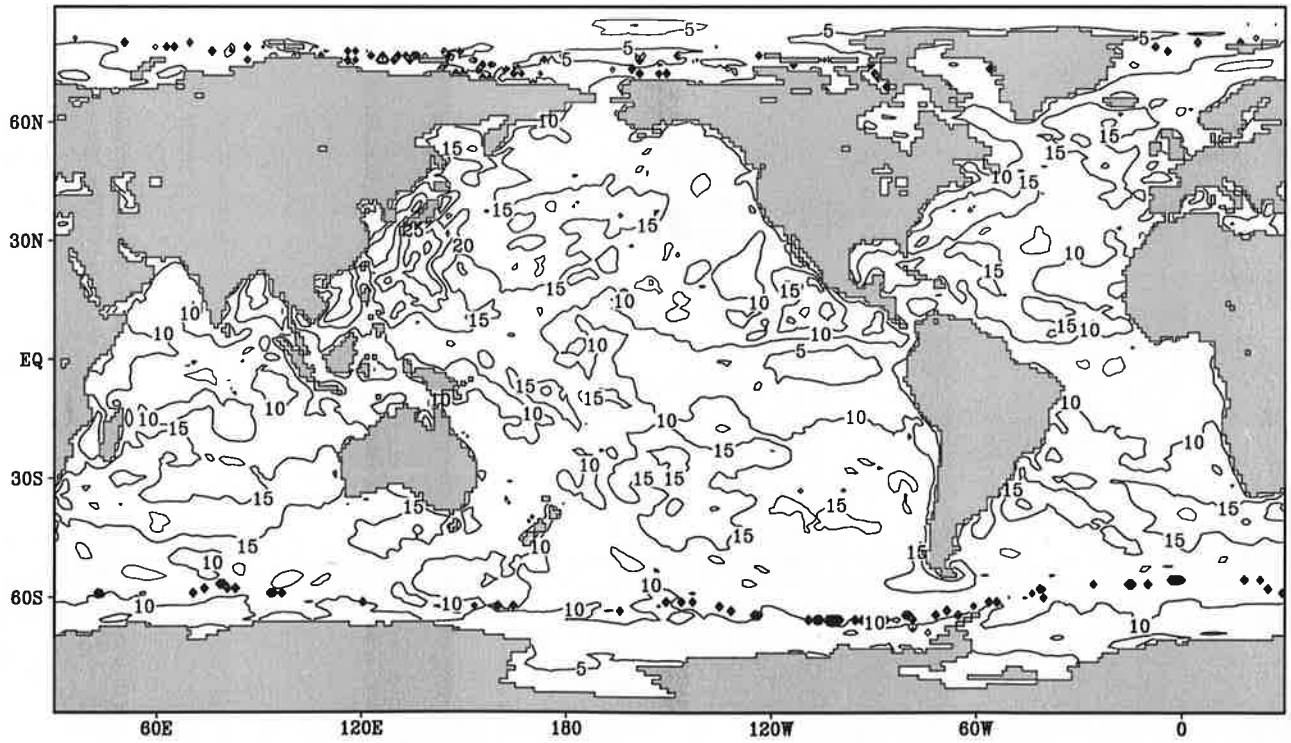

Contour interval: 5 $WK^{-1}m^{-2}$

Fig.11.10 $\frac{\partial Q}{\partial T}$ October

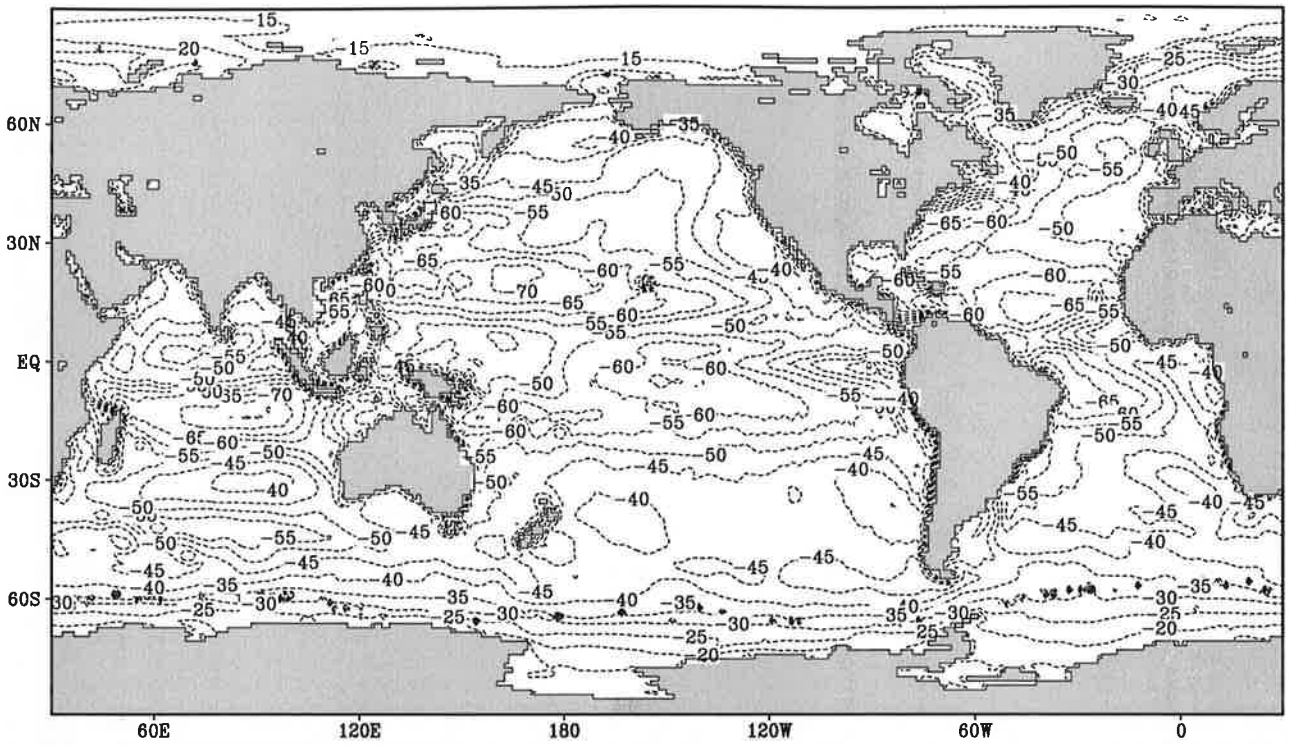

Contour interval: 5 $WK^{-1}m^{-2}$

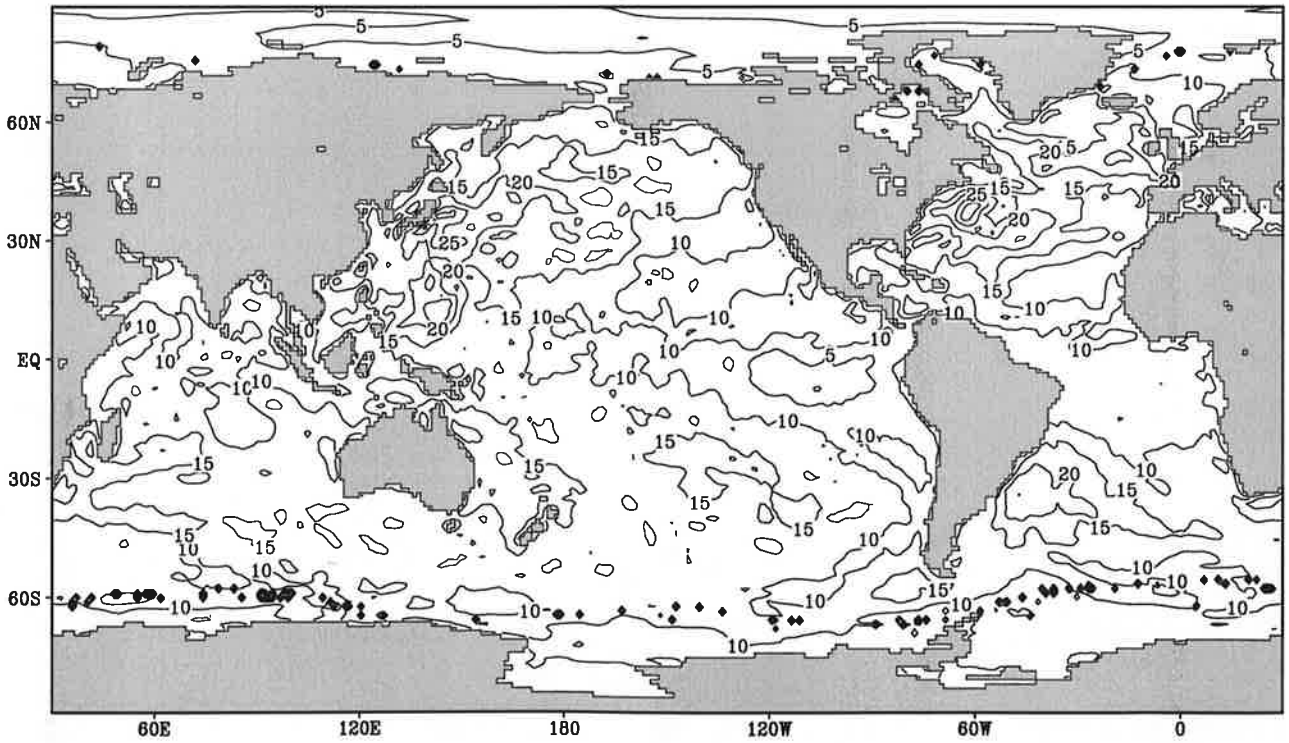

Contour interval: 5 $WK^{-1}m^{-2}$

Fig.11.11 $\frac{\partial Q}{\partial T}$ November

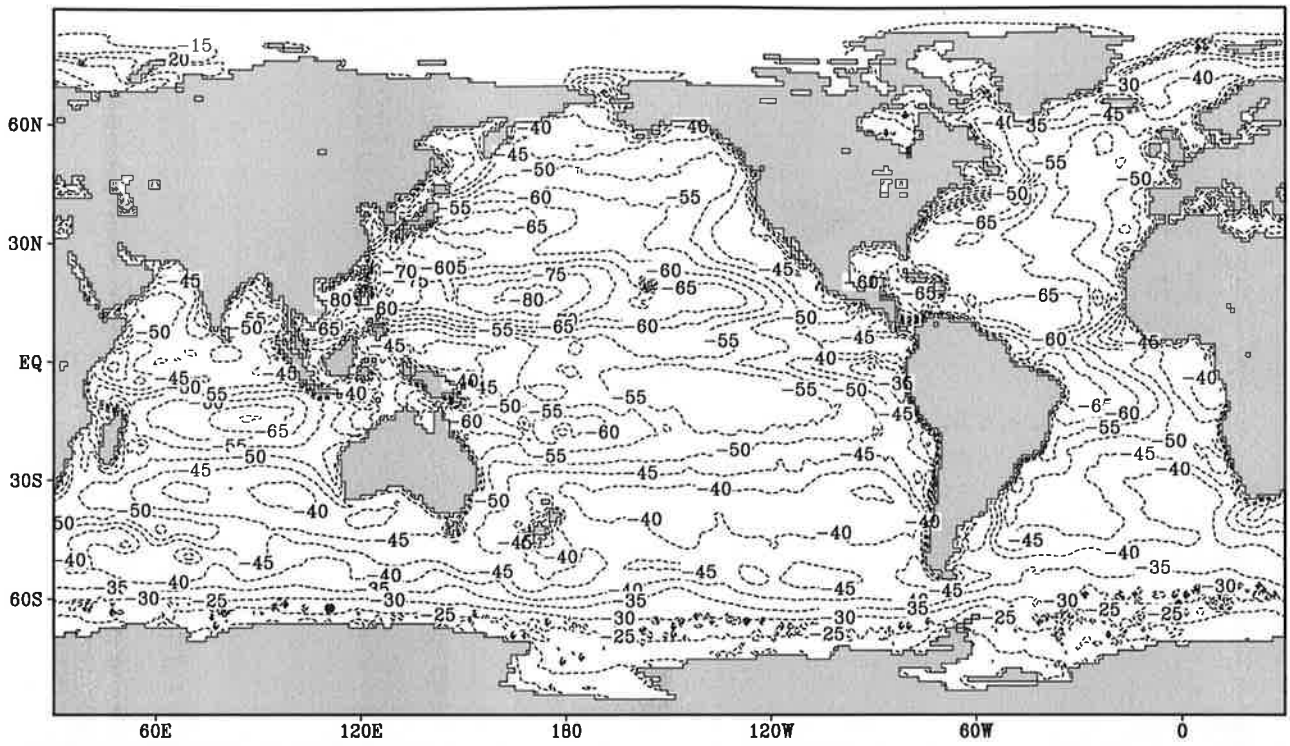

Contour interval: 5 $WK^{-1}m^{-2}$

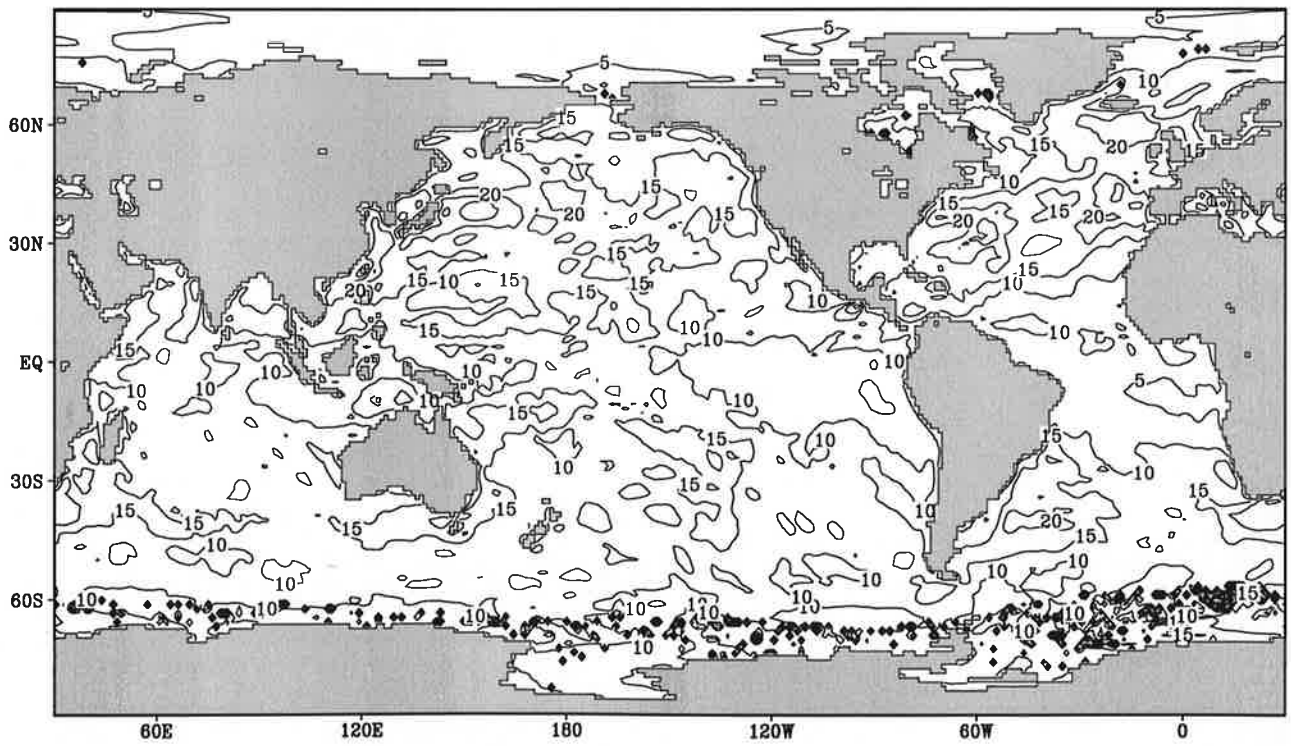

Contour interval: 5 $WK^{-1}m^{-2}$

Fig.11.12 $\frac{\partial Q}{\partial T}$ December

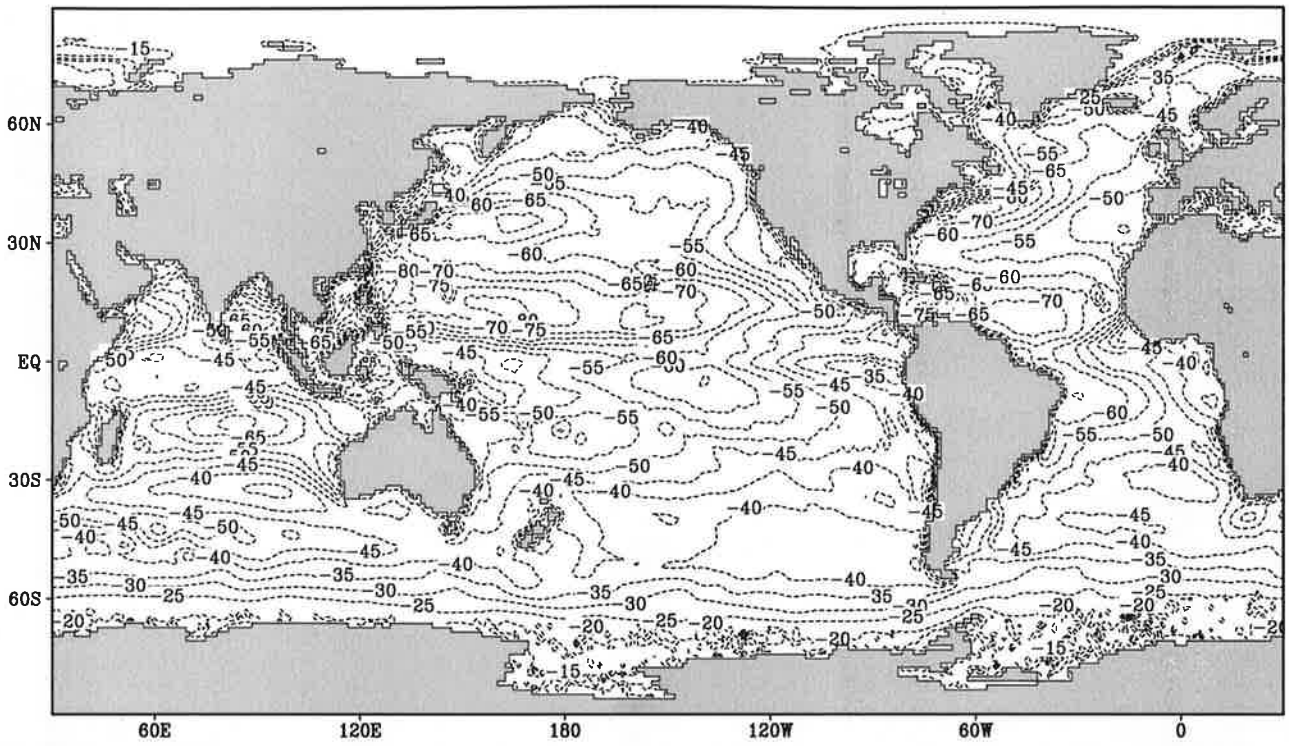

Contour interval: 5 $WK^{-1}m^{-2}$

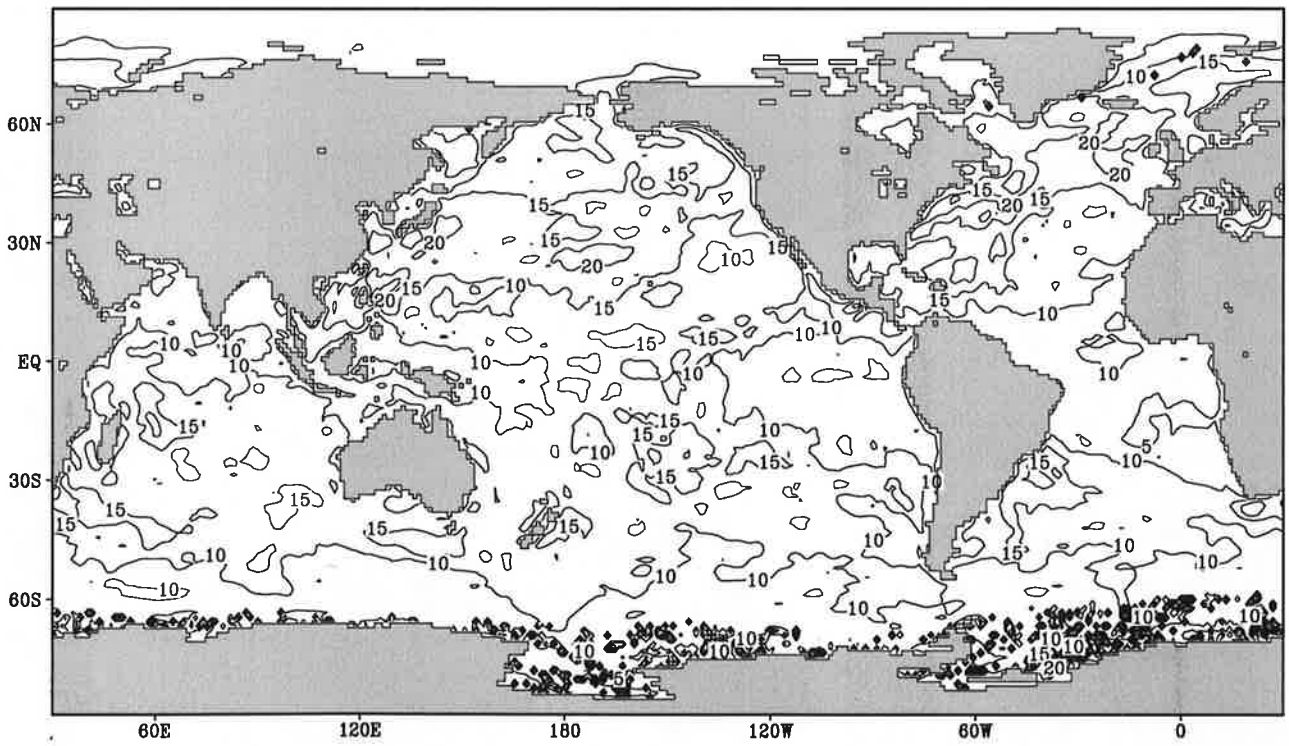

Contour interval: 5 $WK^{-1}m^{-2}$

Fig.11.13 $\frac{\partial Q}{\partial T}$ Annual Mean

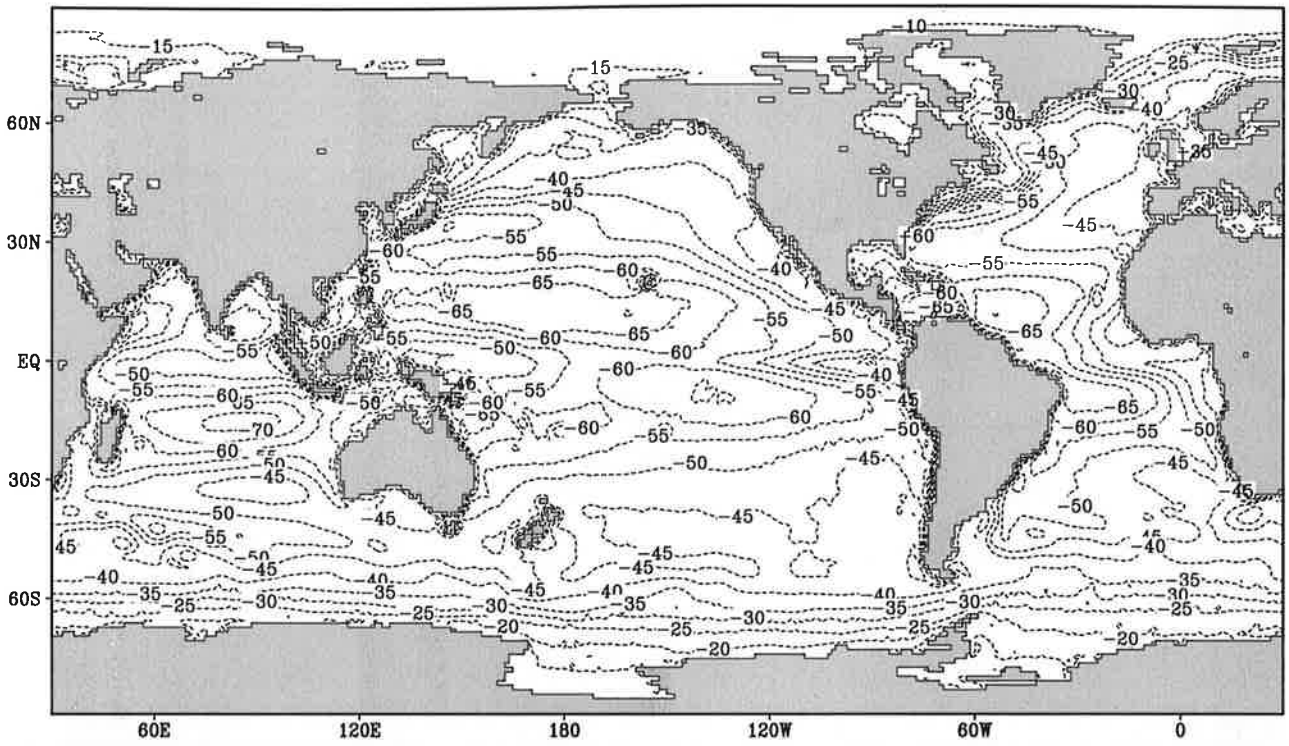

Contour interval: 5 $WK^{-1}m^{-2}$

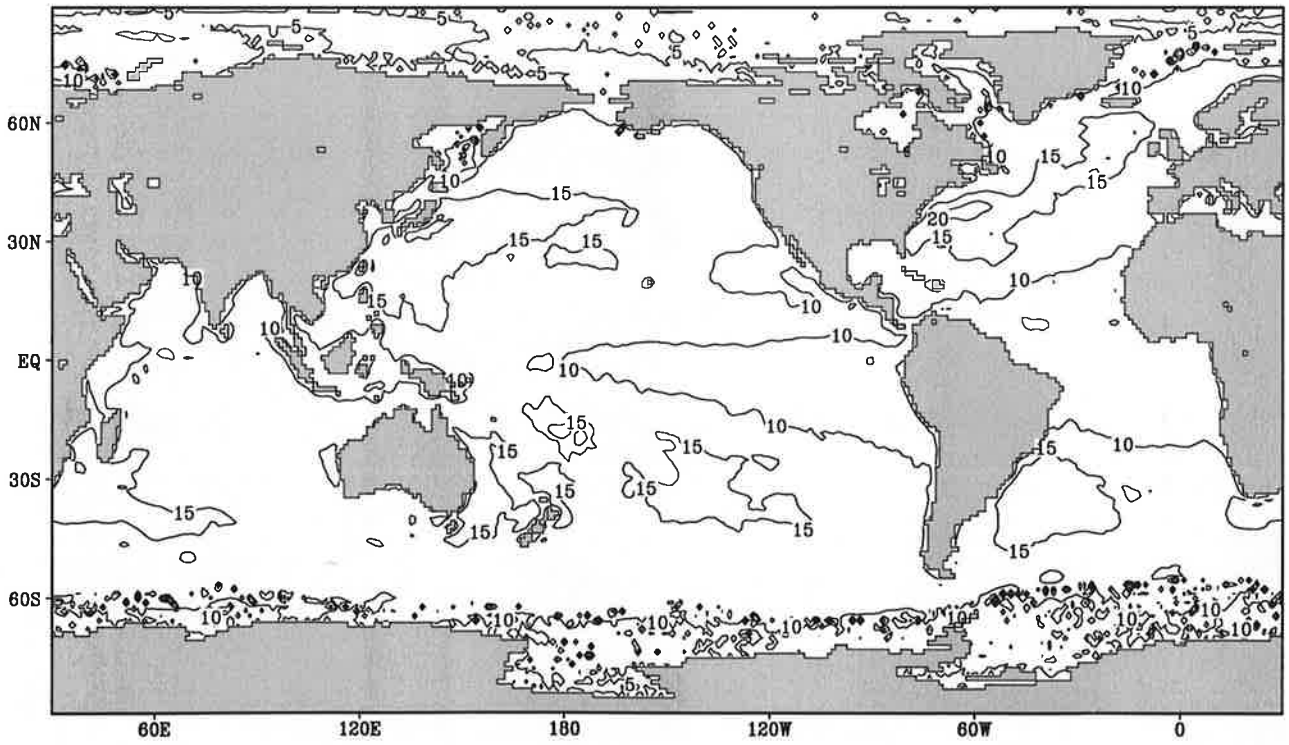

Contour interval: 5 $WK^{-1}m^{-2}$

Fig.12.1 Transfer coefficient for latent heat flux January

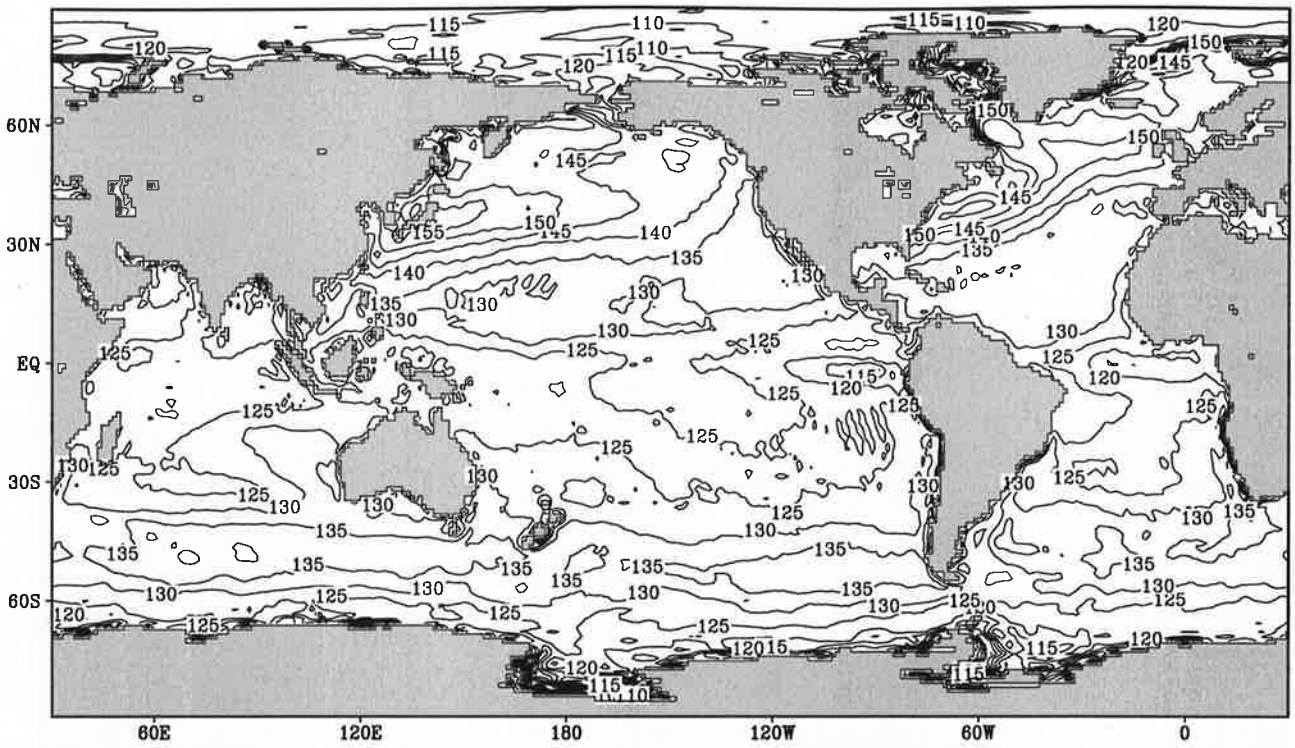

Contour interval: 5 10^{-6}

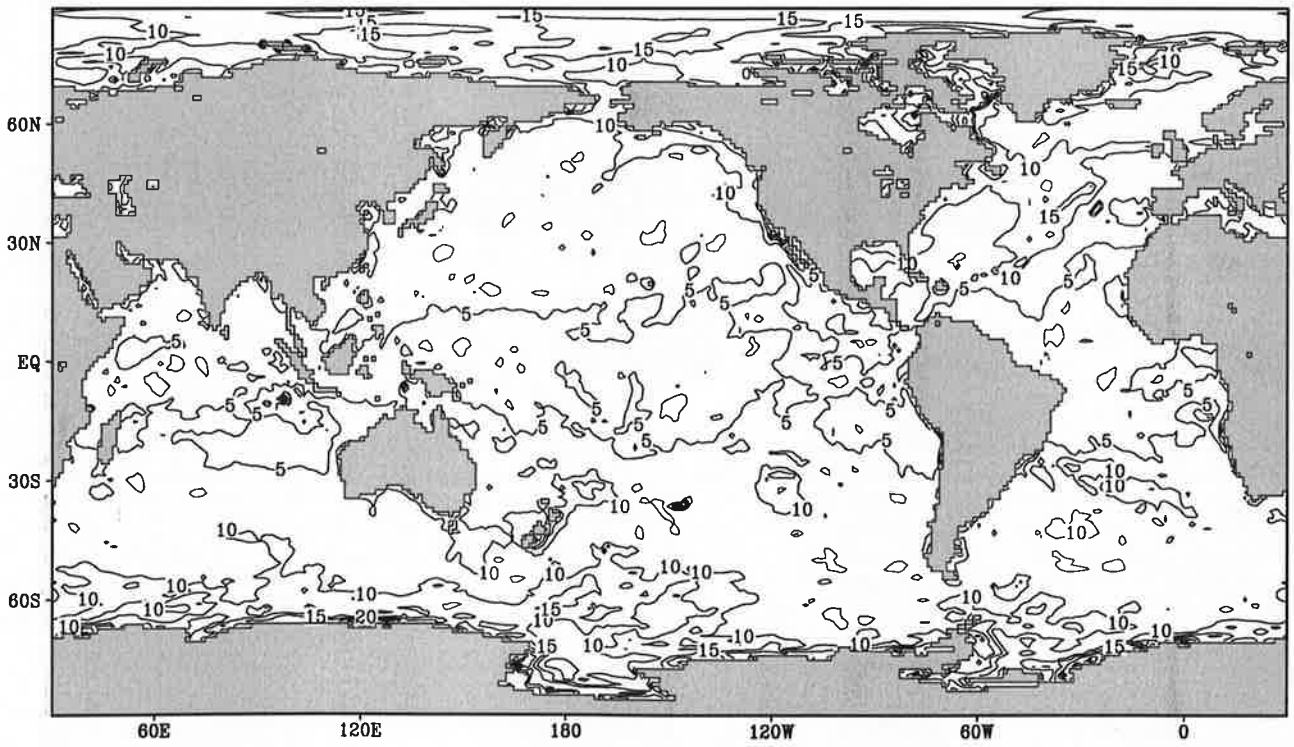

Contour interval: 5 10^{-5}

Fig.12.2 Transfer coefficient for latent heat flux February

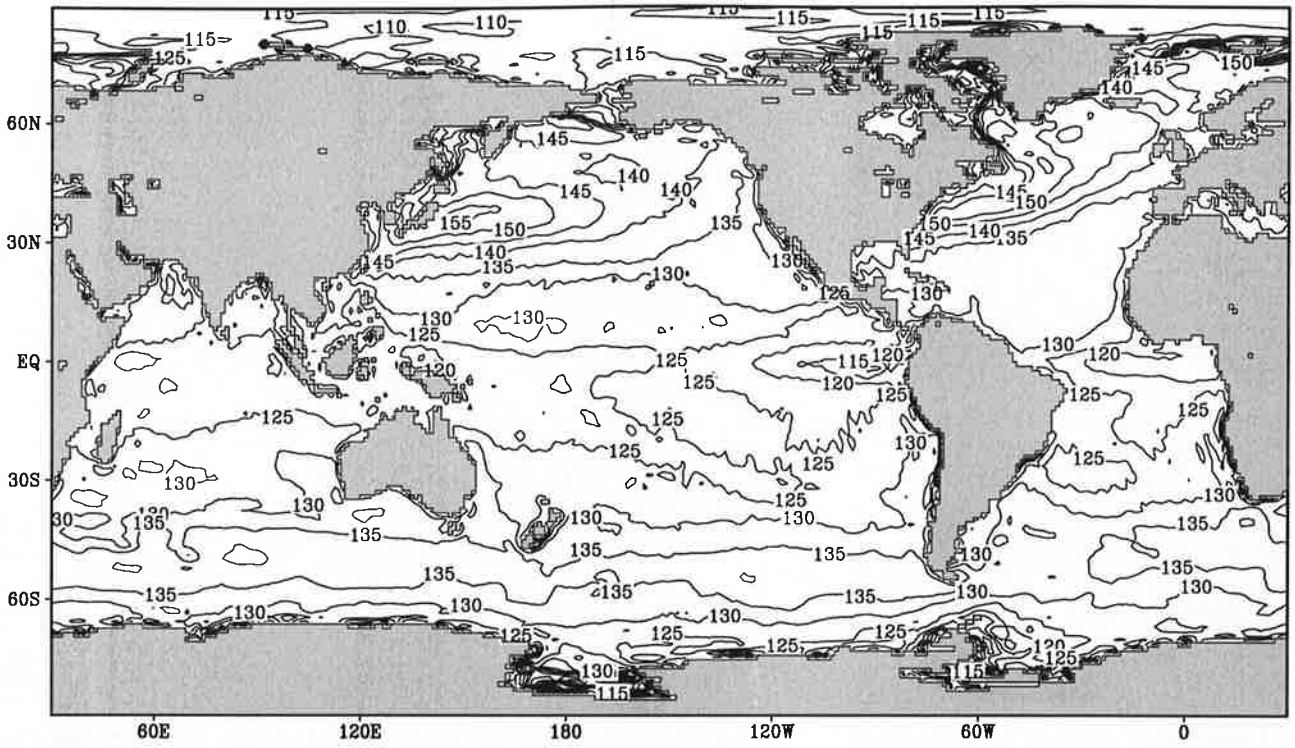

Contour interval: 5 10^{-5}

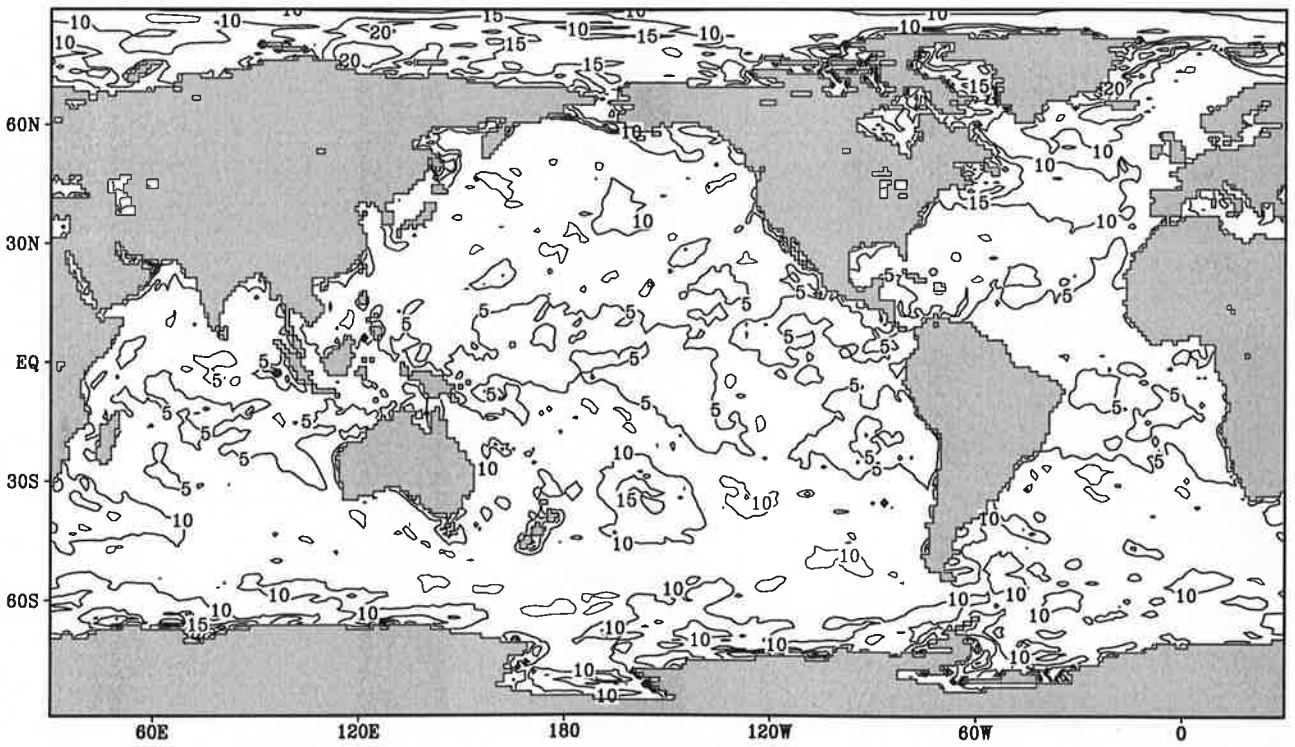

Contour interval: 5 10^{-5}

Fig.12.3 Transfer coefficient for latent heat flux March

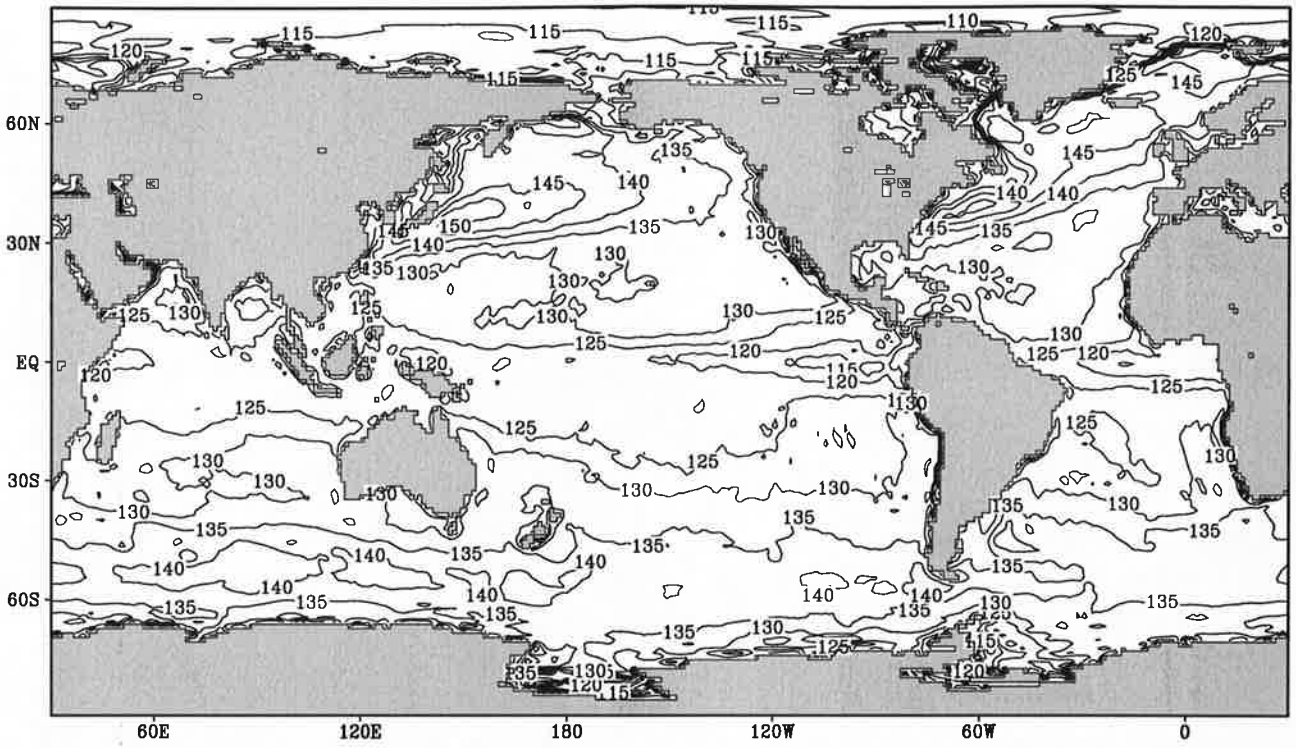

Contour interval: 5 10^{-5}

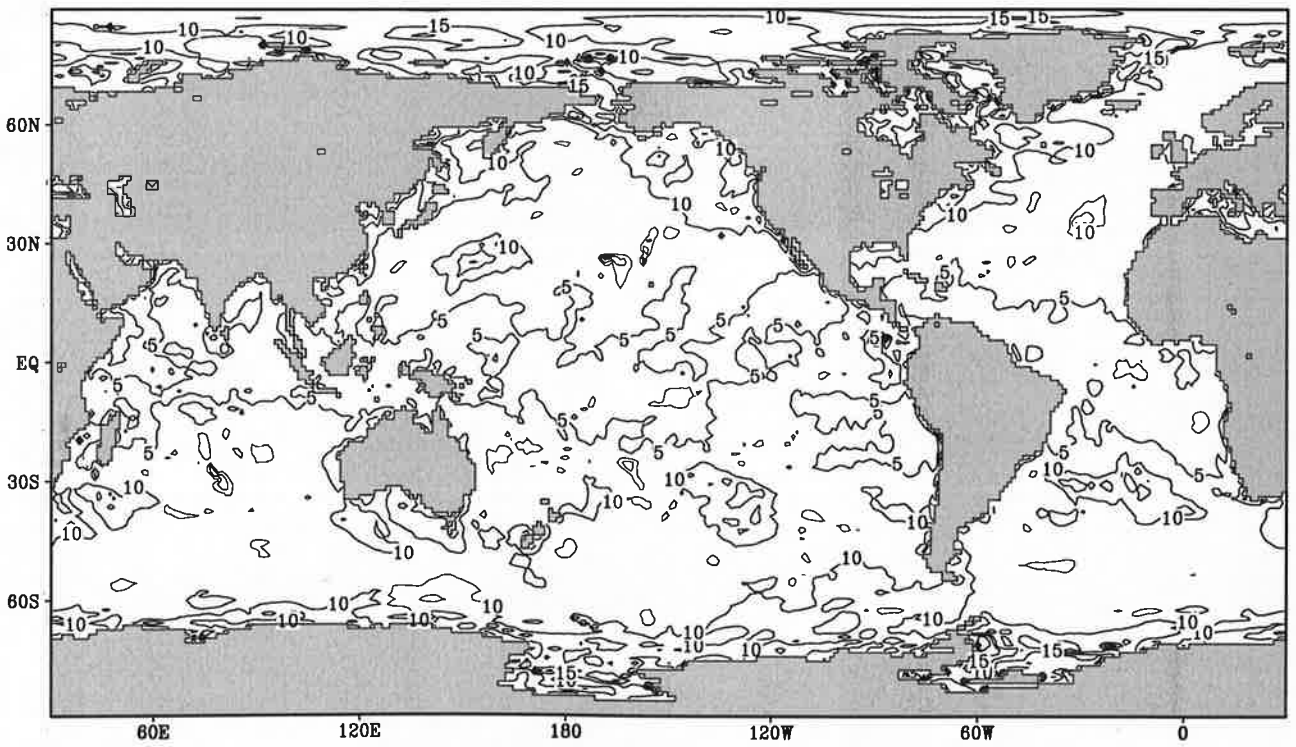

Contour interval: 5 10^{-5}

Fig.12.4 Transfer coefficient for latent heat flux April

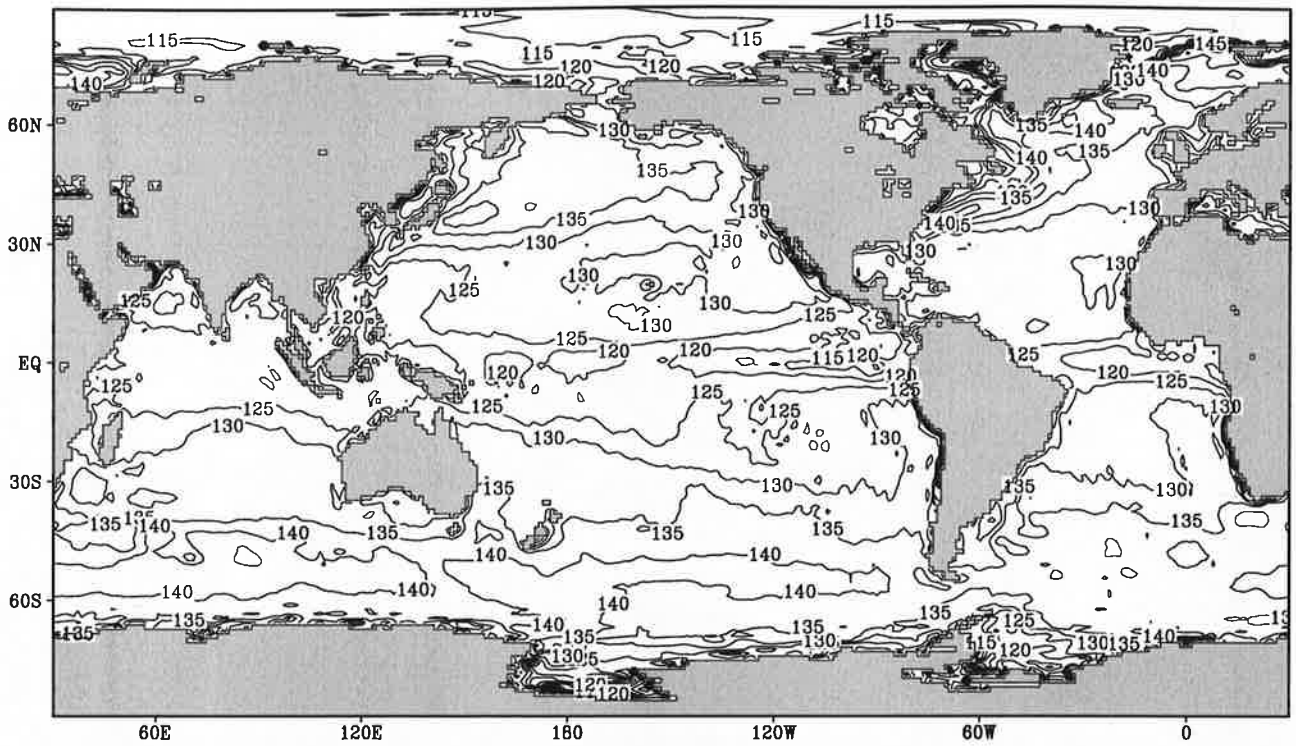

Contour interval: 5 10^{-5}

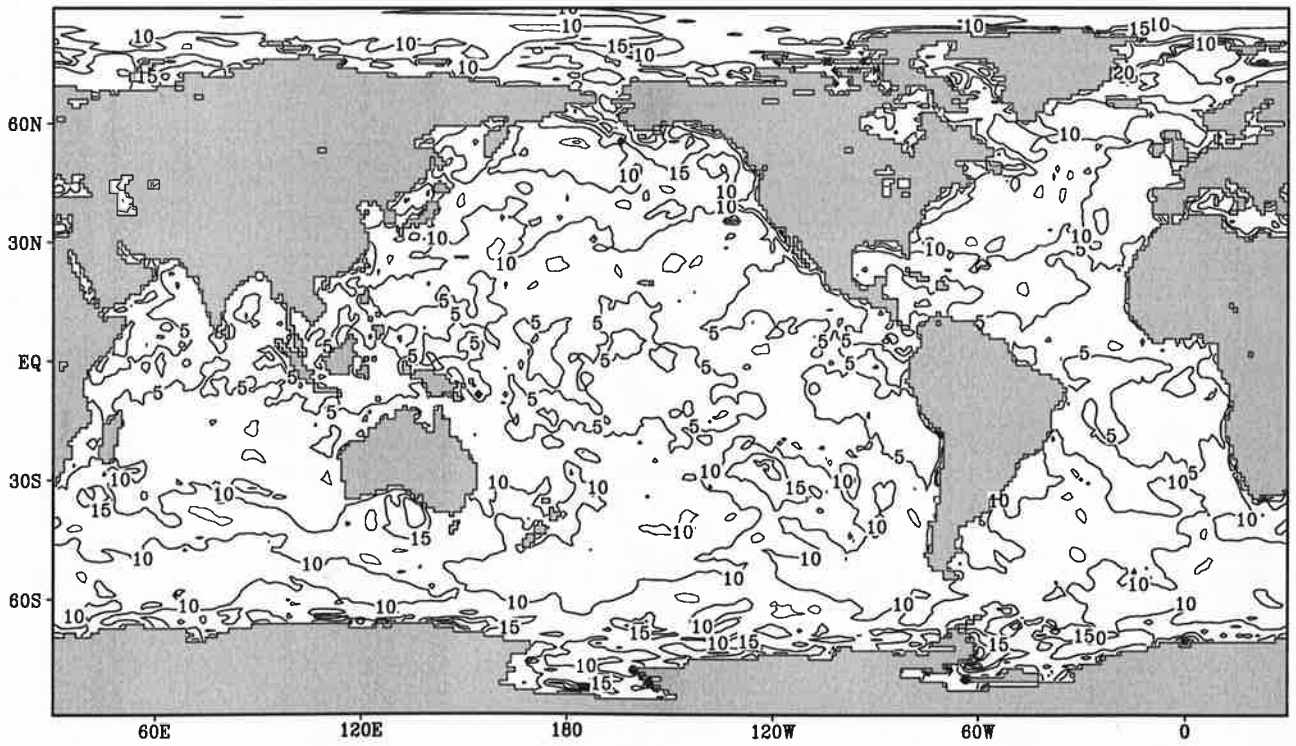

Contour interval: 5 10^{-5}

Fig.12.5 Transfer coefficient for latent heat flux May

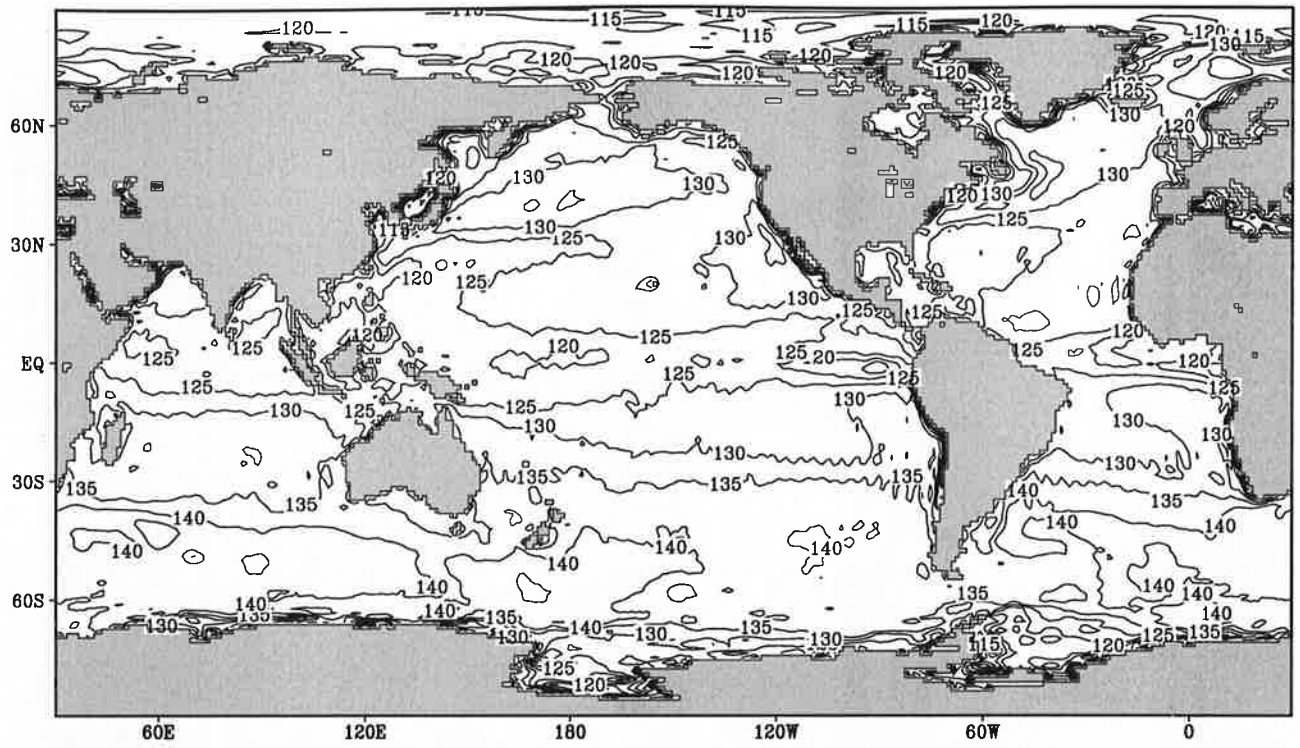

Contour interval: 5 10^{-5}

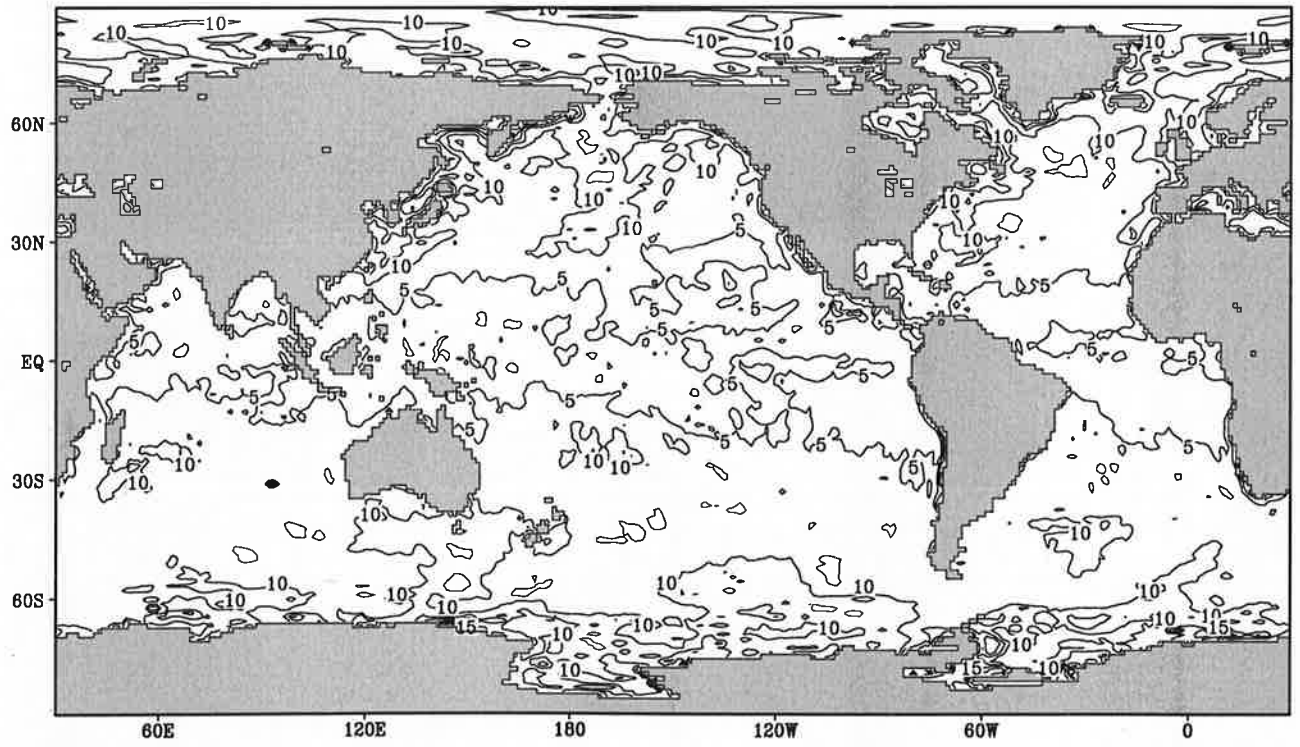

Contour interval: 5 10^{-5}

Fig.12.6 Transfer coefficient for latent heat flux June

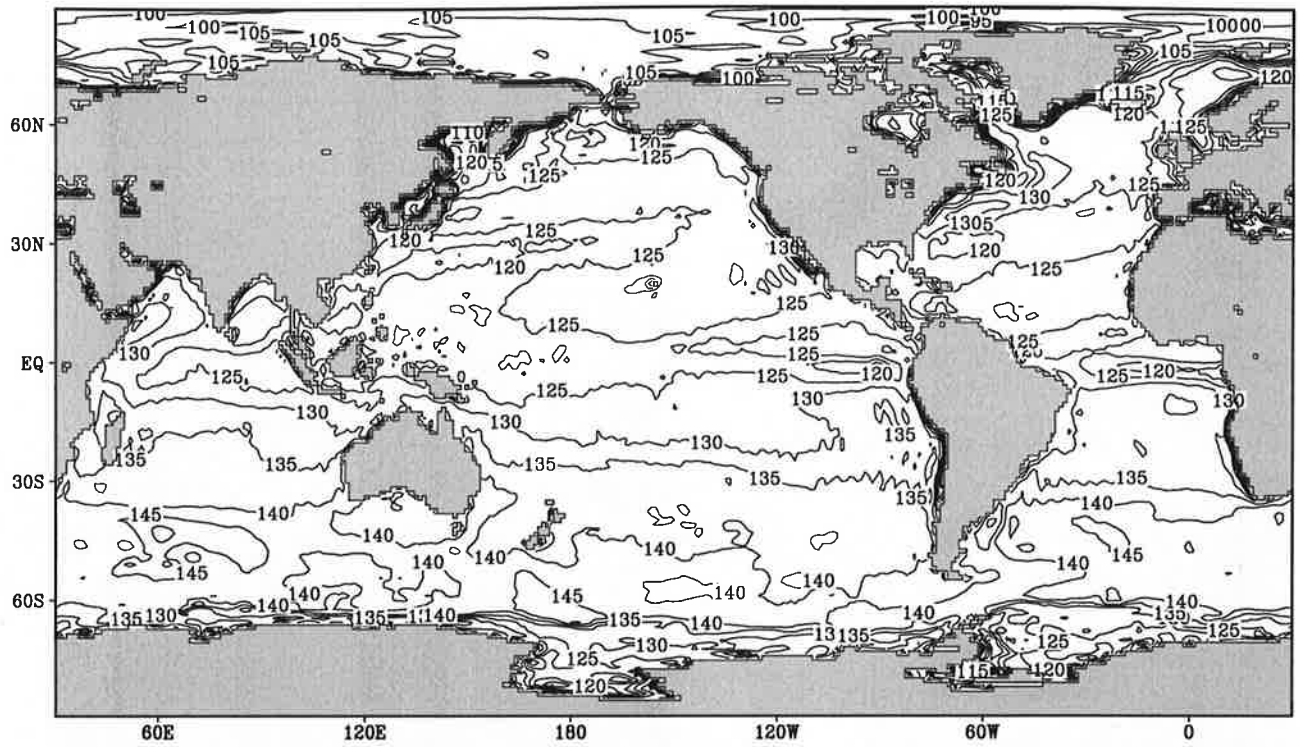

Contour interval: 5 10^{-5}

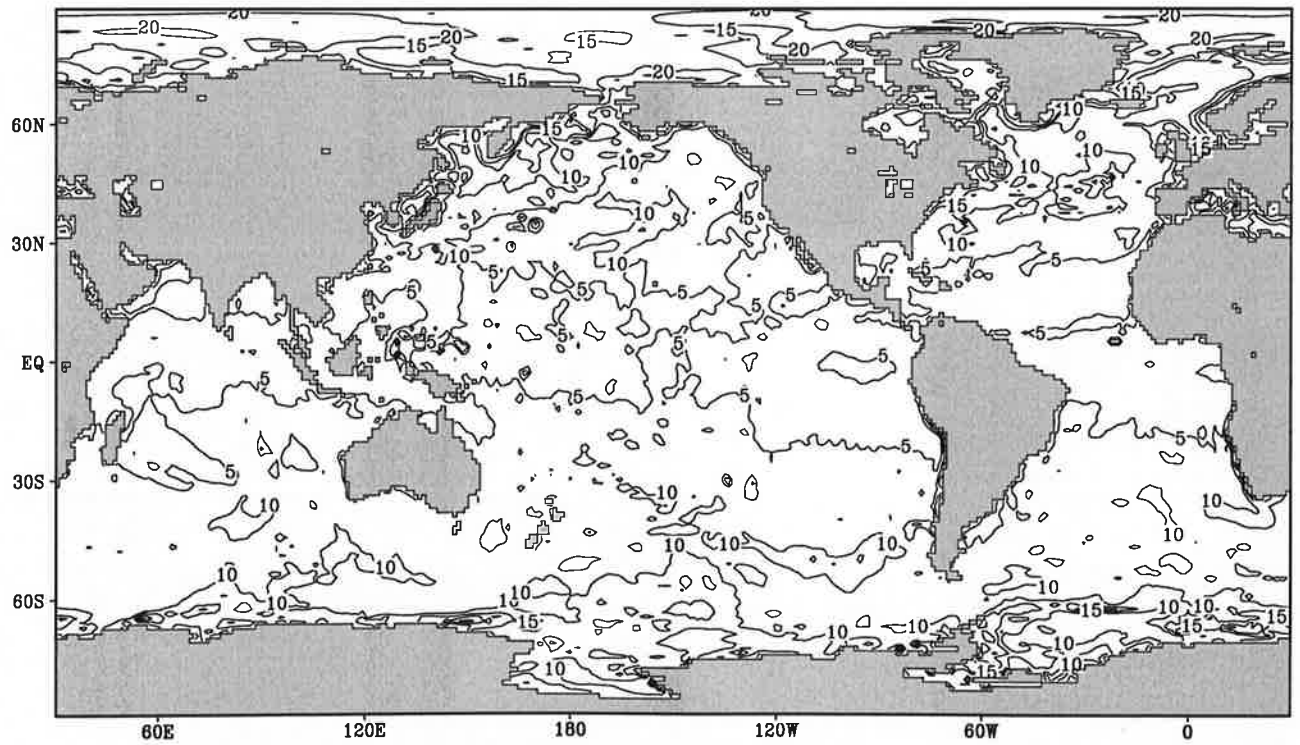

Contour interval: 5 10^{-5}

Fig.12.7 Transfer coefficient for latent heat flux July

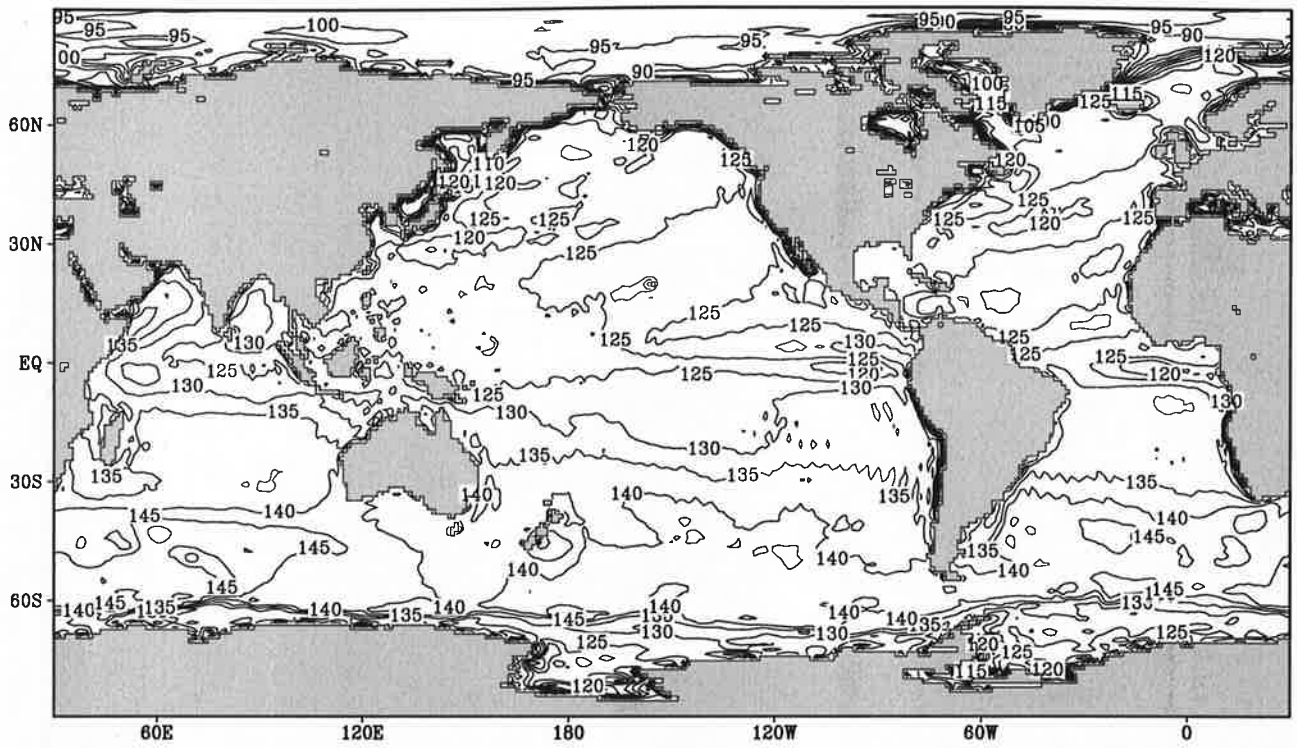

Contour interval: 5 10^{-5}

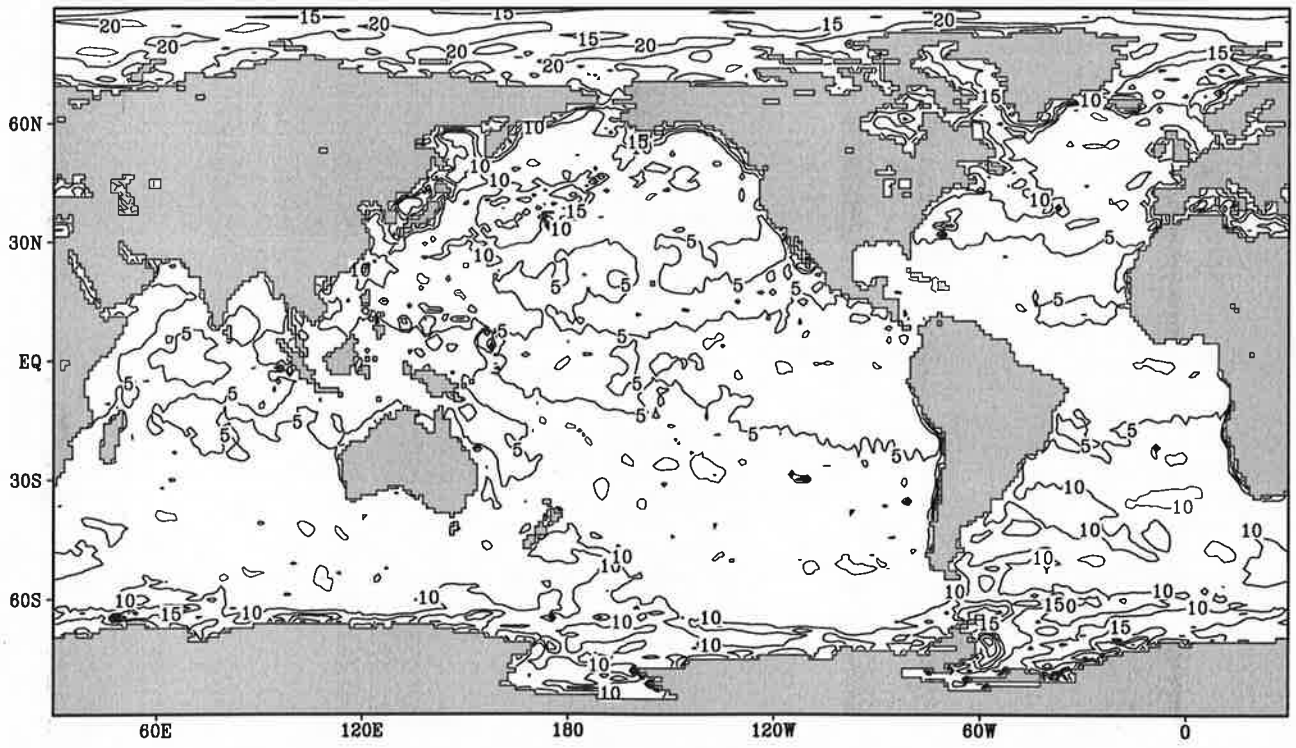

Contour interval: 5 10^{-5}

Fig.12.8 Transfer coefficient for latent heat flux August

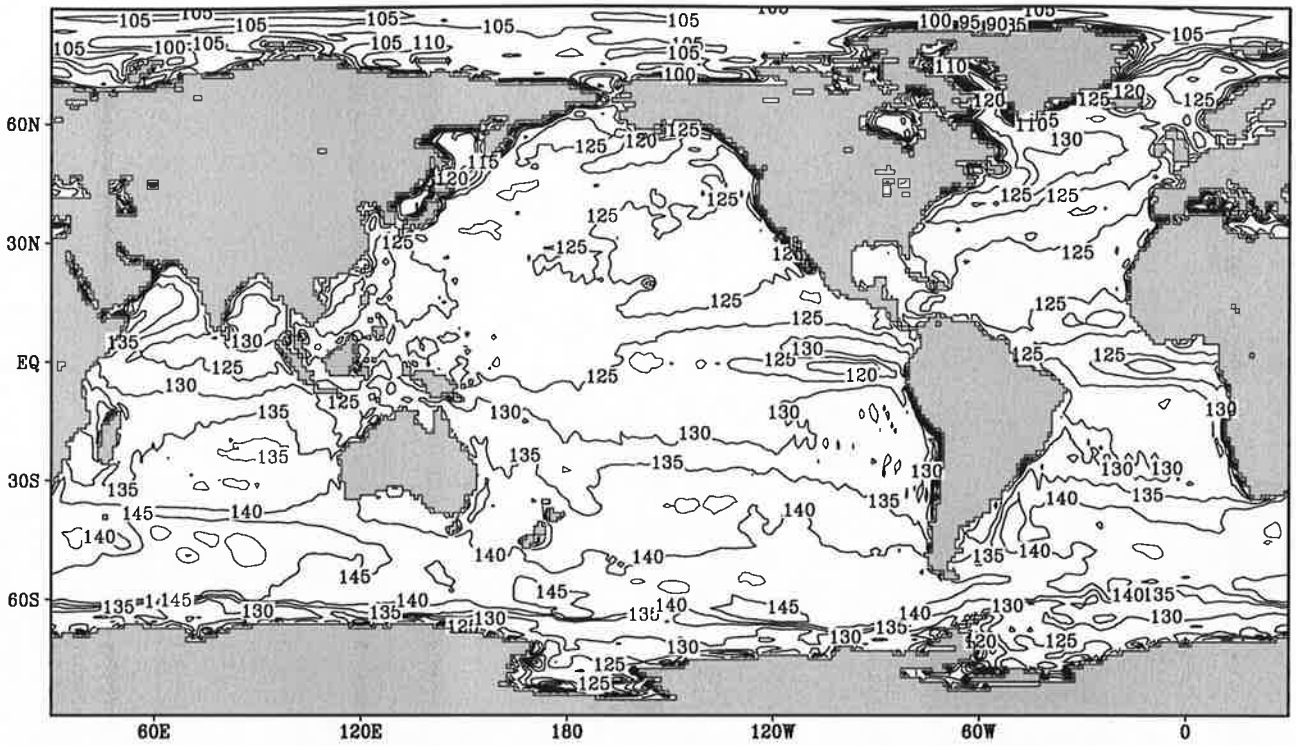

Contour interval: 5 10^{-5}

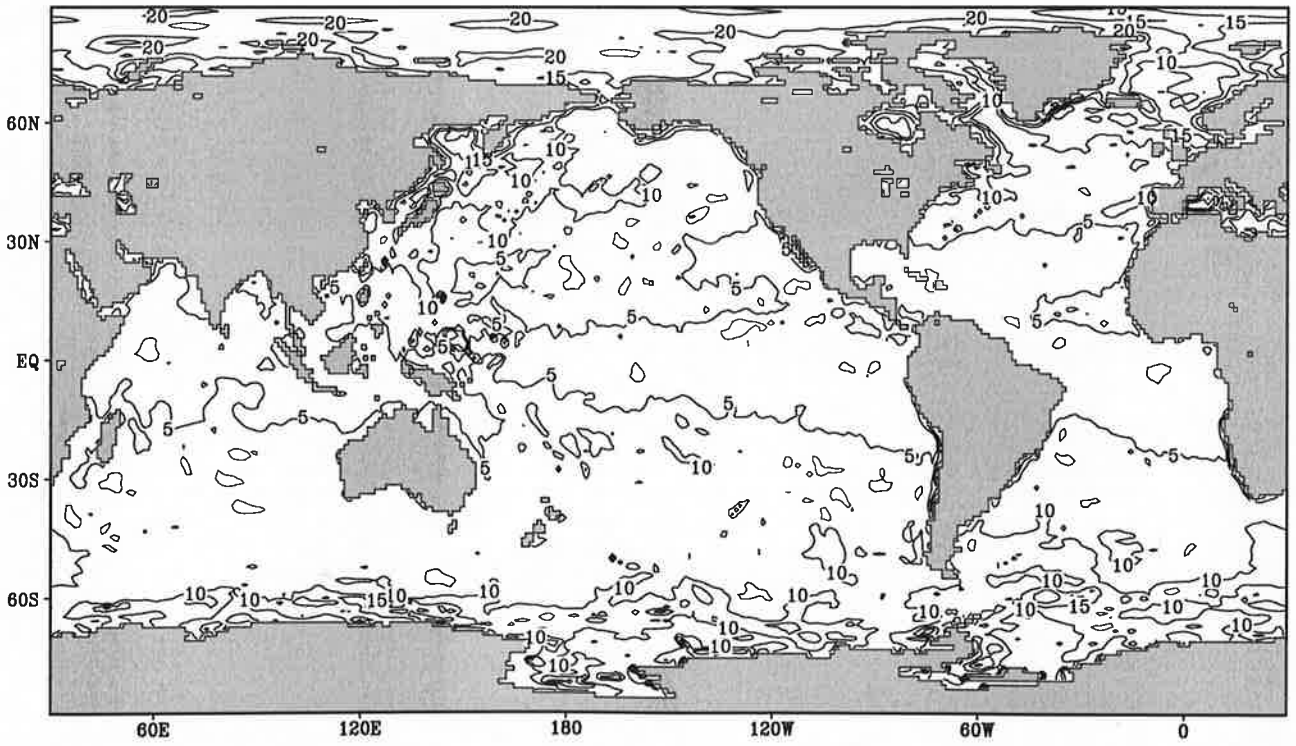

Contour interval: 5 10^{-5}

Fig.12.9 Transfer coefficient for latent heat flux September

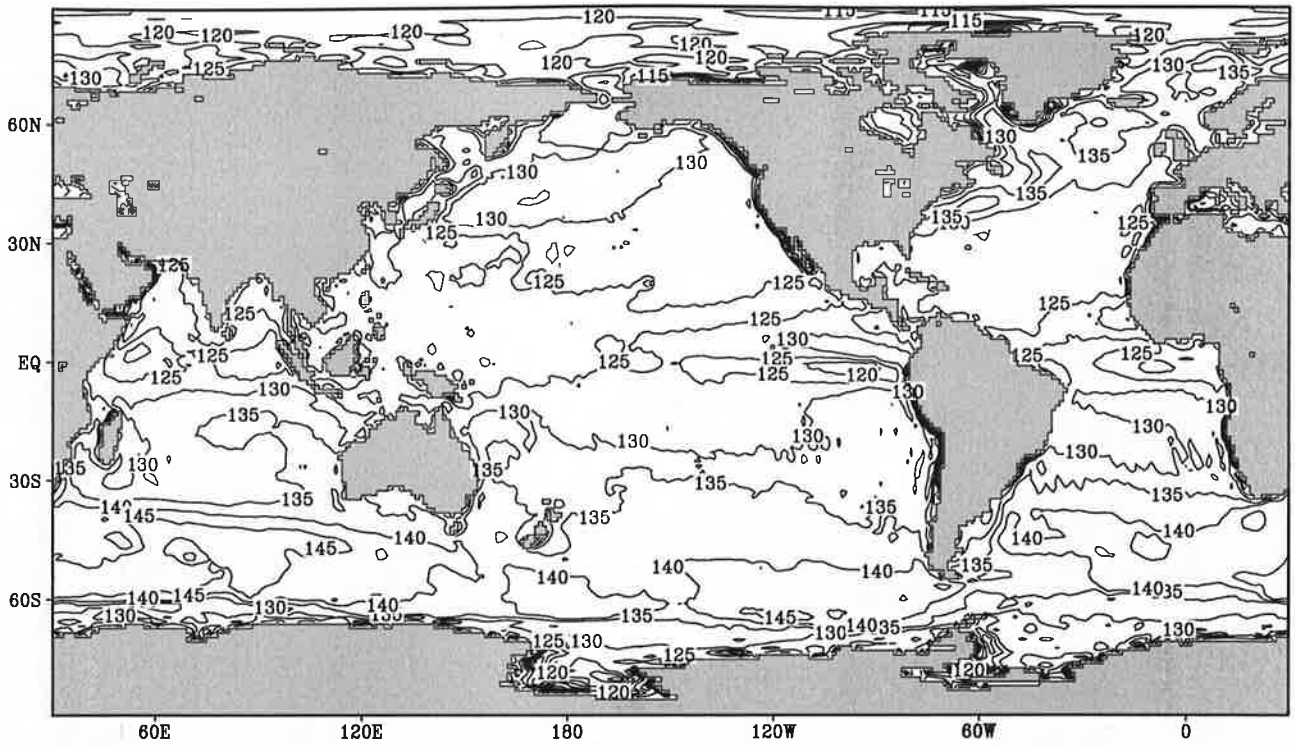

Contour interval: 5 10^{-5}

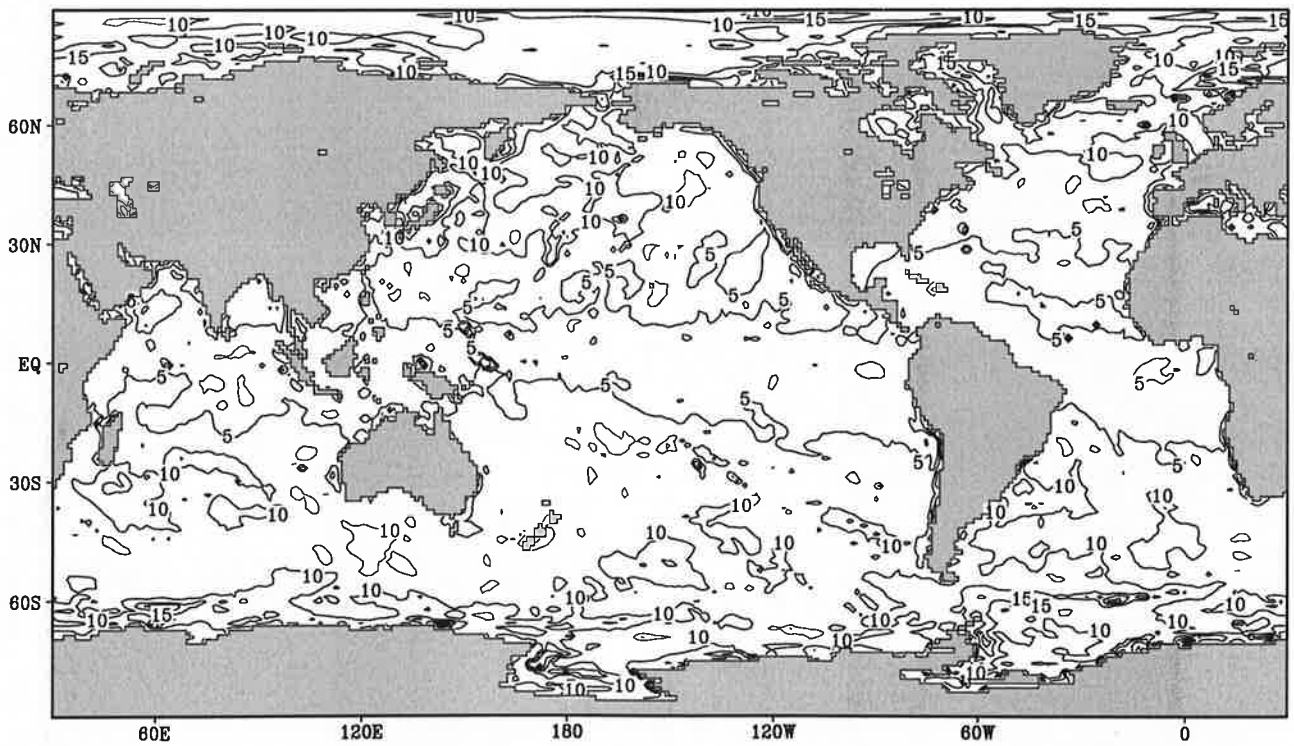

Contour interval: 5 10^{-5}

Fig.12.10 Transfer coefficient for latent heat flux October

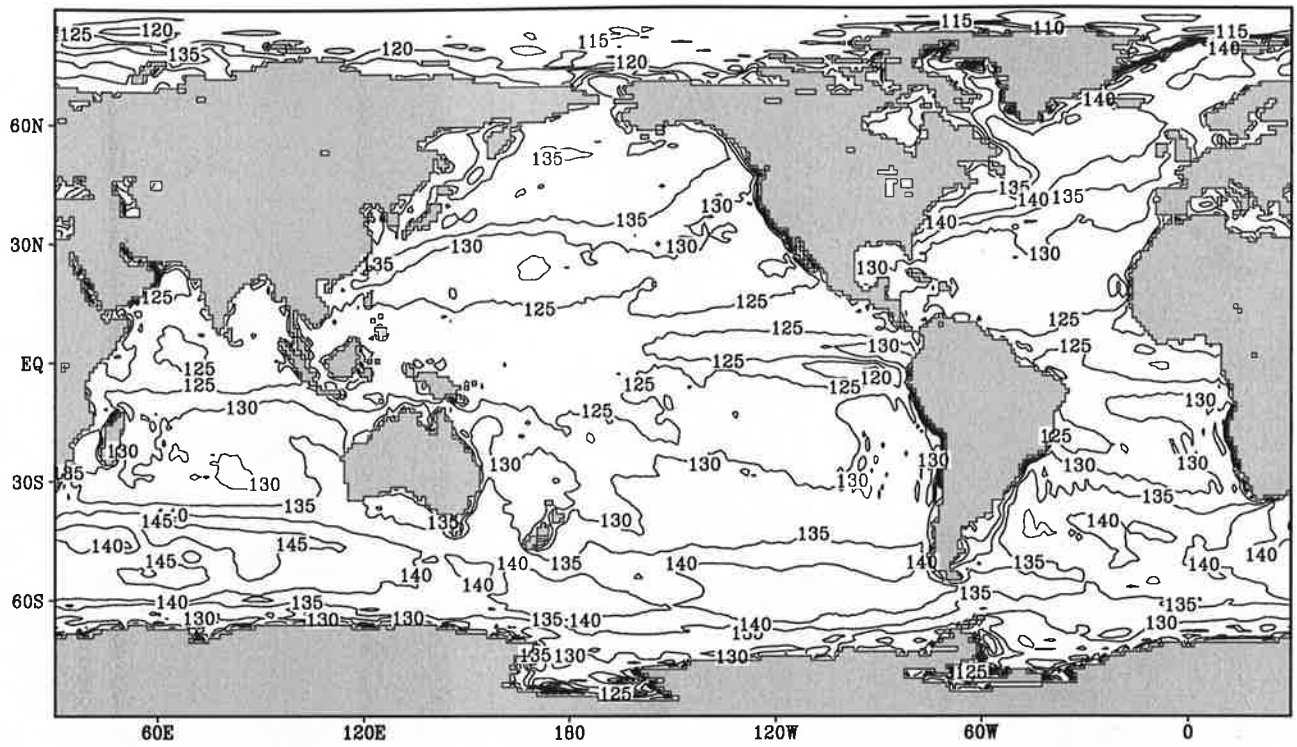

Contour interval: 5 10^{-5}

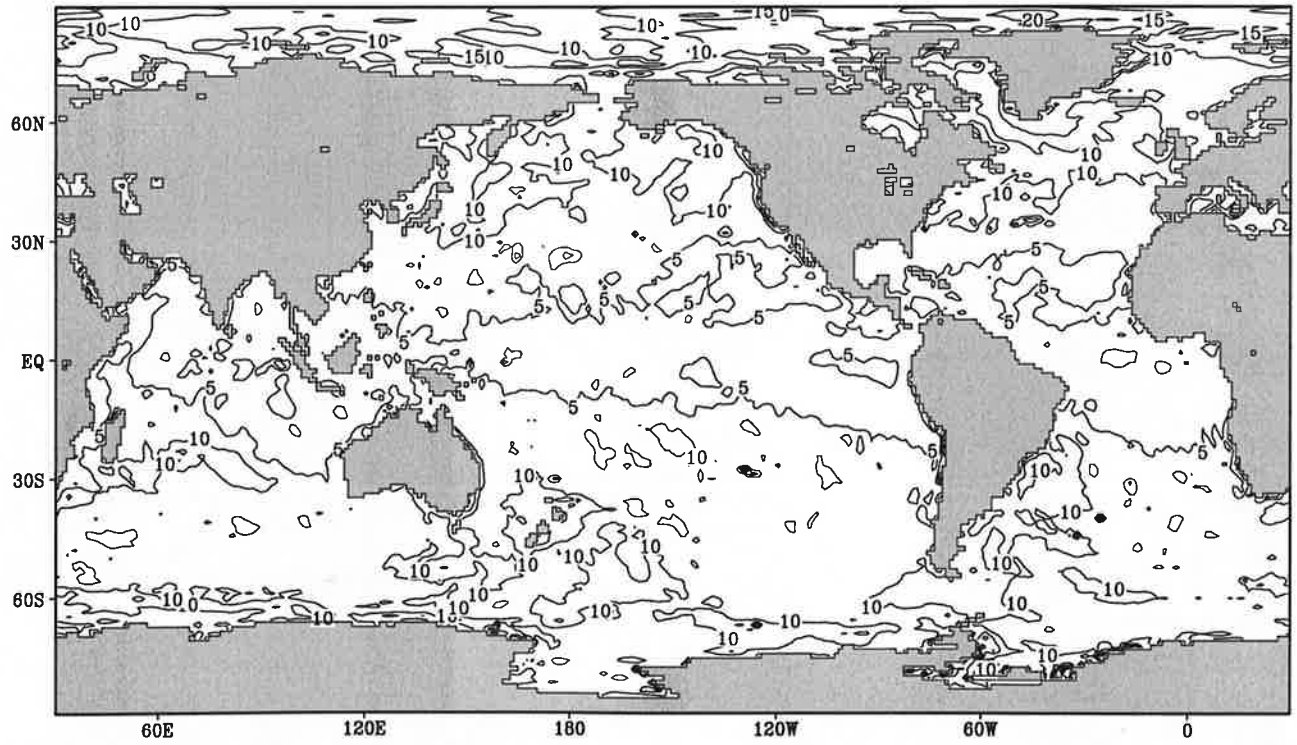

Contour interval: 5 10^{-5}

Fig.12.11 Transfer coefficient for latent heat flux November

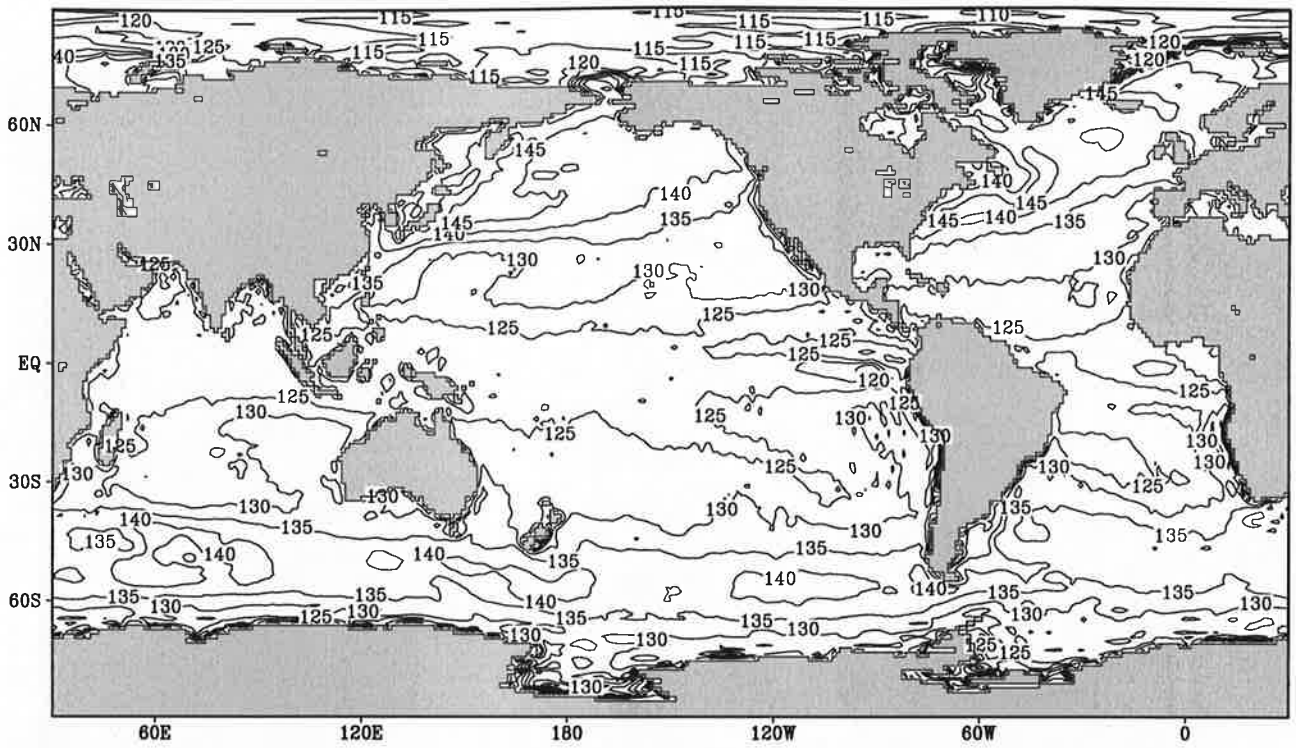

Contour interval: 5 10^{-6}

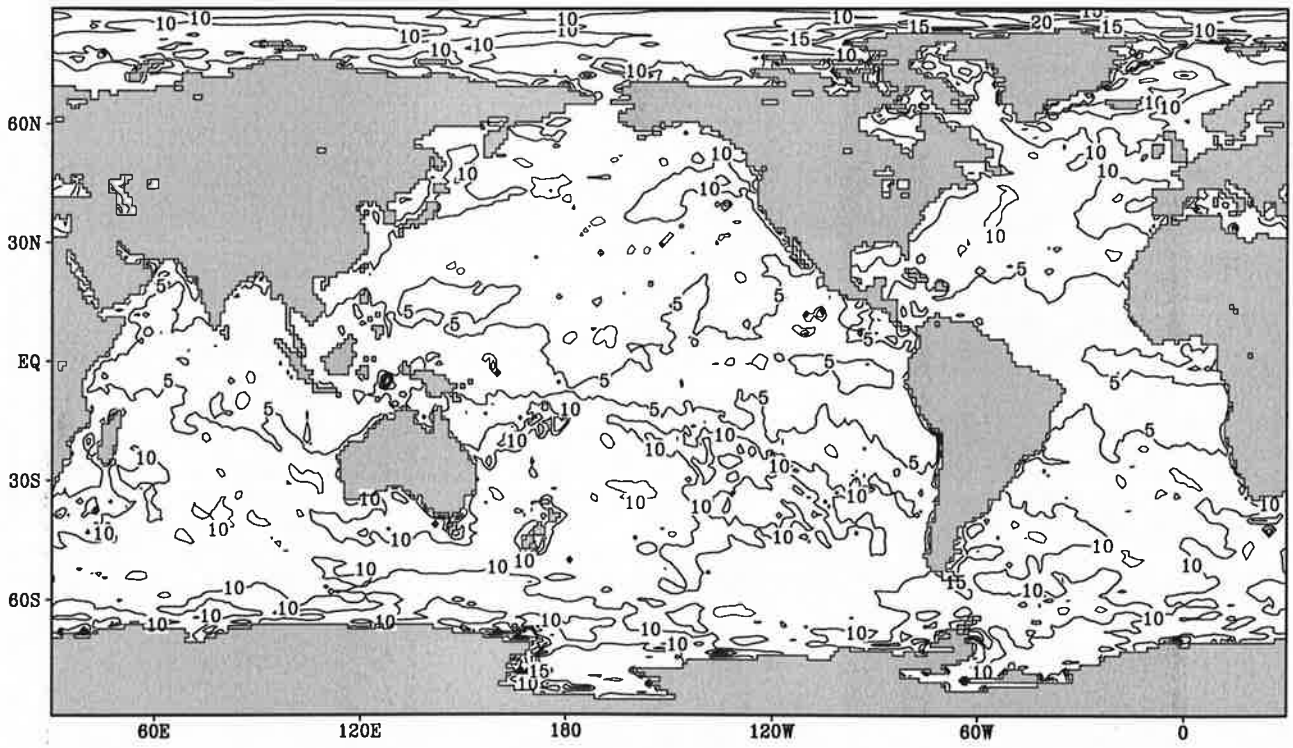

Contour interval: 5 10^{-6}

Fig.12.12 Transfer coefficient for latent heat flux December

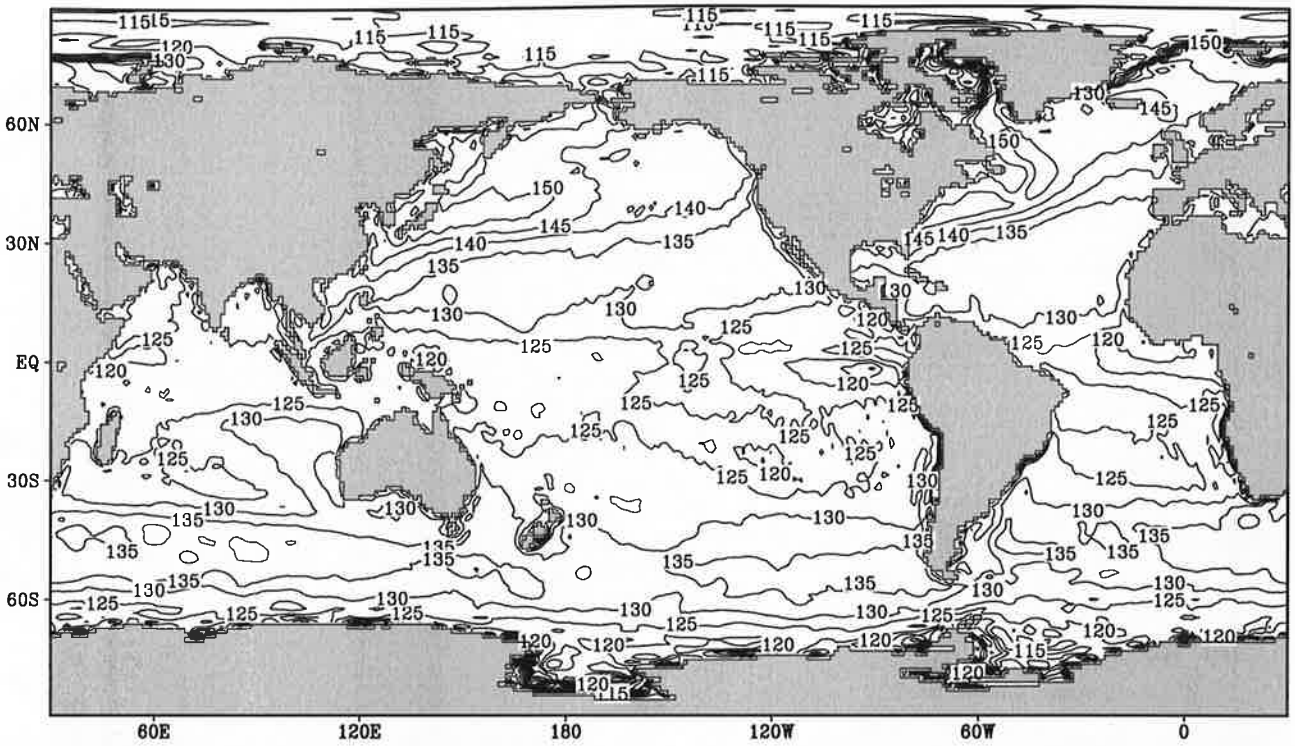

Contour interval: 5 10^{-5}

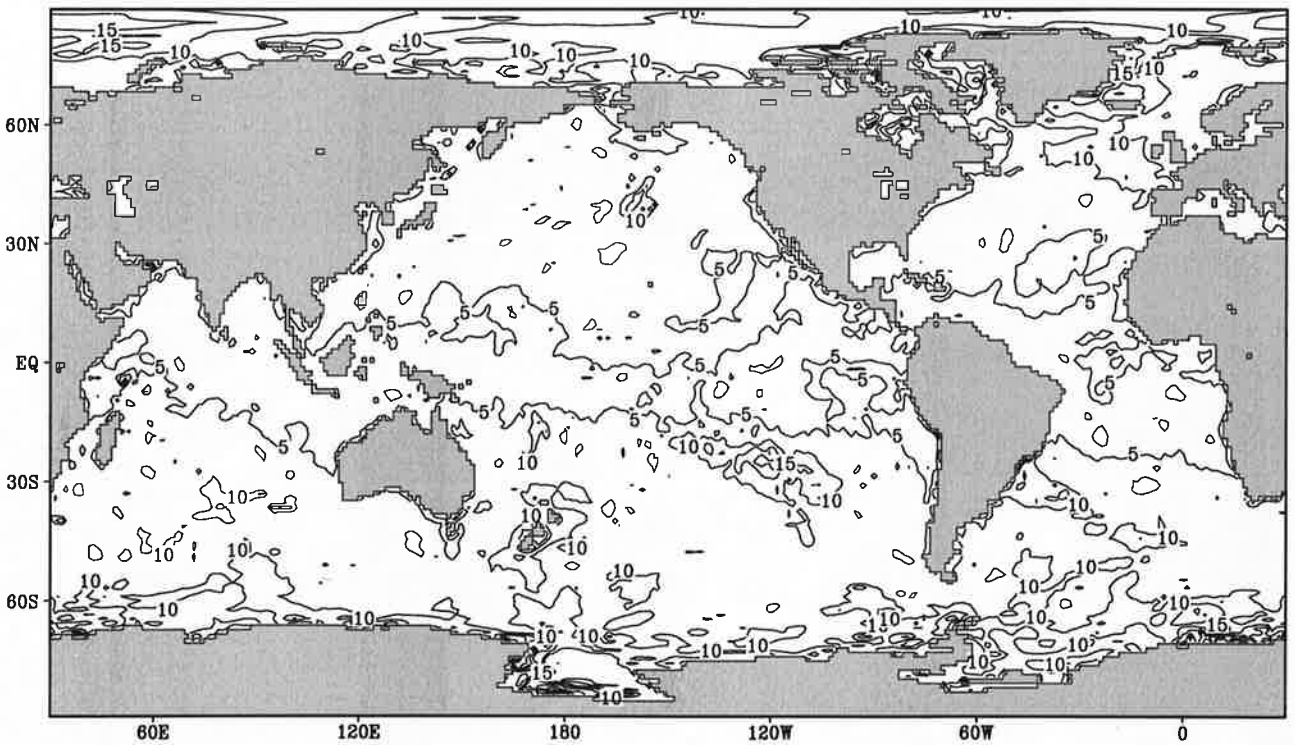

Contour interval: 5 10^{-5}

Fig.12.13 Transfer coefficient for latent heat flux Annual Mean

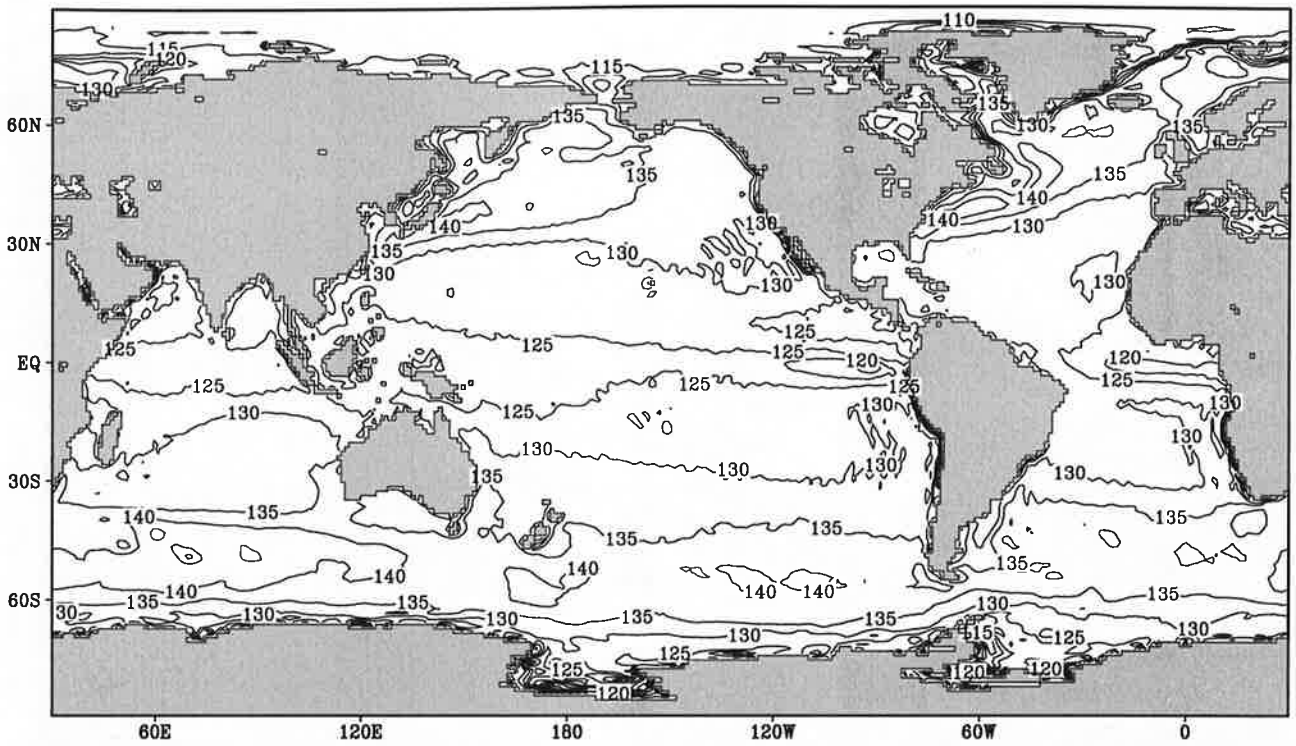

Contour interval: 5 10^{-5}

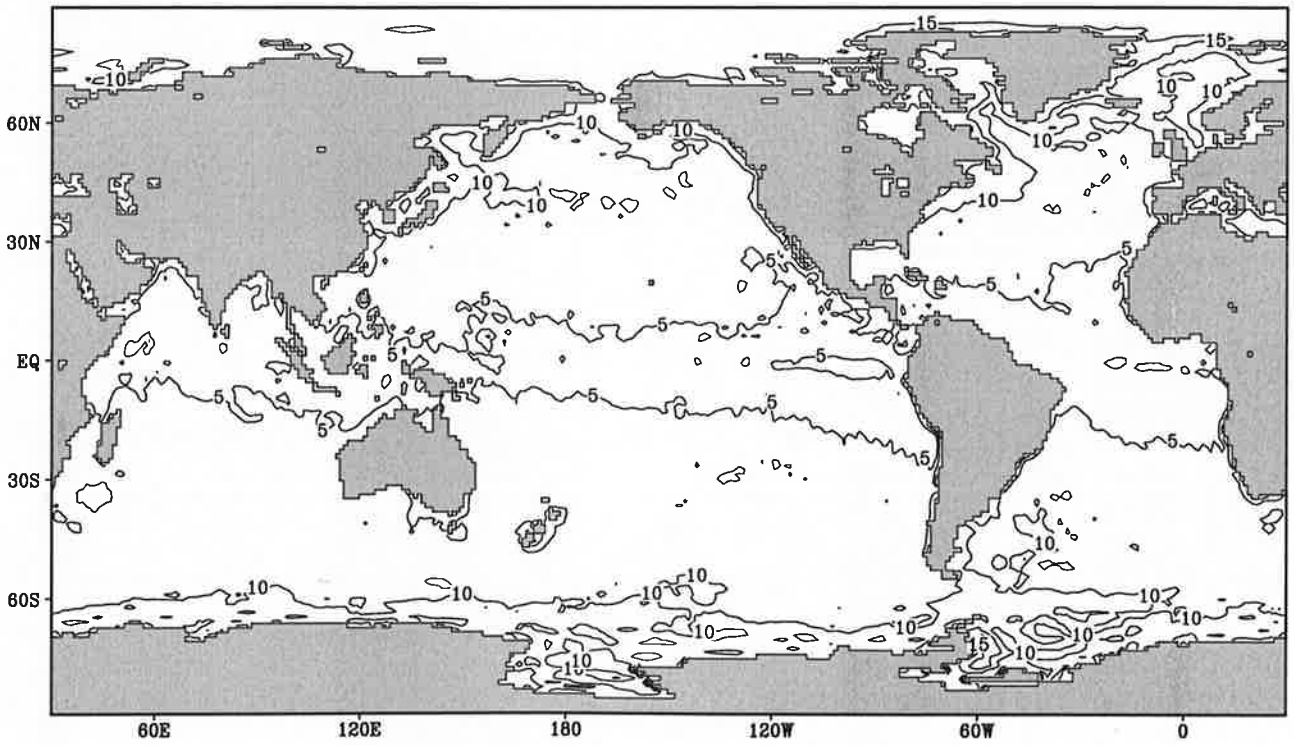

Contour interval: 5 10^{-5}

Fig.13.1 Wind stress January

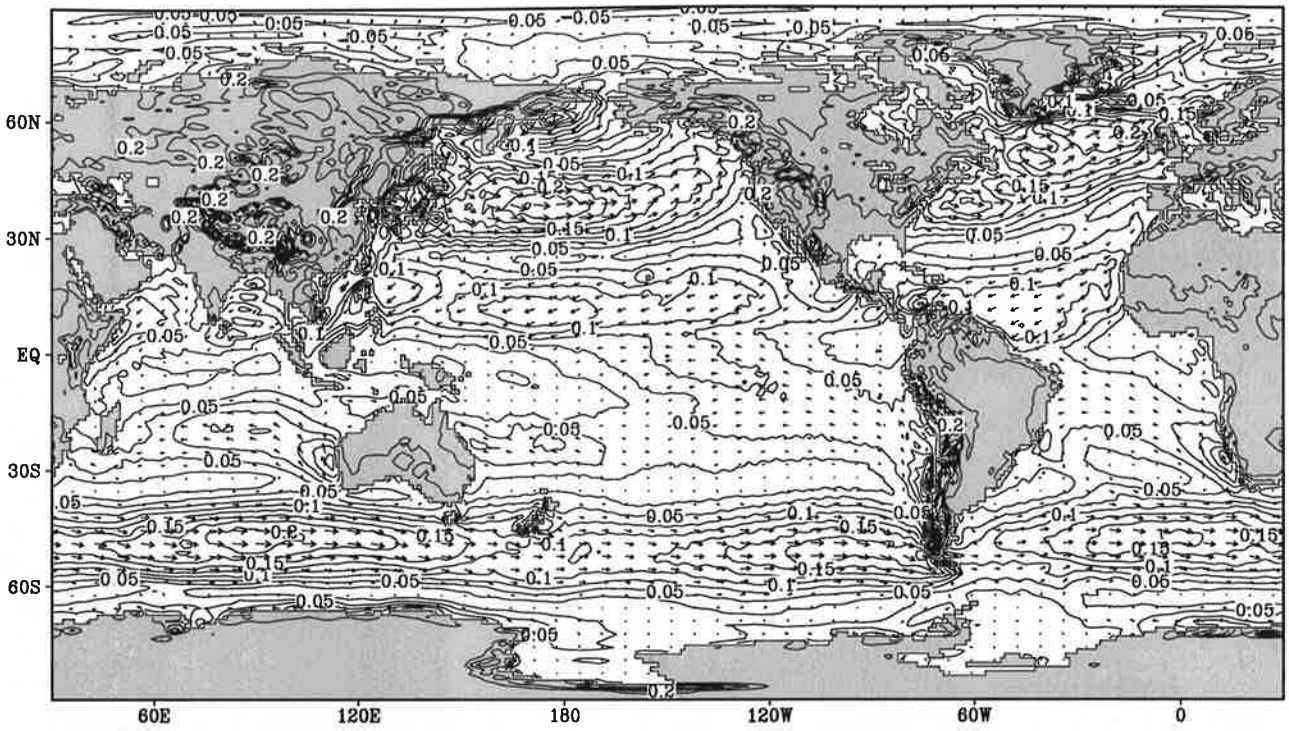

Contour interval ocean: 0.025, land: 0.1 $\vec{0.25}$

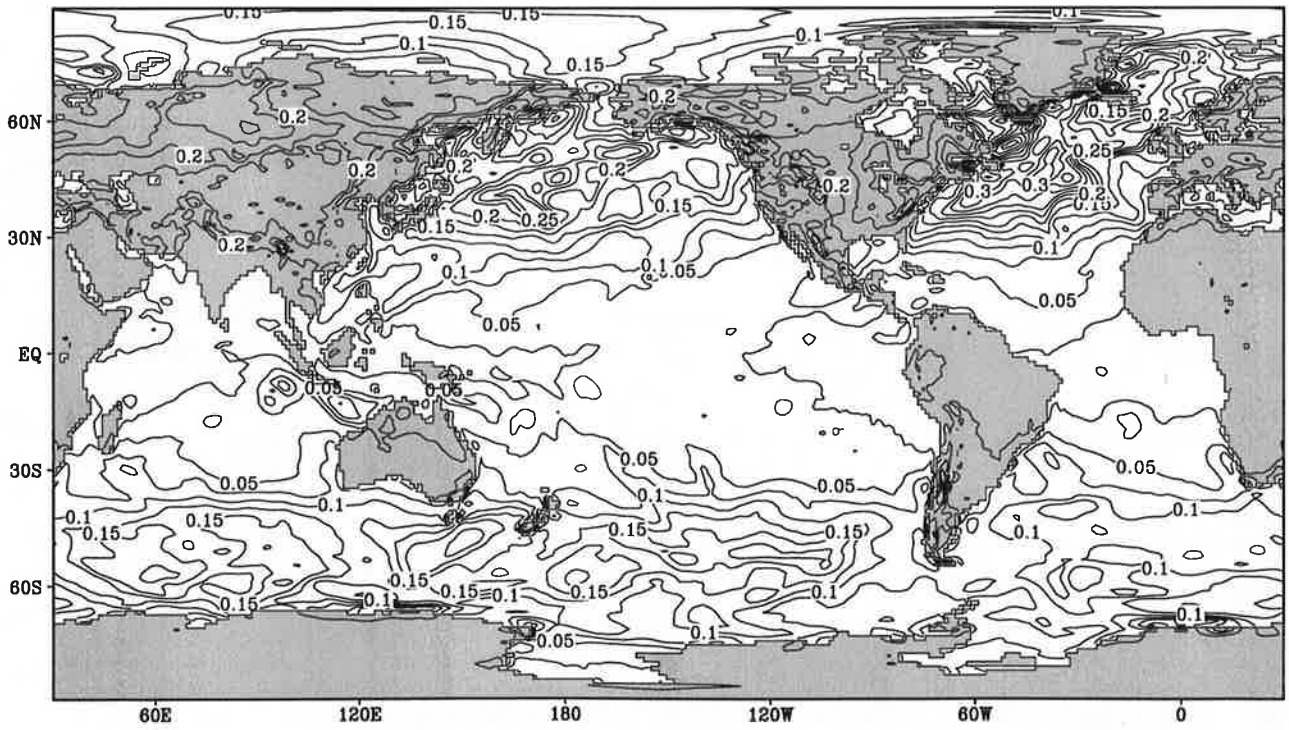

Contour interval ocean: 0.025, land: 0.1

Fig.13.2 Wind stress February

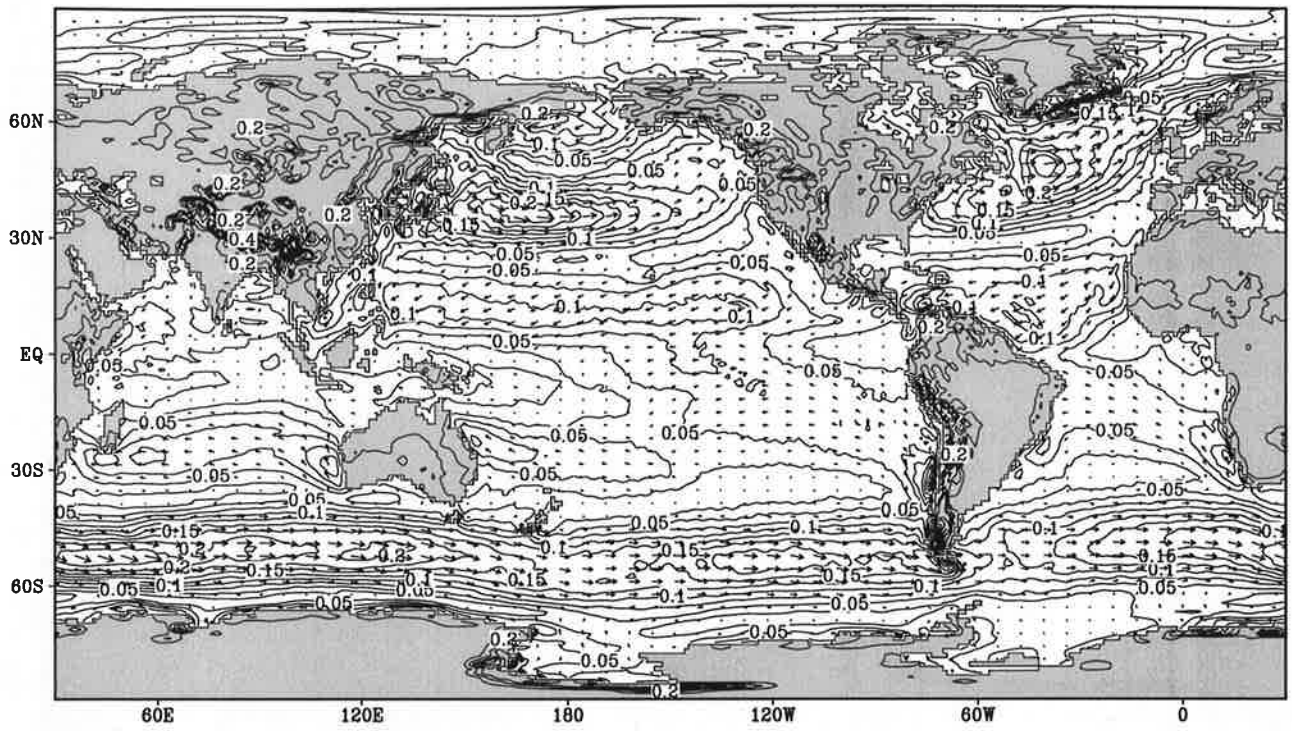

Contour interval ocean: 0.025, land: 0.1 $\vec{0.25}$

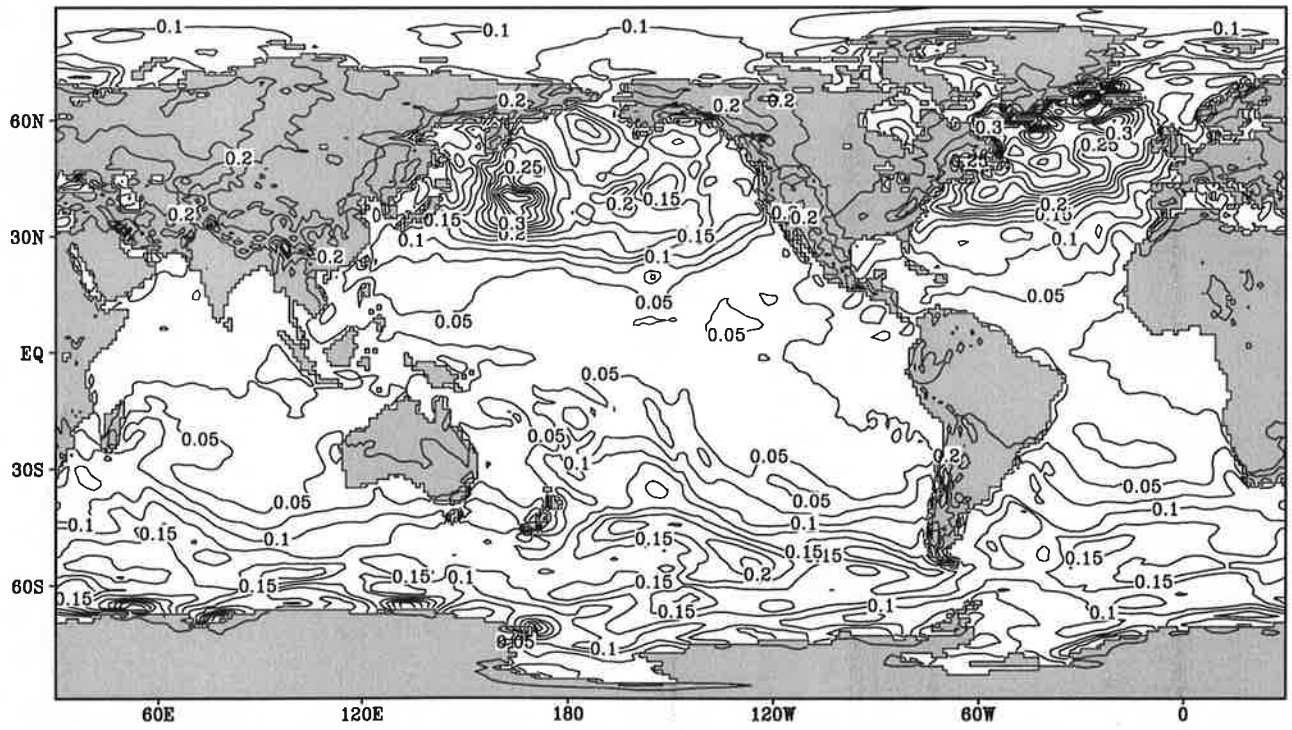

Contour interval ocean: 0.025, land: 0.1

Fig.13.3 Wind stress March

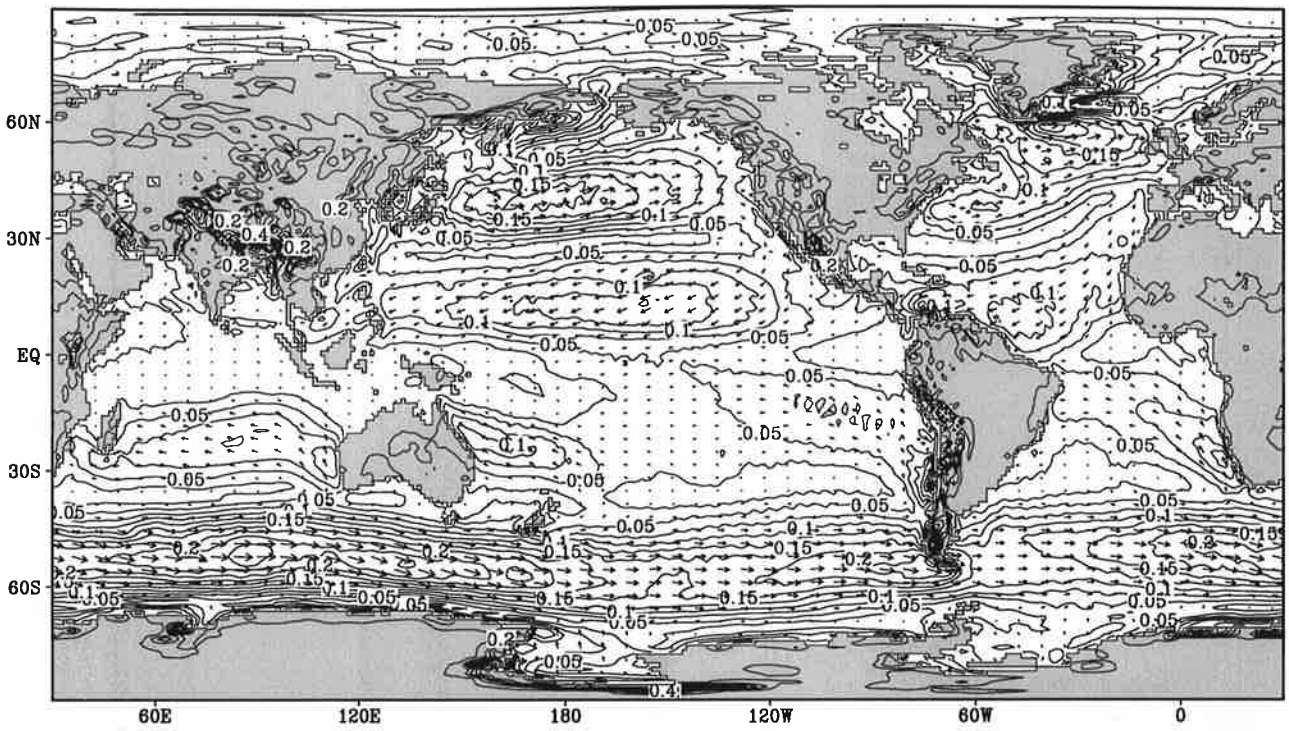

Contour interval ocean: 0.025, land: 0.1 $\vec{0.25}$

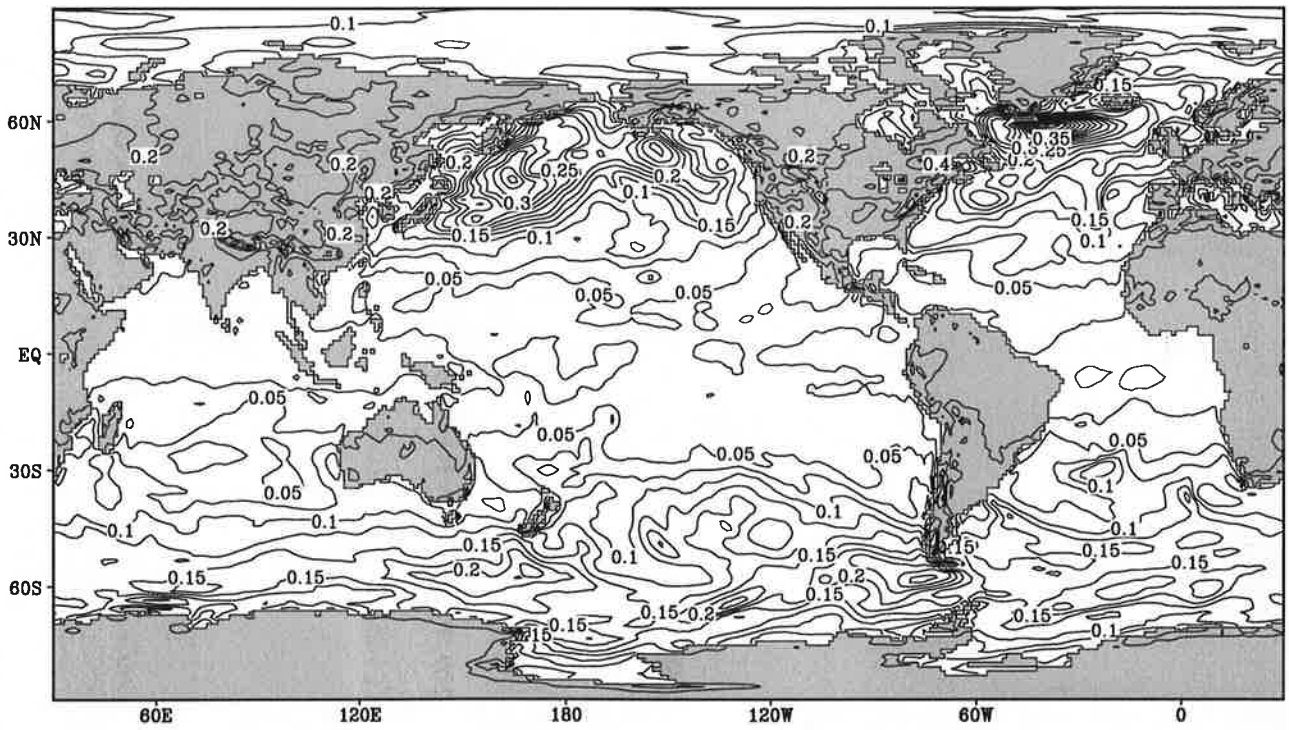

Contour interval ocean: 0.025, land: 0.1

Fig.13.4 Wind stress April

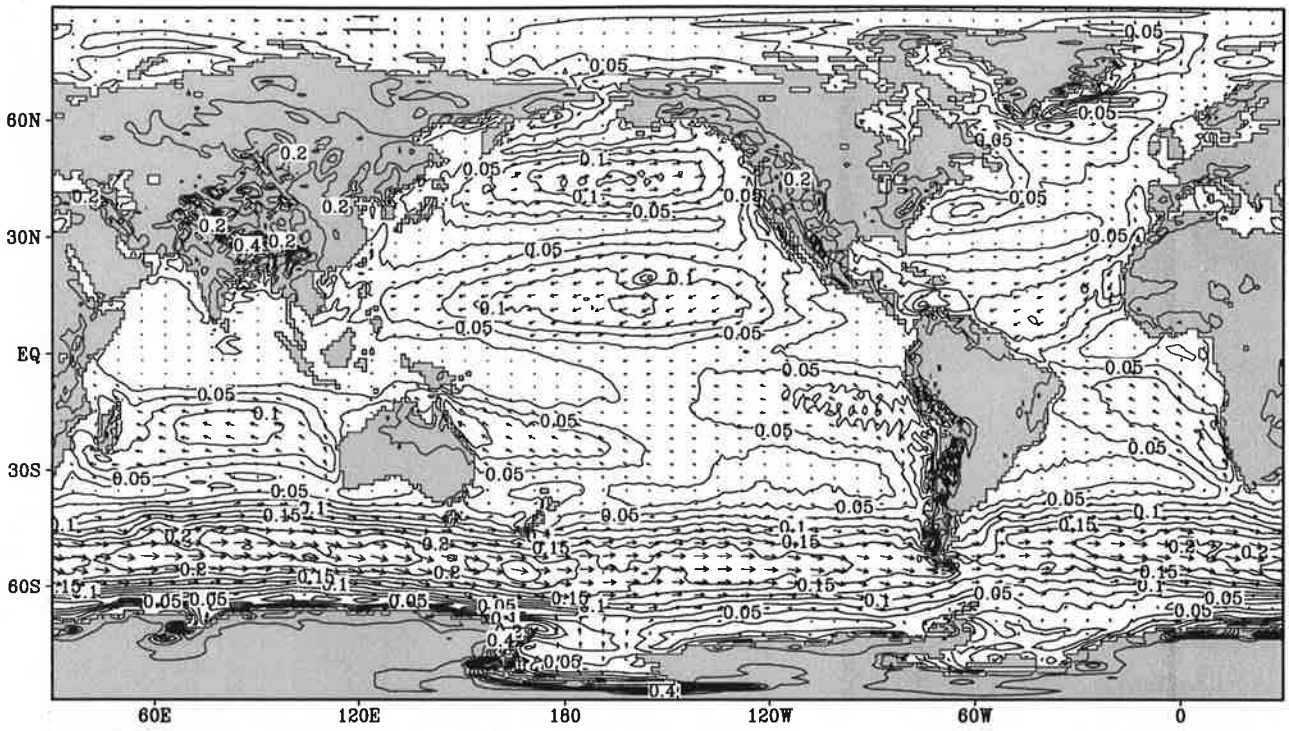

Contour interval ocean: 0.025, land: 0.1 $\vec{0.25}$

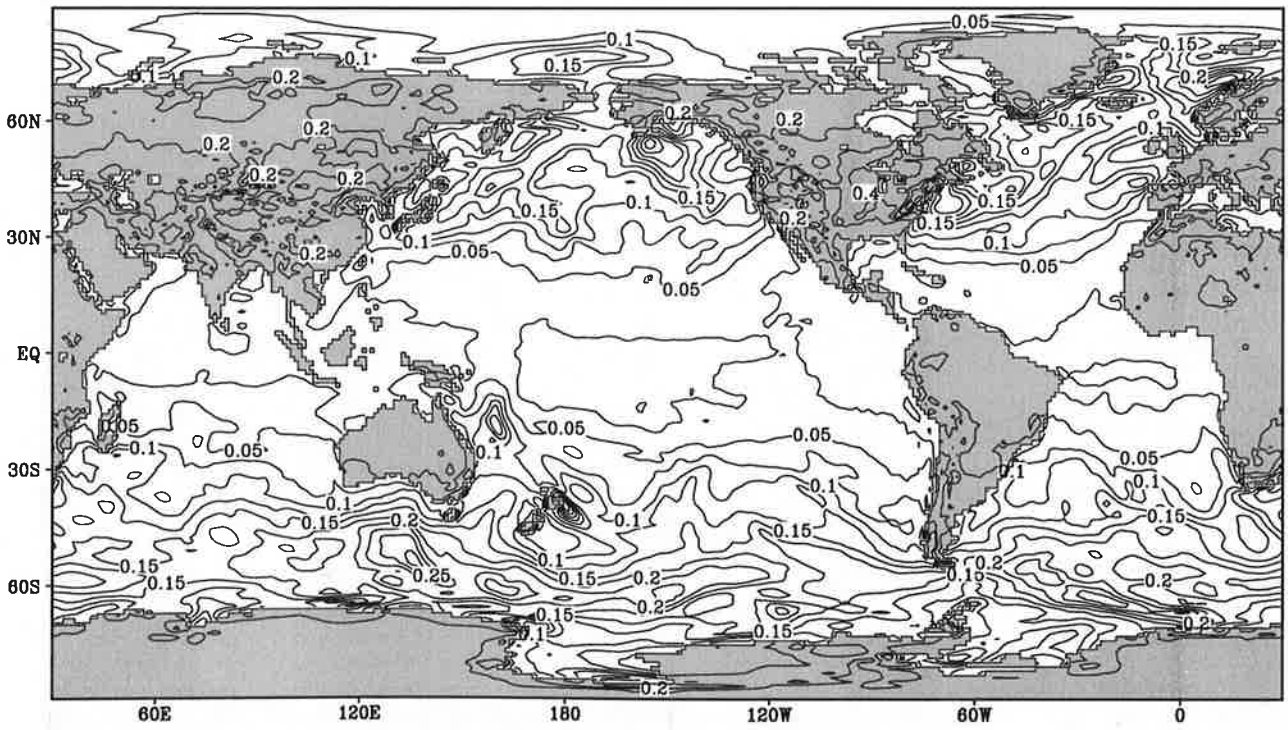

Contour interval ocean: 0.025, land: 0.1

Fig.13.5 Wind stress May

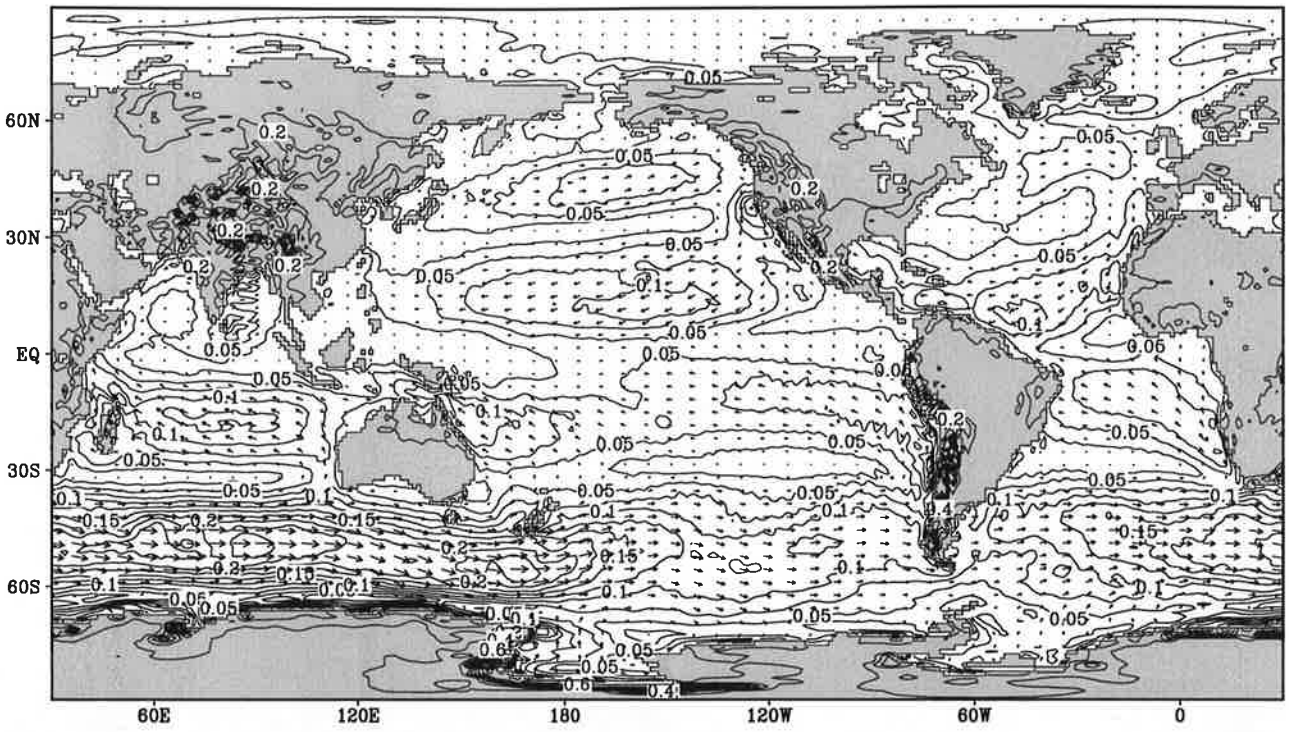

Contour interval ocean: 0.025, land: 0.1 $\vec{0.25}$

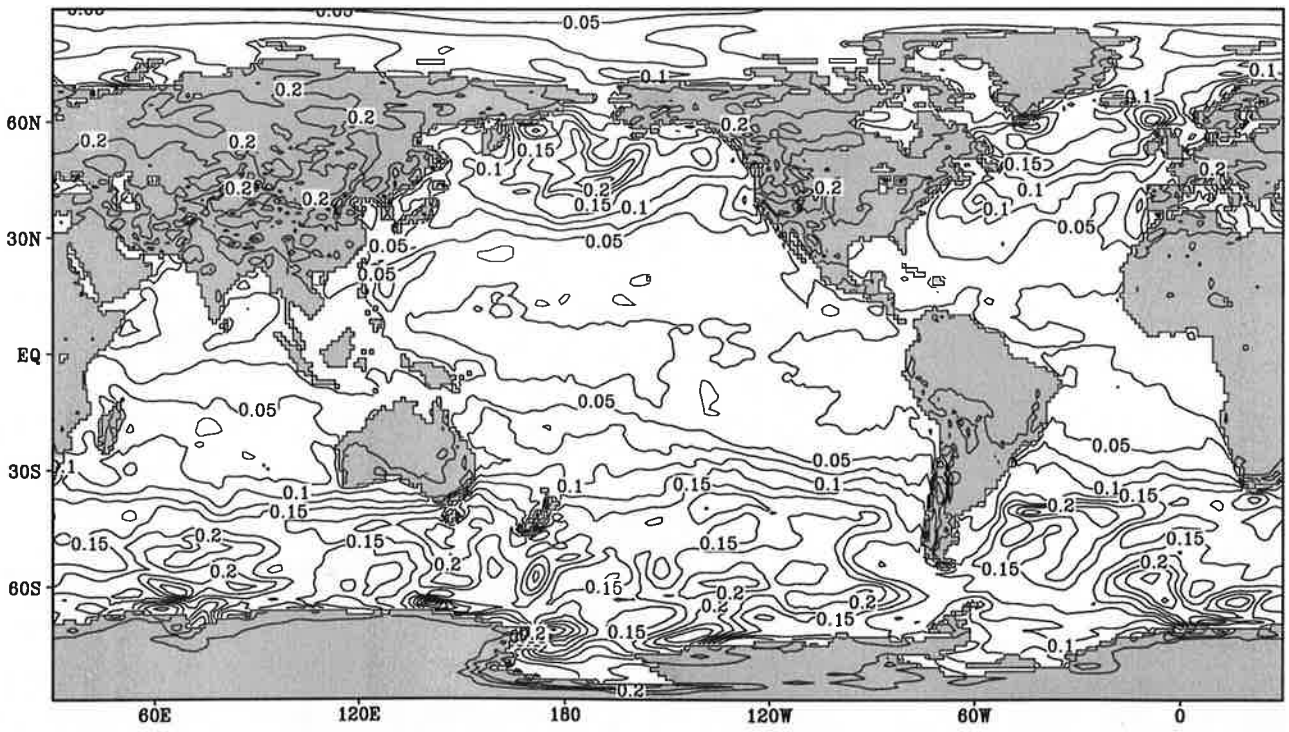

Contour interval ocean: 0.025, land: 0.1

Fig.13.6 Wind stress June

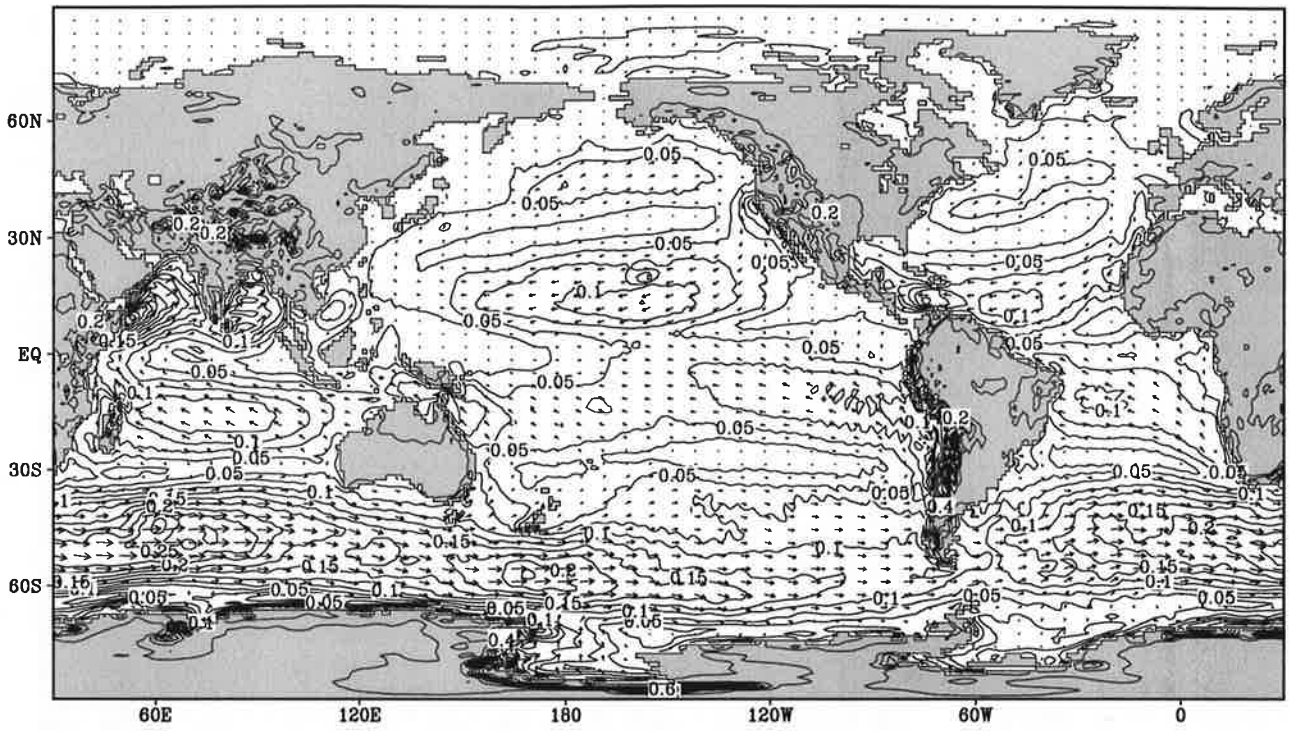

Contour interval ocean: 0.025, land: 0.1 $\vec{0.25}$

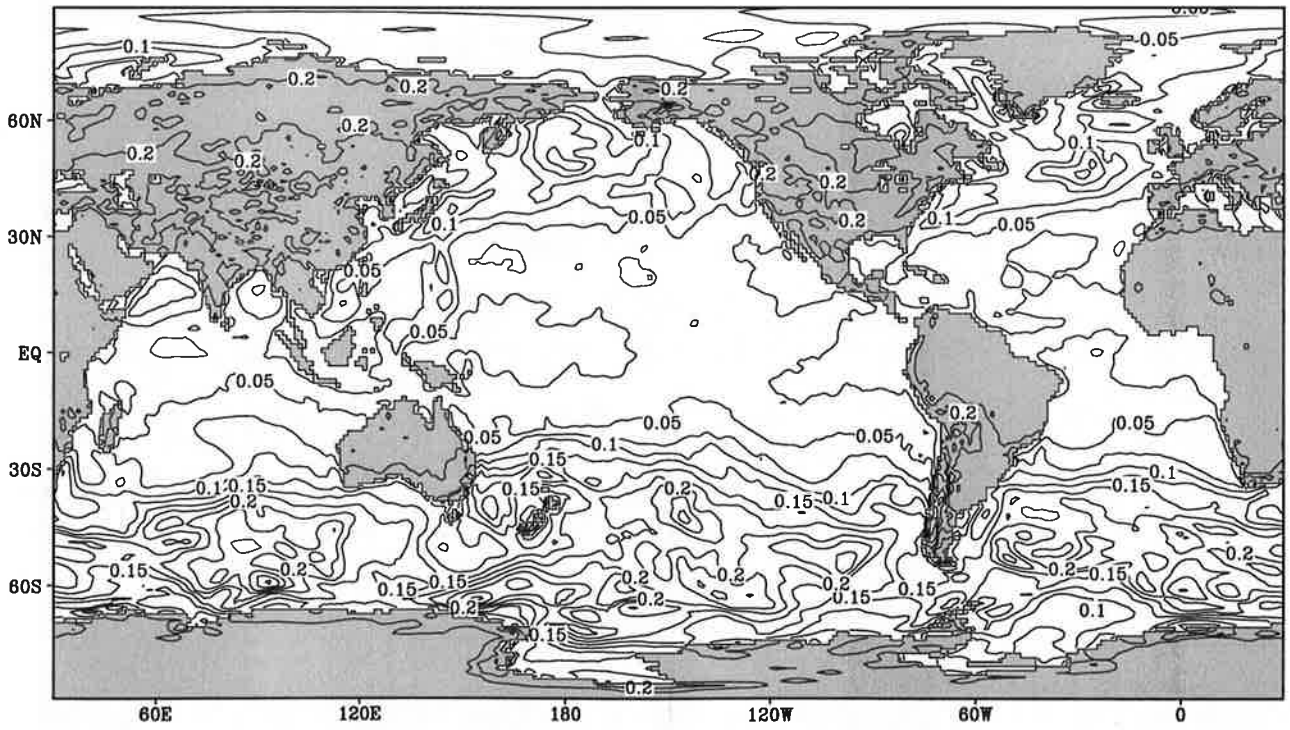

Contour interval ocean: 0.025, land: 0.1

Fig.13.7 Wind stress July

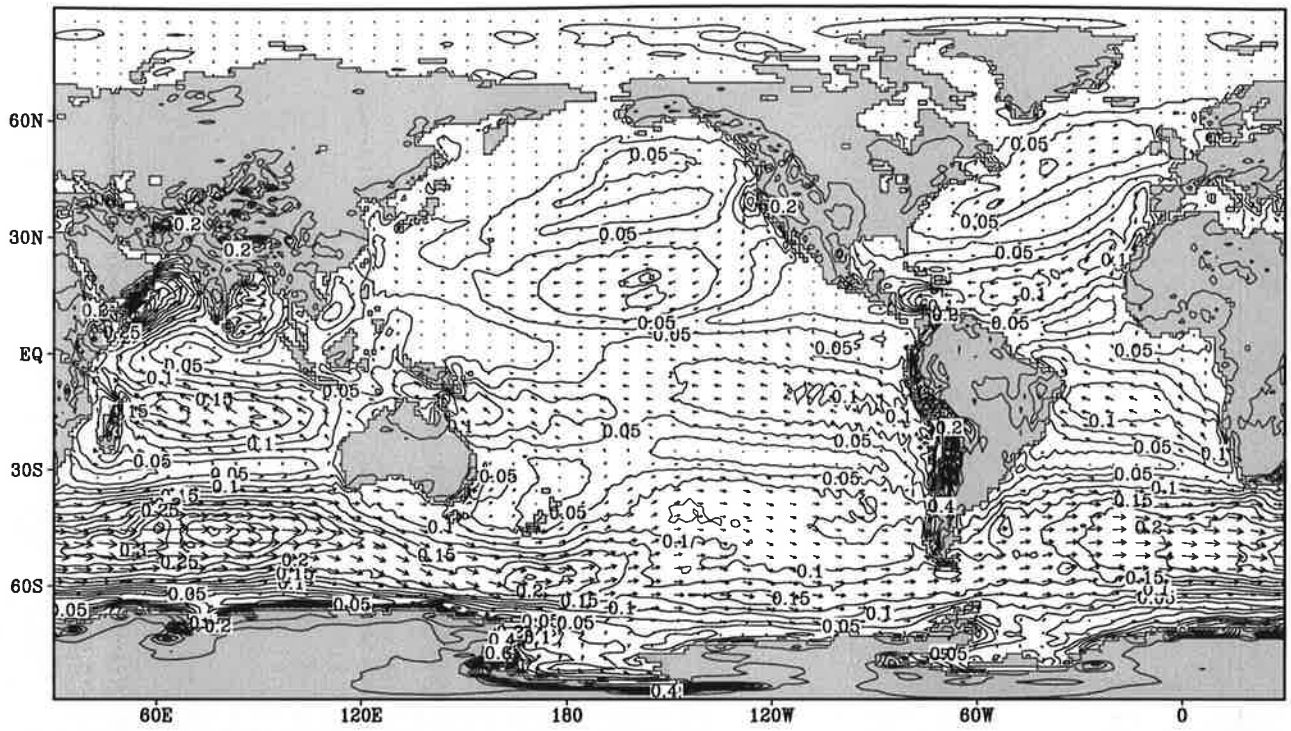

Contour interval ocean: 0.025, land: 0.1 $\vec{0.25}$

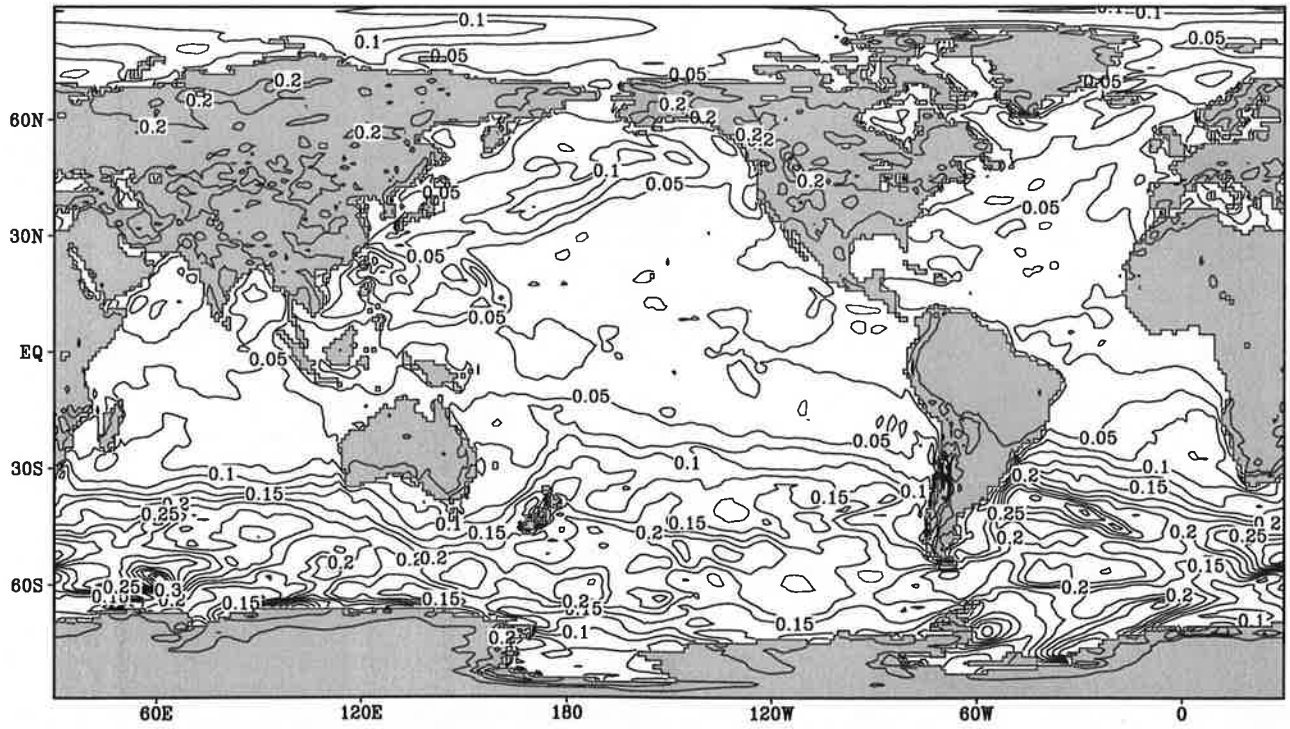

Contour interval ocean: 0.025, land: 0.1

Fig.13.8 Wind stress August

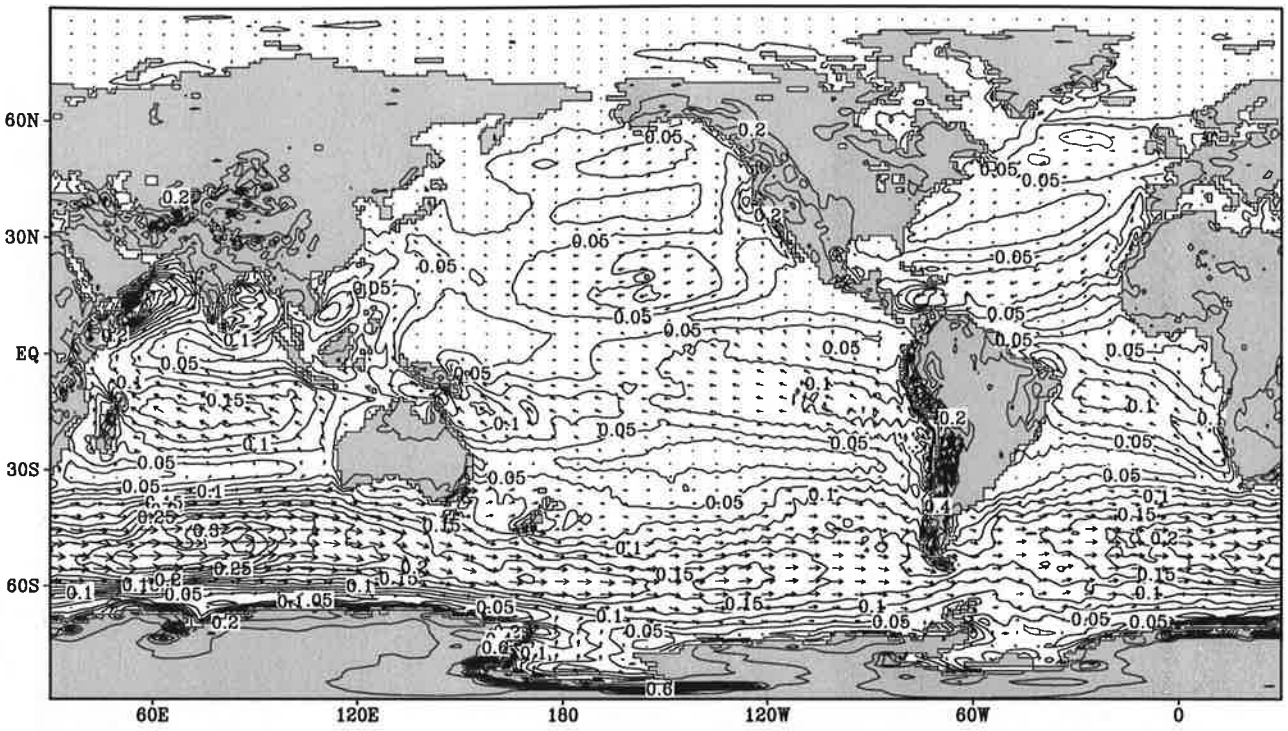

Contour interval ocean: 0.025, land: 0.1 $\vec{0.25}$

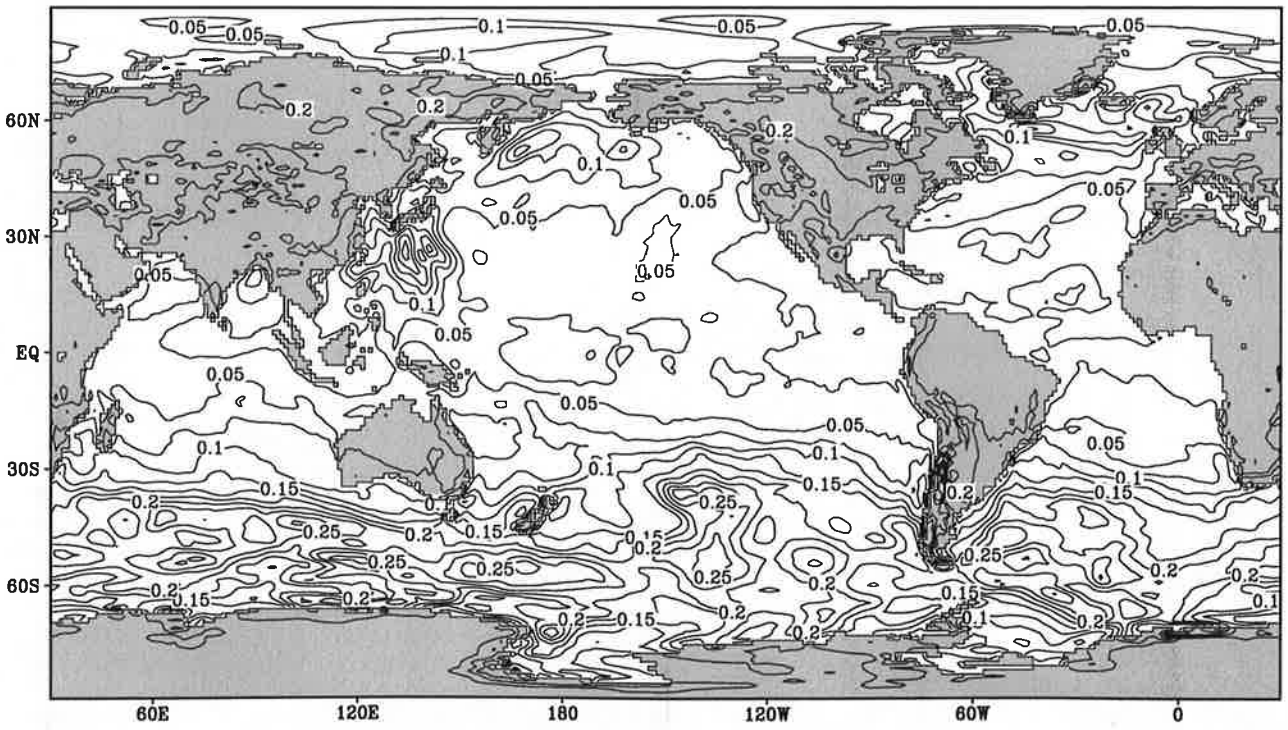

Contour interval ocean: 0.025, land: 0.1

Fig.13.9 Wind stress September

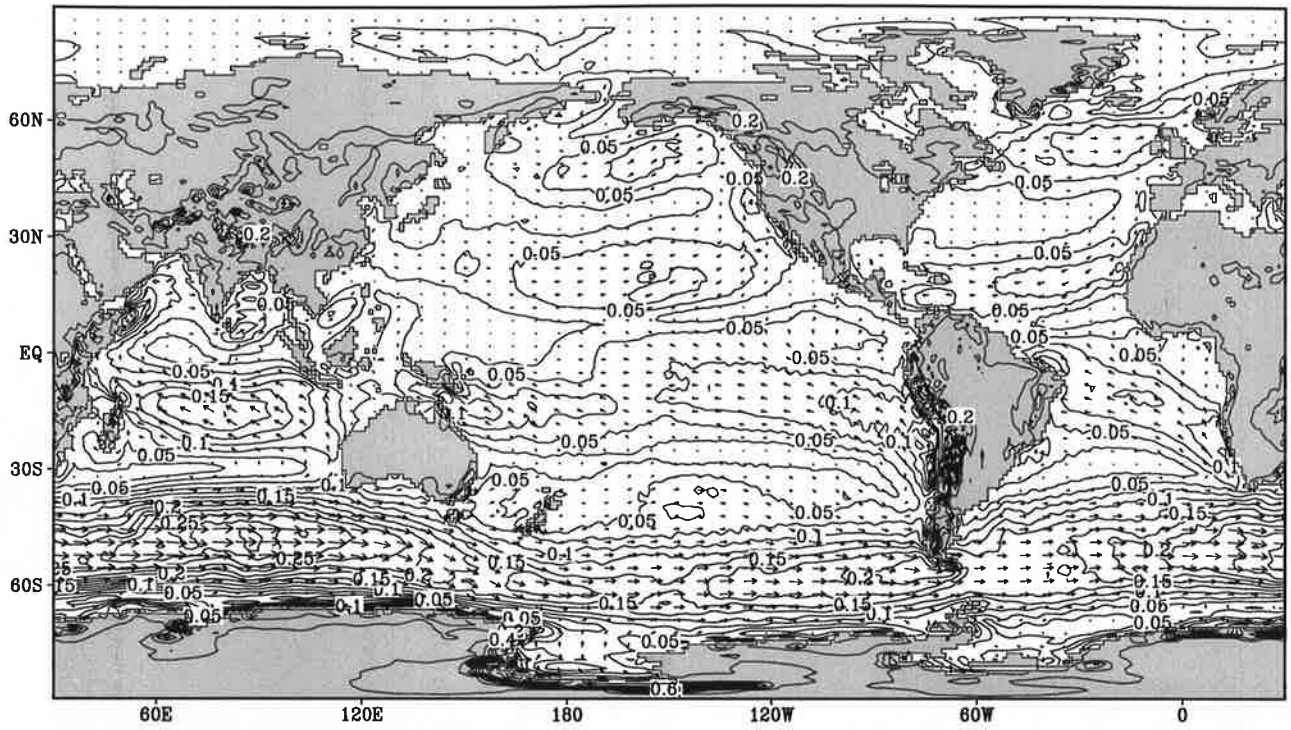

Contour interval ocean: 0.025, land: 0.1 $\vec{0.25}$

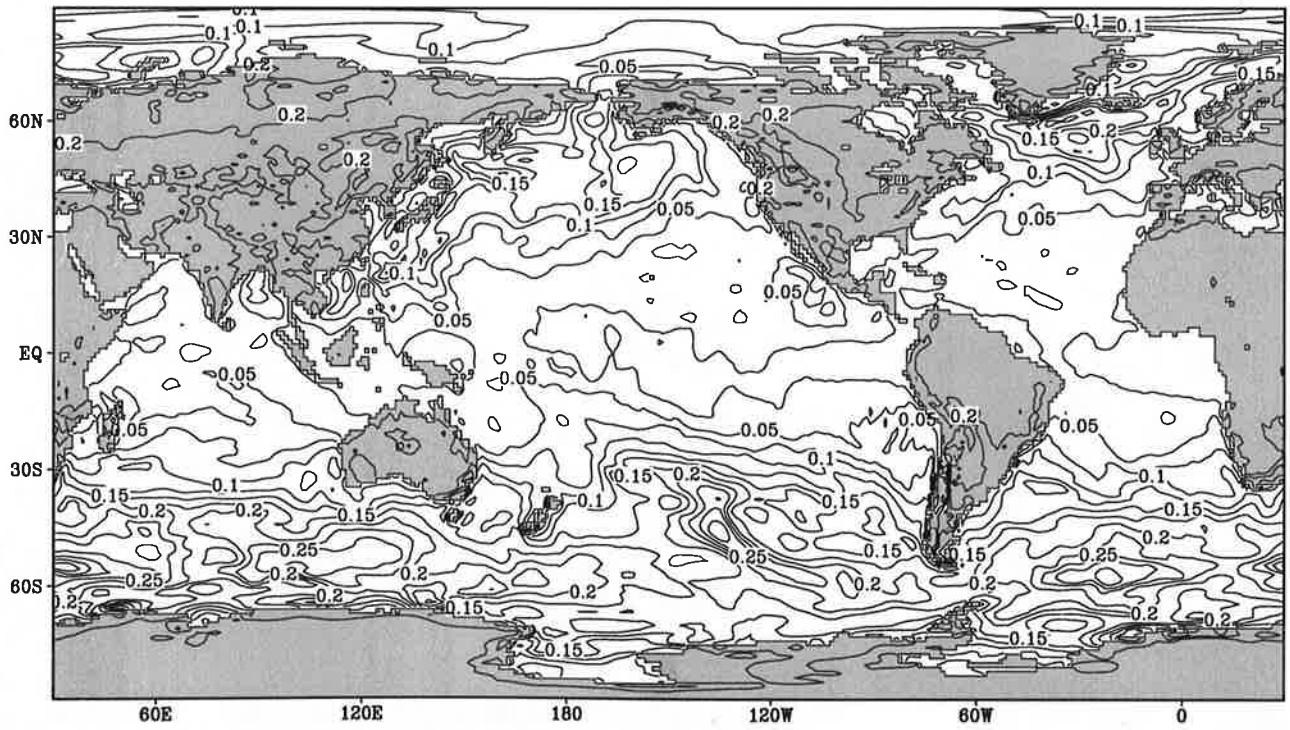

Contour interval ocean: 0.025, land: 0.1

Fig.13.10 Wind stress October

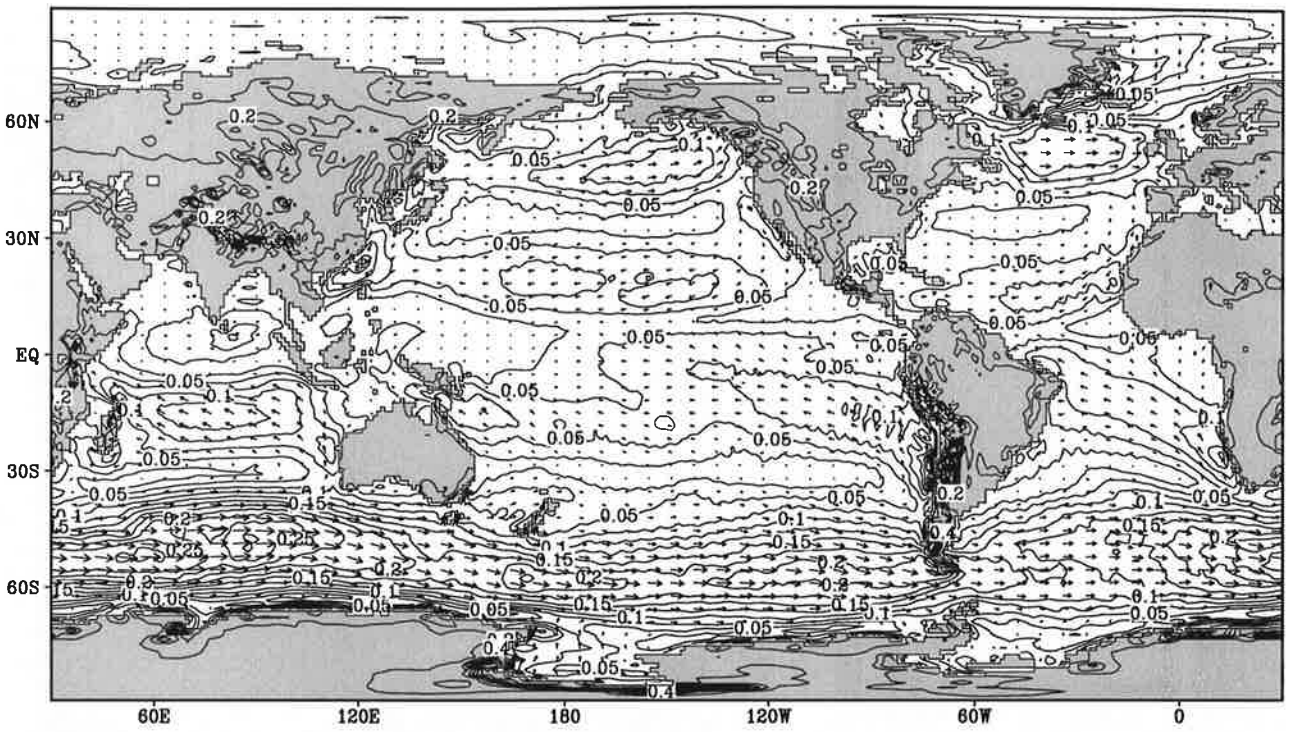

Contour interval ocean: 0.025, land: 0.1 $\vec{0.25}$

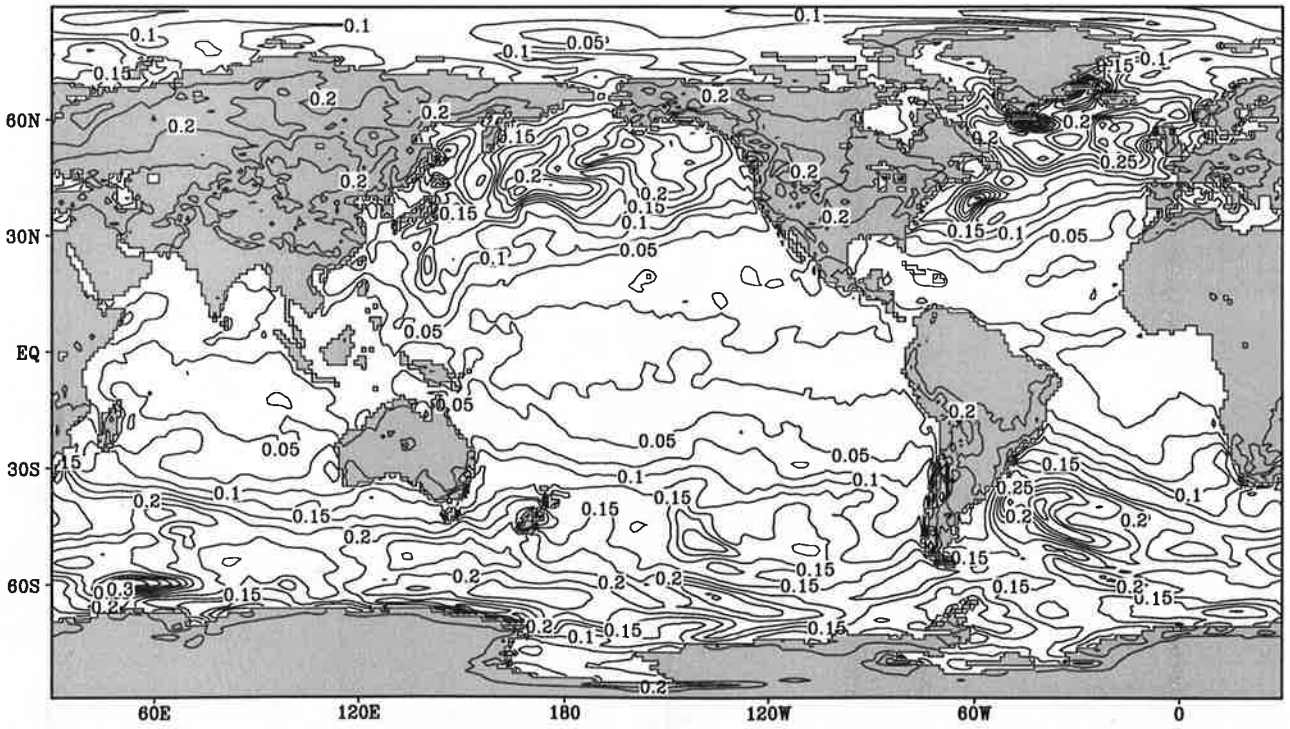

Contour interval ocean: 0.025, land: 0.1

Fig.13.11 Wind stress November

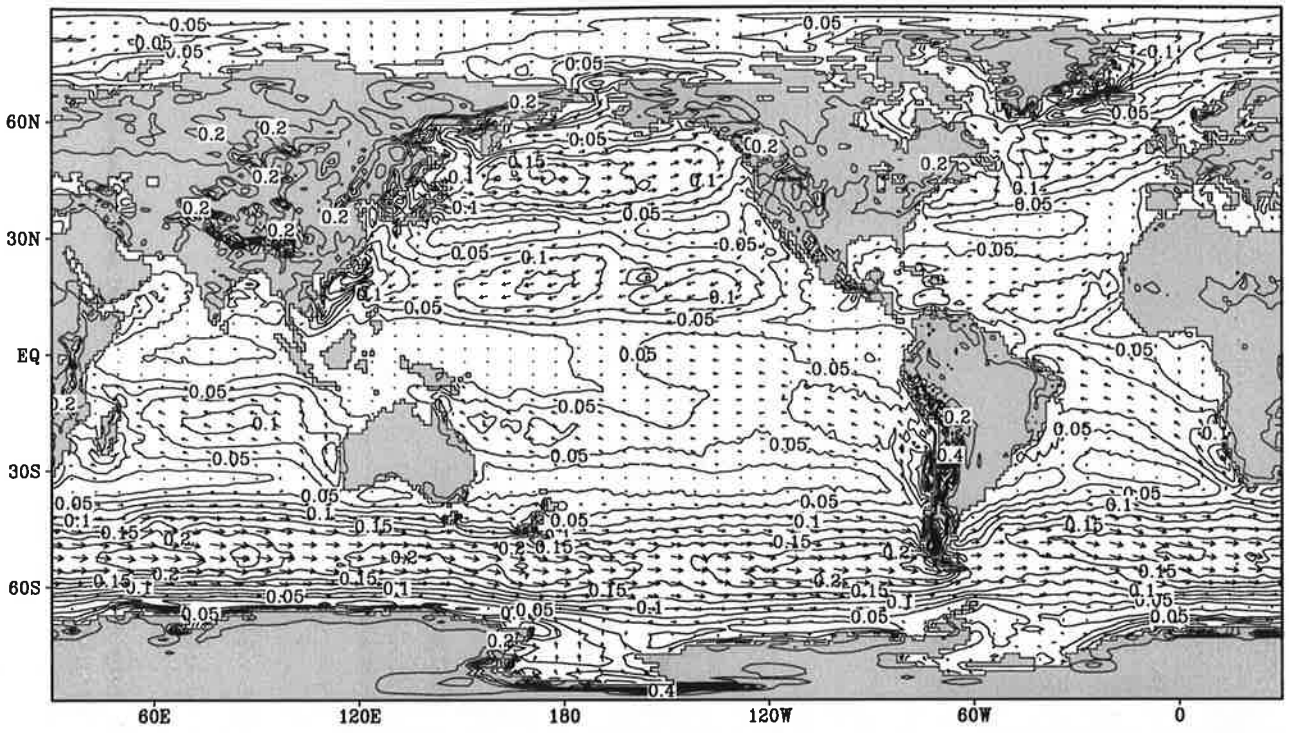

Contour interval ocean: 0.025, land: 0.1 $\vec{0.25}$

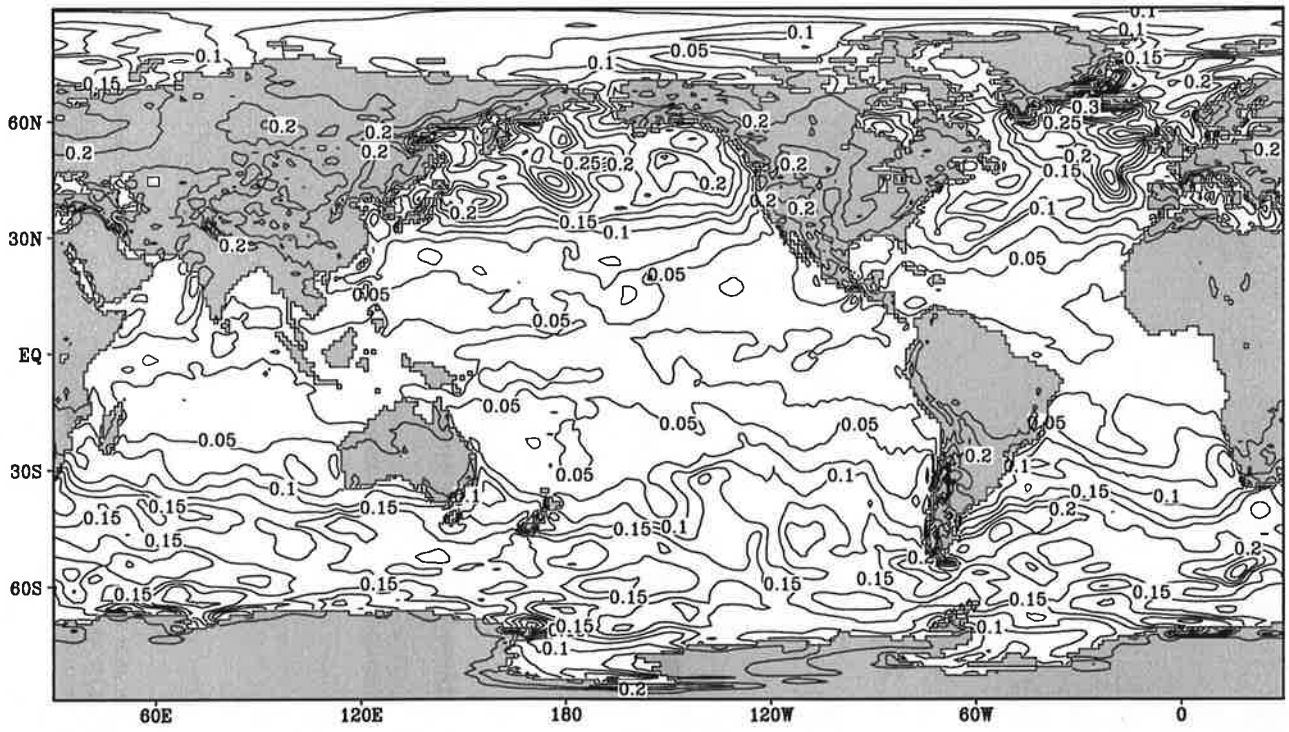

Contour interval ocean: 0.025, land: 0.1

Fig.13.12 Wind stress December

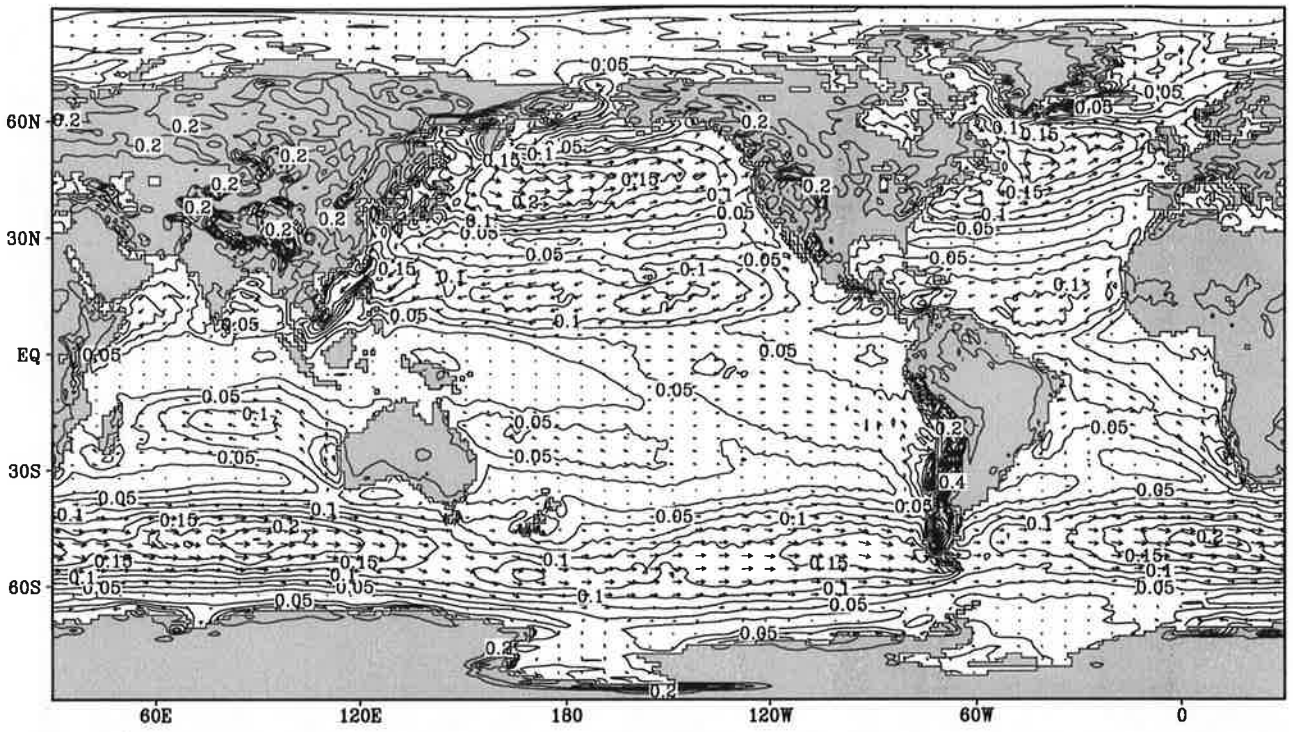

Contour interval ocean: 0.025, land: 0.1 $\vec{0.25}$

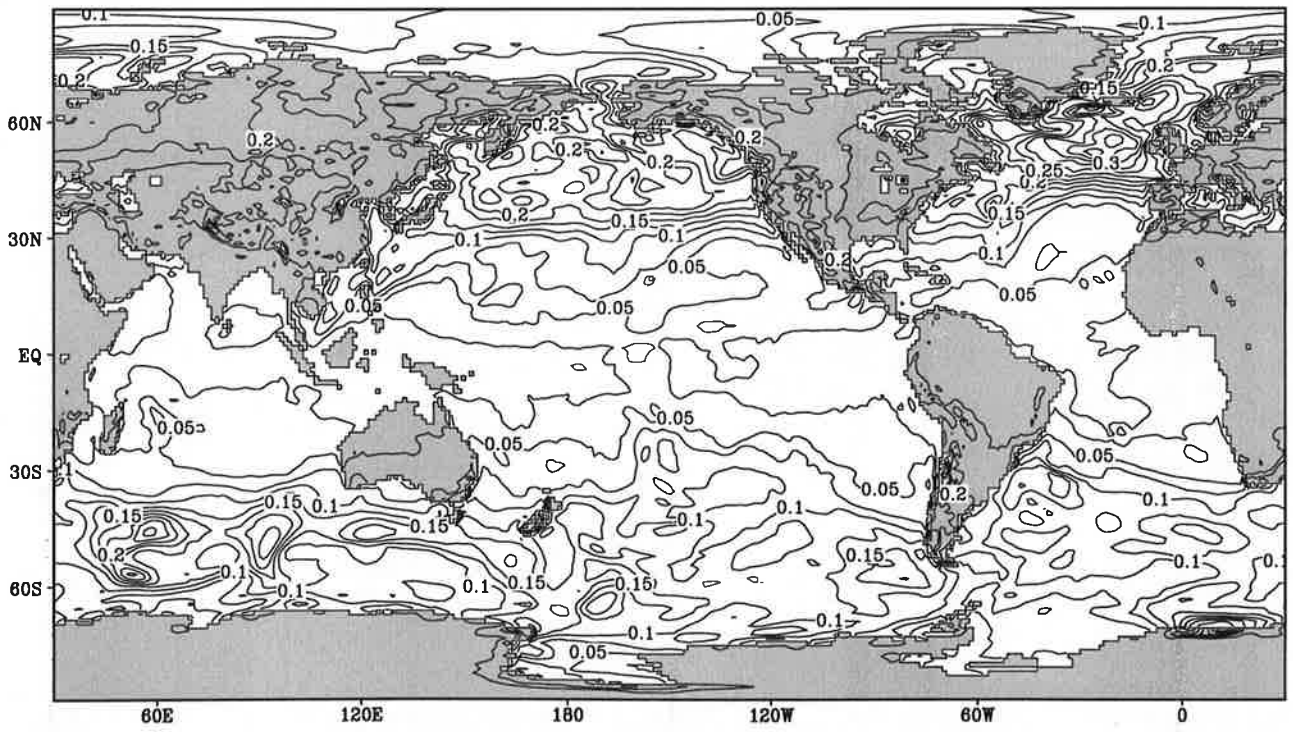

Contour interval ocean: 0.025, land: 0.1

Fig.13.13 Wind stress Annual Mean

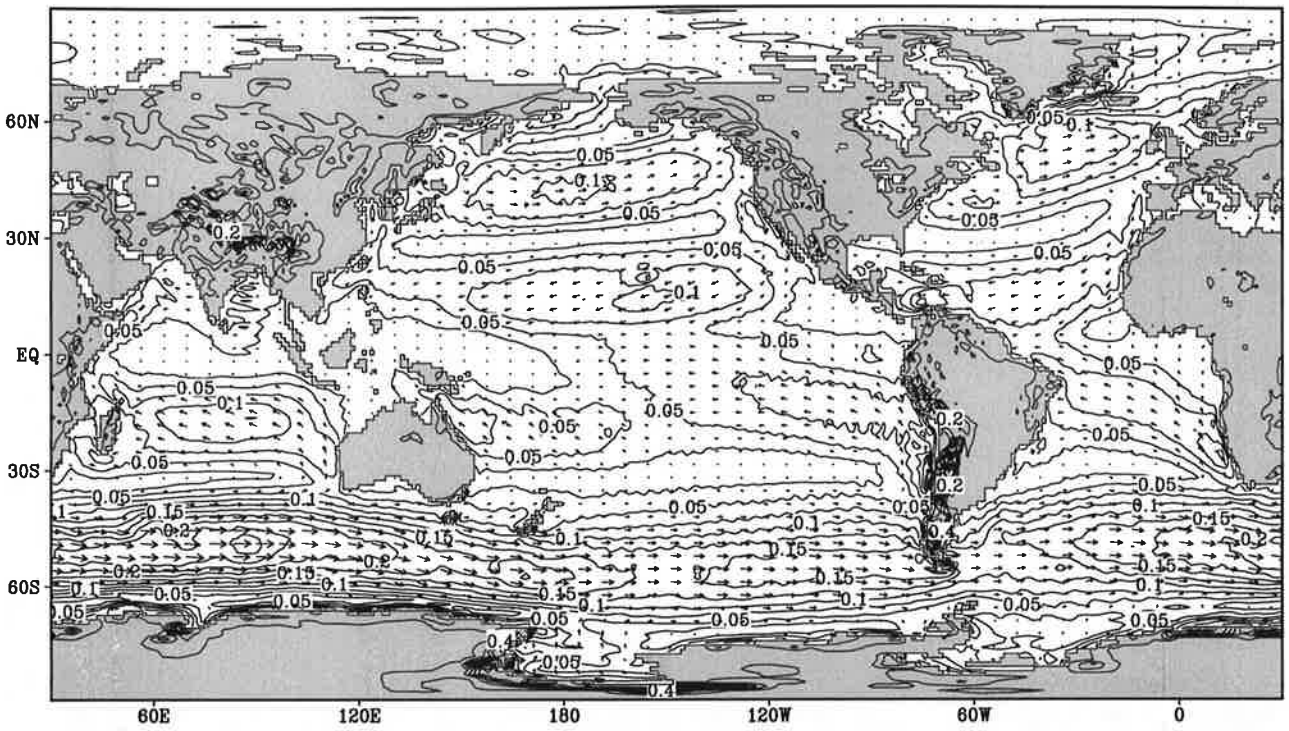

Contour interval ocean: 0.025, land: 0.1 $\vec{0.25}$

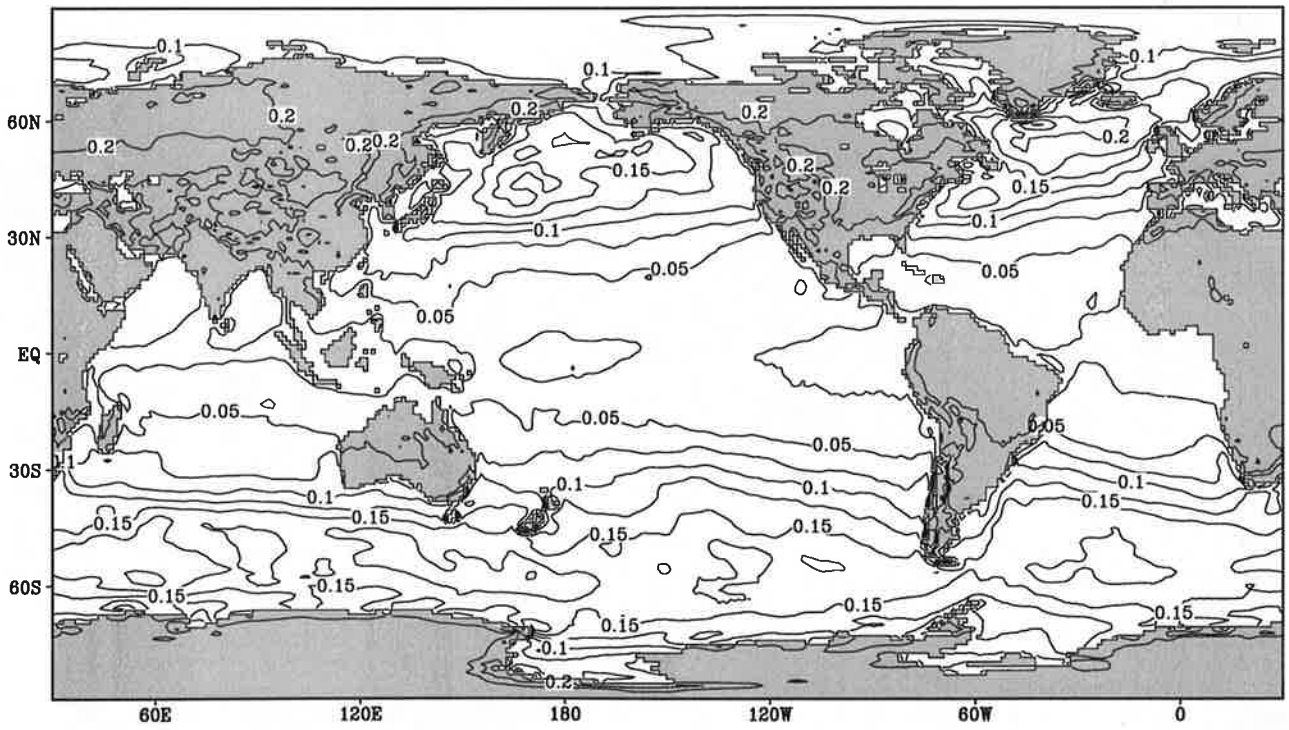

Contour interval ocean: 0.025, land: 0.1

Fig.14 Time-latitude section of zonally averaged daily net downward heat flux

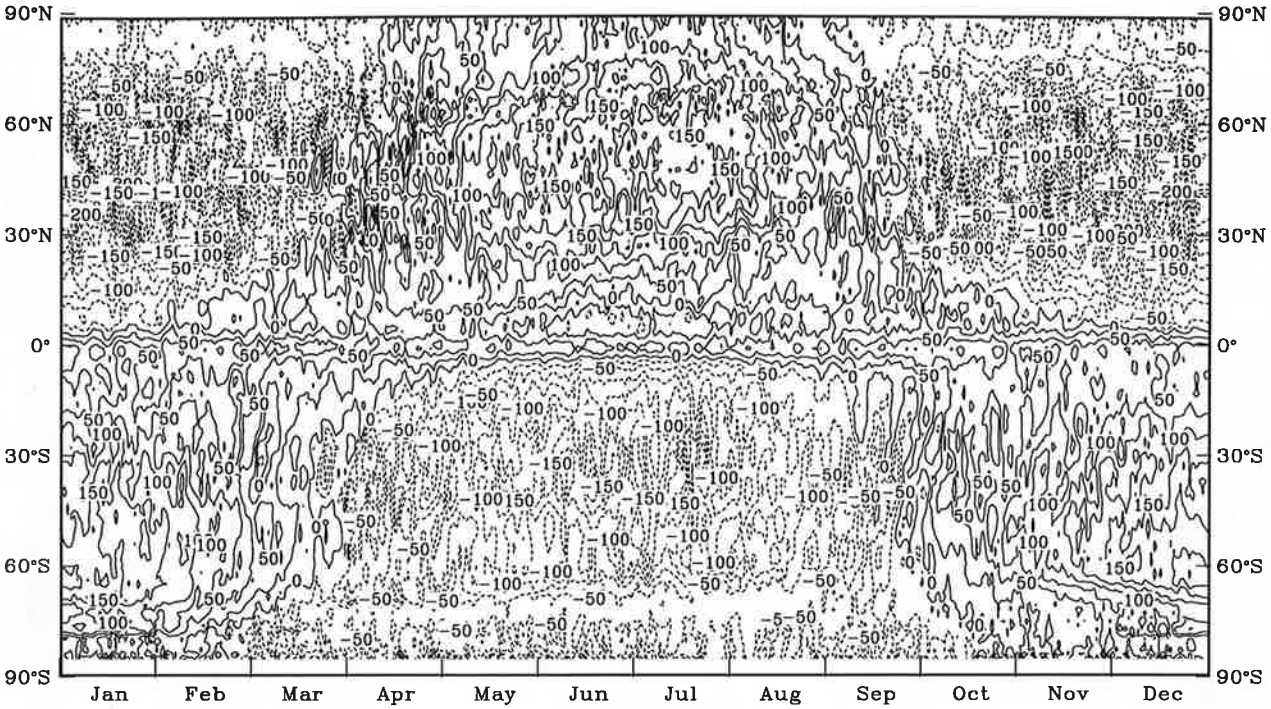

Contour interval: 25 Wm^{-2}

Fig.15 Time-latitude section of zonally averaged daily fresh water flux

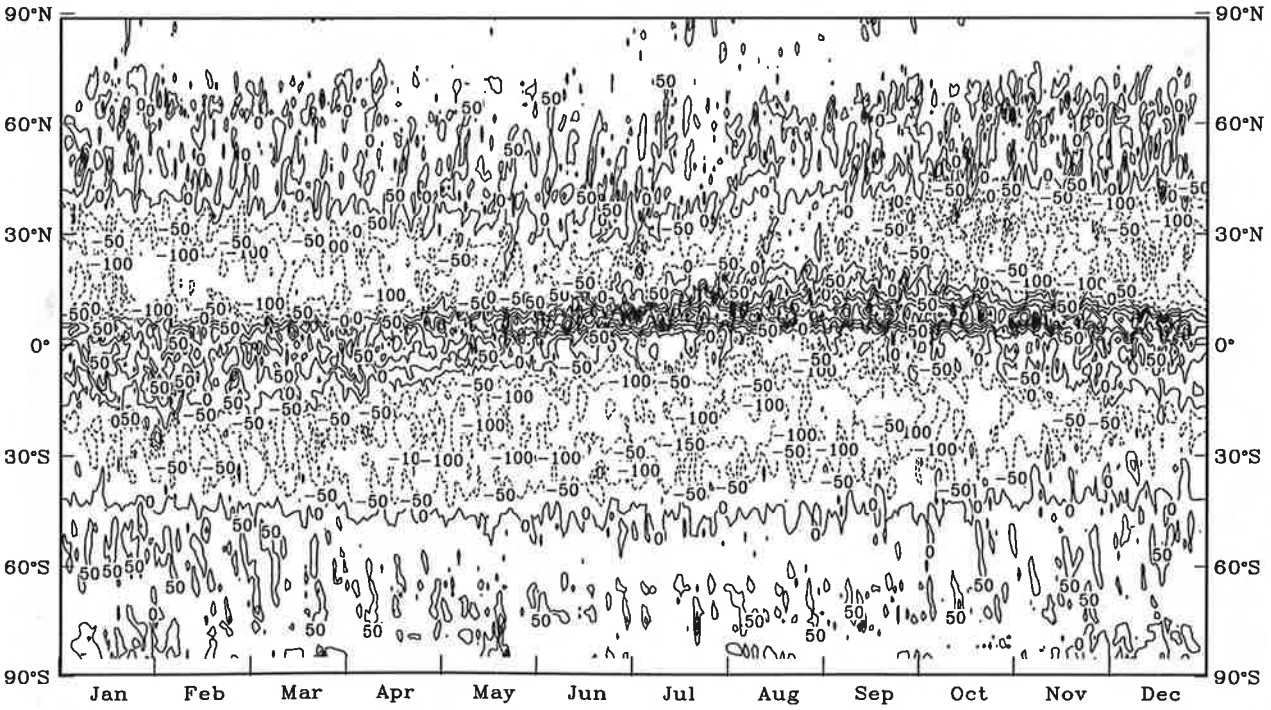

Contour interval: 50 mm $month^{-1}$

Fig.16 Time-latitude section of zonally averaged daily short wave solar radiation

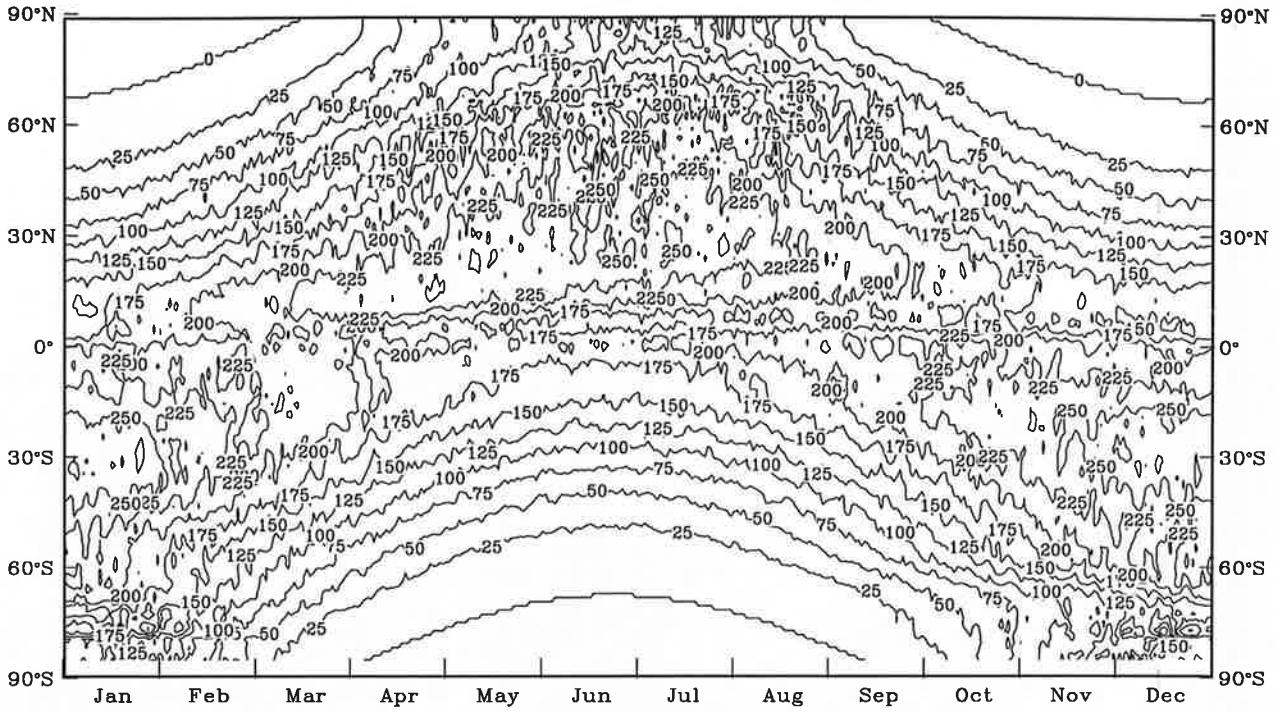

Contour interval: 25 Wm^{-2}

Fig.17 Time-latitude section of zonally averaged daily long wave radiation

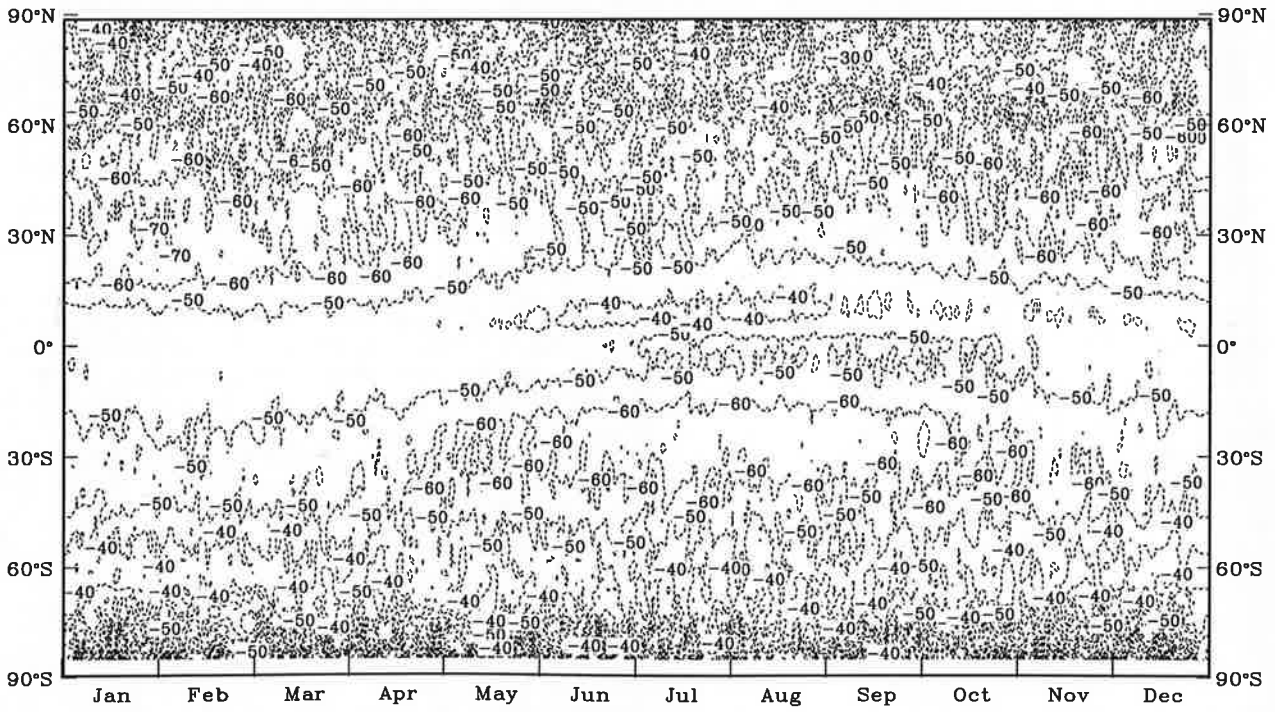

Contour interval: 10 Wm^{-2}

Fig.18 Time-latitude section of zonally averaged daily sensible heat flux

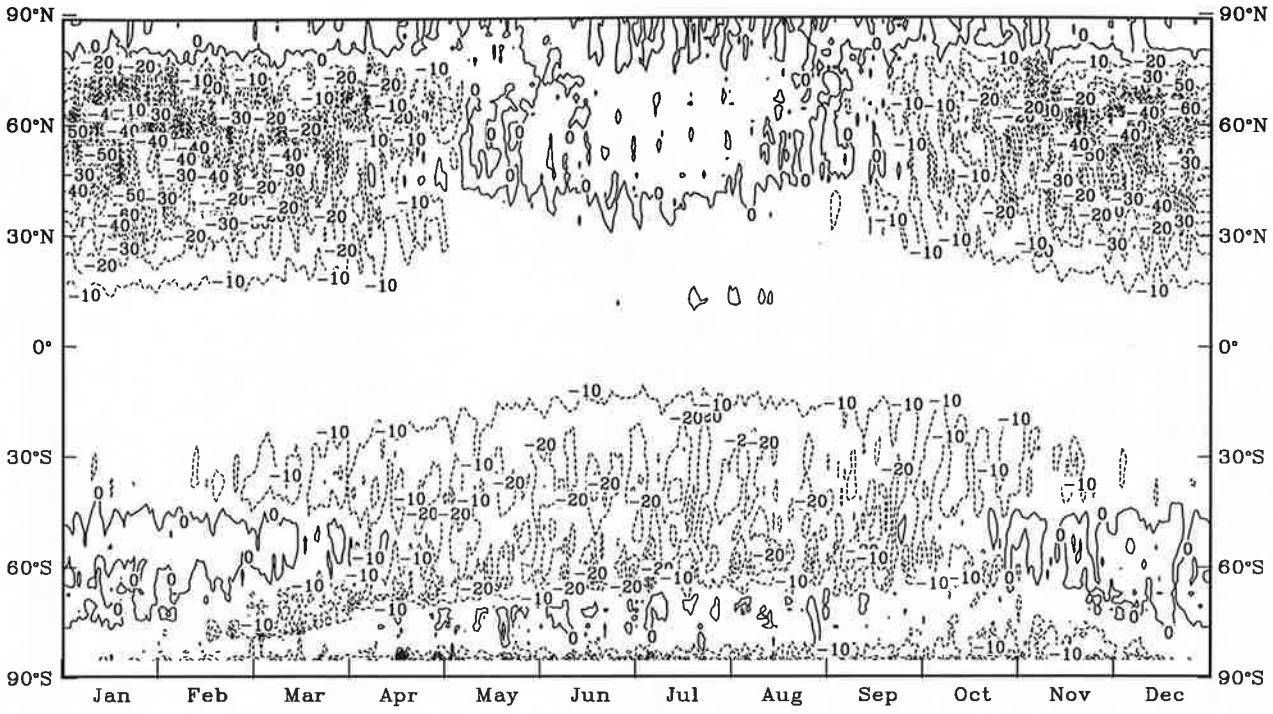

Contour interval: 10 Wm^{-2}

Fig.19 Time-latitude section of zonally averaged daily latent heat flux

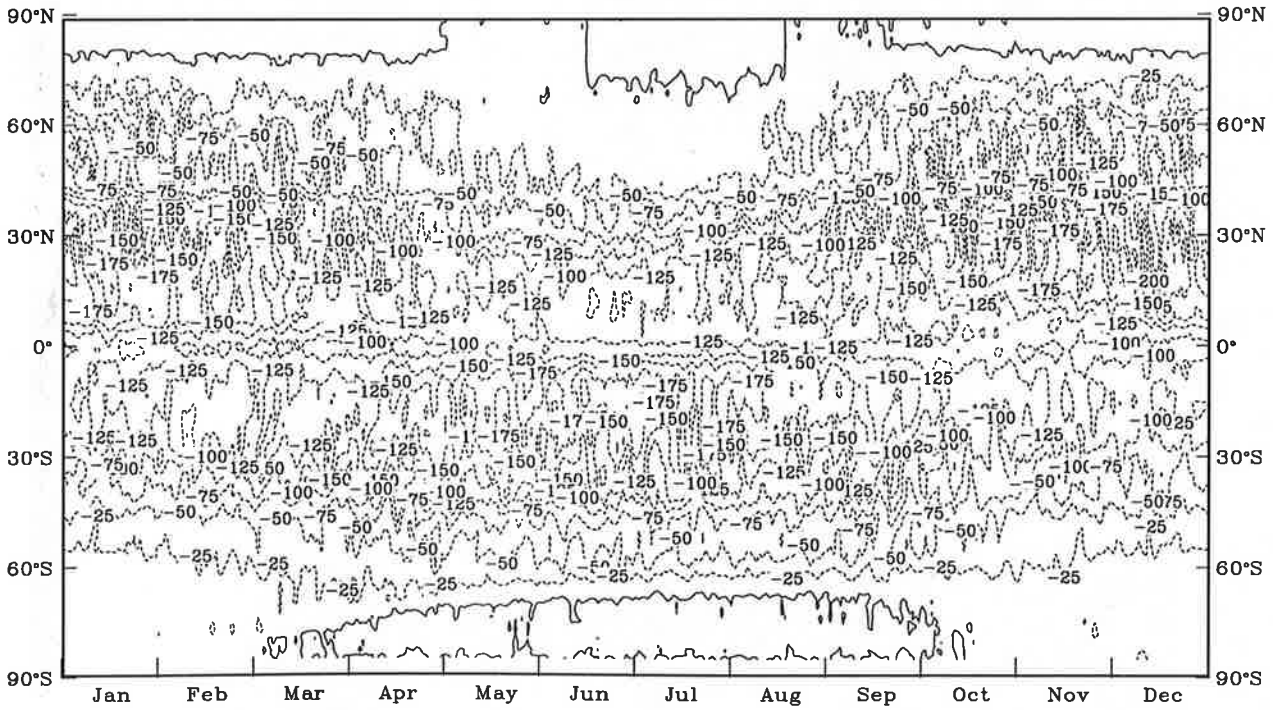

Contour interval: 25 Wm^{-2}

Fig.20 Time-latitude section of zonally averaged daily evaporation

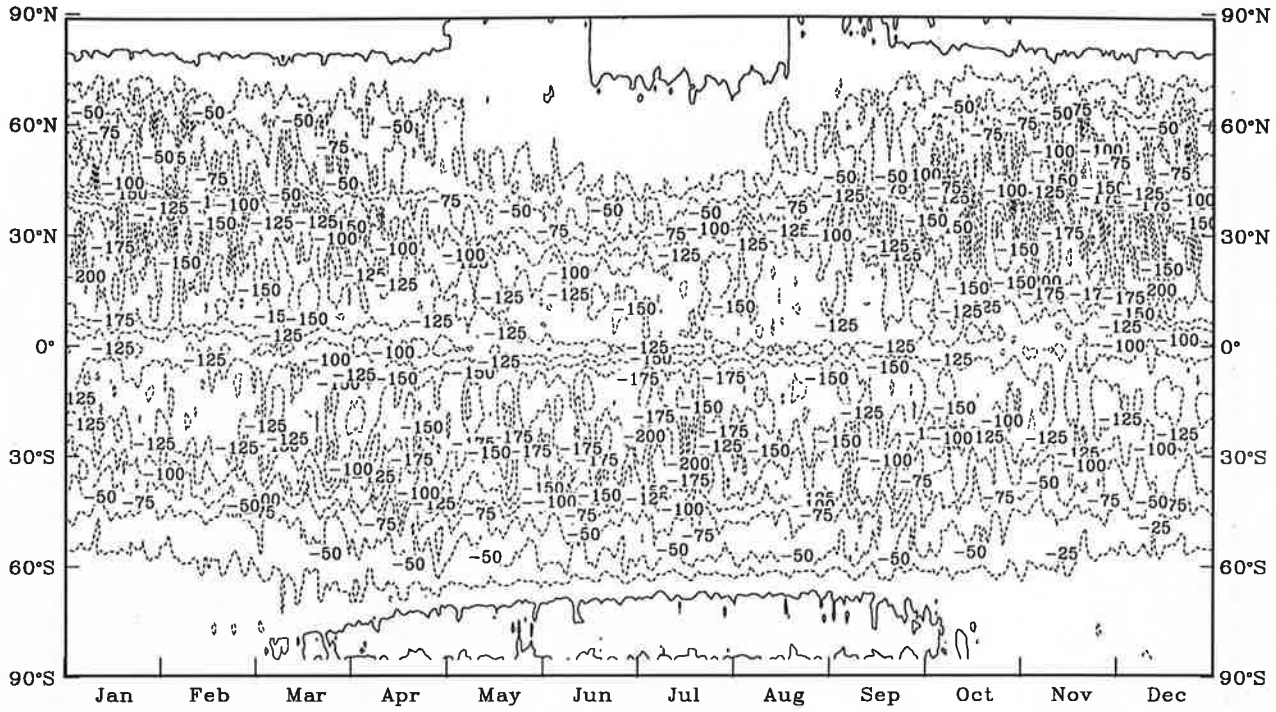

Contour interval: 25 mm month^{-1}

Fig.21 Time-latitude section of zonally averaged daily precipitation

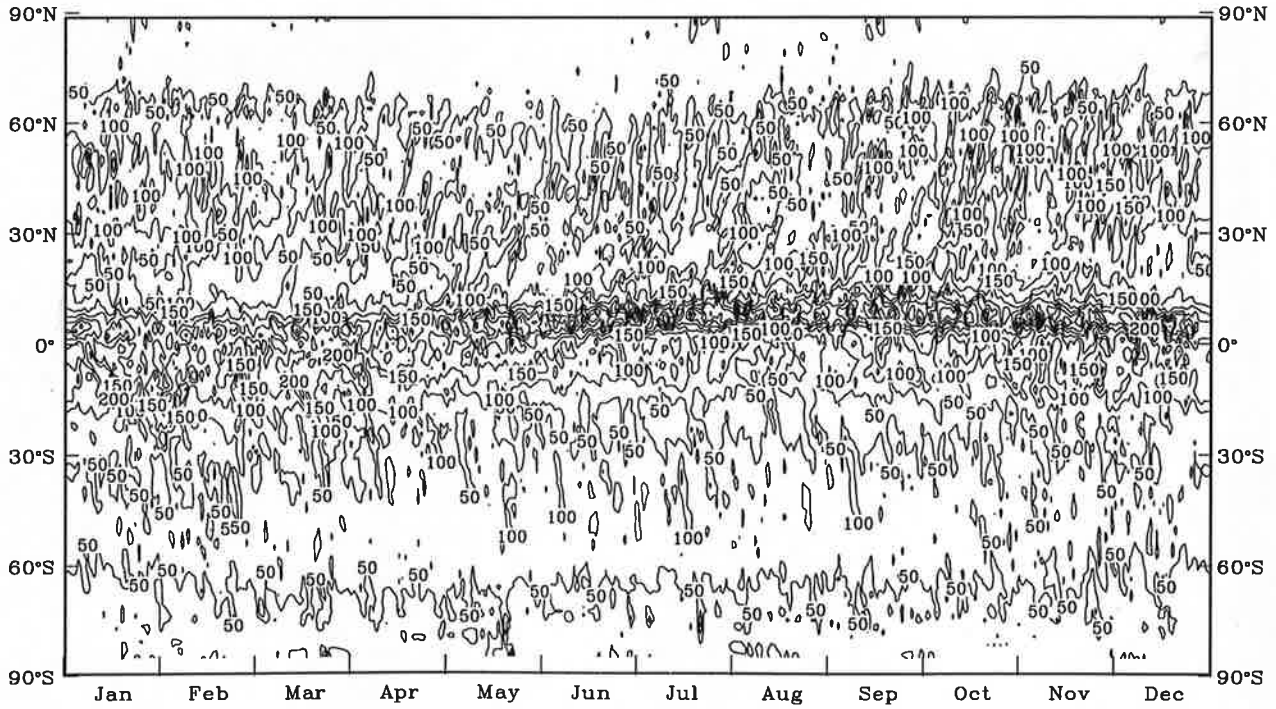

Contour interval: 50 mm month^{-1}

Fig.22 Zonal averages: the flux components Annual Mean

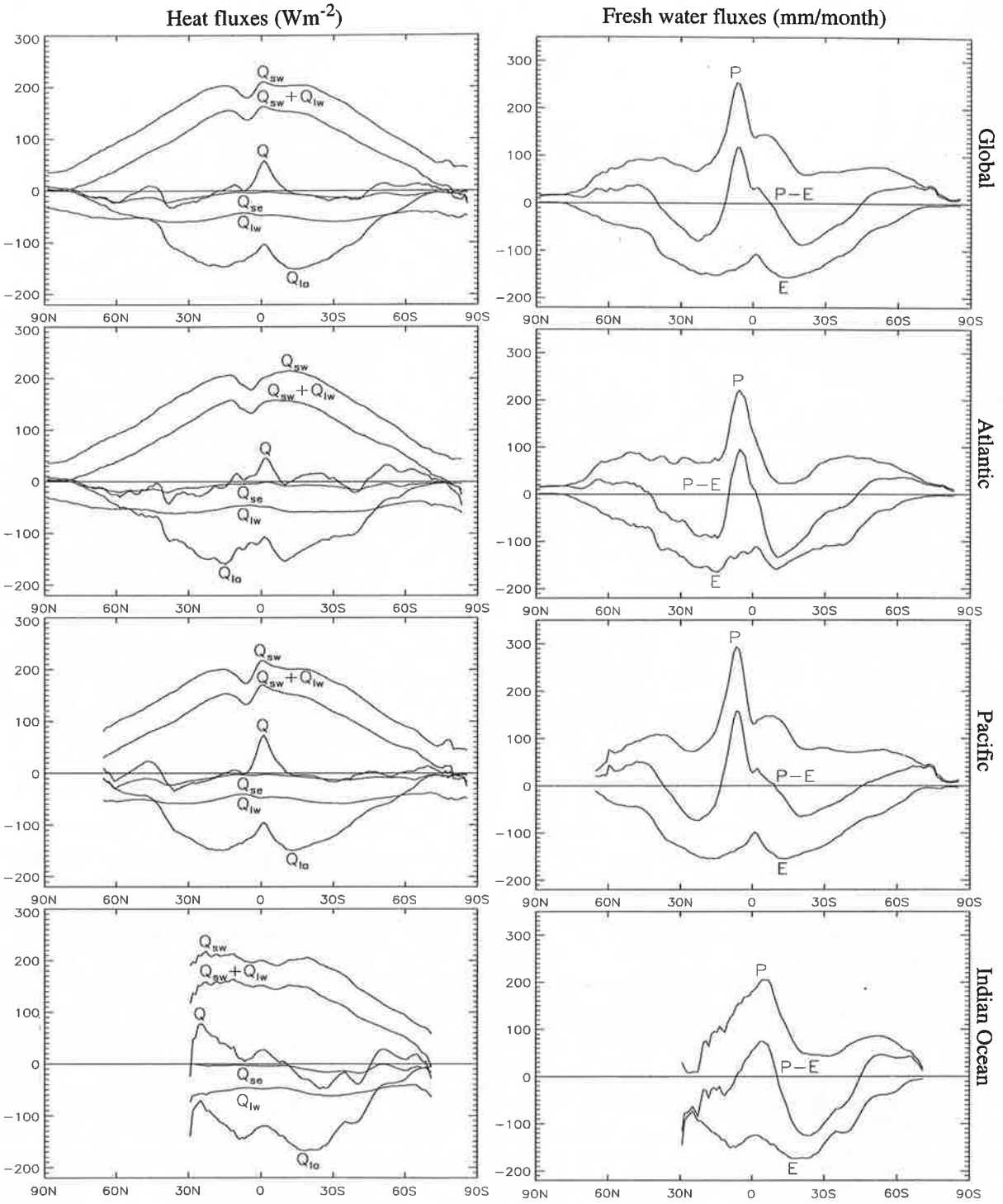

Q_{sw}: Short wave solar radiation
$Q_{sw}+Q_{lw}$: Net radiation
Q: Net downward heat flux
Q_{se}: Sensible heat flux
Q_{lw}: Long wave radiation
Q_{la}: Latent heat flux

P: Precipitation
P−E: Fresh water flux
E: Evaporation

Fig.23 Zonal and oceanic averages: the runoff Annual Mean

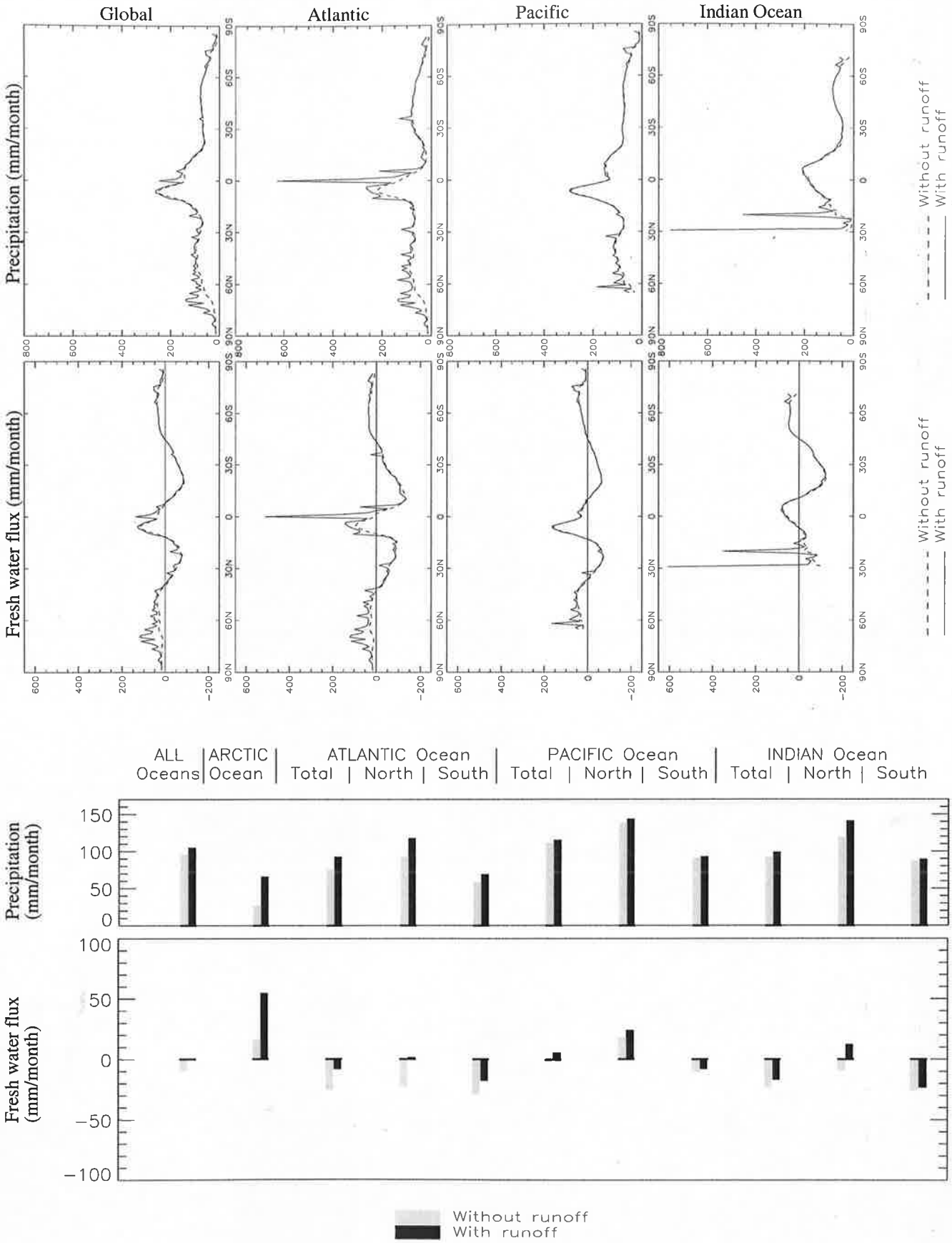

Fig.24 Net downward heat flux: other climatologies Annual Mean

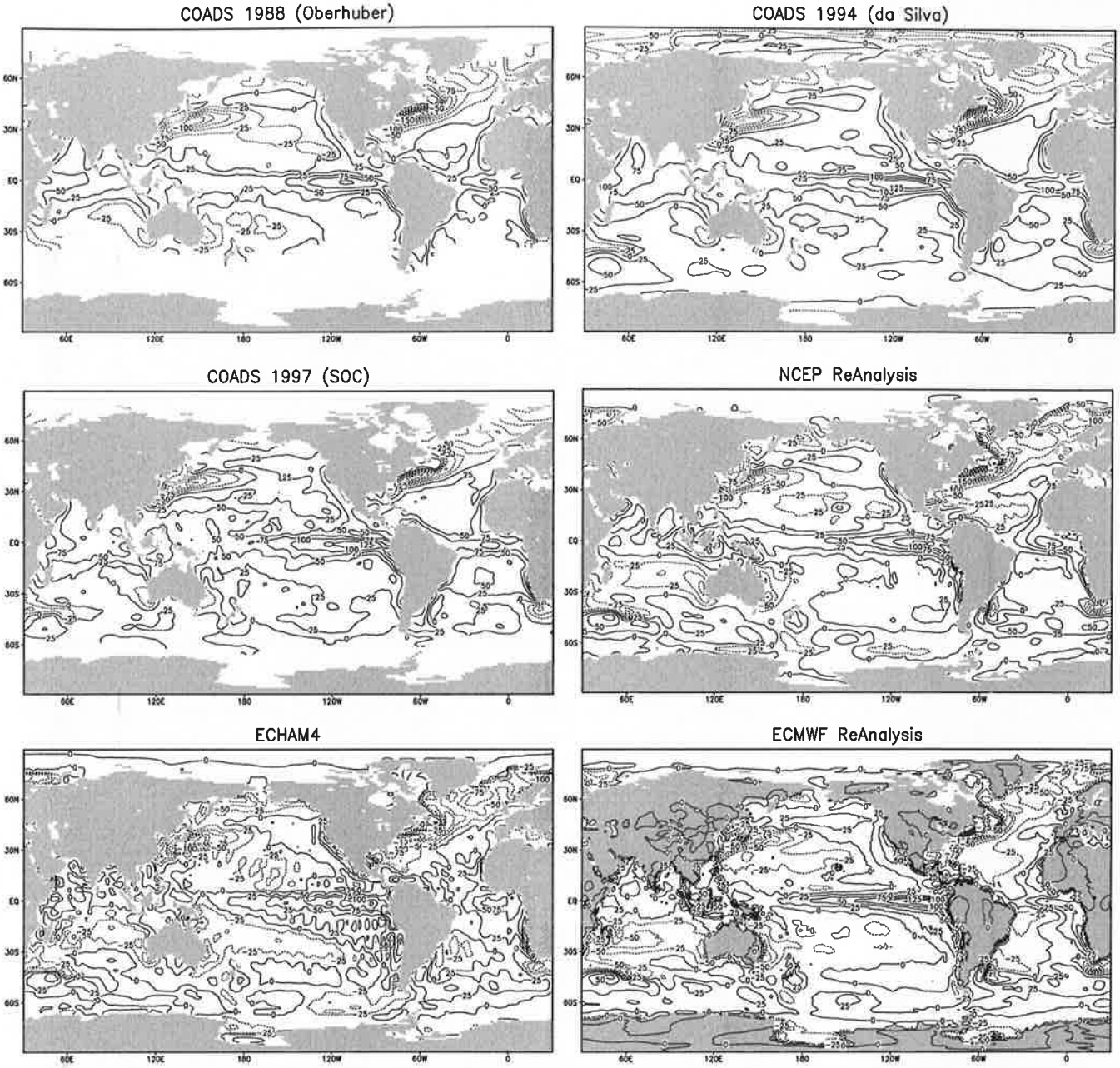

Fig.25 Net downward fresh water flux: other climatologies Annual Mean

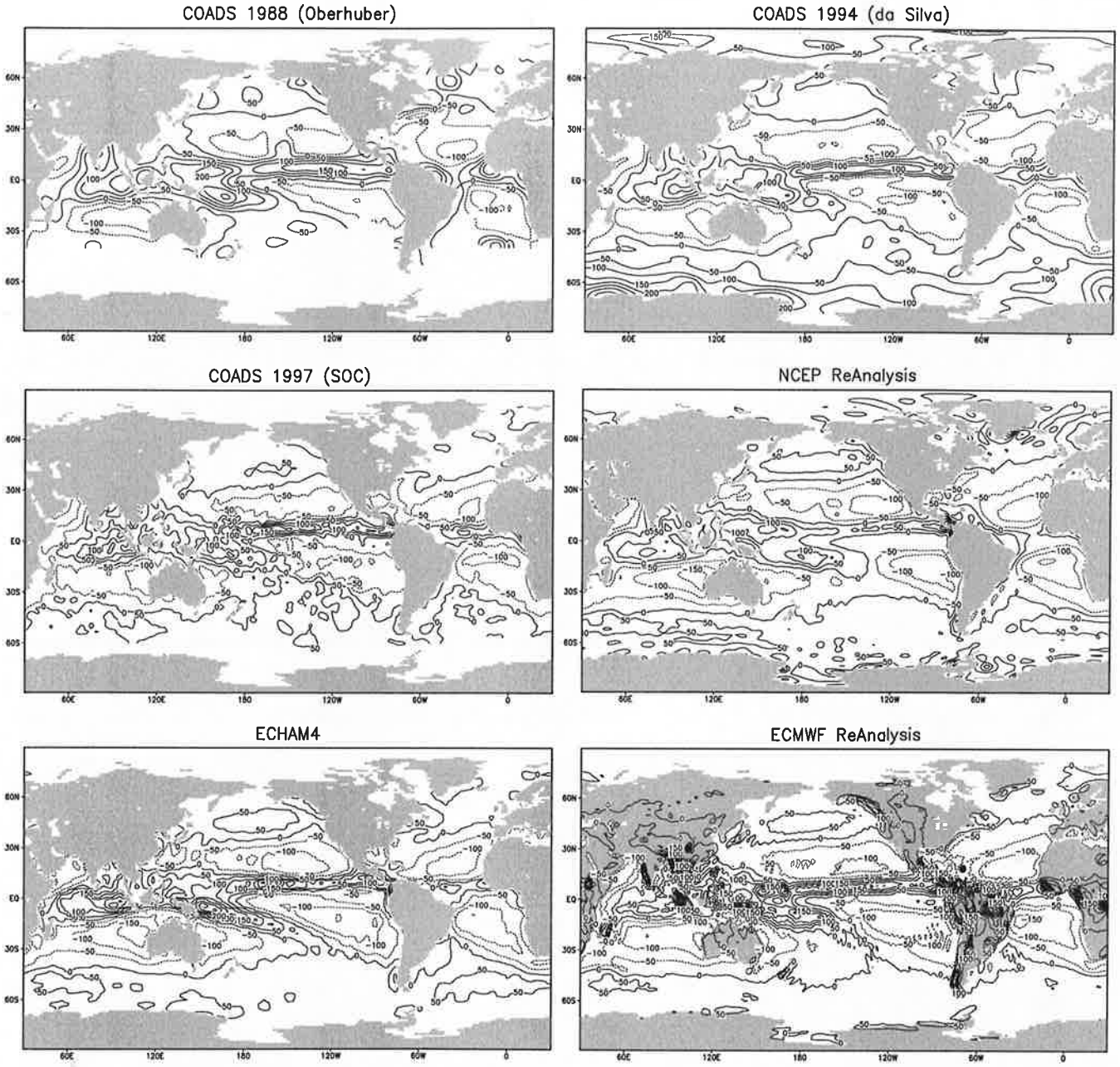

Fig.26 Implied northward meridional transports

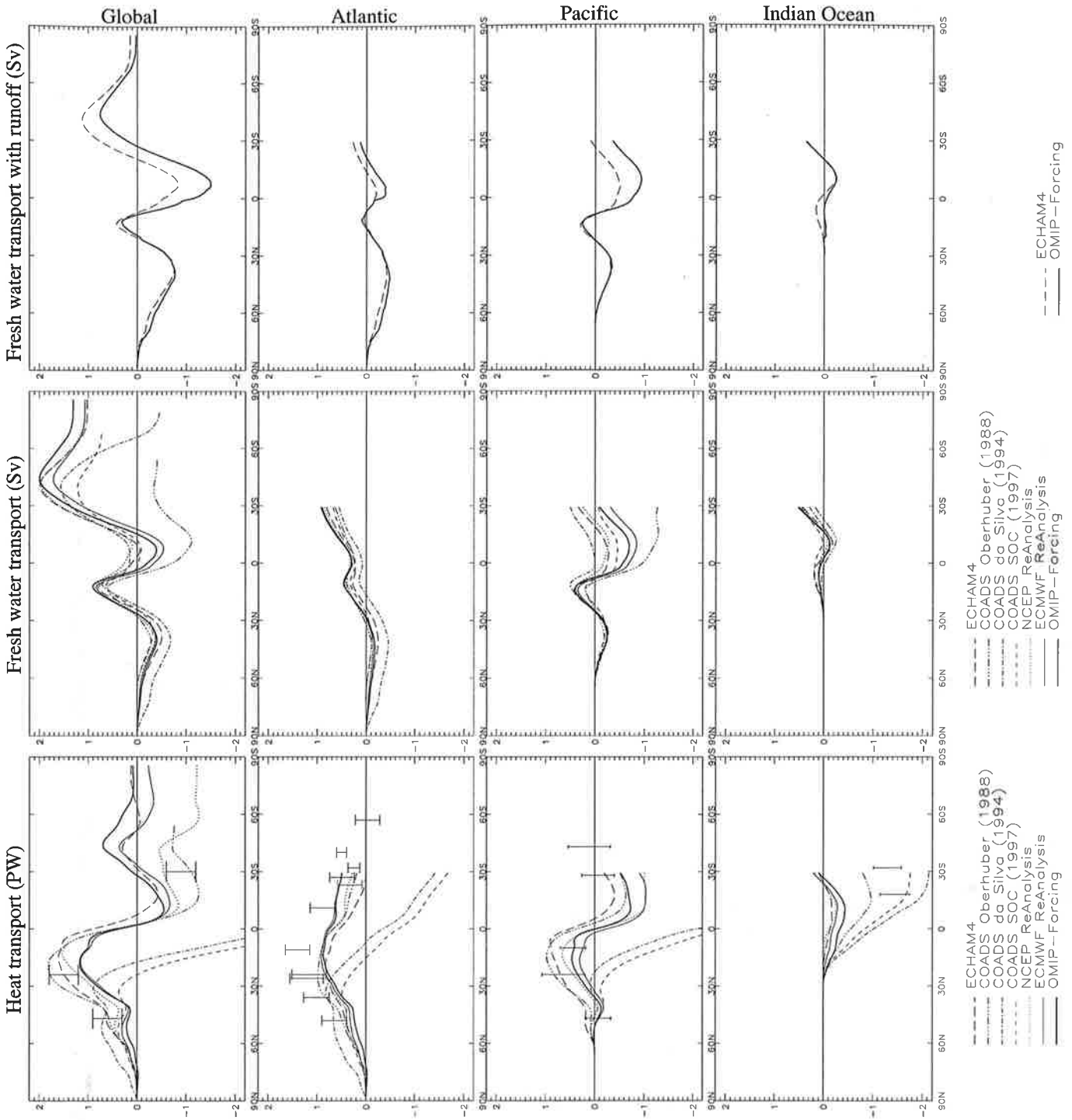

Fig.27.1 Zonal averages - part I January

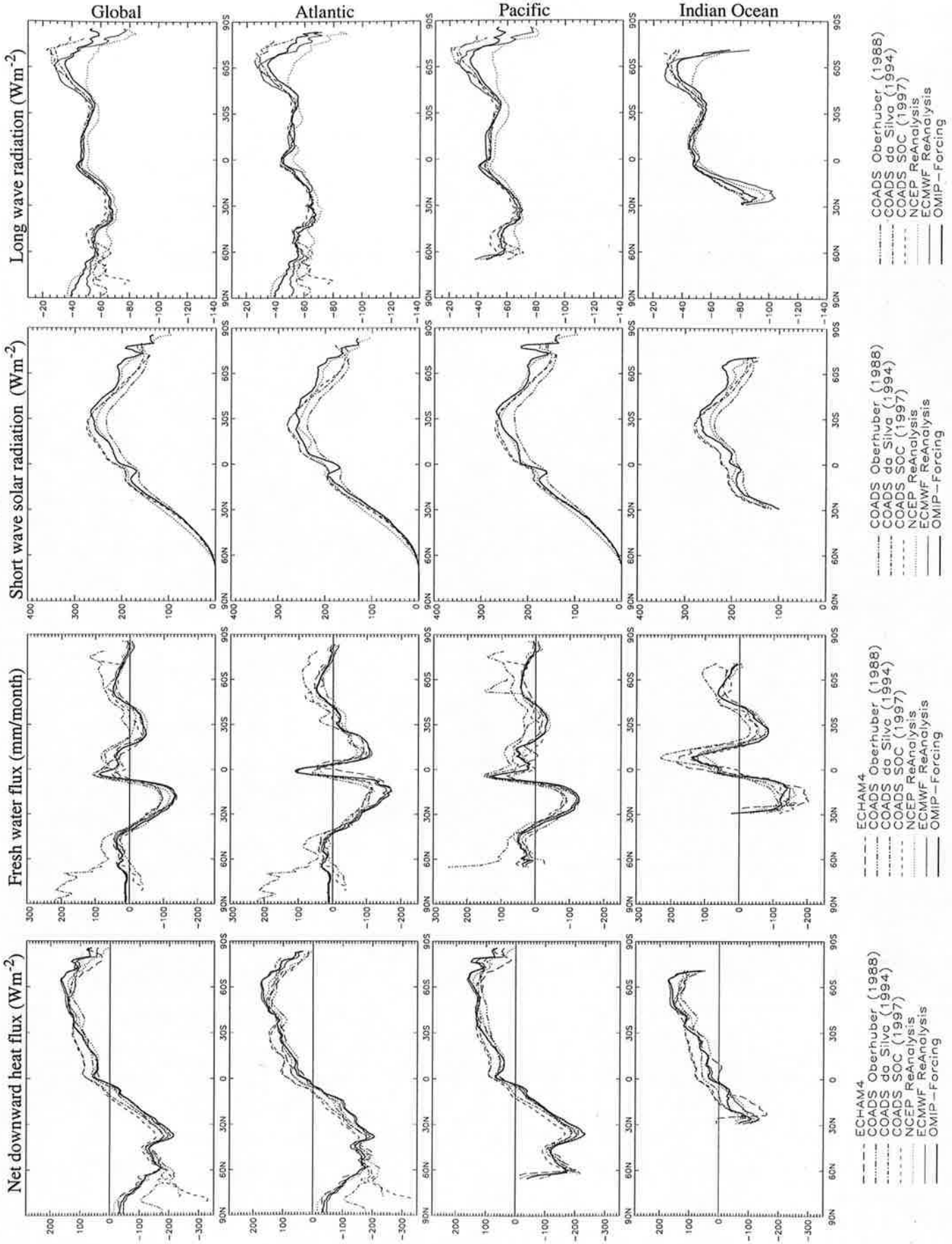

Fig.27.2 Zonal averages - part I February

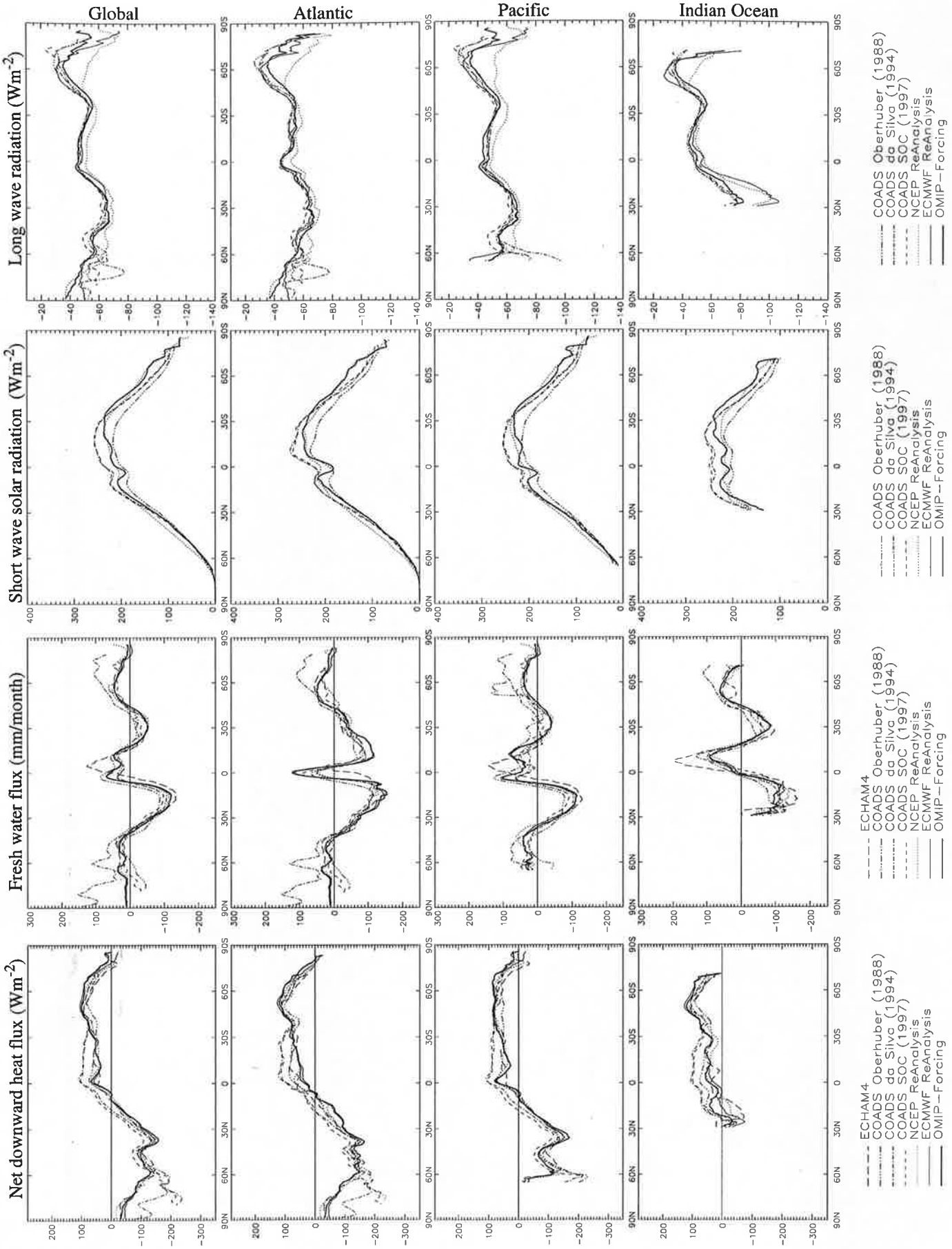

Fig.27.3 Zonal averages - part I March

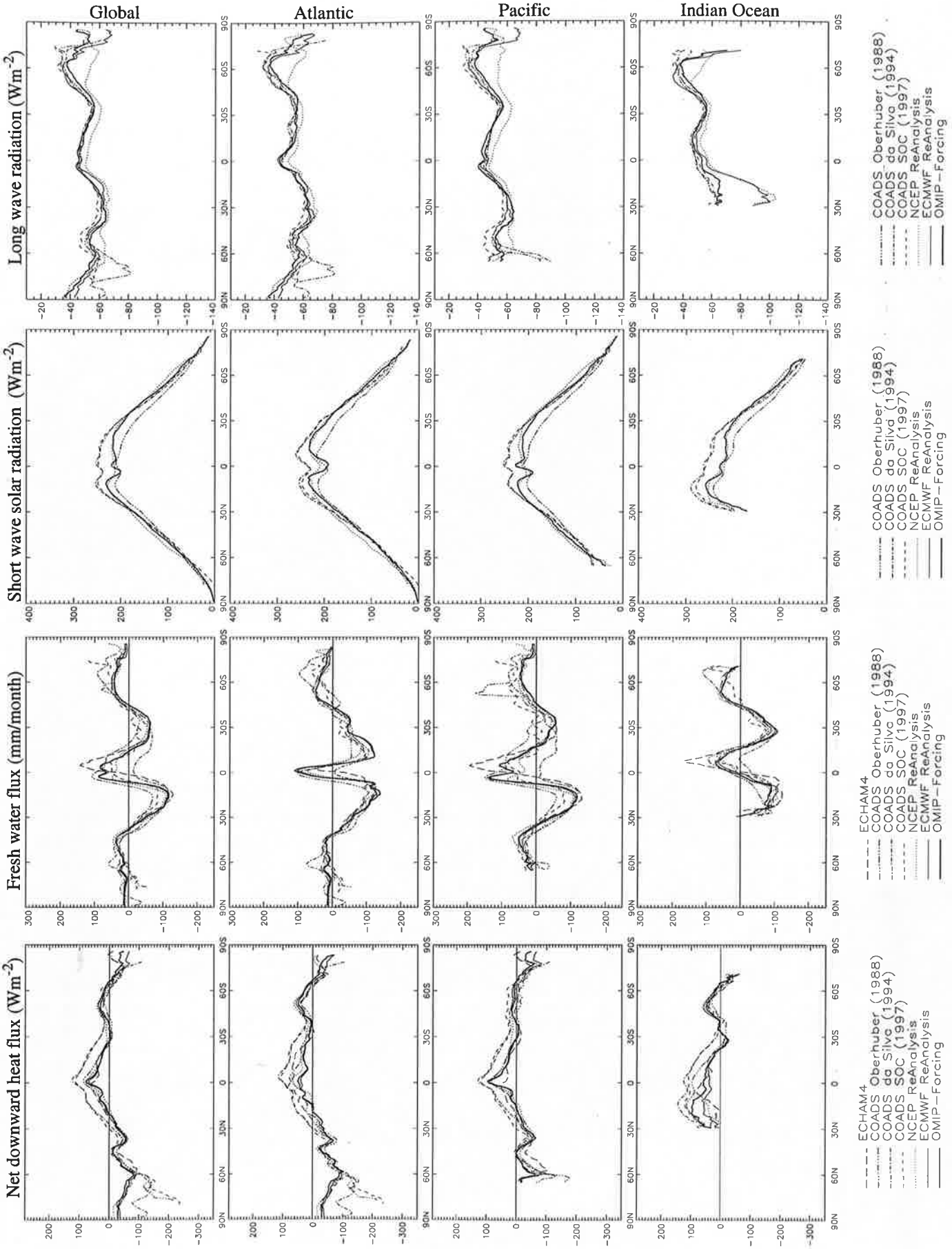

Fig.27.4 Zonal averages - part I April

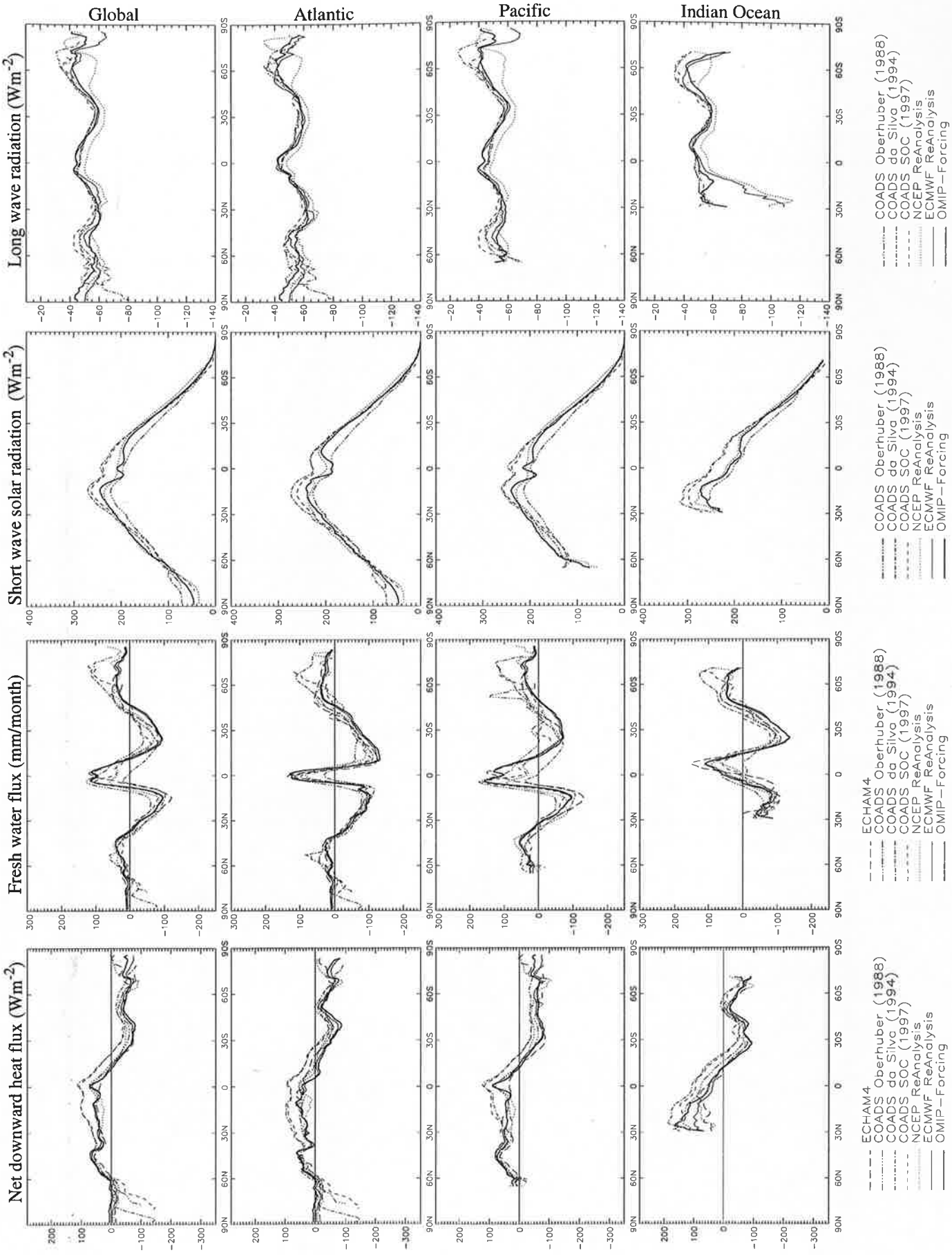

Fig.27.5 Zonal averages - part I May

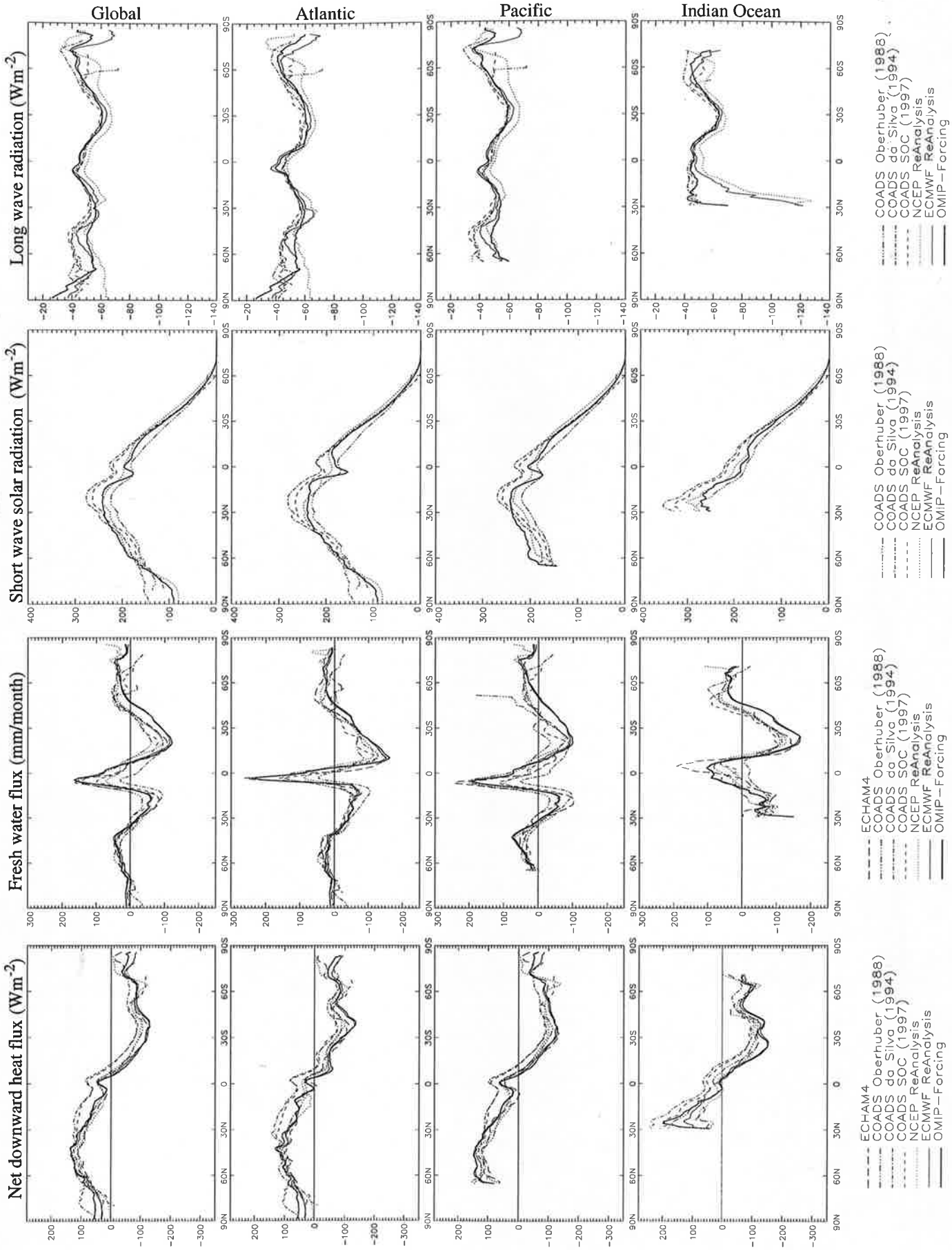

Fig.27.6 Zonal averages - part I June

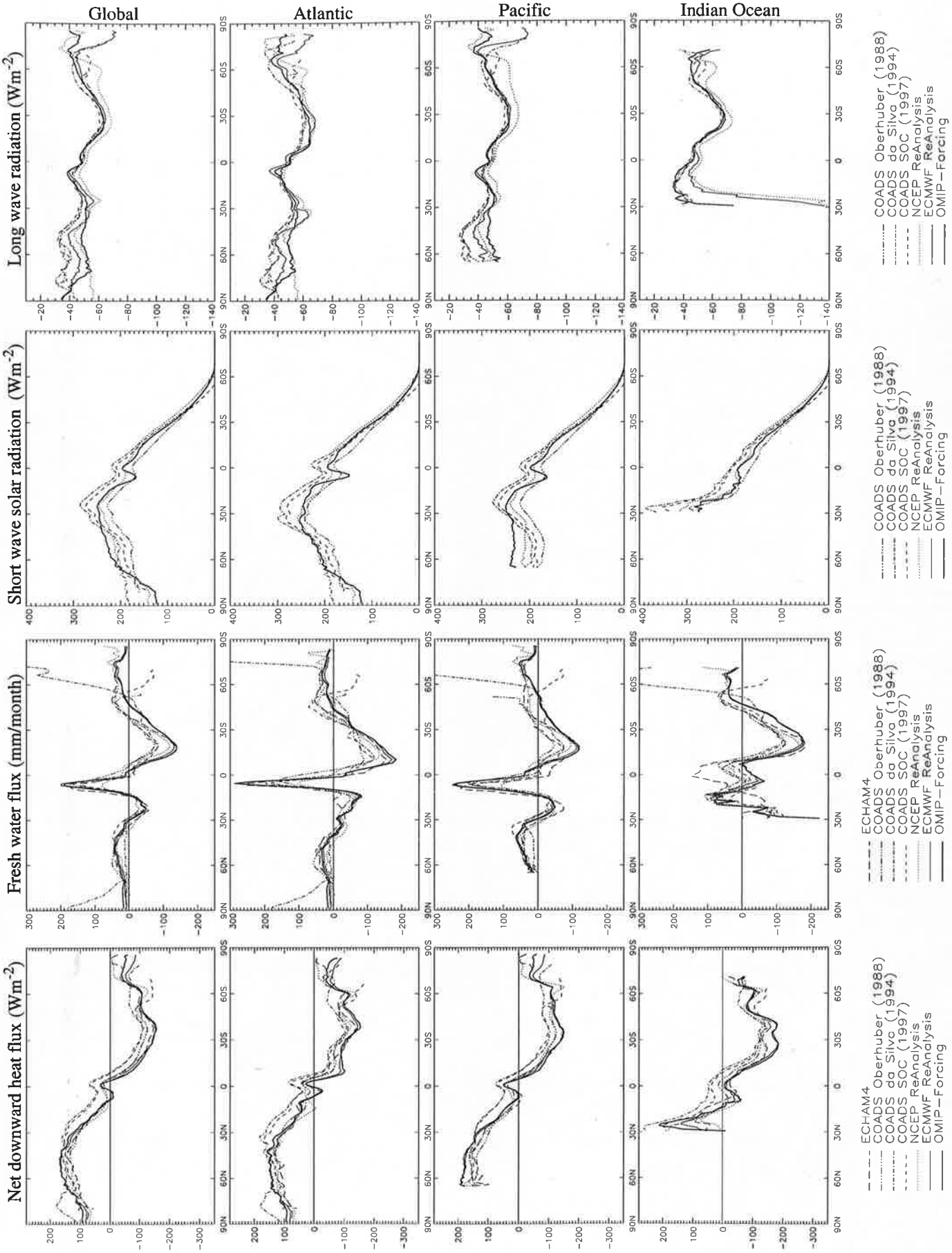

Fig.27.7 Zonal averages - part I July

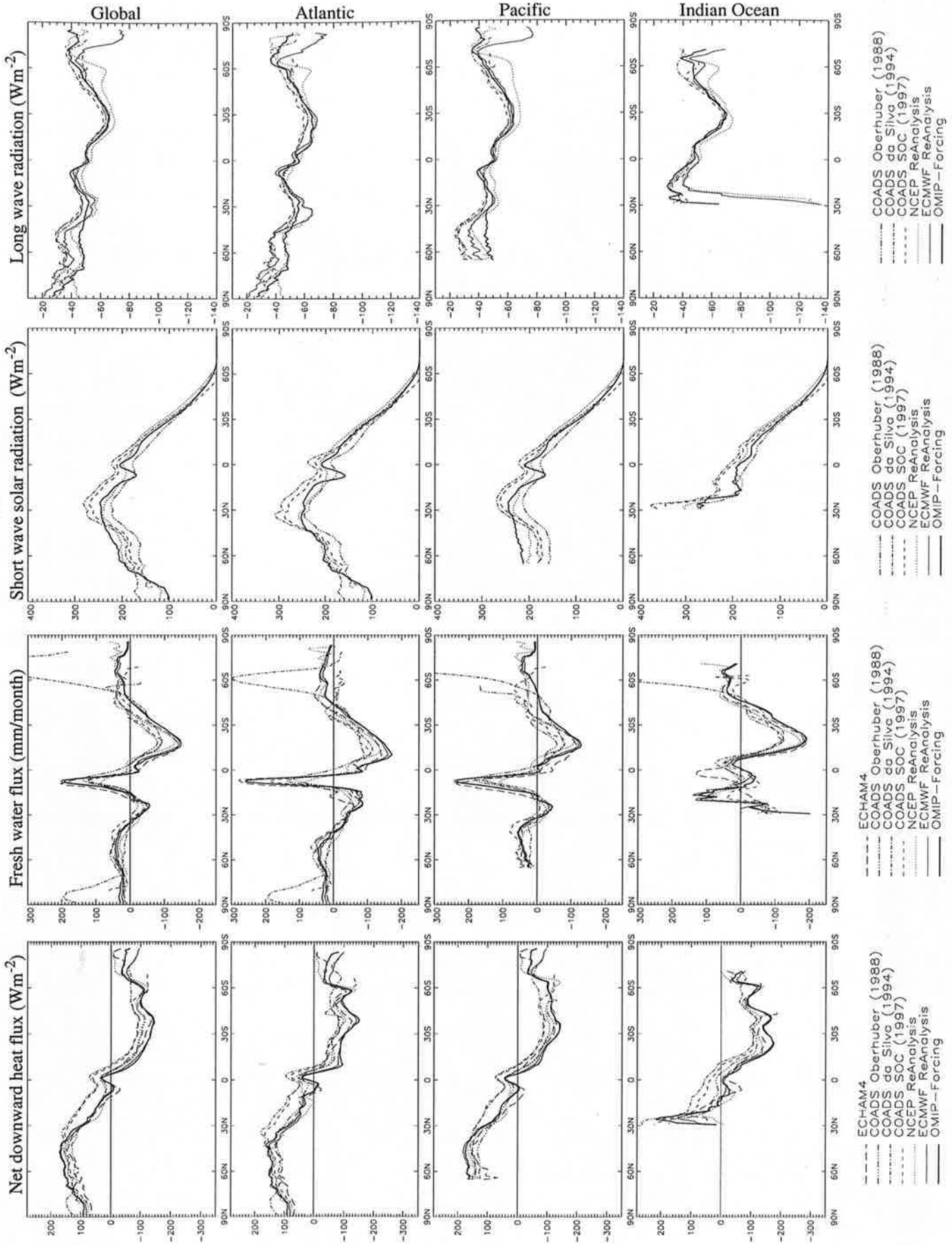

Fig.27.8 Zonal averages - part I August

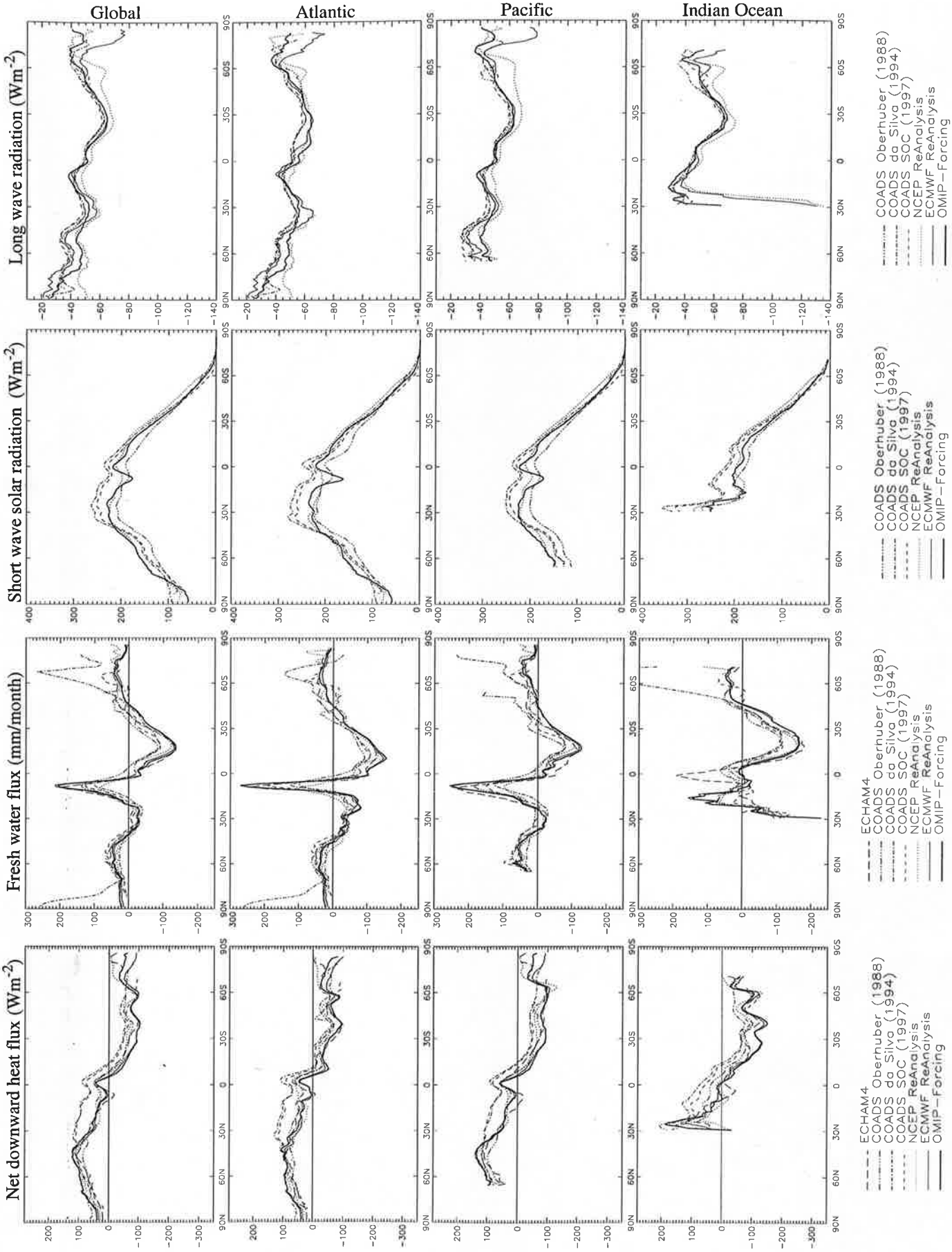

Fig.27.9 Zonal averages - part I September

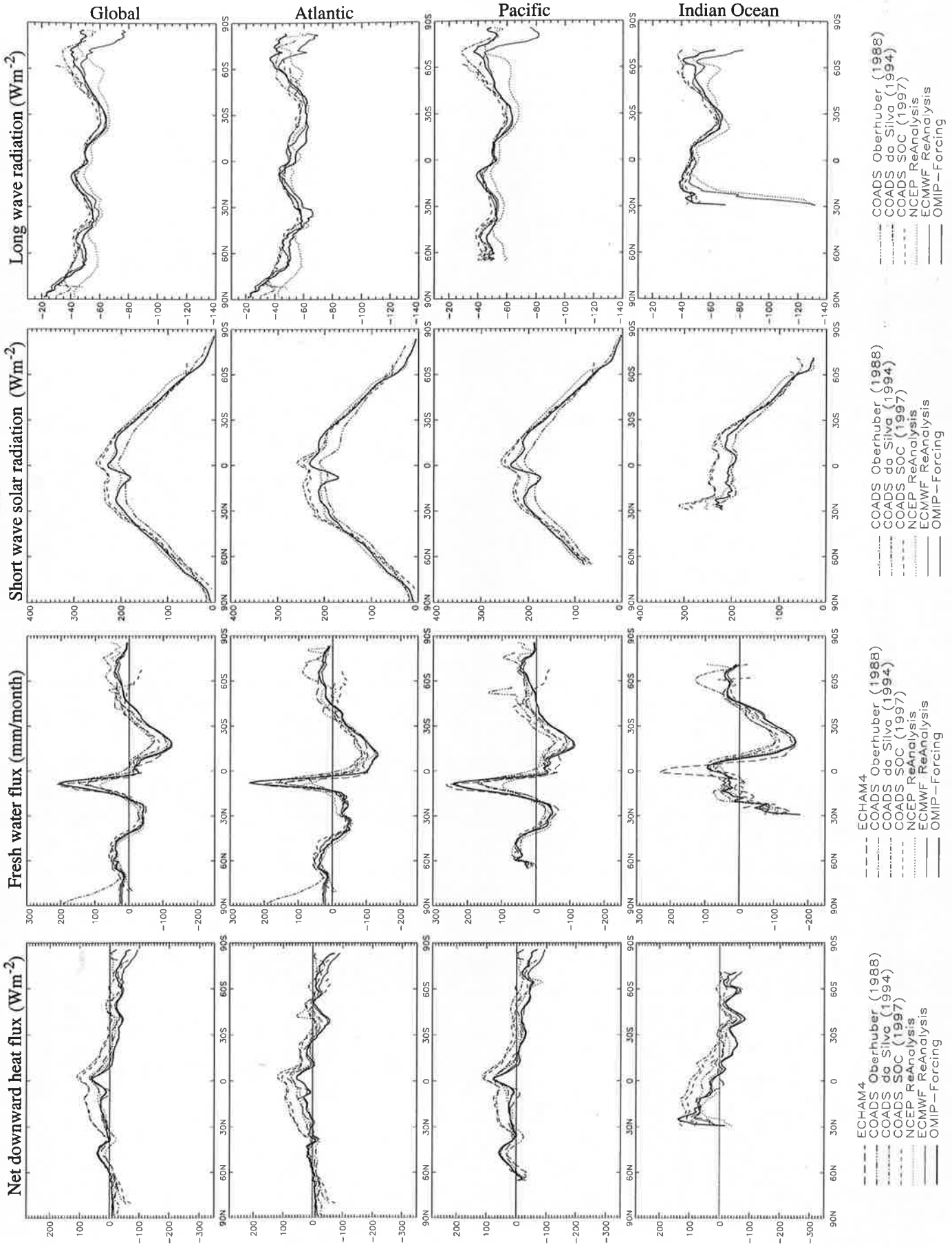

Fig.27.10 Zonal averages - part I October

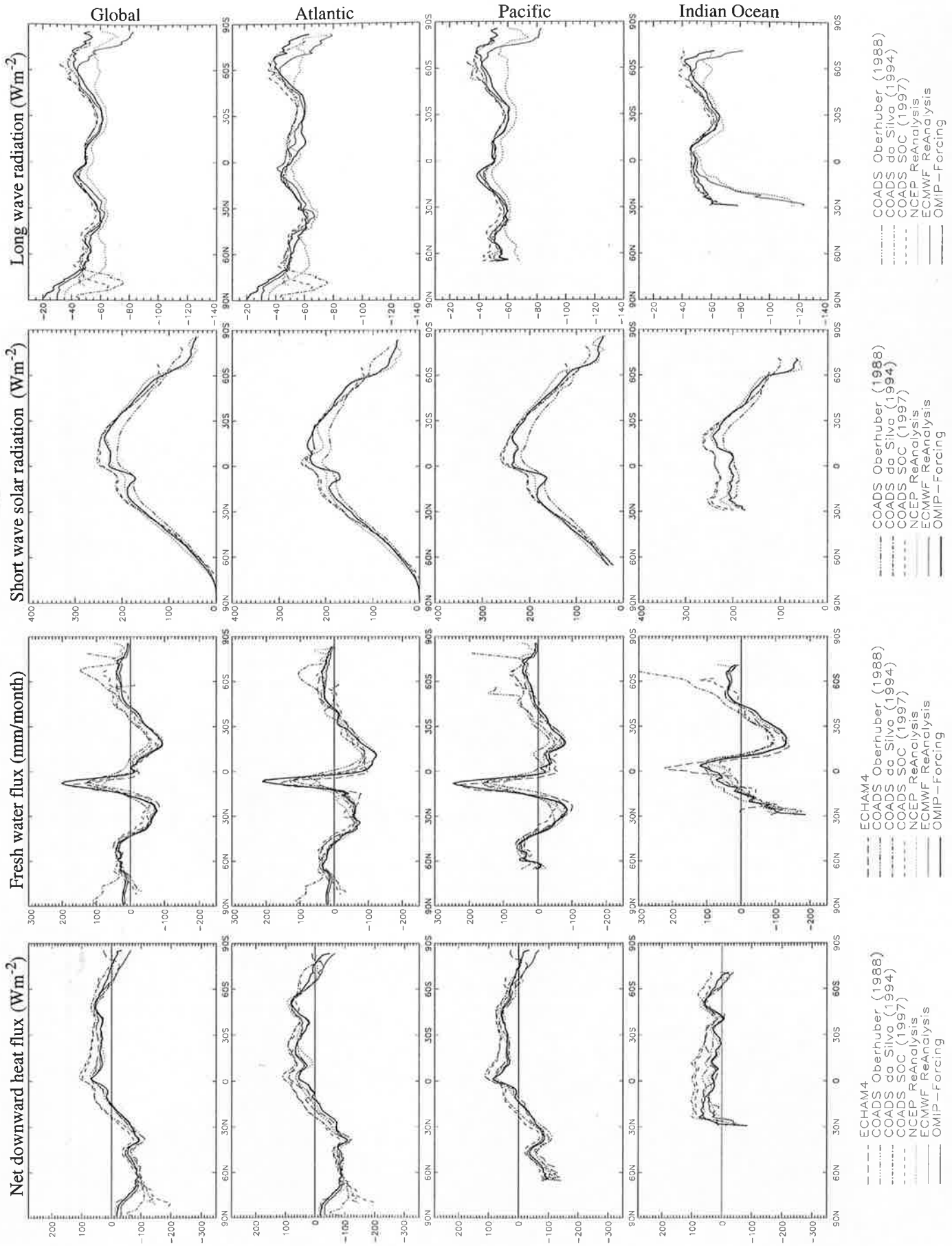

Fig.27.11 Zonal averages - part I November

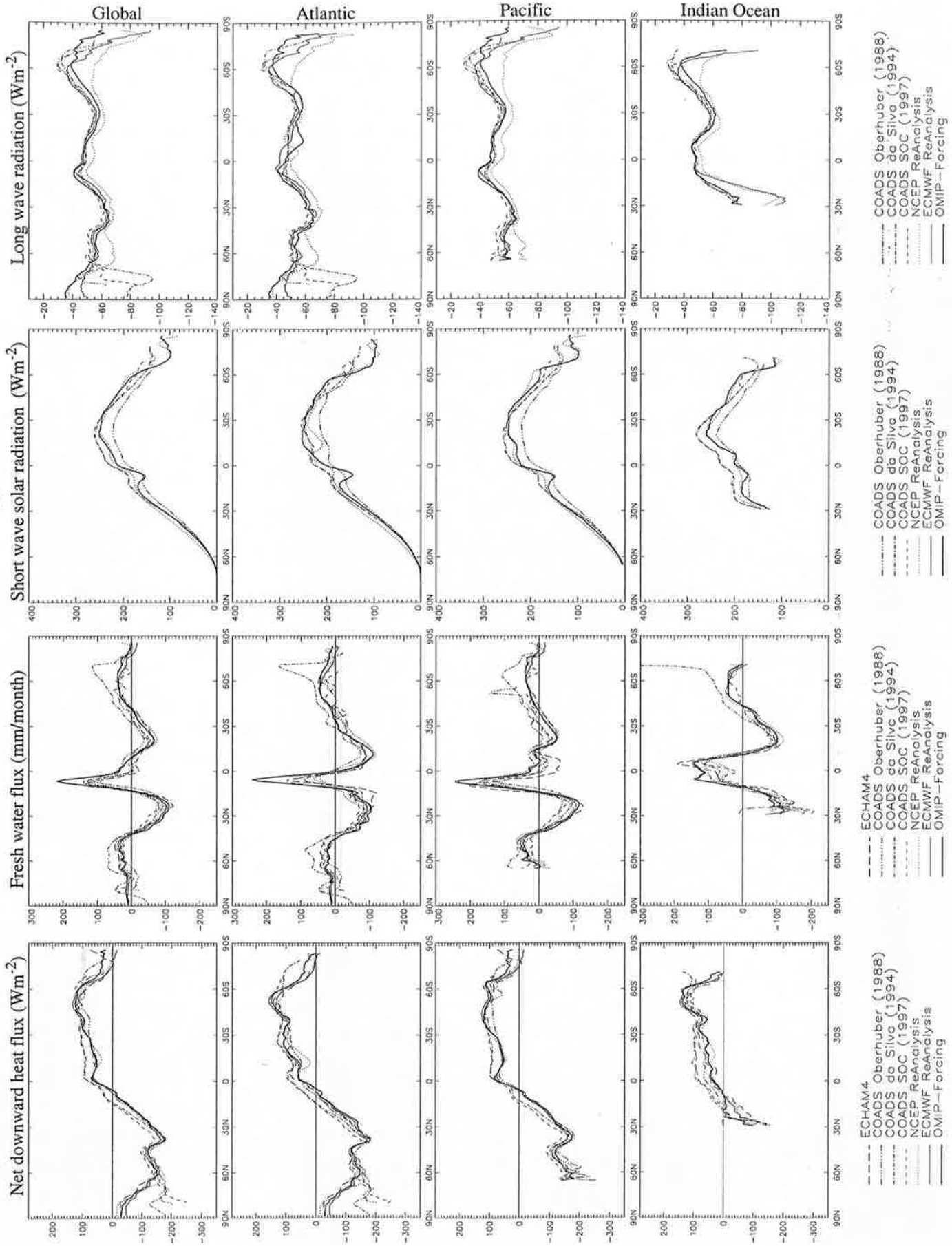

Fig.27.12 Zonal averages - part I December

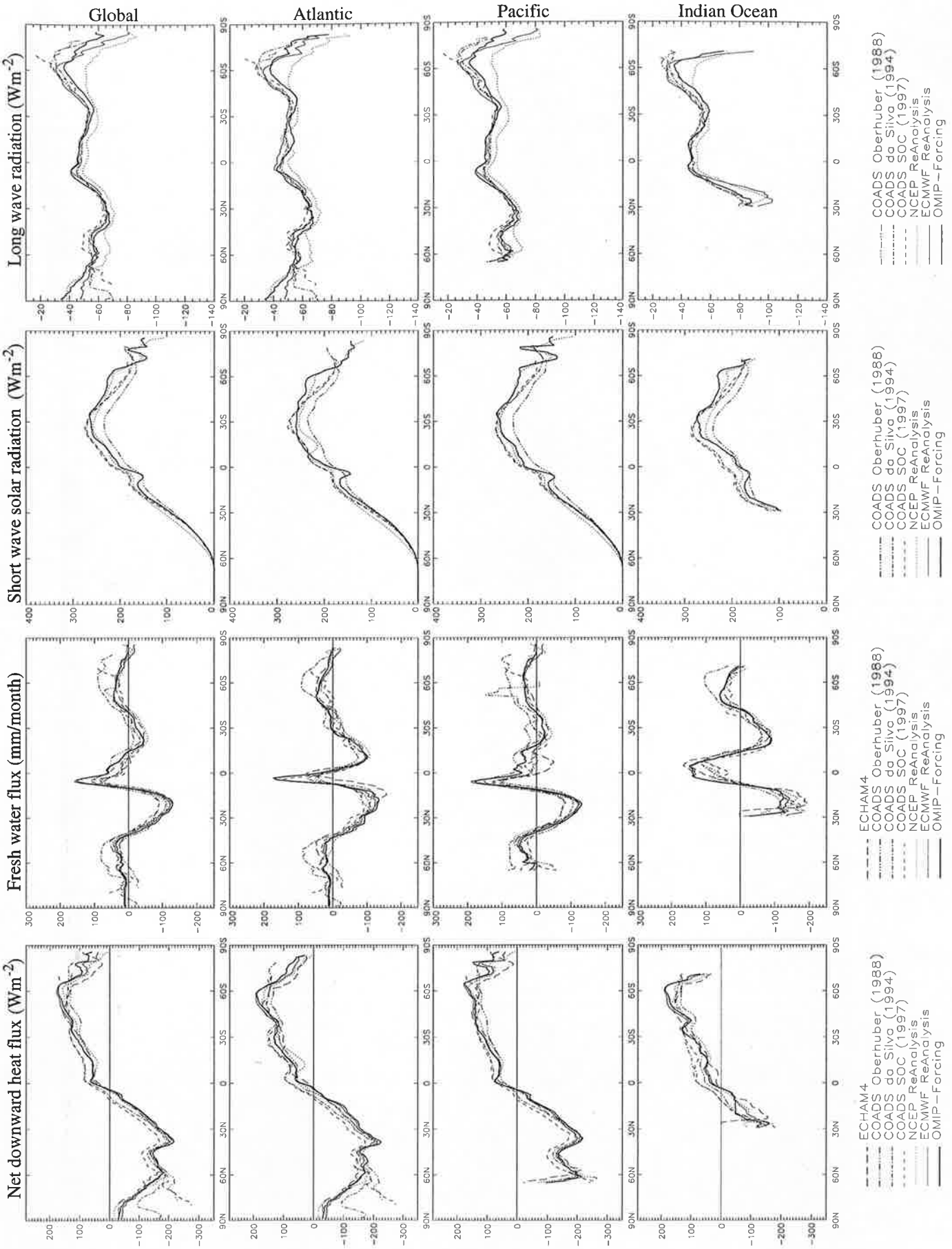

Fig.27.13 Zonal averages - part I Annual Mean

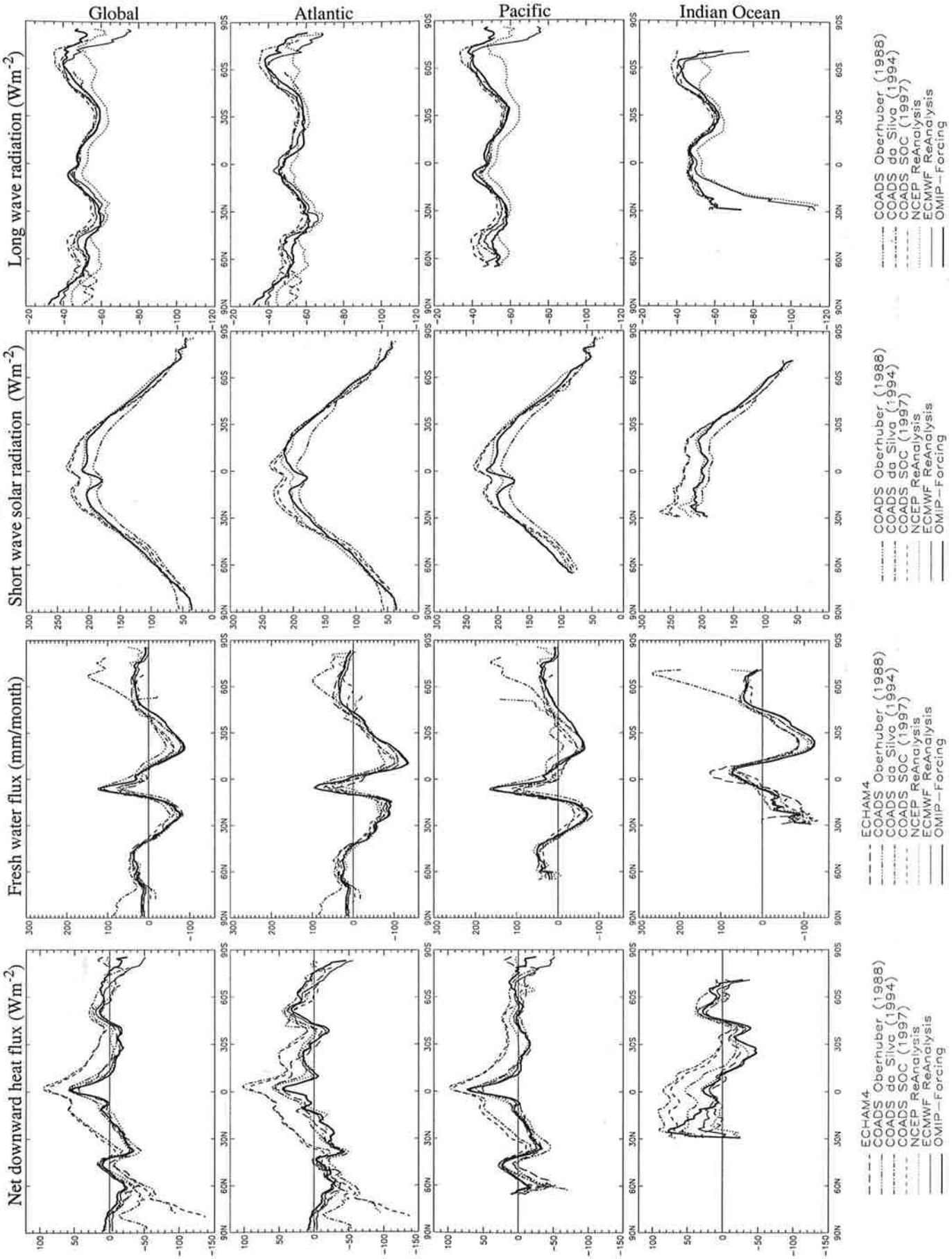

Fig.28.1 Zonal averages - part II January

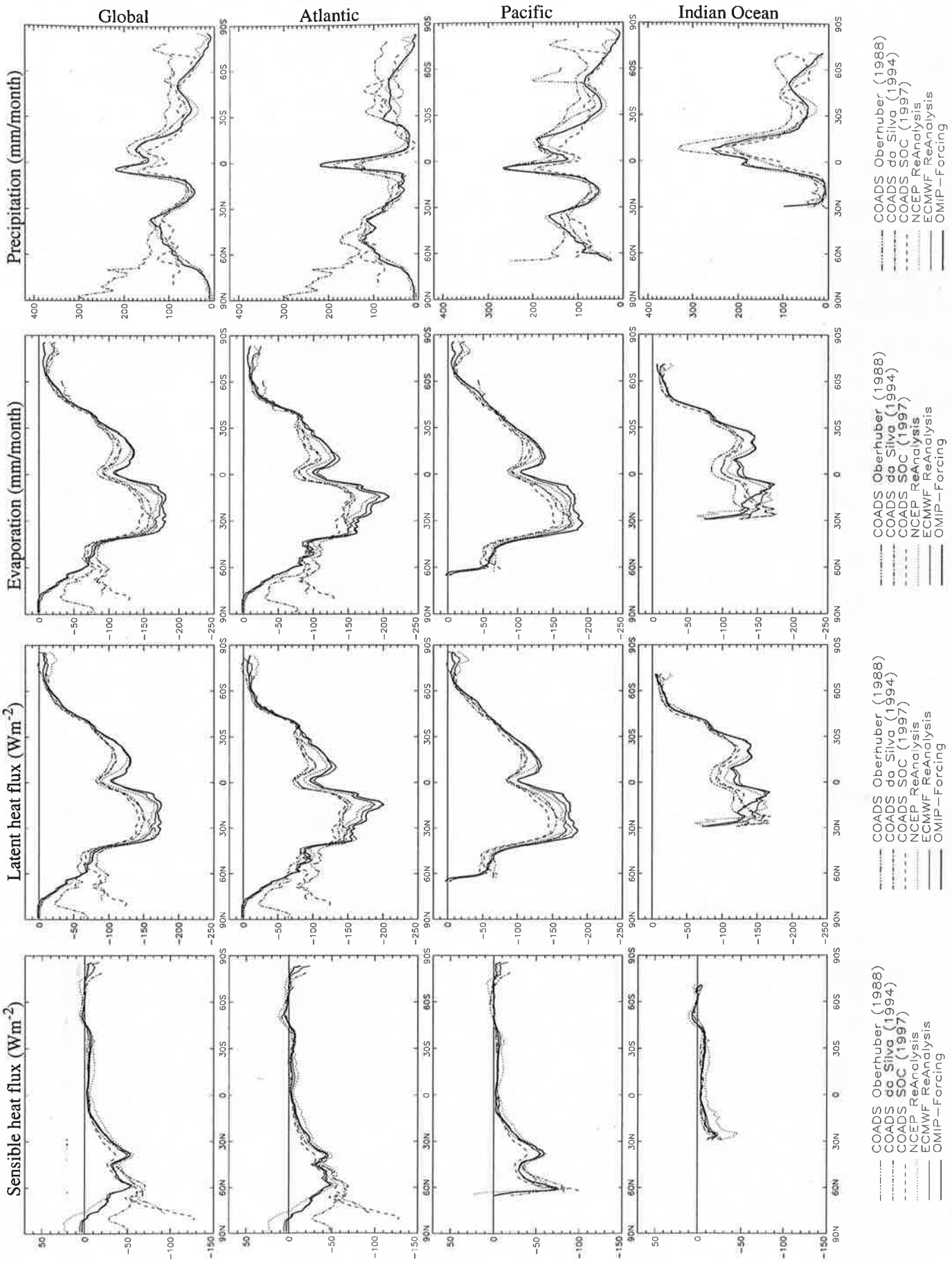

Fig.28.2 Zonal averages - part II February

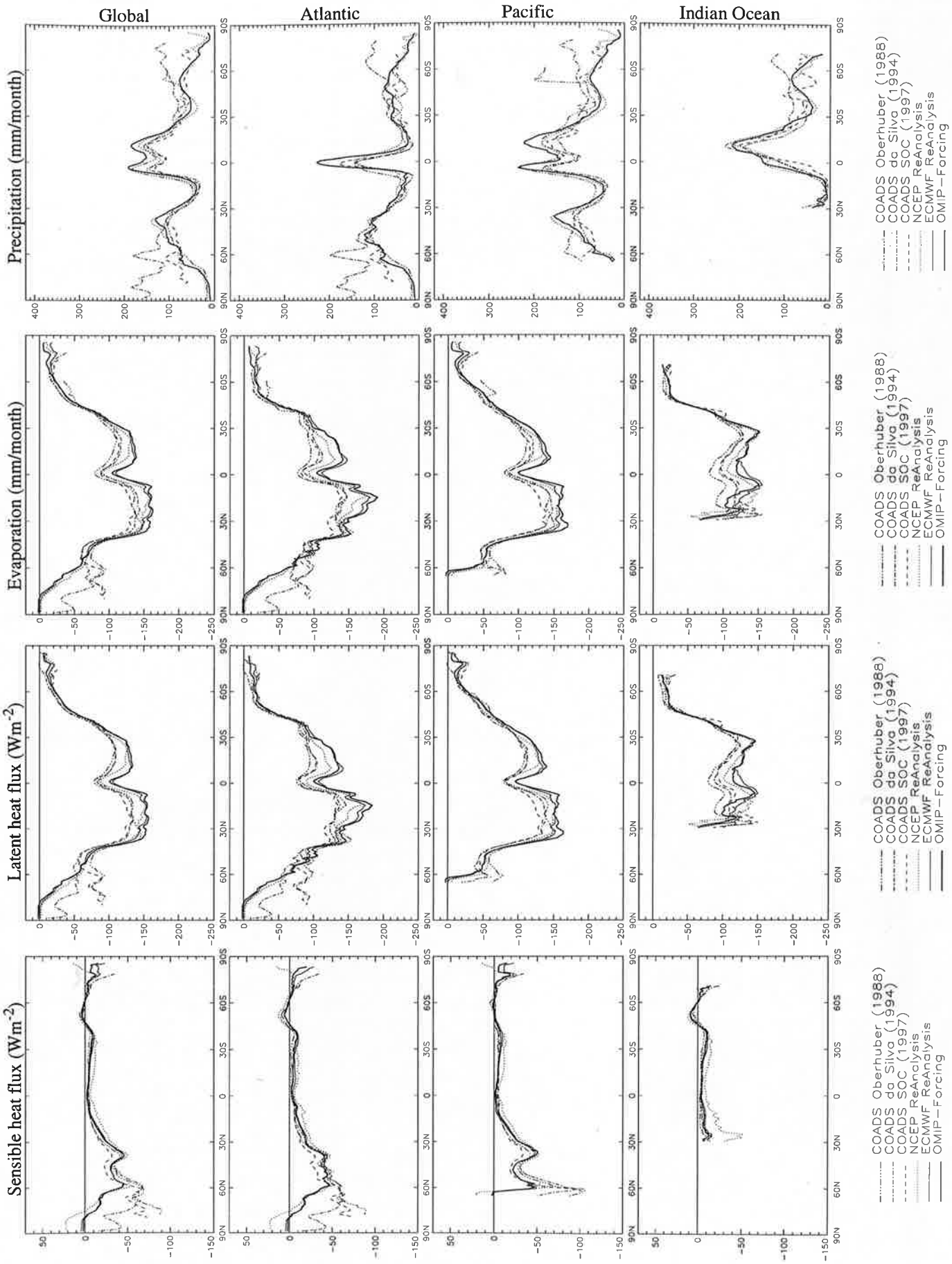

Fig.28.3 Zonal averages - part II March

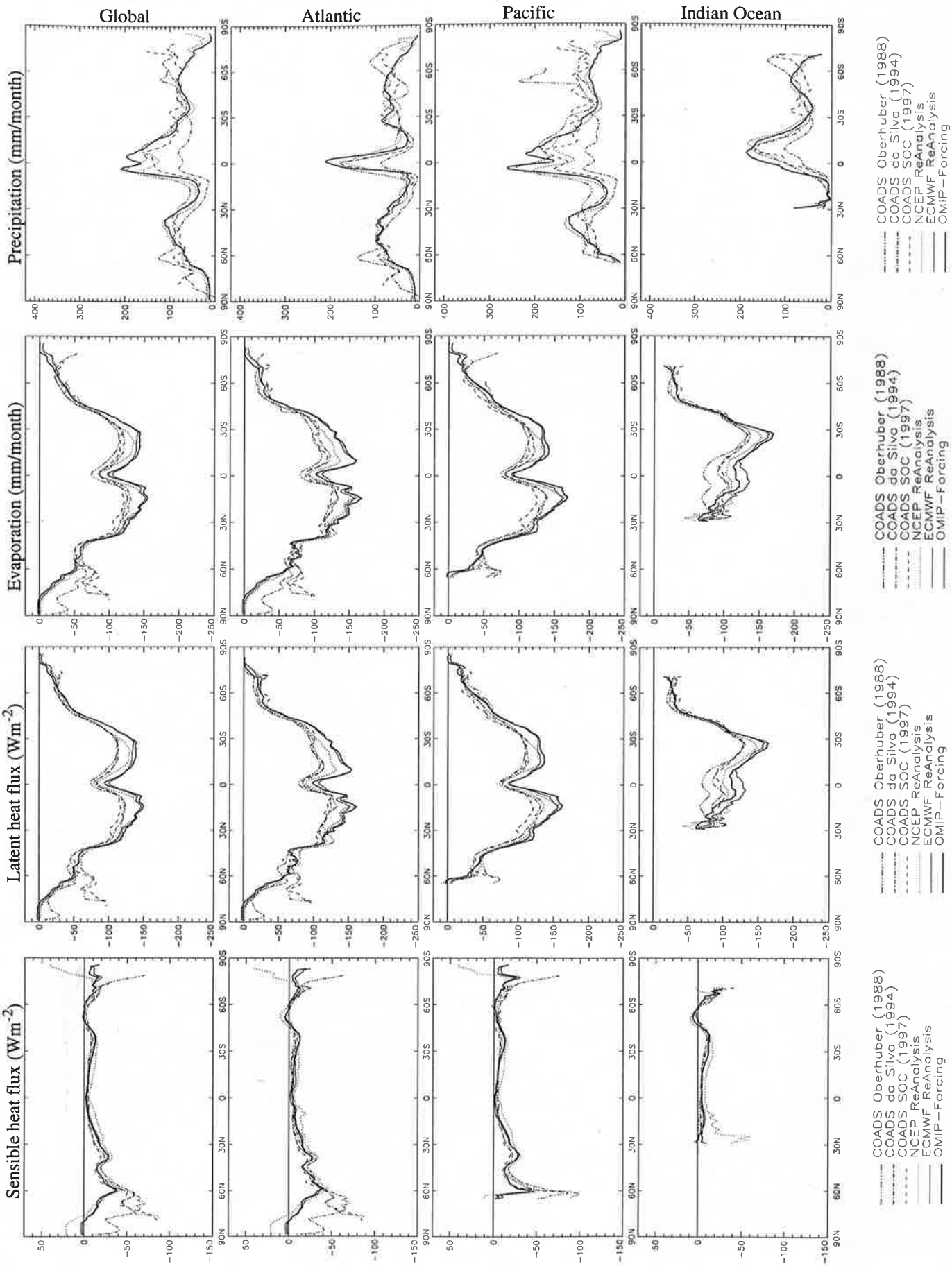

Fig.28.4 Zonal averages - part II April

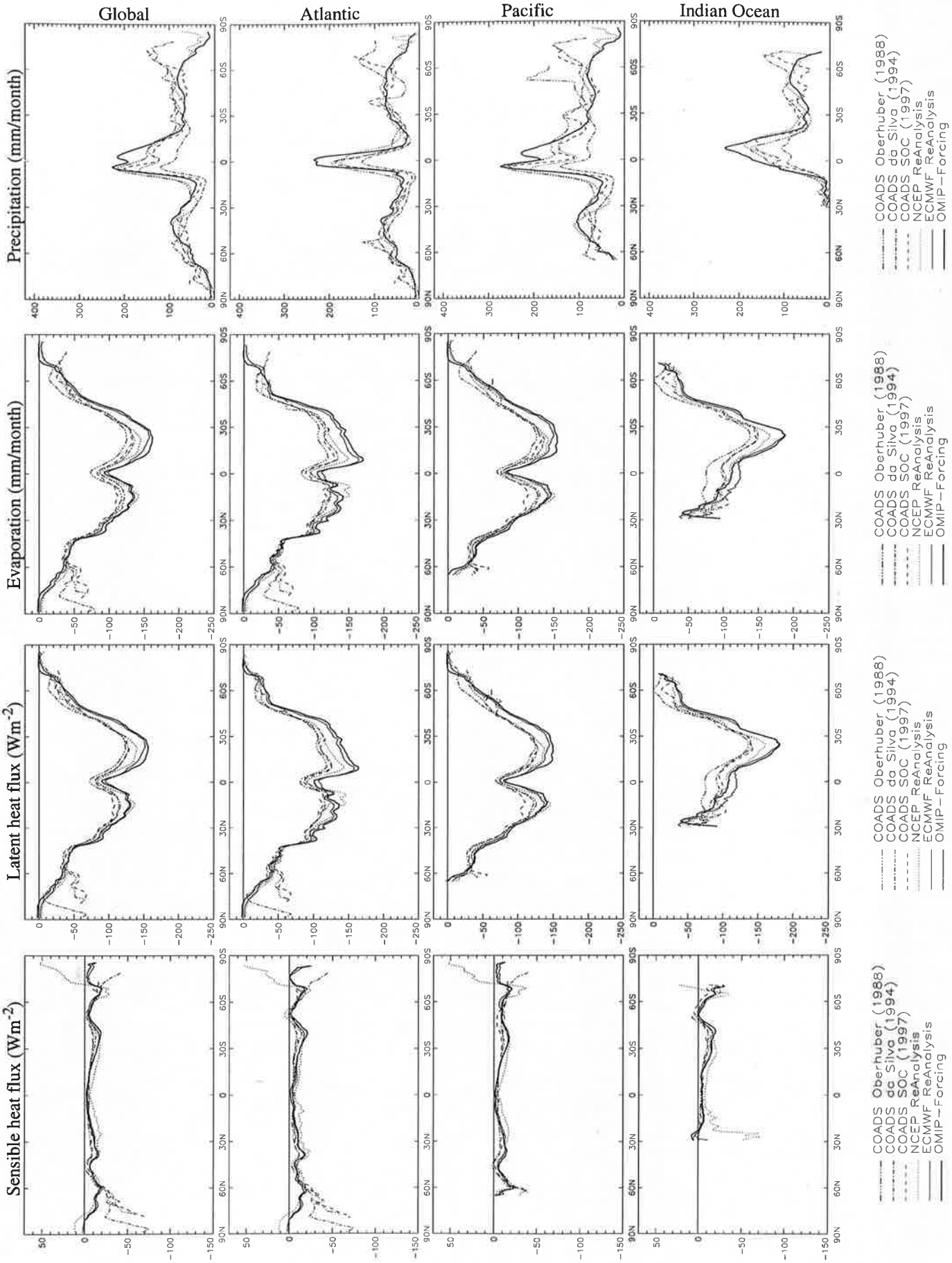

Fig.28.5 Zonal averages - part II May

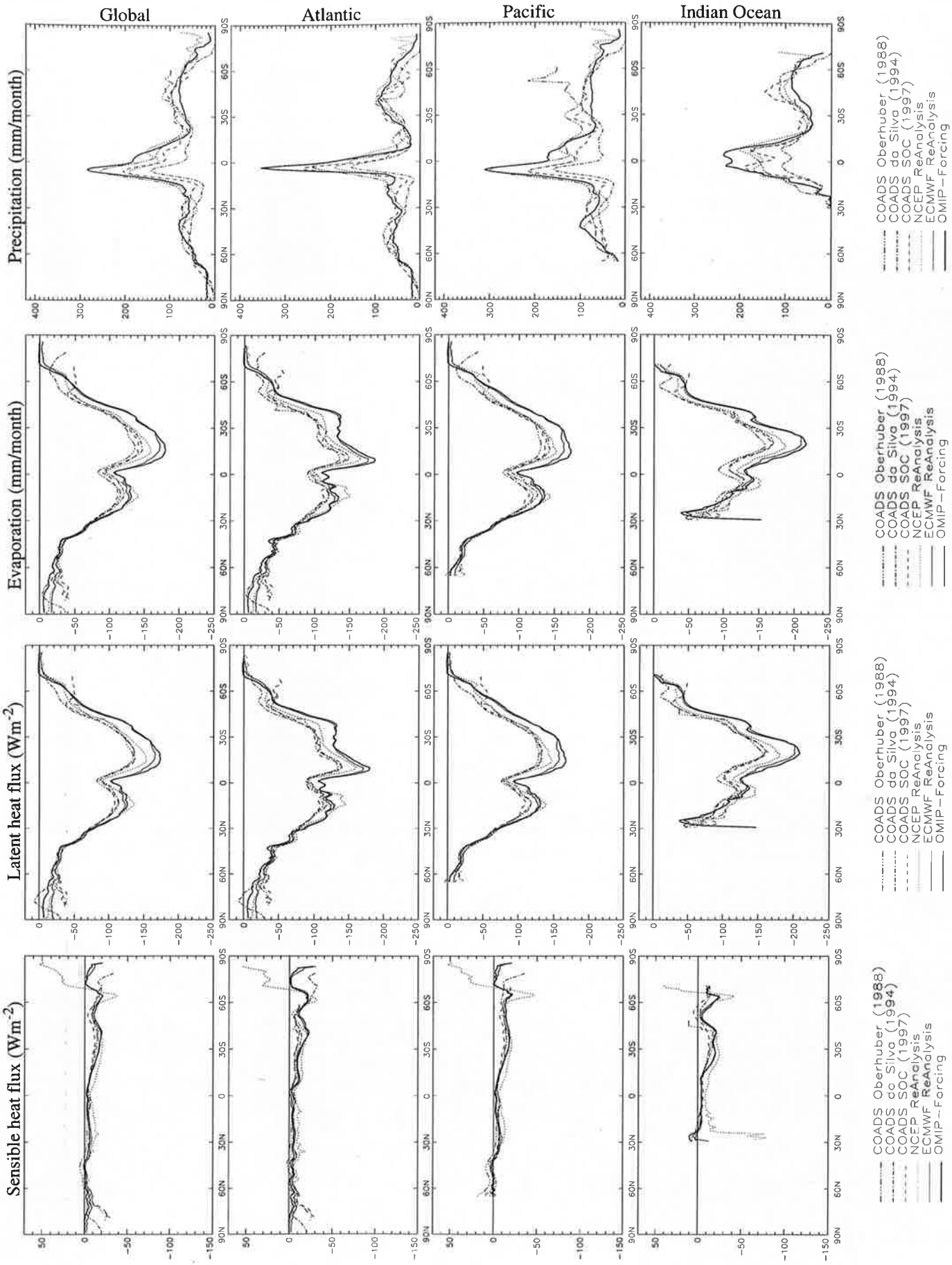

Fig.28.6 Zonal averages - part II June

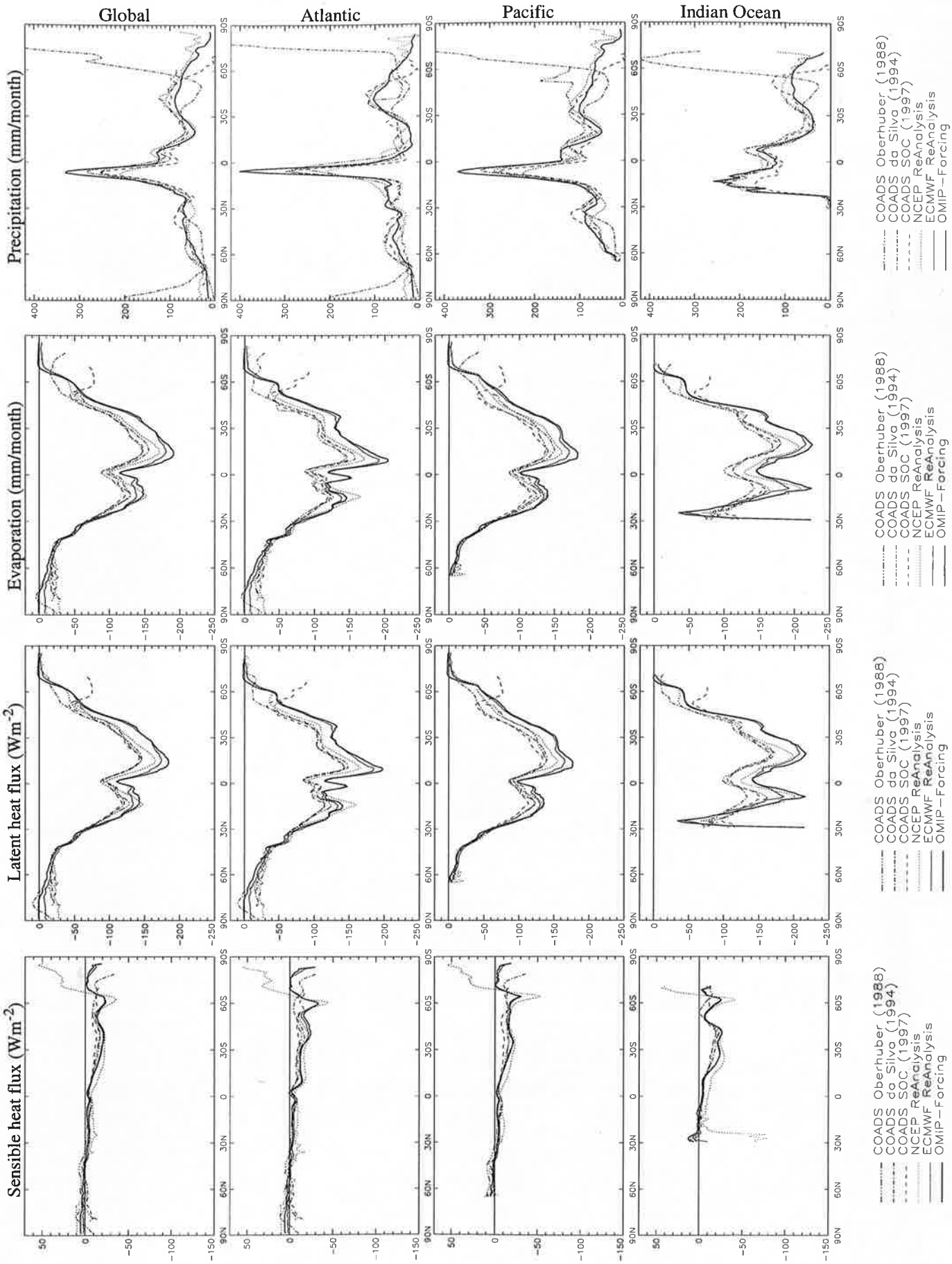

Fig.28.7 Zonal averages - part II July

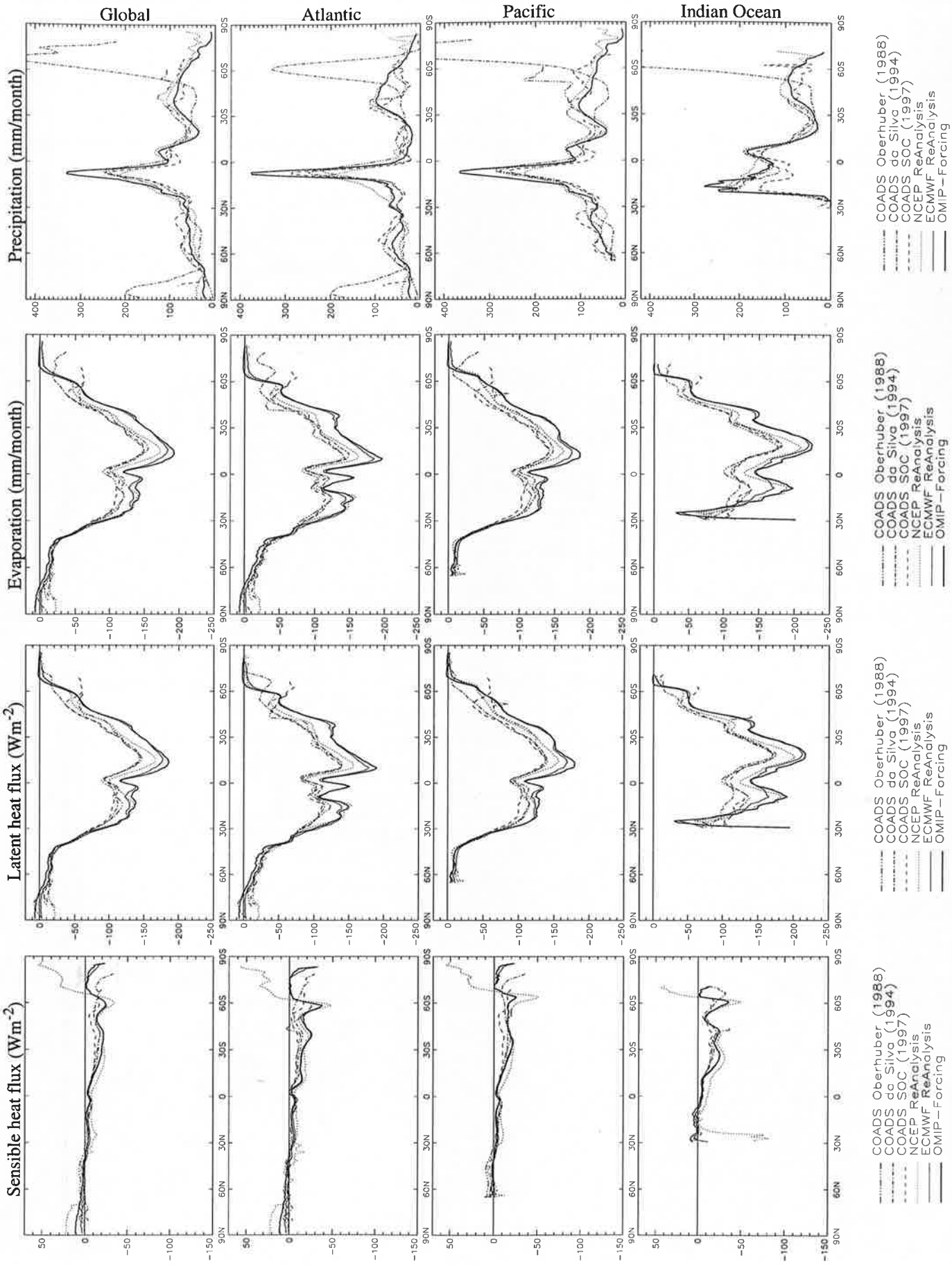

Fig.28.8 Zonal averages - part II August

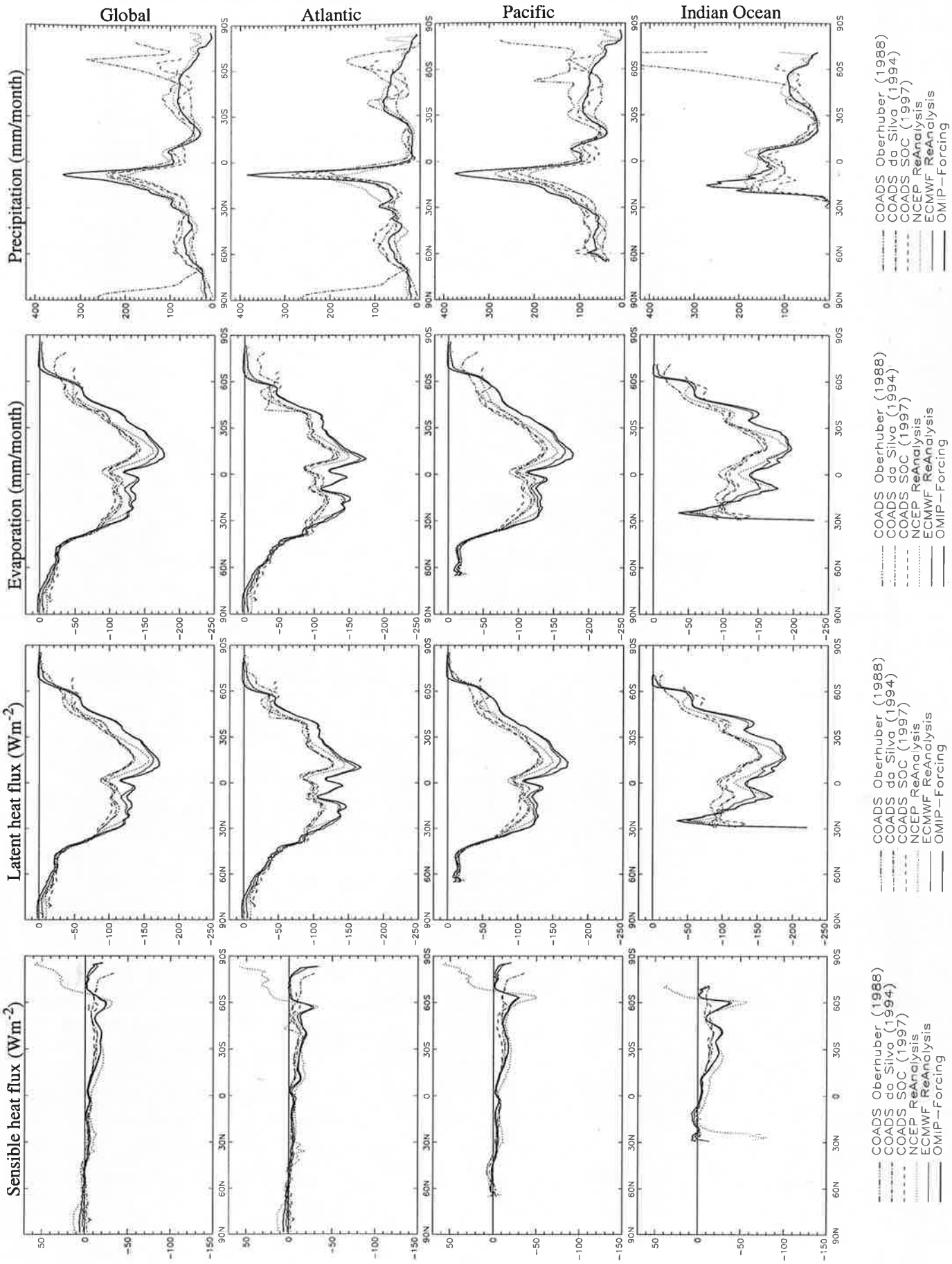

Fig.28.9 Zonal averages - part II September

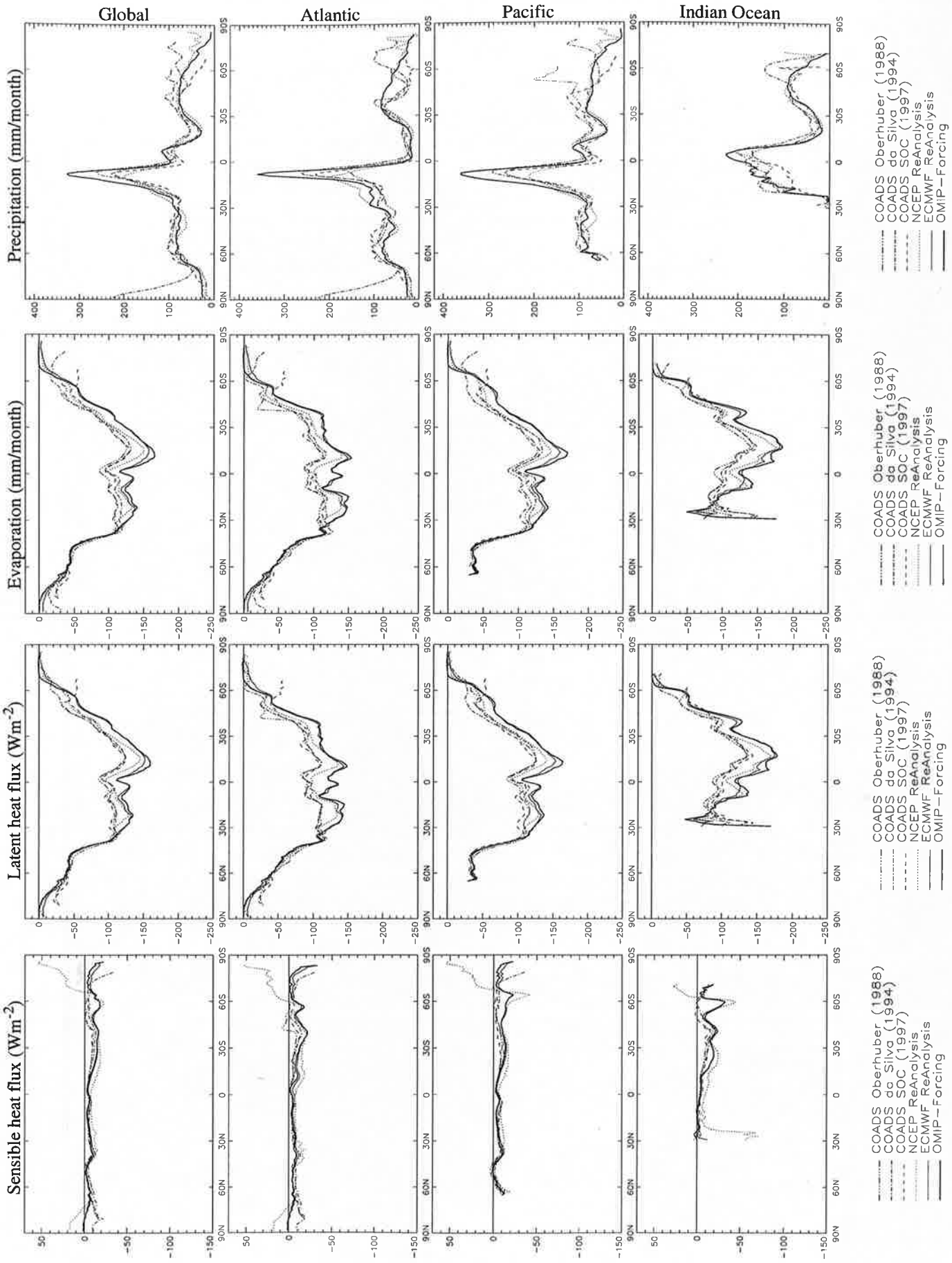

Fig.28.10 Zonal averages - part II October

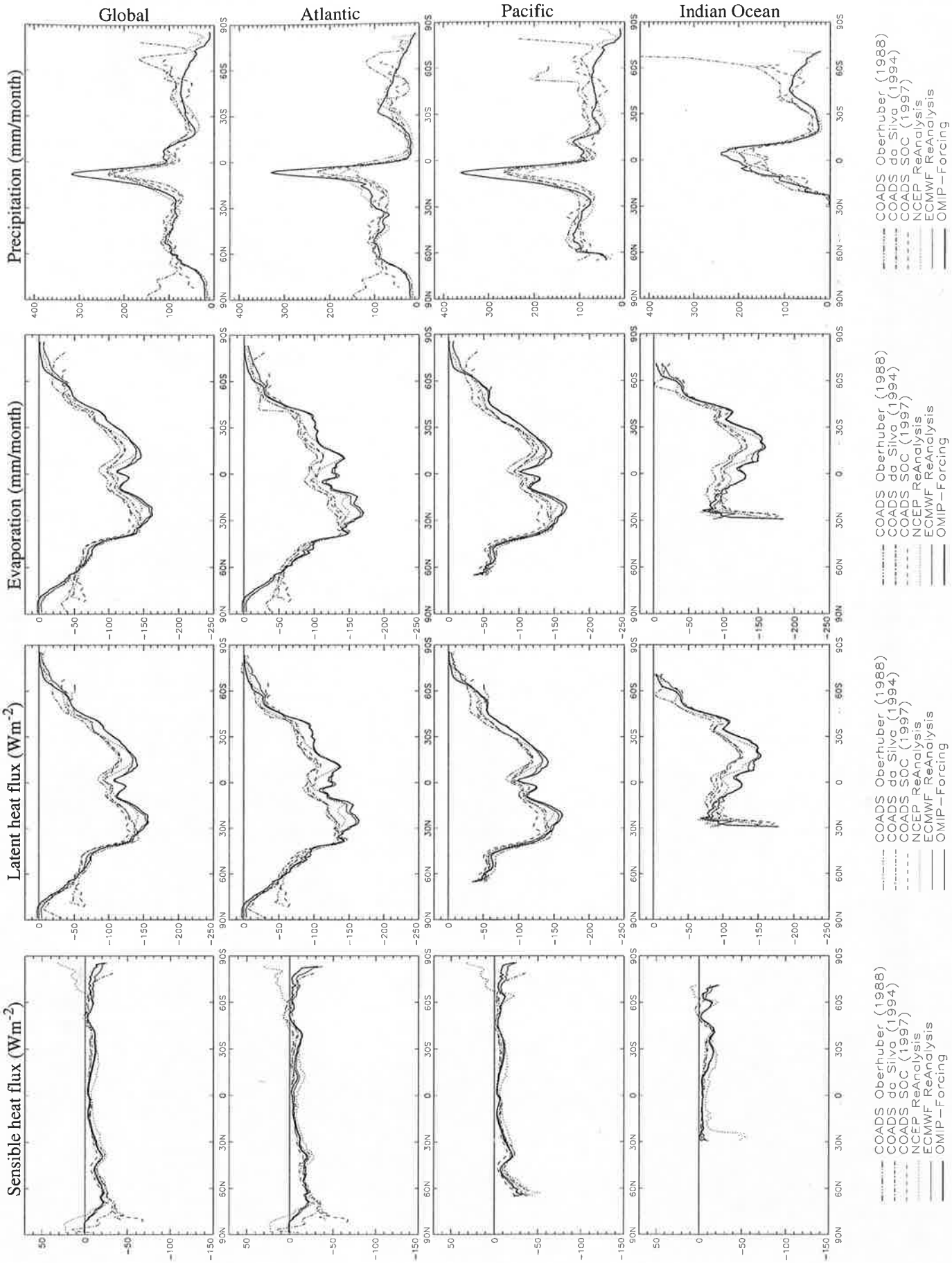

Fig.28.11 Zonal averages - part II November

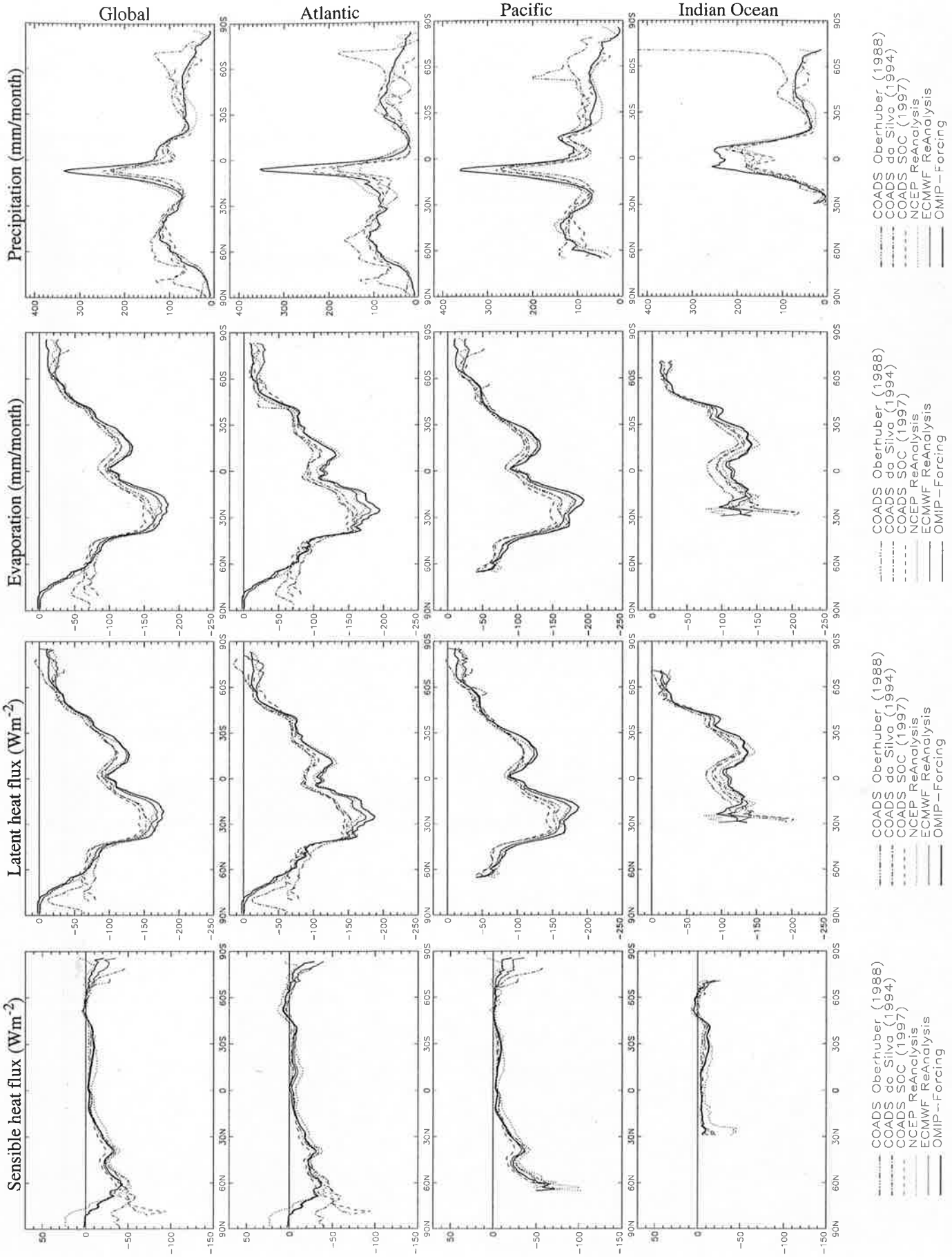

Fig.28.12 Zonal averages - part II December

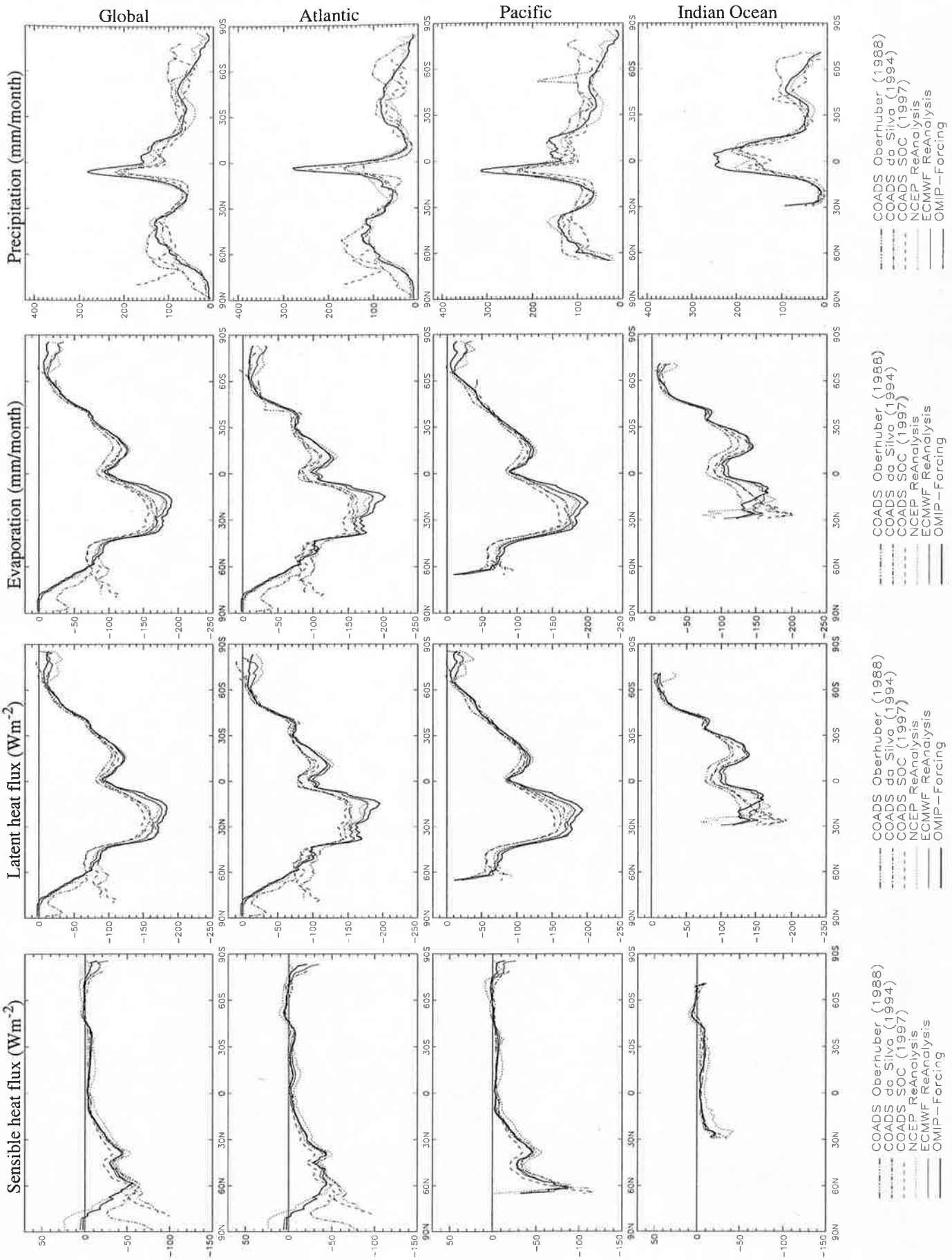

Fig.28.13 Zonal averages - part II Annual Mean

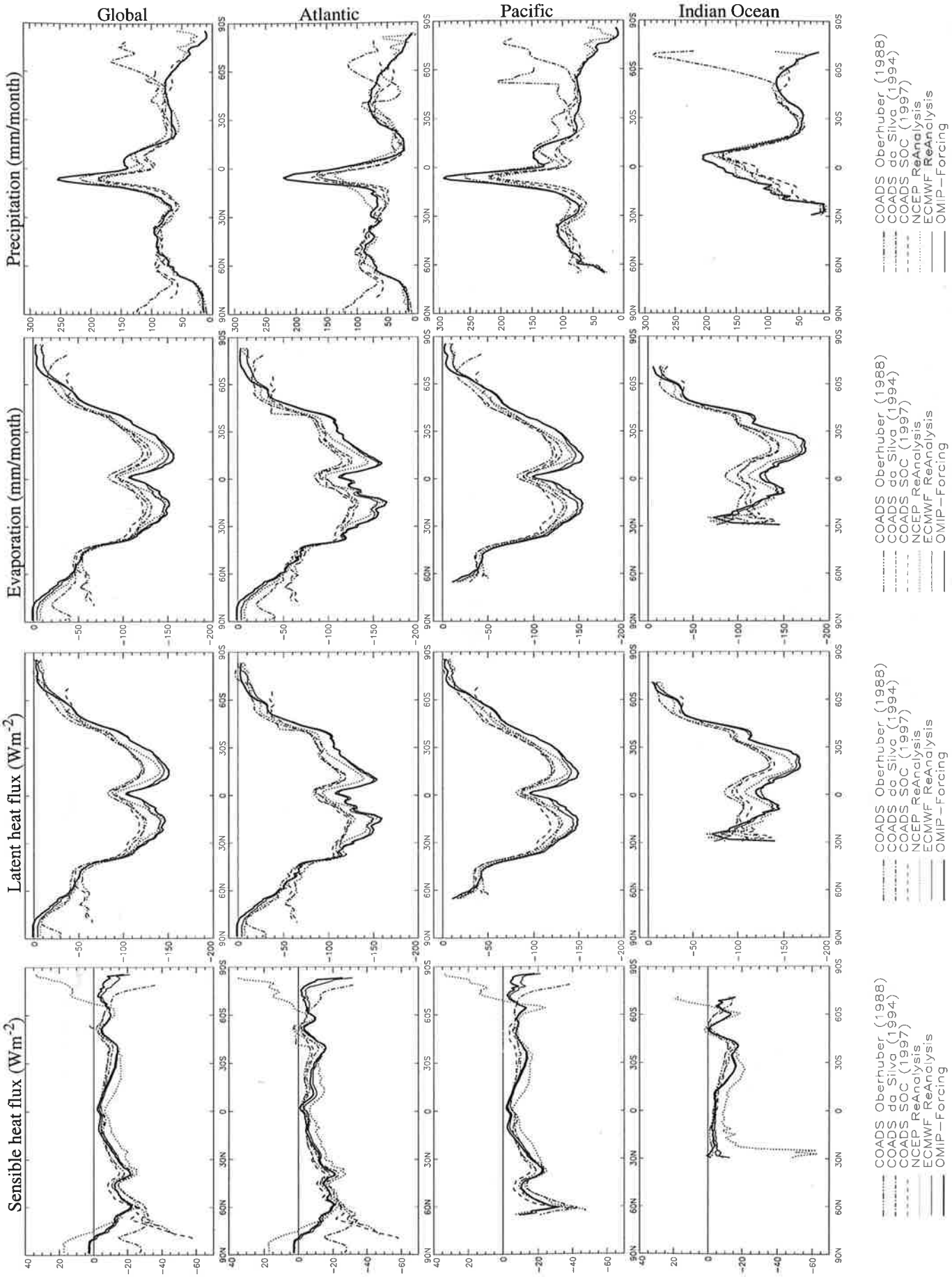

Fig.29.1 Zonal averages - part III January

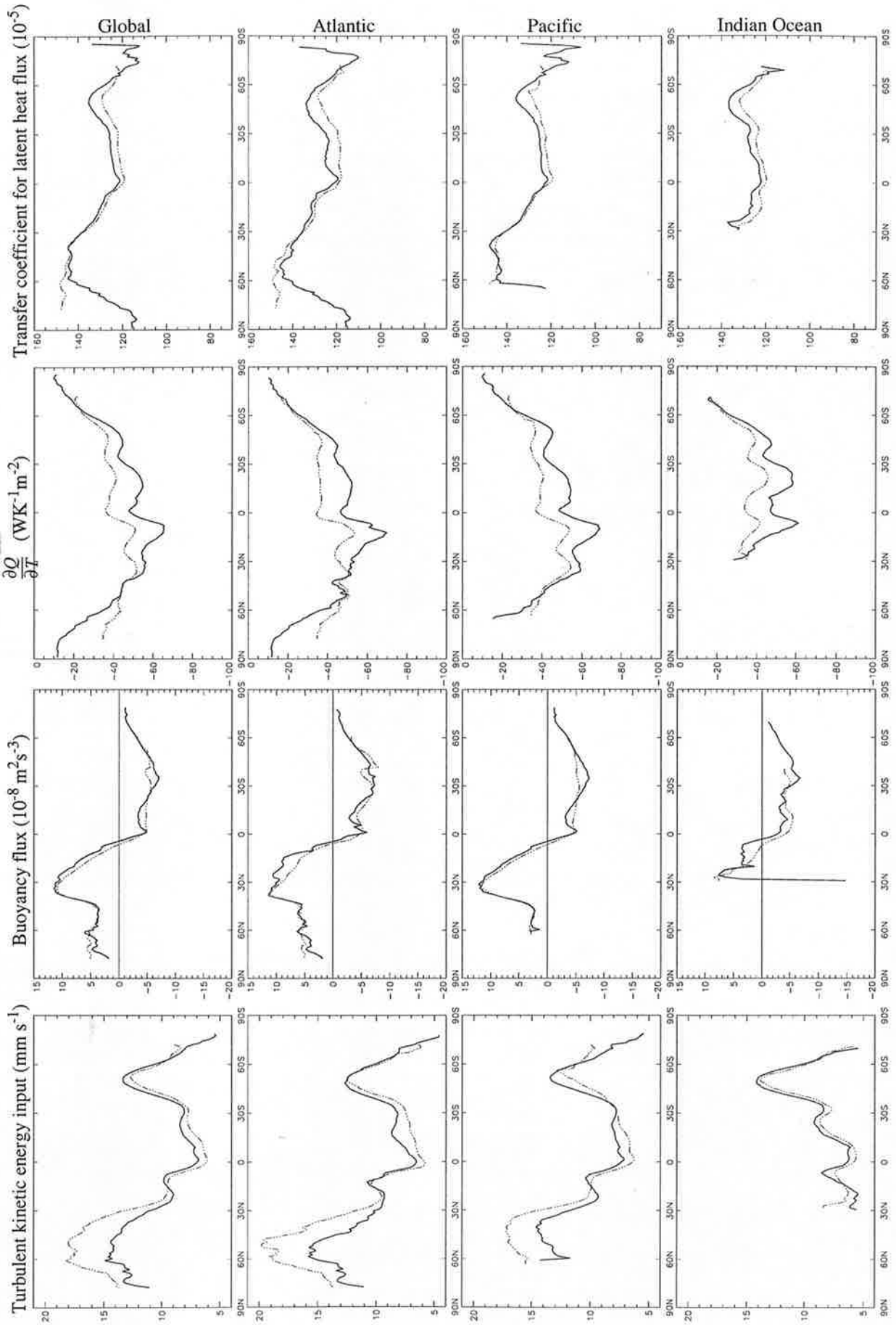

Fig.29.2 Zonal averages - part III February

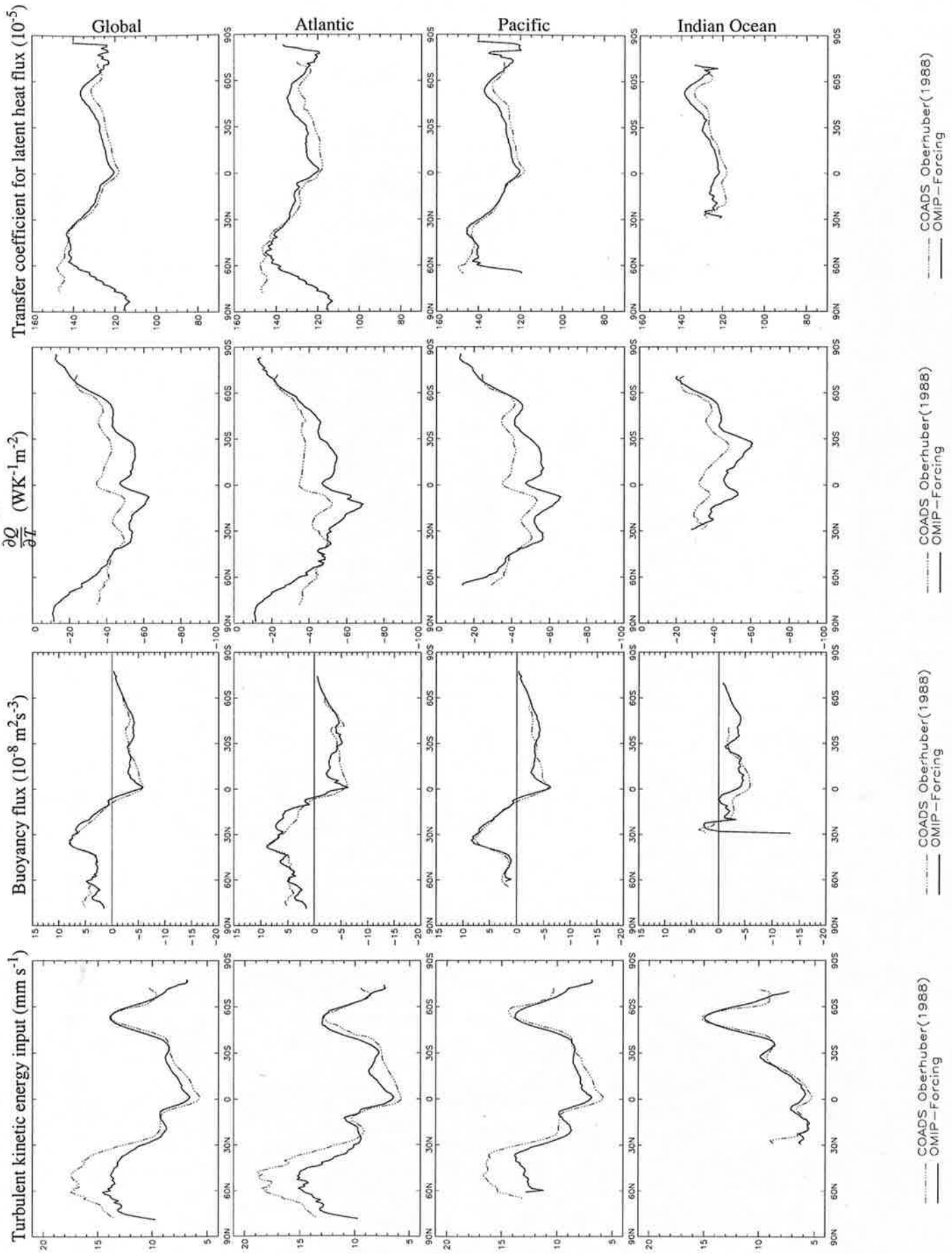

Fig.29.3 Zonal averages - part III March

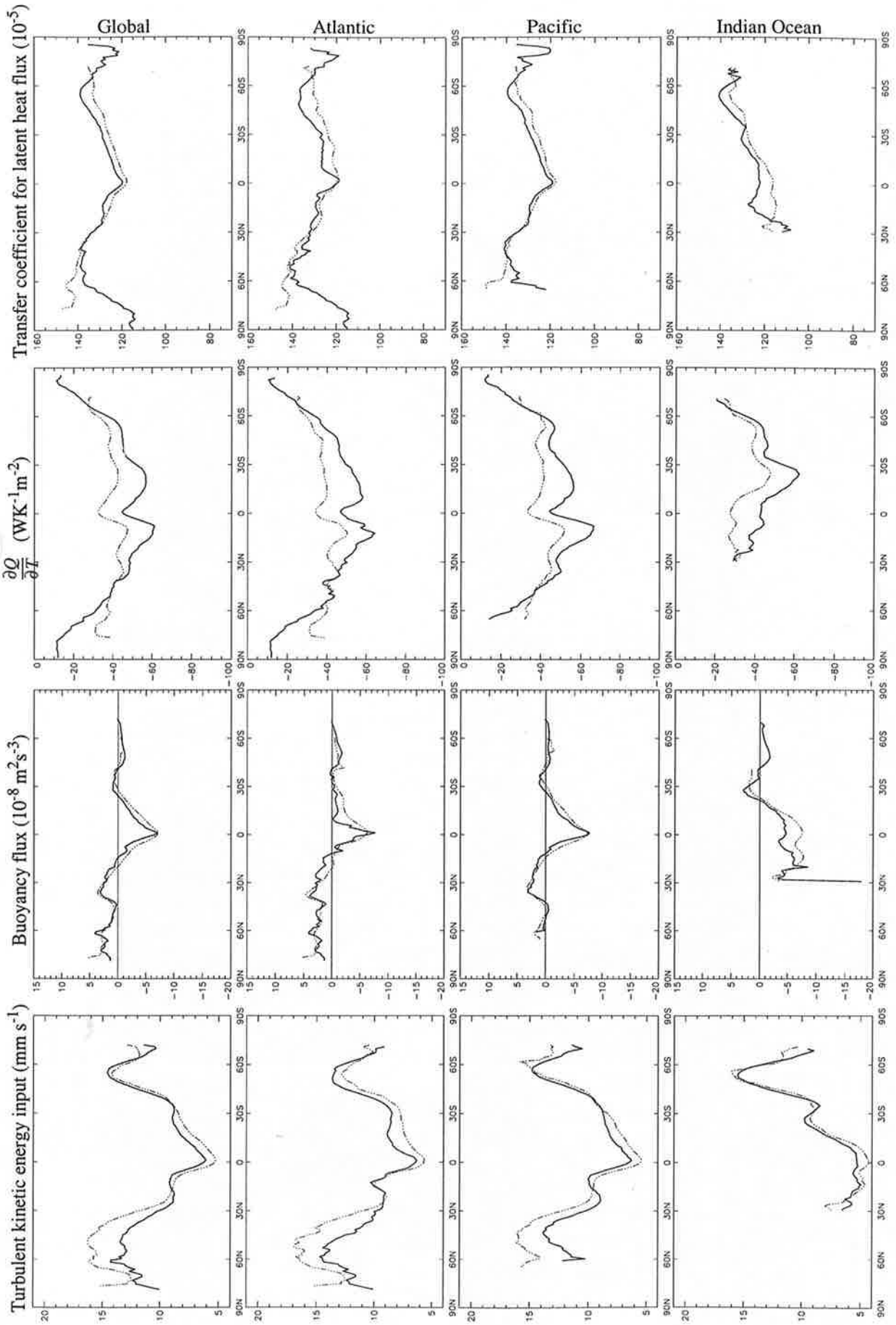

Fig.29.4 Zonal averages - part III April

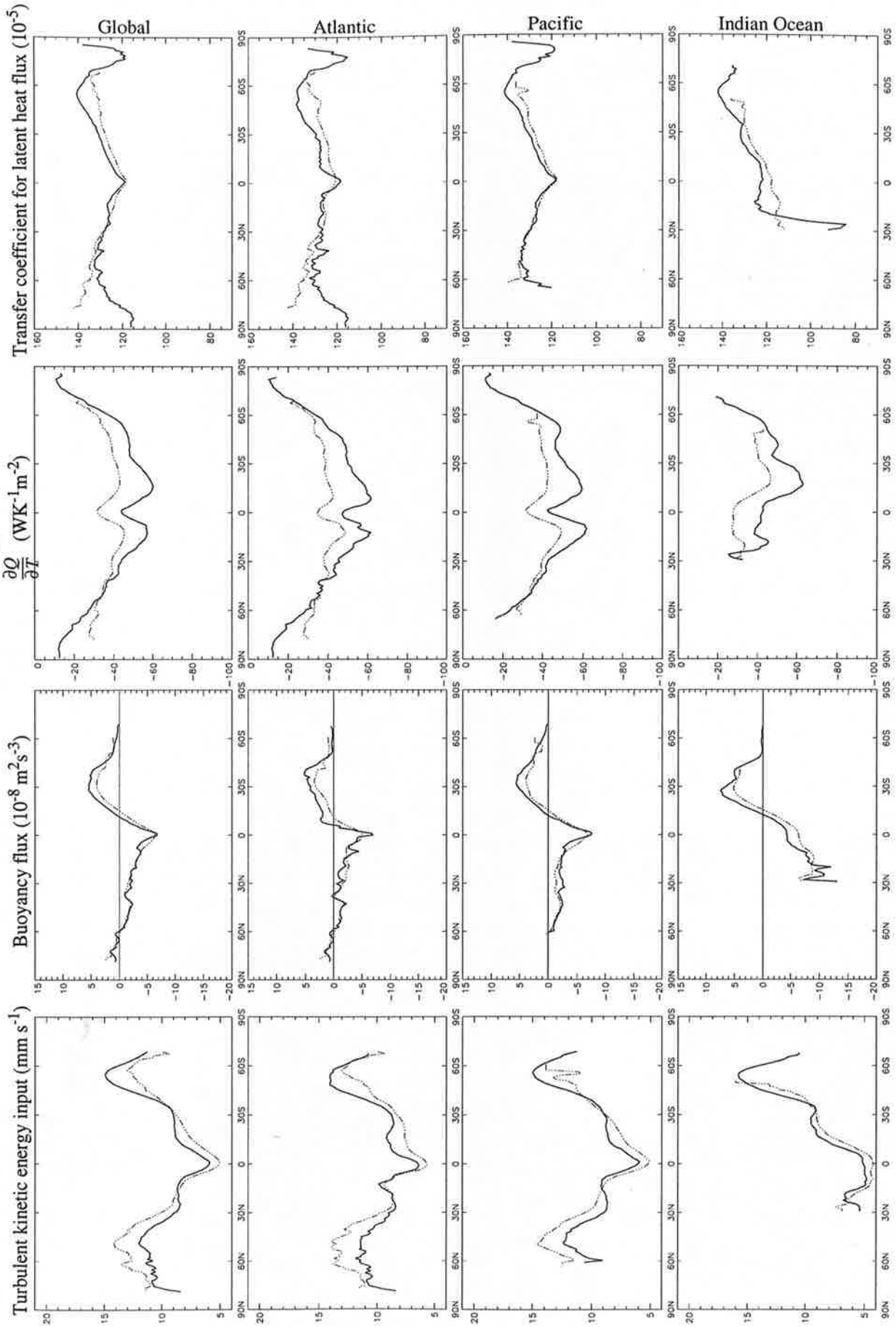

Fig.29.5 Zonal averages - part III May

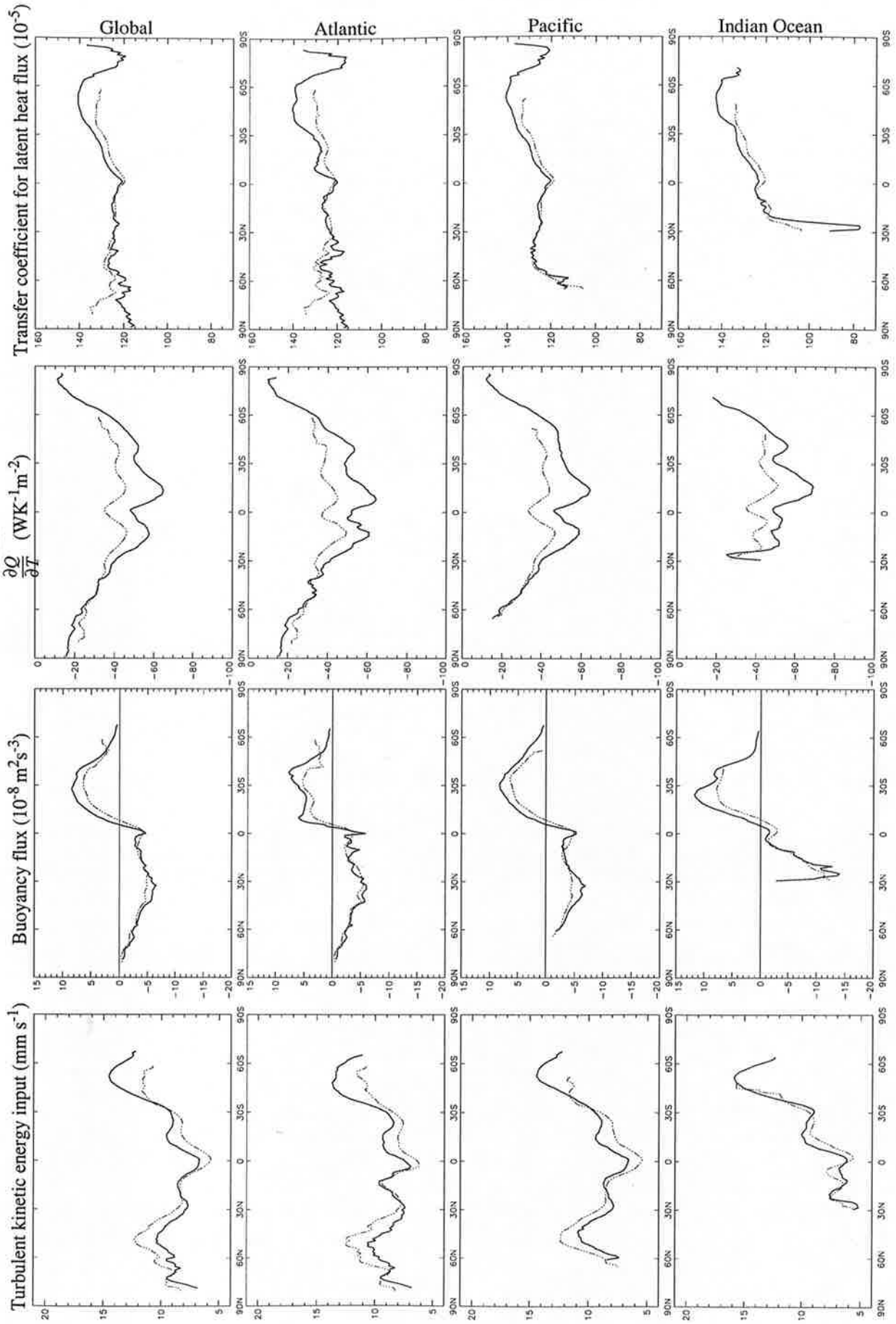

Fig.29.6 Zonal averages - part III June

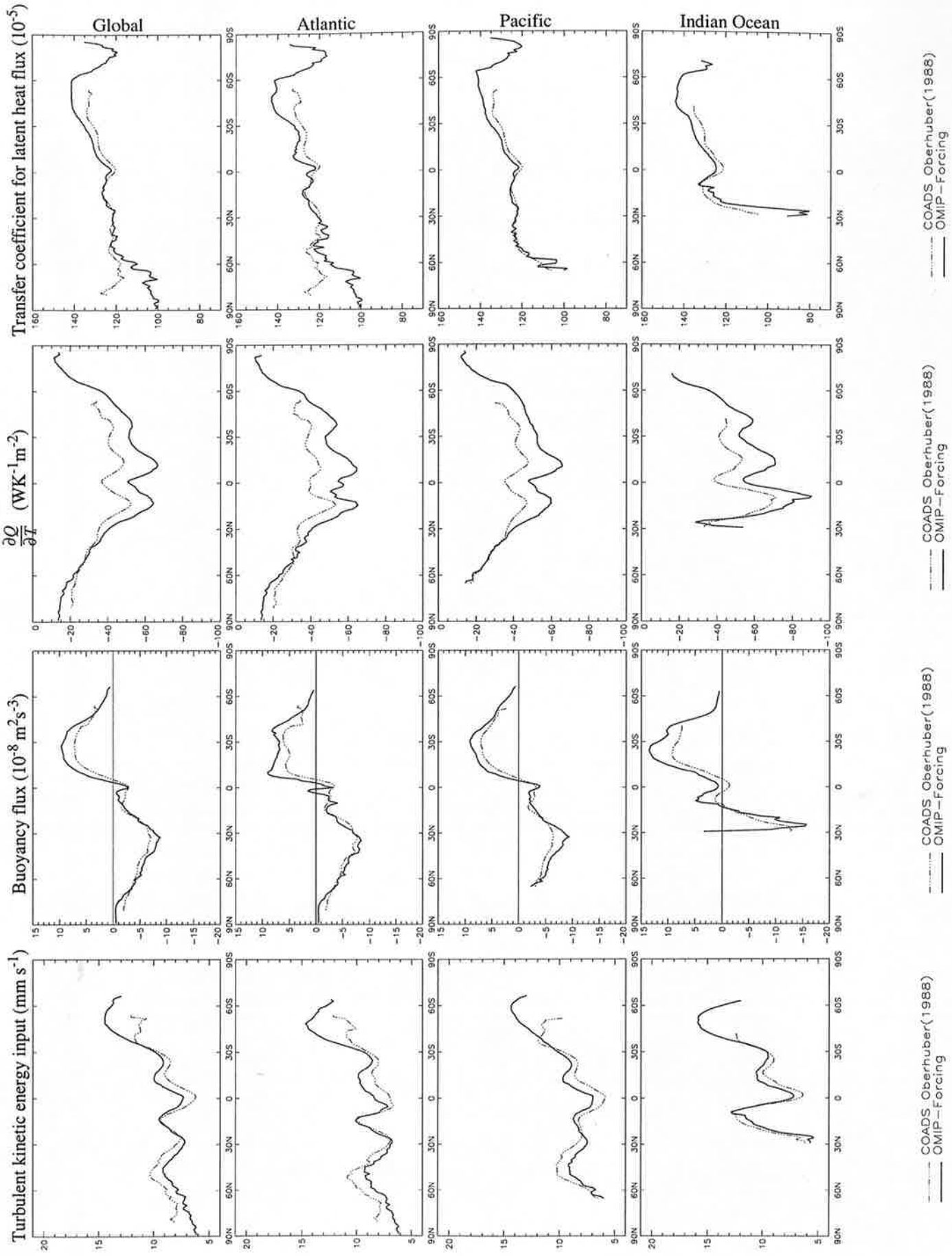

Fig.29.7 Zonal averages - part III July

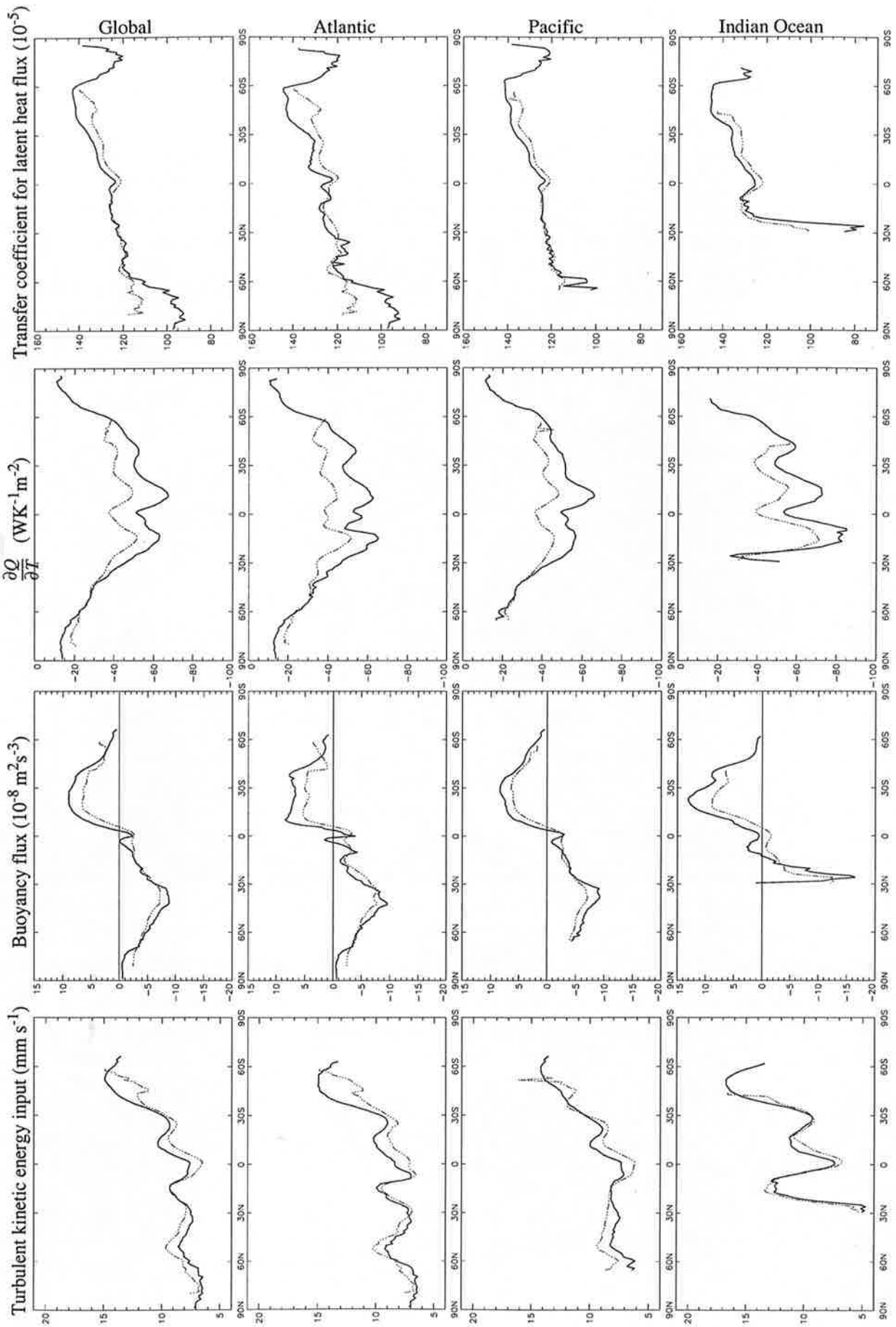

Fig.29.8 Zonal averages - part III August

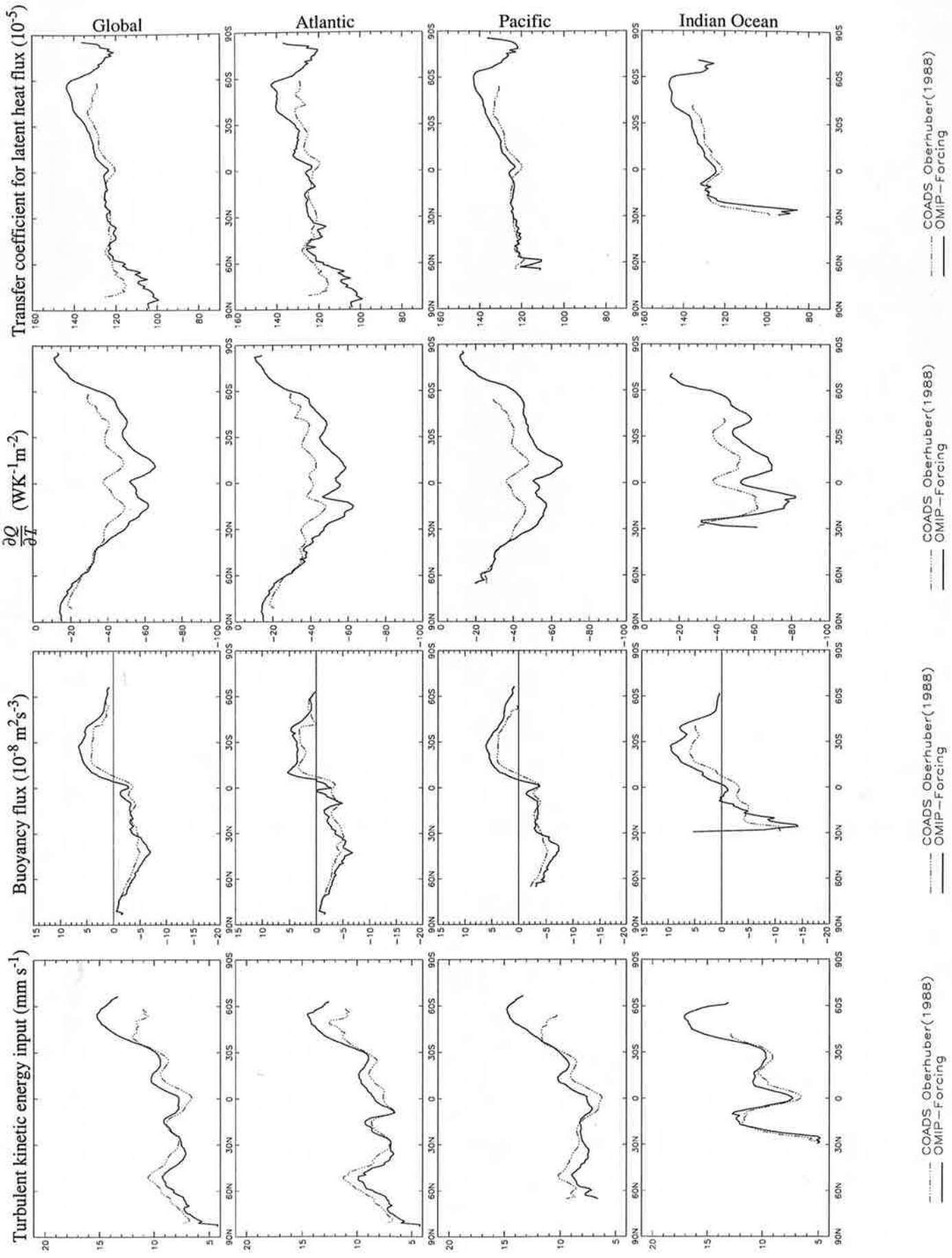

Fig.29.9 Zonal averages - part III September

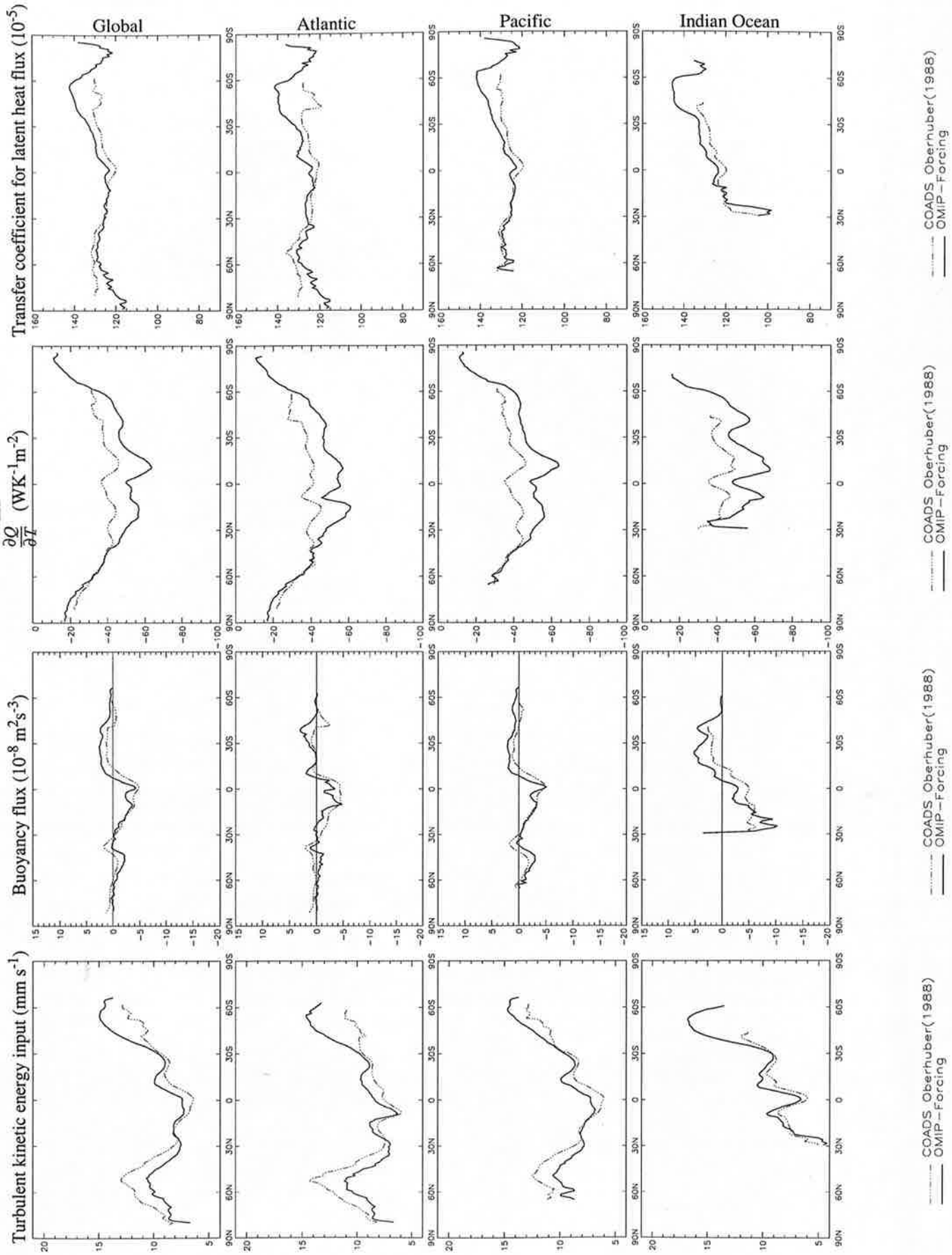

Fig.29.10 Zonal averages - part III October

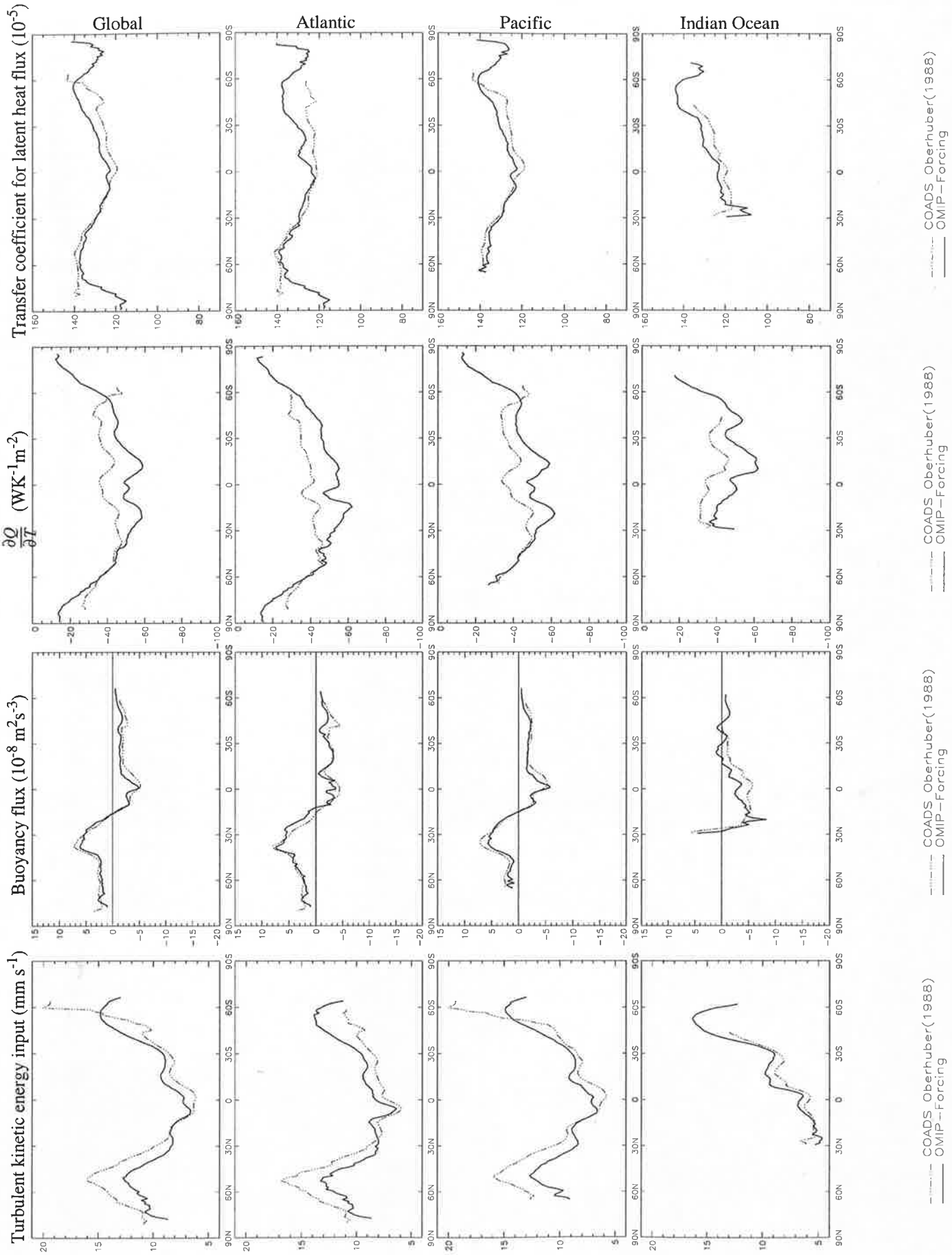

Fig.29.11 Zonal averages - part III November

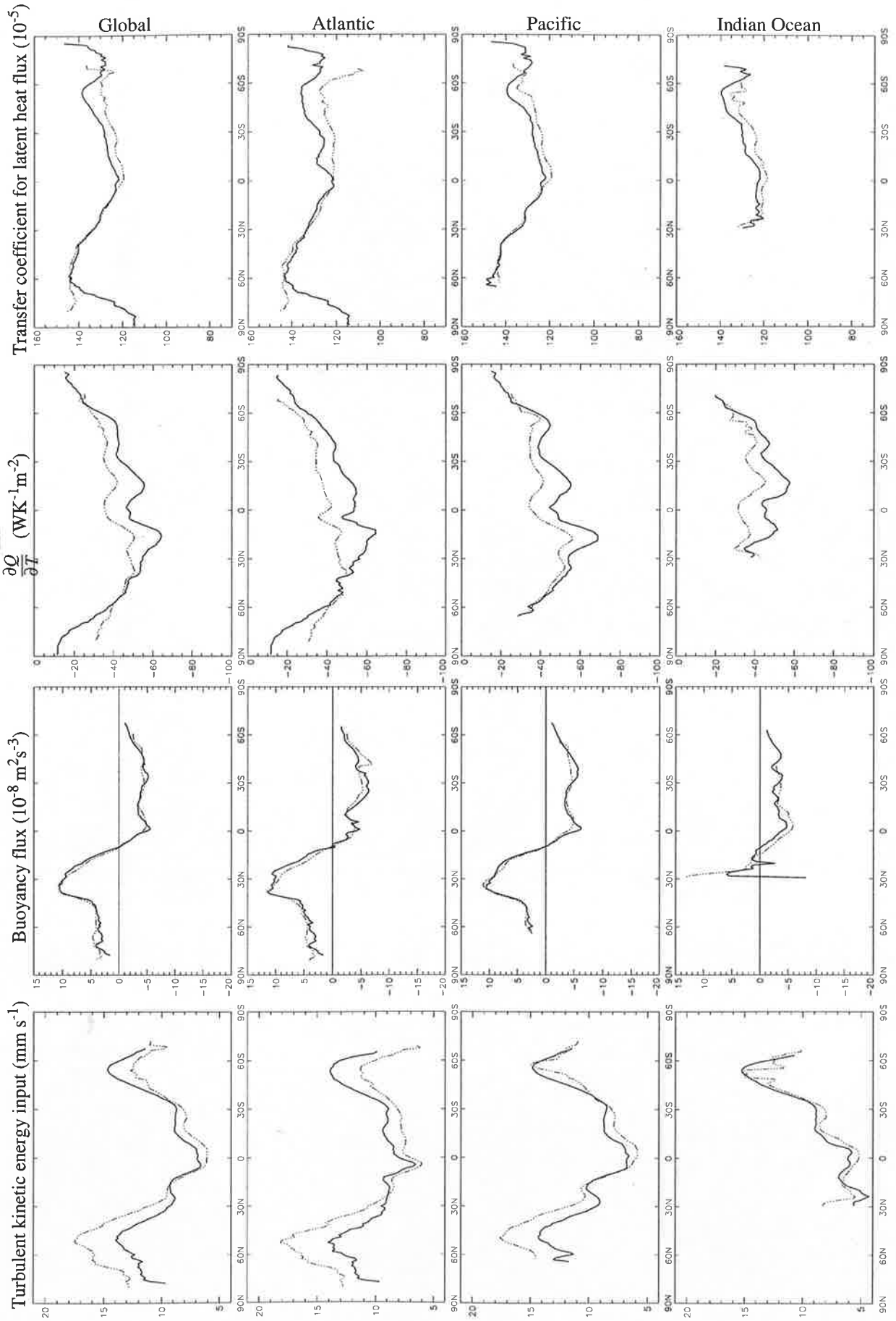

Fig.29.12 Zonal averages - part III December

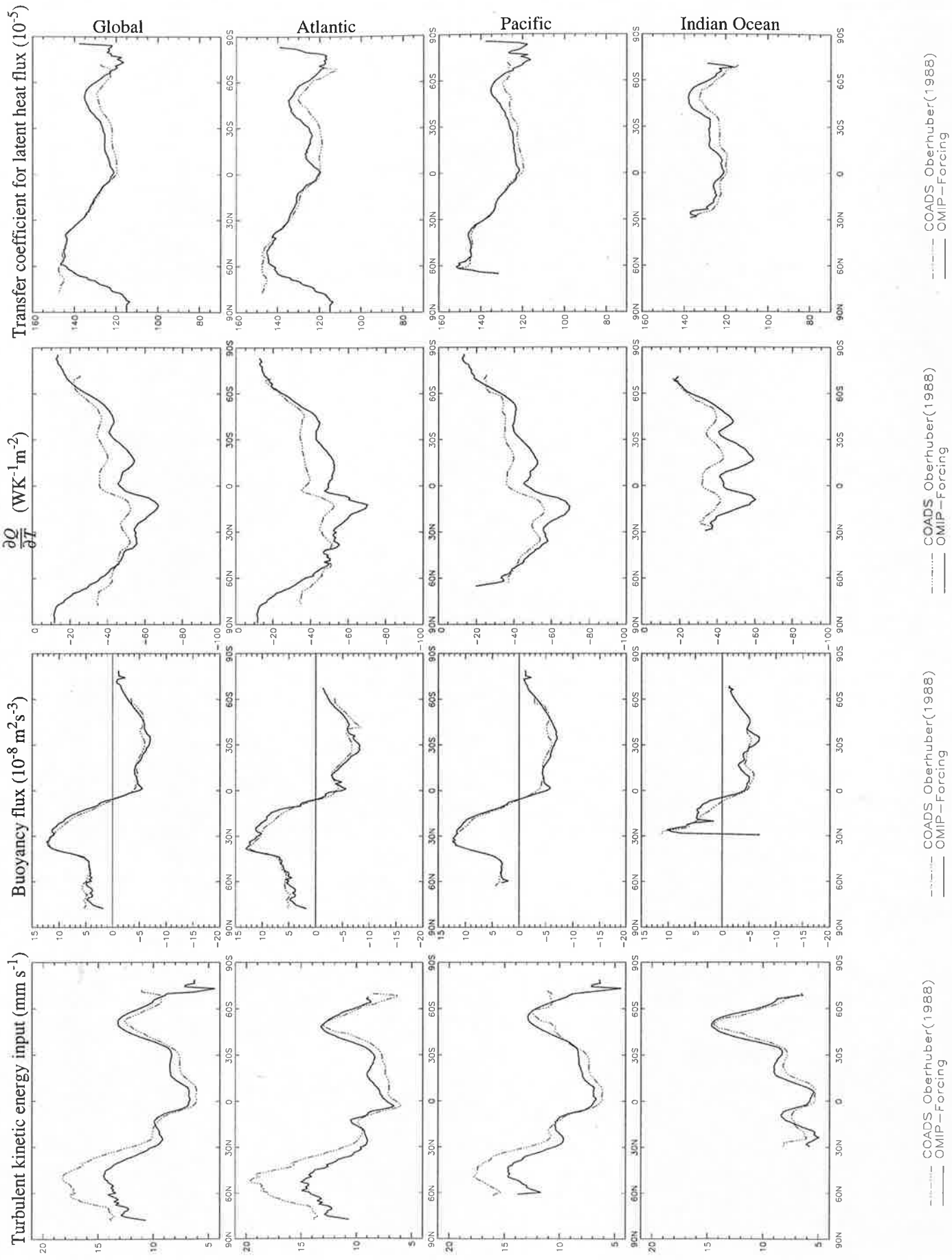

Fig.29.13 Zonal averages - part III Annual Mean

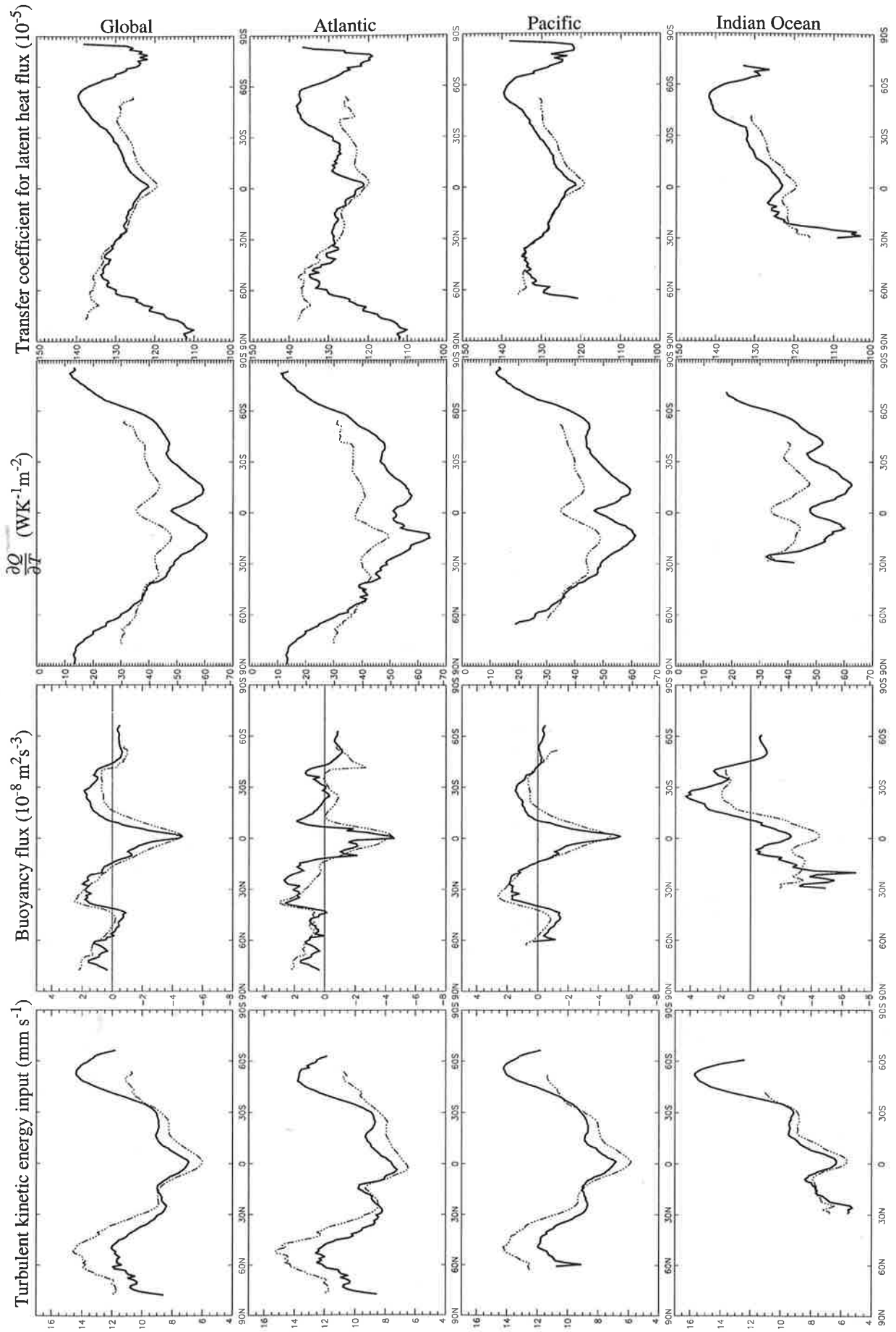

Fig.30.1 Oceanic averages - part I DJF

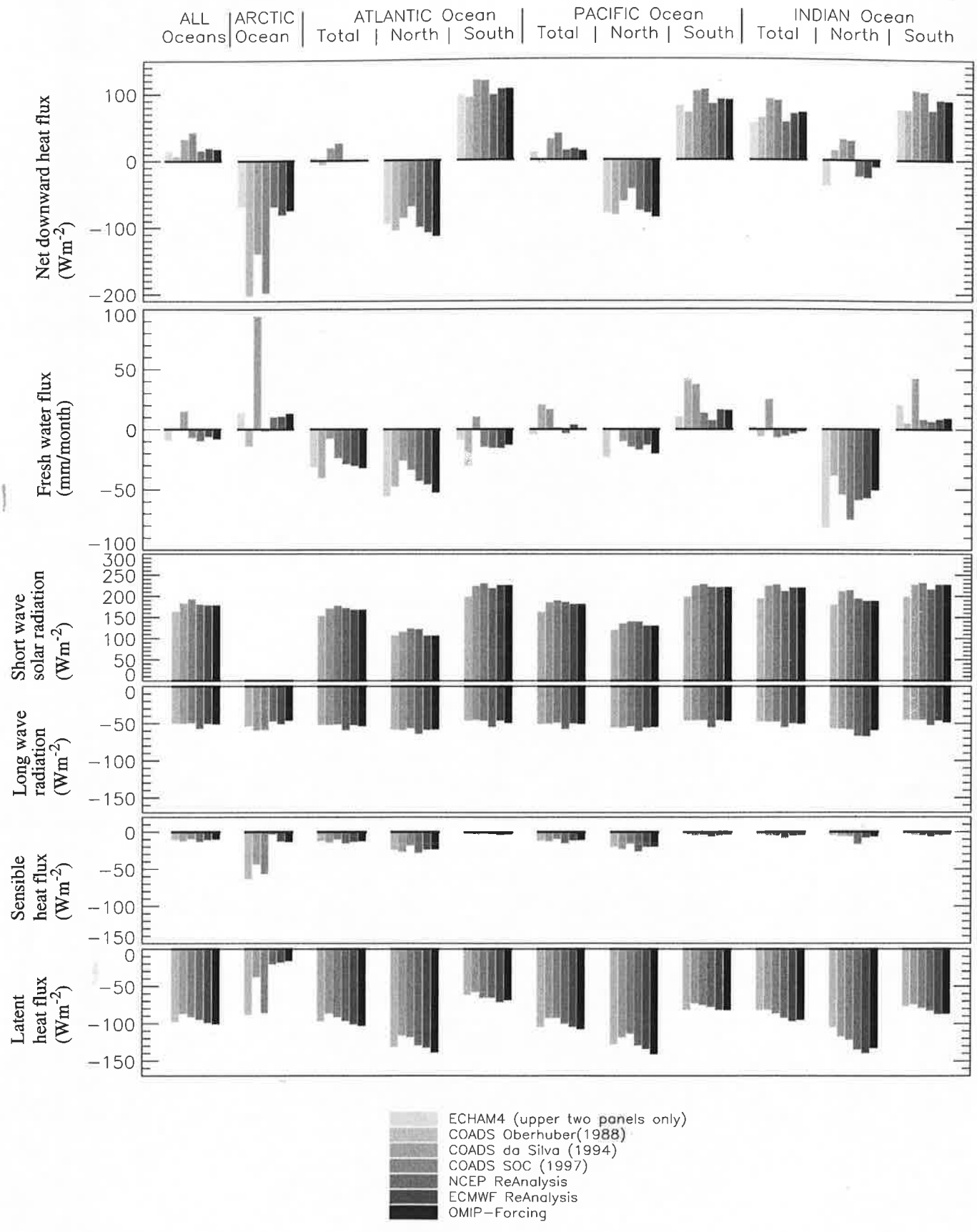

Fig.30.2 Oceanic averages - part I MAM

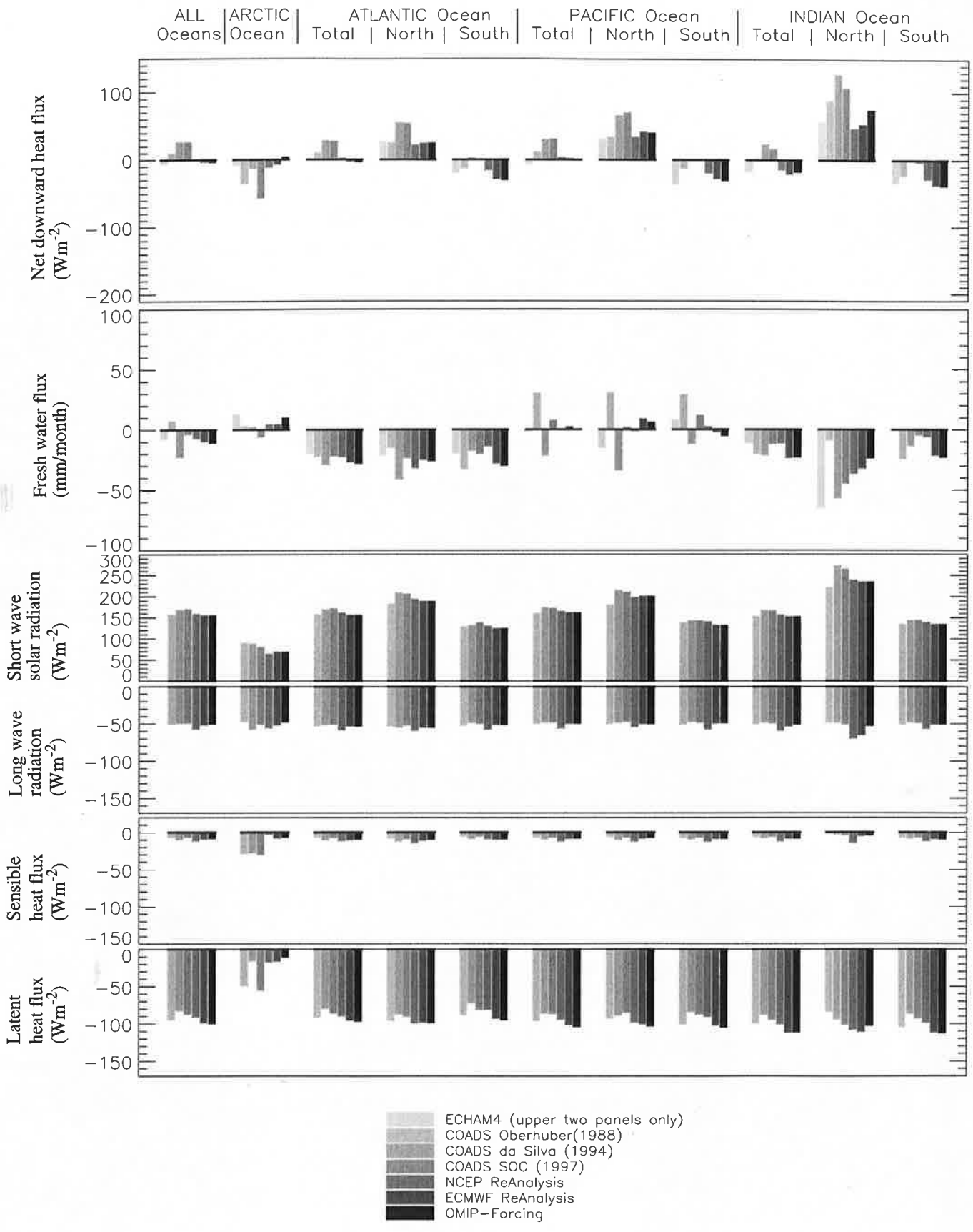

Fig.30.3 Oceanic averages - part I JJA

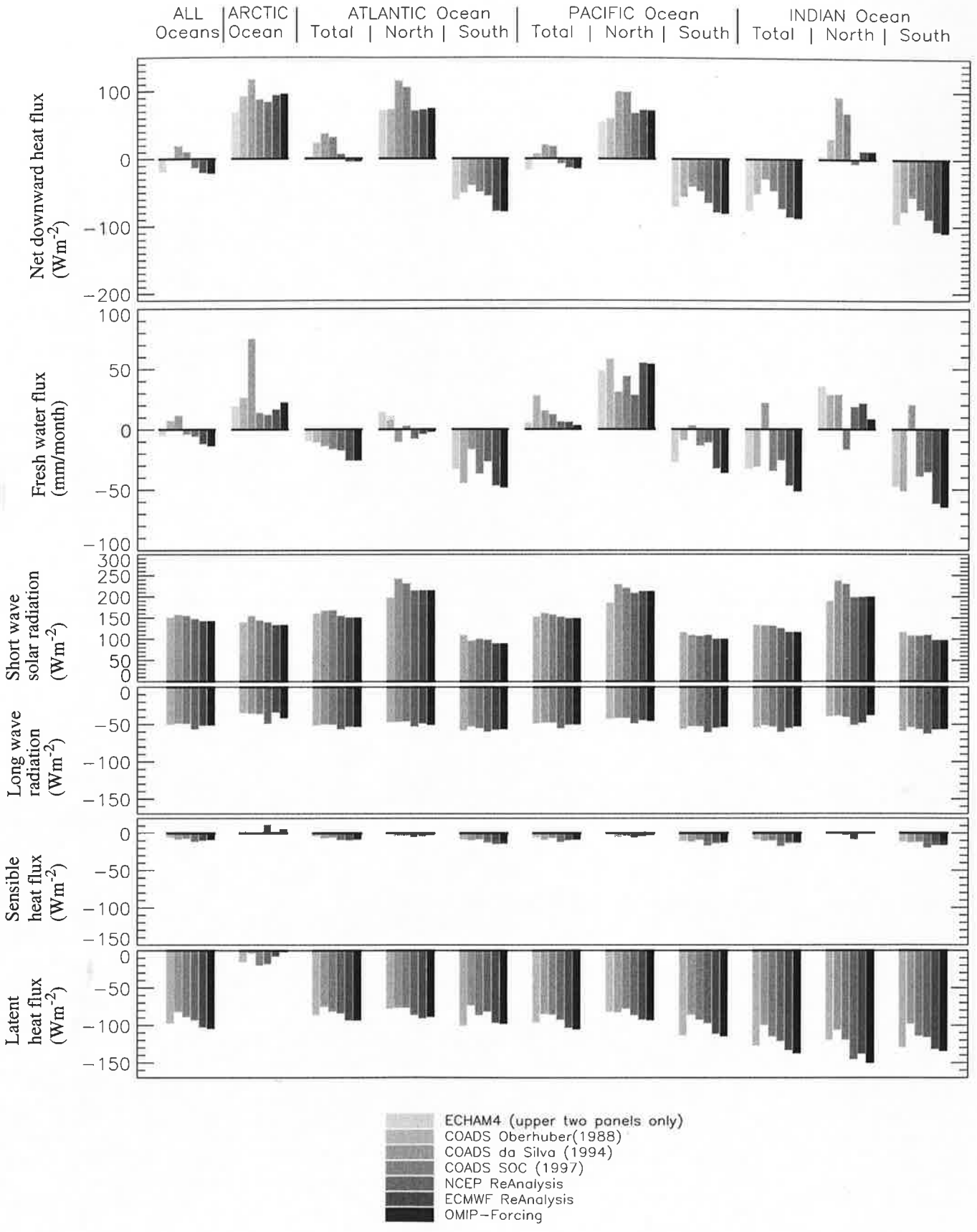

Fig.30.4 Oceanic averages - part I SON

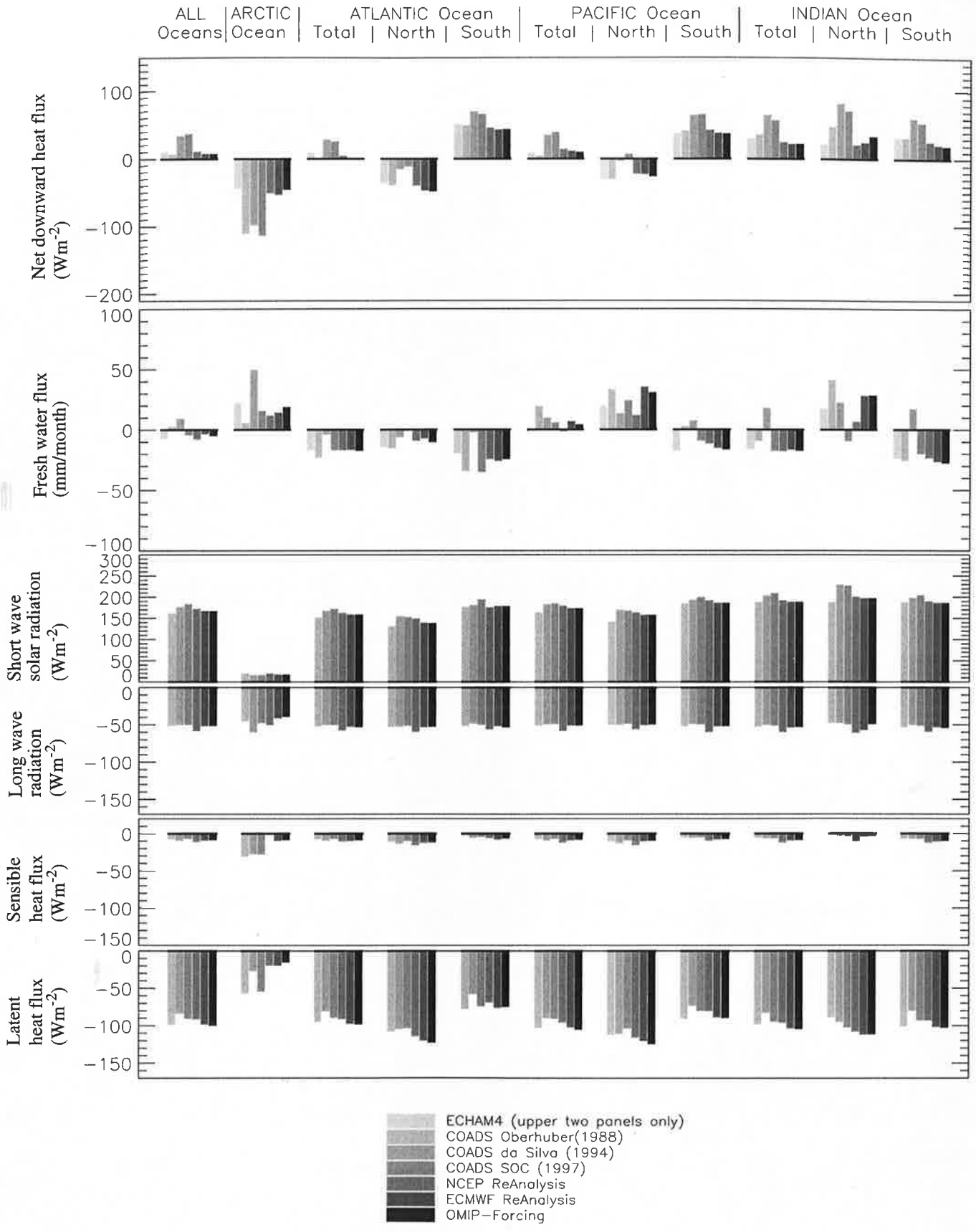

Fig.30.5 Oceanic averages - part I Annual Mean

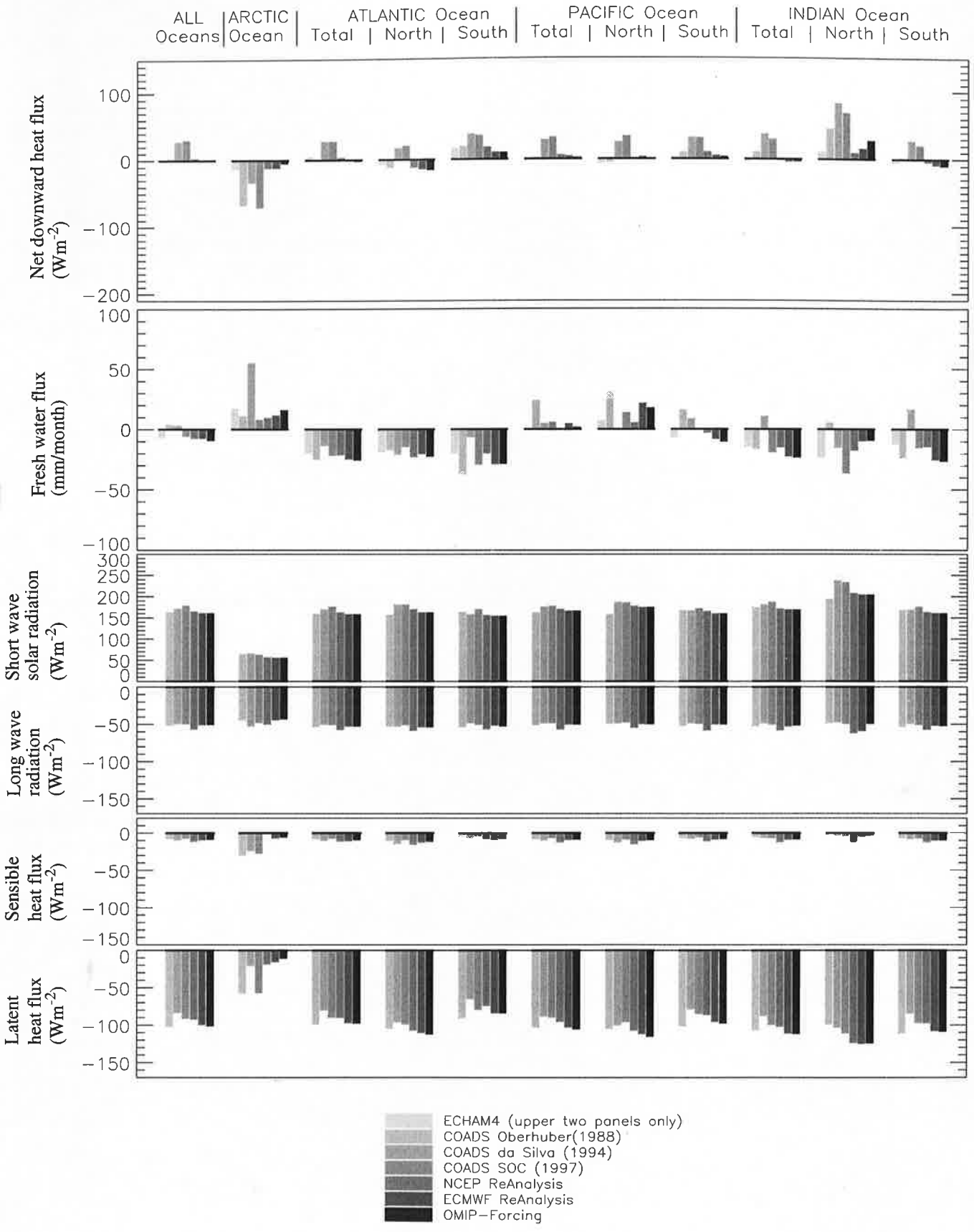

Fig.31.1 Oceanic averages - part II DJF

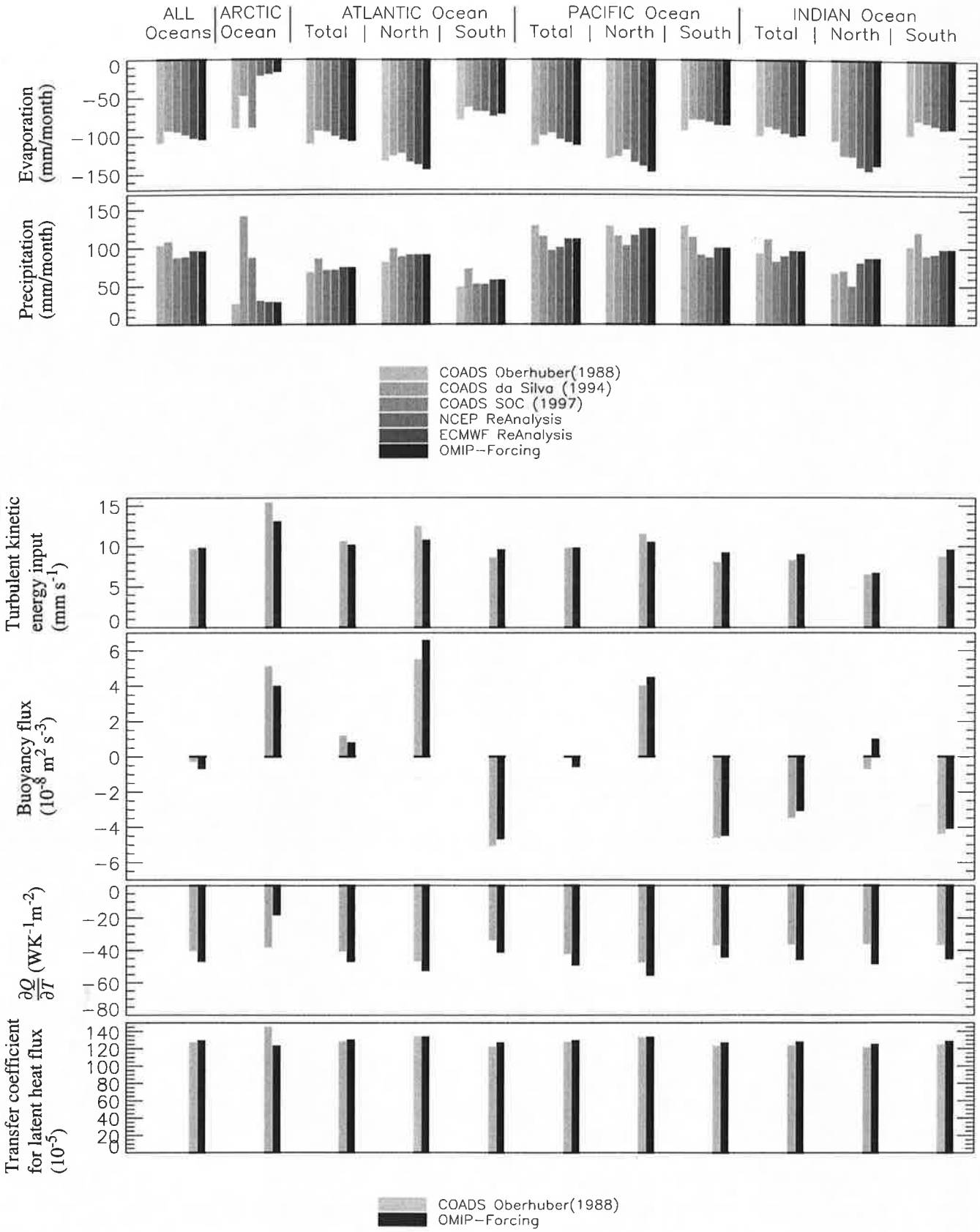

Fig.31.2 Oceanic averages - part II MAM

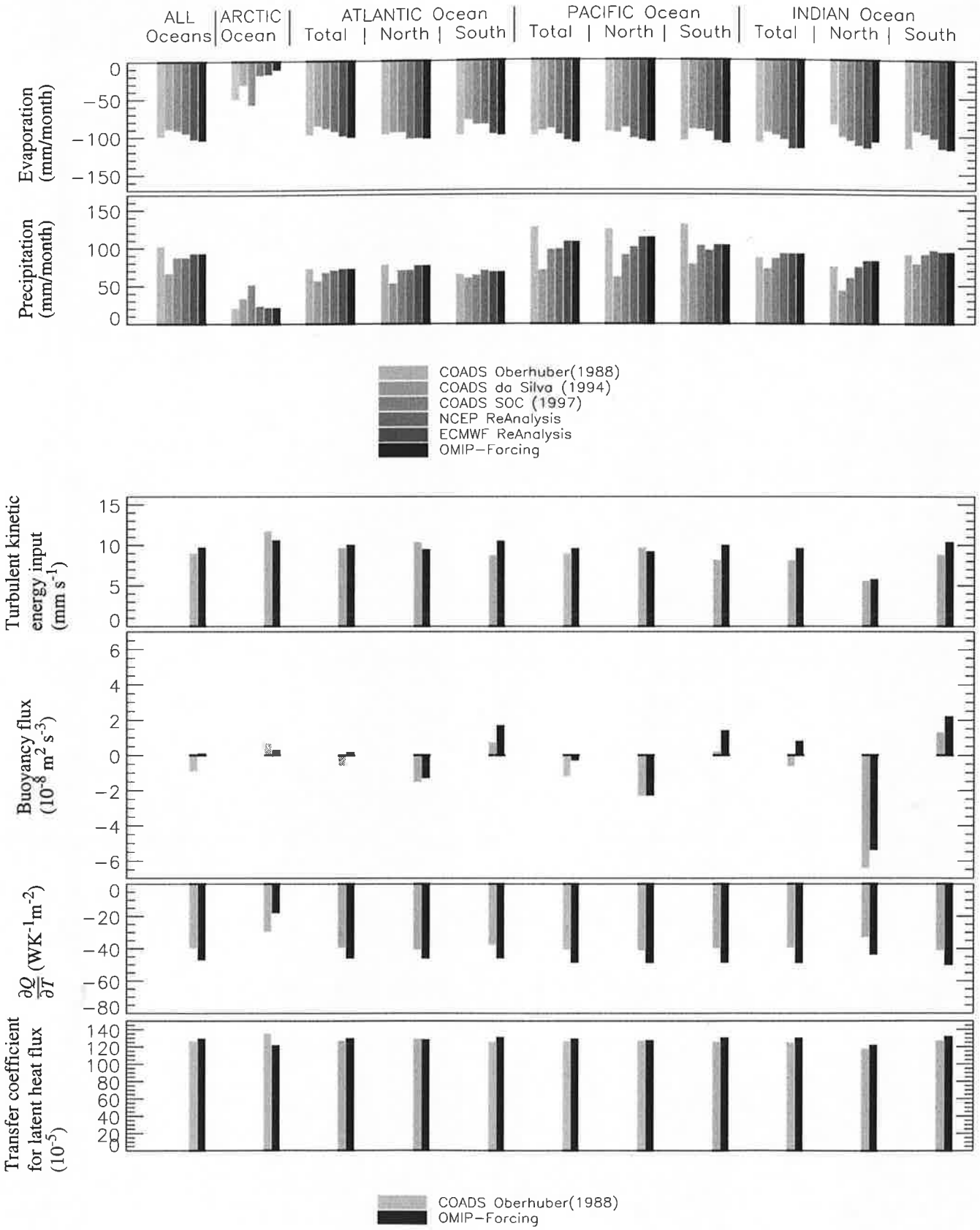

Fig.31.3 Oceanic averages - part II JJA

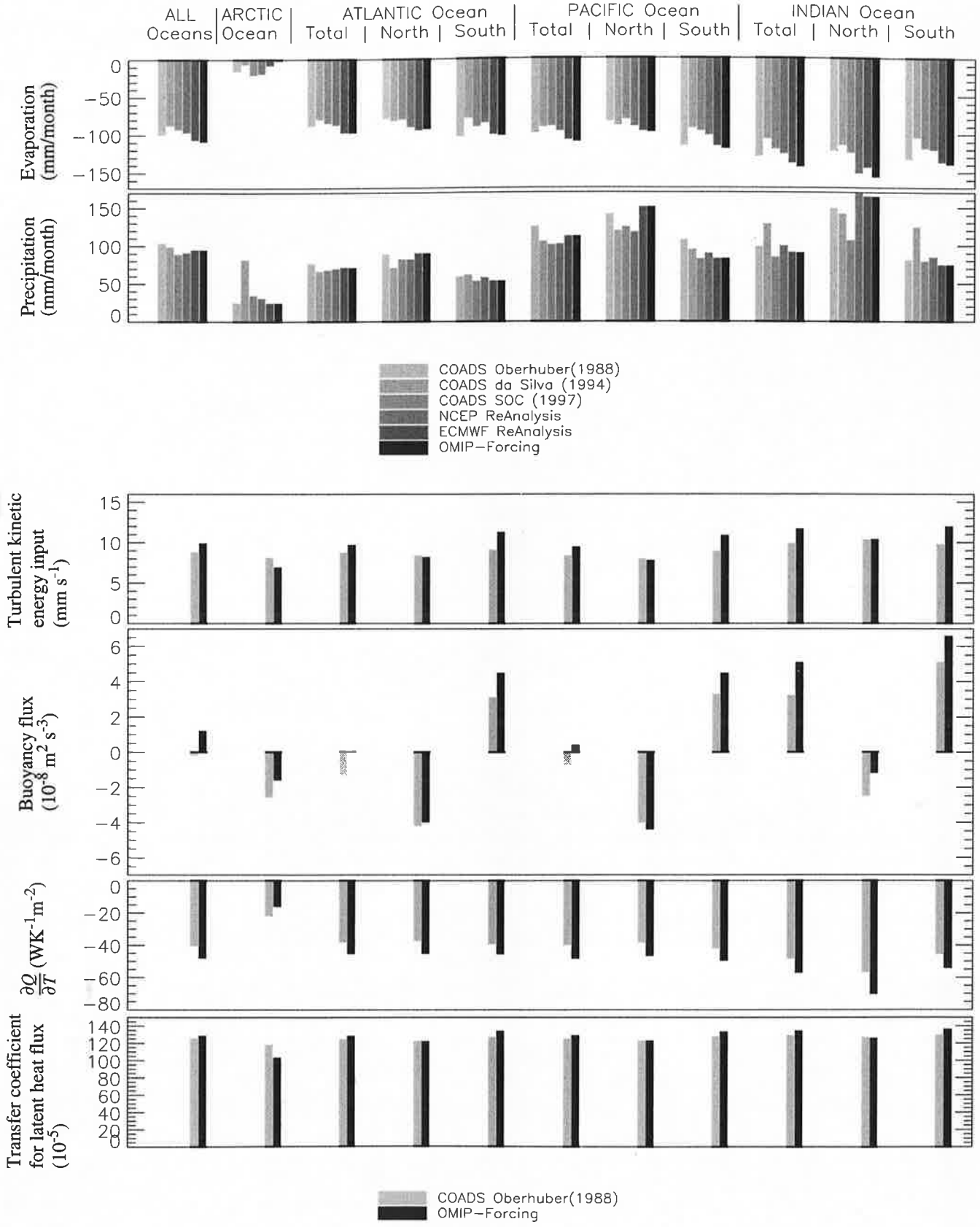

Fig.31.4 Oceanic averages - part II SON

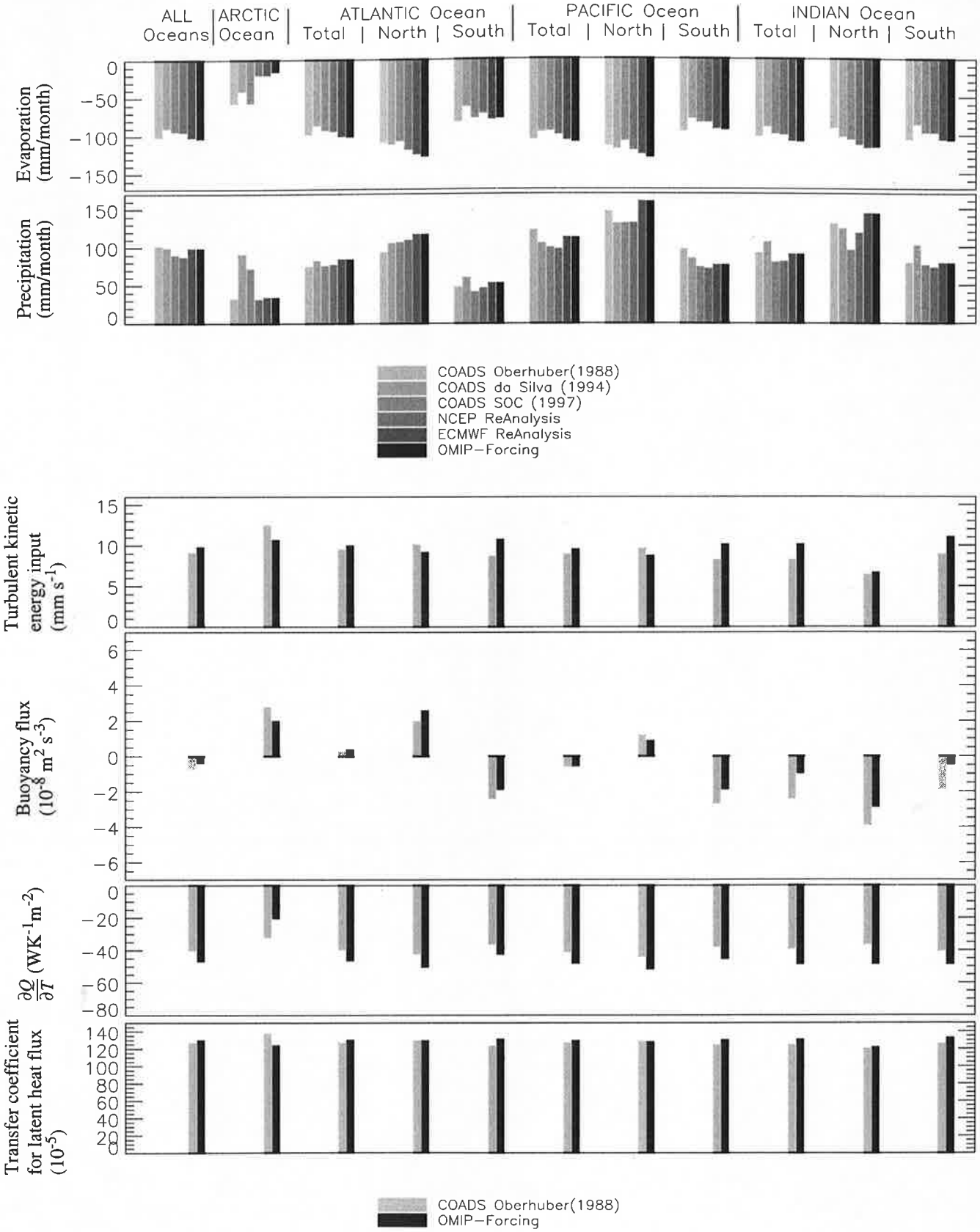

Fig.31.5 Oceanic averages - part II Annual Mean

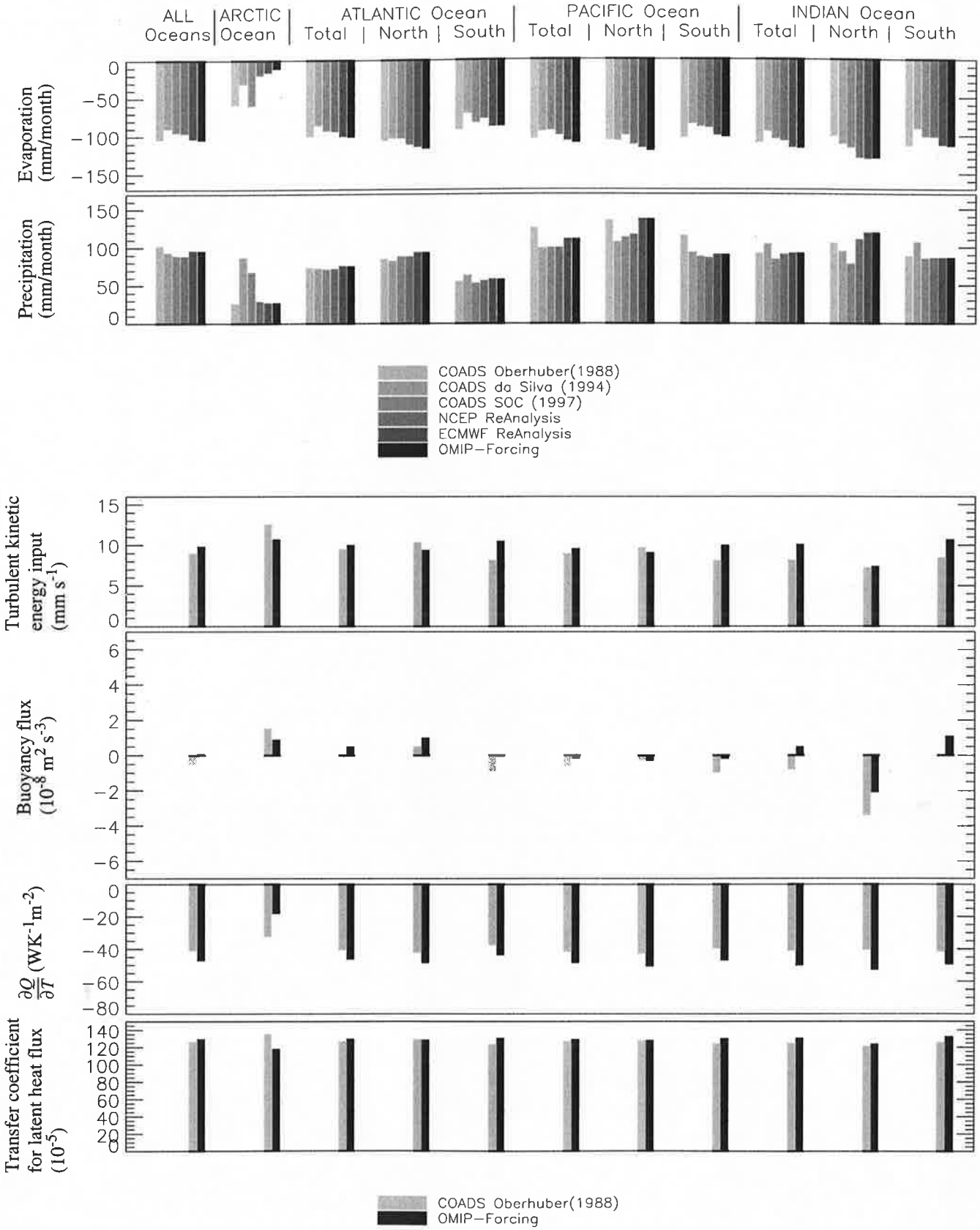

Fig.32 Flux extrema in the Atlantic Ocean

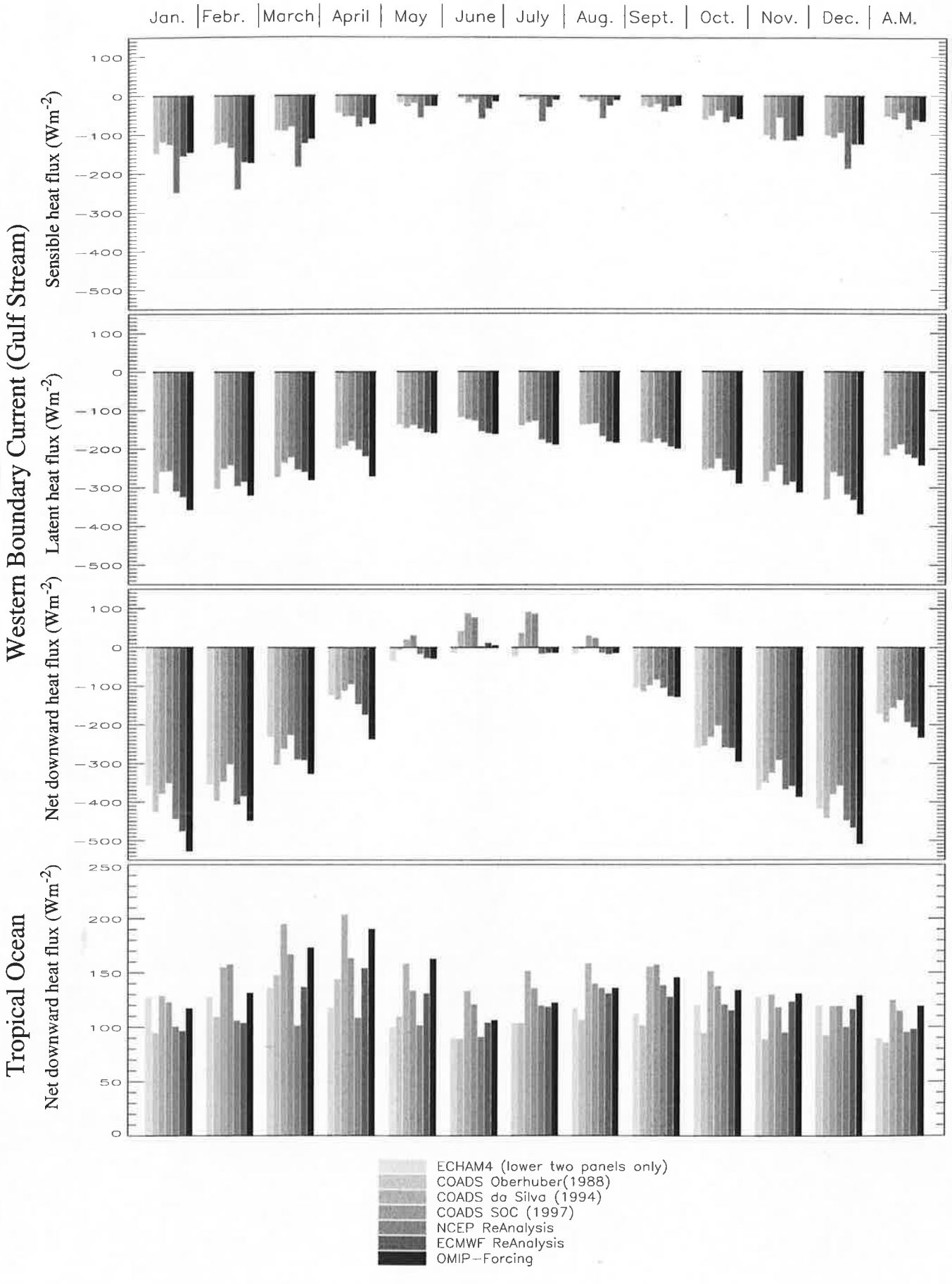

Fig.33 Flux extrema in the Pacific Ocean

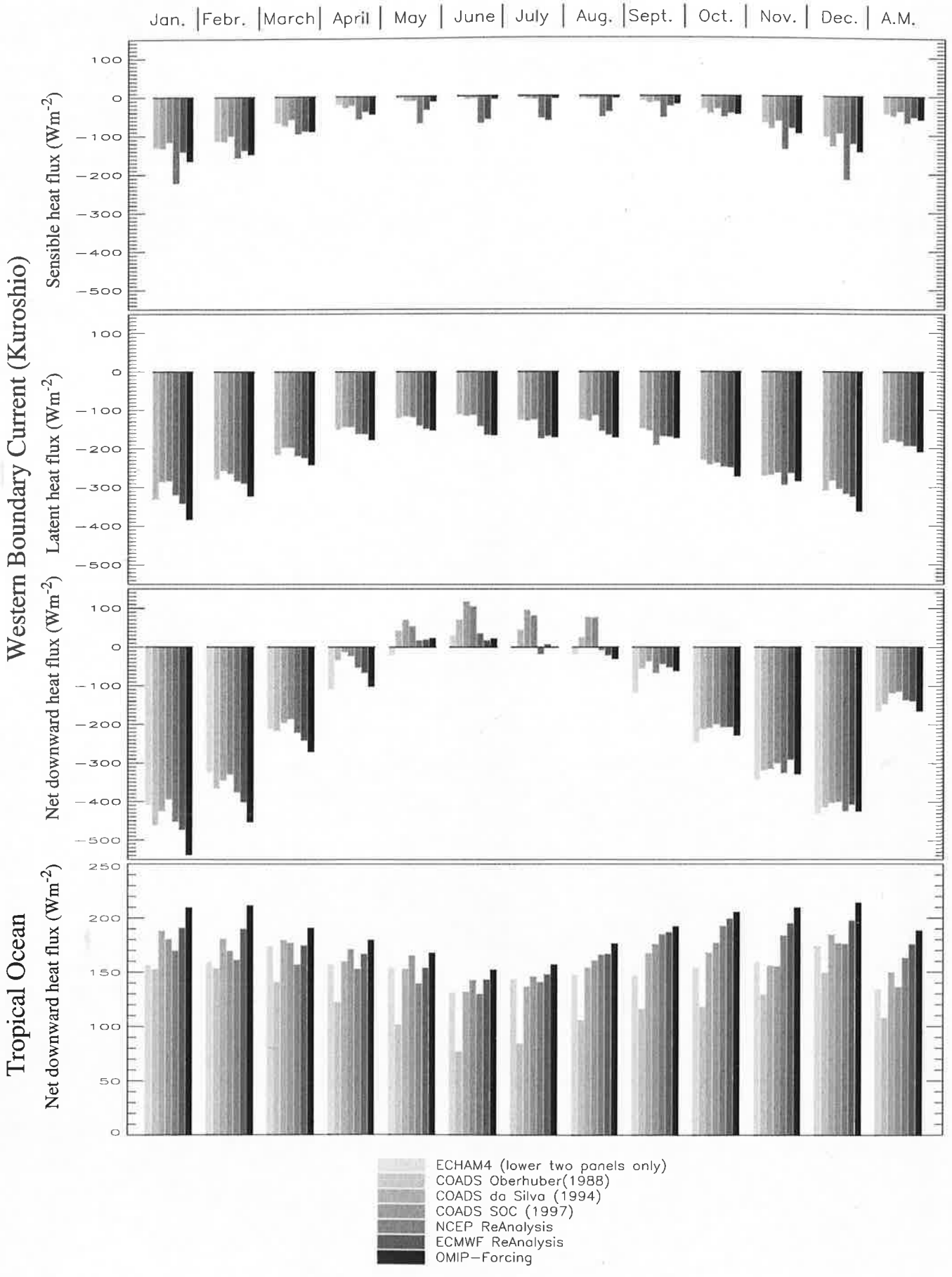

Fig.34 All seven climatologies Annual Mean

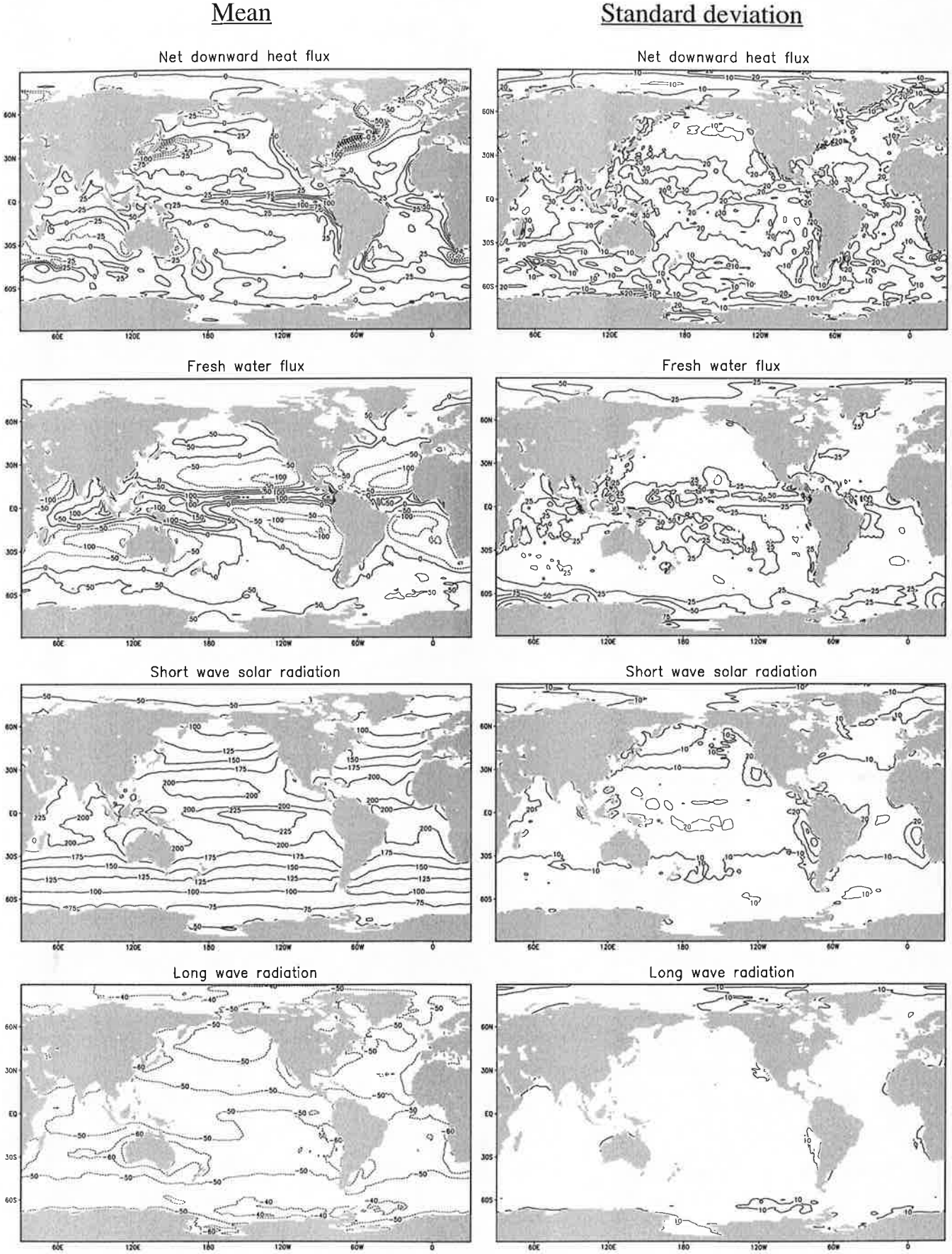

Fig.35 All seven climatologies Annual Mean